THE UNIVERSITY OF SHEFFIELD
Department of Mechanical Engineering

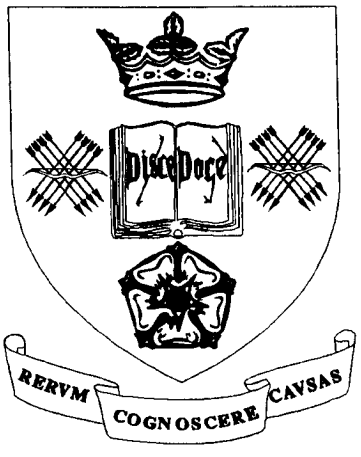

THE AERODYNAMIC PROPERTIES OF TENNIS BALLS

STEPHEN GEORGE CHADWICK

Submitted for the Degree
of
Doctor of Philosophy

November 2003

THE UNIVERSITY OF SHEFFIELD

Department of Mechanical Engineering

THE AERODYNAMIC PROPERTIES OF TENNIS BALLS

STEPHEN GEORGE CHADWICK

Submitted for the Degree of Doctor of Philosophy

November 2003

Several experimental procedures were developed to enhance the understanding of the aerodynamic properties of tennis balls. Four test methods were tried as quantitative assessments of the aerodynamic forces that act on tennis balls, whilst an additional two methods were introduced for qualitative purposes. A computational trajectory model was developed to predict the effect of any modifications to tennis balls proposed in the study.

The test methods adopted utilised two different wind tunnels, projection devices, dropper devices, aerodynamic load cells and motion analysis techniques using high-speed digital cameras. Several different tennis balls were tested: some had the nap modified to investigate changes in aerodynamic forces that may occur during play, others were oversized to investigate the options available for slowing the game down.

C_D and C_L profiles were obtained for a normal sized ball with unmodified nap and then used to develop a set of equations that enable the C_D and C_L of a tennis ball to be calculated at any speed and spin rate. When used in a trajectory model, a 6.5% larger ball was shown to decelerate 5% faster than a normal sized ball when projected with the same initial elevation angle, speed and spin rate. This results in the larger ball landing 1.5 metres shorter and taking more than 19ms longer to arrive at the receiver.

Initial testing showed that the C_D of all tennis balls with unmodified naps was similar and remained constant at around 0.53 up to a wind speed of around $63ms^{-1}$. The nap of the tennis ball was modified to represent early wear characteristics (fluffed) and extensive wear characteristics (shaved). It was found that the C_D of a ball with a fluffed nap is higher than that of a ball with an unmodified nap, which in turn is greater than the C_D of a ball with a shaved nap. The C_D of a ball almost twice the size of a normal tennis ball was found to be independent of Reynolds number up to $5x10^5$, which is clear evidence that the boundary layer around a tennis ball turns turbulent at a low Reynolds number. The ball with the shaved nap was shown to be similar to a classic rough ball however, with boundary layer transition occurring at a low Reynolds number.

The flow around a tennis ball was assessed using pressure profiles and smoke particles, and the separation of flow for all balls was shown to be near the poles. Pressure profile testing provided clear separation details, and showed how the pressure around the ball differs for subcritical and postcritical Reynolds number regimes. Flow through and over the fibres causes the elevated C_D over and above that associated with separation at the apex of a sphere.

Keywords: tennis ball, aerodynamics, flow visualisation, drag, lift, wind tunnel

ACKNOWLEDGEMENTS

I would like to thank Dr Steve Haake, who has been a continual source of advice and guidance throughout this study. I am grateful to Dr Alison Cooke in her role as a supplementary supervisor, and for enabling the continuation of aerodynamic studies at Cambridge University Engineering Department (CUED) when the facilities at Sheffield were decommissioned.

I would also like to thank Andrew Coe and the technical commission of the International Tennis Federation for the funding of this project.

I am grateful to Terry Senior and Richard Kay at the University of Sheffield and Bunny Noon and John Clark from CUED, for their assistance in the design and building of much of the experimental apparatus.

Many thanks go to Richard Dignall, Nicholas Bagshaw and Christina Aguilez for their assistance during testing and image analysis. Mention should also be made of Simon Goodwill, Matt Carré and all the members of the Sports Engineering Research Group, University of Sheffield, who have contributed to this study through informal discussion and the exchange of ideas.

Finally, completion of this PhD would not have been possible without the support of my wonderful wife, Kim. Submission of this thesis signals the start of our married life with weekends together.

CONTENTS

NOMENCLATURE

A	Projected area of a tennis ball (m^2)
a_x/ $\ddot{x}$	Acceleration of the ball in the horizontal direction (ms^{-2})
a_y/ $\ddot{y}$	Acceleration of the ball in the vertical direction (ms^{-2})
C_D	Coefficient of drag
C_L	Coefficient of lift
C_P	Coefficient of pressure
d	Projected diameter of a tennis ball (m)
d_s	Sphere diameter at the base of the fibres (m)
F_D	Drag force (N)
F_L	Lift force (N)
F_W	Force in the wire acting at θ^o to the horizontal (N)
g	Acceleration due to gravity (ms^{-2})
h_w	Vertical co-ordinate of the height of the wheel (m)
h_s	Vertical co-ordinate of the height of the sting (m)
k	Surface roughness height (m)
m	Mass of the ball (kg)
m_{eff}	Effective mass for a ball submerged in a viscous fluid (kg)
N	Rotational speed (rpm)
ω	Equatorial rotational velocity at edge of ball, $\frac{\pi Nd}{60}$ (ms^{-1})
P_{atm}	Atmospheric pressure (MPa)
p_1	Static pressure (MPa)
p_0	Stagnation pressure (MPa)
P_i	Air pressure at the entry to the contraction of the wind tunnel (MPa)
P_{ws}	Air pressure in the working section of the wind tunnel (MPa)
θ_s	Angle between front stagnation point and the separation location (°)

R^2	Pearson Correlation Coefficient
Re	Reynolds number
ρ	Density of air (kg/m^3)
μ	Dynamic viscosity of air (kg/m.s)
Re_{crit}	Critical Reynolds number (the point after which the flow is supercritical)
RN	Critical Reynolds number for a smooth ball in free air
T	Total time taken for a complete trajectory (s)
ΔVR	Difference in voltage reading (VR_W-VR_I) (Volts)
VR_W	Voltage reading at a known wind speed (Volts)
VR_I	Voltage reading with no wind applied (Volts)
V_X/ $\dot{x}$	Horizontal velocity component (ms^{-1})
V_{Xi}	Initial horizontal velocity component (ms^{-1})
V_Y/ $\dot{y}$	Vertical velocity component (ms^{-1})
V_{Yi}	Initial vertical velocity component (ms^{-1})
ΔV_X	Small change horizontal velocity in time Δt (ms^{-1})
ΔV_Y	Small change vertical velocity in time Δt (ms^{-1})
V_R	Resultant velocity (ms^{-1})
V_W	Wind velocity component (ms^{-1})
V_i	Initial velocity of airflow, at entry to contraction of the wind tunnel (ms^{-1})
V_{WS}	Velocity of airflow in the working section of the wind tunnel (ms^{-1})
v_{term}	Terminal velocity (ms^{-1})
Δt	Small change in time whilst velocity changes by ΔV_X and ΔV_Y (s)
x_w	Horizontal co-ordinate of the back of the wheel (m)
x_s	Horizontal co-ordinate of the front of the sting (m)
Δl	Difference in horizontal co-ordinates x_2-x_1 (m)
Δh	Difference in vertical co-ordinates y_2-y_1 (m)

1 INTRODUCTION

1.1 History of the game of tennis

The origins of tennis are shrouded in myth and speculation. Most historians would agree that the earliest recognisable form of tennis was a game restricted to the nobility of thirteenth century France called 'Le Jeu de Paume' (the game of the palm). The first mention of ball manufacture was in 1292 in France, where there were thirteen professionals (Paumiers) making balls in Paris. The requirements of these balls were that they were fairly hard, and round enough to bounce true on a stone surface. They were made of leather or cloth, and stuffed with wool or hair. Originally the ball was struck with the hand, covered in a leather glove to protect the hands of royalty. It was only a matter of time before the glove was supplemented with a wooden handle, thus creating the very first tennis racquet. Following this the game grew in popularity within France, with early French players shouting 'tenez' (i.e. play) at the start of a game. Before long it became known as 'Royal' or 'Real' Tennis, and by the beginning of the seventeenth century there were several hundred tennis courts in Paris.

The game was brought to England in the fourteenth century, introduced by the interrelationships between royal families. Indeed, Edward III built a court inside Windsor castle, and in 1414 Prince Dauphin of France sent some balls for the game to Henry V, a gift recorded by Shakespeare:

> *'When we have match'd our rackets to these balls, We will, in France, by God's grace, play a set.....'*
>
> (King Henry V (1600), Act I Scene II)

Real tennis was played within the houses of the upper classes, and Victorian enthusiasts wanted to develop a game that could be played outside. The game evolved in time to be known as 'Court' tennis, and together with attributes of the games of rackets (squash) and badminton, Major Walter Clopton Wingfield patented a game called 'sphairistike' (play in Greek) in 1874. The new game used balls that were a compromise between the 'fluffiness' of the badminton shuttlecock and the hardness of court tennis and rackets balls.

In the 1850's Charles Goodyear invented the vulcanisation process that enabled rubber to be hardened and India rubber to be formed. The India rubber balls were softer than traditional balls and enabled the game to be played on grass without damaging it. Twenty years later India rubber was introduced into the manufacture of tennis balls and is seen as the change that popularised lawn tennis and brought it to the wider audience.

Unhappy with the soaring popularity of the new game, Marylebone Cricket Club, supported by the All England Croquet Club, took control of the game in 1875 before it could threaten cricket's pre-eminence. New playing rules were required in order to satisfy patent laws, these changed the scoring, lowered the height of the net and changed the configuration of the court surface. The All England Croquet Club had, as an experiment, laid out a tennis court in one corner of the club's property. The experiment proved to be incredibly successful, so much so that they decided to hold a tournament on its grounds in 1877. The first Wimbledon 'Championships' began on July 19 1877 with 22 men vying for the championship. This tournament allowed the new club, the All England Croquet Club and Lawn Tennis Club, to capture control of the game of 'lawn tennis'. The rules of the game and the size of the court have hardly changed in over 100 years since, and are now controlled by the International Tennis Federation (ITF) who publish the rules.

1.2 Background to the modern ball

The earliest tennis balls were made of leather stuffed with wool or hair, and were hard enough to cause injury. Early in the 18th century, the wool was made into 20mm strips and wrapped around a cork nucleus, string wrapped in several directions held the wool in place, and a stitched white cloth completed the ball. Slazenger became the suppliers of tennis balls at the Championships in 1902, introducing a hollow rubber core with a woollen hand stitched cloth (no two balls were alike). By 1909 the external stitching was replaced by understitching, a lengthy and highly skilled process done by hand. In 1924 Slazenger used a cement style resin to adhere the cloth to the core, and these balls were introduced to the Championships in 1929. Advancing production technology led to variations in internal pressure and improved consistency, even the thickness of the core walls became standardised in the 1950's. Since then the basic design has remained virtually unchanged with only minor changes to the surface, which has undergone several modifications to

improve its wear characteristics. In 1982 fluorescent yellow balls were developed for improved visibility.

1.3 Background to modern equipment

The very first tennis racquets consisted of a wooden handle attached to a leather paddle. Between the sixteenth and eighteenth centuries the design of the racquet developed to include sheep gut for strings and a long handle. The configuration of the real tennis racquets used today was developed in the mid eighteenth century, it has a lopsided head to scoop the ball out of the corners and off the wall.

Since the 1960's the influence of sports equipment and clothing manufacturers has had a dramatic effect on the game of tennis. The introduction of the first metallic racquet in 1967 heralded the dawn of a new era, leading to a dramatic increase in ball speed. Open tennis was launched in 1968 in the U.S., heralded as a modern professional sport. The perfection of the service technique and the emergence of professional players allowed service speeds to reach 149mph (Rusedski 1998). With service speeds so high the chances of a reasonable return of serve are lower. Long rallies and enthralling 'chess match' like exploration of tactics and court space are deemed to be a thing of the past. The modern game has developed into:

> *' ..... a trigger happy, bludgeoning of the Lareau by literally blasting him off the court into the crowd with almost every serve ..... the longest rally lasted 4 shots.'*
>
> (Serve and Volley magazine, September 1995)

1.4 Reason for study

Anecdotal evidence suggests that rallies are shorter today than they used to be, and have become dominated by the serve. Whilst this shows advances in the skill of the player and improvements in the design of the equipment, it results in less excitement for the spectator, and in some cases a sense of predictability about the outcome of the match. Although there is no specific data showing a reduction in shots per point, the common thinking is that the

speed of the game, and hence the dominance of the serve, can be measured by analysing the tie breaks. At Wimbledon, the percentage of sets ending in a tie break have risen from 16.5% to 19% since 1970 for the men's game (Haake *et al* 2000).

Whilst the number of visitors to the Championships has not been affected, the rest of the public appear to be literally turning off. It is important that the *game of tennis* is not placed in jeopardy by *tennis the sport.*

It would be naïve to suggest a return to the 'golden years' of enthralling rallies between Borg, McEnroe and Connors. It is not possible to return to the years of wooden racquets that provided these exciting matches, nor is it feasible to change the tennis court dimensions. It is therefore the aim of this project to fully understand the aerodynamic properties of tennis balls, and suggest methods by which the receiver has a greater chance of returning a service.

1.5 Aims and Objectives

The aims of this study are to gain an understanding of the aerodynamic properties of tennis balls through experimentation and theoretical modelling. The objectives of the study are as follows:

1. To develop a method to obtain the aerodynamic forces acting on a tennis ball.
2. To determine and understand any differences in aerodynamic properties between ball designs.
3. To define and use techniques to develop a qualitative understanding of the flow of air over and through the surface of tennis balls.
4. To develop a model to predict the behaviour of a tennis ball's flight through the air.

The following chapters describe a three year study examining the aerodynamic properties of tennis balls.

2 LITERATURE REVIEW

2.1 Introduction

The interest in sports research has grown significantly in recent years. It is apparent that particular sporting events or technological developments within a particular sport are the driving force behind the research, and can be observed by the number of publications released in a particular area of research over relatively short time periods. The flight of the golf ball has been of interest since 1845 when a 'scuffed' gutta-percha ball was discovered to fly further than a new smooth ball. The United States was engaged in a national debate on whether the curve of a baseball was an optical illusion, and in 1870 Freddy Goldsmith threw a baseball between three aligned vertical poles. Cricket research was prompted by the phenomenon of 'reverse swing' and was prolific in the 1980's. One of the first recorded observations regarding the aerodynamics of tennis balls was made by Sir Isaac Newton (Newton, 1672). However, research into the mechanics of the game of tennis is relatively recent.

2.2 Player Studies

It is important that any analytical testing is a true representation of that observed in play. Player studies are not abundant in tennis due to the vast variety of shots produced.

Cislunar Aerospace Incorporated performed a study to investigate the speed and spin imparted on a tennis ball by professionals at the U. S. Open in 2000 (http://wings.avkids.com/Tennis/index.html). This is the only analysis of professional players available, and although the results appear to be comprehensive, the measurement methods were not detailed. Whilst the methods for measuring speed of shots, and the approximations used, are well developed, it is understood that the measurement of spin on a ball is complex and requires detailed analysis. Data was generated using digital photography, presumably from a fixed position with a panning camera, positioned a significant distance from the ball. It is therefore not thought that the information available

for analysis was sufficient to be used as conclusive evidence, however it is useful as a guide to set experimental parameters for testing in this study.

It is important to note that this study showed that less than 1% of shots are struck with negligible spin, and most of this 1% were deemed to be missed hits. Anecdotal experience would suggest that the 'topspin lob' and 'back hand slice' are probably the two shots that impart the most spin on the ball. According to this study however, the highest spin rates are observed on the serve; a 2nd serve struck by Pete Sampras was found to have in excess of 5000rpm of spin on it, the single fastest spinning shot recorded. Many other players regularly generated 4000-5000rpm on the second serve. The spin on the groundstrokes often exceeded 3000rpm, and the vast majority of balls hit at the U. S. Open exceeded 1000rpm.

2.3 Aerodynamics

The aerodynamic properties of tennis balls are governed by conventional aerodynamic theories. The following sections will cover some classical theories and apply them to the flow over a tennis ball. No aerodynamic study is complete without an understanding of the role of the boundary layer.

2.3.1 Boundary layer theory

The air close to an object is gradually slowed from some local velocity to zero on the surface. Deceleration of the air is due to the viscosity of air, and the region in which this velocity change takes place is called the boundary layer. The boundary layer is normally very thin, but may sometimes be seen by the naked eye around large ships moving through the water. As the boundary layer is normally thin, the velocity gradient is very high, and the shear stresses are therefore important. The ideal gas laws cannot be used in analysis of the flow in the boundary layer, as viscosity is not negligible.

With increasing distance from the solid surface, the velocity of the fluid approaches that of the main stream. There is no sharp dividing line between the boundary layer and rest of the flow, with the velocity increasing asymptotically at the edge of the boundary layer. The

boundary layer thickness is commonly defined as the point where the boundary layer velocity reaches 99% of the velocity in the main stream.

There are two main flow classifications observed in aerodynamics; laminar and turbulent. A laminar flow moves with smooth tiers of air passing one over the other without significant exchange of fluid particles perpendicular to the flow direction. As the flow becomes turbulent, the particles flow chaotically throughout the layer and are continually replenished with turbulent mixing. Figure 2.1 shows some typical velocity profiles, it can be seen that a laminar boundary layer has negligible momentum near the wall and increases steadily with increasing Reynolds number, above the critical Reynolds number the turbulent boundary layer has higher momentum near the wall.

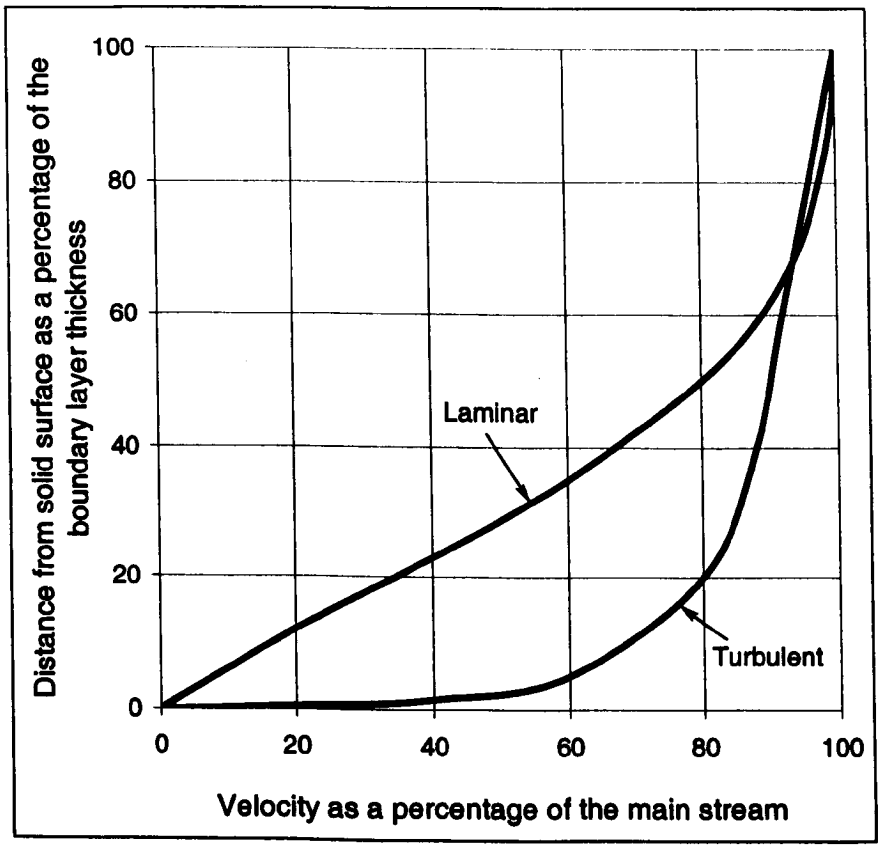

Figure 2.1 Typical velocity distributions in laminar and turbulent boundary layers.

Separation of the boundary layer is induced by the increasing pressure gradient over the rear surface of the ball. The increased momentum of the turbulent boundary layer gives it a greater ability to withstand adverse pressure gradients or roughness, hence it separates from the surface later than flow in a laminar boundary layer. Laminar boundary layers separate near the maximum diameter and therefore create a large wake with a large

pressure drag, the wake produced in a turbulent boundary layer is smaller and hence has a lower pressure drag component.

Much of the classical aerodynamics work concentrates on flow over flat plates but figure 2.2 shows the flow over a curved surface. The velocity is increasing around the surface from points A to B, where the pressure is at a minimum. The dropping pressure between A and B is 'favourable' for stable boundary layer development, and helps accelerate the flow. As the pressure gradient slows between B and C, the pressure acts to decelerate the flow in the boundary layer. The pressure begins to rise after point C, creating an adverse pressure gradient and a thickening of the boundary layer. As the velocity of the fluid reduces in the adverse pressure gradient, the flow starts to change direction, eventually separating at point S. Downstream of the separation point, the flow near the surface is decelerated further causing back flow.

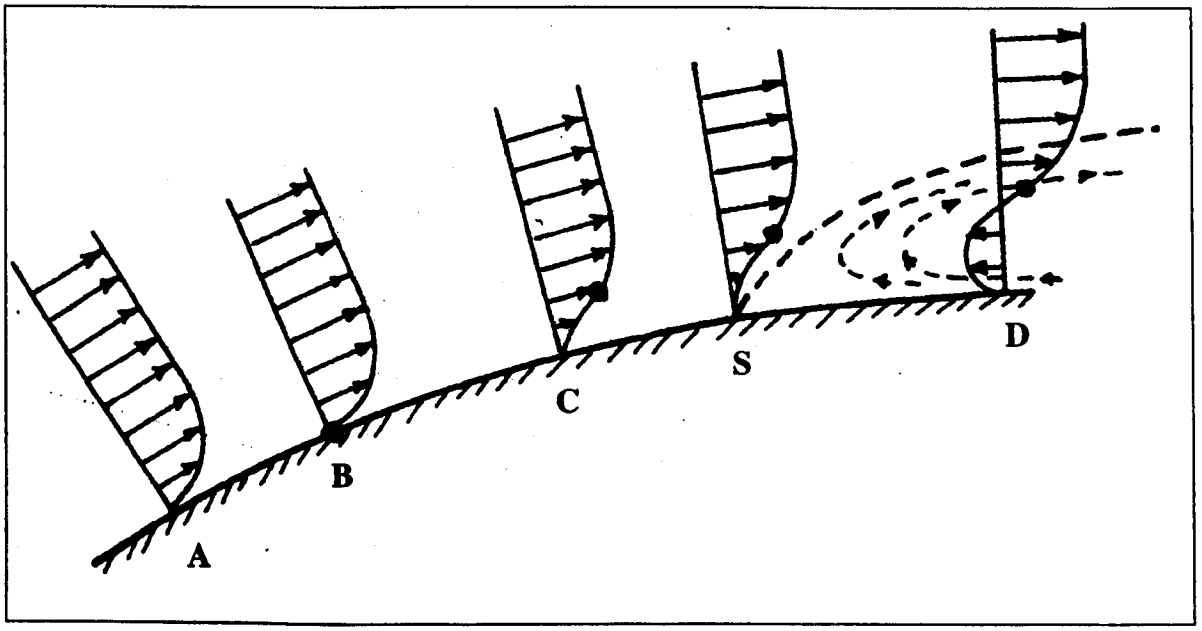

Figure 2.2 Velocity profile shown as it changes over a curved surface (derived from *Introduction to boundary layer theory, Persen L. N., 1972*).

Many classical theories suggest that flow will separate at the apex where the pressure is at a minimum. It is well understood however, that this is not the case and separation occurs on the forward face approximately 80° from the front stagnation point. In order to understand this phenomenon it is useful to investigate flow through a wind tunnel contraction.

Airflow is accelerated throughout the contraction suggesting a positive pressure gradient throughout, however separation can occur at both the entrance and exit. At the inlet to the contraction, the pressure near the walls is greater than that near the centreline due to a reduced radius of curvature of the streamlines (Bell and Mehta, 1988). In general, the boundary layer is less likely to separate in the contraction exit, however short contractions will induce excessive boundary layer growth.

The oncoming flow is turned rapidly over the surface of a sphere, and the relative curvature of the streamlines close to the surface are small compared with free flow. Boundary layer growth is rapid as the flow is rapidly accelerated over a short distance. Hence, the combined effect of the limited momentum near the surface, together with the adverse pressure gradient caused by curvature effects, leads to boundary layer separation on the forward face of a sphere.

2.3.2 Drag

It has been discussed that a boundary layer can be either laminar or turbulent. The Re at which transition from a laminar boundary layer occurs is dependent on the surface roughness of the ball and the quality of the airflow. Achenbach (1973) investigated how the transition point varies with increased surface roughness. The surface was roughened by adding glass spheres to the surface or abrading the surface. A roughness parameter, k/d_s, was used such that the C_D was determined as a function of the Re (where k was the height of the roughness elements and d_s was the original diameter of the sphere). Figure 2.3 is a reproduction of the results presented, it can be seen that transition begins on a smooth ball at a Re of approximately $3x10^5$, and the C_D drops to less than 20% of its original value.

As the roughness parameter is introduced and increased, the transition occurs at a lower Reynolds number, with the earliest transition occurring for the sphere with the maximum roughness tested ($k/d_s=1250x10^{-5}$). In addition, it can be seen that the magnitude of the drop also diminishes, reducing by 60% for the roughest surface. There is an element of recovery after the transition, however it is important to note that the post-critical C_D does not reach its original value.

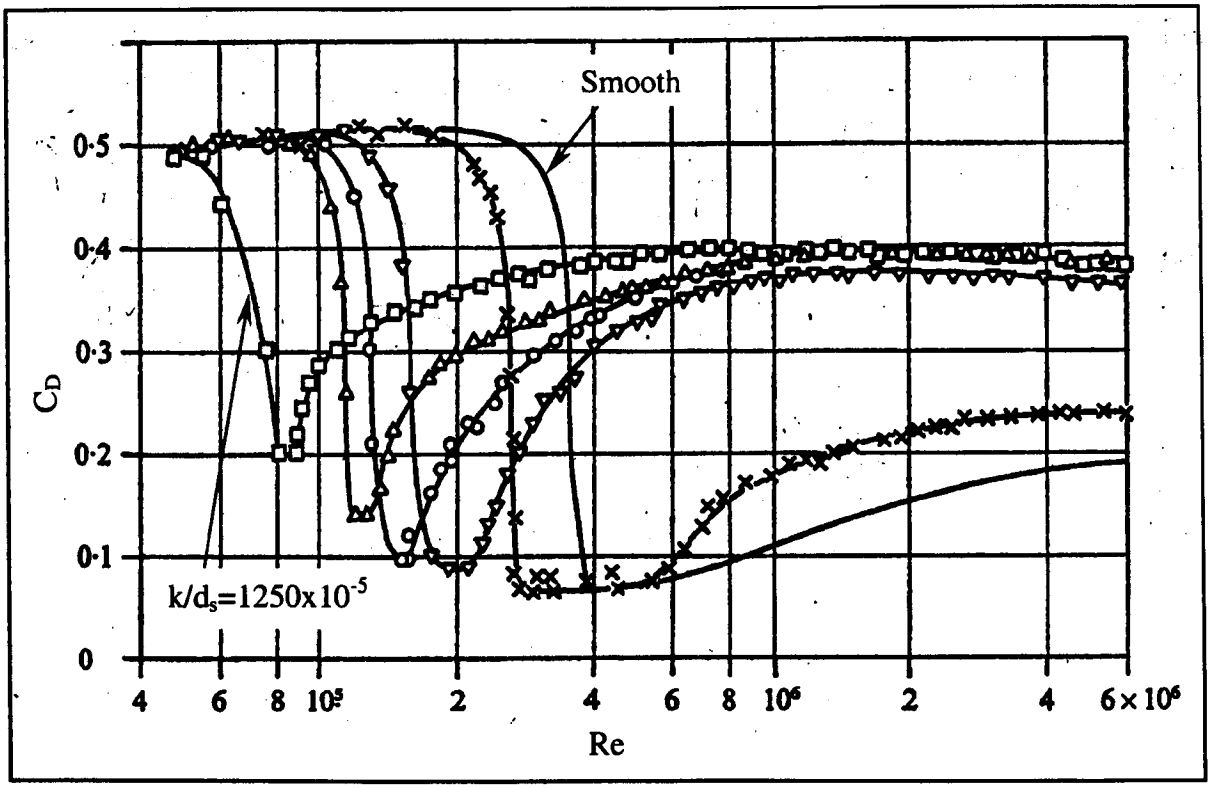

Figure 2.3 Chart to show how the C_D of different roughness spheres changes with respect to Re. (Reproduced from Achenbach, 1973)

The results obtained by Achenbach have been converted to compare the C_D at which transition occurs, and the associated drop in C_D that may be expected. The data is shown in figure 2.4 and it can be used to estimate Re_{crit} and corresponding drop in C_D at transition for a known roughness parameter. In order to consider rougher surfaces such as a tennis ball (should it be considered a classically rough surface), the data has been extrapolated. The additional extrapolated data is depicted by the dashed curve and is assumed to continue following the same trends.

Based on these assumptions, it can be seen that the minimum critical Reynolds number for a sphere appears to be limited to a little over $5x10^4$. The drop in C_D at this Re_{crit} is approximately 0.28, and based on a sphere with a subcritical C_D of 0.5, this will result in a C_D at Re_{crit} of 0.22. This process will be used in later sections to investigate the C_D of tennis balls with various surface roughness.

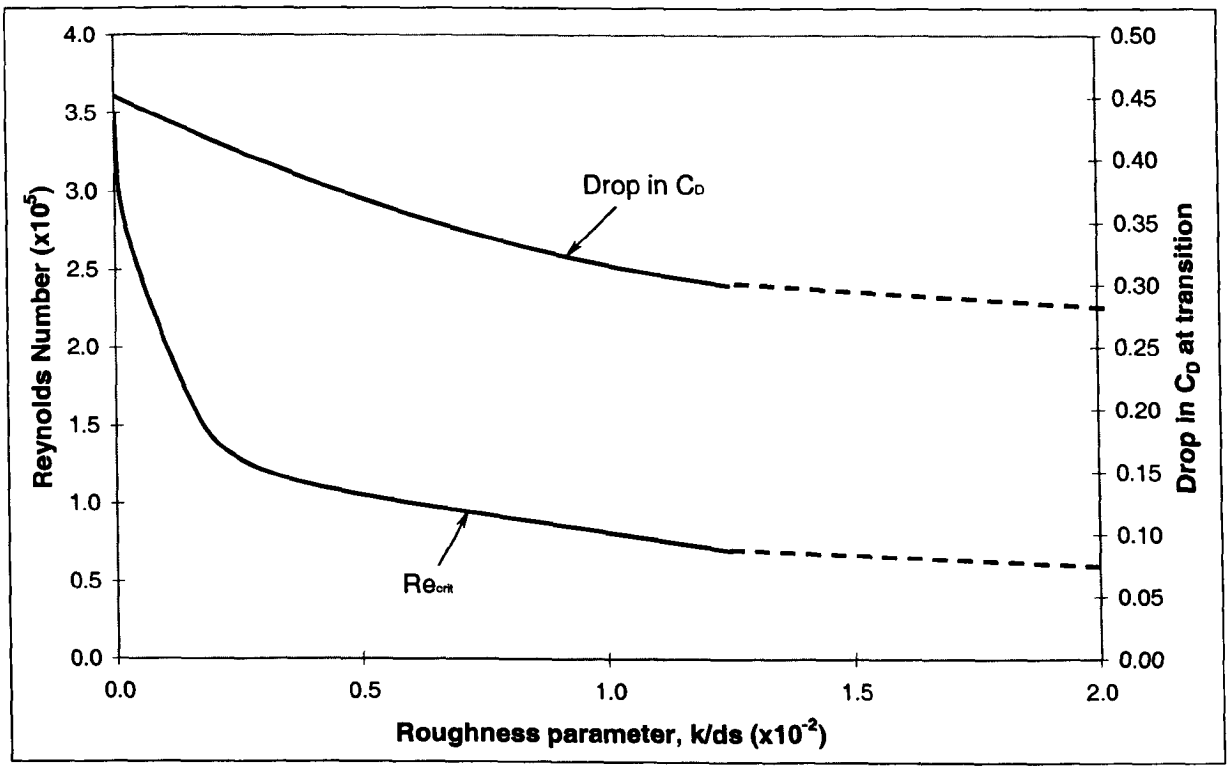

Figure 2.4 Achenbach results presented to show the critical Reynolds number and corresponding drop in C_D that may be expected for a known roughness parameter.

The shape of the C_D plot with increasing Re can be explained in four stages (Mehta & Pallis, 2001), as shown diagrammatically in figure 2.5:

1. For 'subcritical' flow conditions the boundary layer separates laminarly, and apart from very low values of Re (<3), the separation point is just upstream of the maximum diameter ($\theta_s \approx 80°$).
2. As Re increases towards the 'critical' flow regime, the separation point of the laminar boundary layer begins to move downstream as the momentum in the boundary layer increases. A separation bubble is established at the point where laminar separation occurs and transition occurs in the free-shear layer. The flow reattaches in a turbulent state that is better able to withstand the adverse pressure gradient over the rear surface of the ball and separation is delayed At Re_{crit}, the C_D is a minimum, and the separation point is at its most downstream location (140°).
3. In the 'supercritical' flow regime the transition creeps upstream and occurs in the attached boundary layer. C_D increases gradually as the transition and separation locations creep upstream with increasing Re.

4. In the 'transcritical' regime, the transition location eventually moves all the way upstream, very close to the front stagnation point, and the C_D again becomes constant. Since the transition location cannot move further upstream, C_D is independent of Re and the turbulent boundary layer development and separation is based purely on the sphere roughness.

Flow form	Flow characteristics	Separation condition
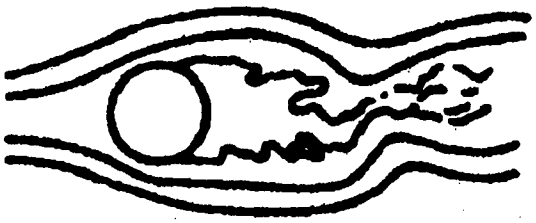	Laminar, with vortex street instabilities	Subcritical $\theta_s \approx 80°$
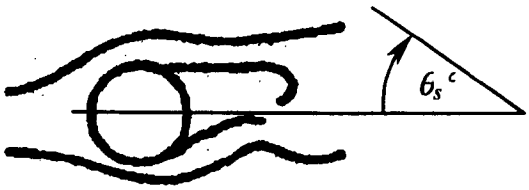	Laminar separation Turbulent reattachment Turbulent separation Turbulent wake	Critical $\theta_s \approx 140°$
	Turbulent separation	Supercritical-Transcritical $\theta_s \approx 115°$

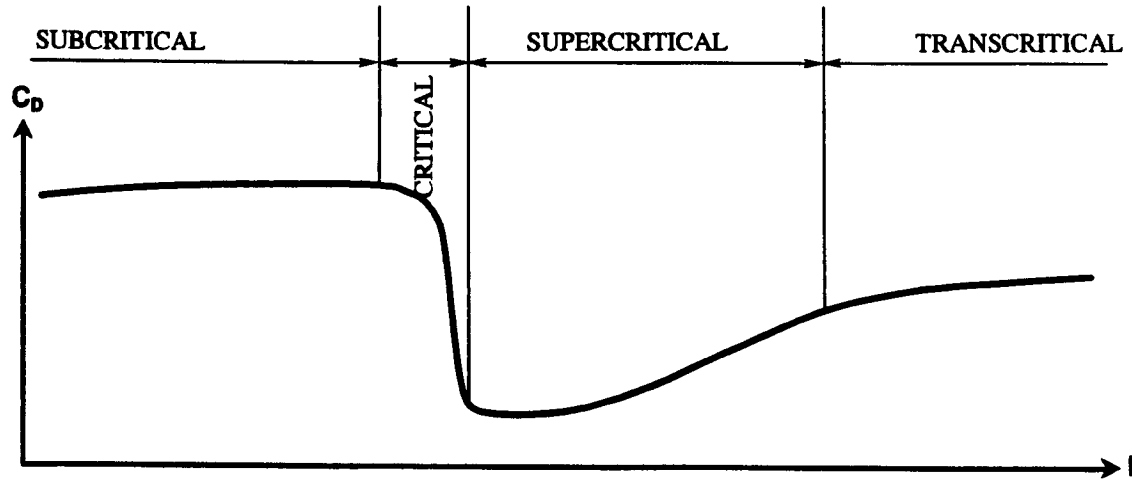

Figure 2.5 Flow and separation changes with increasing Reynolds number.

2.3.3 *Drag on bluff bodies*

A tennis ball is a bluff body, and the understanding of the flow around bluff bodies is fairly well documented. There are two significant components of drag that act on a non-spinning sphere moving through the air, pressure drag and surface drag (skin friction drag). The drag on a bluff body is predominantly due to the pressure difference between the front and back faces. It is widely understood that the shape of the forebody influences the boundary layer separation points and therefore the magnitude of the pressure drag. It is useful to investigate the drag effects on other bluff bodies to enable further discussion regarding the drag around spheres. Figure 2.6 shows the typical drag forces applied to some common shapes. The forces on the flat plate, cylinder and streamline body are depicted at a Re of 10^5 and a projected diameter of d. It can be seen that the flat plate has the highest drag force on it, and the surface drag is a negligible contributor.

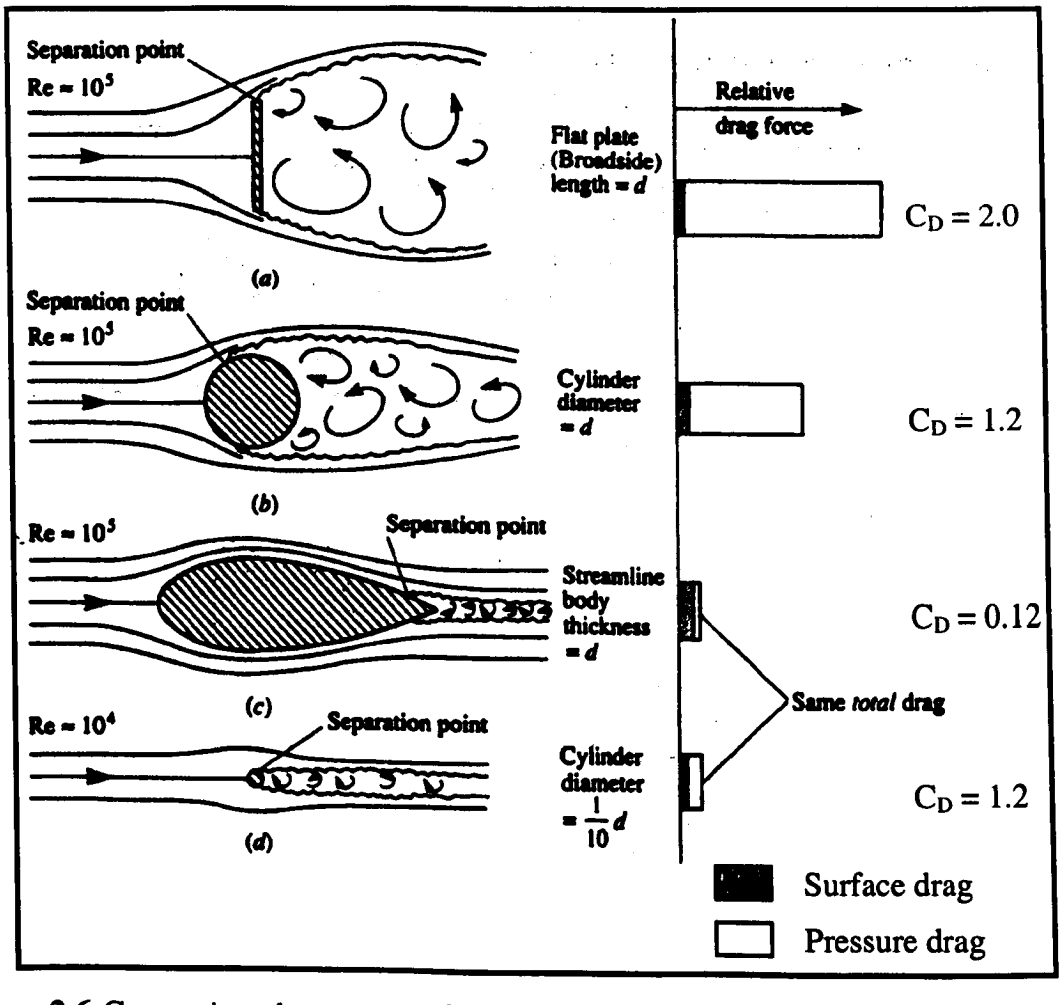

Figure 2.6 Comparison between surface drag and pressure drag for various aerodynamic shapes (Talay, T. A., Introduction to the Aerodynamics of flight, NASA SP-367, 1975)

As the shape of the front end becomes more rounded, the separation point and resulting direction of the post separation flow moves to reduce the overall drag, whilst the surface drag contributions increase. A streamlined body has a low adverse pressure gradient, and therefore enables the flow to remain attached over the rear surface and separation occurs very late, the drag is predominantly due to the surface and is very low.

The small diameter cylinder is shown with the same overall drag force as the streamlined body has acting on it. This has been achieved by reducing the diameter to d/10 and the Re to 10^4. When compared to the larger diameter cylinder, it can be seen that although the size of the object causes the drag force to increase, the C_D is the same.

There has been significant research performed on cylinders and in many cases similar approaches and conclusions can be adopted for spheres. The C_D of a sphere however, is found to be closer to 0.5 (Achenbach, 1973), less than half that of a cylinder. The phenomenon that causes this is known as three-dimensional relief, where not only the overall projected area is reduced, but the shape is also improved to remove the sharp 'corners', as shown in figure 2.7.

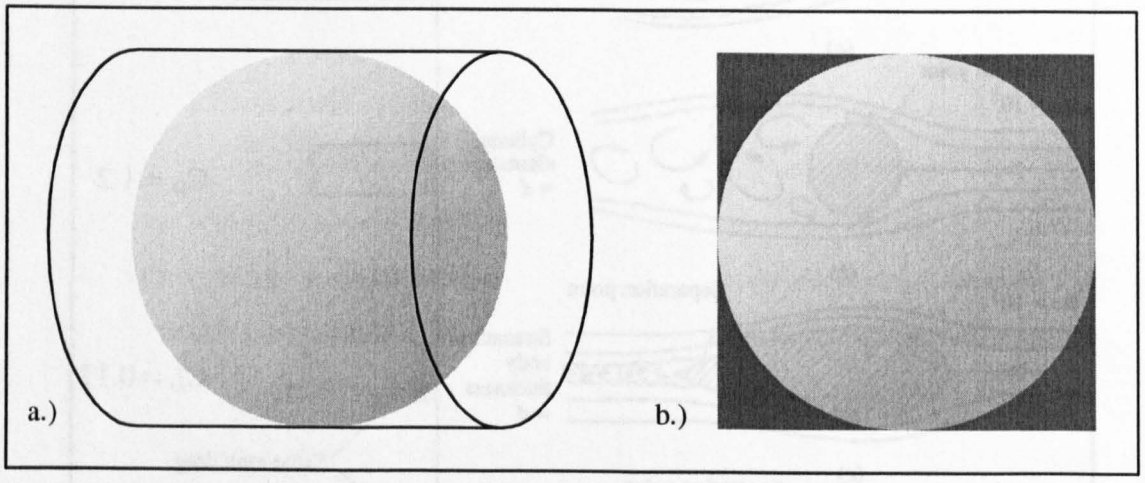

Figure 2.7 Sketch to show a) an oblique view of a sphere positioned within a cylinder and b) a front view showing the sphere in front of the cylinder.

The understanding of the aerodynamic properties of tennis balls is not complete without knowing what happens to the flow when the ball is spinning, the following sections discuss the forces acting on a spinning sphere.

2.3.4 The Magnus effect

Discussions regarding the aerodynamic forces applied to spheres have been occurring for centuries. Sir Isaac Newton noted that tennis balls curve when spin is imparted to them in 1672. In 1742, Robins investigated the curve of a spinning musket ball, and explained it as differences in velocity occurring on opposing sides of the ball. Magnus reported a similar explanation for 'a remarkable phenomenon of rotating bodies' in 1853. A paper on the irregular flight of tennis balls by Lord Rayleigh (Rayleigh, 1877) credited Magnus with the first explanation, and hence the curve in the trajectory of a spinning body is attributed to the Magnus effect.

2.3.5 Lift on a rotating sphere

Lift is generally associated with aeroplane flight and the flow over an airfoil section, however lift is also induced on a body of revolution. The original explanation by Magnus used the Bernoulli effect and suggested that the flow on one side of the ball is faster than that on the other due to the ball spinning, and the resulting pressure differential induces a transverse force.

The mechanics that lead to lift have been investigated significantly since man began to fly. Many textbooks and learning aids agree with Magnus and suggest that lift is induced due to increased velocity of airflow over one side, however this is an induced effect. It is probably more relevant to describe lift force in terms of Newton's 3rd Law of Motion.

In viscous flow the boundary layer is forced to spin with the ball due to viscous friction, which produces circulation around the ball. At the speeds and spin rates encountered by sports balls, the extra momentum applied to the boundary layer on the retreating side of the ball allows it to negotiate a higher pressure rise before separating and the separation point moves downstream. On the advancing side the reverse occurs and the separation point moves upstream, hence there is asymmetric separation and the wake is deflected (Mehta & Pallis 2001).

Positive (upward) lift is required when an aeroplane is taking off, and is created by lowering the rear of the airfoil. The underside of the airfoil forces the air flowing over it to deflect downwards, hence by Newton's 3rd Law, the air applies an equal and opposite force to the aeroplane. The resulting wake behind the wing is deflected downwards, and this relationship can be used to define the direction of lift for a spinning ball. Figure 2.8 shows a ball travelling from left to right in direction v and spinning in a clockwise direction, the resulting wake is shown to be deflected upwards behind the ball hence suggesting a resulting downward lift force. The lift force derived from rotation is combined with gravitational effects and in this case the ball will be accelerated towards the ground more quickly.

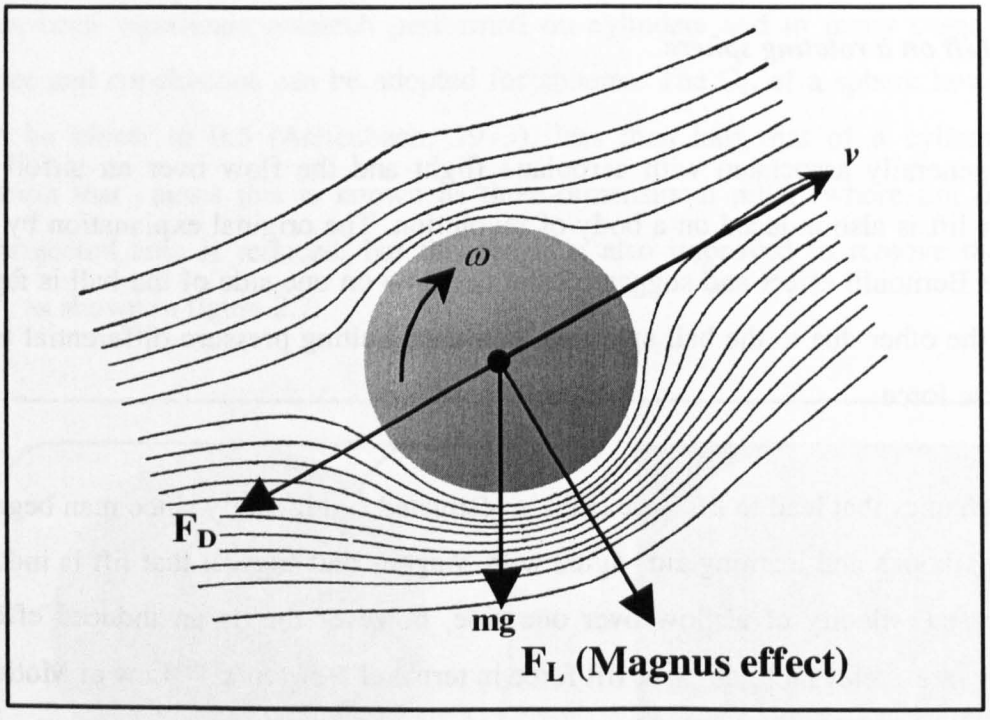

Figure 2.8 Forces acting on a spinning ball.

When backspin is applied the lift force acts in an upward direction, however the magnitude of the force generated on a tennis ball is relatively small in relation to gravity. In the case of a light object such as a beach ball, the lift force generated by spin can easily be greater than that exerted by gravity (Raskin, 1994), and a rising ball is observed during early trajectory.

The dependence of separation location on boundary layer transition Re can either enhance or oppose this effect. The effective Re is greater on the advancing side, hence the flow will

become critical before that on the retreating side. At this stage the separation point will move on to the rear surface on the advancing side whilst that on the retreating side remains unchanged, which causes the side force to switch direction, a phenomenon known as reverse Magnus effect. The reverse Magnus effect occurs over a very limited Reynolds number range, as speed increases further, the flow becomes turbulent on both sides and conventional side force returns.

2.3.6 Lift induced drag

Induced drag is well understood when applied to airfoils and flight, however it is less well defined for a rotating body. On an aeroplane the induced drag is due to 'down wash', created by a mixing of low and high pressure air. If the atmospheric conditions are right (high humidity), this effect can be seen as vortex lines on an airliner during landing. The vortices produce a down wash of air behind the wing, which is very strong near the wing tips and decreases toward the wing root. The local angle of attack of the wing is increased by the induced flow of the down wash, giving an additional downstream facing component to the aerodynamic force acting over the entire wing. This additional force is called 'lift induced' drag because it faces downstream and has been induced by the lifting action of the wing.

For a lifting wing, this type of drag is due to the vorticity produced by it and is expressed as a momentum deficiency in the wake. Whilst a spinning sphere will not necessarily have mixing at the ends of its spin axis, it does produce streamwise vortices, and therefore there is significant additional mixing in the wake. In a similar manner to the wing therefore, there will be less momentum in the direction of motion in the wake.

2.3.7 Forces acting on a sphere

The flight of any object is controlled by the forces acting on it, there are three component forces acting on a spinning tennis ball moving through the air; gravity, drag and lift. Gravity is fixed hence both the drag and lift forces need to be understood in order to develop a full understanding of the aerodynamic properties of tennis balls.

The drag force acts to slow the ball down in flight and the lift force acts to divert the ball from its Newtonian path. The mechanics behind the two forces will be discussed in the following sections, however it can be concluded that the drag force acts in the opposite direction to the direction of motion, and the lift force acts perpendicular to the direction of motion. Figure 2.9 shows a schematic of a sphere with all of the aerodynamic forces acting on it. The direction of the lift force is dependant on the spin direction, and if the ball is not spinning the lift force is assumed to be zero.

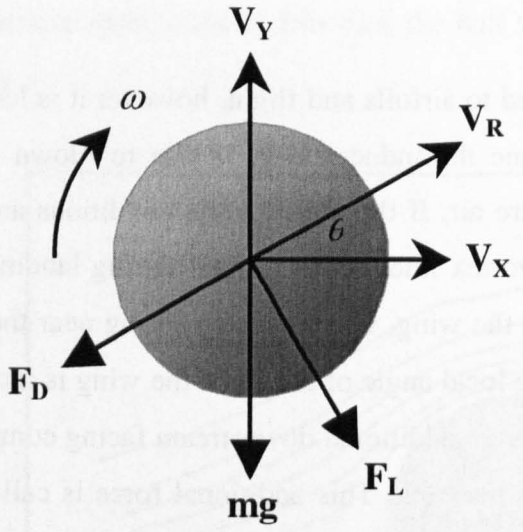

Figure 2.9 A force diagram for a ball spinning in the direction of ω travelling at $V_R ms^{-1}$ at θ degrees to the horizontal.

Figure 2.9 shows the forces acting on a ball spinning in the direction of ω travelling at $V_R ms^{-1}$ and θ degrees to the horizontal. With rotation in the direction shown in the diagram, the equations of motion are as follows:

$$m\frac{dV_X}{dt} = F_L \sin\theta - F_D \cos\theta \tag{2.1}$$

$$m\frac{dV_Y}{dt} = -mg - F_L \cos\theta - F_D \sin\theta \tag{2.2}$$

$$\tan\theta = \frac{V_Y}{V_X} \tag{2.3}$$

Both the drag and lift forces are functions of the object properties and the atmospheric conditions, and can be described by the following equations:

$$F_D = \tfrac{1}{2}\rho v^2 A C_D \quad (2.4)$$

$$F_L = \tfrac{1}{2}\rho v^2 A C_L \quad (2.5)$$

where: F_D and F_L are drag and lift forces respectively

ρ is the density of the fluid within which the object is moving

v is the velocity of the object moving through the fluid, or, the velocity of the fluid moving over the object

A is the *projected* area of the object

C_D and C_L are the drag and lift coefficients respectively

2.4 Aerodynamic effects of sporting projectiles

Previous research directly related to tennis is limited, hence in order to qualitatively understand the behaviour of a tennis ball during flight, other sporting projectiles have also been studied.

2.4.1 Cricket

In an article on the aerodynamics of a cricket ball in the New Scientist, Mehta and Wood (1980) explained how a spin bowler could use the Magnus effect to his advantage by releasing the ball earlier than normal, hence 'giving it more air' and enabling it to deviate during flight. Similarly, if the bowler were to apply topspin to the ball, it will dip unexpectedly in the air. Spin bowling only makes up a small part of the overs bowled in England, as most are bowled by medium to fast paced bowlers.

It is at this increased pace that the art of 'swing' bowling is encountered, a phenomenon which has interested researchers for decades. A cricket ball differs from balls used in any other sport as it is manufactured with a single proud seam. Medium to fast paced bowlers use this seam (possibly together with ball degradation) to cause an asymmetry in the flow

around the ball. The phenomenon of swing was first explained scientifically by Lyttleton (1957), however with subsequent research by Barton (1982) and Sayers (1999), the mechanics of swing are now widely understood.

Figure 2.10 shows the flow around a cricket ball with the seam at an angle to the line of flight. The rough proud seam acts as a trip and causes the boundary layer to become turbulent prior to that on the smooth side. The increased energy present in the turbulent boundary layer delays the separation on this side, thus causing a pressure differential resulting in the side force shown.

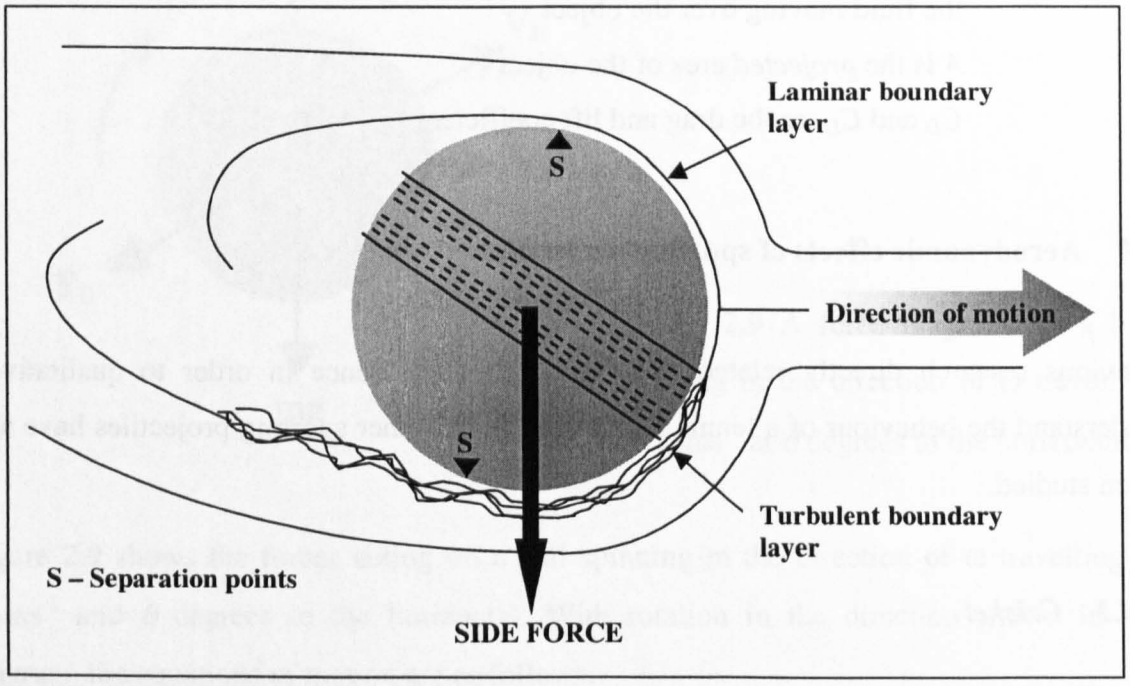

Figure 2.10 Flow over a cricket ball for conventional swing (derived from Mehta, 2000).

At increased bowling speeds, it has been shown that a cricket ball can swerve in the opposite direction to convention. Bown and Mehta discussed the phenomenon of 'reverse swing' in their New Scientist article of 1993. They explained that reverse swing can be mastered when bowling at speeds above $38ms^{-1}$ (85mph) with quarter seam balls as used in first class cricket.

As the ball ages, the surface of the ball is likely to roughen and therefore Re_{crit} will reduce. It is therefore possible that the laminar boundary layer on the upper surface in figure 2.10, required for conventional swing, undergoes transition. The boundary layer separation point on the upper surface will start to move towards the rear face, and the asymmetry, and

therefore magnitude, of the side force begins to reduce. Further increases in Re result in the transition point moving upstream, and will eventually produce a symmetrical flow field with zero side force when transition is coincident with the seam position.

It follows that further increases in Re will continue to move the transition points on both sides further towards the front stagnation point. The flow on the under side now becomes more susceptible to separation as the turbulent boundary layer thickens over the seam, resulting in the separation point creeping upstream. An asymmetry in the flow filed is reinstated, with the orientation reversed such that the side force acts upwards, as shown in figure 2.11.

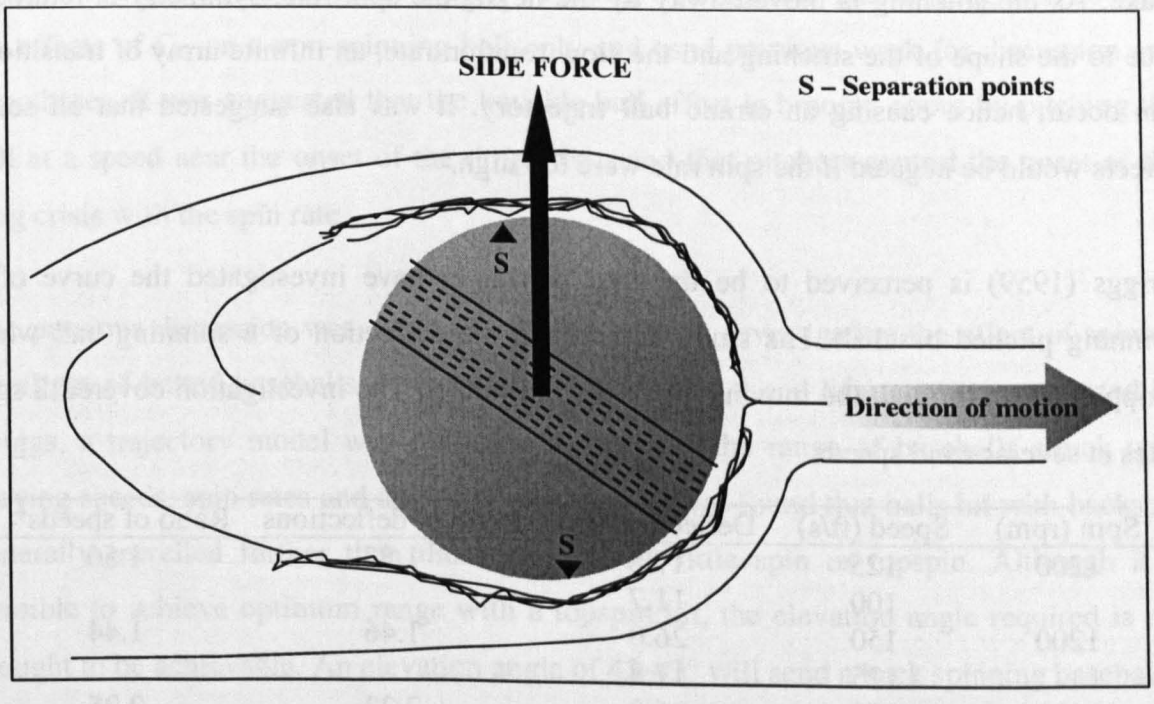

Figure 2.11 Flow over a cricket ball for reverse swing (derived from Mehta, 2000).

Bown and Mehta also showed that reverse swing could be achieved at speeds as low as $29ms^{-1}$ (65mph) simply by bowling the ball with the rough side facing slightly forward rather than the smooth side.

2.4.2 Baseball

The construction of the surface of a tennis ball is more closely related to that of a baseball than a cricket ball, however the seam of a baseball is still proud of the surface. There are

two phases that are of interest to the investigation of the aerodynamic properties of sports balls, the pitched trajectory, and the batted trajectory.

The pitch is most commonly released with spin, however the non-spinning 'knuckleball' is also of interest. The knuckleball gains its name from the way in which it is held, i.e. by the first knuckles or the fingernails. As it is thrown, the fingers are extended such that the ball is thrown without spin (or negligible spin). When a knuckleball approaches the plate it is seen to change direction erratically, Watts and Sawyer (1974) investigated the aerodynamics of a knuckleball. It was concluded that when correctly positioned, the stitching induces turbulence in the boundary layer, which therefore leads to an asymmetric wake. As the stitching is moved away by the negligible spin rate, symmetry is returned. Due to the shape of the stitching and the slow rotation rate, an infinite array of transitions can occur, hence causing an erratic ball trajectory. It was also suggested that all seam effects would be negated if the spin rate were too high.

Briggs (1959) is perceived to be the first person to have investigated the curve of a spinning pitched baseball. His study determined the deflection of a spinning ball when dropped 6 feet through the moving air of a wind tunnel. The investigation covered 2 spin rates at several wind speeds.

Spin (rpm)	Speed (ft/s)	Deflection (in)	Ratio of deflections	Ratio of speeds^2
1200	125	17.8	1.52	1.56
	100	11.7		
1200	150	26.0	1.46	1.44
	125	17.8		
1200	150	26.0	2.22	2.25
	100	11.7		
1200	100	11.7	1.92	1.77
	75	6.1		
1200	125	17.8	2.91	2.79
	75	6.1		
1200	150	26.0	4.25	4.0
	75	6.1		
1800	125	25.8	1.47	1.56
	100	17.5		
1800	125	25.8	2.98	2.79
	75	9.4		
1800	100	17.5	1.81	1.77
	75	9.4		

Table 2.1 Lateral deflection of a spinning baseball in a 6 ft drop across a wind tunnel airflow at various spins and speeds (reproduced from Briggs, 1959).

Table 2.1 shows the results obtained from this investigation, it can be seen that the ratio of any two deflections for a ball spinning at the same rate is approximately proportional to the square of the ratio of the spin rates. When Briggs assessed how this deflection could be translated to a pitched ball, it was found that the deflection was independent of speed. Hence, regardless of speed, a baseball spinning at 1200rpm deflected approximately 11 inches for a 60ft pitch, whilst an 1800rpm spinning baseball deflected approximately 17 inches over the same distance.

Frohlich (1983) investigated how the roughness of a baseball affects its flight, with particular reference to the drag crisis. The seam was assumed to be the driving roughness parameter, hence the grain of the leather covering was ignored. The investigation covered the effects of C_D on a non-spinning ball only and used previous work for discussion and hypotheses. It was suggested that the knuckle ball effect is brought about by pitching the ball at a speed near the onset of the drag crisis, and that pitchers control the onset of the drag crisis with the spin rate.

The previous discussion was continued by Rex (1985), investigating the effect of spin on the flight of batted baseballs. Using a constant C_D of 0.5 and lift parameters reported by Briggs, a trajectory model was produced to estimate the range of baseballs struck with varying speeds, spin rates and angles of elevation. It was found that balls hit with backspin generally travelled further than those struck with little spin or topspin. Although it is possible to achieve optimum range with a topspin hit, the elevation angle required is not thought to be achievable. An elevation angle of 42-43° will send a back spinning baseball 5 to 6m further than a top spinning hit at the same speed, maybe enough to get a home run.

Although the seam is shown to affect the flight of the non-spinning ball, Watts and Ferrer (1986) showed that the lifting force on a curveball does not depend strongly on the seam orientation. In general, it was found that the lift coefficients were principally a function of the spin parameter and surface roughness, with only a weak dependence on the free stream Reynolds number.

2.4.3 Golf

There have been several studies conducted to investigate the aerodynamics of golf balls. Much of the work has dealt with the range of the ball and the objective of the study arises normally from a desire to increase the length of the shot.

Research into the game of golf started as early as 1893, with a paper from Tait on the path of a rotating spherical projectile. In these formative years, the suggestion that the 'hook' and 'slice' was caused by a poor quality shot was not taken well by the golfers of the day, even though it was also suggested that it may be possible to use these strokes to the golfers' advantage. In 1896, Tait furthered his investigation to include wind resistance and coefficient of friction. A trajectory model was produced and calculations made by hand. The spin decay was assumed to be zero throughout the flight, and different speeds, spins and angles were used to assess the range of a golfing stroke.

The golf ball is always (except when putting) struck with backspin, which is imparted by the angled face of the club. A non-spinning ball would travel straight but not very far, and according to Thompson (1910), 'it is spin which gives the interest, variety and vivacity to the flight of the ball'. It is common belief that the properties of the ball play a larger role in determining spin than the properties of the club (Gobush, 1994). Golf clubs with different lofted angles on them are used to project the ball at different elevations. A 'drive' is struck with a club with a small lofted angle, and the induced lift force due to spin, keeps the ball in the air for longer, increasing the range over that of a ball hit without spin. An 'approach' shot needs to be struck with more control than the long range drive, hence it is projected higher, and the induced spin lends itself to a controlled landing. Initial rotation speeds of between 2000 and 4000rpm have been measured for typical long range shots, although maximum spin rates of 8000rpm have been reported by Davies (1949).

After the introduction of the gutta-percha ball in 1845, golfers discovered that it flew further and better when scored or marked; a phenomenon that is now clearly understood to be the early boundary layer transition caused by increased roughness. Several ball designs were introduced, including the 'bramble ball' with a raised pattern that unfortunately

accumulated mud. Rectangular and square depressions were common, but by 1930 the round dimple had almost taken over and become accepted as the standard design.

Bearman and Harvey (1976) investigated the advantages of an alternative dimple shape, the hexagon. The main aim of the study was to measure the C_D and C_L of both conventionally and hexagonally dimpled golf balls, and then use the results to predict trajectories. It was found that the hexagonally dimpled surface not only induced a small increase in C_L, but the C_D reduced by a similar magnitude for most speeds. It was concluded that the superior aerodynamic performance of the hexagonally dimpled ball suggests that, for the same launch conditions, it should travel further than a round dimpled ball.

Much of the investigations deal with topspin or backspin, however the axis of rotation will normally not be horizontal and perpendicular to the direction of motion. Indeed, Tait wrote of the peculiarities called heeling, toeing and slicing, all of which are caused by inducing an element of sidespin on the ball. McPhee and Andrews (1987) developed a three-dimensional computational trajectory model to assess the aerodynamic effects on a spinning golf ball. It was found that with the correct combination of sidespin and crosswind, it is possible to increase the range of a shot by almost 1%.

2.4.4 Athletics

As part of the research into the aerodynamic properties of sporting objects, it became clear that work has been undertaken investigating several objects associated with athletics. Although the shot put is spherical, the aerodynamic properties associated with it are not complex, in fact, the objects of interest are non-spherical, namely the javelin and the discus. There are some similarities between the motion of these items and a ball, however it was soon understood that the mechanics of flight differ significantly. Each of these sporting activities aims to project the object as far as possible, and will be dealt with separately.

The javelin is thrown such that the tail end is below the front, and hence conventional lift acts upwards to keep it in the air longer. As the rules require the nose to strike the ground

first, modern javelins are perpetually unstable such that the restoring moment is enough to ensure legal throws.

A legal discus throw does not require the front to land first, hence they are designed to be perpetually stable. The rotation of the discus adds complexity to its aerodynamic properties, however the theory behind attaining the maximum range is the same. By projecting the discus with its rear below its front the lift force is favourable to increased range.

A similar rotating object to the discus is the frisbee. The rotation of the discus does not affect its flight significantly, however a frisbee is seen to deviate from its original path and nosedive into the ground. For a frisbee rotating clockwise from above, thrown by a right handed player, gyroscopic precession will cause it to veer right from the thrower's perspective.

2.4.5 Tennis

A game of tennis starts with a service, and is followed by several different types of strokes that may have an infinitive number of speed, spin and elevation angle combinations. Most shots are struck with spin, applied by the oblique impact with the racquet.

Although there was some early attention by Newton (1672) and later by Lord Rayleigh (1877), it was not until late in the 20th century that scientific studies were undertaken. Stepanek (1988) is the first and only published study available at the time this current study commenced. Stepanek aimed to simulate the 'topspin lob', a shot struck above the opponent's head with lots of topspin to force the ball down more rapidly. The aerodynamic forces were determined by dropping spinning tennis balls through the moving airflow of a wind tunnel. The study investigated wind speeds between 13.6ms^{-1} and 28ms^{-1}, and spin rates between 800rpm and 3250rpm. It was found that C_D and C_L could be described in terms of the spin parameter, S, shown in the following equations:

$$C_D = 0.508 + \frac{1}{\left[22.503 + \frac{4.196}{S^{\frac{5}{2}}}\right]^{\frac{2}{5}}} \qquad C_L = \frac{1}{2.022 + \frac{0.981}{S}} \tag{2.6}$$

where: $S = \omega / v$

ω is the equatorial velocity of the spinning ball

v is the ball flight velocity

Preliminary investigation showed that the spin rate of this type of shot would be around 3500rpm. The results showed that the this stroke could be played from many points on the court, however the spin rate and angle of elevation needed to be increased the closer to the net it was struck.

Several relevant projects were undertaken at Cambridge University between 1996 and 1997, and Brown and Cooke (2000) brought these together. The investigation begins with the initial unsteady motion, and is broken down into three key sections, vibration, viscous motion and inviscid motion.

Vibration: The pressure variation was measured inside the ball after impact and it was found that significant large scale deformation ends about 5ms after impact.

Initial inviscid motion: Based on a sound wave test developed by Taylor (1942), it was concluded that the inviscid, unsteady motion of a tennis ball does not last long and therefore does not substantially affect the velocity of the ball.

Initial viscous motion: Based on complex mathematical models developed by Batchelor (1967), it was deduced that, for a ball accelerated to $50ms^{-1}$, the steady flow regime was achieved in a time order of 3ms.

Drawing all of these observations together, it was concluded that the tennis ball reaches a quasi-steady aerodynamic state within 10 ball diameters after leaving the racquet. This relates to approximately 3% of the overall trajectory (Cooke 2000), so the initial unsteady motion described above will not make a significant contribution to the overall flight path.

The most recent work on tennis ball aerodynamics has been undertaken as part of a collaboration between NASA Ames Research Center and Cislunar Aerospace Incorporated. Mehta and Pallis (2001) present C_D results obtained for tennis balls of different manufacturers and surface finishes and found that the C_D of a tennis ball is between 0.6 and 0.7. When compared to previous results for rough spheres a C_D of 0.5 may have been expected, it was found that tennis balls did not exhibit the aerodynamic properties that may have been expected by rough balls, and further investigation was undertaken. It was concluded that boundary layer transition is very early for a tennis ball and that separation was induced by the roughness of the ball on an unstable thick turbulent boundary layer. The additional 20-40% of the C_D exhibited in their results was proposed to be due to 'fuzz drag', where each of the fibres in the nap had an associated pressure drag (at a low Re). It was suggested that the non-linear C_D witnessed for very low speed was affected by both the orientation of the fibres and the Re dependence of the C_D of the fibres at very low Re.

2.5 Wind tunnels

Wind tunnels offer a rapid, economical and accurate means of aerodynamic research. Whether the equipment under test is a scaled model of a military aircraft or a model of a skyscraper landscape, wind tunnels can be of use. Low-speed is a classification that is used for wind tunnel testing with incompressible airflow in the test section, which implies wind speeds of less than 250mph (M<0.3). As the airflow is not that of the open atmosphere, some understanding is essential to ensure good quality results.

2.5.1 Wind tunnel types

There are two basic types of wind tunnel, open circuit (Eiffel) and closed circuit (Prandtl). The open circuit tunnel has no guided return of the air, however, as the name implies, the closed circuit tunnel has a continuous path for the air. Open circuit tunnels were the first tunnel types built, and a schematic can be seen in figure 2.12. Air is drawn into the wind tunnel at the right hand end by a driven fan situated downstream of the working section. The air inlet should ideally be open to the atmosphere, whilst this increases the possibility of debris and gusts affecting the test, it does improve the quality of flow. As the air enters

the wind tunnel it goes through a honeycomb section for 'straightening'. Prior to entering the test section, the air travels through a rapid contraction to increase its speed and maintain a relatively stable airflow; the air leaves the wind tunnel through a gentle diffuser at the left hand end and rejoins the air in the surrounding area.

The diffuser is the gradually expanding passage following the test section in which the flow speed decreases and the pressure rises. The recovery of pressure from kinetic energy reduces the power needed to drive the tunnel, and in the case of open-circuit tunnels the diffuser also reduces drafts in the laboratory. The pressure rise is less than that given by Bernoulli's equation because of losses due to skin friction and resulting growth of boundary layer displacement thickness.

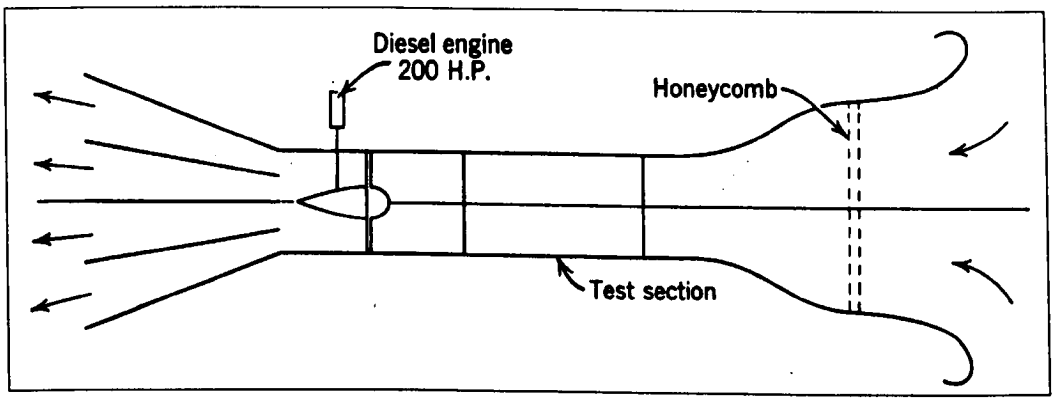

Figure 2.12 Schematic of an open circuit wind tunnel (taken from *Low-Speed Wind Tunnel Testing, Pope A. and Harper J., 1966).*

There are three different types of closed circuit wind tunnel; single, double or annular return, however the single return is most commonly utilised and a schematic can be seen in figure 2.13. The main advantage of the return passage of air is to feed clean air into the settling chamber, free of high turbulence with some control over its temperature. However the power output of the open circuit wind tunnel is increased by as much as 15% due to the fewer screens required.

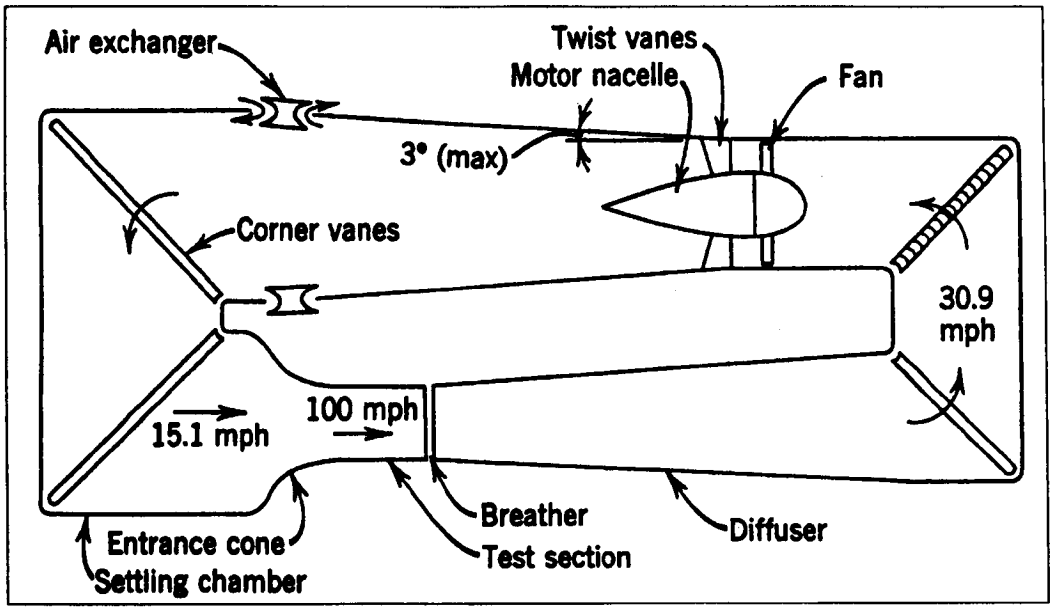

Figure 2.13 Schematic of a single return closed circuit wind tunnel (taken from *Low-Speed Wind Tunnel Testing, Pope A. and Harper J., 1966).*

The test section is a small proportion of the space envelope required, with the rest being required for control of the airflow. The corner vanes are used to smooth the airflow around the corners, whilst the shallow diffuser ensures steady expansion. The main reason for the inclusion of air exchangers is to limit the rise of the airflow temperature, however these are not generally required in low-speed wind tunnels. As the air enters the settling chamber, its velocity is relatively low and uniform. As with the open circuit wind tunnel, the airflow is accelerated into the test section through an entrance cone, and the process starts again.

2.5.2 Wind tunnel components that affect the flow in the test section

The design of a wind tunnel can affect the quality of air flowing into the test section, and the resulting turbulence levels and velocity profiles will be discussed in sections 2.5.3 and 2.5.4. The following sections are included to discuss some of the components of a wind tunnel that affect the flow.

Settling chamber, screens and honeycomb

The settling chamber is the largest cross section in the wind tunnel, and contains a honeycomb and/or screens. It is never long enough for pre-existing tunnel turbulence to

decay significantly, so the name is misleading. A honeycomb with its cells aligned in the flow direction will reduce mean or fluctuating variations perpendicular to the flow direction with little effect on streamwise velocity. Woven-wire screens mainly reduce streamwise velocity fluctuations, with little effect on flow direction because the refractive index of a screen is small.

The honeycomb is always mounted upstream of the main anti-turbulence screens and should be far enough downstream of the start of the parallel-sided settling chamber for the flow to be roughly parallel to the axis. The lateral components of mean velocity and of the larger turbulent eddies can be effectively reduced by a honeycomb. For effective flow improvement the cell length of the honeycomb should be at least six or eight times the cell diameter. For large or high-performance tunnels, aluminium honeycomb used for aircraft construction is better, but care should be taken to remove burrs. A honeycomb naturally produces some turbulence of its own, with eddy sizes of the same order as the cell diameter, which decays very much more rapidly than the original turbulence but more slowly than the small scale turbulence produced by screens. Early wind tunnels often had honeycomb but no screens (and usually a very small contraction ratio also) and suffered from very high turbulence intensity in the test section, although the mean flow was often quite good. Most modern tunnels have both honeycomb and screens.

Screens are normally installed in a settling chamber to improve the mean flow uniformity and reduce the intensity of oncoming turbulence. When installed in a constant area passage, a screen will experience a drag force and therefore reduces the total pressure of the flow passing through it without altering the average velocity locally. In general, the drag force will be greater where the velocity is higher than average, thus the total pressure will tend to equalise over the cross section. In principle, a screen will reduce the velocity defect as it passes through, however to give the maximum reduction of turbulence, the aggregate pressure drop coefficients should be as high as possible. Dense screens are sensitive however, and may produce velocity variation due to imperfections of weave and instabilities of flow through the pores. Several screens in series can give the same velocity variation reduction as a single high-density screen, possibly leaving small fluctuations that are largely the result of weaving imperfections or wrinkles in the last screen.

If a tunnel has no built-in filter, the screens do the filtering, and not only does dirt build-up reduce the open area but the dirt is densest near the bottom of the screen, leading to a vertical gradient of velocity in the test section. Screens should therefore be cleaned at regular intervals, in some cases however, the pressure drop across the first screen or the whole set of screens is monitored (where a significant increase in the pressure drop indicates that the screens need cleaning).

The distance between screens is not critical and a minimum is usually set by the need to mount the screens firmly, in removable frames or otherwise. Screens can be clamped, without adhesive, between two wooden frames. Tight pre-tensioning of the screens is not necessary, and as long as there are no wrinkles, the airflow will pull the screen into a smooth shape. Near the entry of the contraction, the flow starts to slow down near the walls and accelerate nearer the centre line, hence the pressure drop through a screen placed too near the entry will vary over the cross-section. The last screen should be far enough upstream of the contraction that the flow speed is still constant over the cross-section such that there are no velocity variations in the test section.

Contraction

The contraction accelerates the flow from the settling chamber into the test section, further reducing percentage variations in velocity. Early contraction designs has a small radius of curvature at the wide end and a large radius at the narrow end to provide a gentle entry to the test section, however this has been shown not to be the optimum. There is a danger of boundary layer separation at the wide end, or perturbation of the flow through the last screen. Good practice is to make the ratio of the radius of curvature to the flow width about the same at each end. If the radius of curvature at the upstream end is too large, this may lead to slow acceleration and therefore an increased rate of boundary layer thickness growth throughout the contraction, and this can lead to separation at the contraction exit.

The contraction area ratio should be as large as possible to reduce the total-pressure loss through the screens. In medium-size tunnels, the area ratio is limited by the desirability of easy access to the test section while the operator is standing on the floor of the laboratory, implying that the test section floor should be no more than 4-5ft. above the floor of the room. There is no overwhelming reason why a contraction should be symmetrical top and

bottom as modern design codes can easily calculate the pressure distribution on a chosen asymmetric shape. Area ratios of 9 are common in typical wind tunnels, however a wind tunnel with an area ratio of 31 has been developed although it suffered from flow separation in the contraction.

The contraction is the last component before the test section, and should further reduce the variations of velocity components that are created in the return circuit or the laboratory and then attenuated by the honeycomb and screens. The velocity in the high-speed region is determined from Bernoulli's equation. Velocity variations of more than a fraction of a percent in mean velocity (except near the test-section walls) imply either too few screens, too small a contraction ratio or asymmetry in the flow into the settling chamber.

Unsteadiness in the test section is usually the result of flow separation in the tunnel circuit, or unsteadiness in the entry flow of an open-circuit tunnel. A good wind tunnel will have an axial component fluctuation in the test section of less than 0.1 percent of the mean velocity, however it is likely to be about 0.3 percent in student tunnels.

2.5.3 Turbulence

The flow in a wind tunnel is made unsteady by the tunnel design, propeller, quality of surface on the walls, vibrations of the tunnel walls, and any guidance vanes that may be used. The turbulent flow pattern in the tunnel is similar to the flow pattern in free air at a higher Reynolds number. The turbulence level of a wind tunnel can be used to assess the quality of air in the wind tunnel compared with that in the open. It can be calculated in one of three ways; direct measurement, or by use of a turbulence sphere or pressure sphere.

Direct measurement makes use of hot wire anemometry and compares the rms velocity variations to the mean speed at various points in the test section. The turbulence sphere makes use of a smooth ball and a force platform, whereas the pressure sphere takes measurements of the pressure distribution around a smooth sphere. The turbulence sphere requires less complex components and instrumentation, and is discussed in this section.

In this study, a 6-inch ball was used to increase the Reynolds number to compensate for the maximum wind tunnel speed of $67ms^{-1}$. The Reynolds number was derived in 1883 by Osborne Reynolds whilst investigating the transition from laminar to turbulent flow in pipes, and is defined by the following equation:

$$\text{Reynolds number} = \text{Re} = \frac{\rho v d}{\mu} \tag{2.7}$$

where: ρ is the density of the fluid within which the ball is projected

μ is the dynamic viscosity of the fluid within which the ball is projected

d is the projected diameter of the ball

v is the velocity of the ball (velocity of the fluid in a wind tunnel)

The Re is a dimensionless ratio between fluid inertia stress and viscous stress, and most importantly flows at the same Reynolds number are similar. Re can therefore be used to scale models to make them more manageable in wind tunnels of a smaller test section, or in the case of a sports ball, it can be enlarged to increase the scope of the testing possible.

Rather than trying to define the point at which the transition occurs, the point at which C_D becomes 0.3 is used (Dryden *et al*, 1938). Figure 2.14 shows a sample set of results obtained using a smooth ball. The test was performed in a closed circuit wind tunnel with a working section of 1.65m deep by 1.2m high.

It can be seen that the results obtained in this study compare well with those obtained by Achenbach. Transition starts at around $3.2x10^5$ and appears to finish just after $4.2x10^5$, the value of Re when C_D becomes 0.3 is $3.54x10^5$. It is known that the drag coefficient of a smooth ball in free air is 0.3 at a Reynolds number of $3.85x10^5$ (Pope & Harper, 1966), hence the following turbulence factor is obtained:

$$\textit{Turbulence Factor, TF} = \frac{RN}{\text{Re}_{crit}\,(\textit{in the wind tunnel})} = \frac{385{,}000}{354{,}000} = \underline{\underline{1.087}} \tag{2.8}$$

where: RN is the critical Reynolds number for a smooth ball in free air.

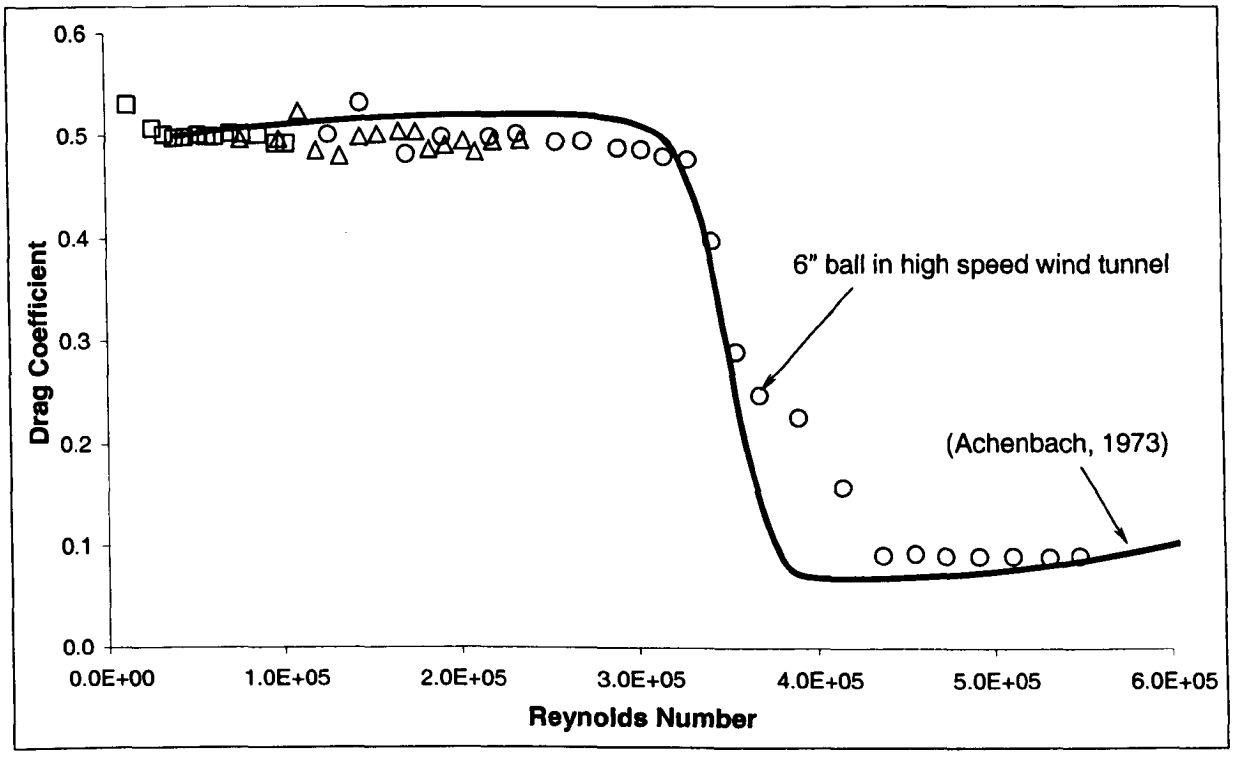

Figure 2.14 Graph to show the transition point of a 6-inch smooth ball in the high-speed wind tunnel, comparison with results presented by Achenbach (1973) for a smooth ball.

A wind tunnel with a turbulence factor of less than 1.1 is satisfactory for accurate testing (Pope & Harper, 1966). Turbulence factors normally range between 1.0 and 3.0, and values above 1.4 normally indicate excessive turbulence for reliable testing on low drag components such as airfoils. The turbulence factor is used to assess the effective Reynolds numbers, Re_{eff}, at any velocity during testing in that wind tunnel. Re_{eff} is obtained by multiplying the actual Re for the given wind speed, Re_n, by the turbulence factor:

$$Re_{eff} = TF \times Re_n \tag{2.9}$$

The relationship between the turbulence factor and the degree of turbulence present is shown in figure 2.15, it can be seen that a TF of 1.087 is equivalent to 0.123%.

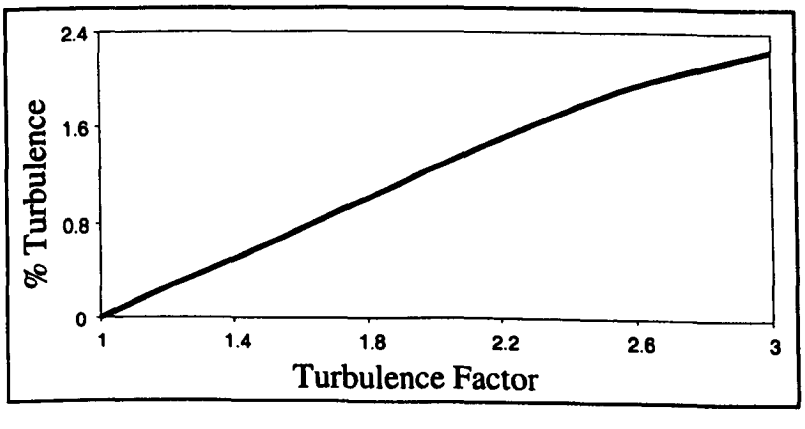

Figure 2.15 Graph showing percentage turbulence expected in the wind tunnel for a given turbulence factor, reproduced from *Low-Speed Wind Tunnel Testing, Pope A. and Harper J., 1966.*

In existing tunnels, the addition of damping screens can reduce the intensity of turbulence, however the loss in power is considerable (between 5 and 20 percent). The positioning of these screens is of great importance, if placed too close to the working section it is possible that the turbulence factor could be increased, therefore they should be placed far enough upstream that the turbulence caused by the screens themselves has time to damp out.

2.5.4 Velocity profile

The variation in the dynamic pressure can be measured at several positions across a single plane of the working section. Sufficient data points should be investigated such that an accurate contour can be assessed. The variation of dynamic pressure should be less than 0.5% from the mean, which implies that a variation of less than 0.25% from the mean velocity is acceptable.

It is not correct to think of a wind tunnel as having uniform flow, particles closest to the walls are constantly being overtaken and passed by those in the central stream. Therefore it is expected that a lowered velocity will be obtained near the perimeter of the cross section under investigation. There are several methods available to improve the flow through the working section of wind tunnels and these were discussed in section 2.5.2. It is understood that the energy available to the wind tunnel will be reduced, however this is far outweighed by the improvement in testing conditions.

2.6 Experimental methods for measuring aerodynamic forces

Any body moving through the air will experience aerodynamic forces, the challenge is to develop a method by which these forces can be measured. The following sections describe the test methods that can be used to calculate the aerodynamic forces on a tennis ball.

2.6.1 Projectile tests

It is ideal to measure the aerodynamic forces acting on a tennis ball whilst actually in flight. The projectile tests use real tennis ball trajectories and calculate the aerodynamic

forces from finite changes throughout the flight. The forces acting on the ball and the related equations of motion were discussed in section 2.3.7.

The first of the tests attempted by Briggs (1959) studied the effect of spin and speed on the lateral deflection of a baseball using air gun experiments. The test used a projectile from the air gun to drive a ball mounted on a spinning tee a distance of 60 feet. At this point the ball hit a vertical surface where it made an imprint. The spin of the ball before impact was measured using a Strobotac and the speed of the ball was estimated using the drop in height of the ball. The results obtained were erratic, and it was postulated that this method equated to a batted ball instead of a pitched ball.

A study to determine the C_D of a tennis ball was conducted by Zayas (1985). A tennis ball pitching machine was used to project the ball horizontally, and the speed was chosen to ensure that the ball landed approximately 8m from the exit. The exit velocity was measured using strobe photography and laser switch photogate apparatus. The horizontal landing velocity and angle were measured using strobe photography at a rate of 7200 flashes per minute. The results from 50 tests were used to calculate the C_D of a tennis ball to be 0.51 with an accuracy of ±15%.

Further work on the golfing shot was undertaken by Zagarola *et al* (1994). This study was undertaken to design an indoor testing range to derive the coefficients of the aerodynamic model of the ball. The experiments used a launching machine consisting of four 25-inch wheels arranged in a square with the bottom and top wheels attached using a timing belt driven in opposite directions. Data of the flight was captured using several timing screens, producing a pulse when the screen is broken.

A study of volleyball by Depra (1998) used a video to record services by a top Brazilian national player. There were four types of service analysed: underhand; floater; floater with jumping; and the overhand service with jump. The service was recorded using two fixed video cameras. The data from the recordings was digitised for every 1/30 second and the Cartesian co-ordinates obtained. A chart of x against y was produced and the author stated that co-ordinates in the z direction were ignored. The chart was then used to derive the C_D, where it was calculated that a volleyball has a subcritical C_D just less than 0.5, with Re_{crit}

occurring around $2.5x10^5$. The C_D results were presented against typical C_D results from other research institutes, which showed that they contained significant scatter but were consistent with typical values.

2.6.2 Drop tests

The inherent control difficulties associated with projectile tests can be overcome by constraining the displacements. The projectile tests investigate how the aerodynamic forces affect the ball as it retards, drop tests investigate how the aerodynamic forces affect the ball as it accelerates through the moving airflow of a wind tunnel working section. A similar method to that used in section 2.3.7 can be used to find the equations of motion for a ball dropping through the moving air of a wind tunnel.

Figure 2.16 shows the associated force diagram for a ball spinning in the direction of ω, dropping through a wind tunnel with air flowing from left to right at velocity V_W.

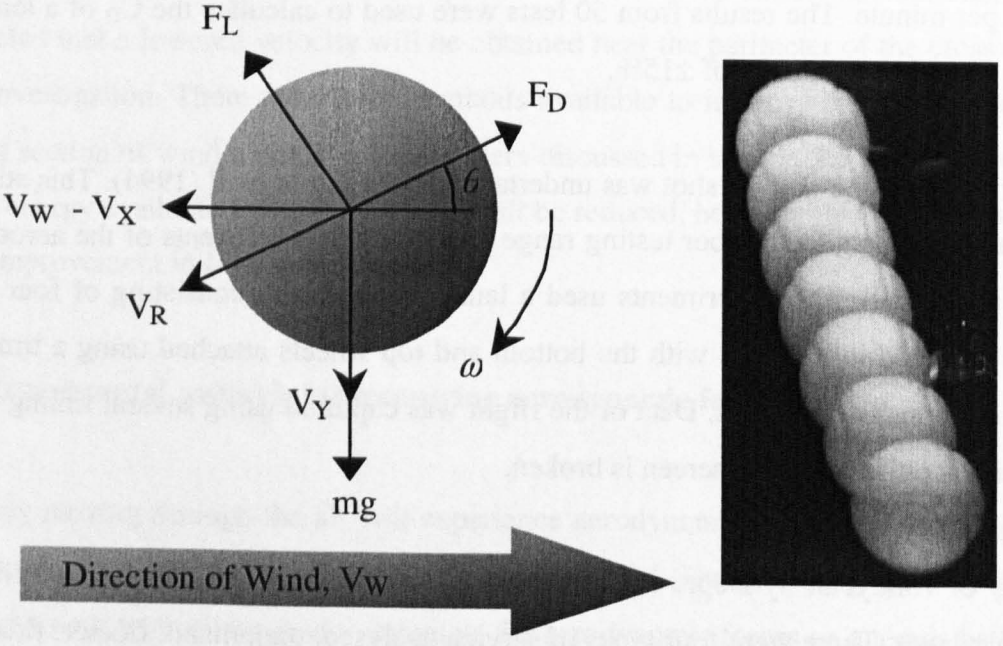

Figure 2.16 Force diagram and typical trajectory for a spinning ball falling through the moving air of a wind tunnel.

The picture on the right hand side of figure 2.16 shows a typical trajectory obtained during a ball drop investigation. The ball drops vertically through the airflow, and although the ball deflects in the direction of the wind with horizontal velocity V_X and vertical velocity

V_Y, the equivalent direction of motion is that depicted by V_R. The relative velocity, V_R, has components V_W-V_X and V_Y acting in the horizontal and vertical directions. For the given force diagram shown in figure 2.16, the equations of motion are:

$$m\frac{d(V_W - V_X)}{dt} = F_L \sin\theta - F_D \cos\theta \tag{2.10}$$

$$m\frac{dV_Y}{dt} = mg - F_L \cos\theta - F_D \sin\theta \tag{2.11}$$

$$tan\theta = \frac{V_Y}{(V_W - V_X)} \tag{2.12}$$

The research regarding baseball deals with the understanding of the aerodynamic effects on the ball when thrown in different manners. One of two tests undertaken by Briggs (1959) studied the effect of spin and speed on the lateral deflection of a baseball. The test used a wind tunnel of octagonal construction measuring 6ft across the horizontal. A spinning device was used to drop the ball through the airflow, and the point of impact was recorded on a sheet of cardboard fastened to the tunnel floor. The lateral deflection of both spin directions was required for calculation of the aerodynamic forces acting on the balls. The spinning mechanism was mounted outside of the wind tunnel, and the ball was dropped into the wind tunnel working section through a hollow shaft that permeated the skin of the wind tunnel slightly. The method of construction meant that the centre of gravity did not always coincide with the geometric centre of the ball, forcing the ball to be projected laterally upon release. In addition to some manual realignment, at least three experiments were made for each spin and wind speed. Experiments were undertaken for speeds up to 150ft/sec (45.5ms^{-1}) and spins up to 1800rpm.

Davies (1949) used a wind tunnel technique whereby the golf ball was dropped through the horizontal wind stream. The corresponding forces acting on the ball were calculated from the drift due to the wind. Rotational speeds of up to 8000rpm and a wind speed of 105 feet/second (≈32ms^{-1}) were used. The speed corresponds to a Reynolds number of 9.4×10^4, a figure substantially less than the value expected of a golf ball leaving the tee. A spinning device was used to rotate a ball between a pair of cups, the cups were parted, releasing the ball into the air stream to fall freely. The distance travelled during the flight of two identical balls spinning at the same rate in opposite directions was used to calculate the

aerodynamic forces. The forces were assumed to act horizontally and vertically and can therefore be calculated using the following equations:

$$F_D = -2mg\left(\frac{x_1 x_2}{y(x_1 + x_2)}\right) \qquad F_L = \frac{mg(x_1 - x_2)}{(x_1 + x_2)} \tag{2.13}$$

where: y is the drop height

x_1 and x_2 are the two distances travelled by the opposing spinning balls

Mehta *et al* (1983) devised a method of dropping a spinning ball through the airflow of a wind tunnel to assess the factors affecting the swing of a cricket ball. The test used five different cricket balls, differing both in material and method of manufacture. Spin was imparted on the ball by rolling it down a ramp prior to entry to the wind tunnel working section. The entry of the ball was controlled to ensure that the seam was vertical throughout the flight. The ball that was found to swing most was the only one with a 2-piece cover, it was stated that the secondary seam on the four piece ball produces a roughness that causes early transition.

An investigation by Stepanek (1986) used a similar wind tunnel apparatus and test method as Davies to determine the drag and lift coefficient of a spinning tennis ball. The trajectory was recorded and a motion analysis method was developed to calculate the deflection of the spinning tennis ball drops. Manipulation of the results enabled calculation of the ballistic trajectories of a topspin lob in tennis. A spinning dropper device was designed to drop the ball through the airflow of the wind tunnel. The tennis balls were modified to include steel inserts for mounting purposes. A small motor with a foam rubber conical follower was pressed against the ball surface and used to impart spin on the ball. Upon release the ball dropped freely through the air stream in the tunnel. The tests were performed for wind velocities up to 28 m/s and spin rate of up to 3250rpm.

2.6.3 Load cell tests

Bearman and Harvey (1976) used a wind tunnel technique to measure the lift and drag forces acting on a golf ball and used the results to predict the trajectory of a golf ball. The study investigated three ball types; round dimples, hexagonal dimples and a smooth sphere.

The wind tunnel used had a maximum speed of approximately $45ms^{-1}$, and to achieve the required Reynolds number, a model of 2.5 times the full scale was produced. The test method used a system of wire supports, motors, strain gauges and a wind tunnel balance. The results from the smooth ball were used to assess the accuracy of the test method, using Achenbach (1972) as the benchmark. The study also used computation of trajectories of the golf ball using the data obtained, which were then compared with data obtained from a driving machine.

Watts and Sawyer (1975) investigated the aerodynamic effects of a knuckle ball (thrown in baseball with no or little spin). The aim of the study was not to measure actual forces, but to identify the orientation of the ball, relative to the airflow, where a lateral imbalance was induced. The experimental arrangement used a subsonic wind tunnel, a device for measuring lift and drag and a strip chart recorder for measuring the forces involved. The device consisted of two beams rigidly attached to a base with foil strain gauges attached near the base. The strain was measured using a Baldwin-Lima-Hamilton micro strain indicator. The wind tunnel velocity used was approximately 50ft/sec ($\approx 15ms^{-1}$), which relates to a Re of $1x10^5$. The study extended to consider the trajectory of the pitched ball, and was based on the fact that that the drag coefficient for a sphere is approximately constant (and therefore the drag force increases with the square of the velocity). A ball rotating at half of one revolution over a 60.5ft ($\approx$18m) pitch was postulated to change direction three times due to the position of the stitching.

Mehta and Pallis (2001) attached polyurethane foam filled tennis balls to a reaction torque cell via an airfoil strut. The torque cell was positioned outside of an open circuit wind tunnel, with the ball positioned in the 380mm square working section. The tare was measured separately to account for the drag force on the sting and strut assembly, using a tare ball held separately to create a more realistic flow. The drag measurements were made over a wind flow rate of $17ms^{-1}$ to $70ms^{-1}$. The ball diameter was measured using callipers, with the final diameter being taken as the average of several measurements on several axes. The C_D of a smooth sphere was determined first and used as a qualification for the test method. Initial testing on tennis balls showed that the seam of a tennis ball has little or no effect on its C_D. Several balls were tested, and all were found to have a constant C_D of

just above 0.6 above a Re of 150,000, it was suggested that the boundary layer was in the transcritical regime at this stage.

2.6.4 Terminal velocity

Terminal velocity studies use the fact that fluids with higher densities will induce higher Reynolds numbers. Figure 2.17 shows a typical experimental set up for a study of this type, the additional mass shown is that of the fluid which both fills the ball and is absorbed into the nap. The motion of the ball is captured using a high-speed camera; motion analysis enables calculation of the velocity.

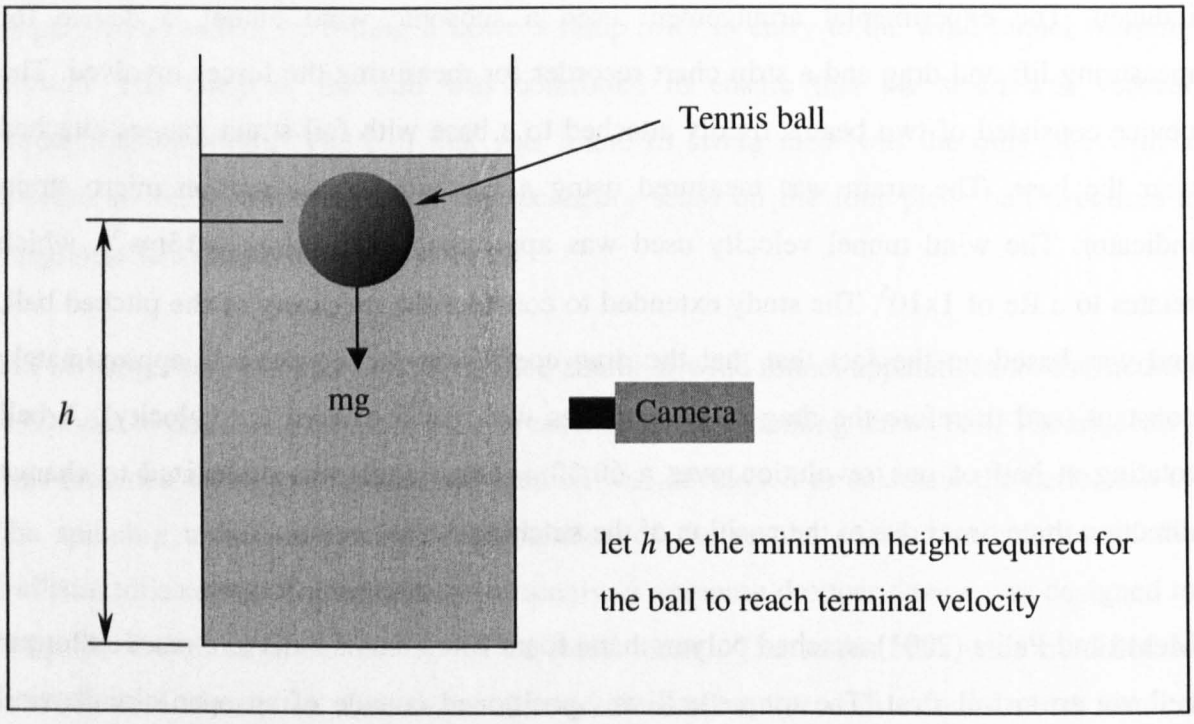

Figure 2.17 Schematic view of the apparatus required to determine C_D using terminal velocity experiments.

The motion of the ball can be explained using the following equation of motion:

$$m\ddot{y} = m_{eff}\, g - F_D \tag{2.14}$$

where: m_{eff} is the effective mass of the ball and fluid

$\ddot{y}$ is the vertical acceleration of the ball

However terminal velocity occurs when $\ddot{y} = 0$, which implies:

$$0 = m_{eff}\,g - \tfrac{1}{2}\rho v^2 C_D A \quad \Leftrightarrow \quad v^2 = \frac{2m_{eff}\,g}{\rho C_D A}$$

$$\Leftrightarrow \quad v_{term} = \sqrt{\frac{2m_{eff}\,g}{\rho C_D A}} \qquad (2.15)$$

Using an approximated volume of fluid, m_{eff} can be determined by adding the mass of the fluid to that measured for the empty ball, and subsequently used to estimate v_{term} (m_{eff} can only be measured accurately for the submerged ball). Assuming the fluid to be water:

$$m_{eff} \approx 0.144\text{kg} \quad \Rightarrow \quad v_{term} \approx 1.5\text{ms}^{-1}$$

Manipulation of 2.14 gives: $$mv\frac{dv}{dy} = m_{eff} - F_D \qquad (2.16)$$

and integration of 2.16 gives: $$y = \frac{m}{\rho C_D A} ln\left(\frac{2m_{eff}\,g}{2m_{eff}\,g - \rho C_D A v^2}\right) \approx \underline{0.13 metres}$$

Therefore a water filled ball will reach terminal velocity, from stationary, in approximately 0.13m, and the column of fluid will need to be taller than this such that v_{term} is guaranteed. It is possible that v_{term} could be achieved in less drop height, possible by increasing the mass of the ball or increasing the density of the fluid. The real v_{term} is obtained by motion analysis, and can be used in equation 2.15 to calculate the real C_D.

2.7 Experimental methods used to understand the flow

Whilst the calculation of the aerodynamic forces is essential when developing an understanding of the movement of the ball in air, it is equally important to understand why and how the forces occur. The following sections describe several test methods developed to qualitatively assess the flow around the ball.

2.7.1 Pressure coefficient, C_P

The pressure coefficient, C_P, is derived to compare the pressure differences observed locally with those measured in the flowing air of the wind tunnel, as seen in equation 2.17.

C_P is a dimensionless coefficient derived in the same way as C_D and C_L. It is commonly used throughout aerodynamic studies and in many cases a pressure reading will be given in terms of C_P rather than the pressure itself. The local pressure, p, is measured at the surface of a tennis ball, and p_∞ is the free stream pressure. The free stream pressure is identical to the static pressure used in the dynamic pressure measurement, hence reducing the number of measurable parameters required.

$$C_p = \frac{p - p_\infty}{q_\infty} \tag{2.17}$$

The dynamic pressure, q_∞, is defined by:

$$\textit{Dynamic Pressure} = \textit{Stagnation/Total Pressure} - \textit{Static Pressure}$$

$$\Leftrightarrow \qquad q_\infty = p_0 - p_1 \tag{2.18}$$

Rearranging equation 2.18 gives:

$$p = p_\infty + q_\infty C_p \tag{2.19}$$

which can be used to show the relationship between p and p_∞.

The value of C_P defines how much the local pressure differs from the free stream pressure in multiples of the dynamic pressure. The local stagnation point occurs when the pressure sensor is facing the oncoming airflow. At the stagnation point, C_P is equal to one; hence the local pressure is a magnitude of q_∞ greater than the free stream pressure.

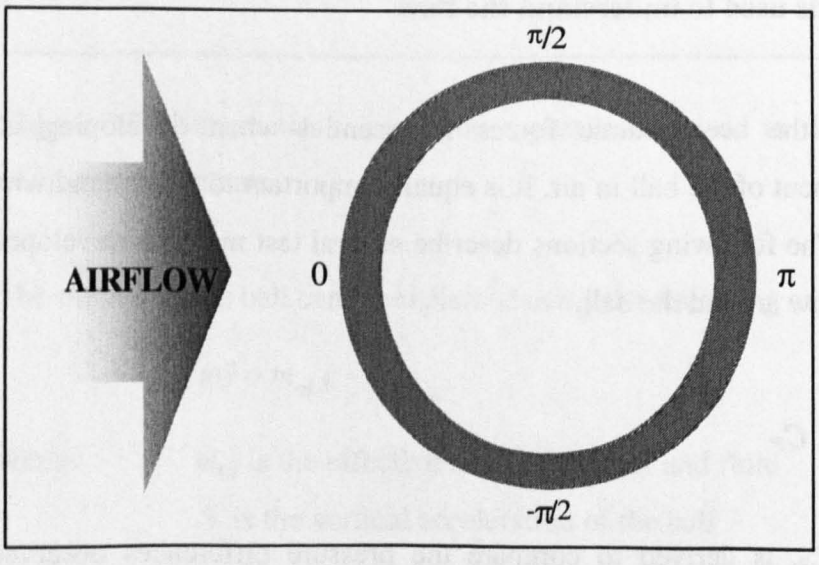

Figure 2.18 Schematic showing a section through a tennis ball at its maximum circumference with airflow impinging at point 0.

Figure 2.18 shows a cross section of a sphere used to define the change in C_P around the surface of the ball. As the velocity of airflow over the surface increases from zero at point 0 to a maximum at the top and bottom (points $\pi/2$ and $-\pi/2$), the pressure reduces from a maximum at point 0 to its minimum at points $\pi/2$ and $-\pi/2$. Hence, it can be deduced that C_P reduces from 1 at the stagnation points, reaching a minimum at the maximum flow rate over the surface.

The theoretical solution

The theoretical inviscid relationship between C_P and the sensing position of the local pressure is given by (Schlichting, 2000):

$$C_p = 1 - \tfrac{9}{4}\sin^2\theta \qquad (2.20)$$

The sensing position is measured as an angle, θ, to the horizontal with the forward facing stagnation point being zero degrees.

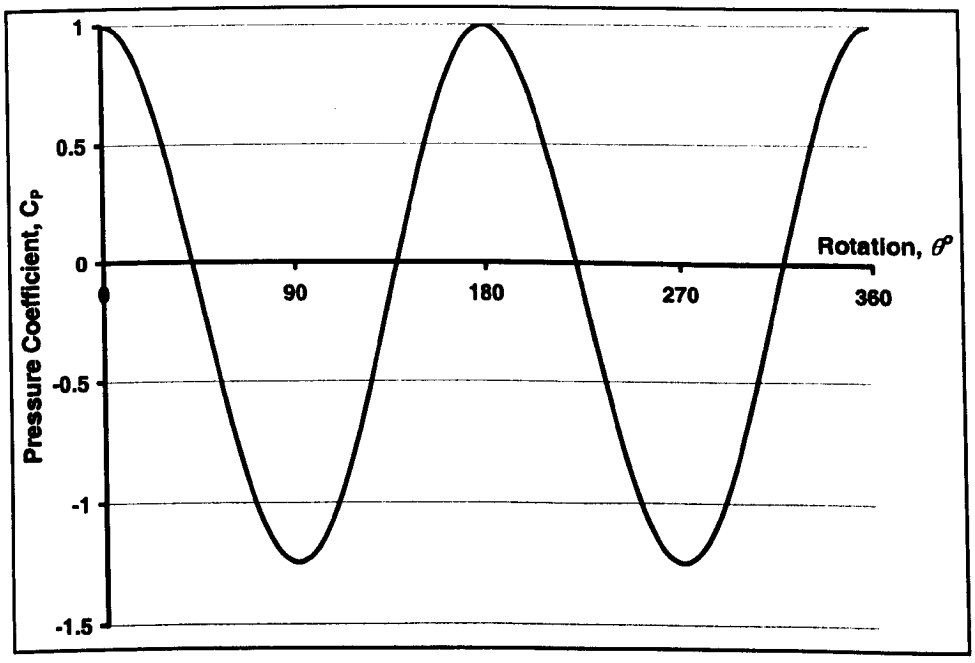

Figure 2.19 Relationship between C_P and pressure sensing point calculated using equation 2.20.

Figure 2.19 shows a graph produced using data created using equation 2.20. It can be seen that C_P starts at a value of 1 and steadily reduces to -1.25 at $\pm\pi/2$ (where $-\pi/2 = 270°$), the theoretical points of maximum velocity. The C_P then rises again in the adverse pressure gradient on the back face, returning to 1 at the rear most point. Hence the theoretical solution contains two stagnation points, with the second positioned at the back of the sphere.

In almost all cases, the relationship between C_P and the flow over the ball cannot be described by equation 2.20. It is more normal that the adverse pressure gradient will cause separation at some point around the surface. Literature relating to flow over spheres (Schlichting, 8th revision, 2000) has shown that the flow over a tennis ball is more likely to be similar to one of those shown in figure 2.20.

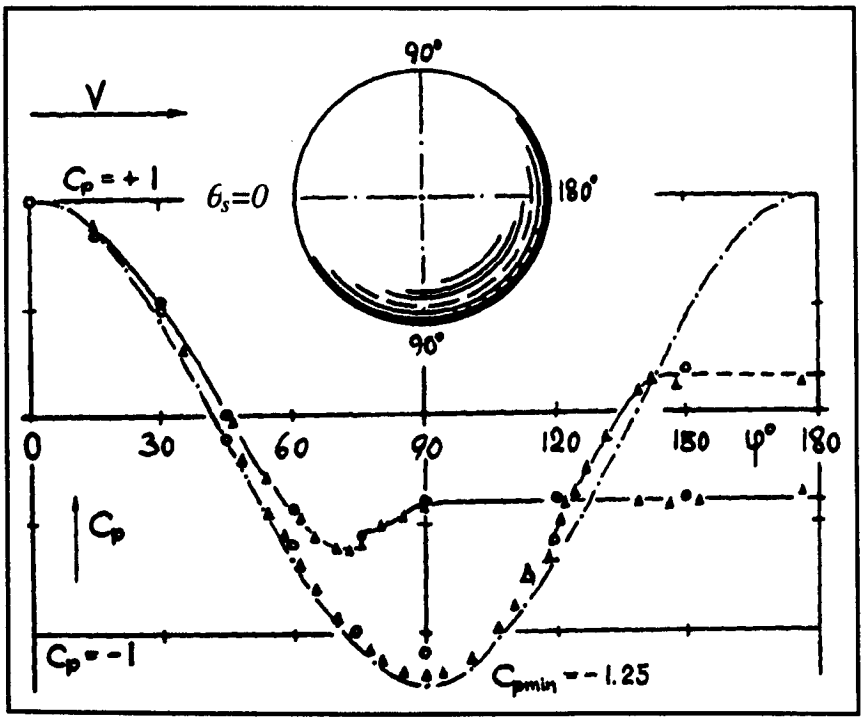

Figure 2.20 Chart showing the typical C_P results obtained around the surface of a sphere for different flow types (Hoerner, 1965).

Figure 2.20 shows data sets for two C_P distributions around the circumference of a sphere. The C_P profile shows the boundary layer separation points, where the point of separation is defined where there is a sudden change in direction of C_P, or where the C_P becomes constant. Separation is easily defined for the laminar flow, occurring near the poles and maintaining a constant pressure in the wake. The turbulent flow, having a thicker boundary layer with more energy, is more tolerant of the adverse pressure gradient on the rear face, making it able to recover significantly. The separation occurs on the rear face creating a small wake with relatively high pressure. It is therefore possible that understanding of these mechanisms could help in defining the flow regime around a tennis ball.

Achenbach (1972) measured the C_P distribution around a non-spinning smooth sphere to assess the effect of blockage in the working section for a range of Reynolds numbers. The Reynolds numbers chosen ranged from 2×10^5 up to 1.4×10^6, and the results were used to show the phenomena of laminar intermediate separation and turbulent reattachment of the boundary layer, where the downstream shift of the separation point causes a recovery in

the static pressure at the rear of the sphere. In this study the C_P and C_f measurements were used to establish the flow regimes around the ball.

Mehta (1985) used the C_P distribution to show why a cricket ball swings. The study used 24 pressure taps installed along the equator of the ball, in a plane perpendicular to that of the seam. With the seam angled at 20° to the oncoming flow, the results showed that at low speeds the pressure distributions were equal on both sides. As the Re increased the pressure on the side of the seam dropped lower than that on the other side, thus causing the ball to deflect towards the seam.

Briggs (1959) was able to assess the C_P distribution around a spinning smooth sphere, however the apparatus is not well defined. Although the phenomena of anti Magnus force had been shown previously by calculation of aerodynamic forces, Briggs used the C_P distribution to aid the understanding, showing that a ball that would conventionally be forced to the right, actually had a lower pressure on the left hand side.

2.7.2 Flow visualisation

Flow visualisation is a qualitative method with no quantification and conclusions are deduced purely by interpretation. The flow over the surface of bluff bodies has been discussed at some length in previous sections, and with this method it is possible to gain an understanding of the separation and boundary layer conditions.

The method is used extensively and can be applied in several different environments. Although the terminal velocity test method suggested the use of water as the fluid, it will be more normal to test tennis balls in airflow. The flow lines are created in several different manners, helium filled soap solution and paraffin vapours are the most widely adopted.

The application of the smoke can be achieved in two ways depending on the aim of the study. If the flow over the bluff body is of interest, then the flow lines are flowed over the ball through a 'comb' positioned upstream. Alternatively, the smoke can be injected into the wake, where the unsteady flow behind the object induces chaotic smoke activity.

The smoke can be viewed through a camera against a black background, however additional lighting helps fluorescence. Time lapsed capture images of the smoke flow can then be captured and compared against one another to help understanding.

Flow visualisation methods have been used widely to discuss the lateral deflection of a spinning ball. Mehta and Pallis (2001) used the deflection of the flow lines travelling over the surface of a 280mm tennis ball to show why the ball dips on a top spinning shot. The deflection of the flow lines showed the asymmetry in the wake, which thus relates to asymmetry in boundary layer separation and hence in pressure, therefore the direction of the lift force can be interpreted. In the interesting case of anti Magnus, the deflection of the flow lines is the reverse of that which may be expected, thus showing lift force acting in the opposite direction. The study covered wind speeds up to $66ms^{-1}$, and no evidence of a change in direction of the flow lines was observed around the oversized tennis ball.

Mehta (1985) discusses the flow over several sports balls, and used flow visualisation techniques as a way of confirming an experimental C_P distribution. Smoke was injected into the separated region behind a cricket ball with its seam positioned 40° below the horizontal, and it was shown that the flow leaving the top surface was smooth and hence proved laminar separation. On the bottom surface however, the flow was 'tripped' by the seam and separated turbulently on the rear surface. The resulting wake was deflected upwards and thus signified a downward lift force.

2.8 Trajectory models

The trajectory model is normally produced to assess the differences that may be observed in flight due to differing aerodynamic parameters that may have been studied. Tait (1896), in his study to define the path of a rotating spherical projectile (golf ball), is one of the first reported studies that use a trajectory model. The trajectory was assumed to be an equilateral polygon of 6' sides, calculating its angle to the horizontal. The equations of motion were formed as differential equations, and the trajectories solved by hand.

With the improvement in computing power, such calculations can be achieved in a fraction of the time. There are several methods used to define the trajectory of sports balls, and the

ability to make use of each method often depends on the assumptions that have been made.

Stepanek (1987) used a radius of curvature method to assess the flight of a top-spin lob in tennis. The model was created assuming that the lift force acted towards the centre of curvature, hence the C_D was ignored.

By far the most commonly used method uses the equations of motion obtained from a force diagram. The trajectory is formed using an iterative process that calculates the change in velocity over a small time period for the equations of motion formed for the given trajectory. As the time period is known, the combination of known parameters can be used to calculate the co-ordinates of the ball.

Davies (1949) used C_D and C_L data obtained by assuming the drag and lift forces acted horizontally and vertically for a spinning golf ball. These same figures were then used in the trajectory model acting in the conventional directions.

Erlichson (1982) investigated various methods for calculating the maximum range of a golf drive. Drag and lift data previously obtained by Davies and Williams (1959) was used for the assessment. Trajectory models were used to determine the optimum angle at which a ball should be projected to give the maximum range. It was found that by changing the drag coefficient, both the range and the optimum angle changed.

Of course, in most cases the ball does not spin on a perfectly horizontal axis. The resulting lift force will therefore contain a sideways parameter, hence creating a three dimensional trajectory. McPhee and Andrews (1987) studied the effect of sidespin and wind on the trajectory of golf balls. The three-dimensional trajectory model was based on a two dimensional model previously presented by Erlichson in 1983. Three differential equations of motion were solved for v_x, v_y and v_z, which were then integrated analytically to obtain the displacements $x(t)$, $y(t)$ and $z(t)$. The equations were solved using a FORTRAN-77 program, producing a computational trajectory from t=0 to the point where the ball returned to ground level (z=0). Although the three dimensional model produces satisfactory trajectories, it was suggested that the approximations used for C_D and C_L were inadequate for the full range of strokes used in the game of golf. Further development of

the model to include empirical coefficients was proposed, however it would not be possible with the current analytical model.

2.9 Aerodynamic coefficients of tennis balls

The studies investigating the aerodynamic properties of tennis balls are normally split into non-spinning and spinning. The non-spinning studies can determine C_D only, which is completely different to that of the spinning C_D. The following sections will deal with the C_D and C_L obtained in non-spinning and spinning studies separately.

2.9.1 Non-spinning studies

Zayas (1985) used a projectile test to find the C_D of a non-spinning ball projected horizontally up to 26.8ms^{-1}. Based on 50 tests, the C_D was found to be 0.51±0.08, which relates to a confidence limit of 15.7%.

Mehta and Pallis (2001) used a load cell in a wind tunnel to estimate the C_D on a non-spinning tennis ball in a Re range, 80,000<Re<300,000. Several new (unused) tennis balls were studied and it was found that the C_D ranged from 0.6±0.01 to 0.63±0.01, and suggested that the additional C_D contribution was due to the method used to define the diameter of the tennis ball and 'fuzz drag'. The accuracy of the C_D results obtained using this test method is improved significantly to less than 2%. Further discussions suggested that the C_D increases with initial ball wear causing the nap to 'fluff up', and decreases with further use as 'the cover becomes worn and the fuzz starts coming off'.

2.9.2 Spinning studies

There has only been one study performed on spinning tennis balls, Stepanek (1987) used a drop method to investigate the aerodynamics of tennis balls for speeds between 13.6ms^{-1} and 28ms^{-1}. A range of spin rates was chosen to create a set of spin parameters up to around 0.6. Extrapolation showed that a non-spinning ball had a C_D of approximately 0.51. A spinning ball was found to have a C_D up to 0.80±0.09 and a C_L up to 0.49±0.1

3 TEST EQUIPMENT AND SET-UP PROCEDURES

This study has utilised several test methods to increase the understanding and define the aerodynamic properties of tennis balls. The following sections describe the apparatus used and outline the set-up procedures necessary for accurate results gathering.

3.1 Wind tunnels

Three distinctively different wind tunnels were used throughout this study. The defined requirements included flow visualisation, pressure profile plotting and aerodynamic force measurement. The following sections describe the physical properties and proposed function for each of the wind tunnels used.

3.1.1 Low-speed

The low-speed wind tunnel has a maximum attainable wind speed of approximately 26ms^{-1} after blockage effects of the apparatus are accounted for. It is open ended with a turbulence factor of 1.71 (0.85%) (Cartwright, 1997) across a working section of 715mm x 512mm. It is understood that this turbulence level is high, however this is typical of tunnels of this type (Pope and Harper, 1966). Screens are fitted to the opening of the wind tunnel to improve flow, the velocity variation is within 0.5% for approximately 90% of the working section area. The ball and sting assembly take up less than 3% of the test section area, hence blockage effects can be assumed to be negligible.

3.1.2 High-speed

The high-speed wind tunnel is not officially high-speed, however it is useful to refer to it as the high-speed wind tunnel for the purposes of this study. It is rated at a maximum wind speed of 150mph (67ms^{-1}), however the highest wind speed attainable with apparatus in place was approximately 61ms^{-1}. Airflow is re-circulating with a turbulence factor, calculated using methods described in chapter 2, of 1.087 (0.123%) across a working section of 1.65m x 1.2m. Screens are fitted ahead of a 7:1 (approx.) contraction to improve

flow, with the velocity variation within 0.5% for approximately 93% of the working section area. The blockage due to the sting and ball assembly was approximately 0.3% of the test section area, hence no correction procedures were required.

3.1.3 Smoke flow

The smoke flow wind tunnel shown in figure 3.1 is specifically designed for flow visualisation analysis. The airflow travels from the bottom to the top of the working section, which is approximately 250mm wide and 500mm high with a depth of approximately 175mm.

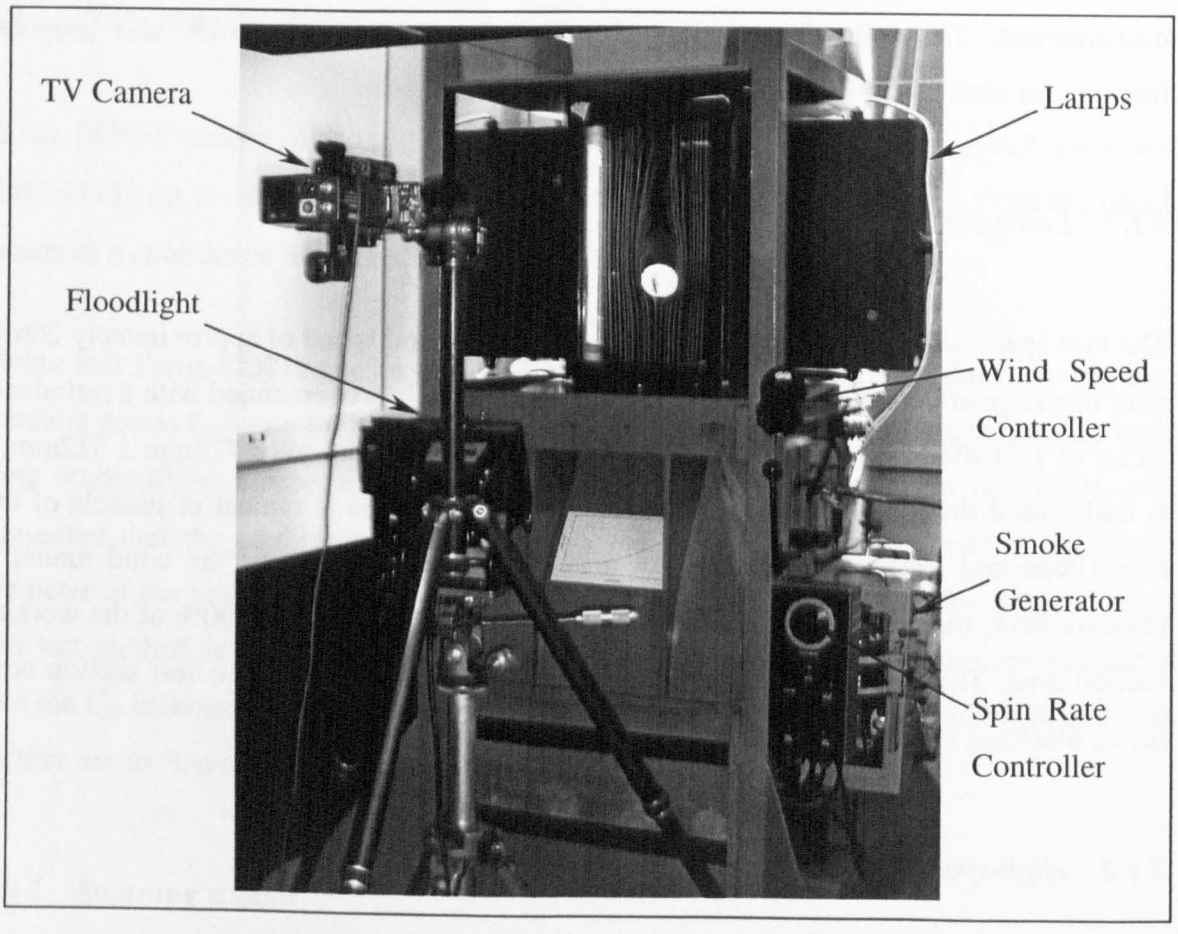

Figure 3.1 Apparatus required to create smoke flow around a tennis ball.

The flow lines are created using a paraffin smoke generator mounted on the side of the wind tunnel, with a comb being used to distribute the smoke at regular intervals. Figure 3.2 shows a picture of a comb, it can be seen that it consists of an airfoil section containing a

hole along its length with several brass pipes inserted into the rear of the airfoil section at regular intervals.

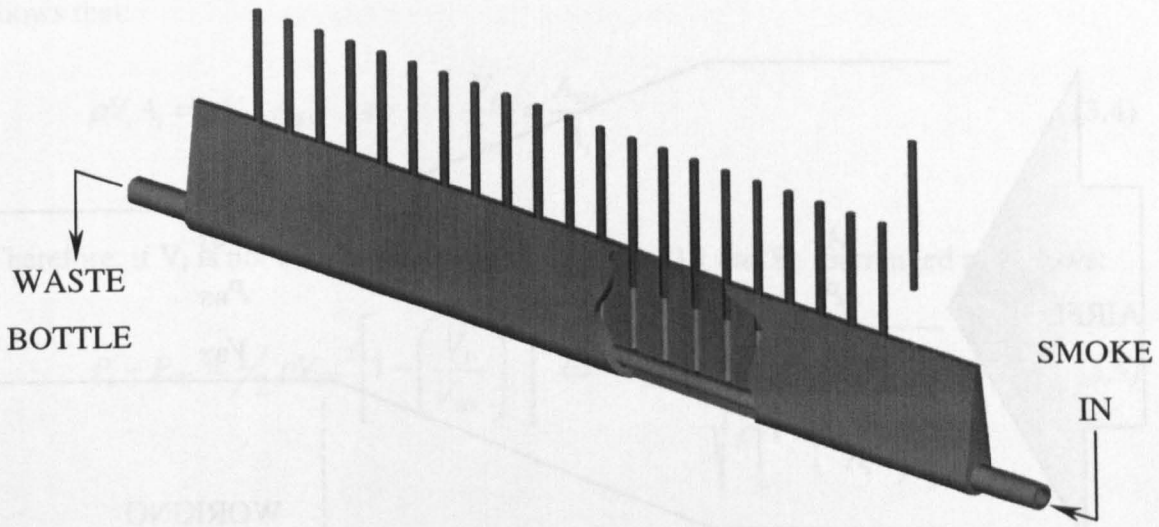

Figure 3.2 Comb used to distribute the flow lines around the ball at equal increments.

The smoke feeds into one end and is then capillaried into the brass pipes. A glass bottle is connected to the other end to capture any condensing paraffin vapours.

3.1.4 Calculating the velocity of airflow

The wind velocity is calculated in one of two different ways: the differences in atmospheric conditions across the contraction section prior to the working section was used in the high-speed wind tunnel; and a pitot static probe within the working section was used in the low-speed wind tunnel.

Pressure difference across the contraction

Static pressure is the measure of the random motion of molecules in the air, measured using a small hole perpendicular to the flow of air. If a reference to pressure is made without further qualification, that pressure is the static pressure. At the start of the contraction, in the reservoir, the pressure is high and the velocity of the air is low (and in the first example is assumed to be stationary), by the end of the contraction the airflow has accelerated resulting in a drop in pressure.

Figure 3.3 shows a schematic of the contraction with the air flowing from left to right. Air in the reservoir has a pressure and velocity of P_i and V_i, and when it reaches the working section it has pressure and velocity of P_{WS} and V_{WS}.

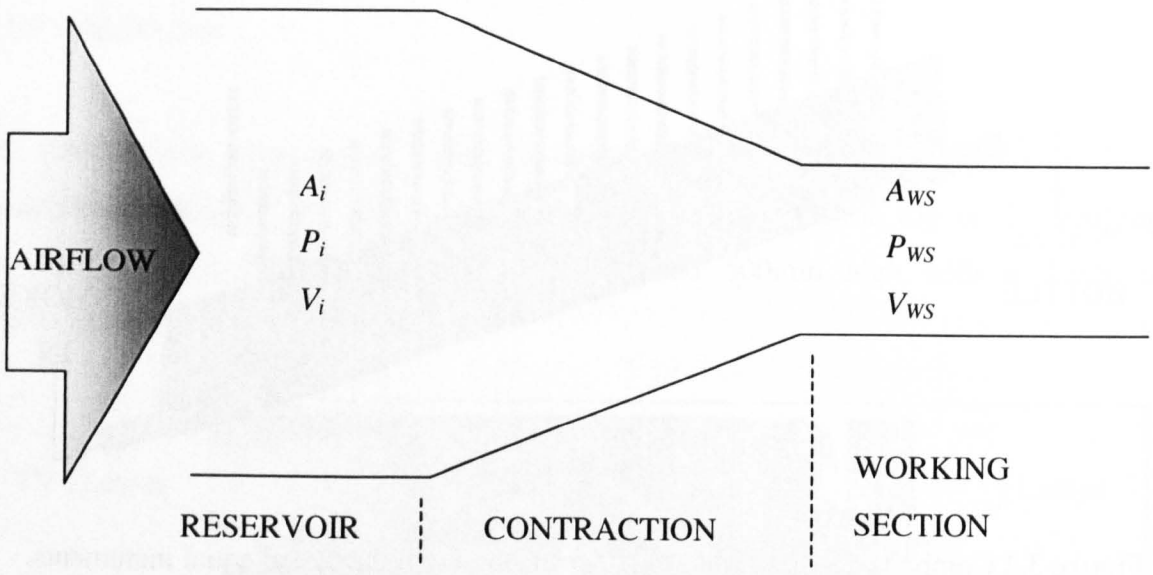

Figure 3.3 Schematic showing a contraction with the velocity and pressure in the before and after.

Bernoulli's conservation of energy equation for inviscid, incompressible flow (ignoring terms related to potential energy) is as follows:

$$P_i + \frac{1}{2}\rho V_i^{\,2} = P_{WS} + \frac{1}{2}\rho V_{WS}^{\,2} \tag{3.1}$$

As the velocity of the air in the reservoir, V_i, is low enough to be assumed to be zero, Bernoulli's equation can be reduced to the following:

$$V_{WS} = \sqrt{\frac{2(P_i - P_{WS})}{\rho}} \tag{3.2}$$

where: $$(P_i - P_{WS}) = Dynamic\ Pressure \tag{3.3}$$

A digital manometer is connected across the contraction of the wind tunnel to measure the dynamic pressure. Readings are taken at each increase/decrease of wind speed and entered into a spreadsheet that is formatted to automatically calculate the new wind speed.

Although the airflow in the reservoir has been assumed to be stationary throughout this study, it is understood that this is not realistic. It is therefore useful to assess the errors that may be introduced using this method. For incompressible airflow, the conservation of mass shows that:

$$\rho V_i A_i = \rho V_{WS} A_{WS} \quad \Leftrightarrow \quad \frac{V_i}{V_{WS}} = \frac{A_{WS}}{A_i} \tag{3.4}$$

Therefore, if V_i is not assumed to be zero, equation 3.1 can be rearranged as follows:

$$P_i - P_{WS} = \tfrac{1}{2}\rho V_{WS}^2 \left[1 - \left(\frac{V_i}{V_{WS}}\right)^2\right] \quad \Leftrightarrow \quad V_{WS} = \sqrt{\frac{2(P_i - P_{WS})}{\rho\left[1 - \left(\frac{A_{WS}}{A_i}\right)^2\right]}} \tag{3.5}$$

In the high-speed wind tunnel, the entrance of the contraction was approximately 3.5m square, and thus the calculated V_{WS} in this study is estimated to be around 1% lower than that obtained using equation 3.5.

Pitot static probe

The Pitot static probe is positioned a short distance up stream of the model under test, it contains two holes, one perpendicular to the flow (p_1) and one facing the flow (p_0) as can be seen below:

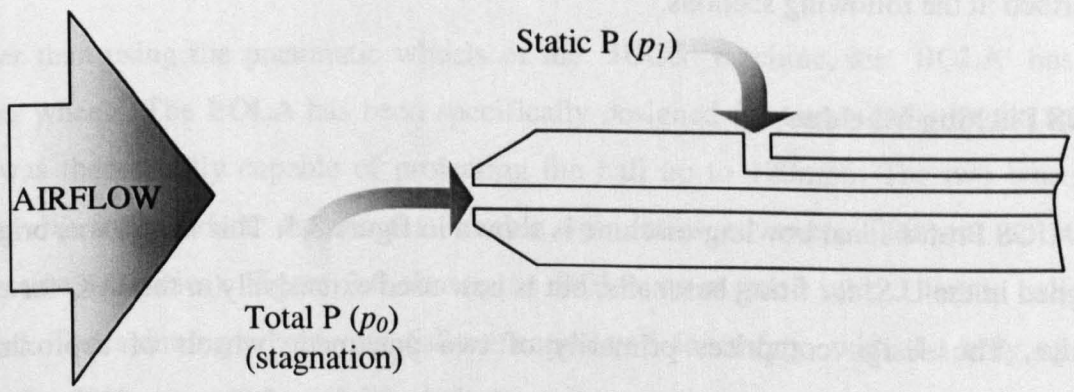

Figure 3.4 Schematic of the front section of a Pitot static probe.

The static pressure, p_1, is felt across a small pressure tapping on the circumference of the tube perpendicular to the airflow. The hole at the front of the tube collects incoming air

until the volume is completely filled. At this point the oncoming air impinges on the front surface of the tube as if it were an obstruction to the flow, hence at the entrance to the tube the velocity of air is reduced to zero, a stagnation point of flow, where the pressure is p_0. The pressure difference, p_0-p_1 is the dynamic pressure, measured using a digital manometer. The figure can be used directly in equation 3.2 to calculate the velocity of air in the working section.

3.2 Projecting devices

There have been four different projecting devices developed and used throughout this study. Horizontal projections were achieved using pitching devices and vertical trajectories through the moving airflow of a wind tunnel were achieved using dropping devices. Two of each type of projection device have been developed and used in this study, and are described in the following two sections.

3.2.1 Pitching devices

A pitching device is used to accelerate a ball as it passes through two wheels spinning in opposite directions. The trajectory is created by aiming the head of the pitching device at an elevation angle to the horizontal, where the resulting flight path can be used to define the aerodynamic forces acting on the ball. Two pitching machines have been used and are described in the following sections.

JUGS Pitching Machine

The JUGS Professional bowling machine is shown in figure 3.5. This model was originally designed in the U.S. for firing baseballs, but is now used extensively in the U.K. for cricket practice. The design comprises primarily of two pneumatic wheels of approximately 400mm diameter, which can be set independently to rotate from 240rpm to 2280rpm.

The wheels and feeding chute are mounted on a yoke, which is connected to a supporting tripod by a ball joint. Balls are fed into the machine via the chute and through the gap between the wheels which is approximately 1/3 of the diameter of the ball. The ball is

gripped and theoretically projected at the linear speed of the wheels. The orientation of the wheels and the direction of travel can be adjusted using the ball joint, which is clamped in place using a large screw wheel. The choice of wheel setting allows control of the ball speed as well as back and top-spin.

Figure 3.5 Picture of the pitching machine mounted on a custom built stand used for projecting the tennis balls up to 100mph

Based on previous work undertaken using this pitching machine, speed of up to 50ms^{-1} (≈110mph) and spin rates of approximately 6000rpm are attainable.

BOLA

Rather than using the pneumatic wheels of the 'JUGS' machine, the 'BOLA' has solid rubber wheels. The BOLA has been specifically designed for tennis balls by the supplier and was theoretically capable of projecting the ball up to 120mph. The two wheels are driven by independent motors that enable spin rates of over 3000rpm (at reduced projection velocities). Figure 3.6 shows the BOLA on a stand with a tennis ball being loaded. The spinning wheels are fully encapsulated for safety, with the only openings being for the input and output of the ball.

The speed and spin was controlled using two dials, and the theoretical ball velocity was displayed on a digital readout, however accurate velocity and spin measurements were also obtained with the use of high-speed digital photography.

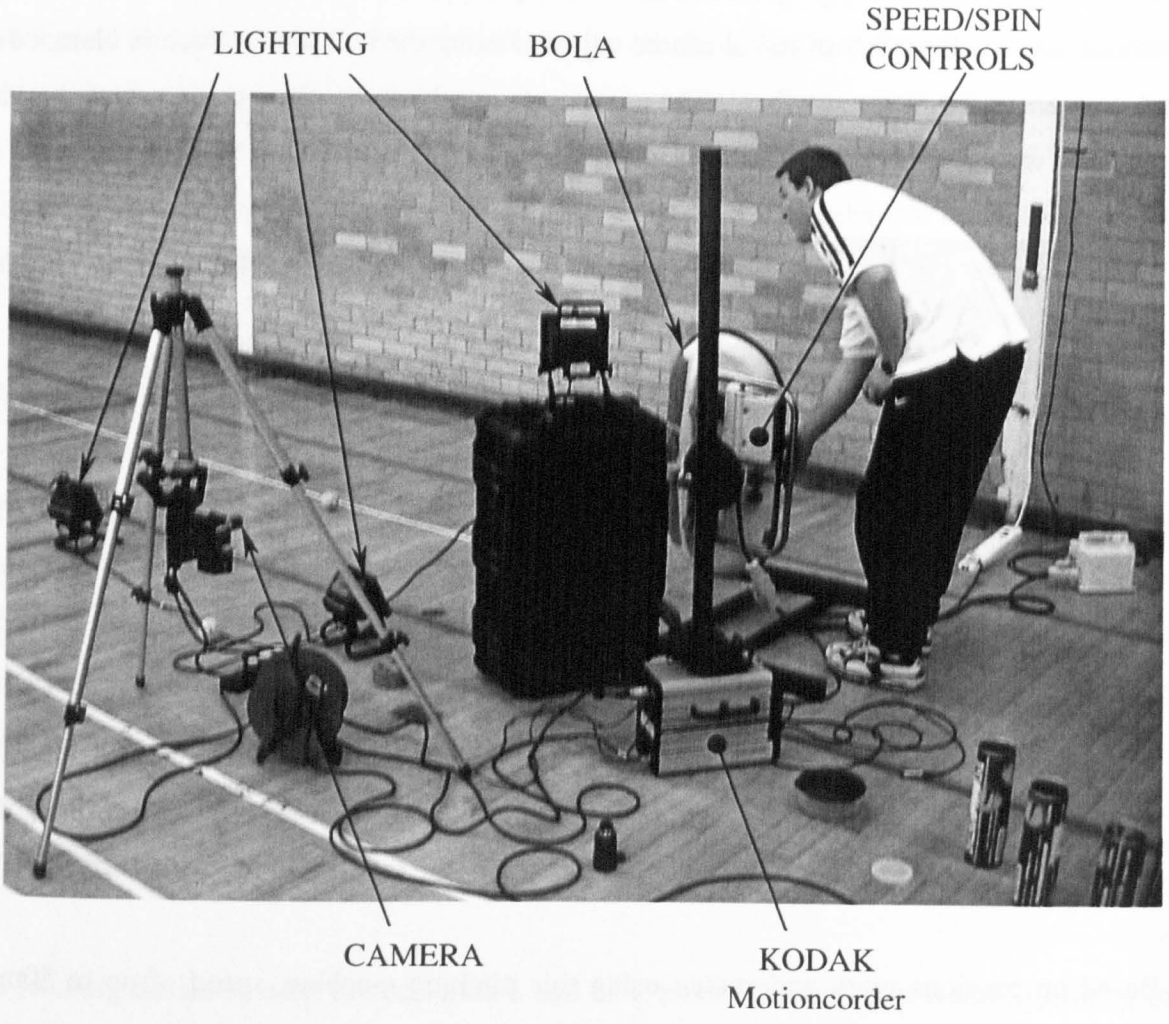

Figure 3.6 BOLA machine with the camera and lighting required enabling the capture of speed and spin data as the ball departs the projecting machine.

3.2.2 Dropping devices

Dropping devices have been developed to assess the deflection of a tennis ball as it travels through the moving air of a wind tunnel. There were two dropping devices used during investigation and they have been differentiated between by their design criteria; non-spinning and spinning.

Non-spinning drop

The non-spinning dropping device consisted of a sheet of aluminium, with a section detached in the centre. The outer plate was clamped to a stand, and the inner plate hinged

to the outer section. This dropping device was designed such that upon a trigger the inner plate would drop. The speed that the inner plate retracted had to be faster than that imparted on the ball due to gravity.

The inner plate was held in place using a solenoid, and a trigger prompted the retraction of the solenoid and therefore released the inner plate. A spring was attached at the hinged end to accelerate the inner plates decent and therefore remove it from the path of the falling ball. Figure 3.7 shows a picture of the non-spinning dropping device just after the solenoid has been triggered. The ball was positioned onto a machined indent on the upper surface of the inner plate using the guide shown.

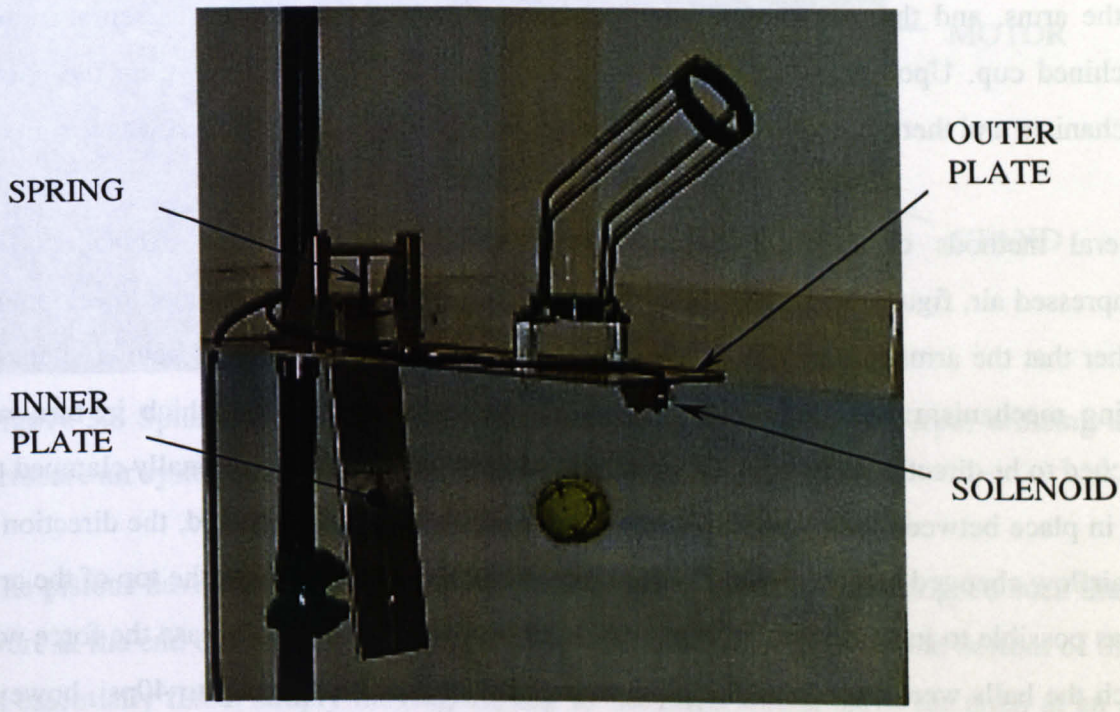

Figure 3.7 Dropping device designed to drop the ball without imparting spin.

It was thought that the more deflection obtained due to the wind the more accurate the results would be. Greater deflection during the ball drop was obtained by minimising the speed of the ball at the entry point to the wind tunnel, hence keeping the height of the dropping device above the wind tunnel to a minimum. The length of the inner plate limited how close the dropping device could be positioned, hence a more flexible device was developed.

Spinning drop

The spinning dropper was designed and built at the University of Sheffield with the help and expertise of Terry Senior. It was designed to apply spin whilst holding the ball in place, and upon a manual trigger, drop the ball vertically through the airflow. The spinning axis was horizontally perpendicular to the flow of air, positioned to apply top and back-spin. As with the non-spinning dropping device, the holding arms have to retract quickly enough not to cause the ball to deflect across the airflow.

The original concept used powerful contraction springs to retract the arms of the dropping device, with the arms contained within a sliding mechanism. A motor was attached to one of the arms, and the rotor arm of the motor passed through a bearing assembly into a machined cup. Upon manufacture, it was found that the arms bound within the sliding mechanism and therefore were not free to slide, and so further development was required.

Several methods of retraction were considered, it was eventually decided to use compressed air, figure 3.8 shows a picture of the spinning dropper after final development. Rather that the arms sliding, they were modified to produce a hinge just below where the sliding mechanism had been. A piston was attached to each arm, which in turn was attached to bi-directional switch. The switch was normally on, hence normally clamped the ball in place between the machined cups. When the switch was depressed, the direction of the airflow changed and the pistons pulled the arms away rotating about the top of the arm. It was possible to increase the air pressure to the pistons, and hence increase the force with which the balls were clamped. The pipes and connectors were rated up to 40psi, however due to inherent out of balance problems with tennis balls, higher working pressures were sometimes used to keep the ball in place when spinning.

The sliding mechanism was used as a clamping mechanism so that the dropping device could be used for all tennis balls to be tested, indeed, it is possible that sizes ranging from a table tennis ball up to 120mm diameter ball could be accommodated. A standard tennis ball is nominally 66mm, hence the distance between the cups was set slightly smaller to grip the ball. It was found that this setting was not suitable for each test, not only was the size different, but the construction and shape also changed. The permanent pressure ball was significantly stiffer than the standard ball, hence required less pressure to hold it in

place, moreover tennis balls change shape at very high spin rates causing them to thin along the axis of spin. To overcome these issues, the spinning dropper was designed such that the arms could be moved closer together.

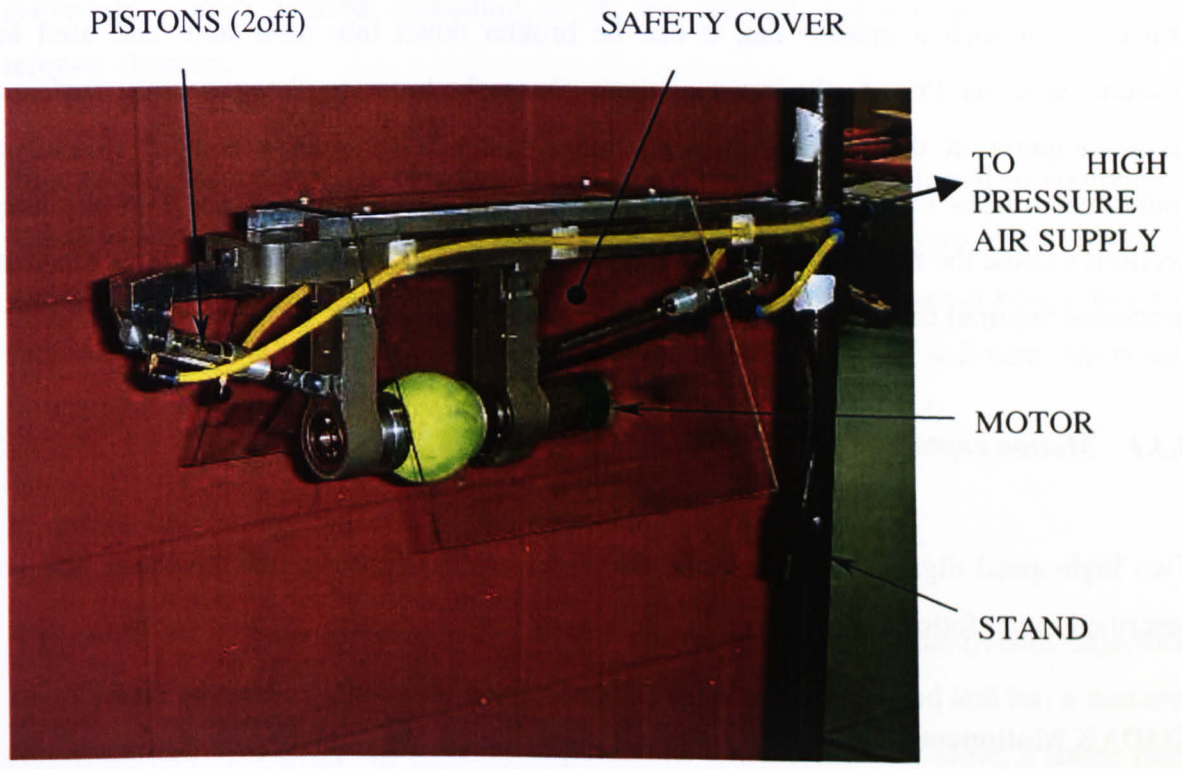

Figure 3.8 Spinning dropping device, capable of rotating up to 7000rpm utilising a high pressure air system for release.

The pistons have limited movement, and the spinning dropper was designed such that they were at the end of their travel when the ball was firmly clamped. As the bottom of the arm is essentially fixed, simply moving the top of the arms would leave the arms at an angle. This was overcome using extension rods that were added between the piston rod and the arm. It was envisaged that several sets of extension pieces would be required, one set for each ball type.

Due to its compact design, the spinning dropper was capable of releasing the ball much closer to the wind tunnel. Given this fact and its aforementioned flexibility, once this dropping device became available it was used for all drop testing.

3.3 Image analysis apparatus and techniques

The aerodynamic forces acting on a ball travelling through the air can be calculated by analysing the shape of the trajectory. Motion capture apparatus is required to capture the trajectory in such a manner that it can be broken down into time steps and used for accurate analysis. Prior to the image analysis phase, the trajectory images were transferred to a computer in the required format. Image analysis software was used to analyse individual images to define the ball co-ordinates at specified time steps. The following sections outline the fundamental apparatus required for motion capture and the subsequent processes required for analysis.

3.3.1 Motion capture

Two high-speed digital motion capture devices were used throughout this study and are described in the following sections.

KODAK Motioncorder

The KODAK Motioncorder high-speed digital camera was capable of capturing images up to 600 frames per second with an exposure rate of 0.0001s. Minimum recording time was approximately 4 seconds, ample for any trajectory in this study. The recording time is offset against viewable image size, at 600 frames per second the visible window was reduced to 360 x 120 pixels, with a resolution of 72 pixels per inch. Images were stored continuously in a dynamic random access memory. A manual trigger was used to stop the continuous recording and store a defined set of images. With the trigger set to 'start', the recording started at the trigger point; with the trigger set to 'end', the camera recorded all images 4 seconds prior to the trigger pulse; and with the trigger set to 'centre', the camera recorded images 2 seconds prior to the trigger and continued for a further 2 seconds.

Images were viewed through the LCD of a Hi8 portable video recorder, they cannot be used or downloaded directly from this digital camera, hence they had to be transferred to 8mm video tape. The video recorder was set to record several seconds before the digital recorder was set to playback, which ensured that no important images were lost. Each

recording was given an identification number, which was noted down against a description of the trajectory.

A means of calibration was required to ensure that the data obtained was applicable, the calibration process differed depending on the test method, and will be discussed in the relevant chapters.

Prior to any formal analysis, the analogue video footage was transferred to computer. A dedicated Iomega *buz* digitising card and *Microsoft® VidCap* software was used for this purpose. Images were digitised at 2 frames per second to match the rate at which they were recorded. Individual images were extracted in sequence using further software, *Microsoft® VidEdit 1.1*, and at this point any unwanted images could be discarded.

Phantom v4

A Phantom v4 high-speed video system was used to record some of the overall trajectories. This camera is capable of recording at up to 30,500 frames per second and has a maximum resolution of 512 x 512 pixels. As the flight of the ball is relatively slow, a frame rate of 400 frames per second was sufficient to capture the information required. The video system was controlled using Phantom v4 software on a PC laptop and the images were stored in the native cine file format. For the purposes of future motion analysis these cine files were converted to AVI's that could then be opened directly into image analysis software which is described in the next section.

It was important to ensure that the focal axis of the camera was perpendicular to the flight of the ball and in the same plane. Calibration for the Phantom v4 camera was achieved using a 2m reference pole positioned along the plane of the trajectory in 1m increments.

Simultaneous triggering

A simultaneous triggering mechanism was designed such that both cameras would start recording with a single impulse. It consisted of a trigger connected to two equal lengths of

BNC cable via a 'T' joint. The trigger was standard issue with the cameras, and the two lengths of cable were stored on a 10m rotary cable tidy.

3.3.2 Image analysis

Image analysis was performed using dedicated software, *Richimas*, a programme that was specially developed within the research group. It was found that most of the tools available from the existing 'single user' software, *Optimas 6.0*, was not required for most of the analysis undertaken by the group. In addition, Richimas used a circle to calculate the position of the ball, the centre of which was exported to a spreadsheet, and the co-ordinates of several images made up a trajectory. Spin rate was calculated by monitoring the change in angle between consecutive images, achieved as a secondary process within Richimas and exported as an additional data set.

The following sections give an overview of some of the similar processes undertaken during the image analysis phase, however the more specific details are outlined in the related chapters.

Scaling factor

Prior to analysing images of the balls, a scaling factor was calculated using the calibration image for each trajectory. The distance between the reference points was compared to the number of pixels and a scaling factor formed, which was then applied to all subsequent images for analyses using that camera set-up.

The aspect ratio is skewed using this particular digitising card and software. When fitting a circle over an image of a ball, it is desirable for the aspect ratio to be corrected. The scaling factor was calculated for both horizontal and vertical corrections separately and a simple correction factor using percentages was applied, where one of the orientations was 100%. The process is performed using *DeBabelizer® Pro version 4.5* from *Equilibrium*. A script is written to change the length and height of a batch of images independently, such that the ball appears round. Whilst performing this operation, it is normal to reduce the size of the images to save space on the computer's hard disk. This is achieved by converting the

image to greyscale and reducing the number of colours used, the process is added to the script and performed at the same time.

The new images, with the correct aspect ratio, were then used to complete the calculation of the co-ordinates that form the flight path of the ball.

Complete trajectory

Figure 3.9 shows a typical image used to track the ball throughout its trajectory. As can be seen the image of the ball is small compared to the size of the complete image, and the spatial resolution is discussed in individual chapters.

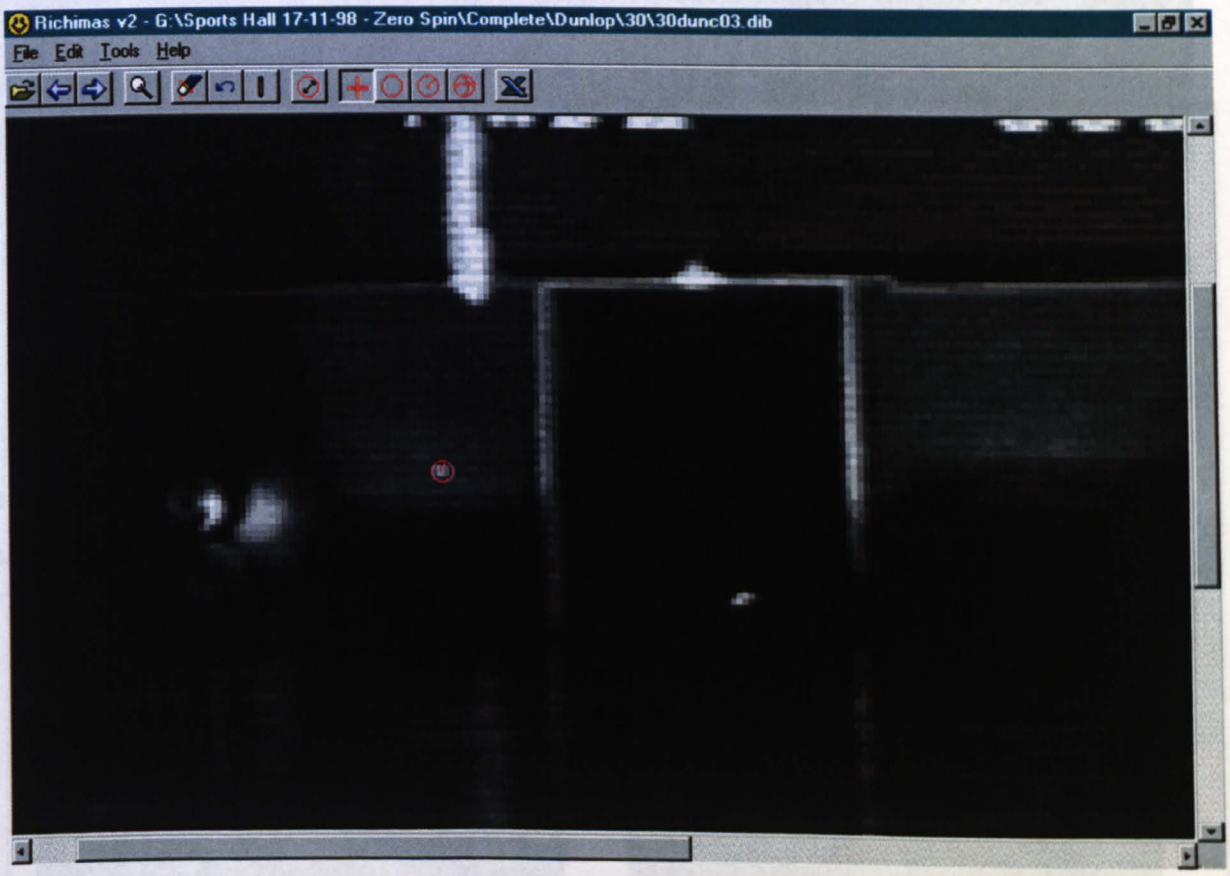

Figure 3.9 Picture showing a typical image used to find the speed and angle of the ball throughout its trajectory.

In an attempt to improve accuracy at the data collection stage, a circle was used to surround the image of the ball rather than a reference point on the ball. This particular picture is the 4th image of the sequence taken from a trajectory of a ball projected at a

nominal speed of 30mph and zero spin. Each image from a single trajectory was opened in turn and the ball tagged with a circle. The co-ordinates of the centre of the ball are exported into a spreadsheet for further manipulation.

Figure 3.10 shows the overlaid images for the trajectory of the normal pressurised ball projected at a nominal speed of 30mph and zero spin. As can be seen, the quality of the images of the ball is fairly poor and knowledge of the shape of a trajectory helps find the ball within the image. If the ball is not visible, then the frame was ignored and allowed for in the time steps in the spreadsheet.

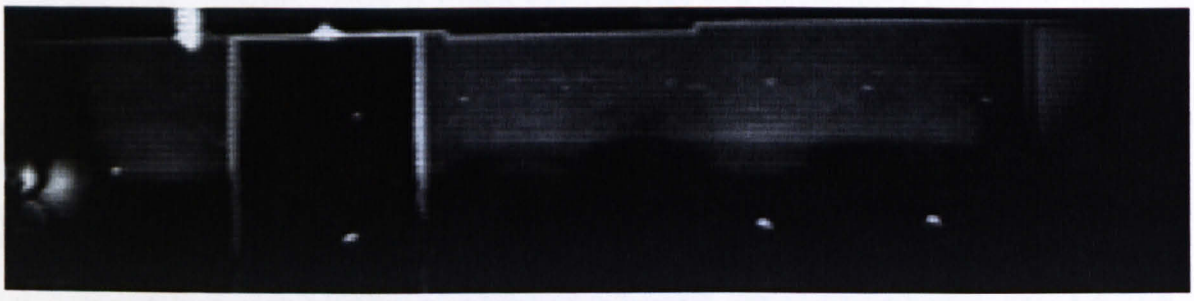

Figure 3.10 Picture showing the overlaid images for the trajectory of a normal pressurised ball projected at a nominal speed of 30mph with zero spin.

Ball markings

In order to conduct the motion analysis, and in particular calculate spin rates, reference points were required on the surface of the ball, figure 3.11 shows a picture of a 'marked-up' normal pressurised ball in two orientations.

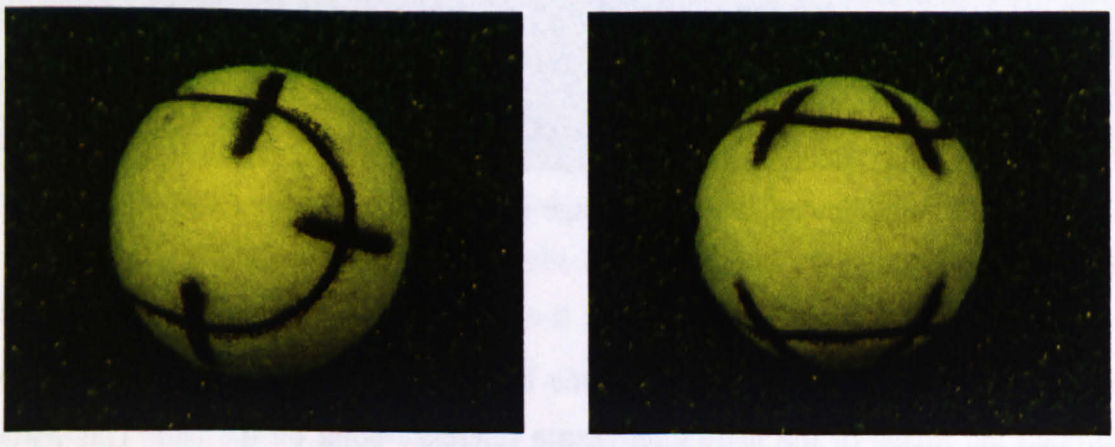

Figure 3.11 Ball markings applied to all balls to allow the calculation of spin.

The ball on the left shows the markings applied to the end of one of the bells of material, and the ball on the right is rotated to show the markings in the middle of the bells of material. The whole seam was blackened and crosses applied at eight regular intervals, where the pattern shown on the left hand picture was repeated for each of the four bell ends. The markings were applied using a standard thick black permanent felt tip pen. At least two of the crosses were required for calculation of spin.

Close up analysis

Figure 3.12 is a magnified image of a normal pressurised ball leaving the pitching machine with a nominal speed of 30mph and zero spin. The camera taking these images is close to the exit of the pitching machine, thus the quality of images is far greater, actual spatial resolution is discussed in greater detail in the individual chapters.

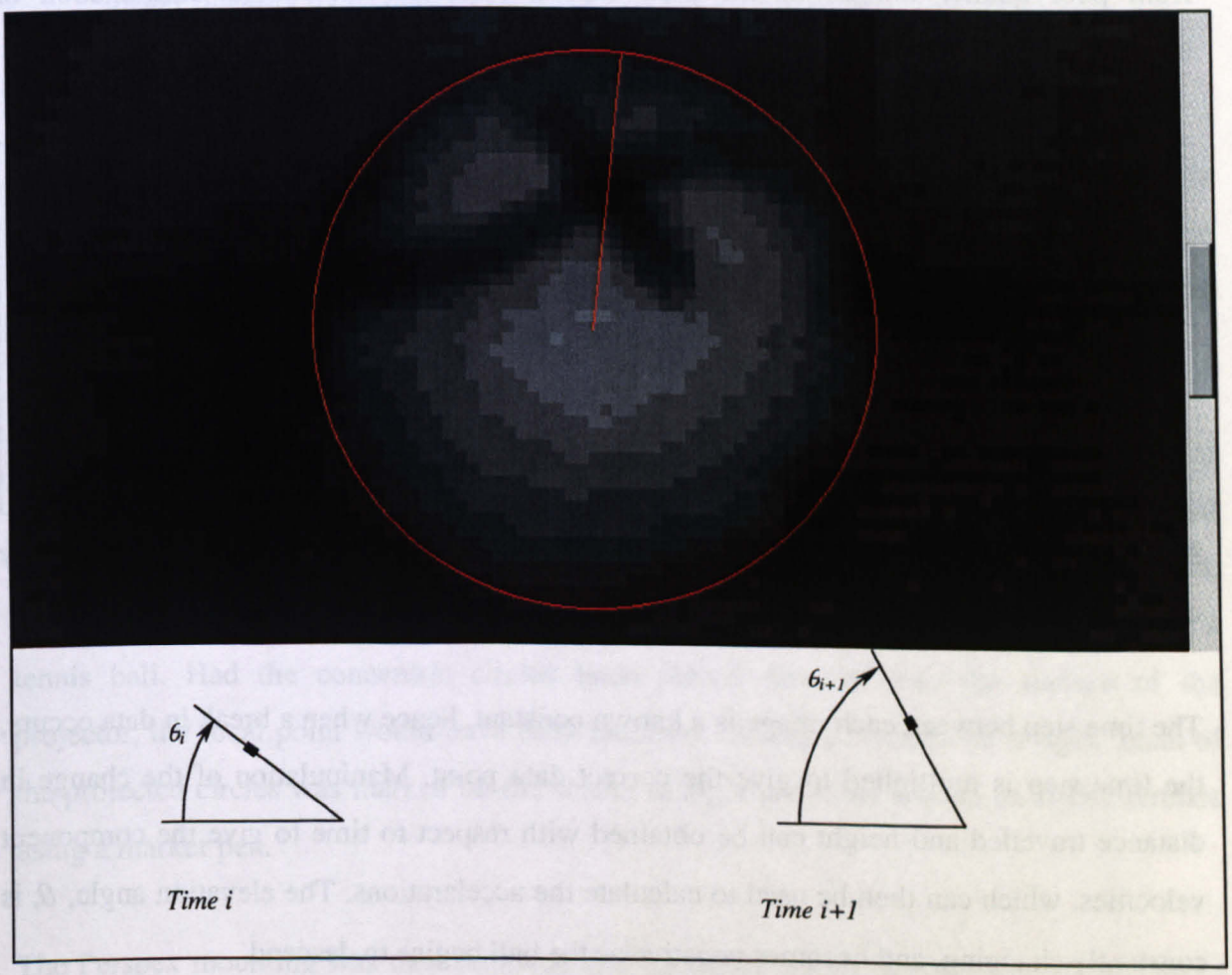

Figure 3.12 Image obtained at the exit of a pitching device, together with a schematic of two balls having rotated $(\theta_{i+1}-\theta_i)°$ in the time step between frames.

The spin rate was obtained using this set of images with use of a line emanating from the centre of the circle and one of the reference points on the surface of the ball. The angle of the line relative to it datum was exported into a spreadsheet. The two images at the bottom of figure 3.13 shows how the angle may change for a clockwise spinning ball. The change in angle, $(\theta_{i+1}-\theta_i)°$, can be used together with the frame rate to calculate the spin rate.

Manipulation of data

When all of the co-ordinates for a particular trajectory have been exported, the trajectory can be seen in a graphical form. Figure 3.13 shows a graph of distance travelled against height above the origin for a normal pressurised ball projected at a nominal velocity of 30mph with zero spin. The co-ordinates are corrected such that at time equals zero the ball travel and height are zero, hence the origin is set. There are gaps in the data set that arise from poor quality images of the ball, caused by either insufficient illumination or interlacing during digitisation.

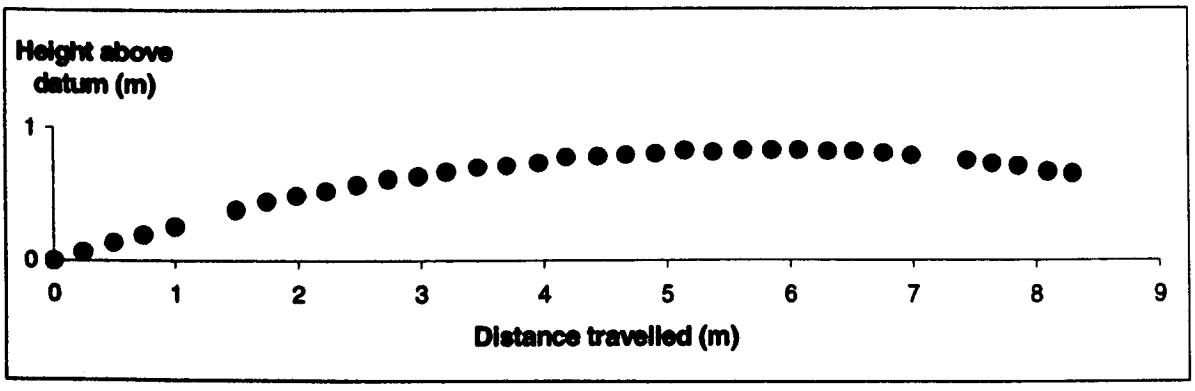

Figure 3.13 A typical trajectory for a tennis ball projected with an initial nominal velocity of 30mph, an angle of 16 degrees to the horizontal and zero spin.

The time step between each image is a known constant, hence when a break in data occurs, the time step is multiplied to give the correct data point. Manipulation of the change in distance travelled and height can be obtained with respect to time to give the component velocities, which can then be used to calculate the accelerations. The elevation angle, θ, is constantly changing, and becomes negative as the ball begins to descend.

3.4 The diameter of a tennis ball

The drag coefficient is calculated using the diameter of the ball, if the ball is smooth this is a trivial matter. However if the ball has a fibrous cloth on it, as a tennis ball has, then defining the diameter can be difficult.

According to the International Tennis Federation rules:

> *'In all tests for diameter a ring gauge shall be used consisting of a metal plate, preferably non corrosive, of a uniform thickness of one-eighth of an inch (.318cm) in which there are two circular openings 2.575 inches (6.541cm) and 2.700 inches (6.858cm) in diameter respectively. The inner surface of the gauge shall have a convex profile with a radius of one-sixteenth of an inch (.159cm). The ball shall not drop through the smaller opening by its own weight and shall drop through the larger opening by its own weight.'*
> *(Appendix I (iv), ITF Rules of Tennis 2000)*

This rule is suitable for the purposes of defining the limits of the size of a ball for a quality control test. However, when considering aerodynamics, the flight of the ball is also affected by the nap, which consists of thousands of fibres. A method has been devised whereby the projected area of a tennis ball can be obtained.

This method uses an overhead projector and a screen. A set of concentric circles of diameter 60mm to 74mm in 1mm increments were drawn in a CAD package and printed out onto a piece of acetate. A piece of transparent Perspex mounted on a small stand, shown in figure 3.14a, was used to enable focus at approximately half of the diameter of a tennis ball. Had the concentric circles been placed directly onto the surface of the projector, the focal point would have been incorrect leading to unreliable images. Each of the projected circles was marked on the screen in eight positions around its circumference using a marker pen.

The Perspex mounting was then removed and each ball placed directly onto the overhead projector, figure 3.14b. The ball did not have to be positioned in the central axis of the concentric circles, however it was important that at least one mark from each of the eight

sets was utilised. Figure 3.14c is a drawing to show the enlarged image of the projected area of a ball, produced using a standard overhead projector. The diameter is calculated using all eight measuring points to give four diameters, the average of which is used in analysis.

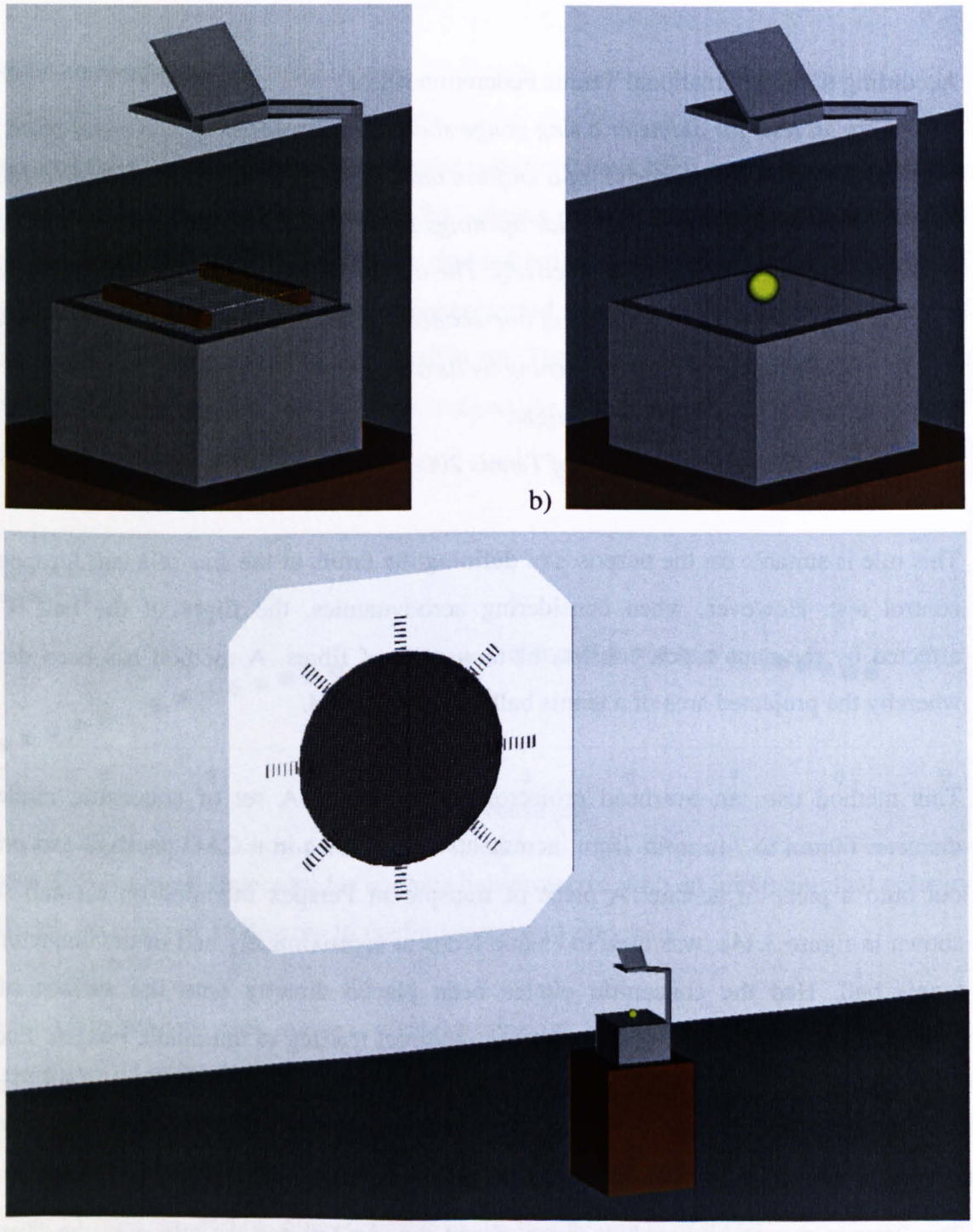

Figure 3.14 Drawings showing the apparatus used to project (a) a set of concentric circles and (b) the diameter of a ball onto the screen, (c) shows the markings obtained from the concentric circles and the enlarged image obtained.

The errors are minimised by the large image used for calculation, and can be assessed using the standard deviation of the four diameters obtained. Additional errors occur when it is difficult to define the edges of the extremely rough balls, confidence limits being applied to define the uncertainty.

The measurements were checked using a completely smooth ball of similar size. The smooth ball can be measured accurately using vernier callipers and compared to the result obtained using the projector. The difference can then be used as a correction factor on all of the other balls obtained using the projection method.

Example:

Table 3.1 shows the calculated projected diameters for three balls with different surfaces; smooth; normal; and fluffed. The smooth ball was calculated to have a diameter of 64.0625 using this method compared to 63.5 obtained using a set of vernier callipers.

Hence the calibration factor is calculated as follows:

$$Calibration\ Factor = \frac{Actual\ Diameter}{Calculated\ Projected\ Diameter} = \frac{63.5}{64.0625} = 0.9912$$

Ball Type	∅ 1 (mm)	∅ 2 (mm)	∅ 3 (mm)	∅ 4 (mm)	Average
Smooth Ball	64.0	64.25	64.25	63.75	64.0625
Normal Pressurised	68	69	68	68.5	68.375
Fluffed Pressurised	70	73	72	73	72

Table 3.1 Sample of calculated projected diameters for three different surface finishes.

Application of the calibration factor reduces the size of the normal pressurised ball to 67.77mm and that of the fluffed nap to 71.37mm. Errors were estimated to be 0.5% for the normal pressurised ball and 1.3% for the fluffed nap. This error is based on standard deviation, with the larger error for the fluffed nap being due to the irregular edge of the ball.

As the edge of the ball becomes more undefined, the diameter chosen is reliant on visual interpretation. It is highly unlikely that the outer most fibre or in the inner most edge will affect the aerodynamic properties of the ball significantly, hence a tolerance was applied to describe the uncertainty. This was applied in terms of distance in mm, in the case of the smooth ball the edge is well defined, hence a tolerance of zero is attached. The normal pressurised ball maintained its compact nap, however several short fibres were protruding, hence a tolerance of ±0.25mm was required. The combed fibres of the fluffed ball required an additional 0.125mm to cover its extremities, hence giving a tolerance of ±0.375mm.

The overall uncertainty of the calculated projected diameters now become 0.87% for the normal ball and 1.84% for the fluffed nap.

3.5 Direct drag measurement

There have been several techniques used to determine the aerodynamic forces acting on a tennis ball throughout this study. The following sections describe the apparatus and fundamental methodologies required to calculate the aerodynamic forces directly, specific test methods are discussed in greater detail in later chapters.

3.5.1 Three component wind tunnel balances

The high and low-speed wind tunnels utilise differing three component wind tunnel balances. An integrated three component wind tunnel balance is mounted above the working section of the high-speed wind tunnel. A generic three component wind tunnel balance was utilised during testing in the low-speed wind tunnel for both non-spinning and spinning tests.

Three component wind tunnel platforms are designed for combined force measurement of primary aerodynamic devices such as airfoils. When air flows over the surface of an airfoil, it is likely that three component of forces will result: drag, lift and pitching moment. When air flows over a non-spinning sphere, it is assumed that drag will be the only force applied.

A spinning tennis ball will deflect the oncoming airflow causing an additional lift/side force, which could be measured simultaneously. The apparatus required to measure the combined forces is large and relatively heavy, and the force related to the spin of a tennis ball is relatively small, hence it was decided that the force due to spin would be measured separately as a side force using the drag component.

Low-speed wind tunnel

Testing in the low-speed wind tunnel utilised a mechanical three component wind tunnel balance manufactured by T.E.M. Engineering Ltd in 1966. The balance uses a parallel motion system to measure drag, lift and pitching moment. Figure 3.15 shows a schematic view of a 'typical' three component wind tunnel balance based on the apparatus used in the low-speed testing. An earth frame is rigidly connected to a stable surface, enabling the force frame to move within it, coupled by four vertical links. The vertical links are connected strip-flexures that permit rotation through small angles. Further links between the earth and force frames are used to translate the measured force by means of a vernier scale.

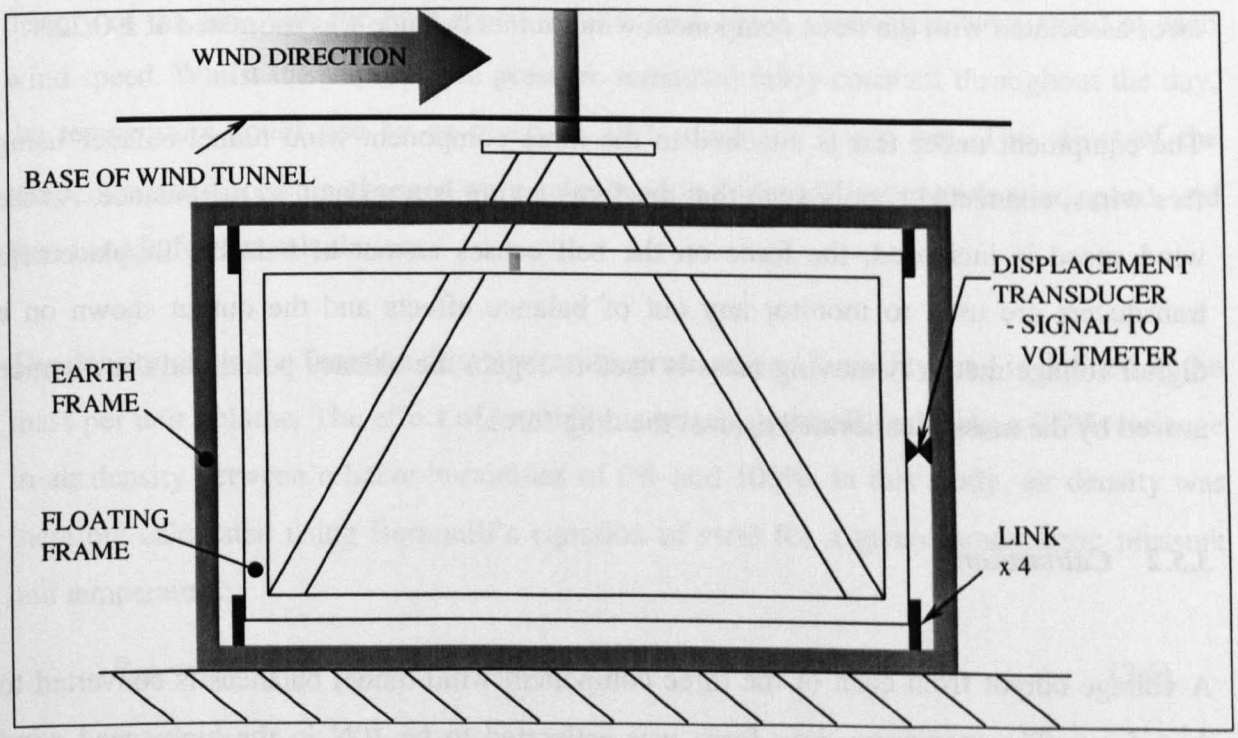

Figure 3.15 Schematic view of a 'typical' three component wind tunnel balance based on the apparatus used in the low-speed testing.

The force readings can be taken either mechanically or electrically. Due to the small forces applied to a tennis ball, the readings obtained from the mechanical scale were deemed to contain too much error. The electrical response is supplied via a transducer system, where the small movements due to the force on the ball cause proportional electrical output. When the test is completed for all wind speeds, the potential difference is normalised against that at zero wind speed, therefore the output from the displacement transducers is directly calibrated against drag force.

This three component wind tunnel balance was used for both non-spinning and spinning testing, and more detailed descriptions regarding the apparatus and specific set-up details can be found in chapters 5 and 6.

High-speed wind tunnel

The three component wind tunnel balance in the high-speed wind tunnel was designed and built at the Cambridge University Engineering Department. Only the drag component is required for this test method, the upper limit of which is 50N. The maximum reading taken during this testing was approximately 120 units to an accuracy of one decimal place. The error associated with the three component wind tunnel balance was estimated at ± 0.22N.

The equipment under test is attached to the three component wind tunnel balance using five wires, connected rigidly such that the force acting is translated to the balance. As the wind speed is increased, the force on the ball causes an out of balance. Displacement transducers are used to monitor any out of balance effects and the output shown on a digital voltage meter. A moving mass is used to regain the balance point, and the distance moved by the mass is calibrated against the drag force.

3.5.2 Calibration

A voltage output from each of the three component wind tunnel balances is converted to drag force. The maximum drag force was estimated to be 10N in the high-speed wind tunnel and 1N in the low-speed wind tunnel. These ranges were used for calibration of both

of the three component wind tunnel balances, and a more detailed description of the calibration test method can be found in chapter 5.

3.5.3 Compensating for tare

The tare is the force associated with the sting assembly alone. The results obtained during testing is the combined force of the sting assembly and the ball, hence the force on the sting assembly has to be deducted. The tare is obtained by performing the tests with the ball removed, and the methodology used differs for non-spinning and spinning tests, therefore a more detailed description can be found in the relevant chapters.

3.5.4 Compensation for atmospheric conditions

Atmospheric conditions change quite slowly, and on a local level can normally be accounted for on a daily basis. These changes occur more quickly when using wind tunnels, especially when testing at higher speeds. When using the low-speed wind tunnel, the temperature and atmospheric pressure was noted before each test and used to find the density of the air. With the high-speed wind tunnel, these parameters were noted at each wind speed. Whilst the atmospheric pressure remained fairly constant throughout the day, the temperature could rise by as much as 10°C during a single test. The effect of the temperature and pressure changes were calculated in a spreadsheet at each wind speed, and then used in further calculations.

The density of air is a function of temperature, pressure and humidity, and is defined as the mass per unit volume. The effect of humidity is relatively small, inducing a 0.9% variance in air density between relative humidities of 0% and 100%. In this study, air density was therefore calculated using Bernoulli's equation of state for a given atmospheric pressure and temperature:

$$P_{atm} = \rho_l R T_l \tag{3.6}$$

where: P_{atm} is the atmospheric pressure

ρ_l is the density of air at the temperature T_l

R is the universal gas constant (287.26J/kgK for all P and T in this study)

When calculating the Reynolds number, the dynamic viscosity is also required. The relationship shown in equation 3.7 (Schlichting, 2000) is used to calculate the dynamic viscosity μ_1 for the temperature T_1, where the dynamic viscosity μ_0 and temperature T_0 are known from standard results.

$$\frac{\mu_0}{T_0^{0.7}} = \frac{\mu_1}{T_1^{0.7}} \tag{3.7}$$

where: μ_0 and μ_1 are the dynamic viscosity at temperature T_0 and T_1 respectively (all temperatures are in Kelvin).

These equations are used at all data points and all results are recorded in a spreadsheet. It is designed such that when a new temperature is inserted, the new density and viscosity are calculated automatically.

4 THE COMPUTATIONAL TRAJECTORY MODEL

4.1 Introduction

A computational trajectory model was created using the results and understanding obtained throughout this study, and has subsequently used to compute and compare simulated trajectories against real trajectories. In the first instance it was used to confirm that the trajectories produced are correct, future analyses can be undertaken to compute how the flight of the ball will alter as the input parameters are changed.

The methods of gathering the data required for the computational trajectory model will be described in subsequent chapters.

4.2 Theory

There are three component forces acting on an object moving through the air; gravity, drag and lift. Both drag and lift forces are functions of the object properties and the atmospheric conditions, and assuming spin around the horizontal axis, can be described by the following equations:

$$F_D = \frac{1}{2}\rho v^2 A C_D \tag{4.1}$$

$$F_L = \frac{1}{2}\rho v^2 A C_L \tag{4.2}$$

where; F_D and F_L are drag and lift forces respectively

ρ is the density of the fluid within which the object is moving

v is the velocity of the object moving through the fluid, or, the velocity of the fluid moving over the object

A is the *projected* area of the object

C_D and C_L are the drag and lift coefficients respectively

The trajectory model is created using the equation of motion, which are developed using the force diagram shown in figure 4.1.

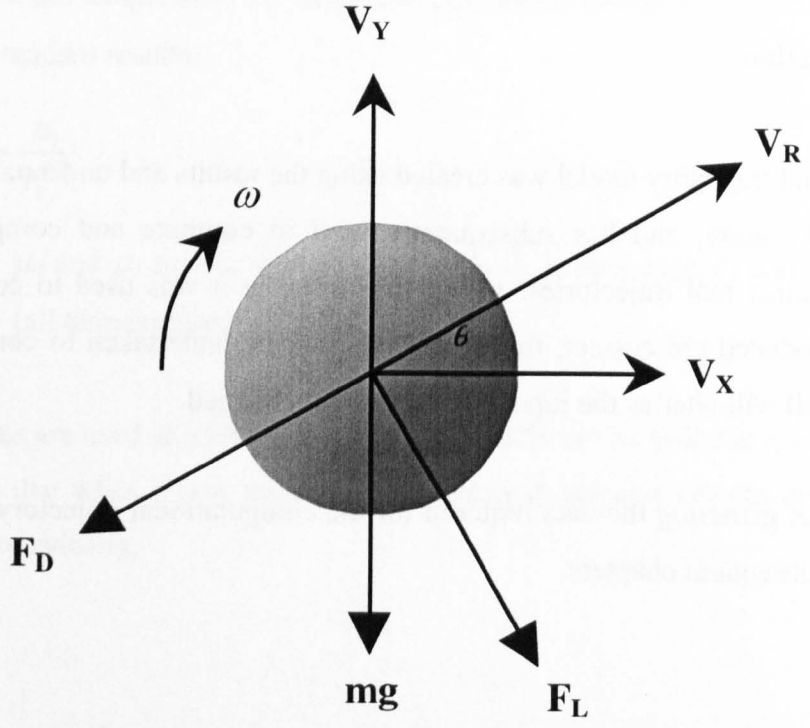

Figure 4.1 A force diagram for a ball spinning in the direction of ω travelling at $V_R ms^{-1}$ at θ degrees to the horizontal.

Figure 4.1 shows the forces acting on a ball spinning in the direction of ω travelling at $V_R ms^{-1}$ and θ degrees to the horizontal. The drag force, F_D, acts in the opposite direction to the direction of motion whilst the lift force F_L, acts perpendicular to the direction of motion, with its direction dependant upon the direction of spin. If the object is travelling without spin, the lift force is assumed to be zero. With rotation in the direction shown in the diagram, the equations of motion are as follows:

$$m\frac{dV_X}{dt} = F_L \sin\theta - F_D \cos\theta \tag{4.3}$$

$$m\frac{dV_Y}{dt} = -mg - F_L \cos\theta - F_D \sin\theta \tag{4.4}$$

$$\tan\theta = \frac{V_Y}{V_X} \tag{4.5}$$

The computational model was developed using an iterative process applied to the equations of motion. The model has been designed with input criteria of: initial velocity; initial spin; initial direction of motion; mass of ball; radius of ball; density of air; and initial height. Figure 4.2 shows a flow chart of the iteration process required to form the trajectory of a ball for a given set of input parameters.

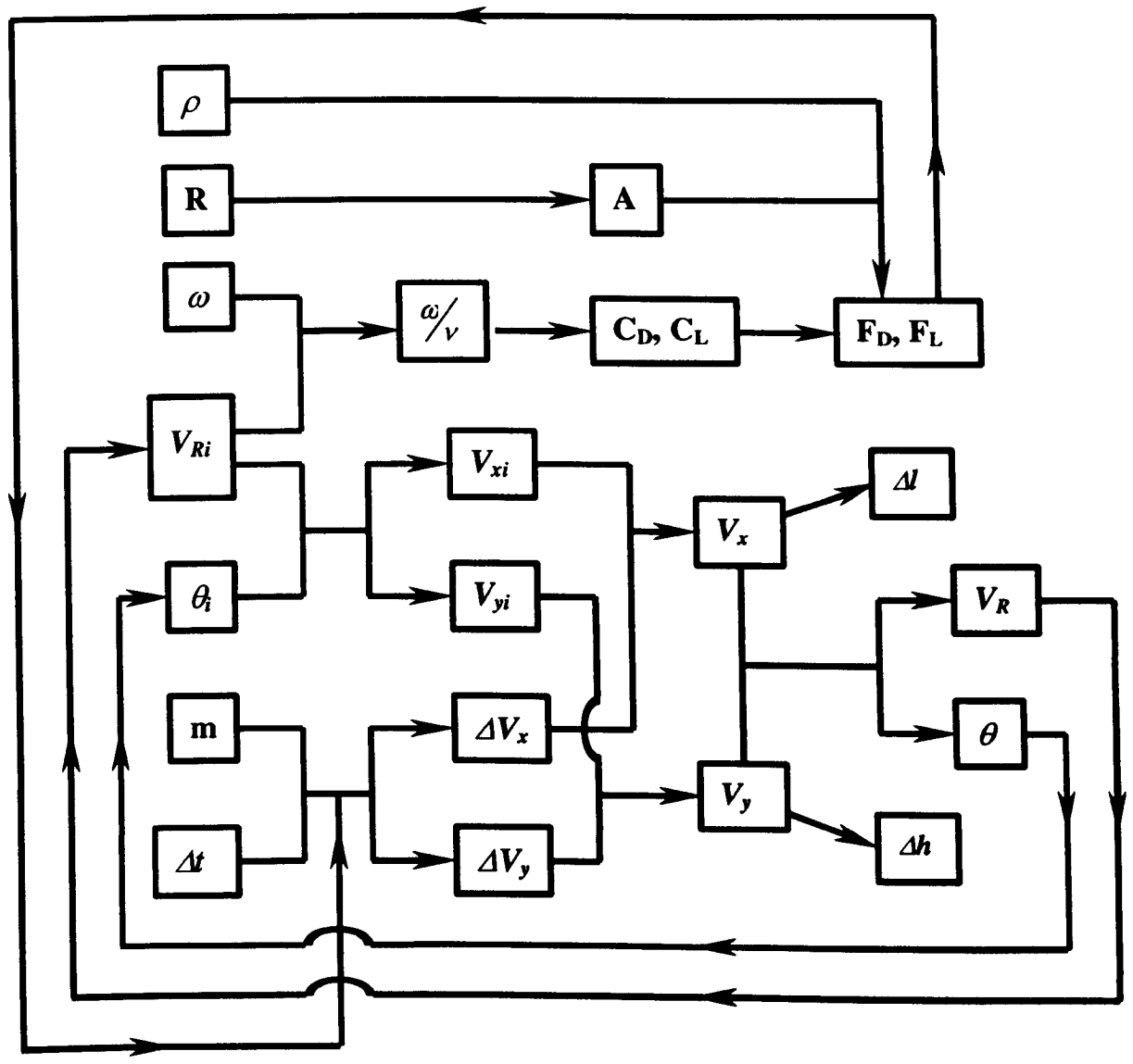

Figure 4.2 Chart showing the flow of information required to compute the trajectory of a tennis ball with a known set of input parameters.

Similar procedures have been developed for different studies for the flight of an object through the air, the procedure chosen for this study is similar to that used by Mehta (1985). The mass of the ball, m, density of air, ρ, and spinning ball radius, R, are constant

parameters defined using the methods and calculations defined in previous chapters. The time step, Δt, is set to suit the frame rate at which the images were captured. The spin rate, ω, initial angle to the horizontal, θ, and outgoing velocity V_{Ri}, is calculated for each trajectory. The spin rate is assumed to be constant throughout the flight, there is no evidence available to enable satisfactory approximation of the spin decay throughout the flight. The angle to the horizontal and effective velocity is calculated at each time step using calculated values of horizontal and vertical velocity components.

The change in horizontal and vertical velocity components, ΔV_x and ΔV_y, is calculated using equations 4.3 and 4.4 respectively. These figures can then be used to calculate the new horizontal and vertical velocity components, where:

$$V_x \text{ at time } t = V_x \text{ at time } t\text{-}1 + \Delta V_x \tag{4.6}$$

$$V_y \text{ at time } t = V_y \text{ at time } t\text{-}1 + \Delta V_y \tag{4.7}$$

The new values of V_x and V_y can then be used to calculate V_R and θ, which are then used to start a new iteration in order to find V_x and V_y at time $t+1$.

The trajectory is computed using the change in height, Δh, and change in length, Δl, at each time step, where:

$$\text{Height above ground at time } t = \text{Height above ground at time } t\text{-}1+\Delta h \tag{4.8}$$

$$\text{Length of shot at time } t = \text{Length of shot at time } t\text{-}1+\Delta l \tag{4.9}$$

Previous work with trajectory models has assumed that C_D and C_L remain constant throughout the flight (Erlichson, 1982). Equations 6.10 and 6.12 developed in chapter 6 enable calculation of C_D and C_L at each time step in line with the changes in V_{Ri}. During analysis, the useful spin parameter range was reduced to $0<\omega/v<2$ due to equipment sensitivity at low wind speeds. Although the model ignores changes in spin rate throughout the flight, the simulated trajectory should recreate a real trajectory more satisfactorily with continual updates in C_D and C_L.

4.3 Validation of the trajectory model

Initial validation was undertaken to ensure the resulting trajectories resembled the flight path of an object. It is well known that a ball struck with top-spin will land shorter than a ball struck at exactly the same speed and elevation with no spin. Conversely, a ball struck with back-spin will have a flatter trajectory and hence travel further than a ball struck at exactly the same speed and elevation with no spin. Figure 4.3 shows three trajectories obtained for a normal pressurised tennis ball struck at 18.1ms^{-1} and at an elevation of 10°, the three spin rates chosen were 2000rpm back-spin, zero spin and 2000rpm top-spin.

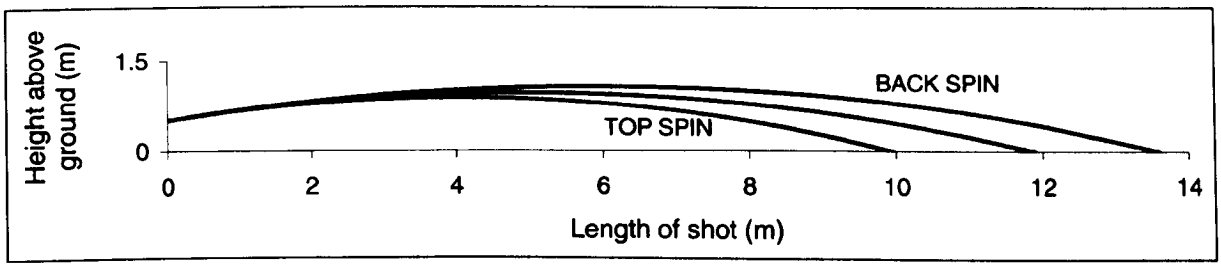

Figure 4.3 Flight paths produced for a tennis ball struck at 18.1ms^{-1} and elevation of 10° using the computational trajectory model for three spin cases: 2000rpm back-spin; zero spin; and 2000rpm top-spin.

The trajectory created for the zero spin case lies between the two spinning cases. The equivalent spin parameter is less than 0.4, and it can be seen that the back-spin case is flatter than that with no spin which in turn is flatter than that with top-spin.

The model created for this study was also compared with models created and documented for other studies. De Mestre and Cohen (2000) applied mathematical techniques to convert the differential equations shown in 4.3 and 4.4 into integral equation that could be solved using *Mathematica*. The lift force was ignored in this study which simplified the mathematical manipulation greatly, and hence enabled this study to be conducted. Initial analysis investigated the test case of a cricket ball projected at 40ms^{-1} at 45° to the horizontal with no drag applied. The trajectory for this set of parameters is parabolic and follows Newton's 2nd law of motion, travelling 162.5m and reaching a maximum height of approximately 40m. As can be seen in figure 4.4, the trajectory model developed for this study returns a similar trajectory.

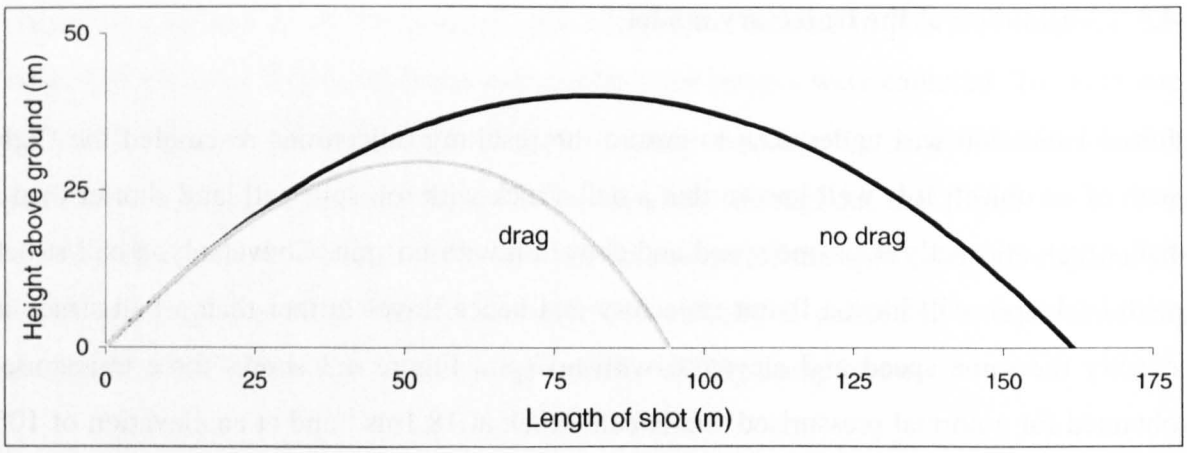

Figure 4.4 Simulated flight paths produced for a cricket ball using input data from de Mestre and Cohen (2000)

When the de Mestre and Cohen model is developed to include a drag parameter, the overall length of shot is reduced to 95.4m with a maximum height of a little less than 30m. The resulting flight path obtained using the trajectory model in this study returns an overall length of 94.4m and maximum height of a little over 29.5m.

Bearman and Harvey (1976) studied the aerodynamic properties of golf balls with differing surface conditions. A small part of their study dealt with the simulated flight of a golf ball with known initial parameters. A typical golf shot would be hit at $57.9ms^{-1}$ at an elevation of 10° with a spin rate of 3000rpm. The range of the resulting shot was computed to be approximately 150m for a conventional ball.

Figure 4.5 shows the flight path produced using the trajectory model developed in this study. The C_D and C_L parameters were estimated using the results published by Bearman and Harvey.

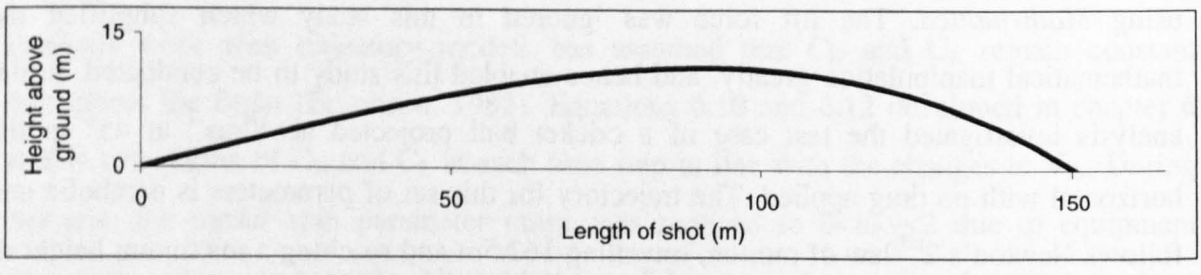

Figure 4.5 Flight path produced for a golf ball using input data from Bearman and Harvey (1976)

The maximum height is found to be just over 11m with a length of shot of approximately 150.5m. It is also worth noting that although significant attempts were made to estimate the spin decay, this study found that the resulting trajectory showed negligible dependence on the spin decay, hence it was decided that it should be ignored.

Thus far the model developed for this study has compared well with alternative models used in other studies. Indeed it has been found to underestimate slightly when compared against de Mestre and Cohen, whilst it overestimates slightly when compared against Bearman and Harvey.

The final trajectory model to be used for validation is directly linked with this study. Stepanek (1988) studied the aerodynamics of tennis balls, concentrating mainly on the topspin lob. A significant part of this investigation dealt with the development of a trajectory model that could be used to define the optimum initial conditions for a topspin lob. Stepanek used a similar mathematical method to that utilised by de Mestre and Cohen, however lift was also included. The manipulation was simplified, and moreover made possible, as lift and drag was assumed to act vertically and horizontally respectively.

The study investigated the aerodynamic parameters required to play the shot and have it land within the base line of the oppositions court. Several positions between the base line and the net were investigated, where the distance from the net decreased with increased spin rate. It was thought that the most rapidly spinning shot would be the most difficult to recreate and was therefore used for illustration. Stepanek (1988) found that the player would have to hit the ball with a velocity of $14.91 ms^{-1}$, a spin rate of 6000rpm and an elevation angle of 40.1° if he were standing 9m within the base line. The C_D and C_L values are published and can be obtained from the ω/v relationship.

Figure 4.6 shows the flight path obtained using the trajectory model developed in this study to replicate Stepanek's analysis. It can be seen that, given a court length of 23.77m, these parameters cause the shot to land outside of the base line at a shot length of 24.06m. When compared against Stepanek, the trajectory model developed for this study compares well whilst overestimating by approximately 1%. It should be reiterated that the model used by Stepanek was simplified and as such small differences would be expected.

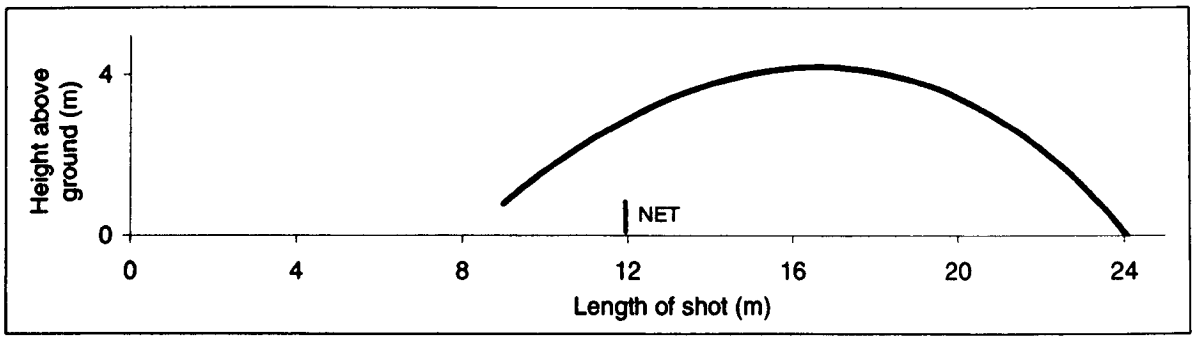

Figure 4.6 Flight path produced for a tennis ball using input data from Stepanek (1988).

None of the trajectories produced using the model developed in this study have exactly reproduced the trajectories calculated using the alternative models. It is important to note that the other models used simplified equations of motion or calculation methods, and therefore some differences would be expected. In addition, the trajectories calculated in this study have both underestimated and overestimated the ranges obtained with other models.

4.4 Test Method

The test method section is divided into two sections; (i) distinguish between the method used to create digital trajectory of a standard tennis ball; (ii) compare these trajectories and the simulated flight path produced using the trajectory model.

4.4.1 Apparatus

The following section includes a brief overview of the equipment used in this part of the study, however a detailed description of all equipment is included in chapter 3.

Pitching machine

The solid rubber wheeled 'BOLA' was used to project the balls with and without spin in a sports hall. Figure 4.7 shows the BOLA on a stand with a tennis ball being loaded. The spinning wheels are encapsulated for safety with the only openings being for the input and output of the ball.

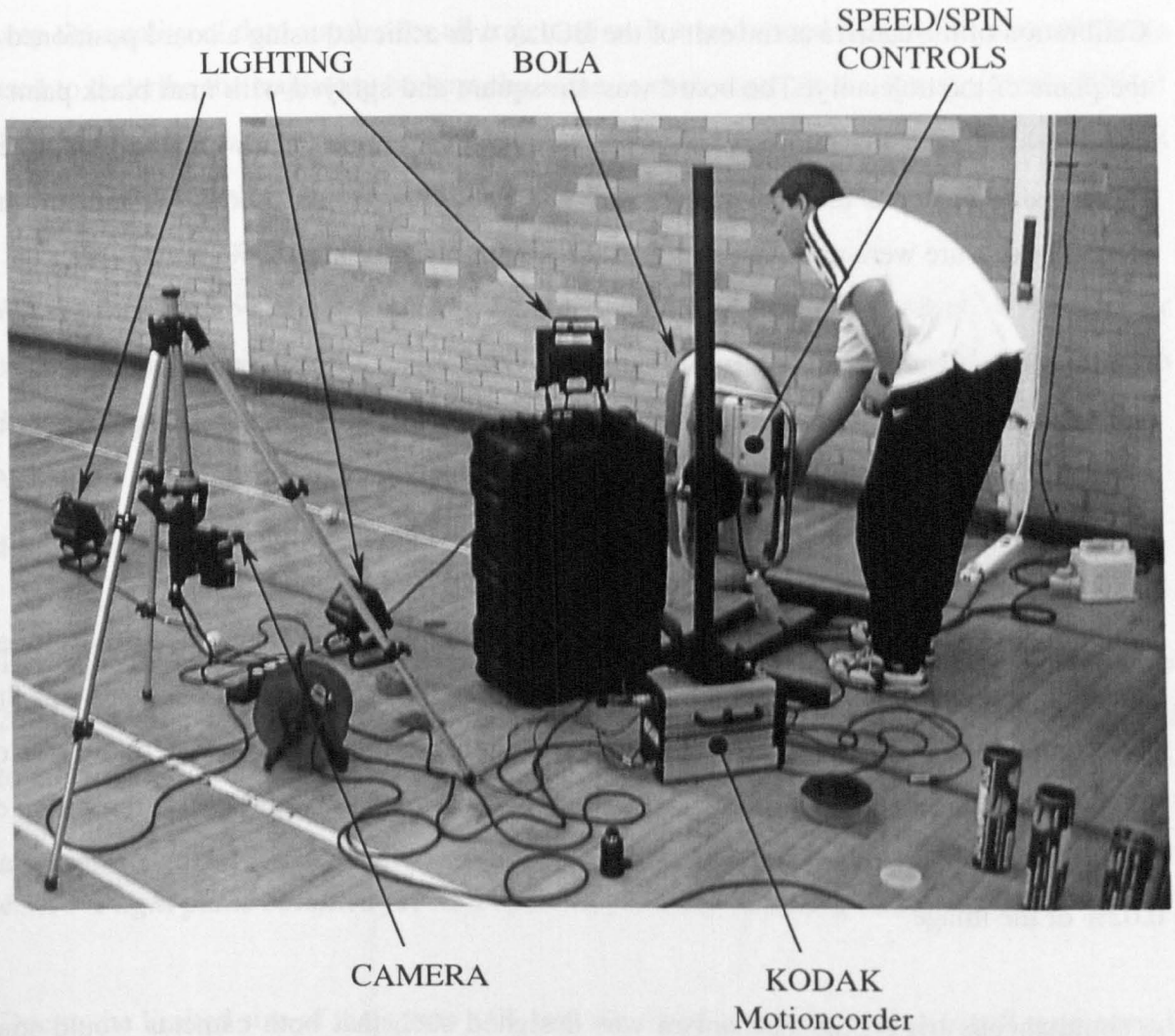

Figure 4.7 BOLA machine with the camera and lighting required to enable the capture of speed and spin data as the ball departs the projecting machine.

Motion capture

Motion capture was achieved using two high-speed digital cameras, one to capture images of the ball as it departs from the projection machine, and the other to capture images of the flight of the ball. The position of the camera and the lighting required to gather the images of the ball as it leaves the BOLA can also be seen in figure 4.7.

Rather than using two identical KODAK Motioncorder high-speed digital cameras however, a PHANTOM v4 was used to capture the complete flight of the ball. The positioning of the cameras enabled calculation of the output spins, speeds and angles, together with the shape of the trajectory and the speed of the ball throughout the flight.

Calibration of the camera at the exit of the BOLA was achieved using a board positioned in the plane of the trajectory. The board was 1m square and sprayed with matt black paint to create a background, white tape was used to mark a 100mm square grid on its surface. High quality data was required to calculate the speeds and spins so both the fastest frame rate and exposure were used, and the spatial resolution was around 25%.

A specially marked up ball was used to produce reference points for use in motion analysis and spin calculation. The markings were applied to the whole seam and in eight positions regularly spaced around the bells using a standard thick black permanent felt tip pen. At least two reference points were required for calculation of spin.

Calibration for the Phantom v4 camera was achieved using a 2m reference pole positioned along the plane of the trajectory in 1m increments. The overall calibration distance was 8m giving nine individual files. As the flight of the ball was relatively slow, a frame rate of 400 frames per second was sufficient to capture the information required. The resolution of the ball is reduced significantly in this configuration, with the ball taking up less than 0.02% of the image.

A simultaneous triggering mechanism was designed such that both cameras would start recording with a single impulse.

4.4.2 Trajectory data

The digital images were manipulated to create trajectory data in Microsoft® Excel in the normal way. The data obtained for the output of the BOLA was used to define the outgoing speed, spin and angle of the ball at the beginning of its flight path. This information was then used as the input parameters for the simulated trajectory model. The selection of trajectories was chosen such that the flight paths for the same ball at different projection velocities could be compared. In addition, to investigate the effect of lift, both top-spin and back-spin were applied to the ball at each projection velocity.

The flight path was recorded at 400 frames per second and data points were plentiful for the slow projection speeds but reduced significantly as the speed increased. In an effort to

keep the quality of data similar for all trajectories, it was decided that the number of points used to describe the trajectory be kept the same in each case. At the lowest speeds 20% of the data points were used raising to 100% for the maximum speed. The analysis represented this with time steps specific to each trajectory.

When all of the co-ordinates for a particular trajectory had been exported, the trajectory could be shown in graphical form. The co-ordinates at the origin were manipulated such that the initial height was 0.5m when time and distance travelled was zero.

4.5 Results

The BOLA was calibrated in miles per hour; therefore the desired theoretical speeds were 25mph, 35mph, 50mph, 70mph, 94mph and 120mph. The elevation of the BOLA was set to 10° for all trajectories.

4.5.1 Flight paths obtained for non-spinning and top-spinning ball projections

Due to the limited size of the sports hall, and the shape of a back-spinning ball trajectory, it was decided that the analysis would be limited to top-spin and zero spin only. The data obtained from top-spin ball trajectories is more abundant due to the looping flight path. Based on the analysis undertaken throughout the study and more specifically in section 4.3, it is therefore assumed that, if the model satisfactorily predicts the flight of top-spinning shots, it will also predict the trajectory of back-spinning shots.

Figure 4.8 shows all of the real data obtained by motion analysis for the non-spinning trajectories. The data has been manipulated such that all trajectories start at the same point. It can be seen that the ball with the slowest projection speed will land earlier than the others, reaching a maximum height of approximately 0.8m. The images of the flight were captured at 400 frames per second, however the analysis rate is set to 0.0125s for all trajectories up to 120mph, when the complete data set is used. This can be seen by the number of data points shown for each flight path, with both the 35mph and the 120mph trajectories containing the most data points.

As the projection speed increases the flight path becomes less curved over the same distance, the 95mph and 120mph trajectories appear to be almost straight. It can also be seen that the 94mph trajectory is above the 120mph trajectory, first impressions may suggest that these are the wrong way around, however this may be explained by differences between actual and theoretical outgoing parameters.

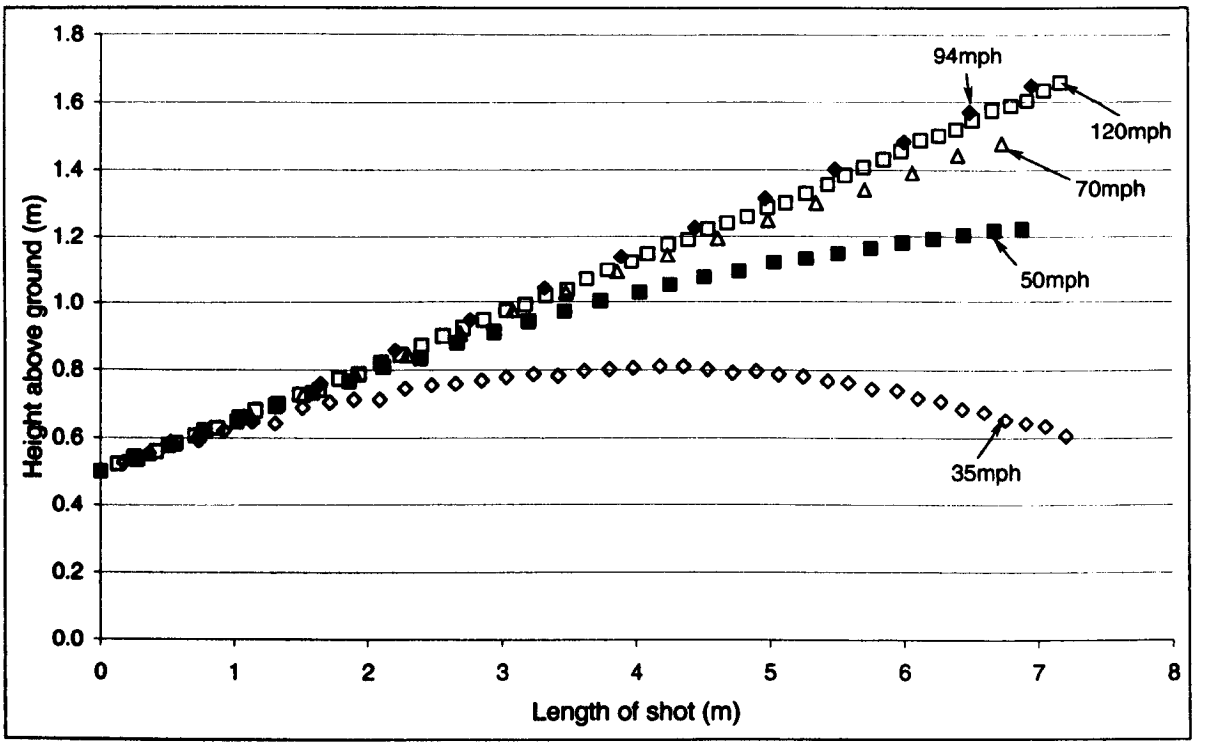

Figure 4.8 Trajectories obtained by motion analysis for all non-spinning projections.

Spin was applied in two stages, figure 4.9 shows the real data set obtained for the intermediate top-spin rate setting. Intermediate spin is defined as the spin rate dial being rotated through half of one turn, and therefore should be half of the maximum spin rate available. As the 120mph trajectory required both wheels to be rotating at maximum speed, it is not possible to impart spin on the ball at the same time.

It can be seen that all trajectories appear to loop more than previously, with the 35mph trajectory reaching a maximum height of approximately 0.7m. The effect of spin has been shown to diminish with increased speed, and this can be seen clearly, where the loop reduces for increasing projection speed. The flight path of the 94mph trajectory appears almost straight compared to the other trajectories.

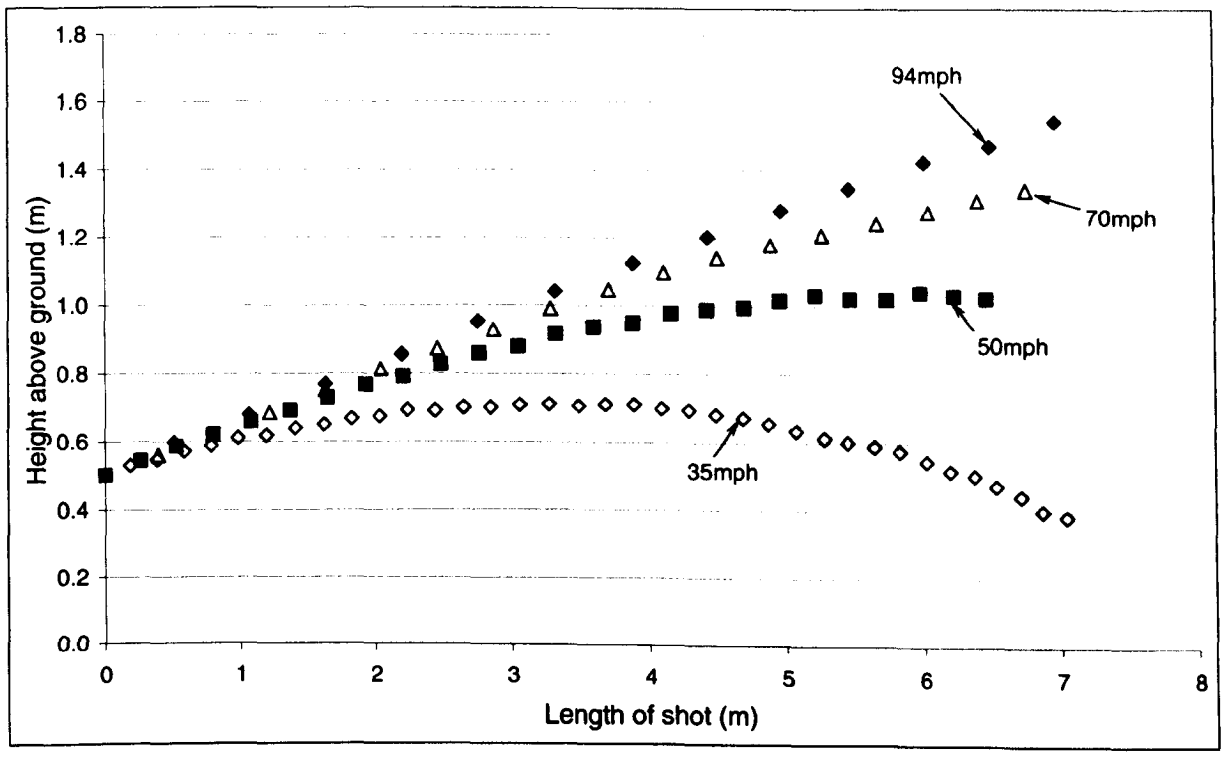

Figure 4.9 Trajectories obtained by motion analysis for all intermediate top-spinning projections.

The spin rate was increased to one full turn and this is defined as the maximum spin rate. Figure 4.10 shows all of the real flight paths obtained for all of the trajectories with the ball projected with a maximum spin rate. A lower projection speed of 25mph has also been included. It can be seen that the combination of speed and spin rate causes the 25mph projected ball to return to the ground within 6m, never actually rising much above its starting point of 0.5m above the ground. As the projection speed increases, the range of the ball increases accordingly.

The 35mph and 50mph look remarkably similar to those in figure 4.9, however there appears to be some anomalies at the higher projection speeds. As suggested for the results in figure 4.8, the outgoing parameters dictate the shape of the trajectory. Table 4.1 shows the theoretical and actual projection speeds and spins obtained at the output of the BOLA. The code used in the description column refers to the theoretical speed in mph and spin rate in rpm where: *ts* is top-spin and *vts* is maximum top-spin.

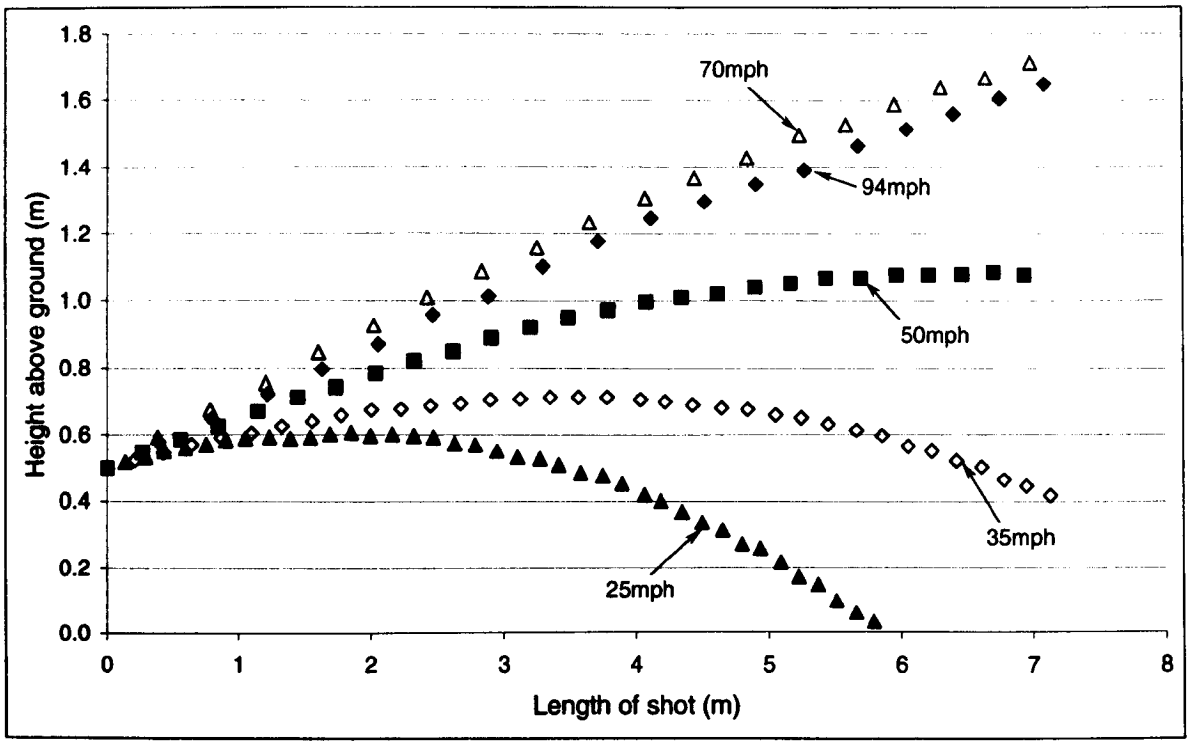

Figure 4.10 Trajectories obtained by motion analysis for all maximum top-spinning projections.

The spin rate was calculated using all of the available outgoing images assuming that it does not change significantly during the first 500mm of flight. With increasing outgoing speed, the number of images available reduced, and in some cases only two images were available. In these cases repeat analyses were undertaken, and the average of these analyses used in the model.

The outgoing angle of flight is more closely related to the flight path, and hence it was calculated using the initial data points of the trajectory. Only the first two complete images could be used to calculate initial conditions, and in order to ensure confidence in the calculated elevation angle, the same set of raw data was analysed five times for each trajectory, and then averaged. The average value was then used as the elevation angle in the trajectory model.

It can be seen in table 4.1 that the calibration at the higher speeds was considerably lower than the actual speed obtained, it should be noted that this will not affect the outcome of the investigation. Although it was desired to have trajectories with zero spin, a small amount of spin was observed (back-spin is denoted by a negative value). At the maximum

projection speed of 63.8ms^{-1}, both motors were running at full power, which meant that no spin could be applied.

Description	Theoretical Velocity (mph)	Actual Velocity (m/s)	Actual Velocity (mph)	Actual Spin (rpm)	Elevation (degrees)
25-vts	25	13.3	29.9	1894	7.7
35-0	35	15.8	35.6	22	8.8
35-ts	35	17.2	38.8	1431	8.3
35-vts	35	18.8	42.2	2326	7.6
50-0	50	22.3	50.1	-174	10.0
50-ts	50	23.5	52.8	2022	9.8
50-vts	50	24.7	55.5	3048	9.7
70-0	70	32.5	73.2	0	9.5
70-ts	70	34.7	78.1	2834	10.4
70-vts	70	34.7	78.0	3580	13.6
94-0	94	46.6	104.9	-162	9.5
94-ts	94	47.1	106.0	2857	10.7
94-vts	94	43.3	97.3	3318	12.0
120-0	120	63.8	143.6	5	9.8

Table 4.1 Theoretical and actual projection speeds and spins to be used in the trajectory model.

Referring back to figure 4.8, the 94mph and 120mph flight paths appeared to converge, it is possible that the small amount of back-spin found in the 94mph trajectory caused the ball to stay in the air a little longer. The anomalies observed in figure 4.10 can be more easily explained by the outgoing elevation angle of 13.6° for the 70mph trajectory compared to 12° for the 94mph trajectory. Although most of the non-spinning balls were projected at approximately 10°, as the ball is squeezed through the two wheels spinning at different rates, it appears that the elevation angle becomes less consistent.

It is potentially more interesting to compare the flight path of balls projected at a similar speed but rotating differently. Figure 4.11 shows the trajectories obtained for the three balls projected at a nominal value of 35mph. It is immediately obvious that the range of the two spinning balls is significantly less than the non-spinning ball. There is little difference between the flight paths of the two spinning ball trajectories. It can be seen that the projection speed has increased along with the spin rate, and therefore the ω/v relationship

remains similar, hence the C_L also remains similar. Furthermore, the elevation angle of the ball projected with maximum spin is significantly less than that projected with intermediate spin, hence with the increased velocity a 'flatter' trajectory would be expected.

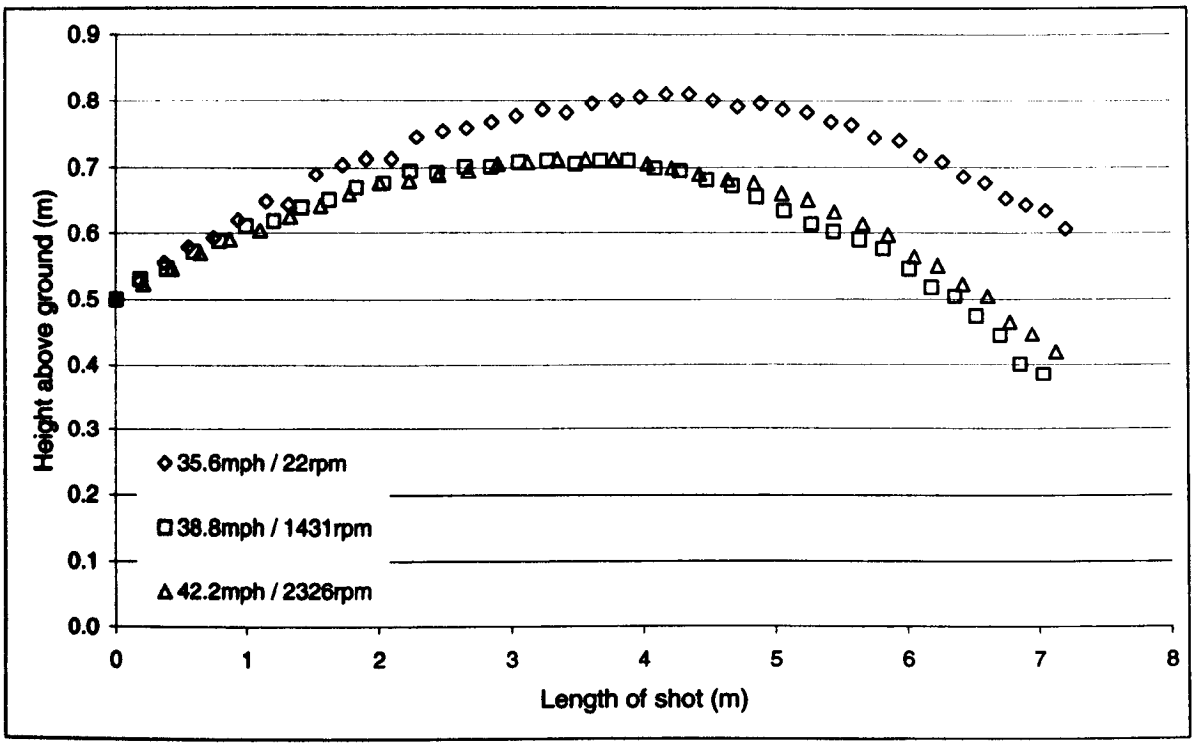

Figure 4.11 Trajectories obtained by motion analysis for all balls projected at a theoretical velocity of 35mph.

Figure 4.12 shows the trajectories created from the 50mph data set and it can be seen that the loop of the ball is less pronounced. A similar phenomenon occurs in this data set as occurred for the 35mph data set, whereby the increased spin rate appears to be counteracted by the increased projection velocity. Conversely, the outgoing elevations of the balls is extremely consistent for these trajectories, hence much of the difference is due to the aerodynamic properties alone.

The spin parameter of the maximum spinning ball is increased by almost 50%, yet the flight path is not significantly different to that of the intermediate spinning ball. The combination of aerodynamic forces that act on the ball during flight is complex, and the model that aims to simulate flight will need to be equally complex.

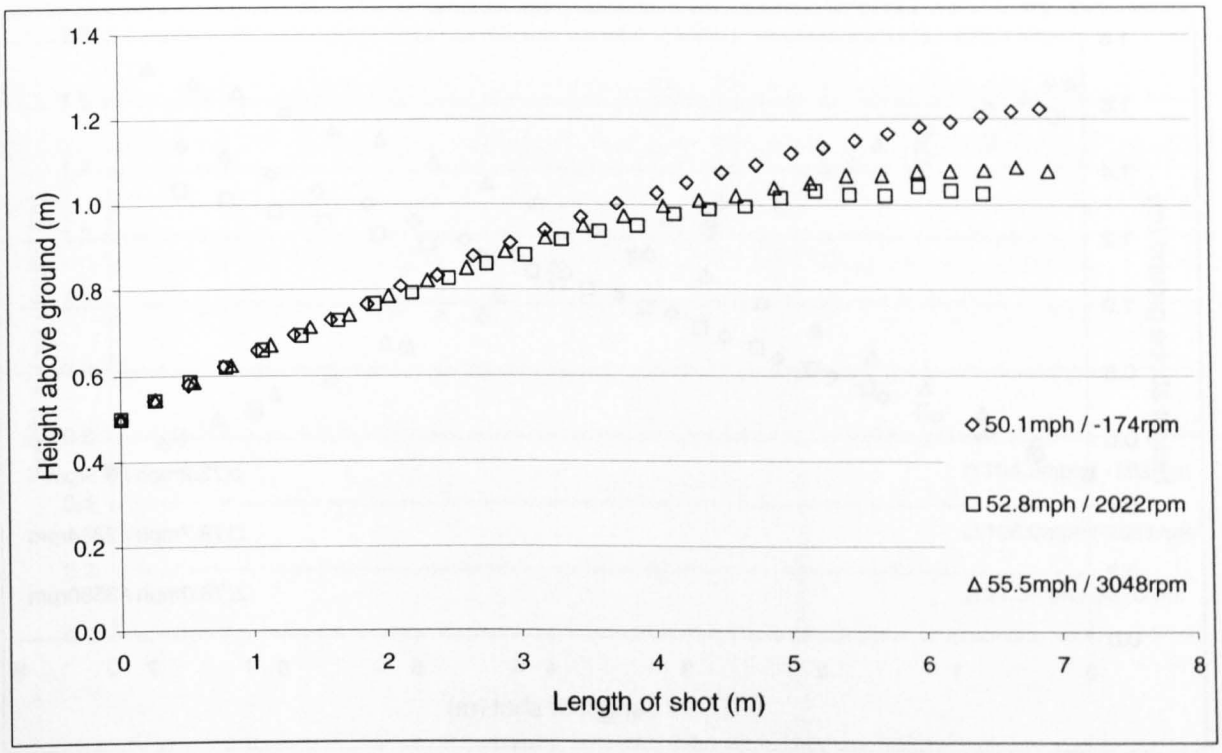

Figure 4.12 Trajectories obtained by motion analysis for all balls projected at a theoretical velocity of 50mph.

The elevation angle was shown to have increased significantly for balls projected at a theoretical projection velocity of 70mph. This anomaly is seen clearly in figure 4.13, where the flight path of the maximum spinning ball travels over that of the non-spinning ball, the opposite of what may be expected. Furthermore, the measured velocity is approximately 7% greater than that of the non-spinning ball, giving the induced lift force less opportunity to act.

The other two trajectories have a similar elevation angle, hence the flight path is more closely defined by the aerodynamic properties of the tennis ball. Whilst the effect of spin is less obvious with the increased speed, a small difference is seen between the non-spinning ball and the intermediate spinning ball. The elevation of the intermediate spinning ball is slightly greater than that of the non-spinning ball, hence the effect of the spin is slightly greater than first impressions may detect.

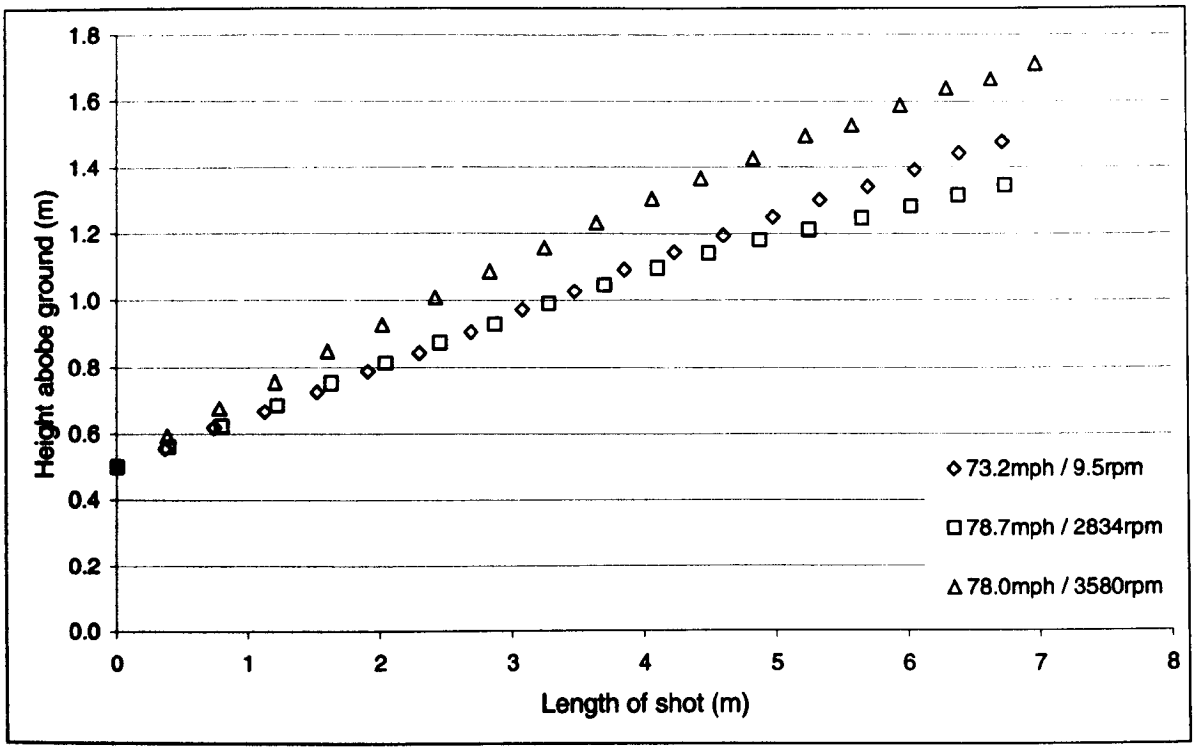

Figure 4.13 Trajectories obtained by motion analysis for all balls projected at a theoretical velocity of 70mph.

The final set of trajectories, for all of the balls projected at 94mph, is shown in figure 4.14. Over the distance available for testing in the sports hall, all of the trajectories are very similar at this projection velocity. There is very little loop observed in the flight path, indeed the balls were probably still rising when they struck the wall at the end of the sports hall.

Looking more closely at the input parameters and flight paths, it can be seen that there is some curvature when the ball is spinning. This is initially confused by the increased elevation of the maximum spinning ball, and the resulting convergence of all three flight paths. It can be seen that most of the data points for the intermediate spinning ball are coincident with that of the non-spinning ball, however the lift force causes it to diverge after about 4m of travel. As with the 70mph trajectories, the elevation increases as the spin applied to the ball is increased, resulting in the ball projected with maximum spin being projected significantly above that of the ball without spin. Even though the projection speed is reduced and the spin rate is significant, at the end of the available data, the two flight paths are almost coincident. The gradient of the maximum spinning ball is such that the remaining flight should show increased curvature towards the ground.

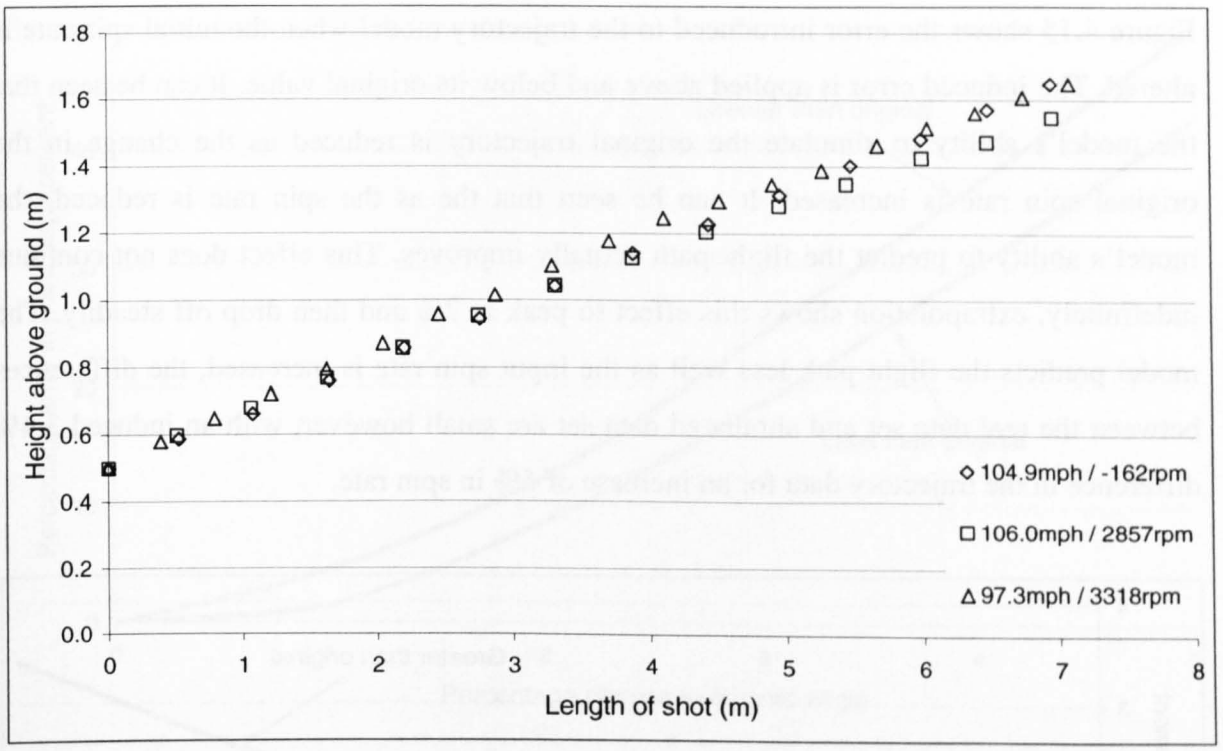

Figure 4.14 Trajectories obtained by motion analysis for all balls projected at a theoretical velocity of 94mph.

It has been shown that two balls projected with significantly different outgoing properties can have a similar flight path. Likewise, two balls with very similar outgoing properties can have significantly different flight paths. An understanding of the sensitivity of the input parameters used to define the trajectory in the model is therefore very important.

4.5.2 Sensitivity of the input parameters

Although there are several input parameters required for the trajectory model, the elevation, projection speed and spin rates are obtained from motion analysis. A model has been developed to compare real data points with simulated data points, hence small changes in the input parameters of the trajectory model can be monitored. The average of the absolute differences between all real data points in a trajectory and their corresponding simulated data point is calculated and used as a datum. Errors are then introduced as small changes in each of the input parameters, and the corresponding average displacement of the absolute distances is then calculated and compared to the datum and converted into a percentage change.

Figure 4.15 shows the error introduced to the trajectory model when the initial spin rate is altered. The induced error is applied above and below its original value. It can be seen that the model's ability to simulate the original trajectory is reduced as the change in the original spin rate is increased. It can be seen that the as the spin rate is reduced, the model's ability to predict the flight path actually improves. This effect does not continue indefinitely, extrapolation shows this effect to peak at 7% and then drop off steadily. The model predicts the flight path less well as the input spin rate is increased, the differences between the real data set and simulated data set are small however, with an induced 3.4% difference in the trajectory data for an increase of 5% in spin rate.

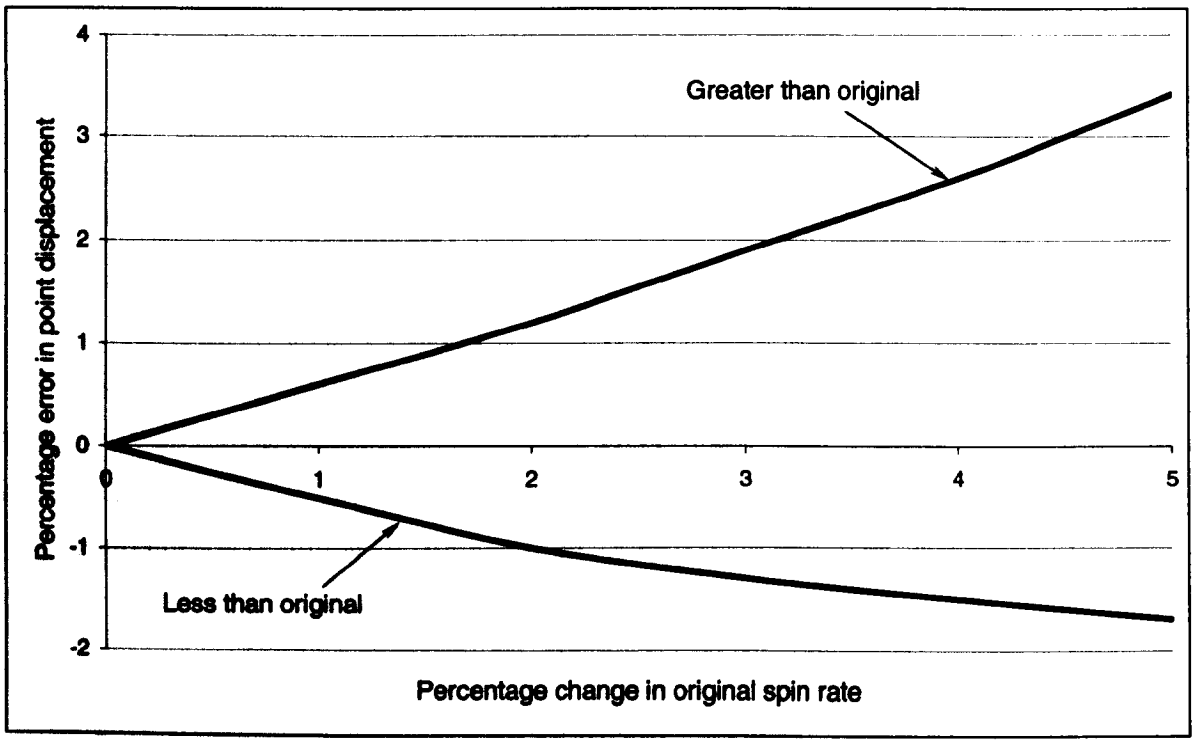

Figure 4.15 Vertical differences between corresponding data points for the real and simulated trajectories induced by small changes in spin rate.

Although additional effort is taken to obtain an accurate elevation angle, the limited number of data points available reduce confidence in the results obtained. Using the same procedure as that applied for the spin rate, figure 4.16 shows the differences between the real and simulated trajectories with induced errors in elevation angle.

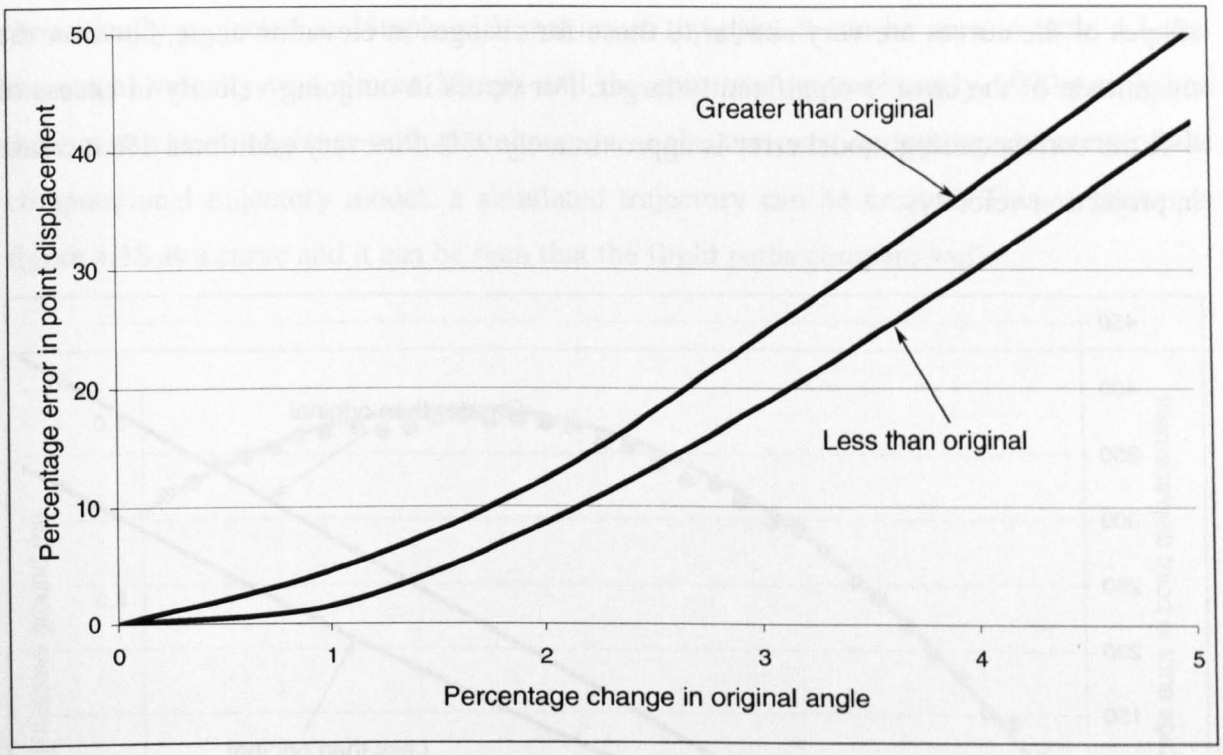

Figure 4.16 Vertical differences between corresponding data points for the real and simulated trajectories induced by small changes in elevation angle.

It is immediately apparent that the differences between the real data set and simulated data set are significantly greater than for spin. It is important to note that an overestimated elevation angle will induce a larger simulation error than an underestimated one, and this trend appears to remain throughout. Although the gradient is relatively small at the beginning of figure 4.16, beyond a change of 2% in the original angle, the increase in difference between the real and simulated data increases to approximately 12% for every 1% increase in elevation angle.

The outgoing velocity is the final input parameter to consider. This is probably the most accurate variable to calculate due to the relatively large change in co-ordinates between consecutive images. It is important to note that a change in the other two parameters will be observed primarily as a change to the vertical displacement, however a change in velocity will significantly alter the range of the trajectory, and is clearly visible when viewed graphically.

Figure 4.17 shows the percentage differences observed in point displacement between real and simulated data sets for small changes in projection velocity. It can be seen that the

shapes of the curves are very similar to those for changes in elevation angle, however the magnitude of the error is significantly larger. For errors in outgoing velocity in excess of 4%, the corresponding model error is approximately 95% for every additional 1% increase in projection velocity.

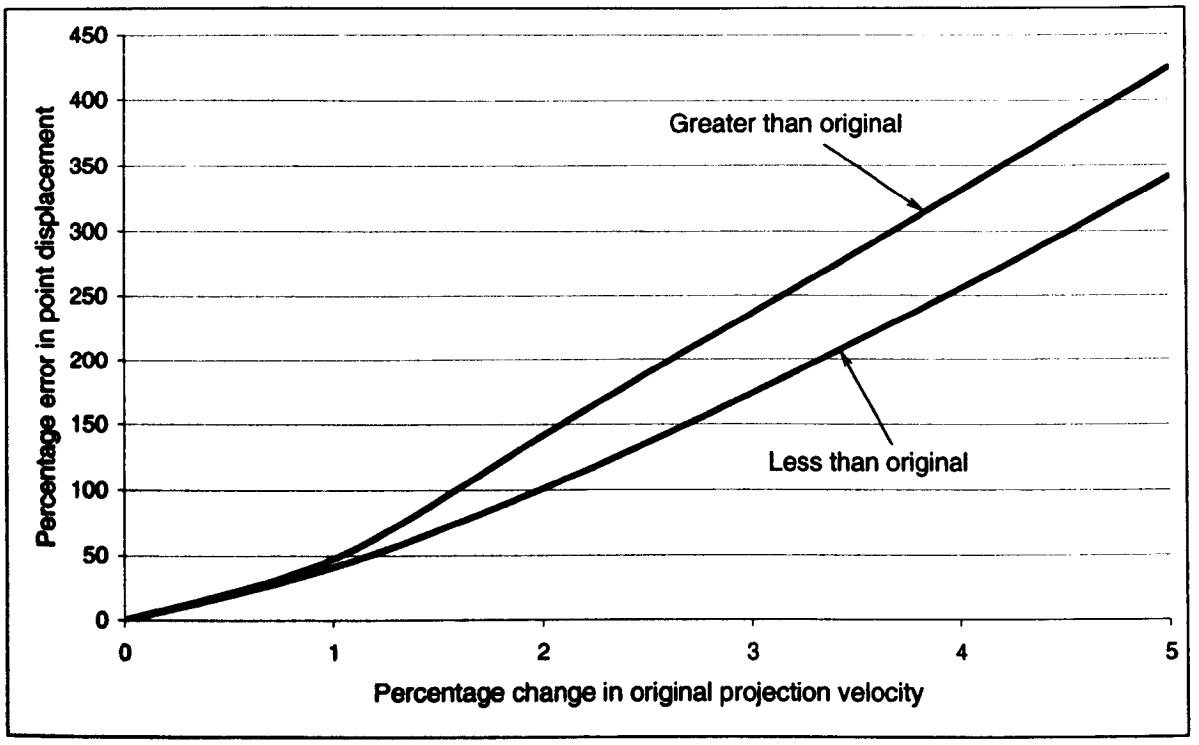

Figure 4.17 Vertical differences between corresponding data points for the real and simulated trajectories induced by small changes in outgoing velocity.

In conclusion, a simulated trajectory that reproduces each data point within 5% of the actual position can be obtained providing the following outgoing parameters are obtained:

- Spin rate measured to within 5% of the actual
- Elevation angle measured to within 1% of the actual
- Velocity measured to within 0.1% of the actual

4.5.3 Flight path comparisons

The most interesting flight paths occur at low speeds where the ball 'loops' significantly. Figure 4.8 shows the data set obtained for the trajectory using the standard ball

theoretically projected at 25mph with maximum top-spin. It can be seen in table 4.1 that the actual velocity was almost 30mph and the spin was approximately 1900rpm. When these parameters, together with the elevation angle, are used as input parameters of the computational trajectory model, a simulated trajectory can be created. This is shown in figure 4.18 as a curve and it can be seen that the flight paths compare well.

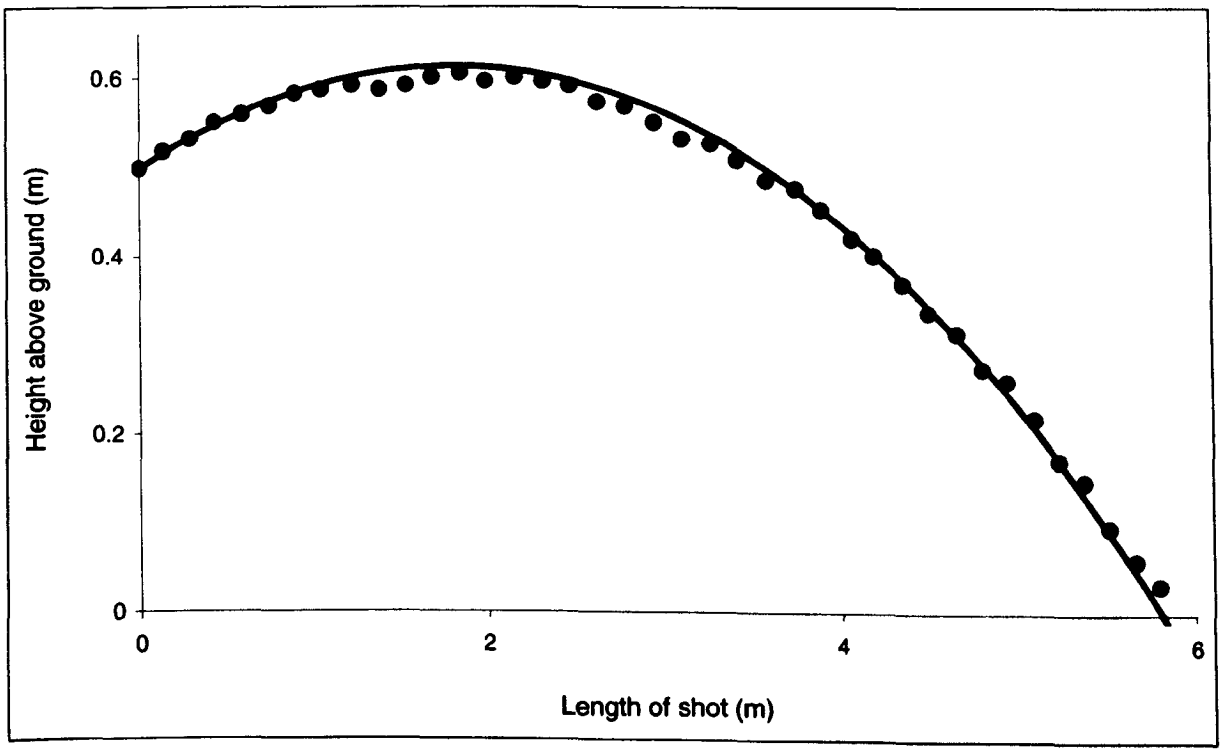

Figure 4.18 Real and simulated trajectories for a standard ball theoretically projected at 25mph and a maximum top-spin rate of 1894rpm.

The time step of some initial simulated trajectories was the same as that of the real data. Errors were caused in initial analyses due to the relatively large value of the time step and hence it was decided that the time step for all simulated trajectories should be 0.001s.

Rather than focussing on one set of data, it is prudent to investigate the trajectories produced for additional speeds and spin rates. It was decided that the 50mph trajectories are significantly different from the 25mph trajectories, yet not so fast that the loop does not exist. Figure 4.19 shows the real and simulated trajectories obtained for a standard ball theoretically projected at 50mph with no spin. It can be seen that the simulated trajectory follows the real trajectory for most of the flight, however it does appear to be deviating

near the end. This deviation will reduce the overall length of shot and the computational model will underestimate the landing point of the ball.

It is important to note that the horizontal distance travelled is the same for both trajectories, and it can therefore be concluded that the two main contributors to this parameter, projection speed and C_D, are correct.

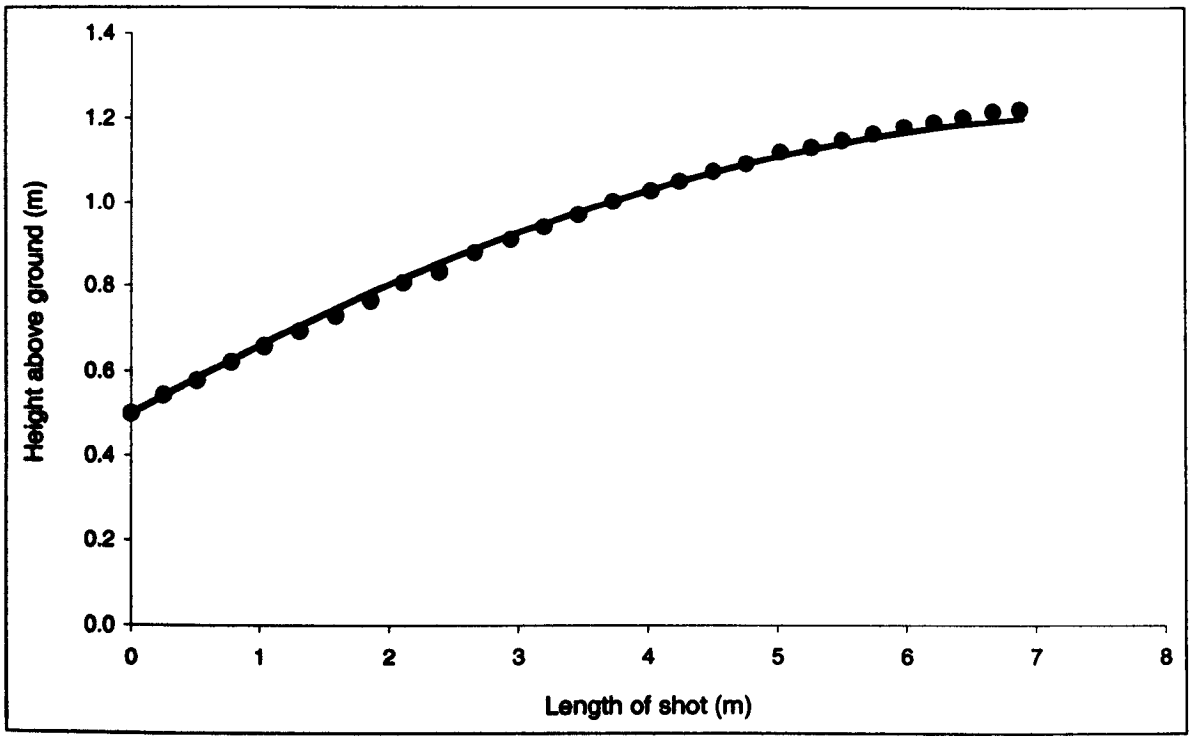

Figure 4.19 Real and simulated trajectories for a standard ball theoretically projected at 50mph and no spin.

The 50mph trajectories were projected with two top-spin rates. Figure 4.20 shows the real and simulated trajectories obtained for a ball projected nominally at 50mph with both intermediate (approx. 2000rpm) and maximum (approx. 3000rpm) top-spin rates. First impressions may suggest that the maximum spinning flight path is looping less and travelling higher than that with medium spin, however this can be explained by the differences in the actual projection velocities presented in table 4.1. The difference is almost 3mph, the reduced distance travelled by the intermediate spinning ball in a similar time is further evidence of the effect.

It is clear that the computational model predicts the trajectory well in both cases. The error has been assessed using the absolute differences between the real co-ordinates and the corresponding so-ordinates from the simulated trajectory. It was found that the average error was approximately 36mm for the intermediate spinning ball and 29mm for the maximum spinning ball. The maximum offset was approximately 65mm for the intermediate spin rate trajectory. This maximum error may be due to an anomaly at a poor data point, or related to a steady offset, both of which have been observed during analysis.

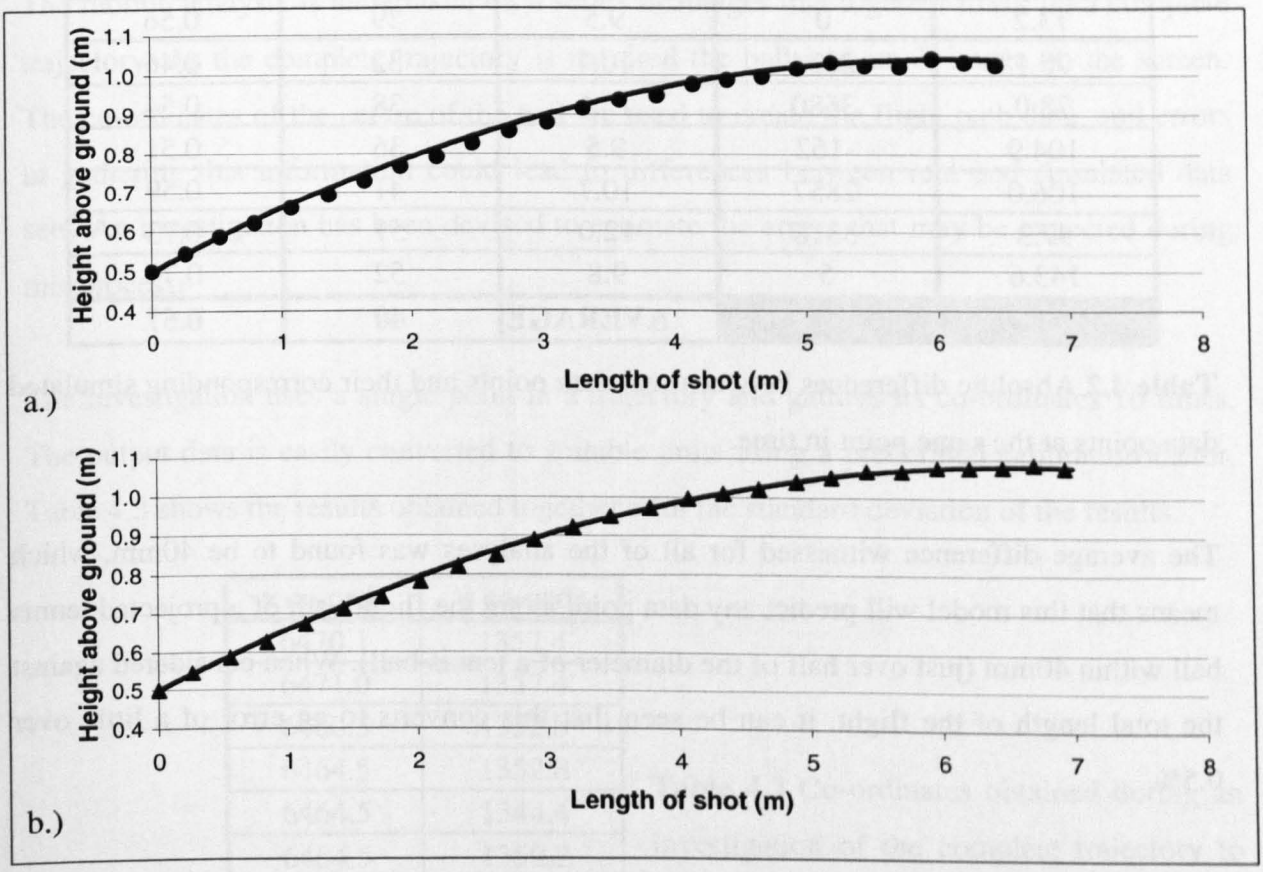

Figure 4.20 Real and simulated trajectories for a standard ball projected nominally at 50mph and spin rates of a) 2022rpm and b) 3048rpm.

The same process can be used for all of the trajectories studied, and the overall set of results can be used as a method of defining how well the trajectory model predicts actual flight path. Table 4.2 shows the actual projection parameters together with the absolute errors obtained. The average difference is defined as an average of the absolute displacements between the real and simulated data points at the same point in time. The error has been calculated using 7m as an approximate length of shot, although the true length of shot would be more accurate and give a lower error.

Trajectory Description			Average Difference (mm)	Error (%)
Speed (mph)	Spin rate (rpm)	Elevation (degrees)		
29.9	1894	7.7	45	0.64
35.6	22	8.8	47	0.67
38.8	1431	8.3	38	0.54
42.2	2326	7.6	38	0.54
50.1	-174	10.0	44	0.63
52.8	2022	9.8	33	0.47
55.5	3048	9.7	29	0.41
73.2	0	9.5	39	0.56
78.1	2834	10.4	32	0.46
78.0	3580	13.6	38	0.54
104.9	-162	9.5	36	0.51
106.0	2857	10.7	41	0.59
97.3	3318	12.0	51	0.73
143.6	5	9.8	52	0.74
		AVERAGE	**40**	**0.57**

Table 4.2 Absolute differences between real data points and their corresponding simulated data points at the same point in time.

The average difference witnessed for all of the analyses was found to be 40mm, which means that this model will predict any data point along the flight path of a projected tennis ball within 40mm (just over half of the diameter of a tennis ball). When considered against the total length of the flight, it can be seen that this converts to an error of a little over 0.5%.

Although it may have been considered that the looping trajectories of the lower projection speeds may be the most difficult to predict, the two highest errors are observed at the highest projection speeds. Most of the spinning projections are predicted with better than average errors, whilst the non-spinning projections contain greater than average errors on the whole.

4.6 Discussion

The computational trajectory model developed as part of this study has been shown to predict the flight of a tennis ball to within 40mm of the balls real position. This figure is an

absolute displacement and could be above or below the trajectory. Whilst this error is significant, it is possible that it can be explained by the data analysis method used. Once the significance of these differences is understood it will be possible to use the model to predict the effect of future changes to tennis balls.

4.6.1 Quality of imported data

The motion analysis is undertaken on a series of images that together make up a complete trajectory. As the complete trajectory is required the ball is a small image on the screen. The co-ordinates of the centre of the ball are used to create the flight path data, and errors in gathering this information could lead to differences between real and simulated data sets. An investigation has been devised to estimate the errors that may be expected during this process.

The investigation uses a single point in a trajectory and gathers its co-ordinates 10 times. The output data is easily converted to suitable units using a predefined calibration factor. Table 4.3 shows the results obtained together with the standard deviation of the results.

	x co-ords	y co-ords
	6470.1	1357.4
	6471.0	1357.4
	6480.3	1352.8
	6464.5	1352.8
	6464.5	1344.4
	6464.5	1359.2
	6464.5	1350.9
	6464.5	1361.1
	6464.5	1337.0
	6464.5	1342.6
	6464.5	1345.3
Std. Dev.	**5.0**	**7.7**

Table 4.3 Co-ordinates obtained during an investigation of the complete trajectory to define the errors expected from the image analysis process.

It can be seen that the standard deviation is small, and when this is converted to absolute differences, it can be concluded that the data analysis error is just in excess of 9mm, approximately 0.13% of the analysed trajectory. This figure is significantly less than the differences obtained comparing the real and simulated data sets.

The elevation angle is calculated using the complete trajectory images. Based on the findings in table 4.3, it is possible that the elevation angle obtained could be as much as 1.5° from its true value. Using the theoretical elevation angle of 10°, this relates to 15% error, which is off the scale of figure 4.16, however it relates to a 200% change in the model's ability to replicate the real data set. This investigation is based on a ball projected at 52.8mph with intermediate spin rate, hence the 200% error can be defined as displacement between the theoretical and actual points of 66mm.

Motion analysis techniques are also used to calculate the velocity and spin rate, as discussed in section 4.5.2. Table 4.4 shows the co-ordinates and angles from ten sets of analyses for the same image for the ball leaving the projection machine.

	Angle (rads)	Angle (degs)	x co-ords	y co-ords
	0.229	13.12	171.0	155.1
	0.270	15.46	170.1	153.6
	0.245	14.04	170.1	154.5
	0.257	14.74	170.1	155.7
	0.256	14.66	170.1	155.7
	0.263	15.07	170.1	154.5
	0.273	15.66	170.1	154.5
	0.232	13.30	170.1	154.5
	0.228	13.05	170.1	155.7
	0.238	13.66	170.1	154.5
Std. Dev.	**0.017**	**0.97**	**0.3**	**0.7**

Table 4.4 Angles and co-ordinates obtained during an investigation of the ball leaving the projection machine to define the errors expected from the image analysis process.

It can be seen that the confidence in the results obtained for the changing angle is limited to approximately 1 degree. When analysing at 400 frames per second, this relates to approximately 40rpm, approximately 2% of the intermediate spin rate. Using figure 4.15 and table 4.2, this difference in spin rate relates to less than 0.5mm displacement between the real and simulated data sets.

The standard deviations of the co-ordinates are small due to the large images and relatively large difference between consecutive images. When analysed further, the small errors observed in the co-ordinates relate to a difference in projection velocity of $0.28ms^{-1}$ at a

frame rate of 400 frames per second. As the projection speed increases, the effect of this analysis error will become less apparent as the distance between images increases. The repeat analysis investigation was performed on a ball calculated to have been projected at 23.5ms^{-1}, hence this error is approximately 1.2%. The corresponding change in the model's ability to simulate the flight path is in excess of 50%, which could be as much as 20mm based on the results shown in table 4.2.

The maximum combined error associated with the motion analysis technique is almost 100mm, significantly greater that the differences presented between the real and simulated data sets. It can therefore be concluded that, although 40mm is a significant offset, it has been shown that this may be due to the motion analysis technique used and the quality of image available.

4.6.2 Prediction of typical shots

One of the main aims of this study is to understand the aerodynamic properties of tennis balls enough to propose methods of slowing the game down. The serve of powerful males on 'fast' courts is a major concern to the governing bodies, however the way the ball impacts with the ground is a major factor in this stroke, and hence lies outside of the scope of this study. The forehand drive is a common shot hit at a high velocity with spin, and it is less dependent on the bounce of the ball.

The forehand drive is struck at approximately 60ms^{-1} with a top-spin in the region of 1000rpm. It is an attacking shot, where the player aims to just get the ball over the net and land it deep in the opponents court. Figure 4.21 shows the simulated trajectory obtained using these parameters and an elevation angle of 2.5°. This study has shown (chapter 5) that the flow around a normal sized tennis ball is similar to that around an 'oversized' tennis ball, and hence it is possible to increase the size of the ball to decelerate it more rapidly. The flight path of a 6.5% larger ball is also shown in this chart, and it can be seen that its range is reduced by a little less than 1.5m. The reduced length of shot is induced primarily by the increase in drag associated with the larger diameter ball, however lift also increases a small amount forcing the ball earthwards more quickly. The velocity of the ball

is reduced to 37ms^{-1} upon impact with the ground for the normal sized ball, however the larger ball has decelerated by an additional 5% by the time it contacts with the ground.

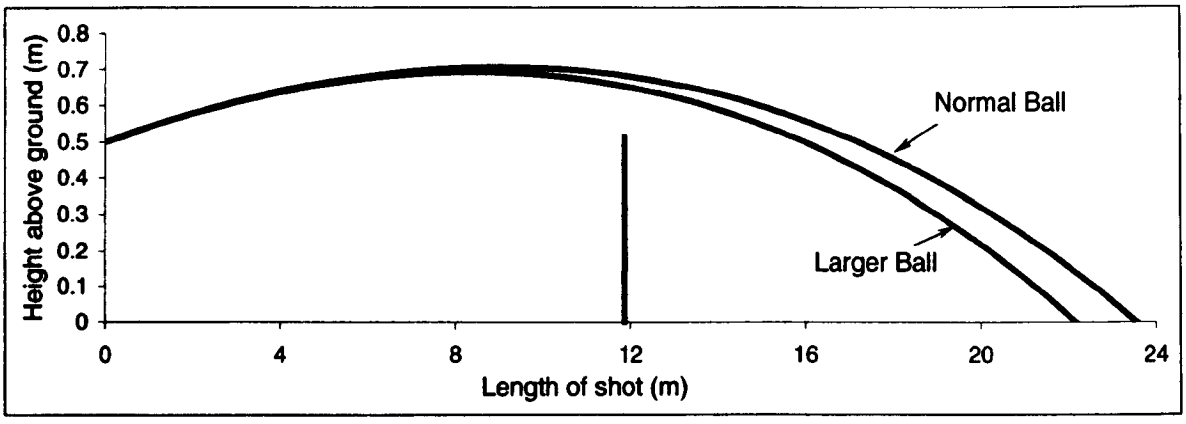

Figure 4.21 Simulated trajectories for a forehand drive struck with 1000rpm of top-spin at 60ms^{-1} at an elevation angle of 2.5° for a normal sized ball and a 6.5% larger ball.

It is interesting to note that the time taken by the larger ball is 20ms less than the normal sized ball, however it has travelled less distance. If the angle of elevation is increased to make the larger ball land in a similar position, it is found that it takes an additional 10ms to arrive there, vital time for the receiver to make a return shot.

The same approach can be applied for a sliced 'approach' shot played with lots of back-spin. Whilst this shot is not struck at a high velocity, and therefore does not need to be slowed down, knowledge of its flight path will help in the overall understanding. Figure 4.22 shows the two simulated trajectories obtained for the normal and larger balls struck with 1500rpm of back-spin at 45ms^{-1} and an elevation angle of 1.25°.

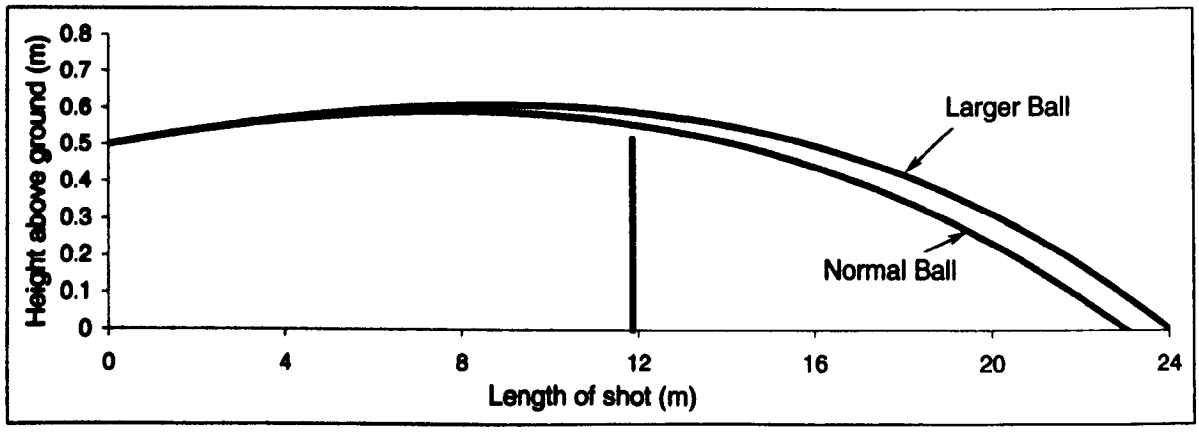

Figure 4.22 Simulated trajectories for a sliced approach shot struck with 1500rpm of back-spin at 45ms^{-1} at an elevation angle of 1.25° for a normal sized ball and a 6.5% larger ball.

It can be seen that although the normal sized ball lands in a similar position just inside the baseline, the larger ball now travels further. The velocity has reduced to 27.6 for the normal sized ball, and a further 8.6% for the larger ball, however the flight path appears to be more heavily controlled by the lift. The initial C_L is identical for both balls, however the F_L is greater for the larger ball due to its increased diameter. Due to the limited data available, spin rate is assumed to remain constant, hence as the velocity of the balls reduces, the spin parameter, ω/v, increases, causing C_L to increase. The more rapidly slowing larger ball will have a more rapidly increasing lift force, and will therefore be inclined to stay in the air for longer.

If the initial outgoing conditions are kept constant except for the spin rate, then an understanding of limiting factors may become clear. Figure 4.23 shows the simulated forehand drive with a normal ball, together with a 1000rpm back-spinning shot and a zero spinning shot at the same speed and elevation angle. It can be seen that the back-spinning flight path takes the ball over 50% further than the top-spinning shot. As the direction of motion is almost horizontal, the lift force is acting almost vertically, and it therefore affects the flight path and range significantly.

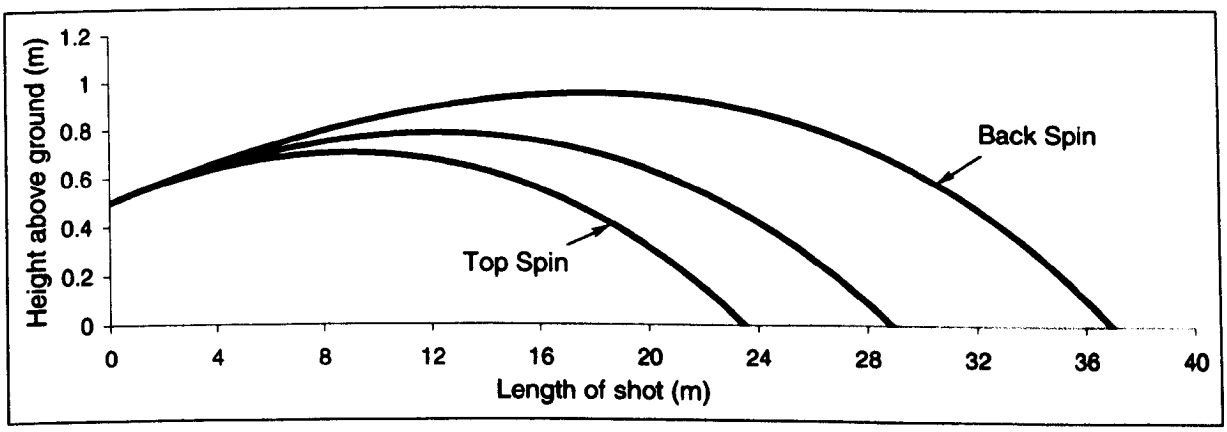

Figure 4.23 Simulated trajectories using initial velocity and elevation angle parameters of $60ms^{-1}$ and 2.5°, but modifying the spin rate to compare top-spin (1000rpm), zero spin and back-spin (-1000rpm).

As the elevation angle is increased the direction of the lift force moves around with it. For a shot struck at 45° elevation, the lift will be acting horizontally and vertically in equal proportions. The aerodynamic forces are not balances, so this soon changes, however the horizontal component remains predominant throughout.

Figure 4.24 shows three simulated trajectories with the same initial conditions as previously used, however the elevation has been increased to 50°. Whilst these specific trajectories are not representative of what may be seen in tennis due to their length, they are a useful aid in understanding the aerodynamic properties of tennis balls.

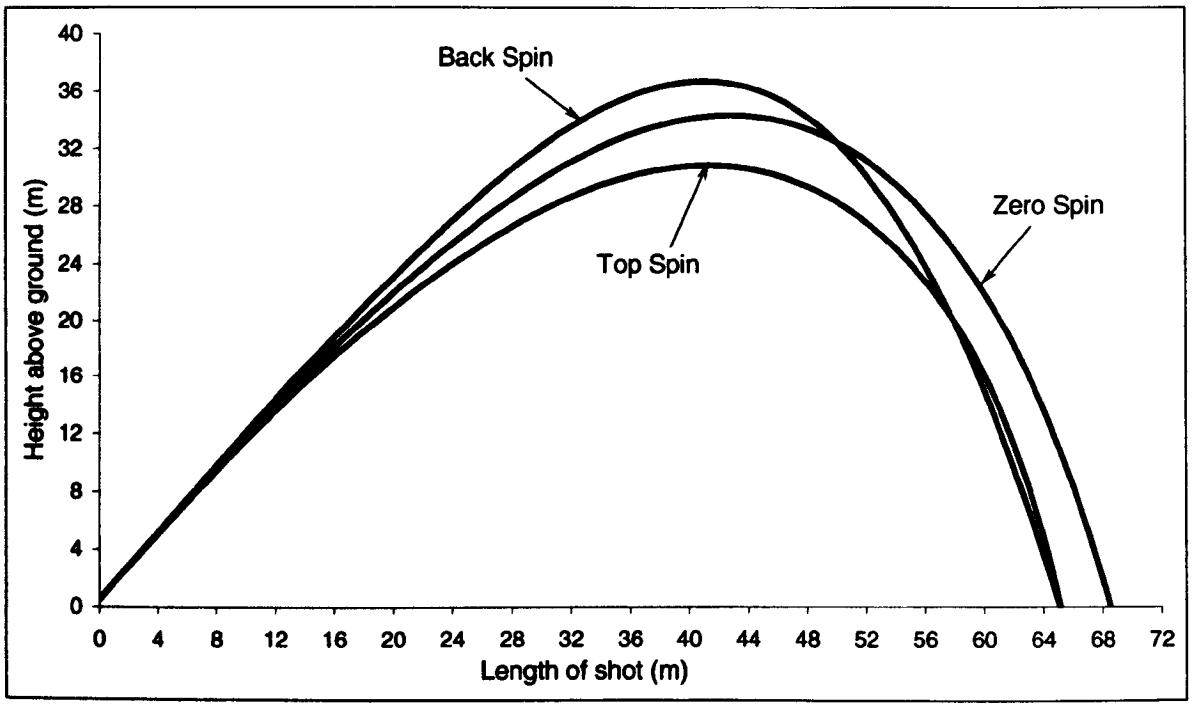

Figure 4.24 Simulated trajectories using initial velocity and elevation angle parameters of $60ms^{-1}$ and 50°, but modifying the spin rate to compare top-spin (1000rpm), zero spin and back-spin (-1000rpm).

It can be seen that the top-spin and back-spin shots land in a similar position. The flight path of the two shots is significantly different and the back-spinning shot will have been in the air significantly longer by the time it reaches the ground. In this instance, the horizontal lift force component on the back-spinning shot has acted to pull the ball backwards, whereas it projects the top-spinning ball forwards in the early stages.

4.6.3 Spin parameter

The spin parameter, ω/v, is used in the calculation of C_D and C_L, which in turn are used in the calculation of the drag and lift forces. Throughout this study it has been assumed that the spin rate does not change significantly throughout a balls flight. Whilst this statement

may be correct, there is no easy way to prove or disprove it, nor has the work been done previously to confirm one way or the other.

The velocity has been shown to reduce significantly during flight, inferring that the spin parameter will rise as the velocity falls. The flight of the ball may be affected by this assumption as the C_D and C_L also rises with increasing spin parameter. As the aerodynamic forces acting on the ball are proportional to the square of the velocity, they are controlled more by the changing speed rather than changing C_D and C_L. The overall effect on the flight of the ball should be minimal, as it was shown in section 4.5.2 that errors in spin rate calculation do not affect the model's ability to predict a ball flight significantly.

4.7 Summary and conclusions

A computational trajectory model has been created to predict the flight of tennis balls, and all trajectories analysed were simulated with a confidence limit of approximately 40mm at any point along the trajectory. The model has been used to predict the flight of two balls with different diameter, and it was found that:

- The velocity of a top-spinning normal sized ball starting at $60ms^{-1}$ 0.5m above the ground, will clear the net and land near the baseline at a velocity of $37ms^{-1}$. A 6.5% larger ball was shown to have decelerated by an additional 5% when it landed a little less than 1.5m shorter.
- When the landing points of the normal and larger balls are forced to coincide, it was predicted that the receiver would get an extra 10ms to react with the larger ball.
- The back-spinning larger ball has been predicted to travel further than a normal ball given the same outgoing properties.

The following chapters describe several methods utilised in the endeavour to characterise the aerodynamic properties of tennis balls, and calculate the C_D and C_L used in the computational trajectory model.

THIS PAGE INTENTIONALLY LEFT BLANK

5 NON-SPINNING BALL TESTING USING A THREE COMPONENT WIND TUNNEL BALANCE

5.1 Introduction

As mentioned in chapter 2, there are three common methods that can be used to find the drag forces on spheres. The use of a three component wind tunnel balance is actually the third method used within this study and produced the best C_D results by far. Both the 'projectile method' and the 'drop method' utilise motion analysis techniques, and it is felt that the digital video equipment and software available to this study was not suitable for the accuracy required in this study. The analyses that relate to these test methods were exhaustive and are fully documented in the appendices for further information. It should be noted that the analysis showed that the algorithms developed in the study returned accurate results with simulated data, even with simulated errors, and it has therefore been concluded that with improved apparatus more accurate results could be obtained.

The three component wind tunnel balance utilises load cells to obtain the drag force, and this chapter will outline the methodology and give some preliminary results obtained. Although it is well known that a rotating sphere will have both drag and lift forces acting on it, this chapter documents the case of a non-spinning ball only, and the flow around a spinning ball will be dealt with separately in chapter 6.

5.2 Theory

The theory behind this method is simpler than that for the previous two methods, where the drag force is obtained directly from the load cell. The drag force is a function of the ball characteristics and the fluid through which it passes. This relationship can be conveniently reduced to the relationship shown below:

$$F_D = f(\rho, \mu, d, v) \tag{5.1}$$

where: F_D is the drag force

ρ is the density of the fluid within which the ball is projected

μ is the dynamic viscosity of the fluid within which the ball is projected

d is the projected diameter of the ball

v is the velocity of the ball (velocity of the fluid in a wind tunnel)

The rules of dimensional analysis can be used to develop the relationships shown in the following equation:

$$C_D = f\left[\tfrac{1}{2}\rho v^2, \frac{\rho v d}{\mu}\right] \tag{5.2}$$

where: $\frac{\rho v d}{\mu}$ = Reynolds number = Re (5.3)

$\frac{1}{2}\rho v^2$ = Dynamic Pressure = q (5.4)

The equation used to define the drag force is:

$$F_D = (\tfrac{1}{2}\rho v^2) \times A C_D = (Dynamic\ Pressure) \times A C_D \tag{5.5}$$

where: $A = \frac{\pi d^2}{4}$ = the projected area of the ball

C_D is the drag coefficient

The fastest shot used in tennis is the serve, and top male competitors have been recorded serving at speeds of 149mph. This relates to a Re of approximately 2.75×10^5. Rather than using a wind tunnel to attain these speeds, researchers often use a larger model sphere to raise the Re (Bearman and Harvey, 1974). It is important that the object being tested remains a true representation of the original and obviously the best method of this is to use the original unmodified version.

As discussed in chapter 2, flow around spheres goes through a transition from laminar to turbulent at high speeds. Roughening of the sphere causes the transition to occur at lower speeds (Achenbach 1972). For a smooth ball this occurs at a Re of approximately 3.5×10^5, whereas in a slightly roughened ball it occurs at a Re of approximately 1×10^5. A tennis ball

is certainly not smooth, in fact it may be considered extremely rough and hence it is entirely reasonable to expect such a transition to occur in play.

It would be ideal to investigate the aerodynamic properties of an actual tennis ball in excess of 150mph. It is not always necessary to test in real conditions, the following methods of obtaining the relevant Re were postulated.

5.2.1 Methods of obtaining a higher Re

Inspection of equation 5.3 shows that there are several methods of increasing Re, many of which have been used previously. These methods are shown below along with a discussion about the relative merits of each.

- Decrease the kinematic viscosity either by increasing the density of the fluid (e.g. use water), and/or decreasing the dynamic viscosity of the fluid (i.e. lower the temperature of a gaseous fluid; or increase the temperature of a liquid fluid). The main disadvantage of this method is that water would be absorbed into the nap thus changing the aerodynamics properties. Furthermore, the required change in dynamic viscosity is large.
- Increase the size of the object being investigated. In addition to the physical change in diameter of the ball, a scaling of the nap would also be required to allow the model to be a true representation of the original object. Scaling of the nap should incorporate an increase in diameter of the fibres, which will probably result in increased fibre stiffness, and more significantly a change in the interaction between the airflow and the surface of the ball.
- Use high wind speeds using a standard tennis ball. This gives a true representation and allows a direct comparison of tennis ball brands.

As the flow through the nap is not fully understood, it was decided that the only fully representative model would be the actual ball, hence a wind tunnel capable of delivering the desired wind speeds was sourced.

5.3 Apparatus

Two methods have been used to find the drag force on a tennis ball using a three component wind tunnel balance. The general apparatus consists of a wind tunnel, a method of mounting the ball, a method of relaying the force, a method of measurement and a method of finding the aerodynamic parameters. The first method was developed using a high-speed wind tunnel, however the three component wind tunnel balance was designed to measure the forces on large bodies, hence accuracy was compromised with the low forces experienced on a tennis ball. The second test method utilised a three component wind tunnel balance designed for testing smaller objects in a wind tunnel with a lower maximum wind speed. Detailed descriptions of the wind tunnels and three component wind tunnel balances can be found in chapter 3.

5.3.1 Mounting of the balls (the stings)

The sting is the component used to translate the drag force on the ball to the three component wind tunnel balance. The ball is mounted at the front of the sting, such that the airflow of the wind tunnel flows over the ball first.

High-speed testing

A high-speed wind tunnel was used to investigate the drag forces on a tennis ball at the speeds experienced in play. The ball and sting assembly consume approximately 0.3% of the test section area, hence good quality results should be expected. The design criteria for the sting is as follows:

1. The length from the cross member to the back wire must be a minimum of 24 inches. This length is a design requirement of the three component wind tunnel balance being used.
2. The overall length of the cross member should be approximately 12 inches, with equal amounts on either side of the main length. The wider this section is, the more stable the sting will be, however the associated drag force increases with length.

3. The distance between the cross member and the tennis ball should be sufficient to prevent disturbance in the wake giving a false reading.
4. Drag forces on the sting and wires should be as little as possible to minimise subtraction errors. The first cross member used was an airfoil, however it was found that the flow around it went through transition, which lead to problems in calculating the drag force on the ball alone. It was decided that a circular section could be used whilst trying other methods to reduce the drag force on the cross member. This will be discussed in section 5.4.3.

Figure 5.1 shows an oblique view of the sting with a ball on the front, it is constructed from 10mm diameter rod parallel to the airflow with a 5mm cross member perpendicular to the airflow.

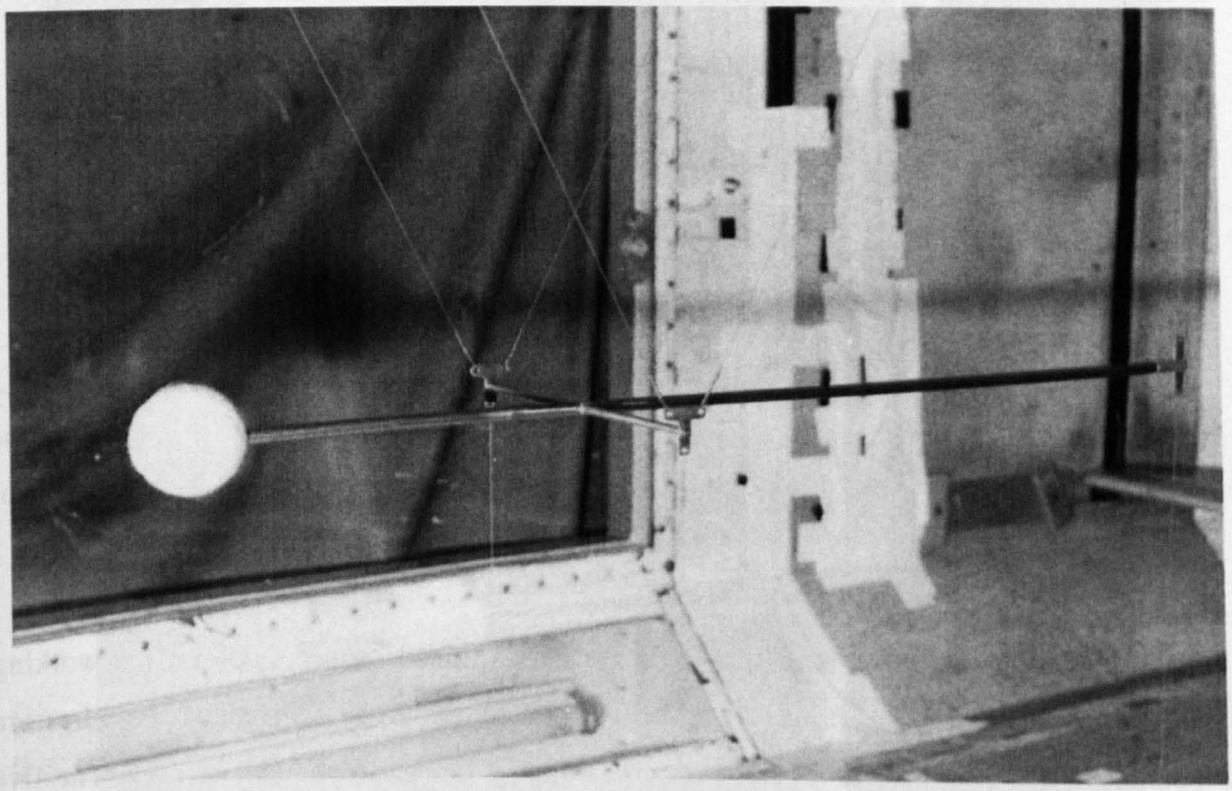

Figure 5.1 Picture of a ball attached to a sting in the high-speed wind tunnel.

Figure 5.2 shows the custom made brackets that are connected at each end of the cross member and at the rear of the 10mm diameter rod. They are oriented to enable movement around the horizontal axis perpendicular to the direction of airflow. Connection to the sting is achieved using M2 screws with a threadless shoulder, the thread engages in the sting and

the shoulder is a close fit with the mating hole in the bracket, thus allowing rotation of the bracket. There are five wires connecting the sting to the three component wind tunnel balance, two at each end of the cross member at an angle to the vertical to help with stability, three wires drop down from the sting. Weights are attached at the bottom of the wires, outside of the wind tunnel, to ensure tension in the system, such that any force acting on the ball is translated directly to the balance. The two weights at the front of the sting are suspended in viscous oil to help with damping.

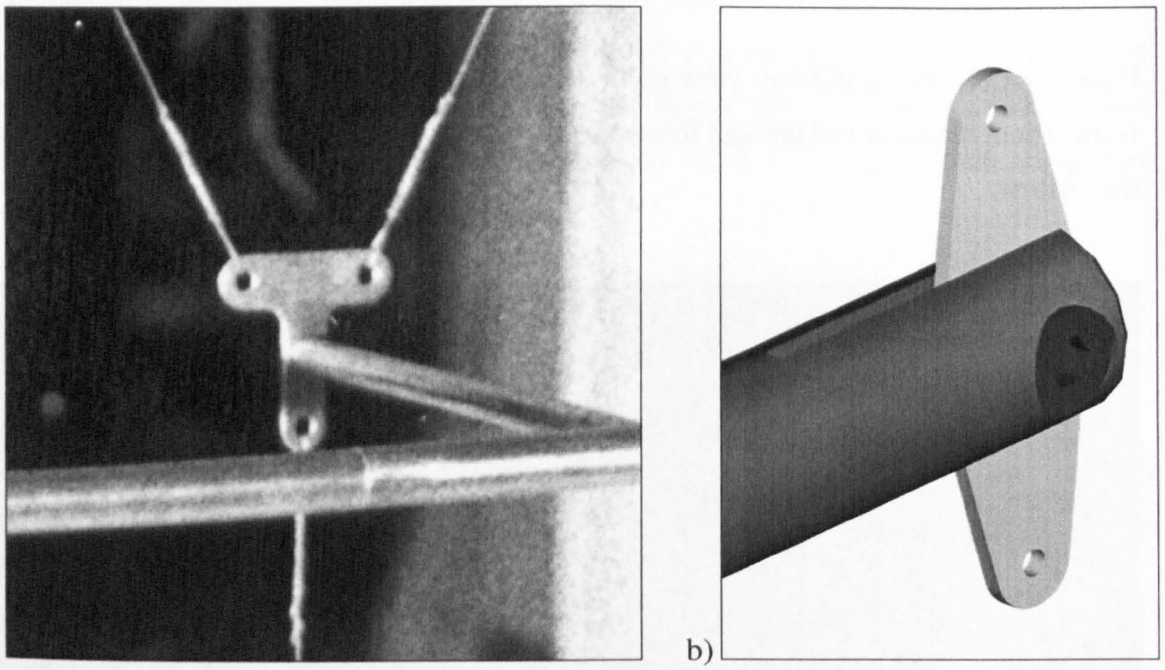

Figure 5.2 Close up image of the custom made brackets used to attach the wires to the sting in the high-speed wind tunnel a) at each end of the cross member and b) at the rear of the 10mm diameter rod.

The wires are of a length such that the sting is positioned in the middle of the working section. Adjustable connectors attach the wires to the balance, when all of the wires are connected the sting can be adjusted to ensure that it lies parallel to the airflow. The five wires are connected rigidly such that the force on the tennis ball is translated to the balance. As the wind speed is increased, the force on the ball causes unbalance. For analysis purposes it is considered that there are three separate objects within the airflow, the ball, the sting and the wires.

Low-speed wind tunnel

A low-speed wind tunnel was used to obtain more accurate results for the drag forces on a tennis ball. The ball and sting assembly take up less than 3% of the working section area, hence good quality results should be expected.

The sting used for this test method used a 25mm diameter bar to translate the force to the three component wind tunnel balance. This sting appears simple in comparison to that used for the high-speed wind tunnel. From the design criteria used for the sting used in the high-speed wind tunnel, only 3 and 4 apply to this model. A brief overview of the theory behind the design of the sting for this test method follows, the numbers relate to the design criteria for the sting of the high-speed wind tunnel test.

3. It was decided that the same distance used between the ball and the cross member in the high-speed testing should be used between the ball and the connection bar in these tests. By doing this it is easier to form a comparison between the two methods. The other advantage to this is that most of the attachments can be used in both methods.
4. It seems clear that a 25mm bar will have a large force acting on it, however it is possible to reduce the force applied. The method used to reduce this force is known as shrouding and will be discussed further in section 5.4.3.

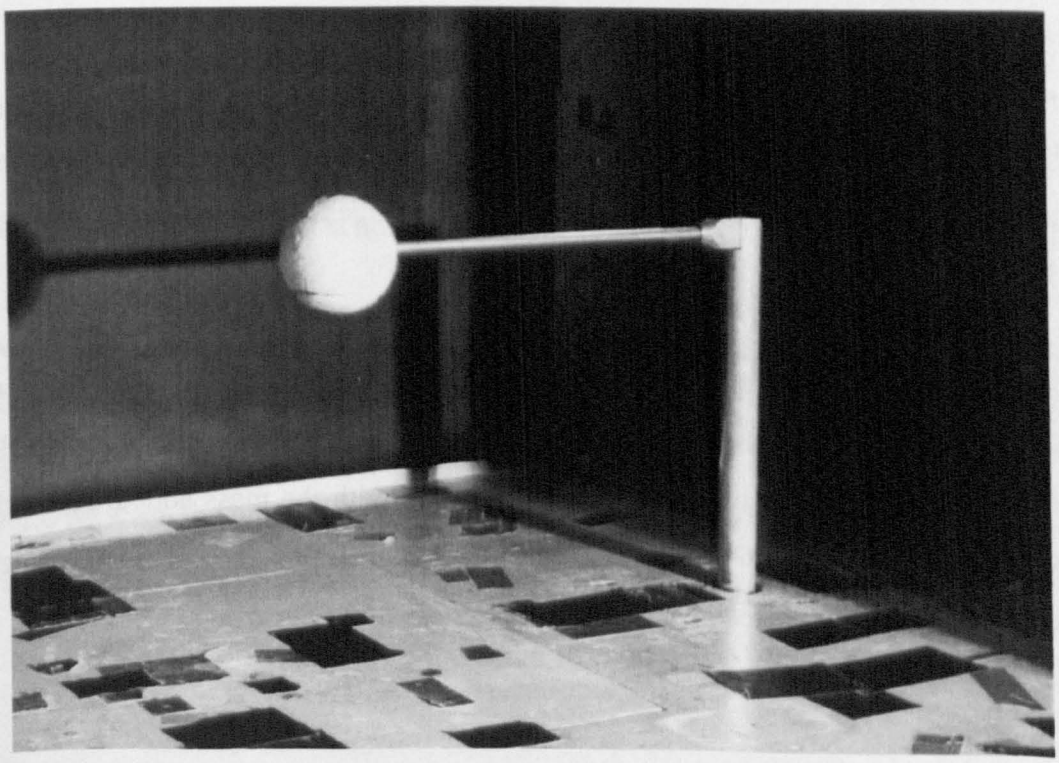

Figure 5.3 Picture of a ball attached to a sting in the low-speed wind tunnel.

The connection bar is bolted to the three component wind tunnel balance beneath the working section of the wind tunnel. The height of the bar is such that the ball is in the centre of the working section. The position at which the connection bar goes through the skin of the wind tunnel to the three component wind tunnel balance is decided by the position of the ball. The airflow is more stable just after the contraction, hence the connection bar was positioned such that the ball was in the front part of the working section.

5.4 Test method

The test method associated with both types of investigation is similar, however the high-speed test method is affected more by changes in the atmospheric conditions. The temperature within the wind tunnel increases at high speeds, hence the high-speed test is more closely monitored throughout.

There are several processes to undertake before testing can commence, the following sections outline each process.

5.4.1 Calibration

A voltage output from each of the three component wind tunnel balances is converted to drag force. The maximum drag force was estimated to be 10N in the high-speed wind tunnel and 1N in the low-speed wind tunnel. These ranges have been used to calibrate the two three component wind tunnel balances.

Figure 5.4 shows a schematic of the apparatus used to calibrate the three component wind tunnel balance for the low-speed wind tunnel tests. The masses are connected to the sting using high strength wire, chosen to minimise stretch with the mass added. A notch is cut into the front of the sting to locate the wire, which is then passed over a large wheel. The wheel is made as friction free as possible with the use of ball bearings.

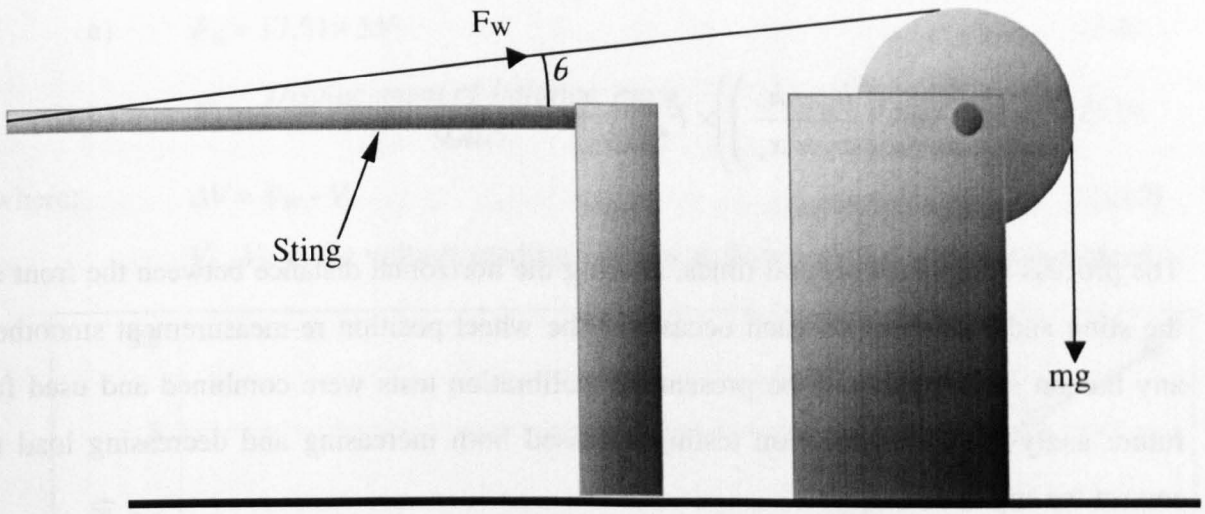

Figure 5.4 Schematic of the apparatus used for calibration of the three component wind tunnel balance.

The wire is attached at a small angle to the horizontal, hence the force, F_W, is applied along the line of the wire. A correction factor is required to convert the applied force to that acting along the line of the sting, F_D. The drawing in figure 5.4 can be simplified to that in figure 5.5, showing the difference in height causing a small angle θ to the horizontal.

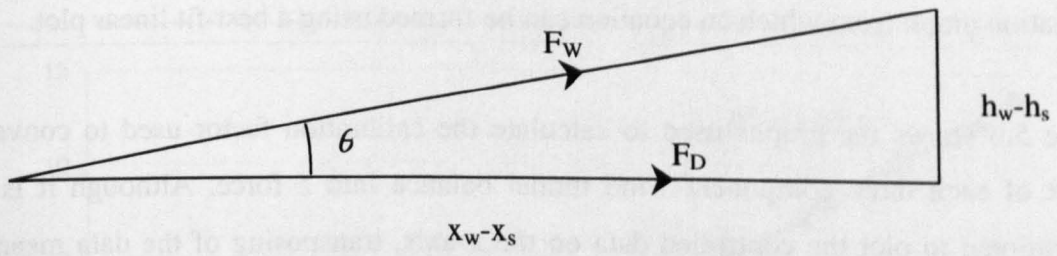

Figure 5.5 Simplified view of schematic in figure 5.4 to calculate the calibration factor.

The correction factor is calculated using trigonometry, where: the difference between the axis of the sting and the top of the wheel gives the difference in height; and the distance between the front of the sting and the back of the wheel gives the horizontal displacement. The angle between the wire and the axis of the sting is required first and is calculated using the following equation:

$$\tan\theta = \frac{height\ of\ wheel - height\ of\ sting}{back\ of\ wheel - front\ of\ sting} = \frac{h_w - h_s}{x_w - x_s} \tag{5.6}$$

Equation 5.7 is then used to find the force, F_D, acting along the axis of the sting:

$$F_D = \cos\left(\tan^{-1}\left(\frac{h_w - h_s}{x_w - x_s}\right)\right) \times F_{applied} \tag{5.7}$$

The process is repeated several times, altering the horizontal distance between the front of the sting and the wheel on each occasion. The wheel position re-measurement smoothed any human errors that may be present, all calibration tests were combined and used for future analysis. The calibration testing assessed both increasing and decreasing load to correct for any inertial effects.

Linear voltage displacement transducers are attached to both of the three component wind tunnel balances to define a balance point. The low forces experienced in the low-speed wind tunnel makes it possible to use the output of the displacement transducer to calibrate directly against drag force. As the force experienced in the high-speed wind tunnel tests exceeded the full-scale deflection of the displacement transducer, calibration was achieved more conventionally against the displacement of the balance mass required to regain balance with added load. The results obtained from all repeats are used to give a single calibration graph from which an equation can be formed using a best-fit linear plot.

Figure 5.6 shows the graphs used to calculate the calibration factor used to convert the output of each three component wind tunnel balance into a force. Although it is more conventional to plot the controlled data on the x-axis, transposing of the data means that the gradient of the line is the calibration factor.

A statistical measure of how closely a set of data points match a polynomial best-fit can be obtained using the Pearson Correlation Coefficient, *R*. An *R* value of one indicates that the two measurements are highly, positively correlated; and a value of minus one indicates that the two measurements are highly, negatively correlated. When a set of data is plotted against a polynomial curve of best fit, an R^2 value of one means that all the points fall on the curve. The very high R^2 values shown on these charts illustrate that the best-fit quadratic curves used have a high correlation with the original data set, hence the calibration factors can be applied with confidence.

The equation obtained for each test method is:

a) $$F_D = 17.51 \times \Delta V \tag{5.8}$$

b) $$F_D = \frac{Displacement\ of\ balance\ mass}{9.405} \tag{5.9}$$

where: $$\Delta V = V_W - V_I \tag{5.10}$$

V_I, V_W is the voltage reading with no airflow and at a known wind speed

a)

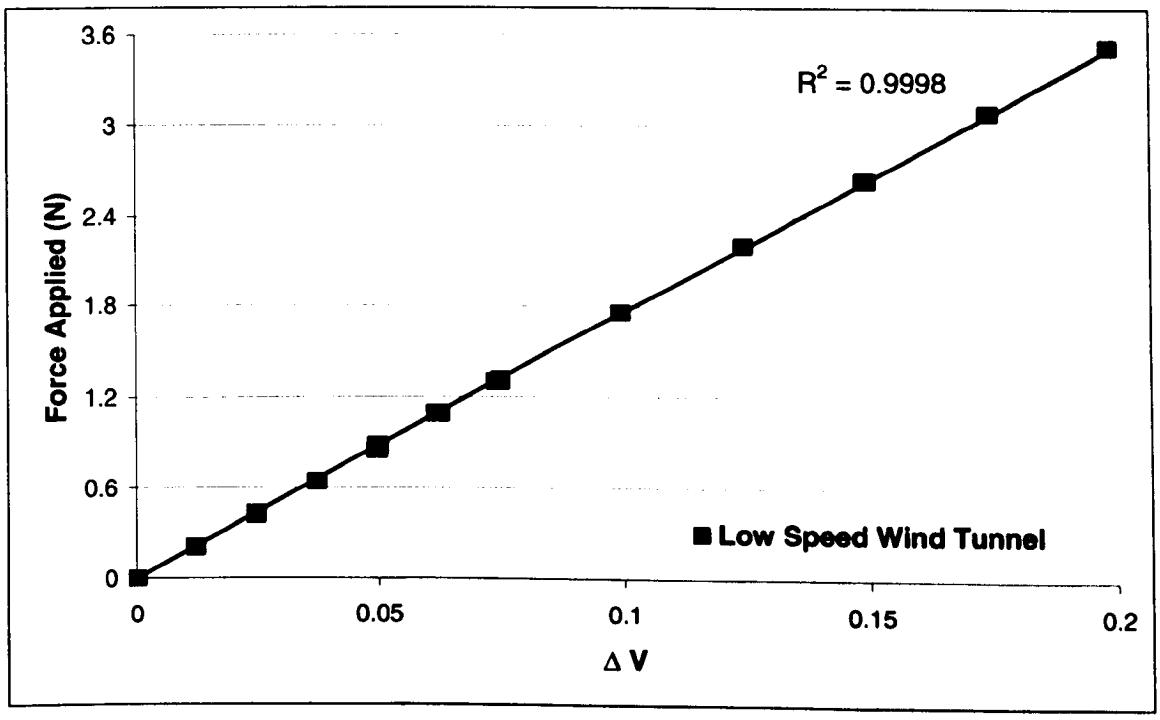

b)

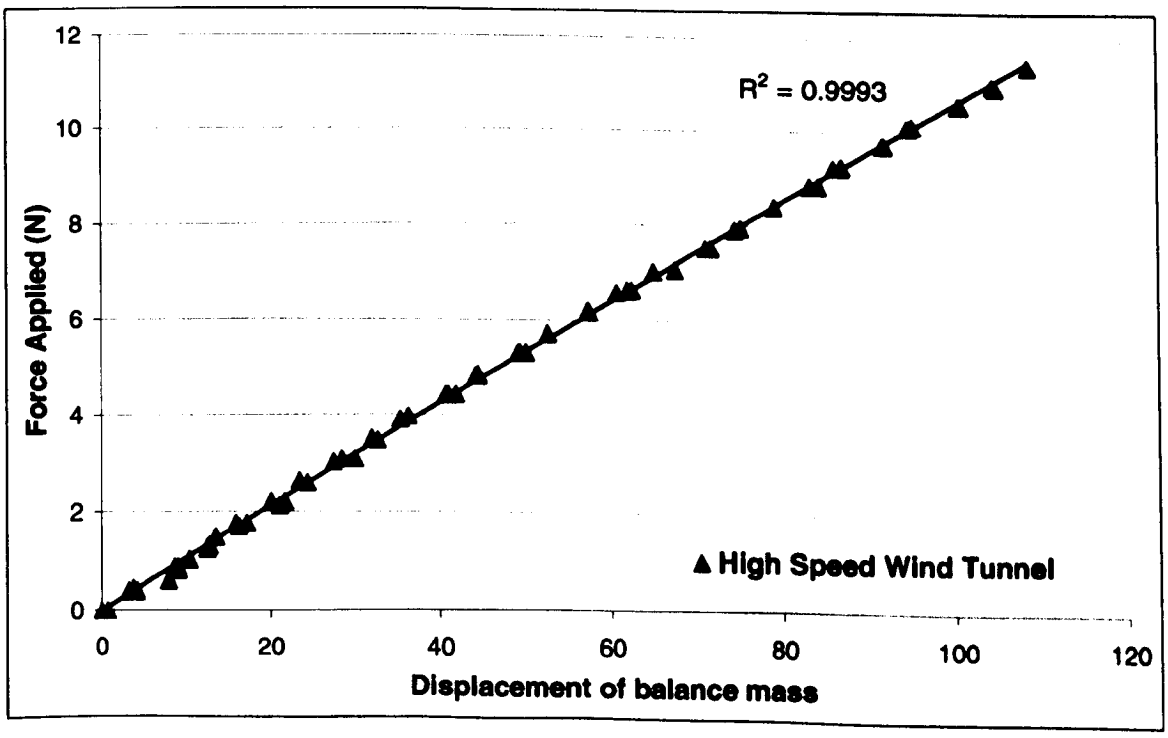

Figure 5.6 Graphs used to calculate the calibration factor for (a) the low-speed wind tunnel tests and (b) the high-speed wind tunnel tests.

5.4.2 Compensating for tare

The tare is the force associated with the sting assembly alone. The results obtained during testing is the combined force of the sting assembly and the ball, hence the force on the sting assembly has to be deducted. The tare is obtained by performing the tests with the ball removed. To ensure that the flow over the sting assembly is similar to that observed during normal testing, the ball has to be placed in its original position whilst not touching the sting. This poses two additional problems; how is the ball positioned in the middle of the wind tunnel and what happens to the bar that would normally hold the ball?

Figure 5.7 shows the set up used to find the force associated with the sting assembly for the high-speed wind tunnel tests.

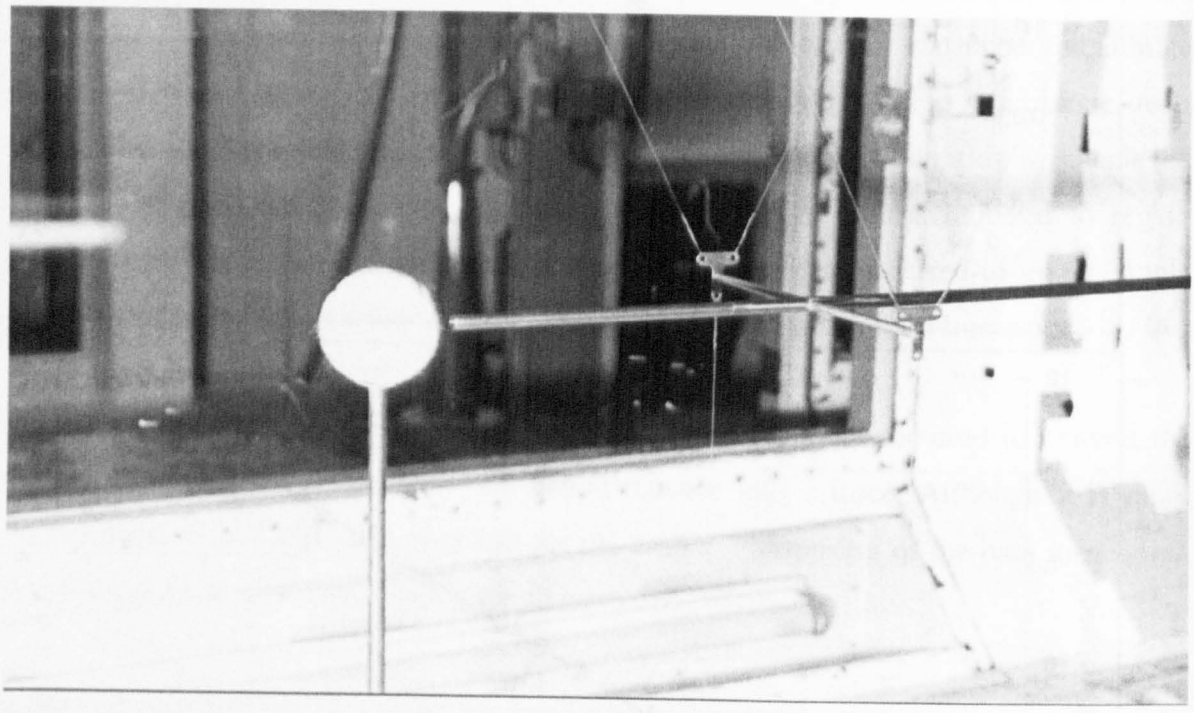

Figure 5.7 Set up used to find the force associated with the sting assembly for the high-speed wind tunnel tests.

The ball is attached to a rod, whose length is determined such that the ball is positioned directly in front of the sting. The other end of the rod is threaded and fits through a hole drilled in the bottom of the wind tunnel. The position of the hole is determined such that the ball is in the same position as it would have been on the sting. Oversized washers are used to help with stability, and the bar is bolted to the base of the wind tunnel. The sting is

designed in such a way that bars of different lengths can be attached between the ball and the cross member, hence a shortened bar is attached. The radius of the ball plus the anticipated deflection of the ball at top wind speeds govern the reduction in length. It is important that the ball does not touch the sting during testing, as this would give an overestimated force on the sting assembly.

The force is obtained by testing over a complete range of wind speeds, whereby a chart can be plotted of force against wind speed. The test method is discussed in detail in section 5.4.8. The process is repeated several times, and all of the data used to obtain the calibration equation.

Figure 5.8 shows the drag force on the sting assembly against wind speed in the high-speed wind tunnel. A similar chart is formed for the low-speed wind tunnel, and can be found in section 5.4.3. A quadratic best-fit equation is formed to calculate the tare at any given wind speed:

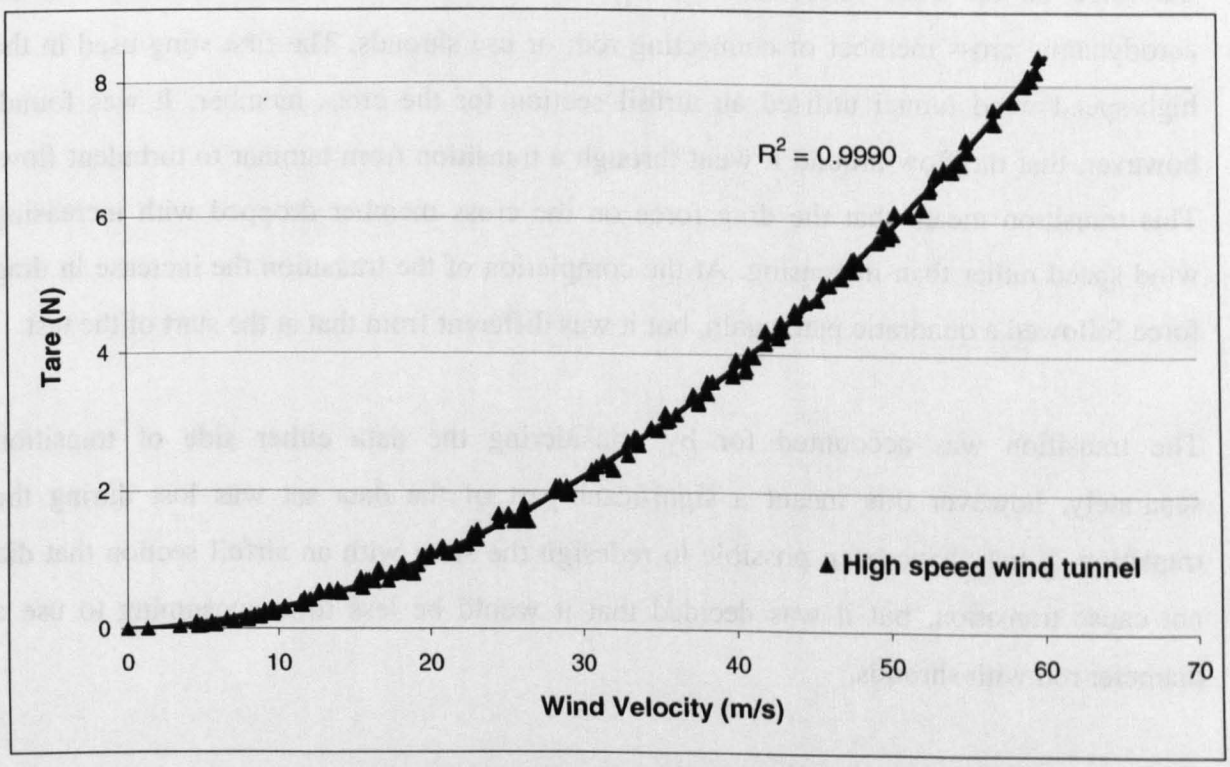

Figure 5.8 Graph to show the calibration factor obtained to compensate for tare in the high-speed wind tunnel.

The high R^2 value calculated (0.9990) illustrates that the quadratic curve of best fit correlates well with the original data shown. The tare for the high-speed wind tunnel tests is described by the following equation:

$$F_D = \frac{WindVelocity^2}{454.545} + \frac{WindVelocity}{113.636} - \frac{1}{120.482} \tag{5.11}$$

There are several ball types tested using these methods, it is important that the flow over the sting represents the flow that would occur if the ball were on the front of it, hence the tare is calculated for each ball type tested.

5.4.3 Shrouding

As mentioned in previous sections, it would be ideal if the force associated with the sting assembly were zero. If this were the case then the force obtained during testing would be the force on the ball. There are two options available to minimise the tare: use an aerodynamic cross member or connecting rod; or use shrouds. The first sting used in the high-speed wind tunnel utilised an airfoil section for the cross member. It was found, however, that the flow around it went through a transition from laminar to turbulent flow. This transition meant that the drag force on the cross member dropped with increasing wind speed rather than increasing. At the completion of the transition the increase in drag force followed a quadratic path again, but it was different from that at the start of the test.

The transition was accounted for by considering the data either side of transition separately, however this meant a significant part of the data set was lost during the transition. It may have been possible to redesign the sting with an airfoil section that did not cause transition, but it was decided that it would be less time consuming to use a diameter rod with shrouds.

A shroud is designed to deflect the airflow over the components perpendicular to the flow. Figure 5.9 shows the shrouding used in the low-speed wind tunnel tests. It can be seen that the shroud covers as much of the connection bar as possible whilst not touching the sting assembly at any point. Should the shroud touch the sting, the force applied to the sting will

not be translated accurately and the results will be unusable. When considering the high-speed wind tunnel tests, the shroud covers the cross member only, the wires cannot be shrouded easily. In this case there will still be a large portion of the sting assembly in the airflow.

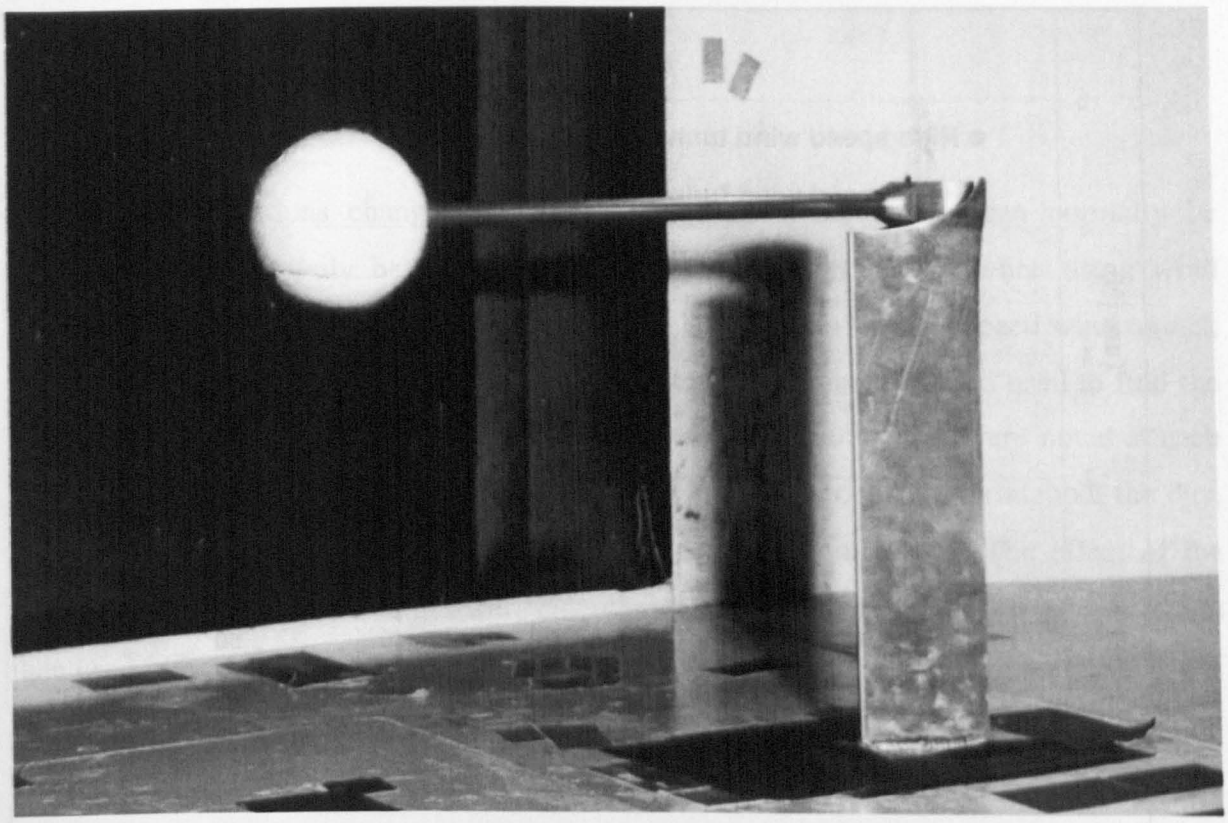

Figure 5.9 Shroud used in the low-speed wind tunnel tests.

The usefulness of the shrouds can be assessed at the time of collecting data for the drag force on the sting alone. Figure 5.10 shows the results obtained for tare against wind speed for the both of the test methods used. The F_D data presented is for both increasing and decreasing wind speeds and it can be seen that there is no sign of hysteresis in the system.

It can be concluded that:

- drag force is reduced by approximately 18% for the high-speed tests with the shrouds in place. The reduction in wind speed is approximately 3%, however the flow became unstable around the shroud at high velocities. It was decided that the benefits from using shrouds was not substantial for this sting configuration, and were not used for C_D tests.

- drag force associated with the sting was reduced by nearly 85% for the low-speed tests with the shroud in place. The reduction in velocity was approximately 2.5% thus the advantages far outweigh the disadvantages in this test method, and shrouds should be used in the C_D tests.

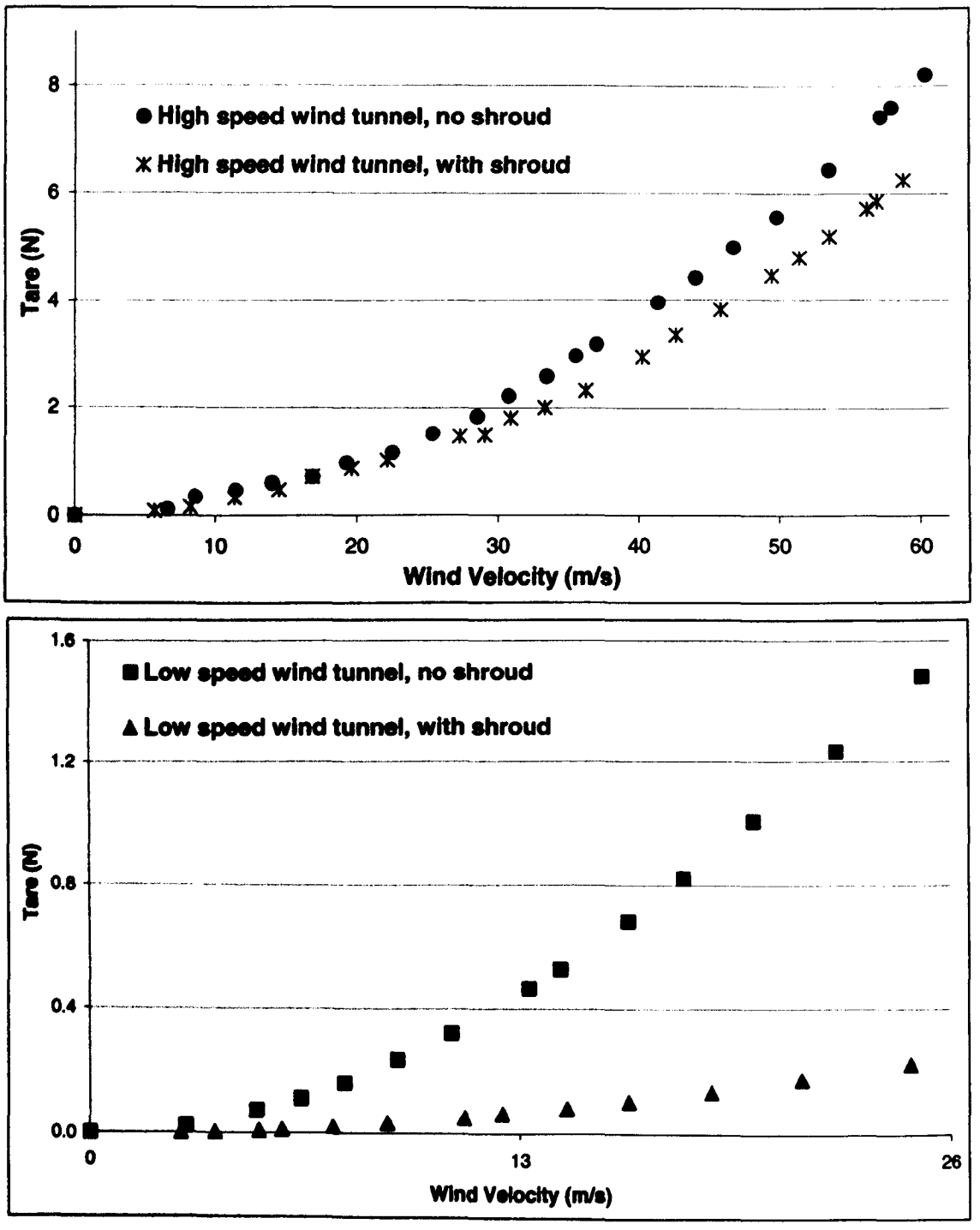

Figure 5.10 Tare versus wind speed for (a) the high-speed wind tunnel tests and (b) the low-speed wind tunnel tests.

Hence the tare for the shrouded low-speed wind tunnel tests can be described by the following equation:

$$F_D = \frac{WindVelocity^2}{3127.209} + \frac{WindVelocity}{697.643} - \frac{1}{483.161} \tag{5.12}$$

5.4.4 Compensation for atmospheric conditions

Atmospheric conditions change quite slowly, and on a local level can normally be accounted for on a daily basis. These changes occur more quickly when using wind tunnels, especially when testing at higher speeds. When using the low-speed wind tunnel, the temperature and atmospheric pressure was noted before each test and used to find the density of the air. With the high-speed wind tunnel, these parameters were noted at each wind speed. Whilst the atmospheric pressure remained fairly constant throughout the day, the temperature could rise by as much as 10°C during a single test. The effect of the temperature and pressure changes were calculated in a spreadsheet at each wind speed, and then used in further calculations, and a detailed explanation can be found in section 3.5.4.

5.4.5 Calculating the velocity of airflow

The wind velocity is calculated in one of two different ways: using the differences in atmospheric conditions across the contraction section prior to the working section; or using a pitot static tube within the working section, and both of these method are discussed in detail in section 3.1.4.

5.4.6 The diameter of a tennis ball

The drag coefficient is calculated using the diameter of the ball, if the ball is smooth this is a trivial matter. However if the ball has a fibrous cloth on it, as a tennis ball has, then defining the diameter can be difficult, issues related to these effects and the calculation method used in this study are described in section 3.4.

5.4.7 The turbulence of the wind tunnels

The turbulence level of a wind tunnel can be used to assess the quality of air in the wind tunnel compared with that in the open. It is calculated using the standard results for transitional airflow around a smooth sphere in free air, and the effects on quality of results that can be expected and method of measurement can be found in chapter 2.

5.4.8 The drag on a ball

Once all of the preliminary testing is complete, the testing to find the drag force on the ball itself can be undertaken. The ball is pierced in the middle of the manufacturer's printed logo such that it is not in the airflow. The hole is formed using a cork borer giving a hole slightly smaller that 10mm diameter rod. The rod is then inserted into the ball until it is tight up against the front wall of the ball. The ball is held on the rod using friction alone in most cases, possible due to the direction and size of the force that is exerted on the ball. Once the ball is in place, the rod is then screwed onto the sting, at which point the ball can be rotated to ensure that the orientation of the seam is the same in each test. Preliminary testing had shown that the seam orientation had negligible effect on the force exerted on the ball, however it was decided that consistency of orientation would remove any doubt.

Before the airflow is started, the digital readout is either set to zero or the zero reading taken. The wind speed is increased from zero to its maximum flow rate to give a complete set of data points. The collection of drag force data differs slightly for each test, hence the following sub sections describe each method separately.

> **High-speed wind tunnel:** the digital readout initially shows an out of balance in terms of voltage. A mass is attached to the balance, moved using a motor and belt system. The motor is controlled using a switch on the control panel, the direction determined by the polarity of the voltage readout. Balance is regained when the voltage returns to zero, and the distance moved by the mass noted in the spreadsheet. At low wind speeds, hence low forces on the ball, the balance point is difficult to determine.

Low-speed wind tunnel: In the low-speed wind tunnel tests, the digital readout shows the potential difference in the displacement transducer. The figure shown on the readout is noted directly into the spreadsheet. There were some occasions where the apparatus would vibrate in the wind causing the readout to fluctuate, the THURLBY 1905 intelligent multimeter was capable of averaging with respect to time was used in an attempt to overcome this.

The force associated with the sting assembly is calculated using the wind velocity, and is then subtracted from the total force to leave the drag force on the ball alone. Figure 5.11 shows an example of a set of results obtained in the low-speed wind tunnel. It can be seen that the force on the sting assembly is small compared with that on the ball, ideally this would be zero to reduce errors associated with subtraction. All of the data that is required to calculate the C_D is available for use in equation 5.5.

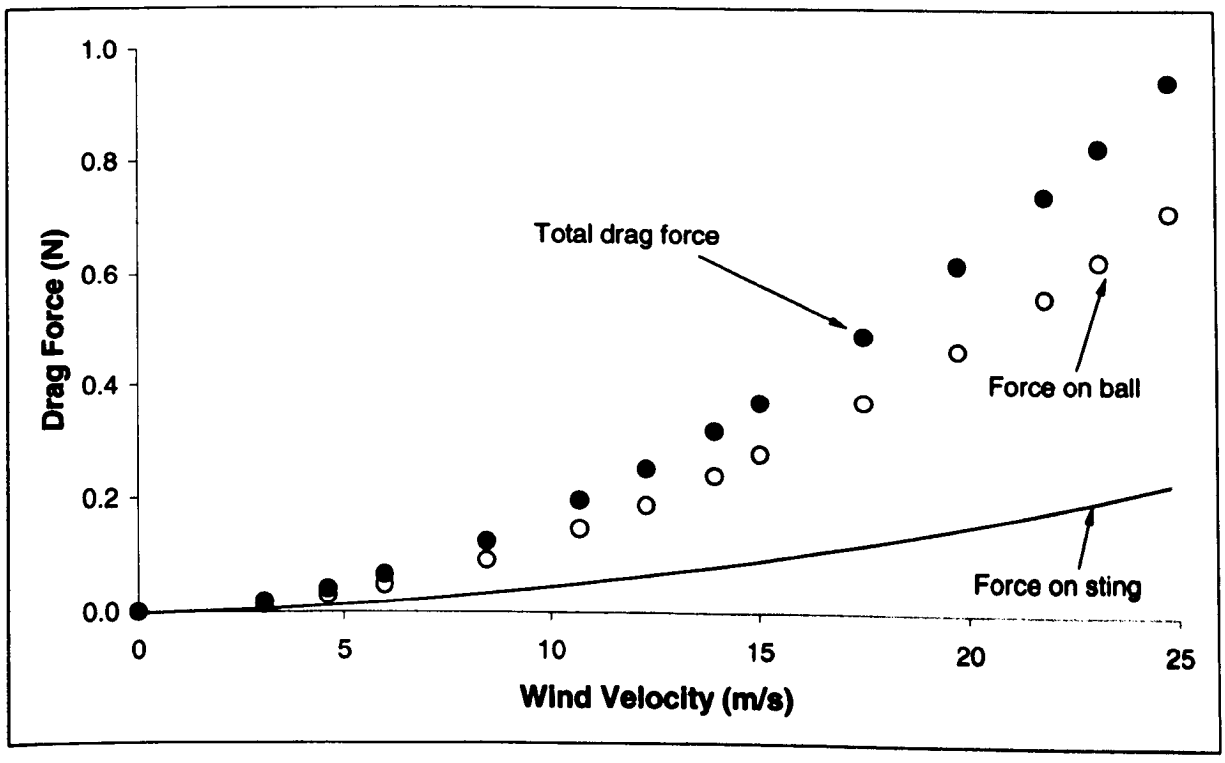

Figure 5.11 Graph showing the force components that are required to find the drag force on the ball alone (results obtained in a low-speed test).

5.5 Results

5.5.1 Smooth Sphere

Initial testing is designed to check that the test method yields satisfactory results compared to previous test data. Testing uses a 2.5inch diameter plastic ball, more commonly used as a jack in bowling. Previous work has shown that the drag coefficient for a smooth ball should be approximately 0.5 (Achenbach, 1973).

Figure 5.12 shows the C_D results obtained for the smooth ball in both wind tunnel test methods plotted on a dimensionless chart against Re, it can be seen that the C_D is approximately 0.5 for all wind speeds. This result shows that both of the test methods are suitable to find drag forces on a ball and that they will give reasonable results. Results are plotted for Reynolds numbers $2x10^4$ and above, which relates to approximately $5ms^{-1}$ and above. Below this, the force on the ball was very small, and the results returned were unsatisfactory.

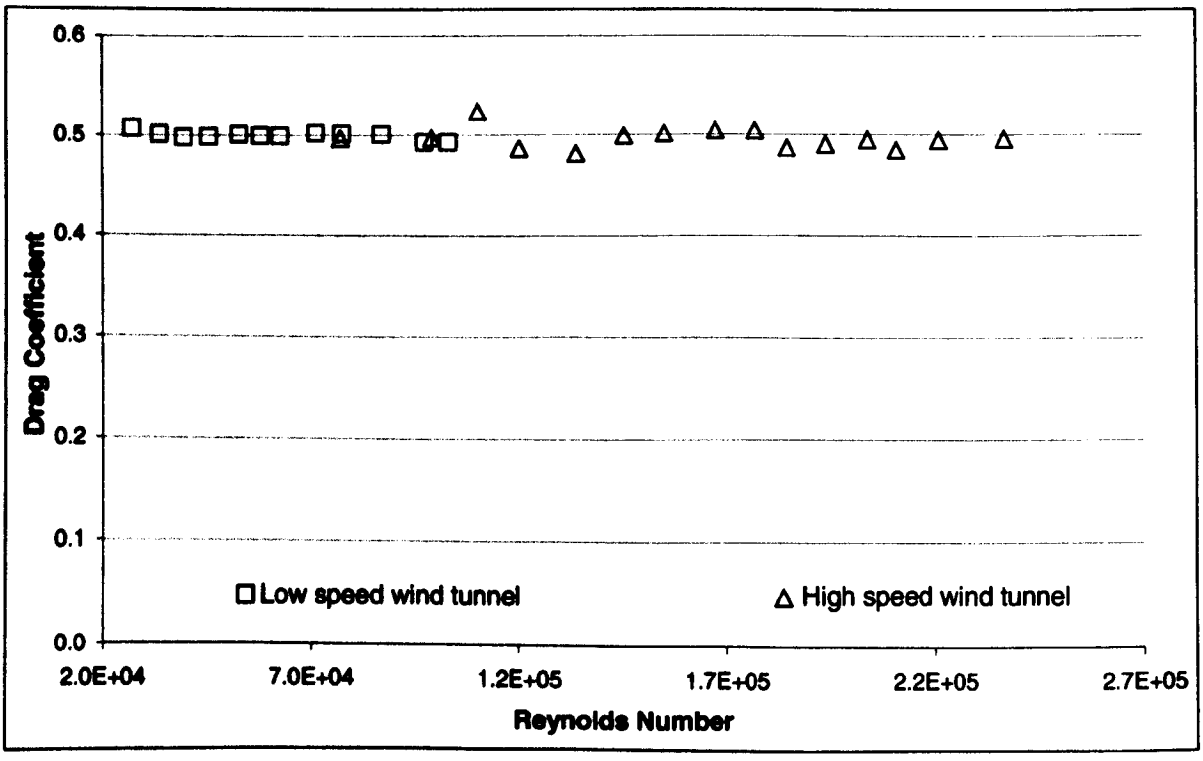

Figure 5.12 Graph showing the drag coefficient obtained for a smooth 2.5 inch ball using both of the wind tunnel test methods.

It can also be seen that the results obtained using the high-speed wind tunnel contains more scatter than those obtained using the low-speed wind tunnel. In fact, the results obtained at low speeds in the high-speed wind tunnel are ignored in this chart due to their inaccuracies. The test was repeated several times in an effort to assess the repeatability and hence the accuracy of the test method. It was found that the C_D results obtained using the high-speed wind tunnel have typical errors of 4.8%, and reduce to less than 2% when using the low-speed wind tunnel. This reduction is due to two factors; primarily the manner in which the force is deduced (balance resolution); however the reduced force applied to the sting (due to the shrouding) in the low-speed wind tunnel testing will also contribute.

5.5.2 Testing of a tennis ball

Initial investigations used a variety of brands of new tennis balls to assess any effect of differing construction. A hole was punctured into each ball, but other than that the balls were handled as little as possible prior to testing such that the nap was representative of the new ball. The ball types tested were, standard sized pressurised, oversized pressurised and standard sized permanent pressure.

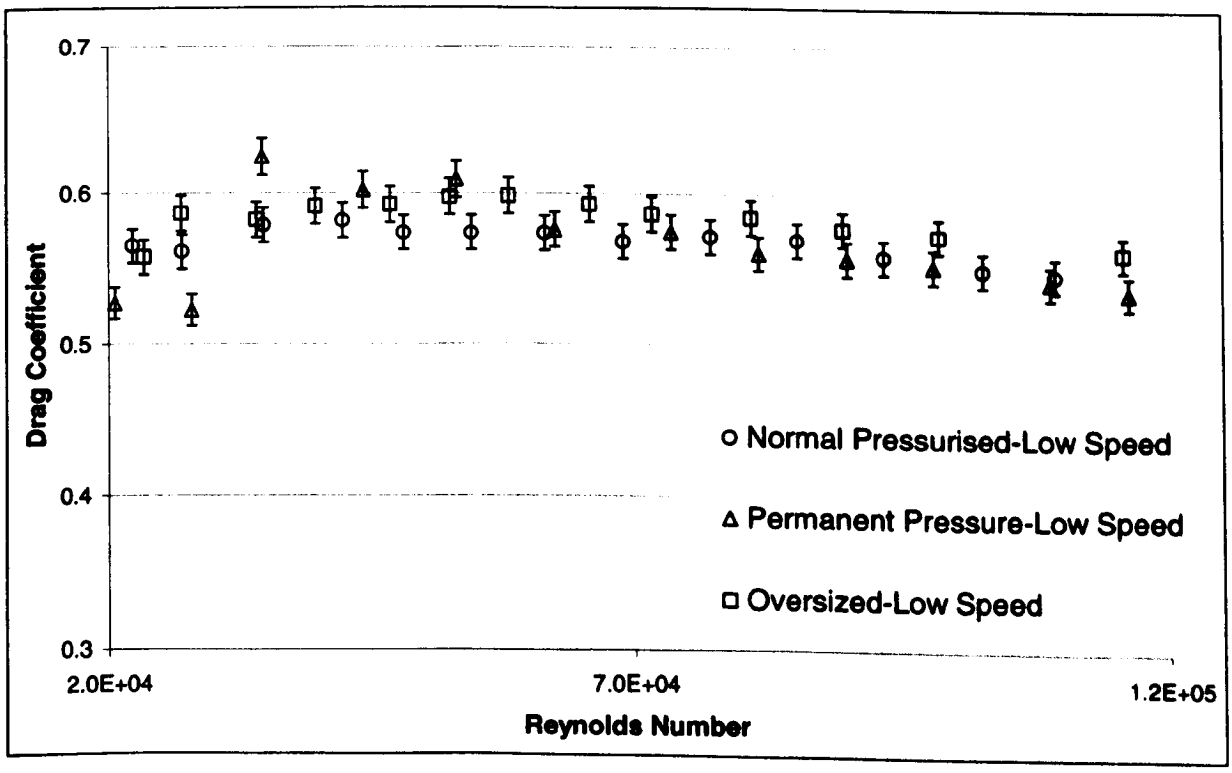

Figure 5.13 Drag coefficient results obtained for three different tennis balls in the low-speed wind tunnel.

Figure 5.13 shows the drag coefficient results obtained for the three different tennis balls in the low-speed wind tunnel. Each ball type returns C_D results between 0.5 and 0.6 for all Reynolds numbers tested, moreover, all three balls follow a similar trend.

A similar chart is plotted for C_D results obtained in the high-speed wind tunnel in figure 5.14. Although there is a significant scatter it appears that the C_D has become stable at a constant value between 0.5 and 0.55. It can be seen from the results obtained for the normal pressurised ball in the low-speed wind tunnel that the high-speed wind tunnel gives a satisfactory continuation of results.

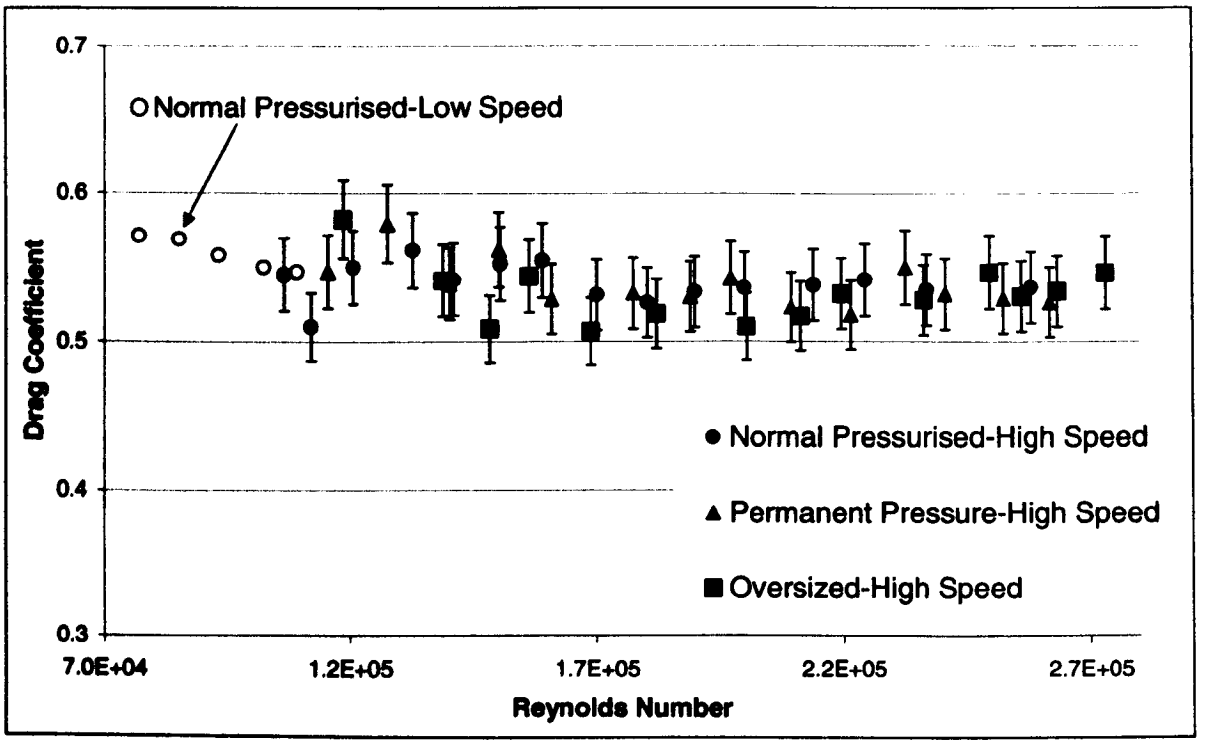

Figure 5.14 Drag coefficient results obtained for three different tennis balls in the high-speed wind tunnel.

Error analysis has been achieved using a repeatability study on a single ball tested in both wind tunnel test methods. All balls were tested at least twice to protect against calibration errors during set-up, however a single normal pressurised ball was tested 10 times in each wind tunnel. The standard deviation between the results was then used to approximate the error in each test method. It was found that the error in the low-speed wind tunnel tests was approximately 2%, however this rose to over 4% in the high-speed wind tunnel tests.

The relatively high error values obtained in the high-speed wind tunnel testing can be reduced using a best-fit quadratic curve applied to the drag force data. Figure 5.15 shows the combined drag force data of ten individual analyses for the normal pressurised tennis ball plotted against velocity in the high-speed wind tunnel.

It can be seen that the curve of best fit correlates well with the original data giving an R^2 value of 0.9996. The quadratic equation can be obtained in the normal way within excel, and this can then be used to plot a new set of results for C_D.

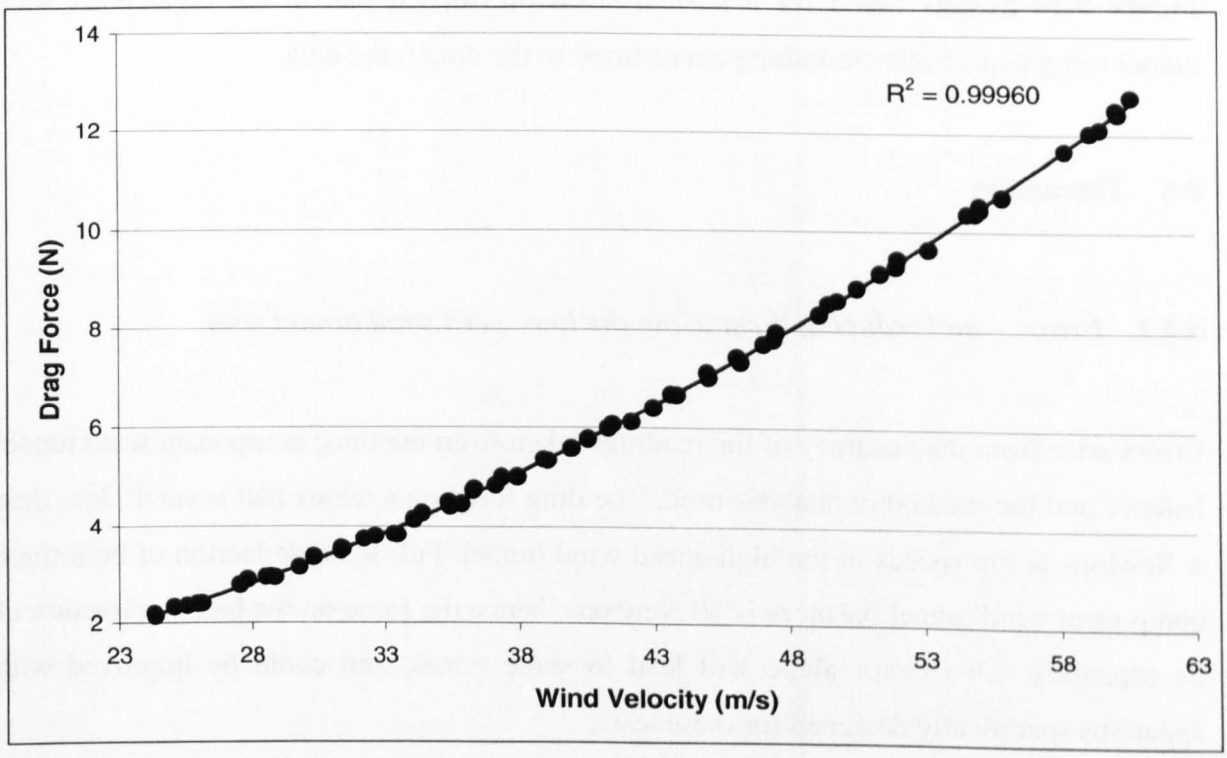

Figure 5.15 Combined drag force data of ten individual analyses for a normal pressurised ball plotted against velocity using the high-speed wind tunnel.

Figure 5.16 shows the results obtained using the best-fit quadratic equation obtained in figure 5.15. It can be seen that the results are now consistent for Reynolds number $5x10^4$ and above, with no sign of transition. The C_D obtained for a normal sized pressurised non-spinning tennis ball is approximately 0.53, and balls of similar surface condition have a similar C_D. The different size and construction appears to have little or no effect on the value obtained for C_D.

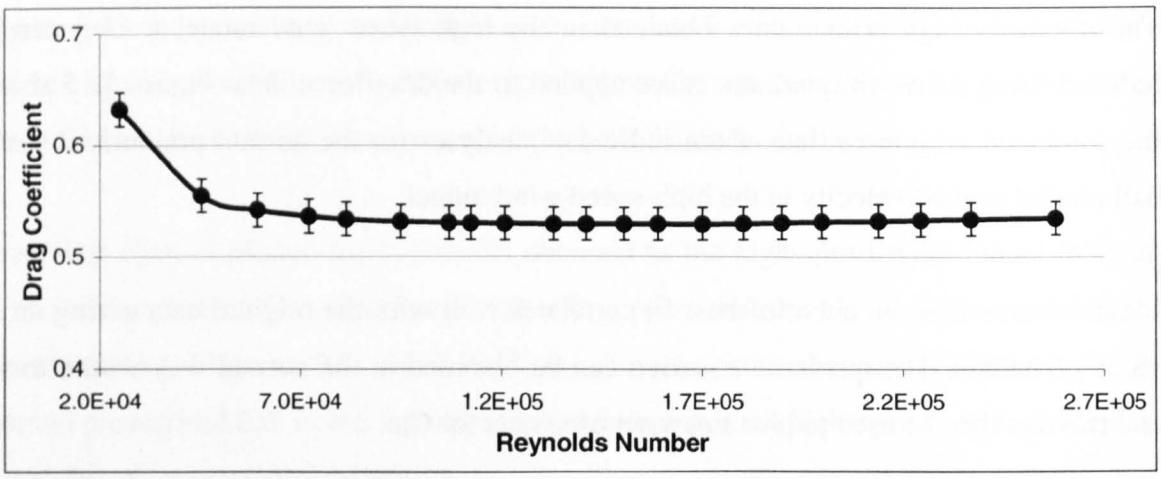

Figure 5.16 Results found for a normal sized pressurised ball in the high-speed wind tunnel using a quadratic smoothing curve fitted to the drag force data.

5.6 Discussion

5.6.1 Errors – and reducing them using the low-speed wind tunnel tests

Errors arise from the accuracy of the readings taken from the three component wind tunnel balance and the method of analysis used. The drag force on a tennis ball is small, less than 4 Newtons at top speeds in the high-speed wind tunnel. Full scale deflection of both three component wind tunnel balances is 50 Newtons, hence the force on the ball is a fraction of its capability. This factor alone will lead to some errors, and could be improved with apparatus specifically designed for these tests.

It was shown that the magnitude of errors depends on the method of analysis used. The method used in the high-speed wind tunnel tests requires a significant amount of visual interpretation of balance point. At low wind speeds, it is possible that the small force on the ball will cause a voltage difference within the system errors. The reading obtained for force is dependent on the interpretation of balance point. On occasion, the mass would be moved to regain balance but the output from the displacement transducer would not show any change. Subsequent requests for displacement of the mass would cause a sudden overshoot. It appeared as though there were some inertial effects in the displacement transducers whilst the encoder attached to the mass was showing movement. On these occasions, time was spent moving the mass forwards and backwards endeavouring to

regain balance, should it not be possible, limits were obtained and the mid-point used as the drag reading.

The results obtained using the low-speed wind tunnel method were found to contain fewer errors than those obtained in the high-speed wind tunnel method. The apparatus was not necessarily superior, more the method by which the drag force was determined. The displacement transducers on this three component wind tunnel balance are used to determine the drag force directly. With this in mind, a modification to the high-speed wind tunnel test was attempted, however the deflection of the displacement transducers was not sufficient to cope with the complete range of force applied.

5.6.2 Comparison with previously presented C_D results

Mehta and Pallis (2001) acquired C_D data for tennis balls using a force platform in a wind tunnel. The C_D of a normal sized pressurised tennis ball from the same manufacturer as used during this study was calculated to be just above 0.6, more than 13% greater than that obtained during this study. Interestingly, an oversized ball was calculated to have a C_D of just above 0.63, it should be noted however, this ball type was supplied by a different manufacturer. It was stated that based on the repeatability of the test method, the larger ball result was comparable with the regular ball. The next section describes some of the factors that lead to differences in C_D, however it is understood that the method of measuring the diameter of the balls differed significantly between the two studies.

Although the results were obtained by a different manner, it is useful to draw comparison with Stepanek (1988). In this study it was found that a non-spinning ball had a C_D of 0.51, a figure closer to that obtained in this study. Just prior to Stepanek's testing, Zayas (1985) used a projectile test to calculate the C_D of a non-spinning tennis ball to also be 0.51, however it should be noted that errors were stated to be ±0.08 (more than 4 times that of the worst errors found in this study).

5.6.3 Factors affecting the drag coefficient

The projected area of the ball has a high influence on the value obtained for C_D, a 2% increase in the diameter of the ball will result in a 4% decrease in the value of C_D obtained. For this reason it is important that the diameter used is a true reflection of that which is affecting the flow of air around the ball. The methods used in this study assume that the diameter of the ball is constant for all wind velocities. Figure 5.17 shows that fibres flatten at increasing wind speeds, and it is hypothesised that this leads to a reducing diameter.

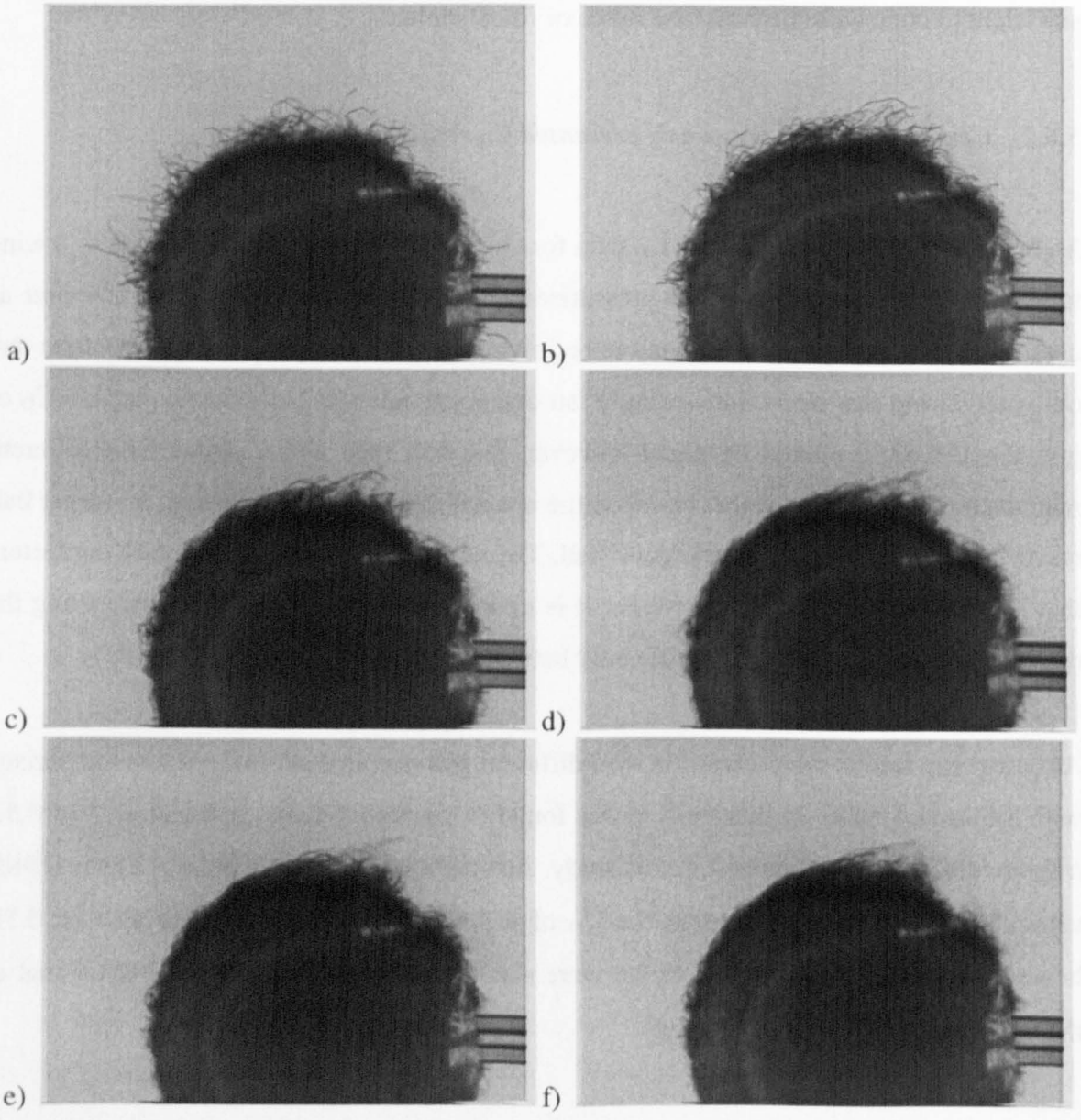

Figure 5.17 Photographs taken of a fluffed pressurised ball at wind speeds of approximately (a) zero; (b) 17ms^{-1}; (c) 29ms^{-1}; (d) 40ms^{-1}; (e) 50ms^{-1}; and (f) 60ms^{-1} in the high-speed wind tunnel.

There is very little difference between images 5.17c to 5.17f suggesting that most of the flattening occurs below $29ms^{-1}$. If this evidence is used in conjunction with the results obtained in figure 5.16, it can be postulated that the initial reduction of C_D at low values of Re is due to the flattening of the nap. The small changes observed after figure 5.17c correlates with the constant C_D obtained at high values of Re.

The method used to determine the diameter of a tennis ball for this set of investigations is described in detail in section 3.4, however researchers at different institutions use different methods that may give a different drag coefficient. At first glance, the C_D results obtained may be assumed to be incorrect, however it may be that the diameter measurement used in the analysis is different and the C_D may well be the same. Although the drag coefficient is a well known parameter, it is possible to normalise the results to a form which does not use diametric effects. Rather than plotting C_D versus Re, a plot of C_DA versus Re (or even velocity) can be created. Issues related to presenting in this form are discussed in greater detail in chapter 10.

5.6.4 Implications for the game of tennis

It was anticipated that a sudden drop in C_D would be observed due to a transition from laminar to turbulent flow in the boundary layer. The results obtained show no transition point, which implies that a tennis ball can be considered to have a constant value of C_D for all values of Re tested, i.e. the C_D of a tennis ball is independent of Re. It is therefore possible to determine methods of retarding the ball more quickly with simple use of equation 5.5. Increased retardation is caused by increased drag force, which can theoretically be induced by; increasing the diameter of the ball; or increasing the C_D of the ball. It has been shown that increasing the size of the ball has negligible effect on the C_D, however methods of changing the C_D of a tennis ball will be discussed in chapter 7.

THIS PAGE INTENTIONALLY LEFT BLANK

6 SPINNING BALL TESTING USING A THREE COMPONENT WIND TUNNEL BALANCE

6.1 Introduction

The trajectory of a tennis ball is determined by the gravitational and aerodynamic forces acting on it during flight. All testing methods undertaken thus far have concentrated on non-spinning spheres and hence only evaluated the aerodynamic drag forces, however a spinning ball also has a lift force imparted on it.

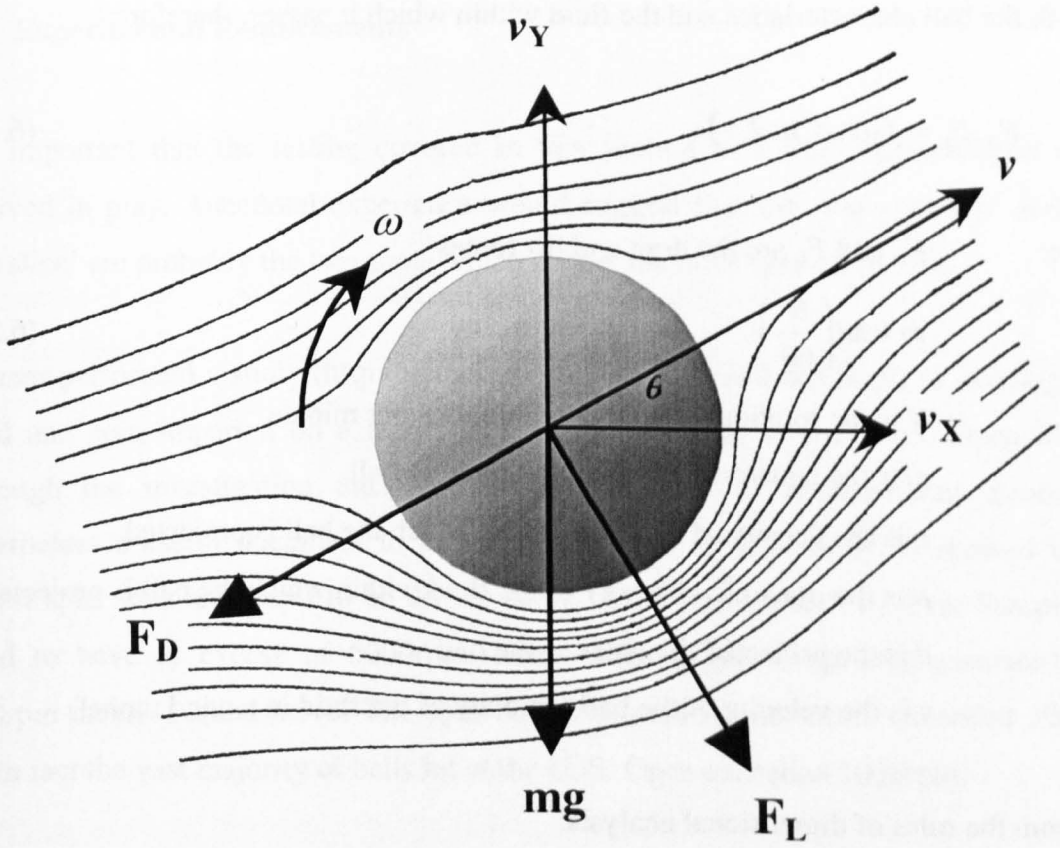

Figure 6.1 Forces diagram showing the flow lines around a ball spinning in the direction of ω travelling at velocity v ms^{-1} and $\theta°$ to the horizontal.

The effect of the spin is to advance the separation of the flow from the surface rotating in the same direction as the projected ball. Conversely, the separation on the surface rotating in the opposite direction as the projected ball is delayed. Figure 6.1 shows a sphere rotating in the direction of ω, travelling at velocity v ms^{-1} and elevation angle $\theta°$. In this scenario,

separation is advanced on the upper surface and delayed on the lower surface as shown by the flow lines.

The previous three sections have shown that load cells return the most accurate results, hence it has been decided to expand this method to measure both drag and lift forces for a spinning ball.

6.2 Theory

The aerodynamic drag and lift forces, F_D and F_L, acting on a spinning sphere are functions of both the ball characteristics and the fluid within which it passes, therefore:

$$F_D, F_L = f(\omega, \rho, \mu, d, v) \tag{6.1}$$

where: F_D and F_L are the drag and lift forces

$$\omega = \pi d\left(\frac{N}{60}\right) \tag{6.2}$$

N is the rotational speed in revolutions per minute

ω is the equatorial speed of the rotating ball

ρ is the density of the fluid within which the ball is projected

μ is the dynamic viscosity of the fluid within which the ball is projected

d is the projected diameter of the ball

v is the velocity of the ball (velocity of the fluid in a wind tunnel)

and from the rules of dimensional analysis:

$$C_D, C_L = f\left[\frac{\rho v d}{\mu}, \frac{\omega}{v}\right] \tag{6.3}$$

where: $\frac{\rho v d}{\mu}$ = Reynolds number = Re (6.4)

$\frac{\omega}{v}$ is the velocity ratio which will be termed the spin coefficient

The equations used to define the drag and lift forces are:

$$F_D = (\tfrac{1}{2}\rho v^2) \times AC_D = (Dynamic\ Pressure) \times AC_D \quad (6.5)$$

$$F_L = (\tfrac{1}{2}\rho v^2) \times AC_L = (Dynamic\ Pressure) \times AC_L \quad (6.6)$$

where: $A = \frac{\pi d^2}{4}$ the projected area of the ball

C_D and C_L are the drag and lift coefficients

6.3 Experimental Requirements

It is important that the testing covered in this section is a true representation of that observed in play. Anecdotal experience would suggest that the 'top spin lob' and 'back hand slice' are probably the two shots which impart the most spin on the ball.

Cislunar performed a study (http://wings.avkids.com/Tennis/index.html) to investigate the speed and spin imparted on a tennis ball by professionals at the U. S. Open in 2000. Although the investigation did not consider accuracy or measurement errors, it is nevertheless a useful document to be used as a basis for this study. It showed that the highest spin rates are found to be on the serve. A 2nd serve struck by Pete Sampras was found to have in excess of 5000rpm. Many other players regularly generated 4000-5000rpm on the second serve. The spin on the ground strokes often exceeded 3000rpm, and in fact the vast majority of balls hit at the U. S. Open exceeded 1000rpm.

As with much of the previous testing it was decided that standard tennis balls would be used for all testing. Discussions that prevented the use of modified balls in previous tests are even more important for the spinning ball where the interaction between the nap of the ball and the air is of great interest.

A ball can be struck at different velocities and in both cases have a similar spin coefficient. According to previous testing, the aerodynamic properties of a spinning ball are independent of Reynolds number (Bearman & Harvey, 1976), hence for a similar spin

coefficient comprising of different spin rates and wind speeds, the C_D or C_L is expected to be the same. This relationship, together with the complexity of the test method, has been used to decide that a low-speed wind tunnel will be used for the spinning ball testing. The relatively low wind speeds attainable are of little concern provided that a variety of spin rates can be achieved.

6.4 Apparatus

The apparatus used in this test method is similar to that used in chapter 5, however the sting carrying the ball and the mounting method is different. The three component wind tunnel balance required for the experiment meant that the low-speed wind tunnel was used for all spinning ball tests. The same three component wind tunnel balance that was used in the low-speed tests in chapter 5, was used for these tests such that the test method was as accurate as possible.

The modification to the mounting meant that the area occupied by the ball and sting assembly was reduced to approximately 1.5%. This reduced blockage implies that both the maximum velocity attainable and the airflow quality were improved.

6.4.1 The spinning sting

The spin was achieved using a 24V electric motor rated at 10,000rpm. The motor was controlled using a mains operated motor controller with the spin rate controlled using a single revolution full-scale potentiometer. The ball was connected to the motor via a circular bar mounted vertically, situating the ball in the middle of the working section. The drag forces on the supporting bar needed to be minimal to reduce subtraction errors in later analysis. However the bar also needed to be rigid enough to support a rotating concentrated mass at one end (on the top). As the ball was in the same plane as the bar, shrouding was not possible as it would affect the airflow around the ball, it was decided that a 10mm diameter bar would be a satisfactory compromise. Figure 6.2 shows an exploded view of the interfaces required for the sting, and the inset shows all of the components fully assembled.

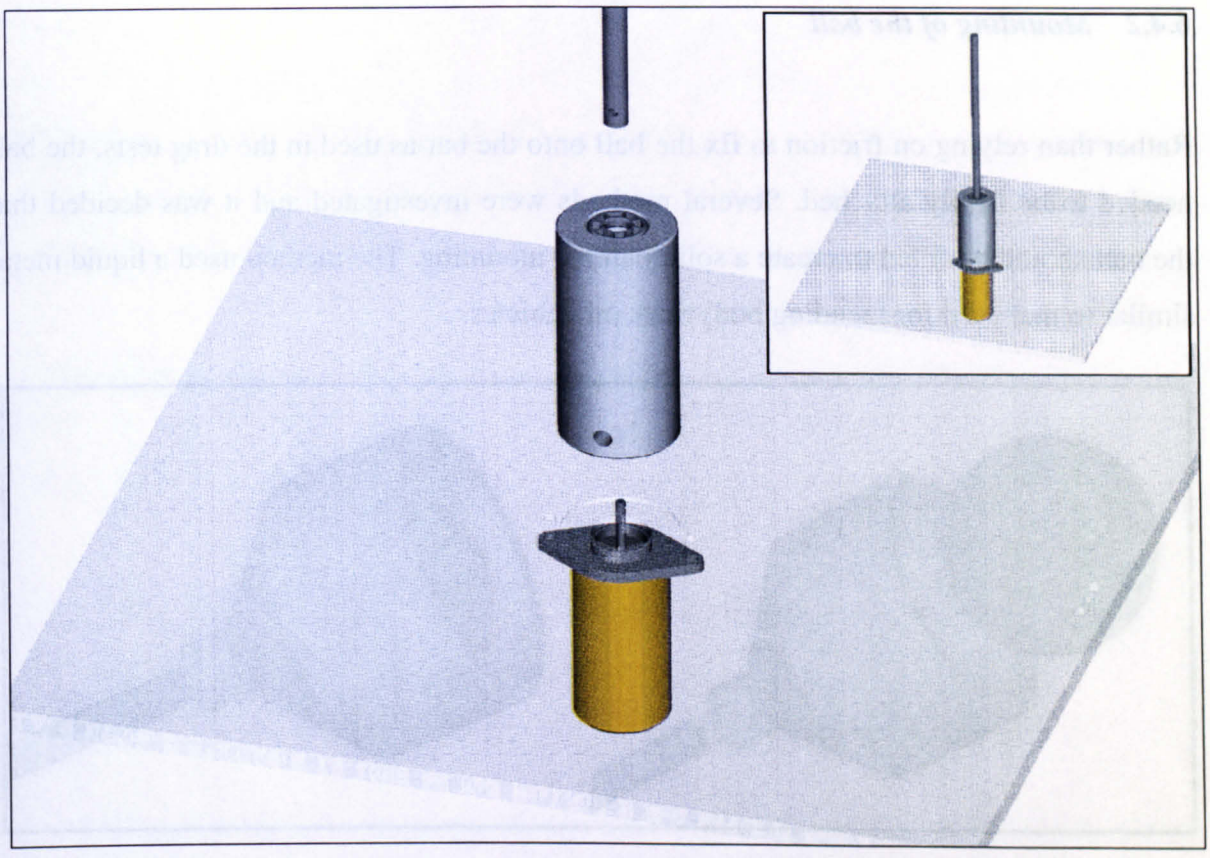

Figure 6.2 Exploded view showing the sting assembly used for mounting the balls. Inset shows fully assembled apparatus.

A bearing housing containing two sets of ball bearings spaced 100mm apart was used to aid stability. The friction in the bearing meant that the maximum spin rate attainable was approximately 7500rpm. The torque required to overcome the inertia of the bearings meant that the minimum spin rate attainable was approximately 300rpm. There are no further enforced limitations of spin rate with the motor control unit enabling flexible settings between these limits.

The bearing housing and motor were mounted on opposite sides of a 400mm square aluminium interface plate, which was then connected to the three component wind tunnel balance. The shape and size of the interface plate was designed to reduce vibrations due to the spinning ball. Although every effort was taken to remove vibrations, a resonant frequency of the complete assembly occurred between at approximately 1000rpm to 1200rpm. The interface plate was connected to the three component wind tunnel balance using four screws and positioned using dowel pins at the interface.

6.4.2 Mounting of the ball

Rather than relying on friction to fix the ball onto the bar as used in the drag tests, the ball needed to be firmly attached. Several methods were investigated and it was decided that the ball should be filled to create a solid ball for mounting. The method used a liquid metal similar to that used for mending bodywork on vehicles.

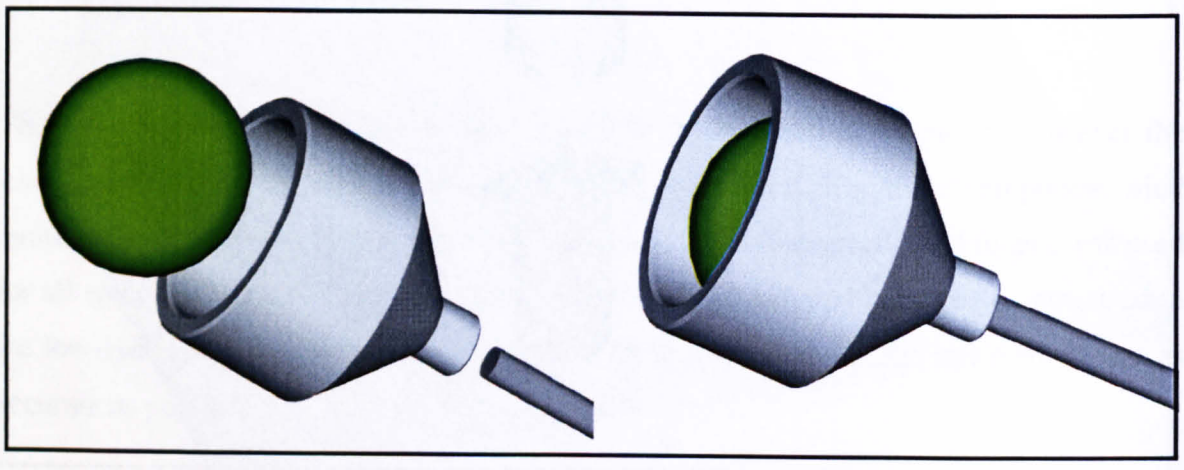

Figure 6.3 Jig used to accurately assemble the ball onto the bar.

A jig was designed to locate the bar in the ball while the filler was still in its liquid state, thus negating the further requirement for machining and mounting of the ball. The jig was designed to ensure that the bar was situated on the central axis of the ball as shown in figure 6.3. Should the ball not be mounted symmetrically, the vibrations caused at high spin rates would not only make it impossible to obtain satisfactory results but could be dangerous.

6.5 Achieving the correct spin rates

The spin rate was determined at the beginning of each test, without wind applied. As a consequence, the spin rate was assumed not to change with increasing wind speed. Initial testing used a direct contact tachometer, however an optical tachometer was the preferred apparatus and was used in all results shown in this chapter. The accuracy is improved significantly using the optical tachometer, as there is no frictional effects caused by contact with the spinning component.

The optical tachometer used a reflective strip of tape to calculate the spin rate. The tape was attached to the bar rather than the ball, thus minimising any change in aerodynamic effects that may occur. The minimum spin rate measurable by the tachometer was 3rpm with a maximum of 99,999rpm. The LCD screen contained five digits, hence the resolution decreased as the spin rate increased. The physical range of the optical tachometer was between 25mm and 1000mm. However it would not work through the Perspex on the door of the wind tunnel, and hence, it was necessary to measure the spin rate prior to testing. An LED was used to indicate correct optical alignment, this was essential at high spin rates on such a small target.

6.6 Test method

6.6.1 Introduction

It is possible to generate results for both drag and lift during a single test, however the apparatus required would be large and heavy using the commercial three component wind tunnel balance available. Although much of the apparatus would be outside of the wind tunnel, a significant part would be within the airflow, and hence would have aerodynamic forces applied to it. Given the relatively low forces expected on the tennis ball, such an apparatus would significantly reduce the accuracy of the test method.

It was decided that a simplified, single vertical bar would minimise any unwanted aerodynamic forces applied. In this orientation it is a side force applied rather than the more conventional vertical lift force. As a consequence, only one force per test can be obtained, with the lift force being obtained with the three component wind tunnel balance turned perpendicular to the flow of air.

The overall forces obtained comprise both the forces on the ball and the support apparatus. The force associated with the support apparatus is measured separately and removed from the overall forces obtained in later testing.

6.6.2 Compensating for drag and lift due to the bar

Figure 6.4 shows a ball positioned on the top of a bar as used in this test method. The testing to compensate for the forces on the supporting apparatus differ from previous test methods. In previous testing, a ball was positioned to simulate the altered flow over the sting. It was observed during early test methods that the projected area of the remaining bar was critical. Therefore, as a compromise, it was assumed that the flow over the bar was not altered significantly with the ball in place and the tare was calculated using a bar that had the ball cut off.

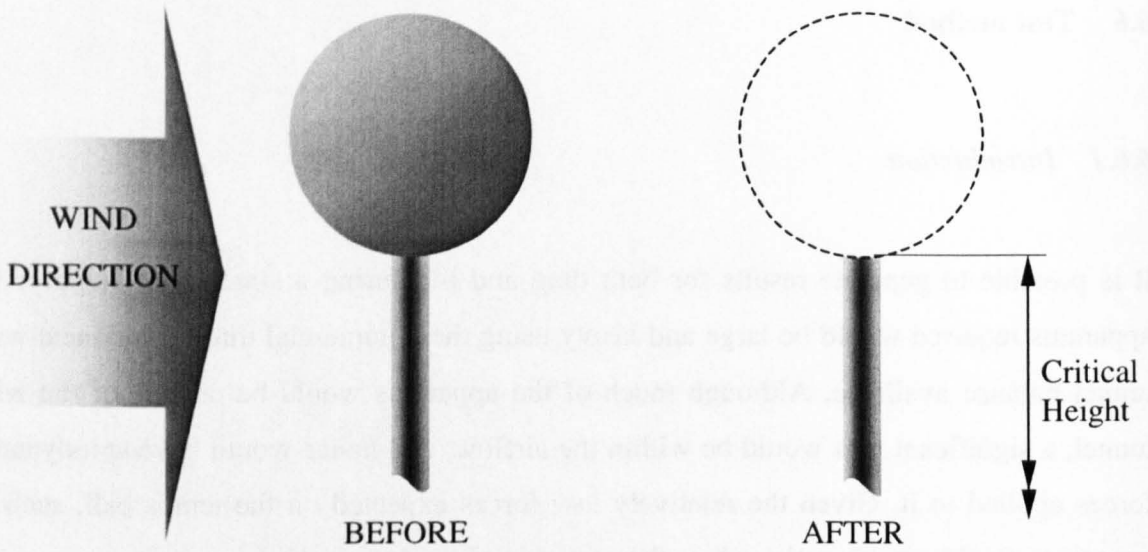

Figure 6.4 Picture depicting the flow of air over the bar with the ball in place and the critical height required for accurate analysis.

The remaining bar was tested at a full range of speeds and spins and results collated for both drag and lift.

Compensating for drag effects due to the bar

Results were obtained for wind speeds up to approximately 26ms^{-1} for three different spin rates, figure 6.5. It is noted that they look similar to those obtained in earlier drag tests with no spin applied. It appears that the spin applied to the long slender bar has negligible effect on the drag force it experiences.

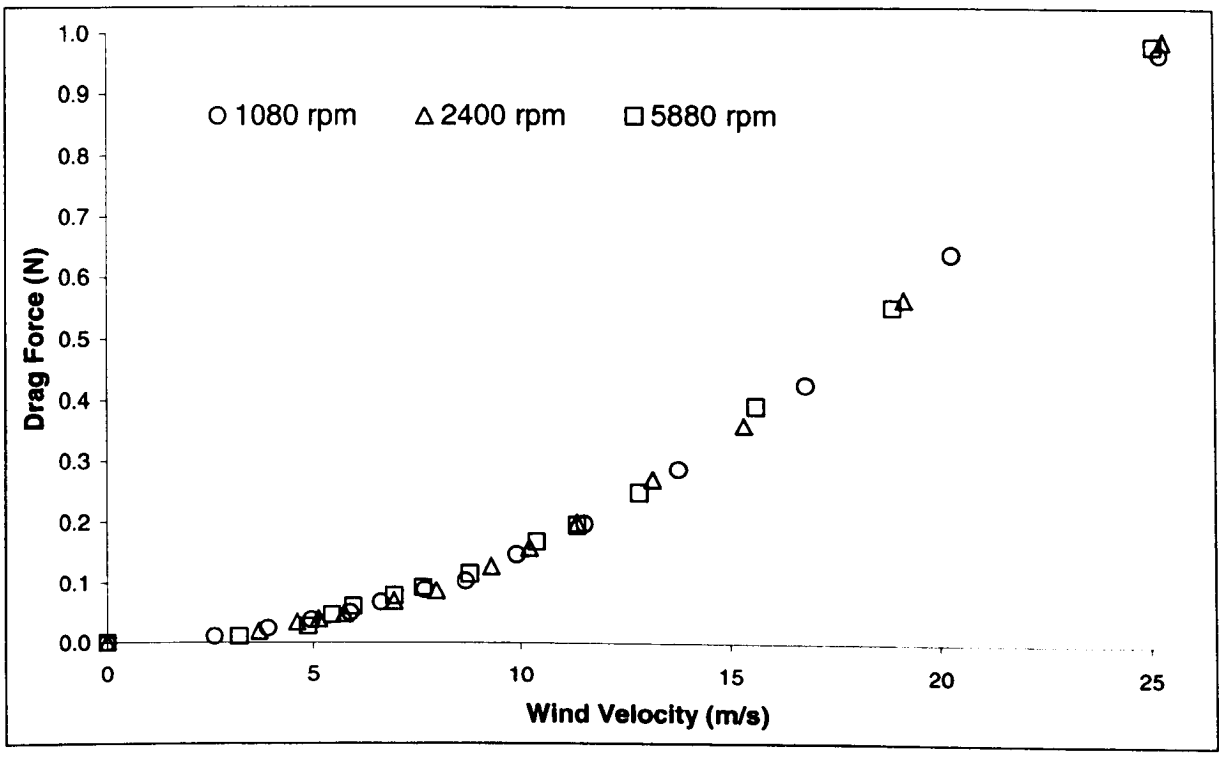

Figure 6.5 Drag force results obtained for the bar alone at three different spin rates.

A polynomial equation was formed to best fit the data, where $F_D = f(v^2)$. Figure 6.6 shows the original data together with the quadratic best-fit curve and its equation.

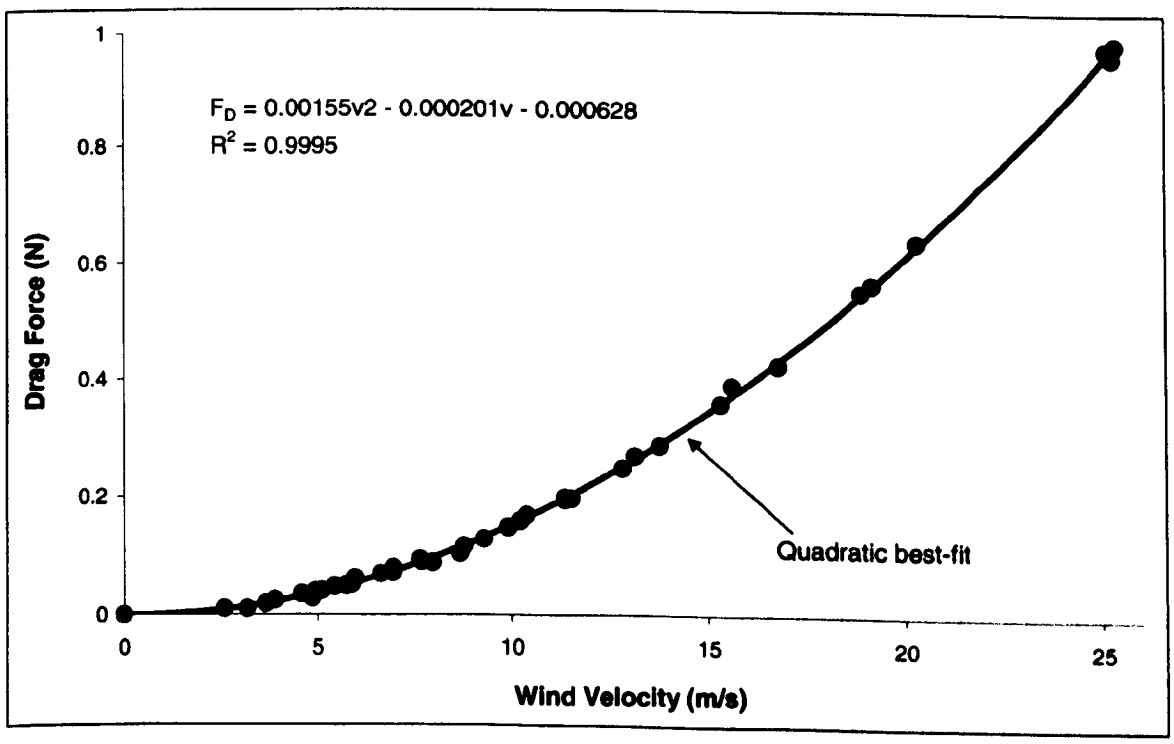

Figure 6.6 Quadratic equation used to compensate for drag force applied to the bar.

The high R^2 value (0.9995) illustrates that the quadratic curve of best fit correlates well with the original data shown. This equation can be used at any given wind speed and spin for results obtained with the ball in place.

Compensating for lift effects due to the bar

When forming a method to compensate for the lift effect on the bar, it became apparent that a more complex relationship was required. Figure 6.7 shows results for wind speeds up to approximately 26ms^{-1} for five different spin rates. The lift force increases with velocity and is heavily dependent upon spin.

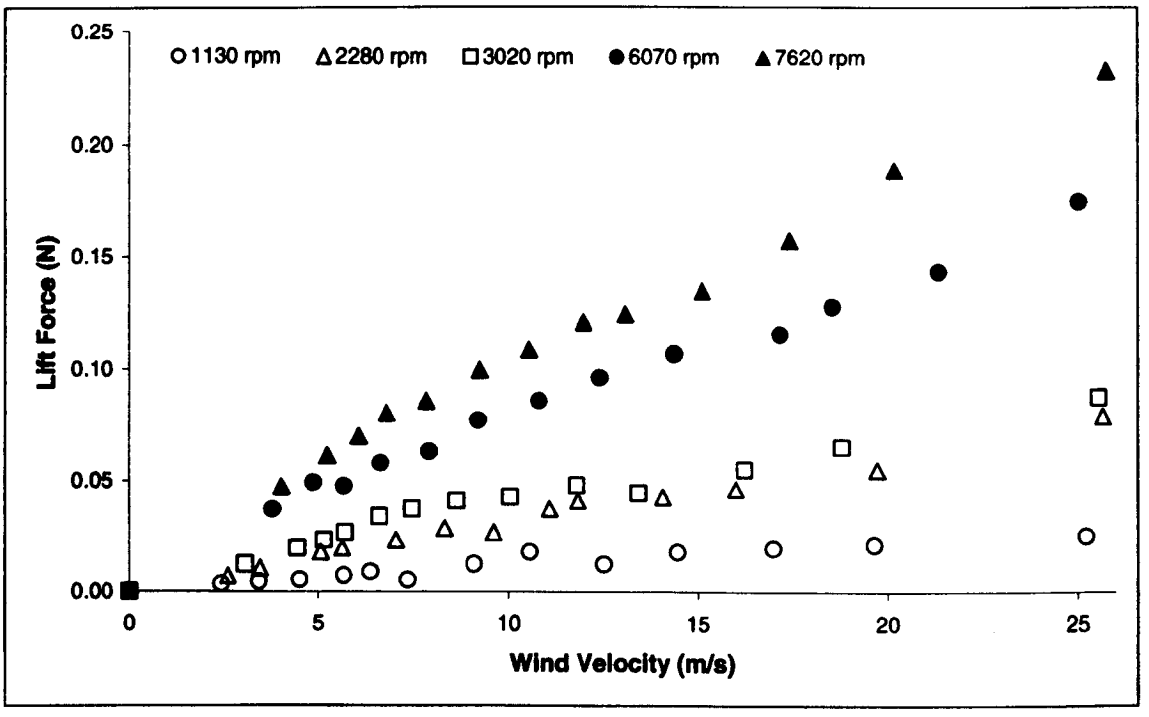

Figure 6.7 Lift force results obtained for the bar alone at five different spin rates.

Initial attempts investigated the formation of relationships with the lift force as this is the easiest way to apply the compensation. After several iterations, a linear relationship between C_L and ω/v was detected and is shown in figure 6.8. The lift coefficient of the bar was calculated using equation 6.6, where the projected area was a function of the bar's length and diameter. It was decided that the spin parameter used in this analysis should be that related to the ball (and its diameter) to simplify future analysis.

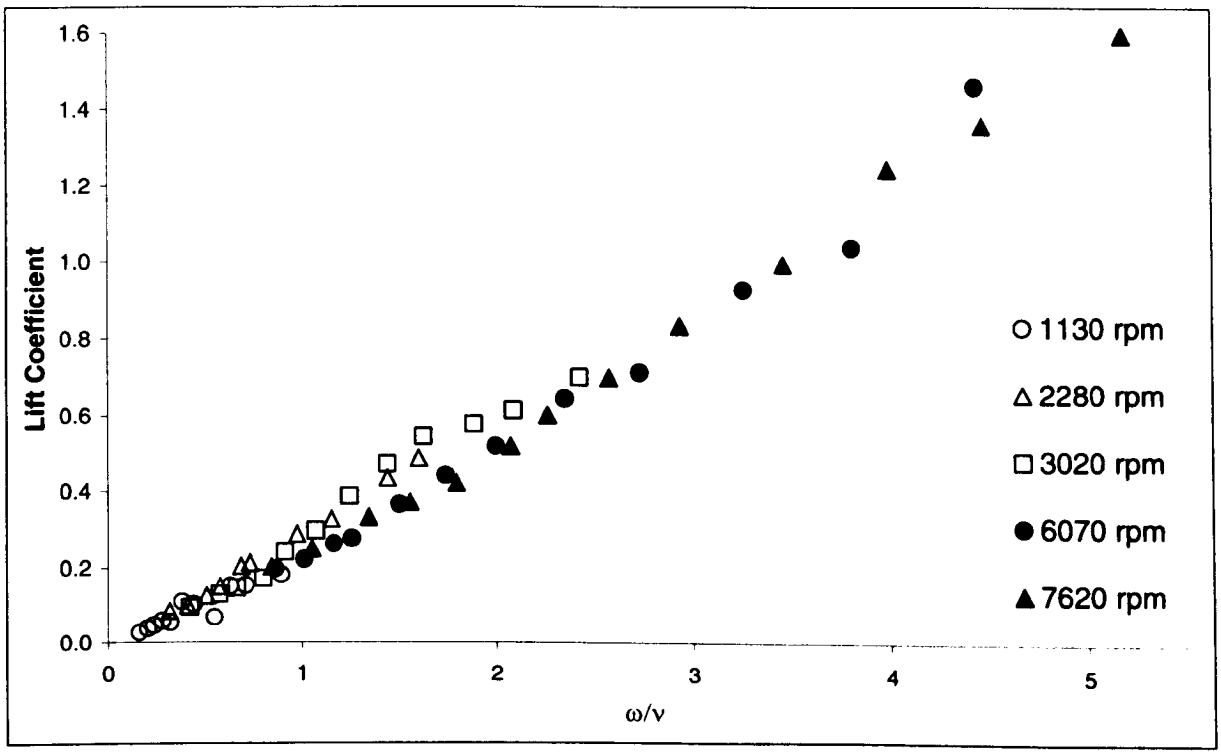

Figure 6.8 Graph to show the relationship between lift coefficient and ω/v (based on the diameter of a tennis ball) obtained for the bar alone at five different spin rates.

Literature had shown this relationship to be more complex, hence this result was surprising. A linear relationship between the lift coefficient of the bar and ω/v was formed for all spin rates and wind speeds.

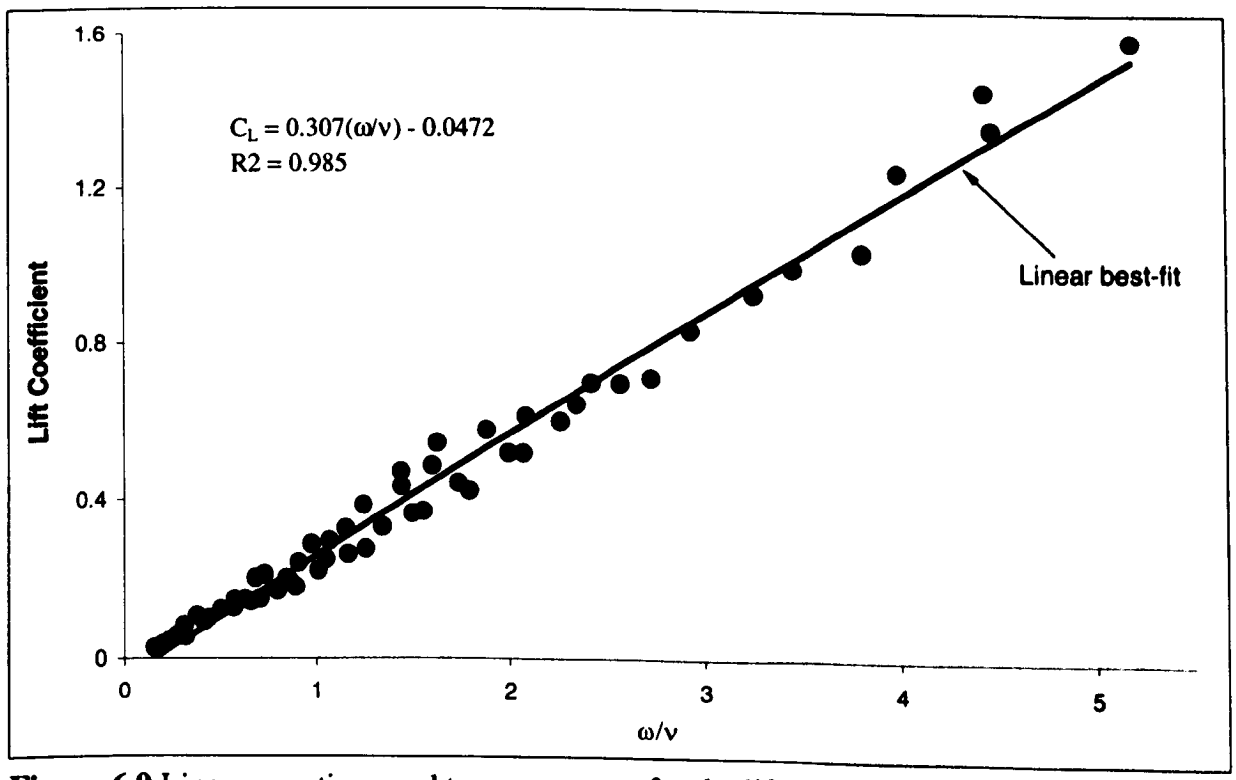

Figure 6.9 Linear equation used to compensate for the lift coefficient of the bar.

Figure 6.9 shows the original data together with the linear best-fit curve and its equation. The R^2 value illustrates that the linear best fit correlates well with the original data shown, however the combination of scattered data from the 3020rpm data set at the upper end has reduced it to 0.985. This equation can be used at any given wind speed for results obtained with the ball in place.

6.6.3 Compensation for atmospheric conditions

Due to the relatively low speeds in this wind tunnel the temperature and atmospheric pressure was noted before each test. The data required and methods of measurement used are detailed in section 3.5.4.

6.6.4 Calculating the velocity of airflow

The wind velocity is calculated using the differences in atmospheric conditions across the contraction section prior to the test section, details of these calculations can be found in section 3.1.4.

6.6.5 The diameter of a tennis ball

The drag and lift coefficients are calculated using the diameter of the ball, and t he method used to calculate the diameter of a tennis ball is discussed fully in section 3.4.

6.7 Results

The following results are separated into those obtained for drag and those obtained for lift. Testing covers wind speed ranging from zero to approximately 26ms^{-1} and spin rates from zero to 7500 rpm.

At the end of this section, both sets of results will be drawn together and discussed together in an effort to understand the effect of spin on the overall aerodynamic properties of tennis balls.

6.7.1 Drag effects on a spinning ball

Figure 6.10 shows the results obtained for drag coefficient plotted against the dimensionless spin coefficient ω/v.

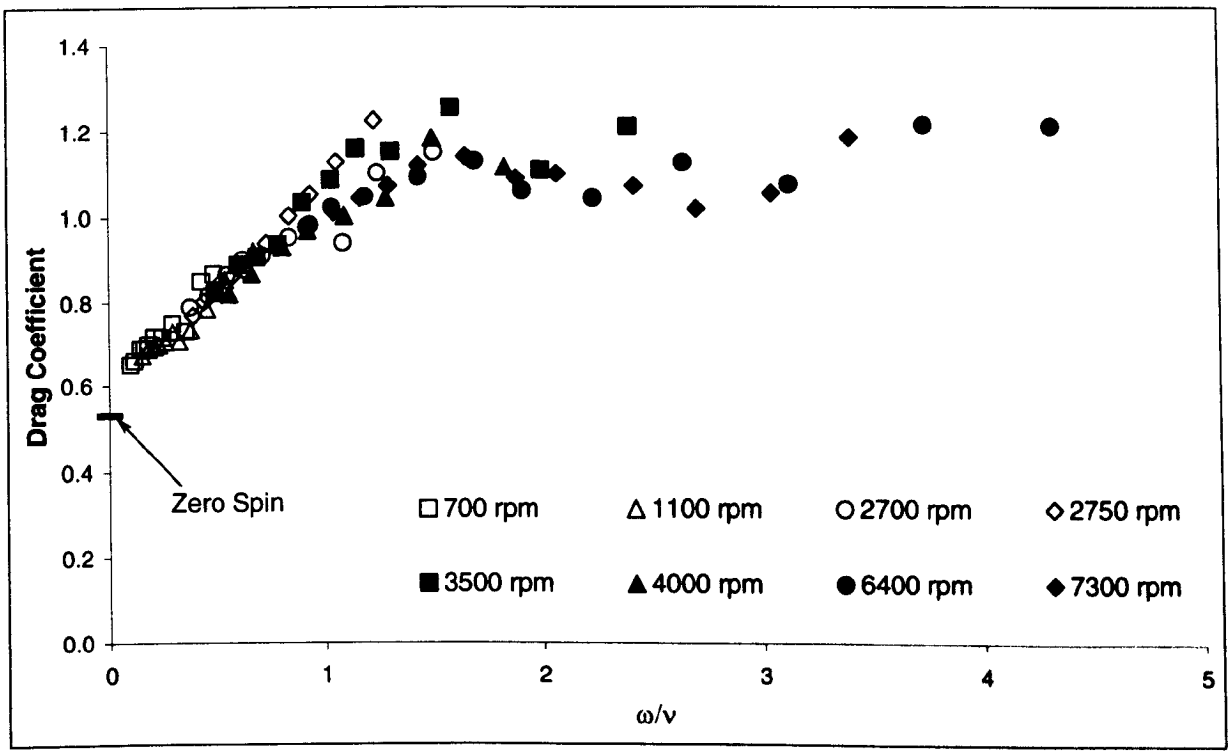

Figure 6.10 Chart to show the C_D results obtained for a tennis ball at 8 different spin rates and wind speeds ranging from zero to 26ms^{-1}.

It can be seen that C_D increases steadily with increasing ω/v, becoming constant at high values of spin coefficient. Testing covered wind speeds ranging from zero to approximately 26ms^{-1} and spin rates from zero to 7300 rpm. Although there is a definite trend the results are quite scattered.

High values of spin coefficient compared to high spin rates and low wind speed. It has already been discussed that the highest spin rates are imparted on the serve, which is also struck at high speed, hence will have a relatively small spin coefficient. Taking the example of Pete Sampras' serve at 5000rpm, his serve speed would have to reduce to less than 9.5ms^{-1} (21.4 mph) to have an ω/v above 2. It is conceivable that some shots in the game of tennis will be struck below this speed, however they will also have significantly less spin applied. It was decided that all data obtained with a spin coefficient of 2 or above

should be ignored. This effectively means that many of the high spin rate data is removed leaving mostly low spin rate data.

Discussions in chapter 5 showed that results obtained at wind speeds less than $5ms^{-1}$ in this wind tunnel were less accurate due to the low forces applied. It was decided that all data at speeds below $5ms^{-1}$ should also be discarded. Figure 6.11 shows the remaining data points that can be used for further analysis. All points that have been discarded at this stage will be reintroduced in later analysis as a way of checking the analysis.

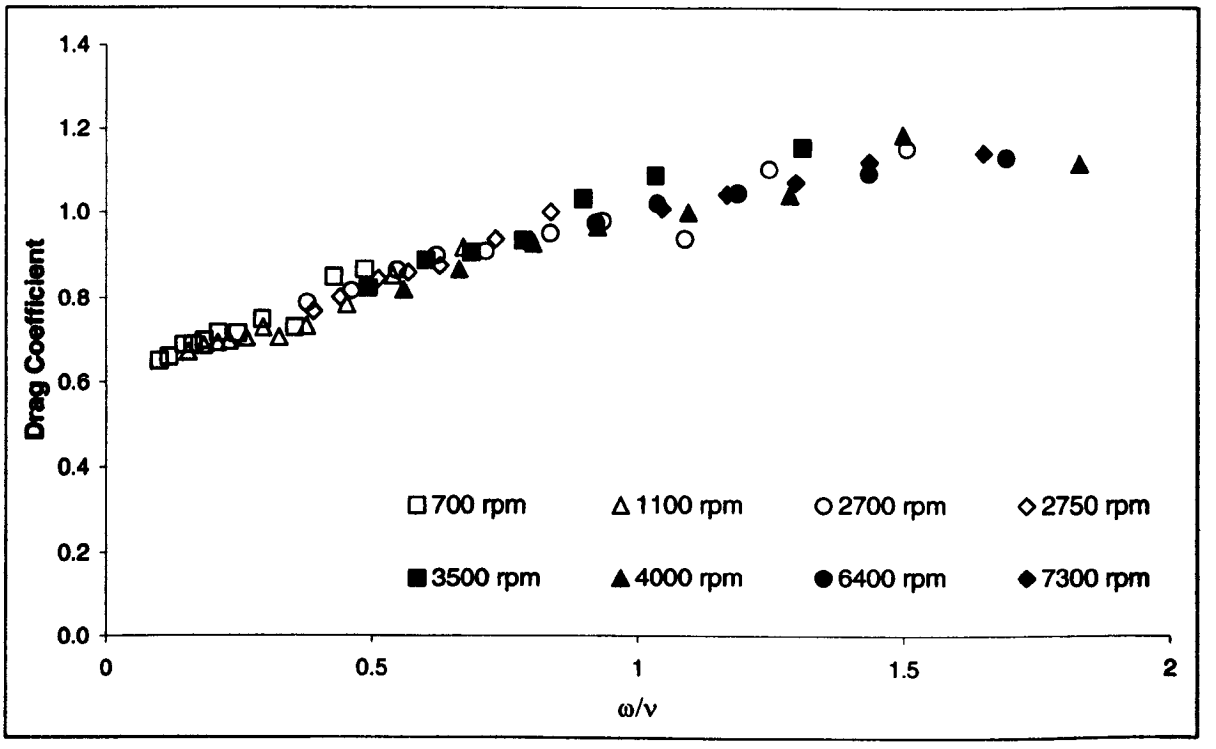

Figure 6.11 Chart of the reduced set of data points of C_D versus spin coefficient with low speed and high spin coefficient data removed.

Extrapolation of the chart in figure 6.11 shows that the C_D of the non rotating ball (i.e. where $\omega/v=0$) is approximately 0.6. It has already been shown using a similar experiment that the C_D of a non-spinning tennis ball is 0.537.

It can be concluded that the drag force on the spinning ball is greater than that on a non-spinning ball at the same wind speed, and an investigation was required to understand the effect.

Careful analysis of the data shows that C_D can be increased due to an inflated force or a deflated wind speed or ball diameter. The sensitivity over the diameter of a tennis ball has already been discussed, therefore it was decided to investigate what change in ball diameter may be expected.

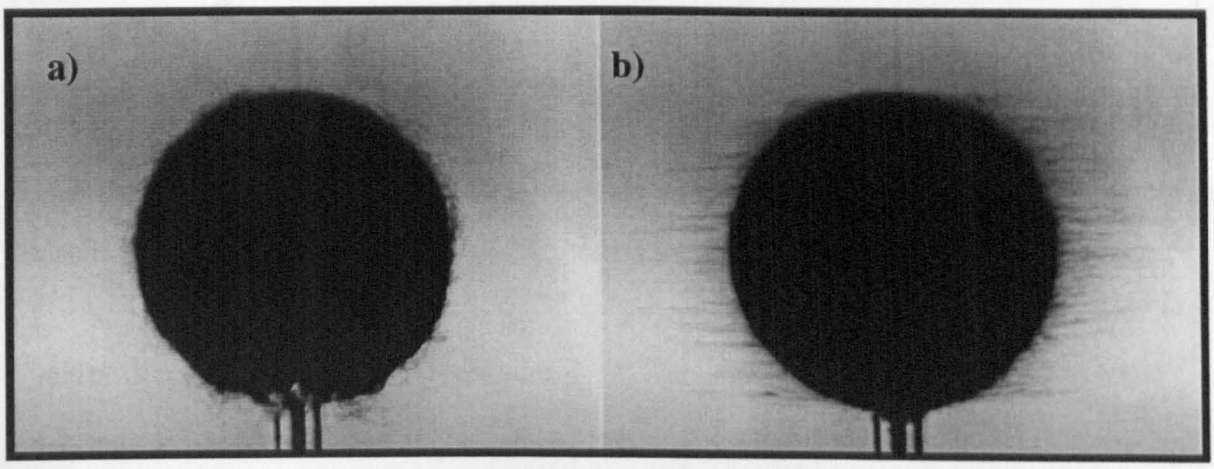

Figure 6.12 Pictures showing a) a non-spinning ball and b) the 'fuzzed' nap of a spinning tennis ball with no wind applied.

Figure 6.12 shows two pictures used to assess the increase in diameter of a spinning tennis ball with no wind applied. Figure 6.12a shows a stationary ball and figure 6.12b shows the same tennis ball spinning at approximately 2000rpm. These images were obtained using a KODAK Motioncorder using a frame rate of 240 frames per second. An individual image of the spinning ball contained insufficient information for analysis, the right hand picture consists of several consecutive images overlaid. Comparison between the images was undertaken using image analysis software, which showed that the diameter of the spinning ball was approximately 15% larger at the extremities of the fibres. The relevant diameter should therefore be between the original size and 115% of that size.

This together with the known C_D for a non-spinning ball means that a more realistic diameter can be determined. It was thus assumed that the real diameter was a fixed value at 7½% greater than the statically measured value. Figure 6.13 shows the chart obtained using the new diameter. It can be seen that not only has the C_D been reduced but the data set has also been elongated on the ω/v scale due to the increase in equatorial velocity. It can be seen that an extrapolation of the data to $\omega/v=0$ corresponds to the values found in the non-

spinning tests. This data set is the source data used to create a best-fit relationship between C_D and the spin coefficient.

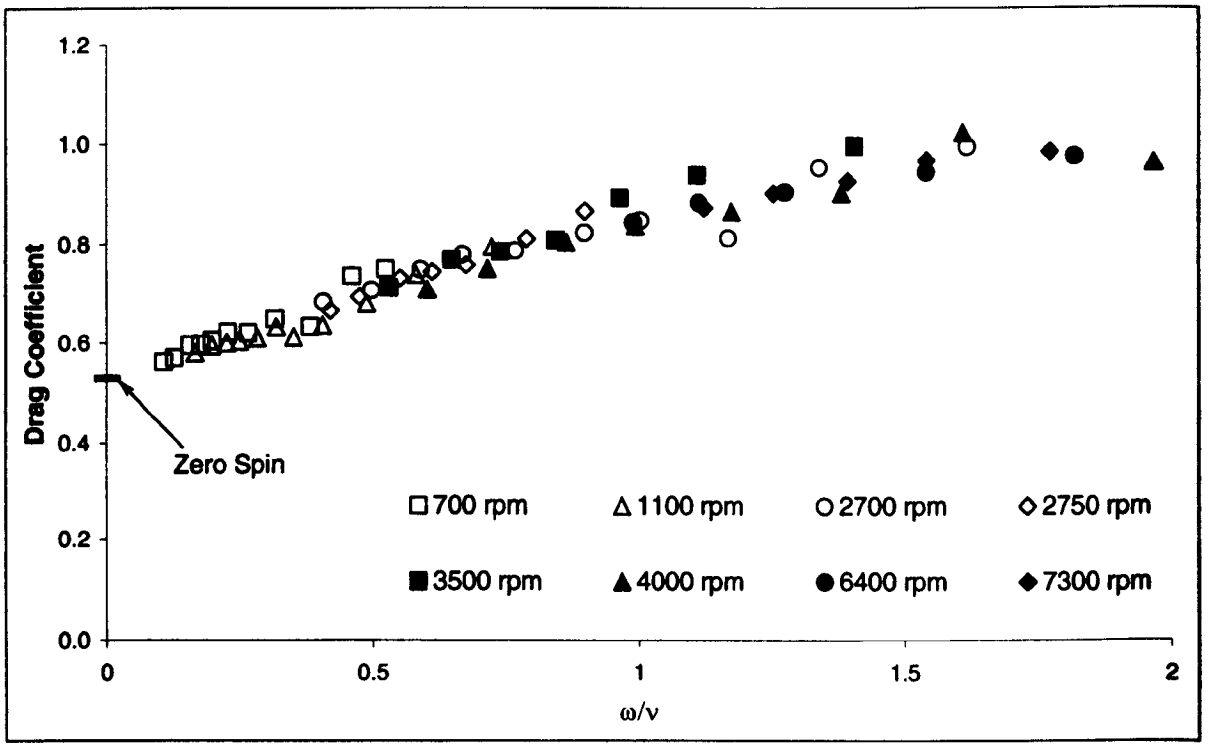

Figure 6.13 Chart showing the reduced set of data points of C_D versus spin parameter with the modified diameter, increased by 7½% for the increased diameter of a spinning ball.

Figure 6.13 shows that the C_D increases steadily as the spin coefficient increases tending to a value of approximately 1.0 at high values of spin coefficient. As they stand, these results cannot be used to predict what C_D would be expected given a speed and spin rate. An equation that describes the relationship between C_D and spin parameter will be required for this purpose.

The definition of the equation that best describes the above data set took several iterations, however using the fact that the C_D is known when the spin parameter is zero enable the derivation of the following relationship:

$$C_D = C_{D0} + f\left(\omega/v\right) \tag{6.7}$$

where: C_{D0} is the drag coefficient at zero spin.

With knowledge that $C_D = C_{D0}$ at zero spin, the initial equation was developed using the relationship $(x)^0 = 1$, it was found that the most successful equation was:

$$C_D = C_{D0} + \left(A\left(\omega/v\right)^B + C \right)^D \tag{6.8}$$

where: *A*, *B*, *C* and *D* are all adjustable cells used in the iterative process.

B and D are negative hence, as the spin rate tends to zero, C_D tends to C_{D0}. Conversely, as the spin rate increases towards infinity, C_D tends towards:

$$C_D = C_{D0} + C^D = CONSTANT \tag{6.9}$$

It was decided that an iterative method using a Microsoft Excel spreadsheet was required. This method uses the 'solver' package within Microsoft Excel that uses the generalised reduced gradient method for non-linear optimisation. As with all iterative processes, small changes in the input data cause changes in the observed output data. The rate of change and magnitude of the output data dictates the input parameter that should be changed next and by how much. The generalised reduced gradient method for non-linear optimisation uses partial derivatives to measure the rate of change of the output data. When a problem contains more than one input parameter, the set of partial derivatives is used to form a vector that is referred to as the gradient. It is possible to solve problems with up to 1000 adjustable cells; equation 6.8 requires four adjustable cells and should be simply solved.

The spreadsheet was set up such that a new set of data is formed for C_D using the equation. A single 'adjustable' cell was created which calculated the sum of the square differences between the real and simulated data sets. The iteration process used by the solver program within Excel modified the adjustable cells until this individual cell was determined to be at its minimum value. It is possible that several sets of values for A, B, C and D could give suitable results. It was also known that C_D tends to a value of approximately 1 at high spin rates, this fact enabled a constraint to be applied, which therefore enabled the generation of more accurate values for the adjustable cells.

The chart in figure 6.14 shows the simulated data set obtained for C_D versus spin coefficient using equation 6.8. The values obtained for A, B, C and D that were used in the equation are also shown. It can be seen that the simulated C_D increases steadily and tends to approximately 1 at high values of ω/v.

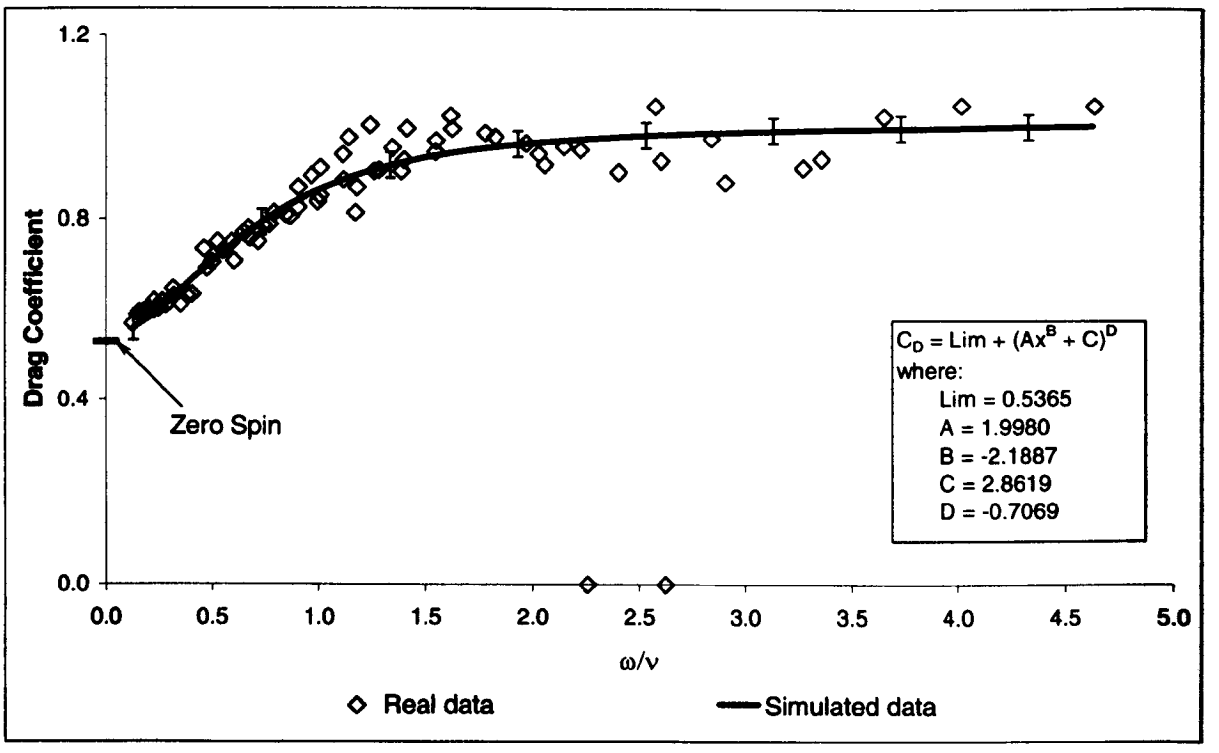

Figure 6.14 Chart showing the simulated data set obtained for the relationship between C_D and spin coefficient using equation 6.8.

Errors have been estimated by comparing the simulated C_D results with the real C_D results at each ω/v data point. The real data was either side of the simulated data and varied in magnitude, therefore an average of all of the absolute differences was used. The average difference has been applied using error bars at a constant value of 0.028 on the chart, which is equivalent to approximately 3% at the maximum value and just over 5% at the minimum value.

The equation that describes the relationship between C_D and spin coefficient is:

$$C_D = 0.5365 + \left(1.9980\left(\omega/v\right)^{-2.1887} + 2.8619\right)^{-0.7069} \qquad (6.10)$$

and it has limiting values of: $\omega \to 0$ $C_D \to 0.5365$

$\omega \to \infty$ $C_D \to 1.0120$

6.7.2 Lift effects on a spinning ball

Now that the method has been developed to determine the relationship between C_D and spin coefficient, the same procedure can be used for C_L. The lift force that is obtained during test is that of the ball and the bar combined, the method by which the C_L of the bar is accounted for is a little different from that normally used. It is more normal to present the correlation between force and speed, however no correlation was found between the F_L of the bar and speed, however there was a linear correlation between C_L of the bar and spin parameter (see section 6.6.2). This does not mean that the C_L of the bar is directly subtracted from a C_L that may be calculated for the combined system, the lift force of the bar is still required. The wind speed and spin rate can be used to define the spin parameter (based in the ball diameter) and therefore the C_L of the bar using the equation defined in section 6.6.2. The F_L of the bar is calculated using equation 6.6 where the projected area relates only to the section of the bar in the airflow. Although this method sounds far more complex than the procedure used to calculate the C_D, the process is automated and the C_L of the ball is calculated with no more manual input than required to calculate C_D.

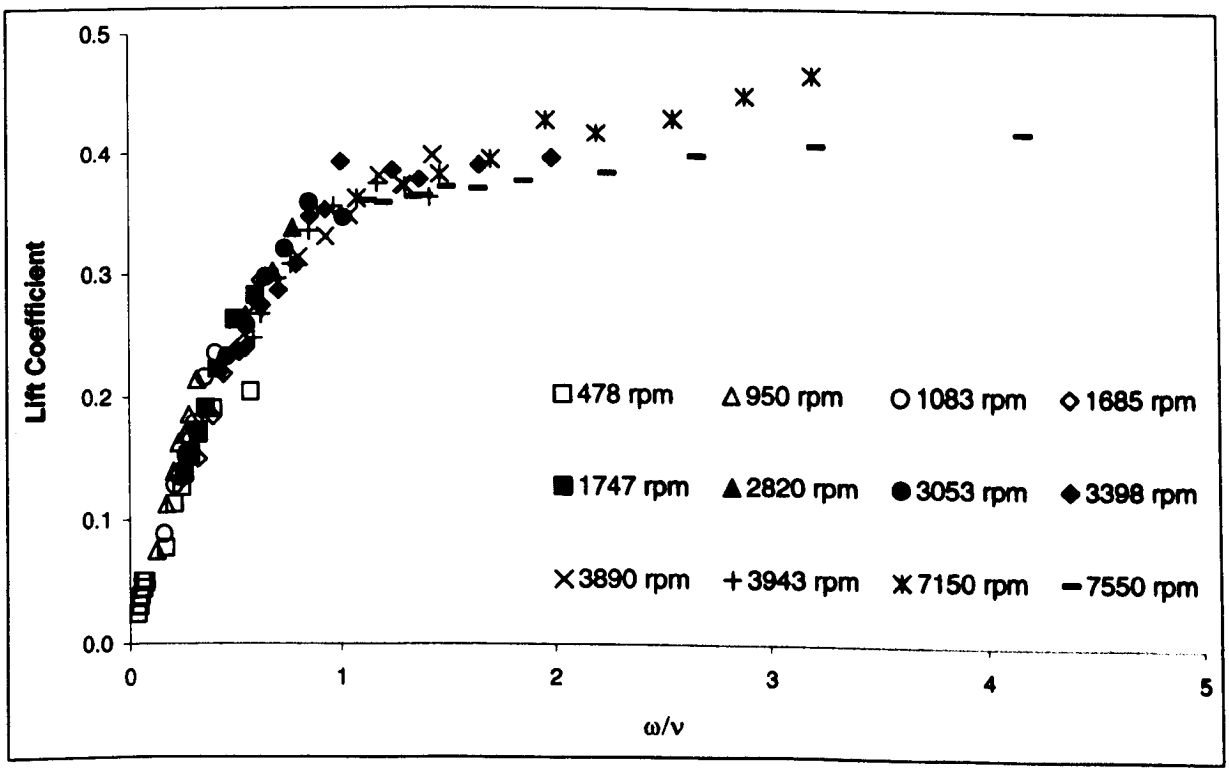

Figure 6.15 Chart to show the C_L results obtained for a tennis ball at 12 different spin rates and wind speeds ranging from zero to approximately $26ms^{-1}$.

Figure 6.15 shows the results obtained for twelve different spin rates over the complete wind velocity range. The dependence of C_L on the diameter of the ball is the same as with C_D as discussed in section 6.7.1. The results shown are corrected using the same factor that was used previously to compensate for the increased diameter of the spinning ball.

The curve that describes the relationship between C_L and the spin coefficient is similar to that shown for C_D and the spin coefficient. The major difference is that C_L is equal to zero when the tennis ball is not rotating. It can be seen that the C_L does appear to tend towards a constant value at high values of spin coefficient. This data set is reduced for analysis using the same assumptions mentioned in the previous section. Figure 6.16 shows all of the data above a wind velocity of $5ms^{-1}$ and below a spin coefficient of 2.

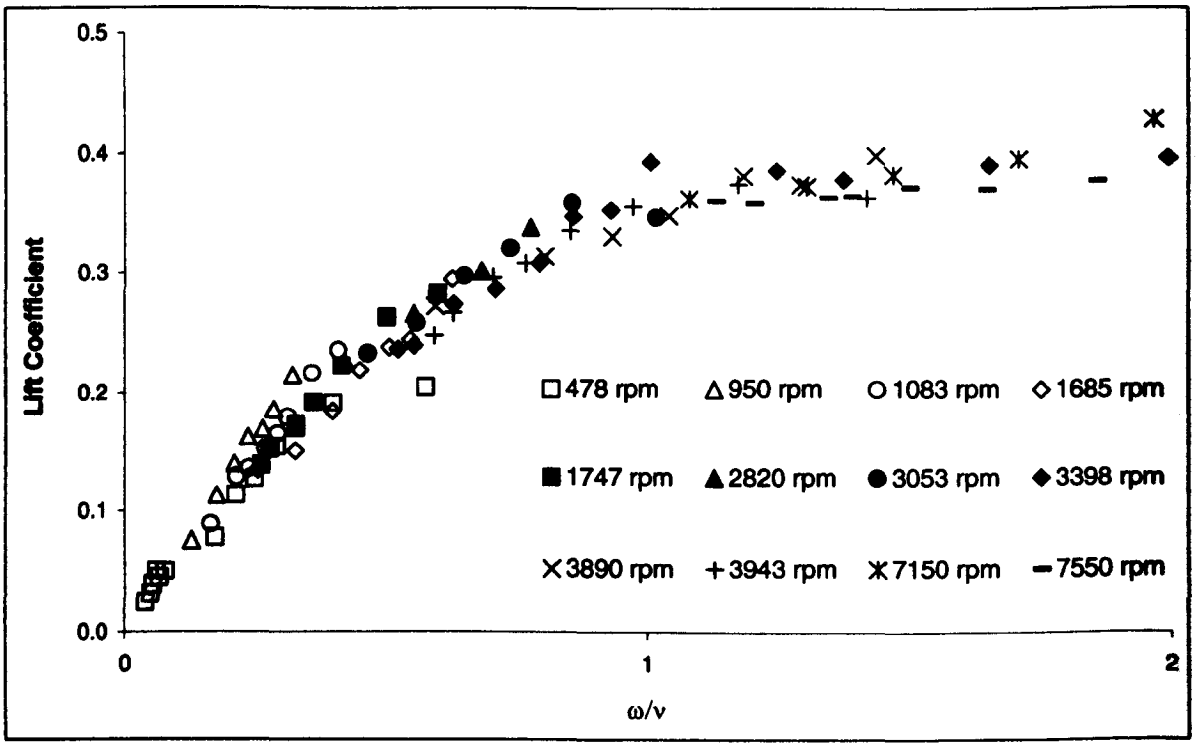

Figure 6.16 Chart showing the reduced data set for C_L versus spin coefficient.

The spreadsheet used for this analysis is the same as that used for C_D with four adjustable cells. As with the manipulation of C_D data, a single cell was created which calculated the sum of the differences between the real data set and the simulated data set created with an equation. The iteration process modified the adjustable cells until differences cell was determined to be at its minimum value. The maximum value of C_L obtained as ω/v tends to

infinity was not as clear as that observed with the C_D data, hence simulated data using the equation was plotted after each iterative process, and visually compared to the real data set.

The C_L data set shows superior correlation when compared to the raw C_D data set presented earlier, hence the equation to describe the relationship should be as accurate if not more accurate. The equation used to describe the relationship between C_L and the spin coefficient is similar to that used for C_D and is given by:

$$C_L = C_{L0} + \left(A\left(\omega/v\right)^B + C \right)^D = 0 + \left(A\left(\omega/v\right)^B + C \right)^D \qquad (6.11)$$

where: C_{L0} is the C_L at zero spin (equal to zero)

A, B, C and D are constants obtained by iteration

The chart in figure 6.17 shows the simulated data obtained for C_L versus spin coefficient using equation 6.11. The values obtained for A, B, C and D that were used in the equation are also shown. It can be seen that the simulated C_L increases steadily and appears to be tending to a constant value at high values of ω/v.

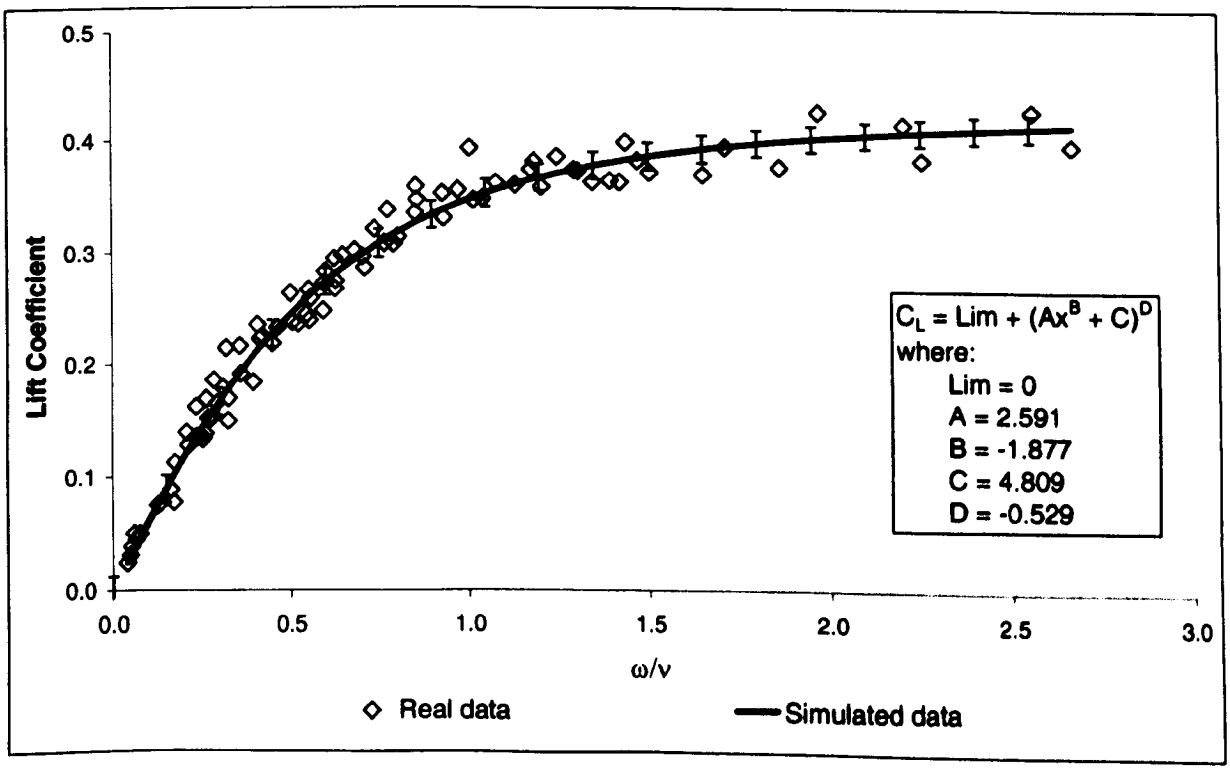

Figure 6.17 Chart showing the simulated data obtained for the relationship between C_L and spin coefficient using equation 6.11.

Errors have been estimated by comparing the simulated C_L results with the real C_L results at each ω/v data point. The real data was either side of the simulated data and varied in magnitude, therefore an average of all of the absolute differences was used. The average difference has been applied using error bars at a constant value of 0.012 on the chart. The magnitude of C_L is lower than C_D, and if the error for each is considered as a percentage of its maximum value, the errors are very similar, as shown below:

- Error obtained for C_D is 0.028 at a maximum of approximately 1 $\Rightarrow$ 2.8%
- Error obtained for C_L is 0.012 at a maximum of approximately 0.43 $\Rightarrow$ 2.8%

The equation that describes the relationship between C_L and spin coefficient is:

$$C_L = \left(2.591 \left(\omega / v \right)^{-1.877} + 4.809 \right)^{-0.529} \qquad (6.12)$$

it has limiting values of: $\omega \to 0$ $C_L \to 0$

$\omega \to \infty$ $C_L \to 0.436$

6.7.3 Comparison between simulated and real data

Although care has been taken at every stage to ensure that the simulated data represents the original data, it is not until the final relationship with ω/v is formed that more meaningful representations can be formed. The equations developed for drag and lift against ω/v can now be used to simulate data for changing spin or velocity. This is achieved by fixing either the wind velocity or spin rate and varying the other. As the original data was gathered at a fixed spin rate with increasing wind velocities, it is useful to attempt to recreate it using equations 6.10 and 6.12.

The investigation compares real and simulated data at four spin rates for a full range of wind velocities tested in this study. The selection of spin rates was chosen in order to display a cross section of the complete set of analyses.

Comparing the drag data

Figure 6.18 shows the results obtained for C_D against wind speed for spin rates ranging from 1100rpm to 6400rpm. It can be seen that the simulated data compares well with the real data, with nearly all of the data points within the errors expected from the test method. The C_D increases with spin rate and in all cases is seen to reduce as the wind velocity increases. For a ball rotating at 1100rpm, the increase in C_D due to the spin almost levels off at $15ms^{-1}$. A ball rotating at 6400rpm, however, continues to decrease at the higher velocities. It can be concluded that a ball struck with high spin will retard more quickly than one struck with little or no spin.

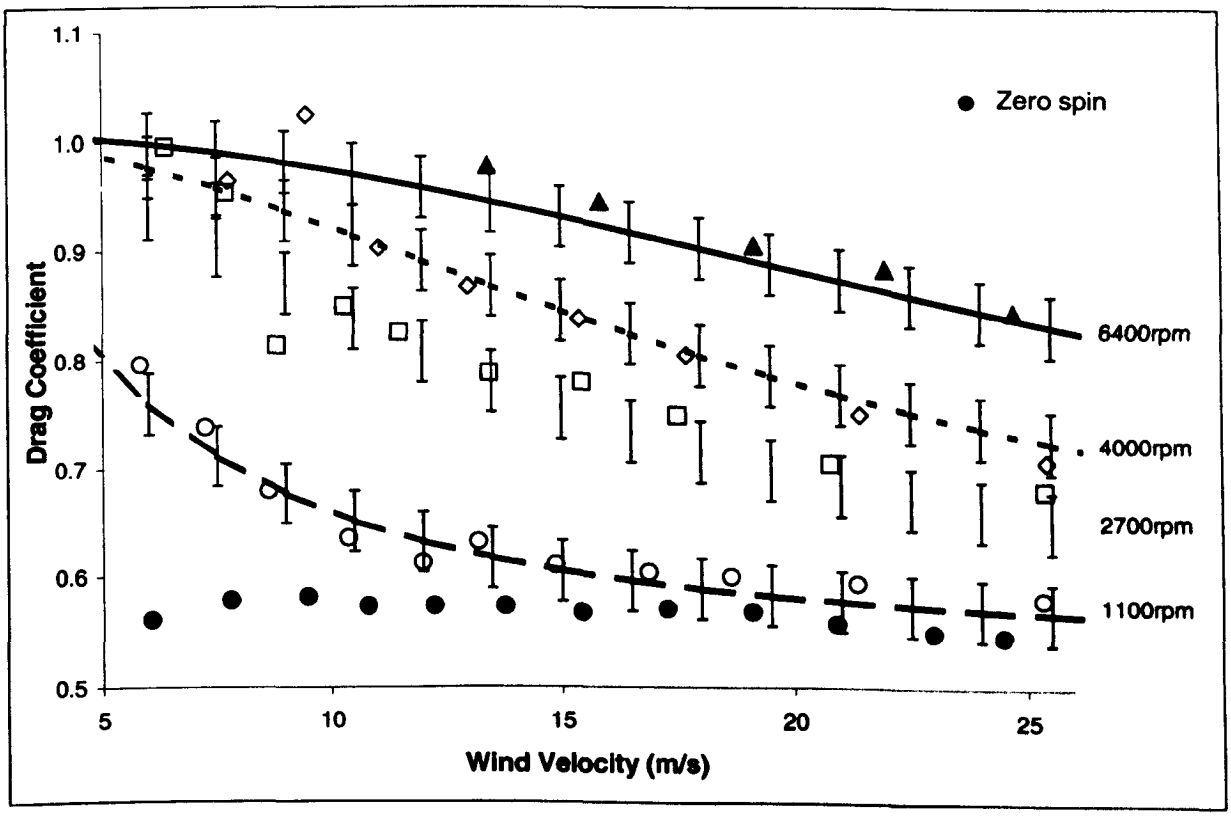

Figure 6.18 Chart plotting real and simulated values of C_D against wind speed for spin rates ranging from 1100rpm to 6400rpm.

It is possible that the spin rate varied during the test, whether it be due to the increased force applied by the wind or irregularities in the motor controller. As mentioned earlier, the spin rate was only measured at the beginning of each test, and hence any changes in spin rate could not be recorded. Given the consistency of the data, it is likely that the spin rate did not change throughout each set of data.

Comparing the lift data

Figure 6.19 shows the results obtained for C_L against wind speed for spin rates ranging from 478rpm to 7550rpm. The C_D and C_L tests were performed separately, hence identical spin rates are not available, the selection of spin rates has been chosen to cover the complete test spectrum.

It can be seen that the simulated data compares well with the real data, with nearly all of the data points within the errors expected from the test method. It appears that there may have been an increase in spin rate during the 3,398rpm test but either side of this the results compare well. Conversely, it appears that there may have been a slight reduction in spin rate during the 7550rpm test with several consecutive points situated just outside of the average errors.

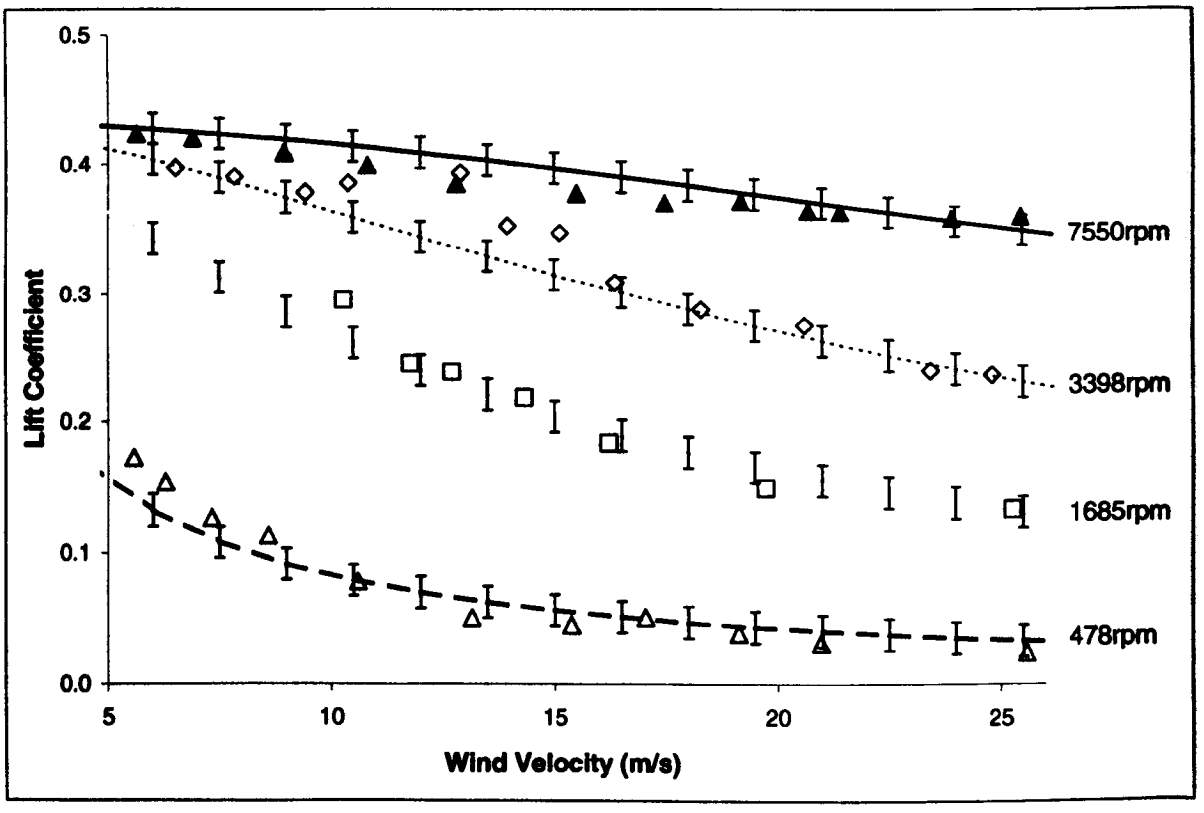

Figure 6.19 Chart plotting real and simulated values of C_L against wind speed for spin rates ranging from 478rpm to 7550rpm.

The C_L increases with spin rate and in all cases is seen to reduce as the wind velocity increases. For a ball rotating at 478rpm, the increase in C_L due to the spin has reduced by

approximately 60% at 15ms^{-1}, however a ball rotating at 7550rpm has a C_L reduced by less than 20% within the speed range studied.

6.1.1 Using the C_D and C_L spin equations to discuss ball flight

In chapter 5, it was shown that the C_D was independent of Re for all wind speeds tested, it is therefore assumed that extrapolation of the C_D and C_L calculations using the equations obtained in this study is suitable.

The results obtained in this study covered spin rates up to 7500rpm and maximum wind velocities of approximately 26ms^{-1}. Although the spin rate exceeds that which may be observed in play, the wind velocity is approximately 40% of that of the fastest serve. Figure 6.20 shows the calculated C_D plotted against both speed and spin. The maximum velocity has been increased to 67.5ms^{-1} (152mph) to cover the maximum speeds seen during play.

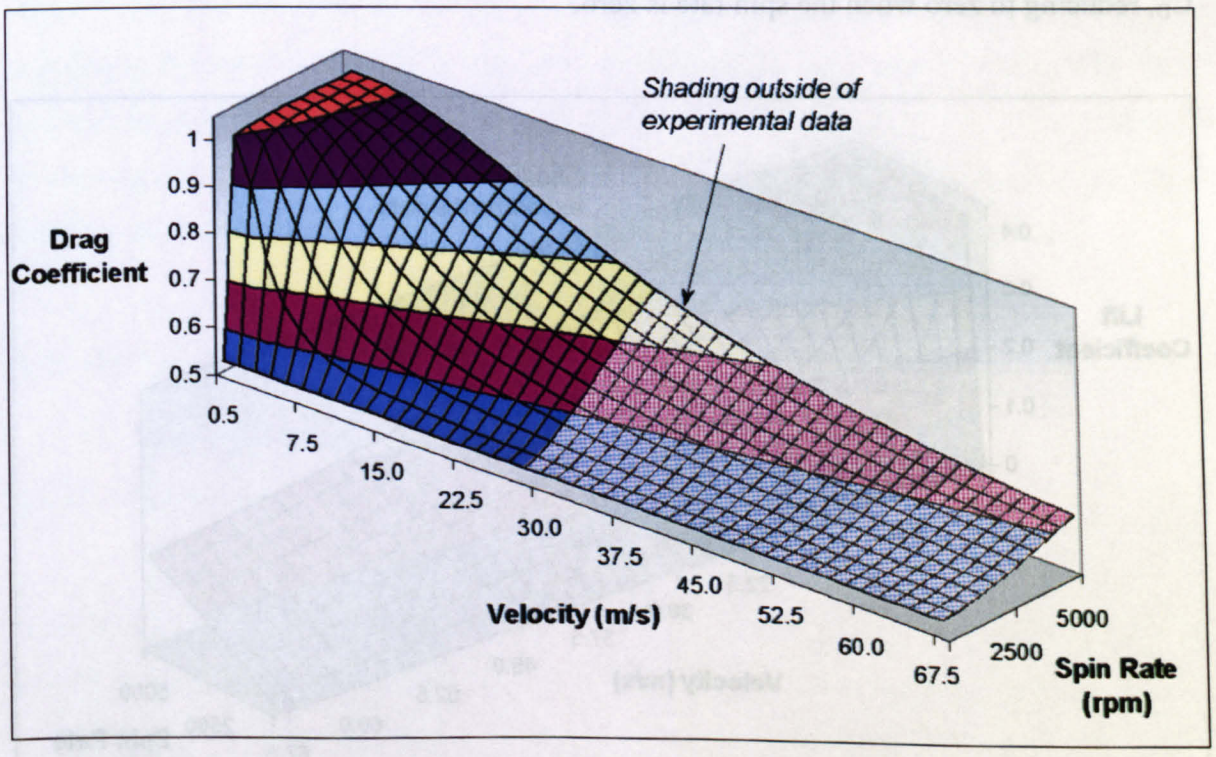

Figure 6.20 C_D plotted against velocity and spin rate extrapolated to cover shot speeds observed during play.

It can be seen in figure 6.20 that C_D is high when the speed is low and the spin is high, tending towards the C_D of a non-spinning ball with increased velocity. The C_D of a service struck at approximately 66ms^{-1} does not alter significantly with spin rate, rising to just above 0.6 at maximum spin rates. The drag force of such a serve is approximately 16% greater than that of a non-spinning shot, and therefore the deceleration will be 16% higher.

In the case of a drop shot, the initial velocity is low and the spin rate is high. It is clear that the C_D increases rapidly with increased spin rate at low velocities. The C_D of a ball struck with an initial velocity of 15ms^{-1} and spin rate of 3000rpm is approximately 60% greater than its non-spinning equivalent. The drop shot is delicate and requires precision positioning to prevent your opponent from returning it. The deceleration of this spinning shot is approximately 60% greater than a non-spinning shot, and therefore the range is significantly reduced, this has to be accounted for by increasing the initial velocity.

A similar chart can be produced to show the relationship between C_L and changing speed and spin rate. Figure 6.21 shows that the C_L plot follows a similar trend to that shown for C_D, reducing to zero when the spin rate is zero.

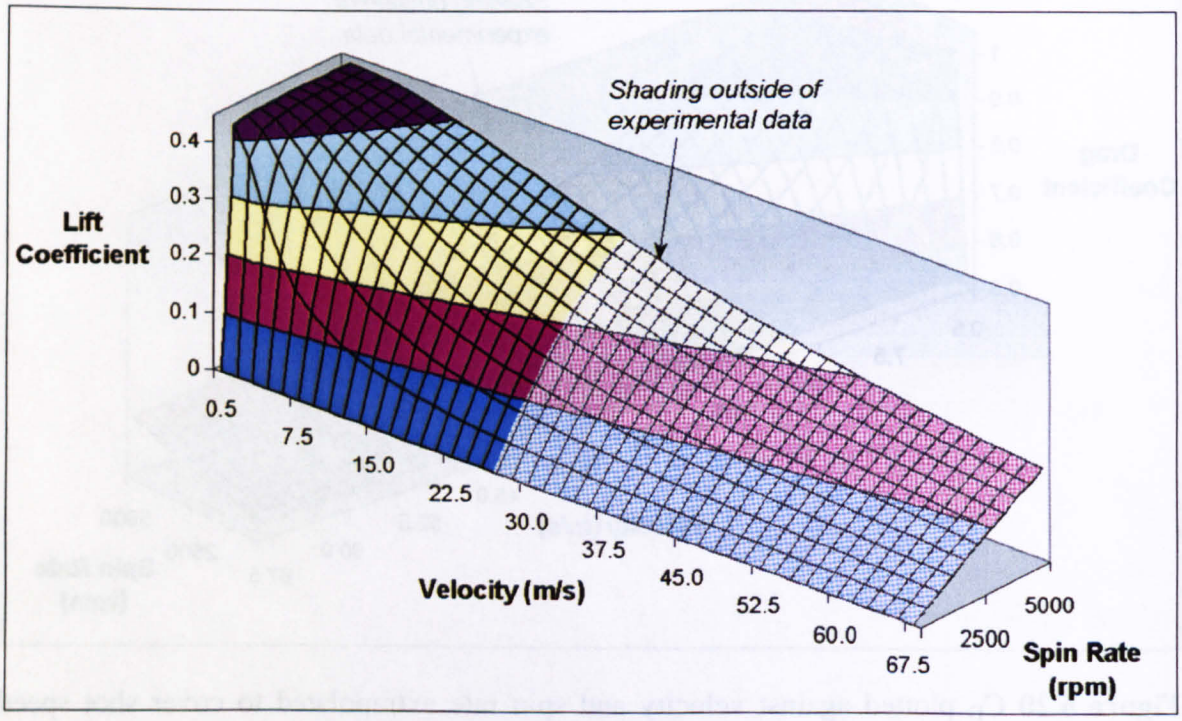

Figure 6.21 C_L plotted against velocity and spin rate extrapolated to cover shot speeds observed during play.

The information shown in the chart covers the speed and spin rates reportedly observed during play. It is shown that although the C_L diminishes with increased speed, provided that spin is applied to the ball, a lift force will be acting on it. This result shows that flight path of even the fastest shots observed will be deflected from their normal trajectory due to lift.

The trajectory of a spinning ball is complex due to the varying axis of rotation for each shot. The axis of rotation was vertical in this study but is normally assumed to be horizontal for analysis, however it is more likely to be a combination of the two in real play. A service is struck with an almost vertical racket and therefore the axis of rotation will be mainly vertical causing the spinning ball to deflect sideways. Most shots in tennis are struck with an almost horizontal racket leading to a mainly horizontal axis of rotation, the range of the ball will therefore be increased or decreased depending on the direction of spin.

Such complexity means that it is difficult to draw simple conclusions from the results in figure 6.21. The example of the drop shot was used when assessing the C_D chart, it is possible to further that analysis to include the effect of C_L. The impact velocity was $15ms^{-1}$ and had an under spin of 3000rpm, signifying a C_L of approximately 0.3. The resulting lift force is acting upwards, increasing the range of the shot. The required increase in impact velocity due to increased C_D is therefore reduced and maybe negated altogether.

6.8 Discussion

6.8.1 Components of drag for a spinning ball

In section 6.7.1 it was shown that the fibres of the spinning tennis ball straighten out, and it has been proposed that this leads to an increased C_D due to an increased projected area. It is also likely however that drag will be generated as the air flows through the individual fibres. It can therefore be concluded that the increase in drag observed for a spinning tennis ball are not only due to classical induced drag mechanisms, but also individual to the surface properties of tennis balls. This effect is discussed in more detail in chapter 7 for non-spinning tennis balls, however the mechanisms are identical.

6.8.2 Comparison with previous work

The drag and lift effects of a tennis ball have been investigated previously by Stepanek in 1988. The aerodynamic forces were assessed using the drop method discussed in appendix B. Analysis used the start and end point of the trajectory as developed by Davies (1949). Testing was limited to air velocities between 13.6 and 28ms^{-1} and spin rates between 800 and 3250rpm. This range of test parameters will give a maximum spin parameter of approximately 0.75, however the published results only go up to approximately 0.6.

Figure 6.22 shows the C_D and C_L results obtained using the equations presented by Stepanek. C_D and C_L 'Chadwick' are curves produced using the spin equations developed in this study. It should be noted that there was an abundance of data available in this study, it was reduced to increase the accuracy of C_D and C_L results within the physical constraints of the game of tennis. It can be seen that the two sets of data compare well for the range of speeds and spin rates tested by Stepanek. Initial impressions suggest that both the C_D and C_L curves tend towards a constant value.

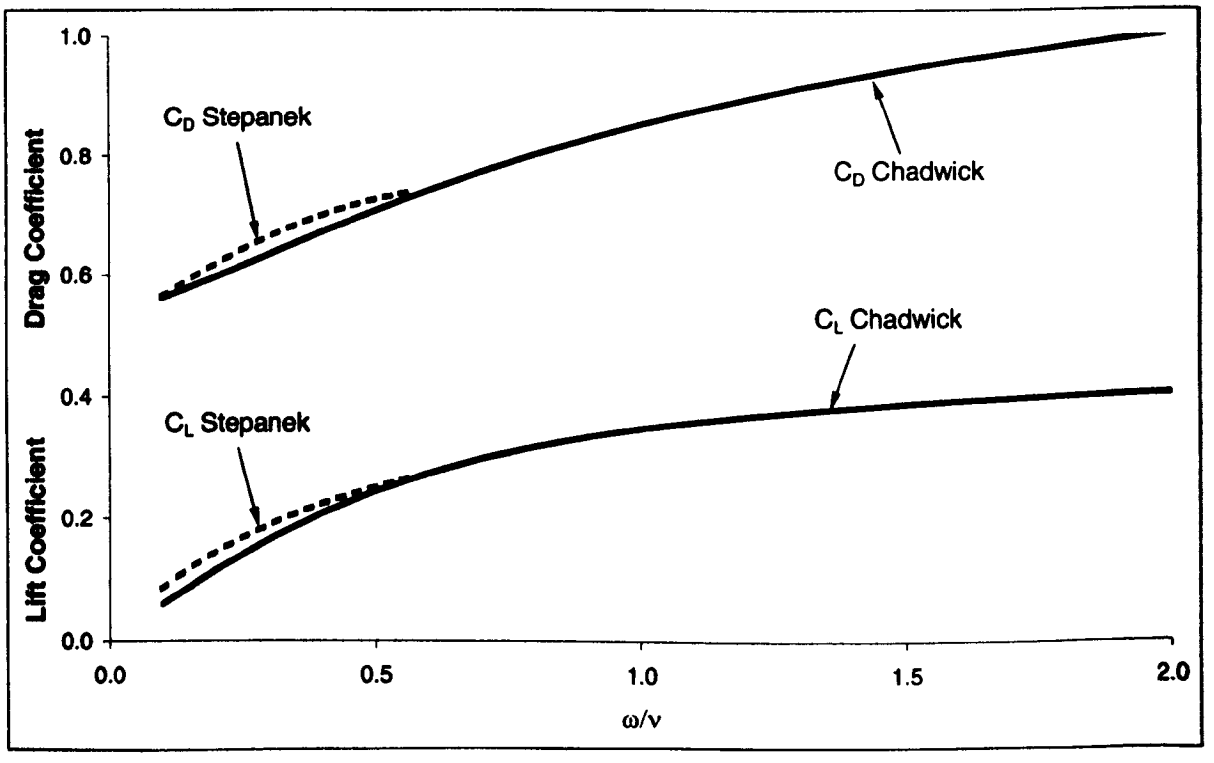

Figure 6.22 C_D and C_L results obtained in a previous study by Stepanek compared with the results obtained in this study.

Table 6.1 shows the limits of the equations published by Stepanek. It can be seen that, in comparison to this work, Stepanek underestimates C_D and overestimates C_L at high spin rates. There are small differences obtained where the spin rate is zero, however this is expected given the different test methods used and the potential inconsistencies in measurement of the diameter of a tennis ball. Comparisons at high spin rates shows that the C_D calculated by Stepanek is approximately 21% lower than obtained in this study, and the C_L is almost 14% higher. It would appear that the limited data obtained by Stepanek, and therefore the extensive extrapolation, has caused inaccuracies in the calculation of C_D and C_L at high spin rates.

	Chadwick		Stepanek	
	C_D	C_L	C_D	C_L
As $\omega \rightarrow 0$	0.537	0	0.508	0
As $\omega \rightarrow \infty$	1.012	0.436	0.796	0.494

Table 6.1 Limits of the C_D and C_L spin equations produced in this study compared to those published by Stepanek.

Confidence limits were estimated by comparing C_D and C_L calculated by equation and obtained by experimentation. The C_D and C_L values were calculated at each wind velocity tested. The absolute difference was subsequently calculated, and the average of this was used in the estimation of errors. Table 6.2 details the differences obtained in this study. It can be seen that the difference is very small, and when converted to a more meaningful percentage rate, the difference in C_D and C_L are identical.

	Chadwick		Stepanek	
	C_D	C_L	C_D	C_L
Difference	0.028	0.012	0.086	0.11
Difference (%)	0.28	0.28	10.8	22.3

Table 6.2 Differences obtained between simulated and real data obtained by experimentation for C_D and C_L in this study compared to those published by Stepanek.

The results published by Stepanek are also shown in table 6.2. The percentage figures have been created using the high spin rate limits in table 6.1. It is clear that the differences

obtained by Stepanek are significantly greater than those obtained in this study. The results obtained in appendix B of this study showed that the Davies method calculated variable results, and this may explain the large differences published.

6.8.3 Implications to the game of tennis

Figure 6.1 shows that the drag force acts in the opposite direction to the direction in which the ball is projected, and the lift force acts perpendicular to the drag force and the axis of rotation. The axis of rotation is vertical in this test method, however in the game of tennis, the axis of rotation is likely to be somewhere between horizontal and vertical.
The results showed that C_D increases with increasing spin rate and decreases with increasing impact velocity. It has therefore been shown that drag due to lift contributes to the overall drag significantly, where a spinning ball has a greater C_D than a non-spinning ball struck at the same impact velocity. As the C_D increases, the range of the stroke decreases, hence a tennis player will need to strike the spinning ball harder in order for it to travel the same distance as the non-spinning ball. It is therefore apparent that a tennis player has several decisions to make before playing a stroke.

It was also shown that C_L increases with increasing spin rate and decreases with increasing impact velocity. The C_L acts upwards in the case of under spin and downwards for a top-spinning ball. If the effect of C_L is combined with C_D, it can be seen that an over spinning stroke will fall significantly shorter than a non-spinning ball. An under spinning ball may travel further than the non-spinning case depending on the dominance of C_D and C_L during the flight, an effect that is discussed in more detail in chapter 4.

The effect of spin impacts more than just the C_L and flight path. The impact of the ball with the ground and the subsequent trajectory is significantly affected by the spin of a ball. The bounce of the ball will differ depending on the surface on which it is impacting. As this study does not cover the impact characteristics of tennis balls, it is not intended to discuss the details. It is clear however, that a spinning ball will bounce differently from a non-spinning ball and hence add further complication for the receiver.

7 C_D OF NON SPINNING BALLS USING A THREE COMPONENT WIND TUNNEL BALANCE - MODIFIED NAP

The drag force on a tennis ball with unmodified nap has been discussed and the results shown in chapter 5. It is extremely unlikely that the nap will remain unchanged throughout its life, hence it is important to investigate what effect such changes may have on the C_D. This chapter acts as an extension to the results obtained in chapter 5, and as such does not concentrate on set-up or test method, but focuses on improving understanding with additional results.

It is also useful to develop an understanding of what causes the drag on a tennis ball. The C_D of a smooth sphere is well understood, hence a method has been devised whereby the surface of the smooth ball is modified to include nap and the resulting C_D used for investigation.

It was decided at an early stage that an oversized ball is not suitable to obtain C_D results for a tennis ball because of the inability to scale the effects of the nap. The larger ball was used to investigate whether transition may occur at a higher velocity.

7.1 Test Method

The results obtained in this chapter have been obtained using the same test method and apparatus as that used in chapter 5. The same two wind tunnels have been used, and will be described by the relative maximum wind speed of each, i.e. low-speed and high-speed.

The diameter of the ball is measured in the same way as described in section 3.4. The changes in projected diameter have been applied in all cases unless otherwise stated.

7.2 Modified tennis balls

The nap on the tennis ball will change throughout its life, initially becoming fluffed with contact with the racquet and ground, and eventually becoming void of fluff with prolonged

impacts. The life of the tennis ball in major competitions is nine games, hence it will not reach the final stages of wear, however it is useful to investigate a well worn ball to develop an understanding of how C_D is affected.

The nap on the balls has been fluffed using a comb. After testing was completed on the fluffed nap, the fibres were shaved off using electric hair clippers and tested again as the shaved nap condition.

7.2.1 Low-speed

Figure 7.1 shows the results obtained in the low-speed wind tunnel for the three nap conditions. The results shown for the normal unmodified nap are repeated from chapter 6, and used here to enable comparisons against the modified nap conditions.

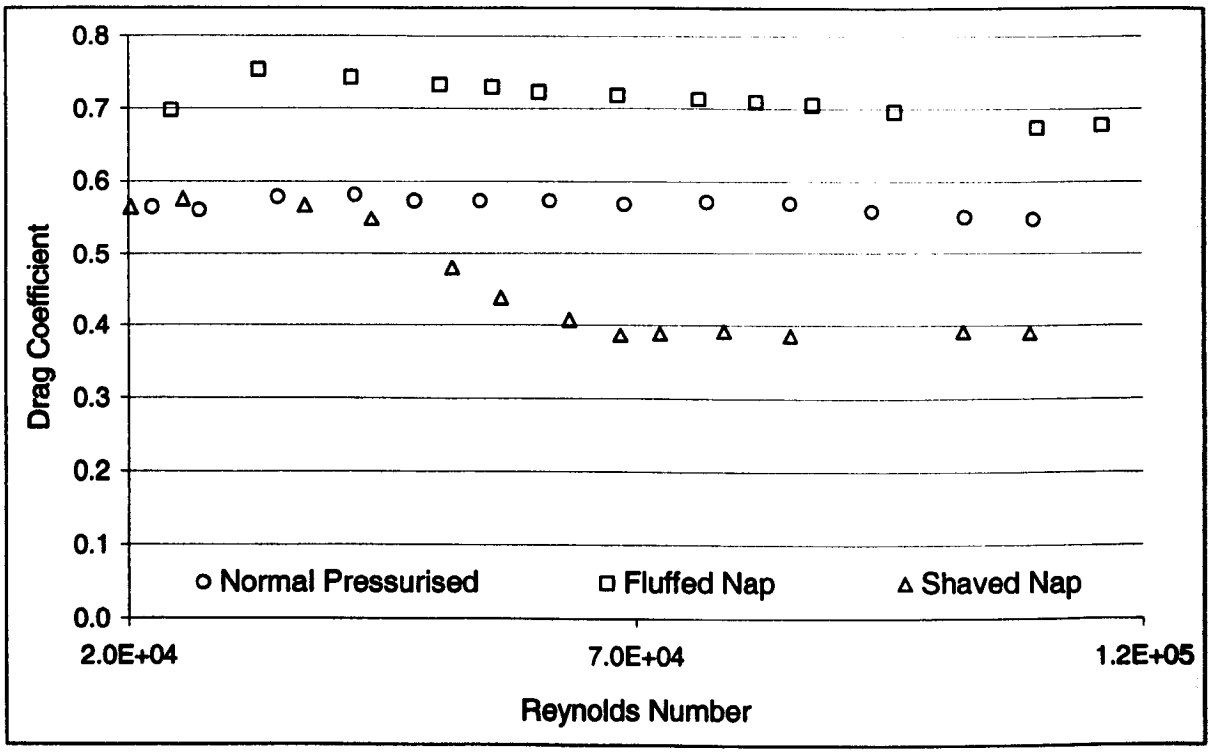

Figure 7.1 C_D versus Re results obtained for three nap conditions in the low-speed wind tunnel.

It can be seen that the C_D of the fluffed nap is higher than the normal unmodified nap, which in turn is higher than the shaved nap condition. The C_D of the fluffed nap steadily reduces throughout the test, suggesting the fibres are flattening with increased wind speed

as discussed in chapter 5. The C_D of the normal nap shows a similar reduction, however the effect is far less obvious.

It should be observed that the C_D of all balls is in excess of 0.5 at low wind speeds. The majority of the drag on a tennis ball is due to pressure drag, and in chapter 8 it is shown that the wake is large for all surface conditions tested.

The C_D for the shaved nap condition changes significantly during the test. It can be seen that the C_D is similar to that of the normal unmodified nap at low Re and reduces to approximately 0.4 at a Re of approximate 70,000, and the C_D remains constant at approximately 0.4 for all addition wind speeds tested.

A single set of data should not be used to draw major conclusions, hence the test using a ball with a shaved nap was repeated three times. Not only were these tests performed at separate times, they were performed on different balls. Figure 7.2 shows the C_D results obtained against Re for the three tests performed on shaved balls.

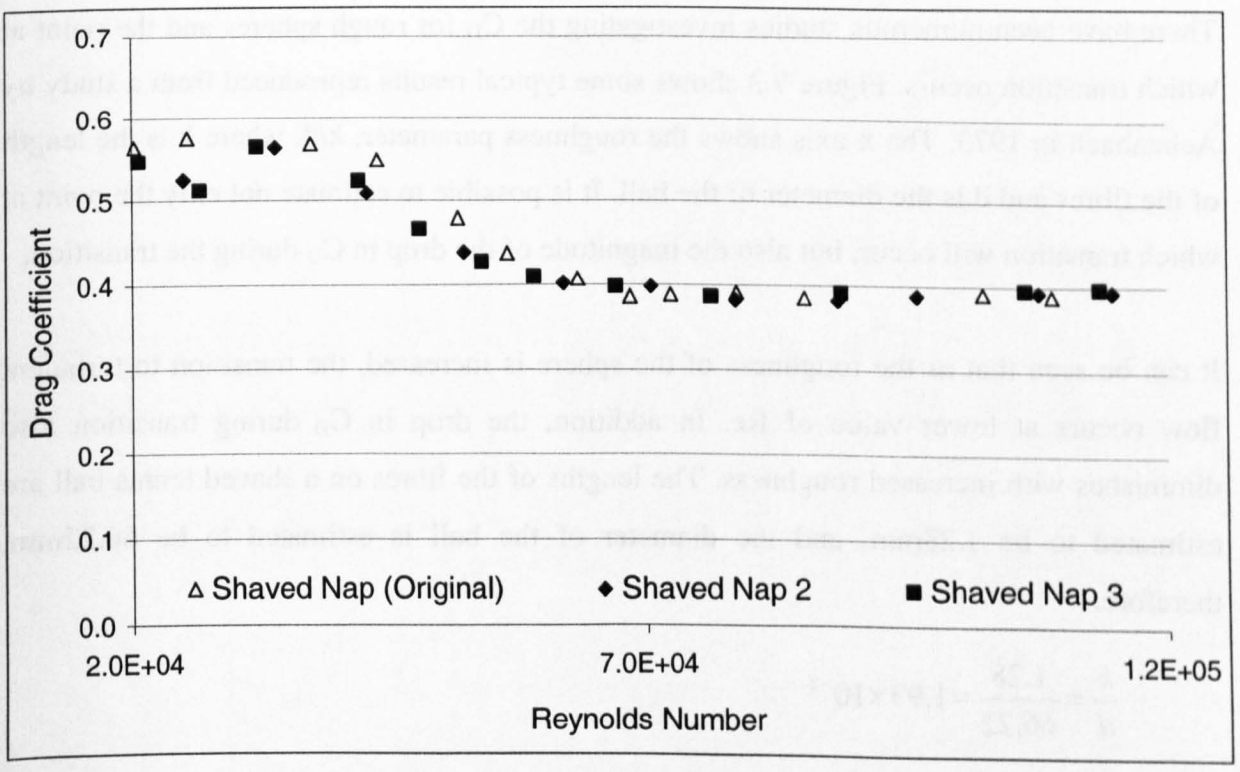

Figure 7.2 C_D versus Re results obtained for three shaved balls in the low-speed wind tunnel.

It can be seen that each ball shows the same drop in C_D at approximately the same Reynolds number. The second and third data sets were created using the same ball, hence it is conceivable that the nap was shaved differently causing the slight difference where the drop occurs. Regardless of where the drop occurs, this is a definite sign of transition, where the flow of air over the ball is starting laminar and turning turbulent at an early stage.

Transition occurs on the shaved ball condition rather than the other nap conditions due to the stiffness of the fibres. With the long fibres removed from the nap, the remaining fibres are short and stiff, making it act more like a rough ball. The transition for a non-spinning smooth sphere was discussed in chapter 5, and the drop in C_D was shown to be in excess of 0.4. The transition shown for the shaved ball could easily be missed or its relevance ignored with a drop in C_D of approximately 0.15. A study of previous work can help to show both the magnitude of drop that would be expected and when it would be expected on a ball of this type.

Magnitude of drop in C_D during transition

There have been numerous studies investigating the C_D for rough spheres and the point at which transition occurs. Figure 7.3 shows some typical results reproduced from a study by Achenbach in 1973. The x-axis shows the roughness parameter, k/d, where k is the length of the fibres and d is the diameter of the ball. It is possible to estimate not only the point at which transition will occur, but also the magnitude of the drop in C_D during the transition.

It can be seen that as the roughness of the sphere is increased, the transition to turbulent flow occurs at lower value of Re. In addition, the drop in C_D during transition also diminishes with increased roughness. The lengths of the fibres on a shaved tennis ball are estimated to be 1.28mm, and the diameter of the ball is estimated to be 66.22mm, therefore:

$$\frac{k}{d}=\frac{1.28}{66.22}=1.93\times10^{-2}$$

Although the chart does not contain data for spheres with this roughness it is possible to extrapolate to obtain an approximate solution. It can be seen that transition would be

expected to occur at a Re of approximately $5x10^4$, and the drop in C_D would be less than 0.3. In figure 7.2, it can be seen that the drop in C_D is approximately 0.15 and super critical flow is established around $7x10^4$, hence the results obtained compare well with those obtained previously on standard rough spheres.

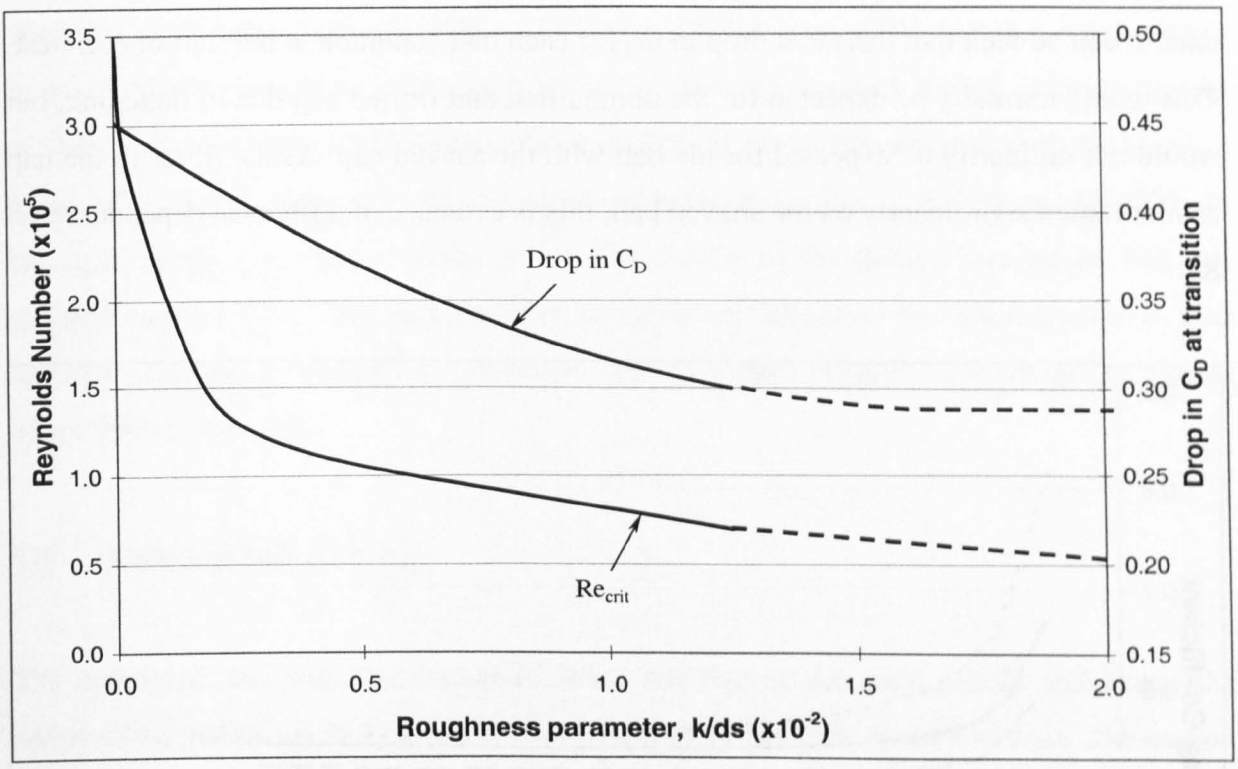

Figure 7.3 Chart showing the drop in C_D expected and the Reynolds number at transition (Achenbach, 1973) for spheres of different roughness.

Mehta and Pallis (2001) obtained some results for 'razor shaved' tennis balls and observed a similar trend. Re_{crit} was estimated to occur at around 100,000, and the C_D was shown to rise in the supercritical flow regime, tending towards 0.5 in the transcritical flow regime.

It is clear that the post Re_{crit} C_D is not shown to rise in the results presented in this low-speed study. The analysis presented in this low-speed study confirms that the shaved ball can be assumed to be a rough ball, in which case a transcritical C_D of 0.4 would be expected based on Achenbach's work. The results obtained by Mehta and Pallis however, showed that the transcritical C_D of a razor shaved ball could rise above 0.4 in the transcritical regime. It could therefore be hypothesised that transcritical flow was not fully developed during this low-speed testing, and further increases in Re could cause the C_D of the shaved ball to rise further.

7.2.2 High-Speed

Figure 7.4 shows the C_D versus Re results obtained for the three ball conditions in the high-speed wind tunnel. Rather than plotting the individual data points, they are shown using the method developed in chapter 6 using best-fit curves for both the sting and ball data. It can be seen that there is a drop in C_D for each ball condition at the start of each test. This would normally be expected for the unmodified and fluffed nap due to flattening, but would not ordinarily be expected for the ball with the shaved nap. As the fibres in the nap cannot flatten significantly on the shaved ball, this is evidence of a fibre C_D dependence on Re.

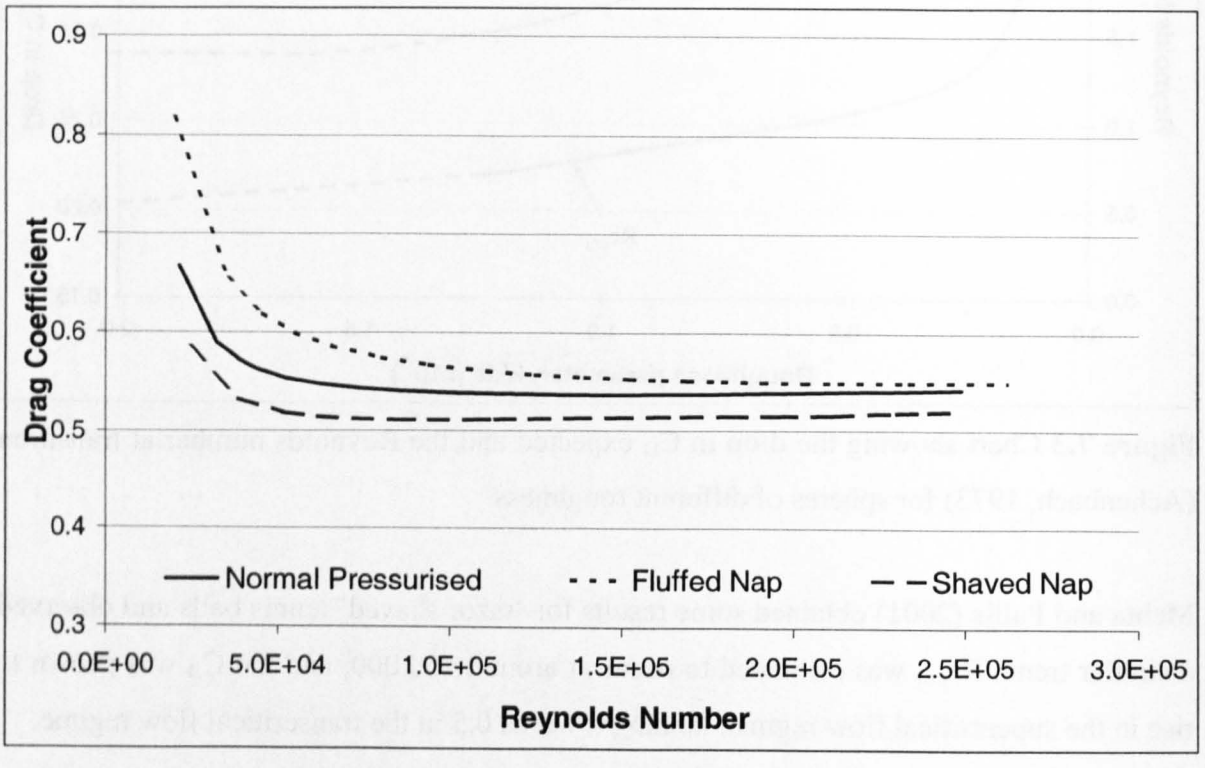

Figure 7.4 C_D versus Re results obtained for three nap conditions in the high-speed wind tunnel.

The C_D for the ball with the unmodified nap was found to be 0.53 in chapter 5. It can be seen that the C_D for the ball with the fluffed nap is greater than that for the ball with the unmodified nap, which in turn is higher than that for the ball with the shaved nap. The C_D of the shaved ball is around 0.5 and it can therefore be concluded that the transcritical flow was not fully developed in the low-speed tests.

The duration of the drop varies for each ball condition, and as would be expected from discussion in chapter 5, the fluffed nap takes a long time to settle. Although it is the final C_D obtained which is of most interest to the game of tennis, the drop is important for understanding the flow around a tennis ball. Mehta and Pallis (2001) observed similar drops in their studies. Although the magnitude of C_D was different, the magnitude of the drop can be directly compared. Figure 7.4 shows a steep drop at the start that is not shown in the results presented by Mehta and Pallis, however their testing started at Re of around 80,000. For a pressurised ball that had been used for 3 games (assimilated to fluffed nap), a drop in C_D of approximately 0.04 was observed between and Re of 80,000 and 140,000. At the same stage, it is shown in figure 7.4 that the C_D of the fluffed pressurised ball has dropped around 0.02. The fact that this unexpected behaviour has been shown in two different studies at completely different test facilities suggests that there is further investigation required.

7.3 Oversized ball with nap

The oversized ball was approximately twice the size of the normal ball, and hence the scope of Reynolds numbers that could be investigated was increased two-fold. The nap on the oversized ball was similar to that on the normal ball, hence it had not been scaled in line with the increase in ball size. In its original condition, the oversized ball had a similar roughness parameter, k/d, as that of the shaved normal sized ball, however the fibres were not as stiff. When the oversized ball was shaved, the roughness parameter reduced to approximately 9.5×10^{-3}.

Testing on the oversized ball was undertaken in the high-speed wind tunnel prior to the low-speed tests. For this reason there is only data available for the unmodified nap, it was thought that modification of the ball could make comparison between wind tunnels void.

7.3.1 High-speed

Figure 7.5 shows the C_D versus Re results obtained for the unmodified oversized ball in both of the wind tunnels. The increases in blockage effects due to the larger ball were negligible, with the overall blockage remaining less than 0.5%.

It can be seen that the C_D results obtained in the high-speed wind tunnel are a continuation of those obtained in the low-speed wind tunnel, tending to an average value of approximately 0.53/0.54. There does not appear to be any sign of transition over the range of Reynolds number tested. The maximum Re tested on the oversized ball related to a wind speed of approximately 125ms^{-1} (285mph) for the normal sized ball.

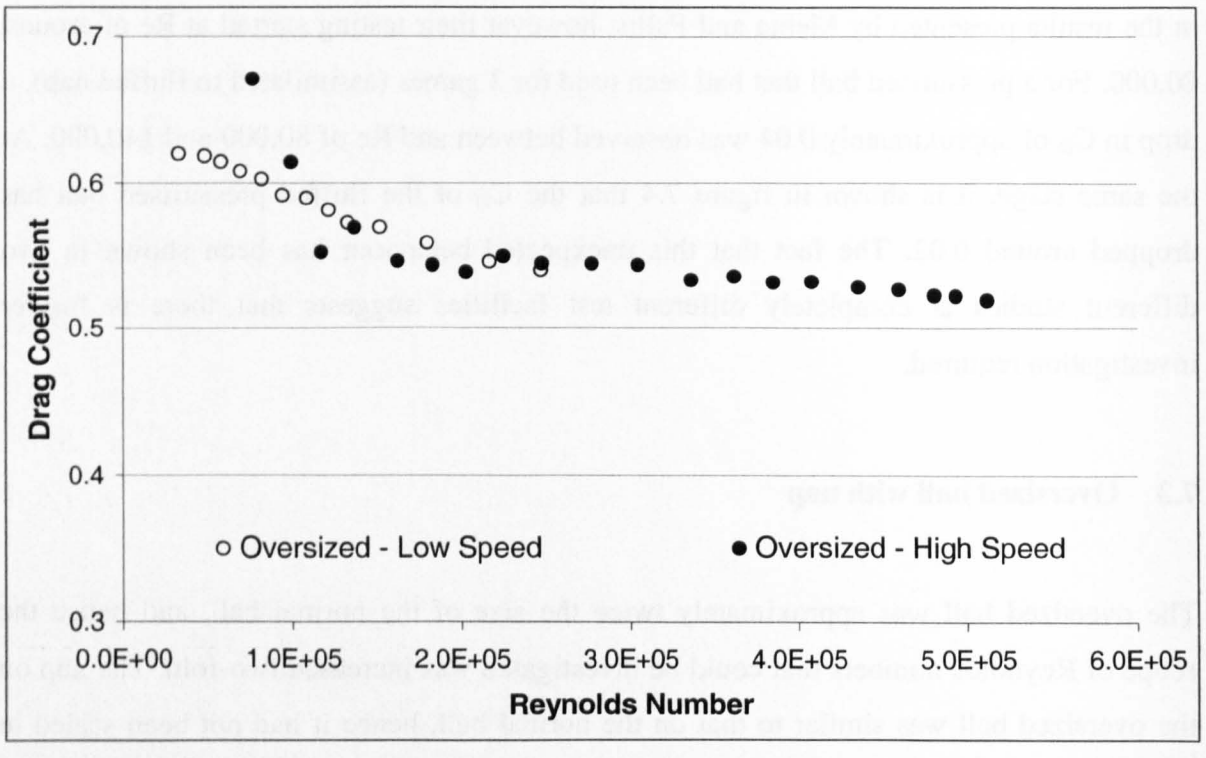

Figure 7.5 C_D versus Re results obtained for the unmodified oversized ball in the high-speed wind tunnel.

The most interesting results that arises from this set of results, is that there is no indication of a transition at all, even though the Re has exceeded the Re_{crit} of a smooth ball in free air of 385,000. This is the clearest sign thus far of the flow regime around a tennis ball, there is no sign of transition, therefore it must have happened very early and the flow around the ball must be turbulent.

The general gradient of the data set drops throughout the wind speeds tested in a similar manner to the data set shown for normal sized tennis balls. There are some erroneous data points shown at low speeds in the high-speed wind tunnel, and it is proposed that these are due to the inadequacies of the measurement technique used in the high-speed wind tunnel

at low forces. Ignoring these points, the C_D drops from just above 0.6 to around 0.55 in the low-speed wind tunnel, a closer look at these results will help further the understanding.

7.3.2 Low-speed

Figure 7.6 shows the C_D versus Re results obtained for the various nap conditions of the oversized ball in the low-speed wind tunnel. The blockage due to the ball and sting apparatus was increased a small amount due the increased size of the ball, however it was still significantly less than 4% of the working section area. The C_D plot for the unmodified nap is shown to be in excess of 0.6 at low wind speeds, reducing to less than 0.55 at the highest wind speeds available in the low-speed wind tunnel. It can also be seen that the trend and magnitude is similar to that of a normal sized unmodified tennis ball. This effect has been repeated for several different balls and it is now clear that it is of real significance. There is no sign of a severe drop in C_D that may be expected during transition, so it can therefore be concluded that transition has occurred below an Re of approximately 30,000 (equivalent to a wind speed of $3ms^{-1}$).

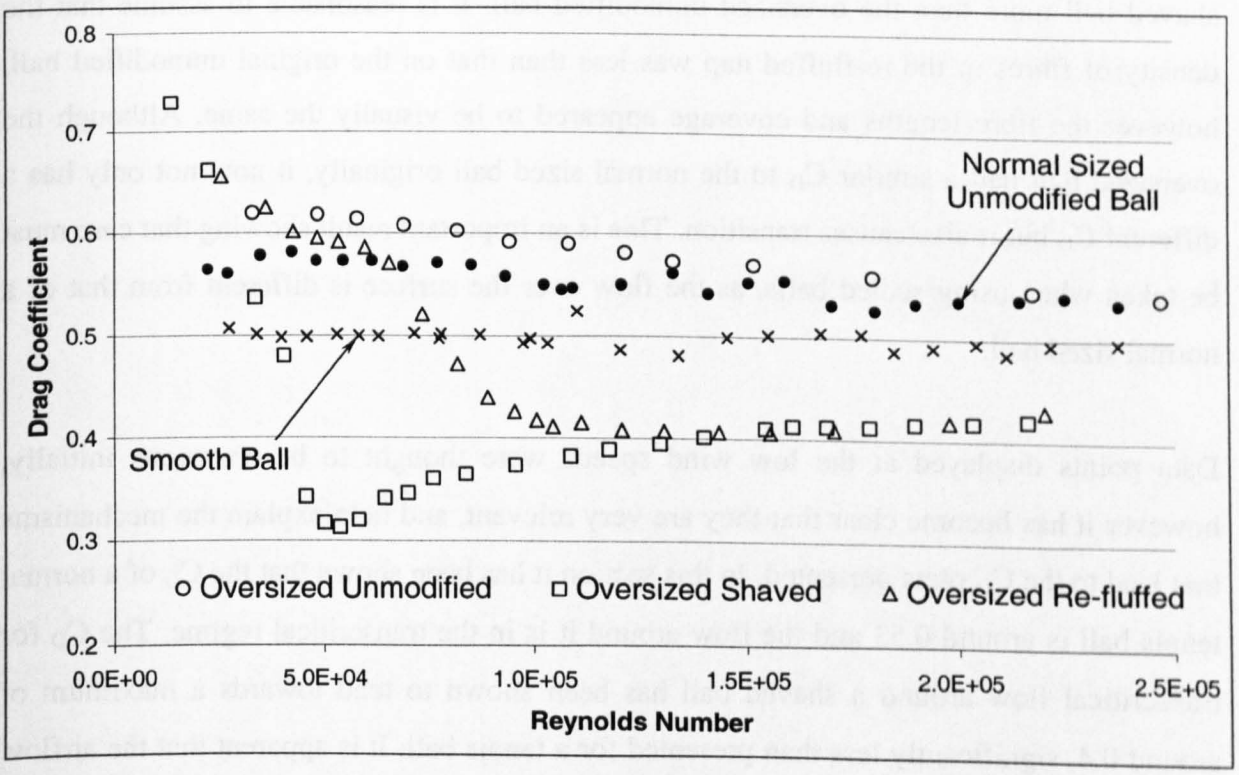

Figure 7.6 C_D versus Re results obtained for the oversized ball with three different nap conditions in the low-speed wind tunnel, whilst drawing comparisons against the normal sized unmodified and smooth balls.

When the oversized ball is shaved the C_D plot becomes more like that obtained for a standard rough sphere. Referring back to figure 7.3, it can be seen that a transition should occur between $5x10^4$ and $1x10^5$ with a drop in C_D of 0.3 to 0.35 for a roughness parameter of $9.5x10^{-3}$. As the transition occurs at a low wind speed, the magnitude of C_D before the drop is not clear. Using the unmodified C_D plot for guidance it can be assumed that the C_D would be in excess of 0.6 for laminar flow, therefore the C_D drop is approximately 0.3 at a Re of approximately $5x10^4$. The only difference between these results and those presented for the normal sized ball is that the C_D continues to rise beyond 0.4, and is still rising at the maximum wind speeds tested. It is not clear whether the C_D would continue to increase up to 0.5 as it did for Mehta and Pallis (2001), indeed at a Re of 220,000 their razor shaved ball had a C_D of approximately 0.475, which is still over 10% higher than that shown in figure 7.6.

The final results obtained for the oversized ball in the low-speed wind tunnel involved combing the nap. As there was only one of these balls, it was hoped that this would return the ball to its original condition such that it could be used in other tests. It is clear from the results obtained that this was not the case, in fact these results resemble the normal sized shaved ball more than the oversized unmodified ball. It is reasonable to assume that the density of fibres in the re-fluffed nap was less than that on the original unmodified ball, however the fibre lengths and coverage appeared to be visually the same. Although the oversized ball had a similar C_D to the normal sized ball originally, it now not only has a different C_D but it also causes transition. This is an important result showing that care must be taken when using scaled balls, as the flow over the surface is different from that of a normal sized ball.

Data points displayed at the low wind speeds were thought to be erroneous initially, however it has become clear that they are very relevant, and help explain the mechanisms that lead to the C_D plots presented. In this section it has been shown that the C_D of a normal tennis ball is around 0.53 and the flow around it is in the transcritical regime. The C_D for transcritical flow around a shaved ball has been shown to tend towards a maximum of around 0.4, significantly less than presented for a tennis ball. It is apparent that the airflow over a tennis ball is complex and the alternative effects that could cause the C_D plots presented in this section will are discussed in section 7.5.

7.4 Smooth ball with fluff added

It is apparent that the airflow around a tennis ball does not act like that around a smooth ball, the magnitude of C_D is too high. Moreover, it does not act like that around a rough ball, there is no sign of transition and the C_D is too high for conventional transcritical airflow over a rough sphere.

A further test was developed to enable a greater understanding of what is happening to the flow around a tennis ball. The test method starts with a smooth ball whose C_D is well known, the ball is subsequently modified by attaching tennis ball nap to it. Rather than attaching the woven felt to the ball, only the fibres were added, hence investigating the airflow through the fibres rather than the surface of the felt. The fibres were added in several stages until the whole front face of the ball was covered. Figure 7.7 shows the incremental stages of covering.

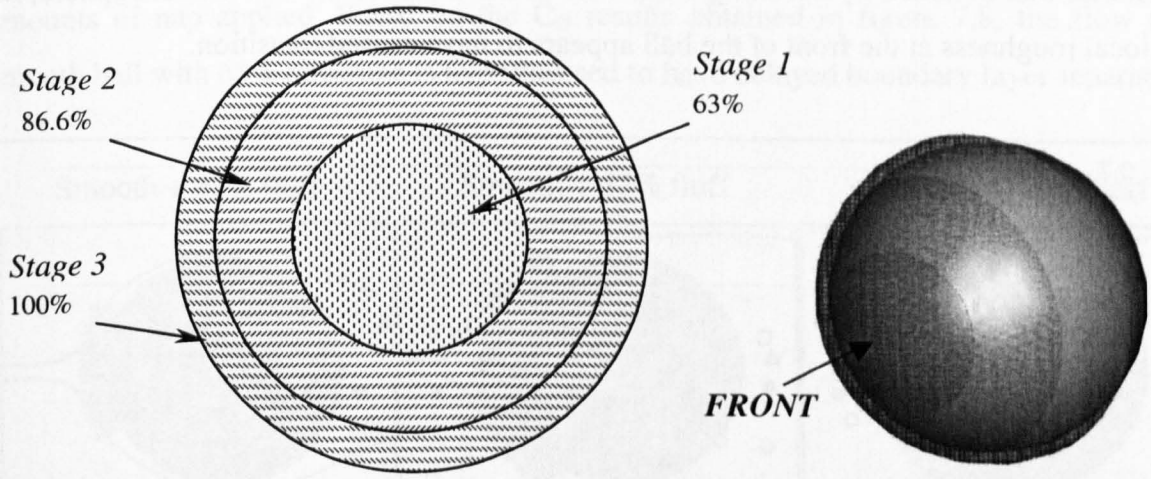

Figure 7.7 Image showing the three stages of coverage (image from front of ball).

It can be seen that coverage started on the front surface of the ball at the stagnation point, with subsequent rings of fibre being added afterwards. Although the fibres were added in three equal amounts, the percentage coverage figure suggests that most of the fibre was added from the start. This percentage coverage figure was calculated using the projected area covered with fibres rather than surface area, hence the high figures. Testing was undertaken at each stage of coverage giving four data sets including that for the smooth ball.

The diameter of the ball was measured before the fibres were added and was not amended due to any change in diameter due to the fibres. The adhesive used to attach the fibres is a fraction of 1mm and hence should not change the C_D significantly. Any changes observed in C_D are therefore due to an increased projected area forcing the airflow wider around the ball, or a drag caused by the airflow travelling through the fibres. It is more likely to be a combination of both effects, and the results obtained in this section will help to develop an understanding of the flow through the nap of a tennis ball.

7.4.1 High-speed

Figure 7.8 shows the C_D versus Re results obtained in the high-speed wind tunnel for the smooth ball before and after tennis ball fibres have been added. It can be seen that the C_D for the smooth unmodified ball is approximately 0.5. When the first layer of fibres is added the C_D rises above 0.55 and drops to below 0.5 at a very low wind speed. This result resembles that obtained by attaching a trip wire to the front surface of a smooth sphere, i.e. the local roughness at the front of the ball appears to have caused transition.

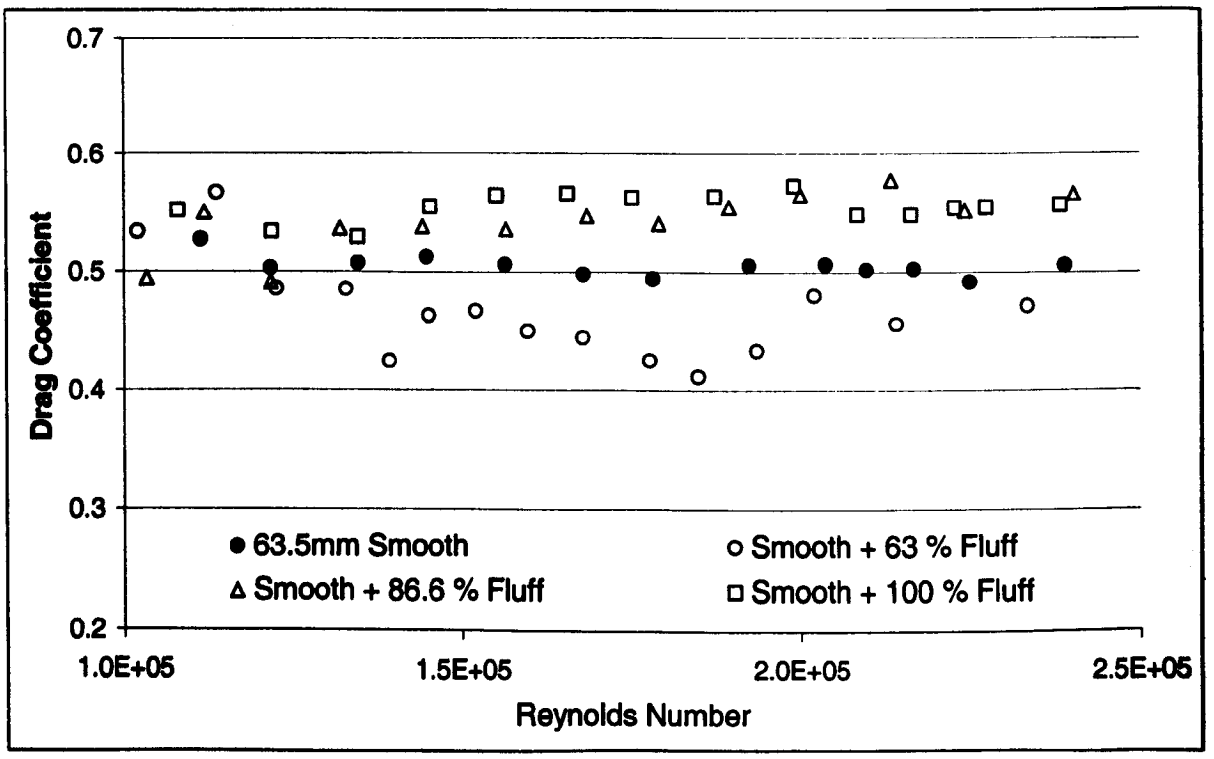

Figure 7.8 C_D versus Re results obtained in the high-speed wind tunnel for a 63.5mm smooth ball before and after fibres have been added.

The addition of the second annulus of fibres causes the C_D to increase above that obtained for a smooth ball for all of the wind speeds tested. The flow passing over and around the ball is now similar to that around a normal tennis ball. It would appear that the increased number of fibres has increased the C_D resulting in a plot is similar to that of a normal tennis ball. It is proposed that the increase in C_D is due to both the changes in diameter and the increased viscous effects of the flow through the fibres. The fibre coverage on these balls is significantly less dense than that on the tennis ball, and hence it is thought that the diameter should not change significantly.

The final data set obtained when the whole front surface is covered with fibres is similar to that for 86.6%. It can be concluded that the airflow over this surface is not significantly different from that with less coverage, and subsequent additions of material will not affect the flow providing it is of similar dimensions to that covering the rest of the ball.

Figure 7.9 shows three images depicting the flow over the smooth ball with increasing amounts of nap applied. Based on the C_D results obtained in figure 7.8, the flow over smooth ball with 63% coverage is hypothesised to have delayed boundary layer separation.

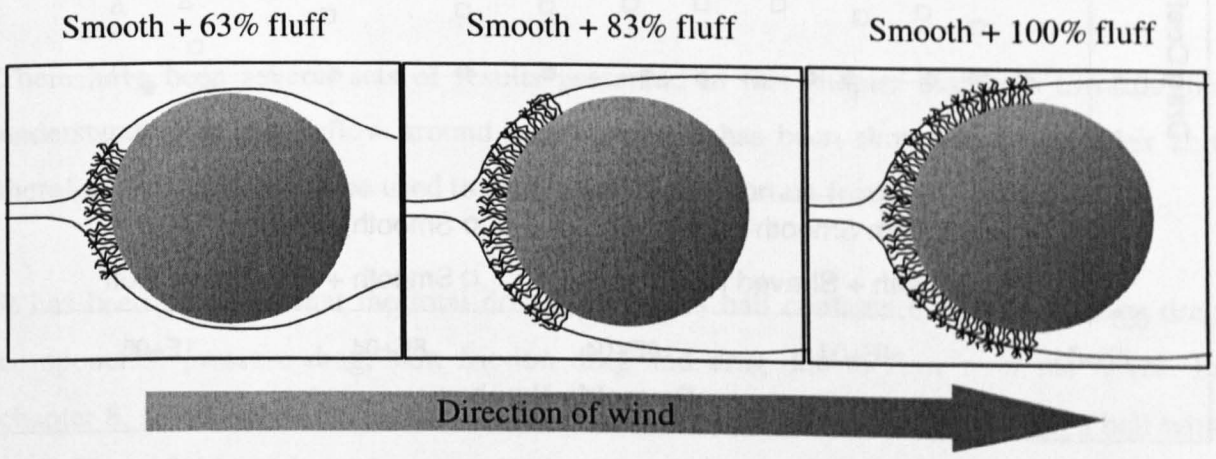

Figure 7.9 Drawings to show how the hypothesised flow over the three different levels of coverage, based on the C_D results obtained.

With additional nap adhered to the front face, the C_D increases suggesting a broader wake and a separation near the poles on the front face. This result does not coincide with the classical rough sphere results presented by Achenbach (1973), where it is suggested that the transcritical flow always separates on the rearward face. As there is very little

difference between the C_D of the balls with 83% coverage and 100% coverage, it is assumed that the flow separates from the ball at a similar position. Although the flow over the nap of a tennis ball is not yet fully defined, it is assumed here that some of the air flows through the nap.

7.4.2 Low-speed

Figure 7.10 shows the C_D versus Re results obtained in the low-speed wind tunnel for the smooth ball before and after tennis ball fibres have been added. A single smooth ball has been used for both the low-speed and high-speed wind tunnel tests, hence rather than adding felt to the ball, it is removed to resemble the shaved ball used in previous testing.

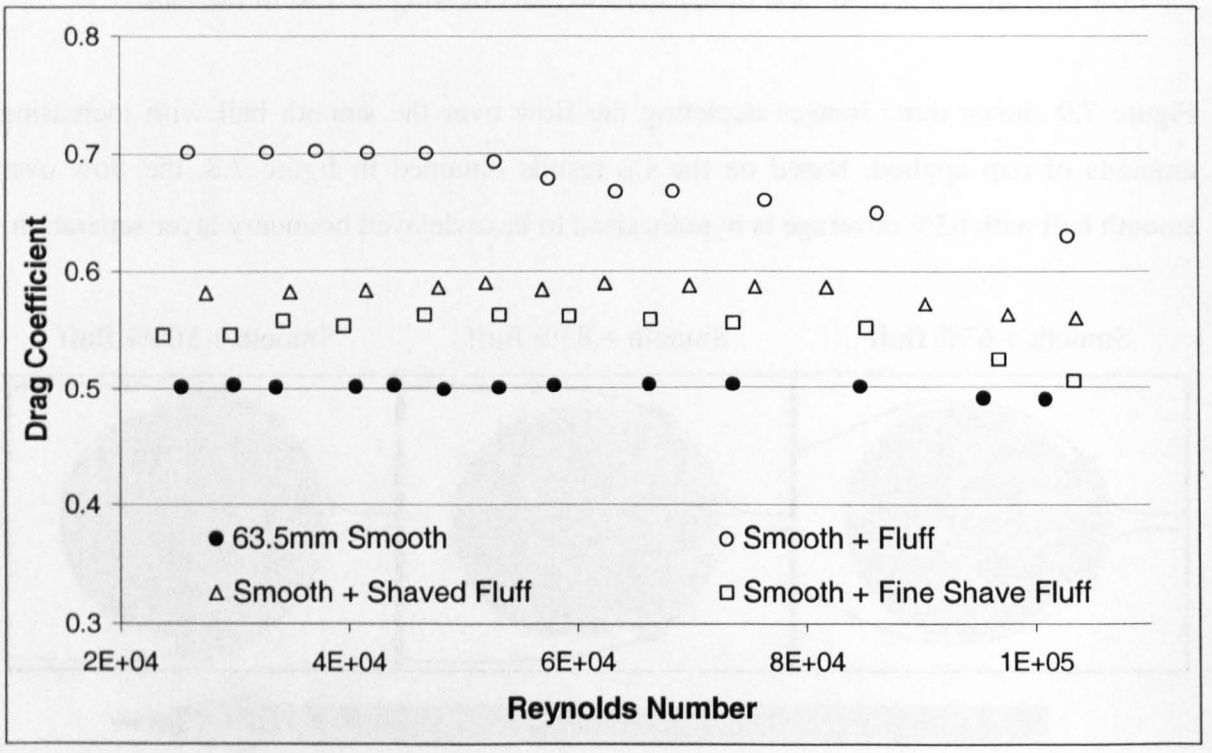

Figure 7.10 C_D versus Re results obtained in the low-speed wind tunnel for a 63.5mm smooth ball before and after fibres have been added.

As can be seen, the C_D for the smooth ball is approximately 0.5 for all values of Re tested, and is increased above 0.6 when the front face is covered in fibres. The C_D plot for the fibre covered ball drops throughout the testing and is approximately 0.63 at the maximum wind speed tested. Unfortunately, due to the ball's reduced size, there is no overlap between the testing in the two wind tunnels, however the C_D is still reducing at the

maximum wind speed measured in the low-speed wind tunnel and it is feasible that it could reduce below 0.6 at increased wind speeds. This drop in C_D may be due to the flattening of the fibres, suggesting that the relevant projected diameter of a ball with fibres on it may be greater than the diameter that would be obtained using the ITF guidelines.

The fibres were initially shortened to investigate the flattening effect, and as can be seen, the C_D is reduced for all wind speeds. It is also apparent that the reduction in C_D is no longer observed, however the C_D remains greater than that of the smooth ball. As the fibres are cut closer to the surface of the ball the C_D reduces further, however it remains greater than that of the smooth ball and it is apparent that there is no transition observed for the closely shaved ball. Due to the fibre density, the surface is not considered to be as rough as the shaved tennis ball, and no transition is initiated, hence the additional drag is due to air flowing through the short fibres.

7.5 Discussion

7.5.1 Contributors to the C_D of a tennis ball

There have been several sets of results presented in this chapter that help towards the understanding of the airflow around tennis balls. It has been shown to be complex and therefore this section will be used to draw all of the important features together.

It has been proposed that the total drag on a tennis ball contains elements of three drag components; pressure drag, skin friction drag and drag due to flow over the fibres. In chapter 8, a ball with a fluffed nap is shown to have a slightly larger wake than a ball with a shaved nap, which may imply a slightly greater pressure drag component. It is proposed that the skin friction drag be due to relatively rough surface of the nap, or more accurately, the junctions of the nap fibres. And it is suggested that the drag due to the flow through the fibres could be attributed to pressure drag on a microscopic scale. Overall, the tennis ball can be thought of as a very rough sphere with a porous coating (Mehta & Pallis, 2001).

Initial drop in C_D

The increased C_D and low Re was initially discarded as erroneous data, however it has been shown to be repeatable, moreover, the smooth ball data is of consistent quality. It is fully understood that a tennis ball is a bluff body and therefore the drag acting on it is predominantly due to the large wake produced by early separation, with as little as 2% of the total drag of a smooth ball being due to viscous drag (Achenbach, 1972). However, if this were the only drag acting on a tennis ball, then the data presented would be more similar to classical rough ball plots, with the C_D being around 0.5 (subcritical) and 0.4 (transcritical). It has been proposed that the effective projected diameter of the ball reduces with increased wind speed, which may also be partly true, however the flow visualisation showed that some of the airflow also passes through the fibres.

There are conflicting conditions occurring in the data presented, the C_D is reducing when a rise in the C_D of a sphere would be expected in the supercritical regime. It is therefore concluded that there must be a more dominant effect.

The fibres in the nap of a tennis ball are normally randomly configured when not moving or no wind is applied. Hence part of the drop in C_D will be due to the effect of aerodynamic drag and the flattening of fibres at increased wind speeds, as shown in figure 7.11, showing a fluffed tennis ball, a) before the test started and b) during test, in the high-speed wind tunnel.

a)  b) 

Figure 7.11 Fluffed pressurised tennis ball at wind speeds of approximately (a) zero and (b) 60ms^{-1} in the high-speed wind tunnel.

Assuming that this effect does not account for the entire drop, and there is additional air being forced through the fibres, then the rest of the effect can be explained by microscopic pressure drag on each of the fibres, termed 'fuzz drag' by Mehta and Pallis (2001).

Figure 7.12 shows classical C_D plots for a sphere and a cylinder for Reynolds numbers from 0.1 up to 10,000,000. If the fibre were considered to be a very thin cylinder with a diameter of 25 microns, then the Re would range from 5 to around 100 for the wind speeds tested in this study.

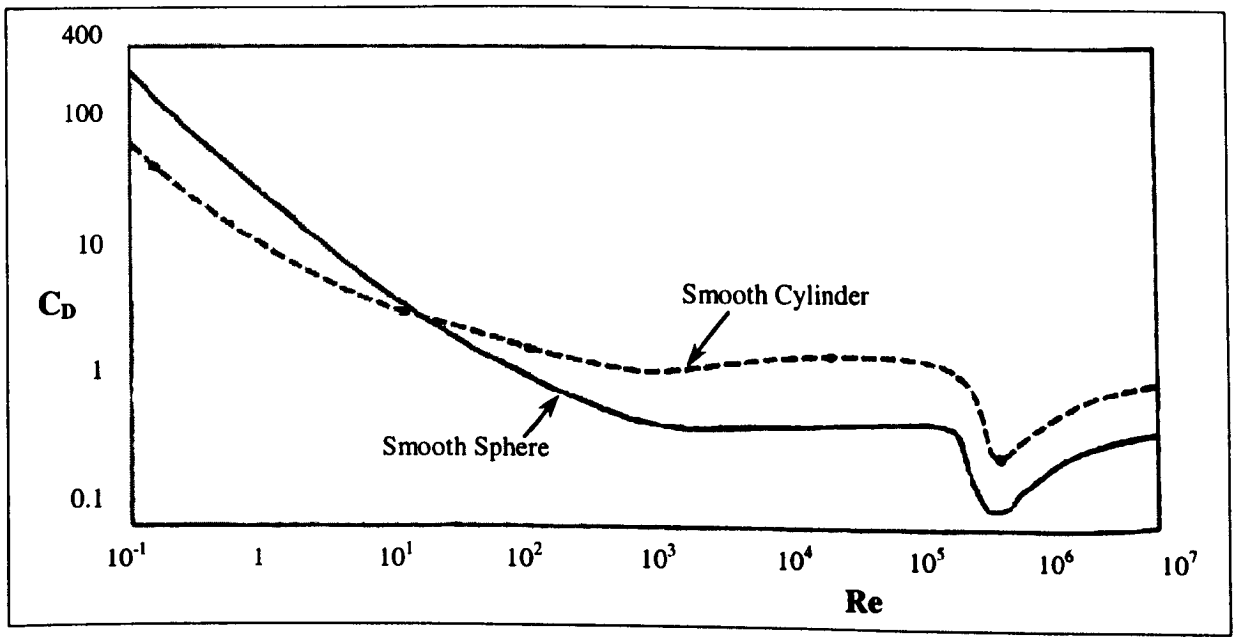

Figure 7.12 C_D for spheres and cylinders at Reynolds numbers from 0.1 up to 10,000,000.

At a Re of 5, it can be seen that the C_D of a cylinder is around 5, and given the fact that there are several hundred fibres in the airflow, the additional drag may be substantial. Even at the maximum wind speed, the C_D of the filaments is greater than 1, and may therefore remain a significant contributor to the overall drag.

Separation mechanisms - why is C_D above 0.4 in the transcritical regime?

In section 7.3.1 it was shown that an oversized ball covered in a similar covering to tennis balls did not go through transition, even at Reynolds numbers beyond $5x10^5$. This was a clear sign that transition must have occurred relatively early and therefore was not observed in the range of Reynolds numbers tested.

In the supercritical flow regime the C_D is expected to rise, and in the transcritical flow regime the C_D is expected to be constant and around 0.4. The data presented for a tennis ball with an unmodified or fluffed nap is consistently in excess of 0.5, and there must therefore be an alternative separation mechanism, two plausible separation mechanisms are discussed in this section.

The first mechanism to be described assumes that the air is forced to flow outside of the nap at increased wind speeds. Figure 7.11 showed a fluffed tennis ball, a) before the test started and b) during test, in the high-speed wind tunnel. It can be seen that all of the fibres on the front face become flat as the airflow impinges normally on it. The fibres on the top surface are seen to flatten more like a set of dominoes, where front fibres are prevented from becoming completely flat due to the resistance of the fibres beneath. The resulting shape is seen to be more like a step down rather than the rounded rear face of a sphere, and hence may act like a trip.

A trip wire on the front facing surface of a sphere will induce premature transition, however it is proposed that a trip positioned near the apex will induce separation. It is therefore hypothesised that the pressure drop across the step down to the rear surface of the ball is too great for the turbulent boundary layer to overcome and separation occurs.

This mechanism is supported by the 'Brown' effect, which comes from a dissertation by Brown (1997), where a noduled ball was discussed as a possible way to increase C_D and hence slow the game of tennis down. The nodules were added in 6 stages, however the effect on C_D was similar in all cases. Figure 7.13 shows a typical set of results obtained in the study, where it was found that the C_D dropped to a minimum of just less than 0.3 at a Re of approximately $9x10^4$ as the boundary layer went through transition. As the Re increased, C_D is shown to rise steadily in the supercritical regime. At a Re of approximately $2.5x10^5$ (Re_{Brown}), the C_D rises rapidly to in excess of 0.85. Brown concluded that the increased C_D obtained using nodules could therefore be used to slow the game down. Whether or not the use of nodules would be a realistic option in the game of tennis, this study can be used to aid understanding of the flow through the surface of the ball.

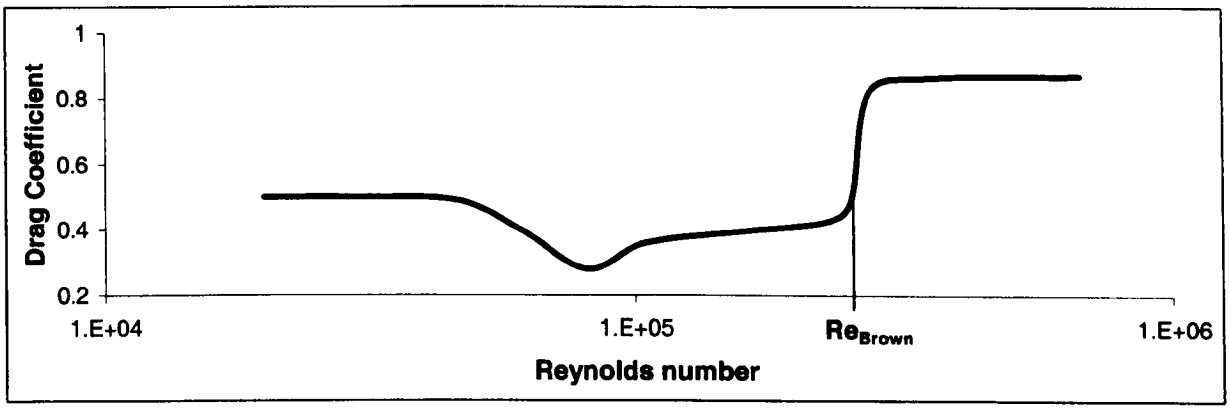

Figure 7.13 Typical results obtained by Brown (1997) to show Re_{Brown}, and the C_D of a ball covered with nodules.

Interpretation of the C_D plot reveals that the air flows through the nodules, and transition occurs relatively early. The turbulent separation point continues to creep forward with increased Re in the supercritical regime. Indeed, up until a Re of approximately $2.5x10^5$ the C_D plot resembles a C_D plot of a roughened ball in the transcritical phase, and the air is flowing through the nodules. After Re_{Brown}, the air is forced over the nodules rather than through them, and the additional C_D can be shown to be a function of the additional projected diameter to the outer edge of the nodules. This is an important result and helps show that the flow over the surface of tennis ball may not flow through the fibres at increased wind speeds.

It should be noted that there is no large increase observed in the C_D of a tennis ball, therefore the Brown effect for a tennis ball must occur at very low velocities, outside of the test constraints in this study. In the flow visualisation section, it appears that air flows through the nap of both the normal and fluffed surfaces at $4ms^{-1}$, within the C_D testing range, which would imply that the Brown effect should have been observed in the C_D results had it occurred. If the airflow is assumed to continue to flow through the fibres, even at high wind speeds, then an alternative (or additional) separation mechanism needs to be discussed.

The second mechanism assumes that air is always forced through the fibres and the roughness of the ball induces separation. As a tennis ball is a bluff body, the drag acting on it is predominantly due to the large wake produced, and if it were considered to be a 'normal' rough sphere, it would have a subcritical C_D around 0.5. It has also been shown

that C_D becomes independent of Re in the transcritical flow regime, with the transition points located near the front stagnation and boundary layer separation occurring around 100°, relating to a C_D of around 0.4. It should be noted however, that the transcritical separation points just described are in the region of adverse pressure gradient, and it could therefore be expected that the separation point could continue to move upstream.

With increasing roughness, the boundary layer growth rate is increased resulting in a tendency towards earlier separation. The skin friction coefficient also increases with increasing roughness resulting in a boundary layer that is more resilient to separation. It can therefore be seen that the separation location on a rough sphere is determined by the behaviour of these competing effects. It is entirely possible that for certain types of roughness, such as the round glass beads investigated by Achenbach, that a limit is reached whereby the boundary layer thickening effects are overridden by those due to increasing skin friction coefficient, and the flow remains attached longer. The roughness elements of the tennis ball may be more effective at thickening the boundary layer however, and it is therefore proposed that the absolute limit for turbulent boundary layer separation in the transcritical regime is the same as that for laminar boundary layer separation.

If the turbulent separation location in the transcritical regime is similar to a laminar separation in the subcritical regime ($\theta_s \approx 80°$), then it is suggested that the pressure drag should also be equivalent ($C_D \approx 0.5$), thus giving a total C_D in excess of 0.5.

7.5.2 Sellotape

An interesting result was obtained whilst trying to create a practice ball that could be used for cricket. In an attempt to get the ball to swing in the air, sellotape was attached to one side to make it the smooth side. It was thought that, if the ball were to deviate at all, it would swing away from the smooth surface. However, the opposite occurred, and the ball deviated a large distance towards the sellotaped surface.

After several conversations and hypotheses, it was decided that a ball covered in sellotape should be tested in the wind tunnel. Rather than applying it to one side and testing for the lift force, it was decided to cover the complete surface and investigate the drag. Figure 7.14

shows the C_D versus Re results obtained for the sellotape covered ball in the high-speed wind tunnel. It can be clearly seen that the C_D is reducing as the Re increases settling at approximately 0.4 towards the end of the test. This is a clear sign that the flow over the surface of the sellotape covered ball is turbulent.

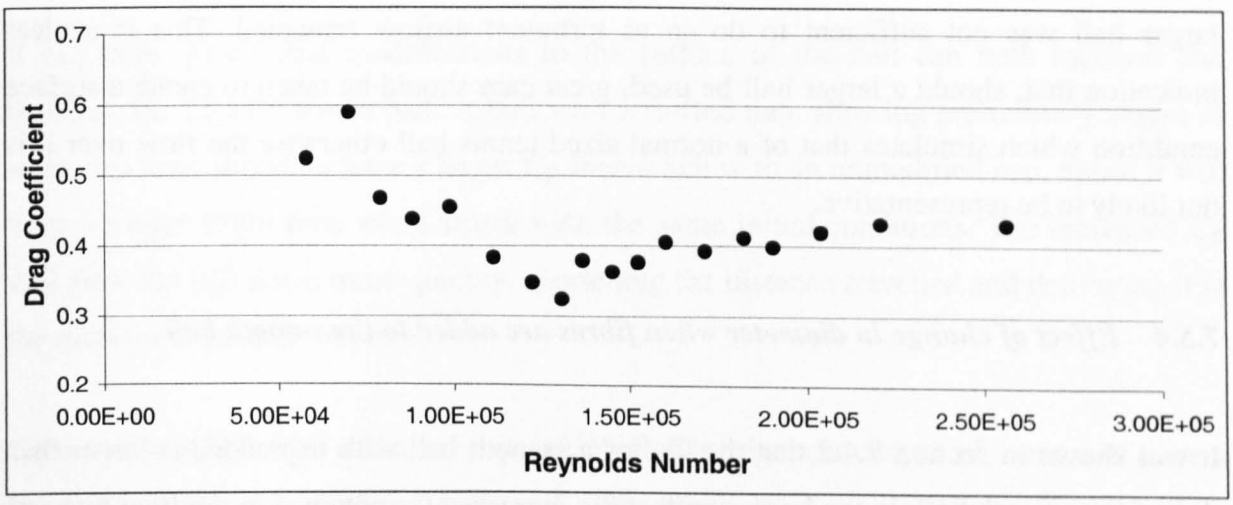

Figure 7.14 C_D versus Re results obtained in the high-speed wind tunnel for a tennis ball covered in sellotape.

Relating this back to the ball with one side covered with sellotape, the side that was thought to be smooth was in fact rough enough to cause transition. Based on discussions in the previous section however, transcritical separation occurs early on the tennis ball nap side, whereas 'conventional' delayed transcritical separation occurs over the sellotape covered side of the ball, thus resulting in an asymmetric wake. The net lift force is therefore directed towards the sellotape covered surface causing it to deflect in the air.

In the case where the flow over the sellotape covered side of the ball is laminar, then it is possible that the anticipated swing direction would have been obtained, with additional drag being induced due to skin friction through the nap and microscopic pressure drag on the fibres.

7.5.3 Confidence in the results obtained using the larger ball

It has been stated several times throughout this report that confident use of a larger ball is difficult to condone. The increased diameter of the ball is simple to create, however the

nap should also be scaled. Not only should the nap be scaled to make the fibres longer, but the stiffness should also be increased to simulate those on the smaller ball. In this chapter, it was found that although the fluff on the larger ball had been replenished, the flow around it was transitional. It should be noted that although the small amount of nap added to the smooth ball was enough to simulate the flow over a tennis ball, the replenished nap on the larger ball was not sufficient to do so as turbulent airflow remained. This is a clear indication that, should a larger ball be used, great care should be taken to create a surface condition which simulates that of a normal sized tennis ball otherwise the flow over it is not likely to be representative.

7.5.4 Effect of change in diameter when fibres are added to the smooth ball

It was shown in section 7.4.2 that the C_D for a smooth ball with nap added is larger than that of the smooth ball. It can be shown that the increased C_D obtained in the final two sets of results in that section may be due to an increased projected diameter. The fibres on a shaved ball have been estimated to be 1.28mm, which implies a 2.56mm increase in diameter. The core diameter of the smooth ball is 63.5mm, hence this represents a 4% increase in diameter. This increase in diameter will relate to an 8% drop in C_D, therefore the C_D of the shaved smooth ball will drop from approximately 0.55 to 0.506, a figure similar to that obtained for the smooth ball, and rough spheres from previous studies (Achenbach, 1974).

7.5.5 Effect of the turbulence factor

The turbulence factor in the high-speed wind tunnel is approximately 1.087, compared to 1.71 in the low-speed wind tunnel. The turbulence factor is calculated by comparing the Re of the point at which transition occurs in a given wind tunnel to that in still air. The higher the turbulence factor the more turbulent the flow, hence the more likely transition is to occur.

Transition was observed for the shaved nap condition on the normal sized ball in the low-speed wind tunnel, however it was not observed in the high-speed wind tunnel, and it is

therefore hypothesised that the increased turbulence within the low-speed wind tunnel promoted transition in the flow around the ball.

7.5.6 Implications to the game of tennis

It has been shown that modifications to the surface of the ball can both increase and decrease the C_D of a tennis ball. A ball with a fluffed nap, showing preliminary stages of wear, has been shown to have a larger C_D than a ball with an unmodified nap, hence it will have a longer flight time when struck with the same initial conditions. The increased C_D will slow the ball down more quickly, shortening the distance travelled and delivering it to the receiver at a lower velocity.

Conversely, a ball with a shaved nap, which shows advanced stages of wear will have a lower C_D than an unmodified ball, and given the correct circumstances it will reduce further due to a change in flow regime. The reduced C_D will slow the ball down less quickly, delivering it to the receiver moving at a higher velocity.

The interaction between the air and the surface of the ball maintains a constant C_D for all velocities tested providing there is predominant nap coverage.

7.6 Summary and conclusions

The C_D results of balls with several different ball coverings have been studied. It has been shown that a ball with a fluffed nap will have a higher C_D than one with an unmodified nap, which in turn will have a higher C_D than a ball with a shaved nap. It was concluded that the increase in C_D for a ball with unmodified and fluffed nap conditions was due to both increases in the relevant diameter and flow through the fibres.

The flow over the ball with a shaved nap has been shown to become turbulent in the low-speed wind tunnel.

The use of a larger ball confirmed that the flow over the unmodified nap must be turbulent and in the transcritical regime. The high C_D values observed are due to early separation,

which is induced by the very high roughness of the tennis ball nap and the interaction of the airflow through and over the fibres. It has been concluded that there may be three drag components acting on a non-spinning tennis ball: pressure drag, skin friction drag and drag due to flow around the fibres.

It was shown that, although the small amount of nap added to the smooth ball was enough to simulate the flow over a tennis ball, the replenished nap on the large ball was not sufficient, and turbulent airflow remained.

Tests on a smooth ball with nap attached to its surface suggested that separation occurred early on the front surface of the ball, and that subsequent addition of nap did not affect the flow any further.

8 FLOW VISUALISATION

Earlier chapters have described and discussed the quantitative methods utilised to calculate the aerodynamic properties of tennis balls. Although extremely important, the C_D of an object can be meaningless without the understanding of what causes the object to have a C_D and what the magnitude refers to. This chapter aims to develop the understanding of the aerodynamic properties of tennis balls with the use of flow visualisation.

There are normally three component forces acting on a tennis ball during normal flight, gravity, drag and lift. As gravity acts on all objects and is constant, it is not included in this part of the study. It is the aim of this part of the study to investigate the type of flow around a non-spinning ball and how it is affected by the changing condition of the nap. As with previous chapters, the discussions regarding lift with be dealt with separately from those relating to drag. Comparisons in flow can be viewed and discussions relating to the magnitude of C_D can be formed.

8.1 Apparatus

This test method requires a smoke flow wind tunnel, a method of smoke generation and a recording medium to enable further analysis. Figure 8.1 shows the apparatus used in-situ during a test.

8.1.1 Wind tunnel

The wind tunnel used is specifically designed for flow visualisation, and the airflow in the test section travels from bottom to top. The test section is approximately 250mm wide and 500mm high with a depth of approximately 175mm.

The flow lines are created using a paraffin smoke generator with a comb to distribute the smoke at regular intervals. Further details of the flow visualisation apparatus used can be found in chapter 3.

8.1.2 Wind speed

Wind speed is controlled using a handle connected to a shutter at the exit of the test section. The connection between the handle and the shutter is geared such that it takes 14 turns of the handle to fully open the shutter from being completely closed. Wind speed was calibrated against number of turns; with the maximum velocity attainable being $4ms^{-1}$, as shown in figure 8.1.

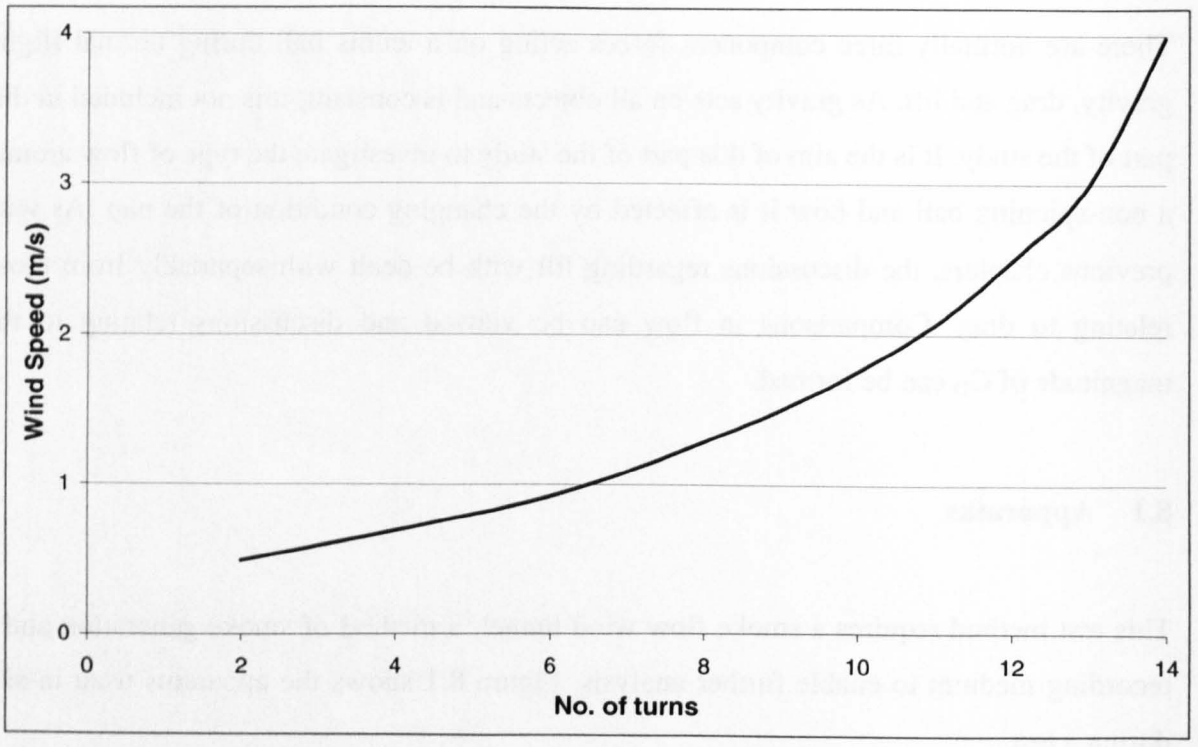

Figure 8.1 Calibration chart showing wind speed against number of turns for the flow visualisation wind tunnel.

8.1.3 Recording of images

Images of the flow lines around the ball were captured using two methods. The high-speed digital camera (KODAK Motioncorder) that was used in previous test methods was used initially as it was thought that snap shots of the flow would be required. The second method used a colour TV camera capturing real time pictures directly to the video recorder. Most tests were performed with both cameras during development, however all images shown in this chapter have been obtained using a high quality TV camera.

8.1.4 Lighting

The flow lines were illuminated using the standard lighting supplied at the sides of the wind tunnel. Two 60 Watt bulbs were filtered through a 10mm slit either side to create a plane of light on the same plane as the smoke flowing around the ball. As the light was localised, the front of the ball was in shadow, and a 500 Watt floodlight was also required for overall illumination.

8.1.5 Stings

The non-spinning sting consists of a 25mm diameter bar, turned down to 10mm for a length of 70mm. The overall length of the bar was such that the ball was located in the centre of the test section. The outside diameter of the sting was chosen such that it can be fixed through a collet on the rear face of the wind tunnel. The ball was punctured using the same procedure described in previous chapters. Attachment of the ball was by friction alone using the assumption that the maximum wind speed was not sufficient to displace it. The 10mm diameter section was long enough to enable the bar to be pushed up tight on the inside surface of the ball. As the sting was positioned at the rear of the ball, it was assumed that it did not affect the airflow over the sides of the ball.

The spinning sting is slightly more complex, consisting of a 10mm diameter ball shaft which is free to rotate inside a bored out brass rod. Figure 8.2 shows the ball mounted directly onto the 10mm steel bar fixed in place using an M4 cap head screw. Additional fixing is required to ensure that the ball is not dislodged by out of balance forces created at high spin rates. The outside of the bearing collar is to be located in the back of the wind tunnel, and the steel bar is free to rotate inside it. The bearing collar is constrained laterally using a circlip on the inside surface and a grooved collar on the outside of the wind tunnel. The grooved collar is prevented from rotating on the ball shaft using an M2 set screw located on a 'flat' on the shaft. Spin is generated using a motor and a belt system connecting the ball shaft to the motor shaft. The drive belt is tensioned around the groove collar and a similar component on the drive shaft of the motor.

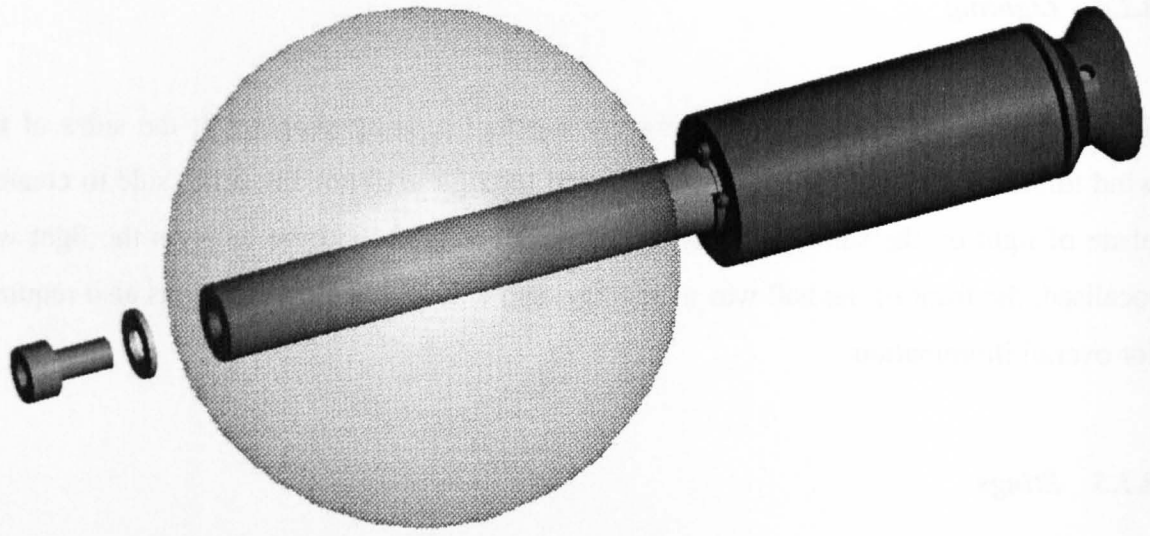

Figure 8.2 Sting used for both non-spinning and spinning flow visualisation tests.

The spin is controlled using a motor controller attached to the wind tunnel. The minimum spin rate attainable was approximately 300rpm, a limit imposed by the low torque rate available from the motor. Four spin rate setting were used, with the maximum spin rate being approximately 1000rpm.

8.2 Test method

All images shown in this chapter have been extracted from footage recorded using the TV camera, hence the following descriptions focus on this test method only. The test method for both a spinning and non-spinning ball are similar except for the inclusion of the spin setting, the following descriptions therefore apply to both unless otherwise stated.

8.2.1 Creating the smoke

The smoke flow lines are created using paraffin vapour. As it takes a while for the paraffin to reach the required temperature, this is always the first process undertaken at the start of a test session. The paraffin is heated in small amounts in a glass tube, wound with copper wire and sealed in conductive cement. The current supplied through the copper filament is initially high to create the vapour rapidly. When the paraffin vapours are observed in the tube, the supply current is reduced and testing is ready to commence.

The smoke is drawn through the wind tunnel and only become visible when the fan of the wind tunnel is activated. The comb can be manually moved sideways to correctly position the flow lines depending on the test requirements. The non-spinning ball tests require a single flow line impinging on the central axis of the ball, whereas the spinning ball tests have a flow line equally spaced either side of the central axis. Once the flow lines have been correctly positioned it is important that they are not moved until the test is complete, should they be moved comparisons cannot be drawn and the test will become void.

8.2.2 Positioning of the ball

It is important to position the ball such that the flow lines pass around the maximum diameter of the ball. As the flow lines are not steady when the wind tunnel door is opened, it was found that minor alterations were best made by manoeuvring the sting from the rear of the test section. The orientation of the ball was set such that the seams were on the rear face of the ball, however preliminary testing had showed that the seam had no effect on the flow around the surface of the ball. Once the ball was in place testing could commence and a video recording be captured.

8.2.3 Image capture

Real time images of the flow around a tennis ball were captured directly to Hi8 video tape using a TV camera. The wind speed was set to minimum (approximately $0.5ms^{-1}$) and the tape was set in motion. After approximately 5 seconds of recording the wind speed was increased. The tape remained running whilst the wind speed was altered and the completion of the new wind speed was signified with a hand signal in front of the camera. This process was repeated for up to nine wind speeds, with each being noted in a log book for future reference.

It was decided that increasing the wind speed over a ball whilst maintaining a fixed spin rate would be the most convenient way to view the flow, hence the recording process was identical over the spinning ball.

8.2.4 Digitisation

These images are useful seen in video format, however a single image of the typical flow is required for report purposes. It was decided during discussion with experts that it is more useful to capture images using a slow shutter speed (in the order of 0.5s) rather than an instantaneous snap shot. The equipment available was not capable of such a process, hence several images were extracted from the video and superimposed to create a single image.

The digitisation of the video was achieved using the methods described in section 3.3. The real time images were digitised at 20 frames per second, hence 10 overlaid images cover approximately 0.5 second.

8.3 Results

The results have been separated into three distinctive sections to look at the effects of both changing surface properties and spin.

Initial testing investigated flow around non-spinning tennis balls, modifying the nap to reflect the changes that may be observed during play. The C_D of balls with different surfaces was be discussed in chapter 7, hence this investigation of the flow around and through the different surfaces will help understand how differences in flow affect the C_D.

Positioning of the ball for these tests was not a simple matter as the required flow line plane was small, hence it was decided that the flow around a cylinder with nap on it may be easier to set up. It is well known that the flow over a cylinder is different to that over a sphere, moreover the three dimensional relieving effect of the sphere leads to a lower C_D than that of a cylinder. A sphere's three dimensional properties also mean that the vortex shedding is different to that from a cylinder, however it should be noted that this part of the study concentrates on the flow over the maximum circumference which should be very similar to that of a cylinder.

The final section deals with the flow around a spinning tennis ball. The additional aerodynamic forces encountered due to spin are significantly greater in magnitude than

those created by modification of the nap. The number of test sets to be analysed can be reduced by ⅔ by simply concentrating on the normal ball with unmodified nap only.

The flow visualisation images shown in this chapter have modified to show black flow lines on a white background. This has been achieved during the image processing stage and was undertaken to improve the quality of the images on paper.

8.3.1 Effect of changing ball parameters

As the flow is symmetrical over the top and bottom surfaces, it was decided that it would be more useful to concentrate on one surface alone, thus increasing the quality and quantity of information that can be taken from the image. The distribution of flow lines has been set such that a single filament impinges on the front most surface of the ball slightly above the stagnation point.

This set of testing uses a standard tennis ball and modifies the nap to simulate the changing conditions that may be observed during play. The three ball conditions used are as follows:

- normal pressurised ball
- normal pressurised ball with its nap combed to make it fluff up
- normal pressurised ball with its fluffed nap shaved off

Although there are as many as nine wind speeds of each ball, only three wind speeds have been chosen for discussion in this section. Figure 8.3 shows the flow around the three ball types at a wind speed of approximately $0.5ms^{-1}$ and zero spin.

The first thing to note in figure 8.3 is the fact that the flow lines appear to flow through the nap of the normal and fluffed balls inferring that viscous drag is a significant factor in the overall drag on the ball. At this low wind speed it is difficult to observe any significant difference between the flow around the normal and fluffed ball, and in both cases the separation point appears to be on the front face and the flow appears to be diverging as it leaves, creating a large wake. Chaotic mixing in the wake can be clearly observed in all three images.

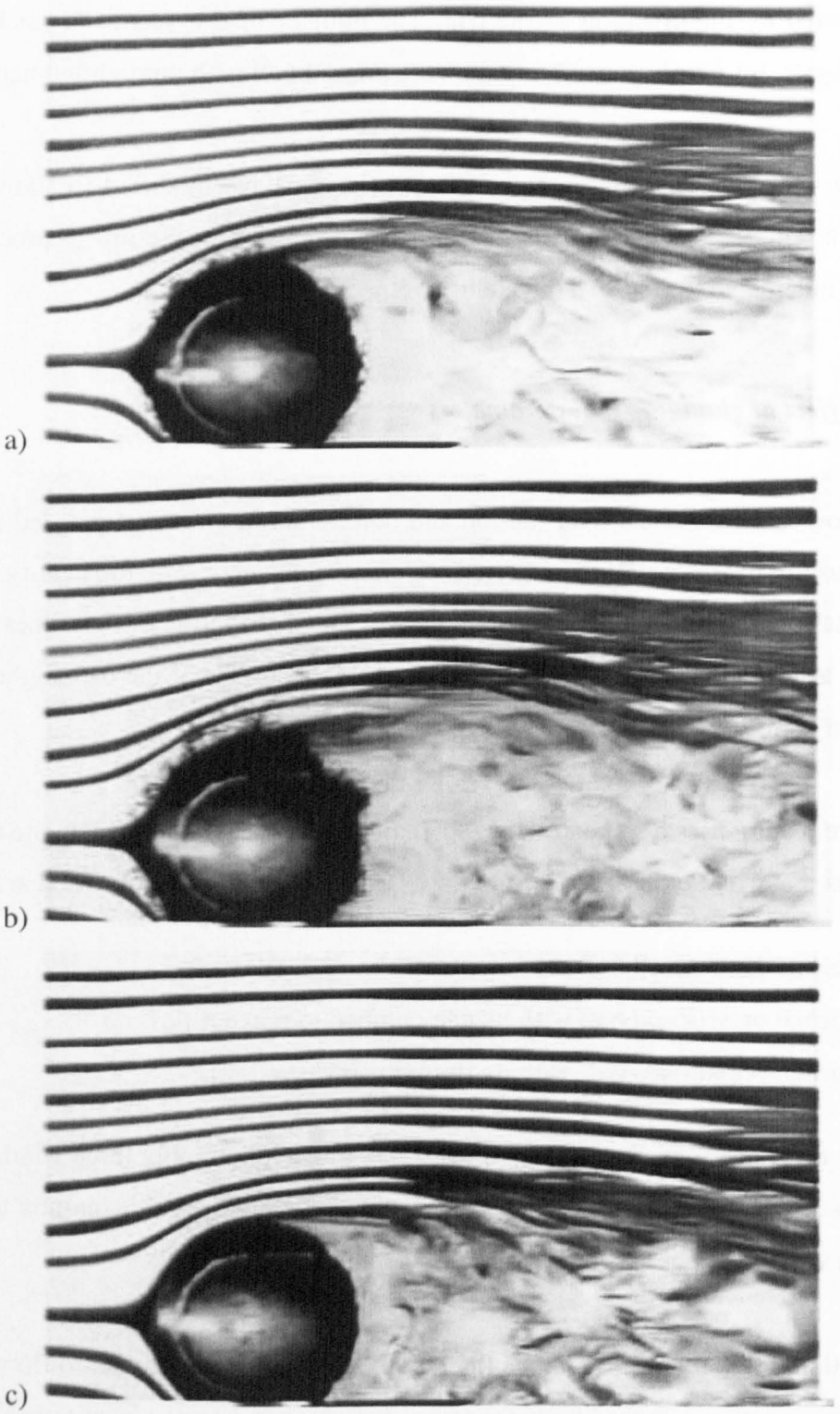

Figure 8.3 Flow around a) normal nap, b) fluffed nap and c) shaved nap non-spinning tennis balls at a wind speed of approximately $0.5ms^{-1}$ ($Re = 3.5x10^3$).

The flow around the shaved ball is completely different to that of the other two. The approximate point of separation can be observed just upstream of the point of maximum diameter, maybe a little later than that on the other two balls. The air is flowing over the

surface and separation can be clearly defined. Reference to the results obtained in chapter 7 shows that transition occurs at a Re of around 70,000 for the shaved ball, which is equivalent to wind speed of a little over $16ms^{-1}$, hence it is likely that the flow in figure 8.3c is laminar.

The random dark areas behind the balls are signs of unstable flow. The air separating from the surface of the ball is travelling fast compared to that behind the ball where it is almost stationary, thus an imbalance is created. As the flow departs from the ball it attempts to fill the void behind the ball and hence begins to converge further down stream.

Previous test methods in this study have shown that the drag on an unmodified and fluffed nap does not change significantly with increased wind speed. The shaved nap however, is seen to have a small transition at a low velocity, viewing the flow at a higher wind speed may show this. Figure 8.4 shows the flow around the three ball types at a wind speed of approximately $2ms^{-1}$ and zero spin.

It is immediately apparent that the flow lines are less dense than those in figure 8.3. This occurs as the wind speed increases because the volume of paraffin vapour available is fixed. The differences in flow around the three ball types are less apparent than they were at the lower wind speed. There is less sign of turbulent mixing in the wake, but this is mainly due to the lack of smoke available for illumination. Far more investigation of the separation area is required to differentiate between the three flows.

It is well known that the drag force on a bluff object is due to pressure differences between the front and rear faces, and relates to the boundary layer separation points, and therefore size of the wake. This can be measured accurately using image analysis, however it is possible to compare these images visually to draw conclusions on the comparative magnitude of C_D for each ball. It can be seen that the wake behind the shaved ball is smaller than that for the normal and fluffed balls, suggesting that the C_D due to pressure drag will be smaller. If these three balls were assessed using the ITF method of measuring diameter, they would likely be the same, however, this is a clear sign that the normal and fluffed balls have a larger effective diameter.

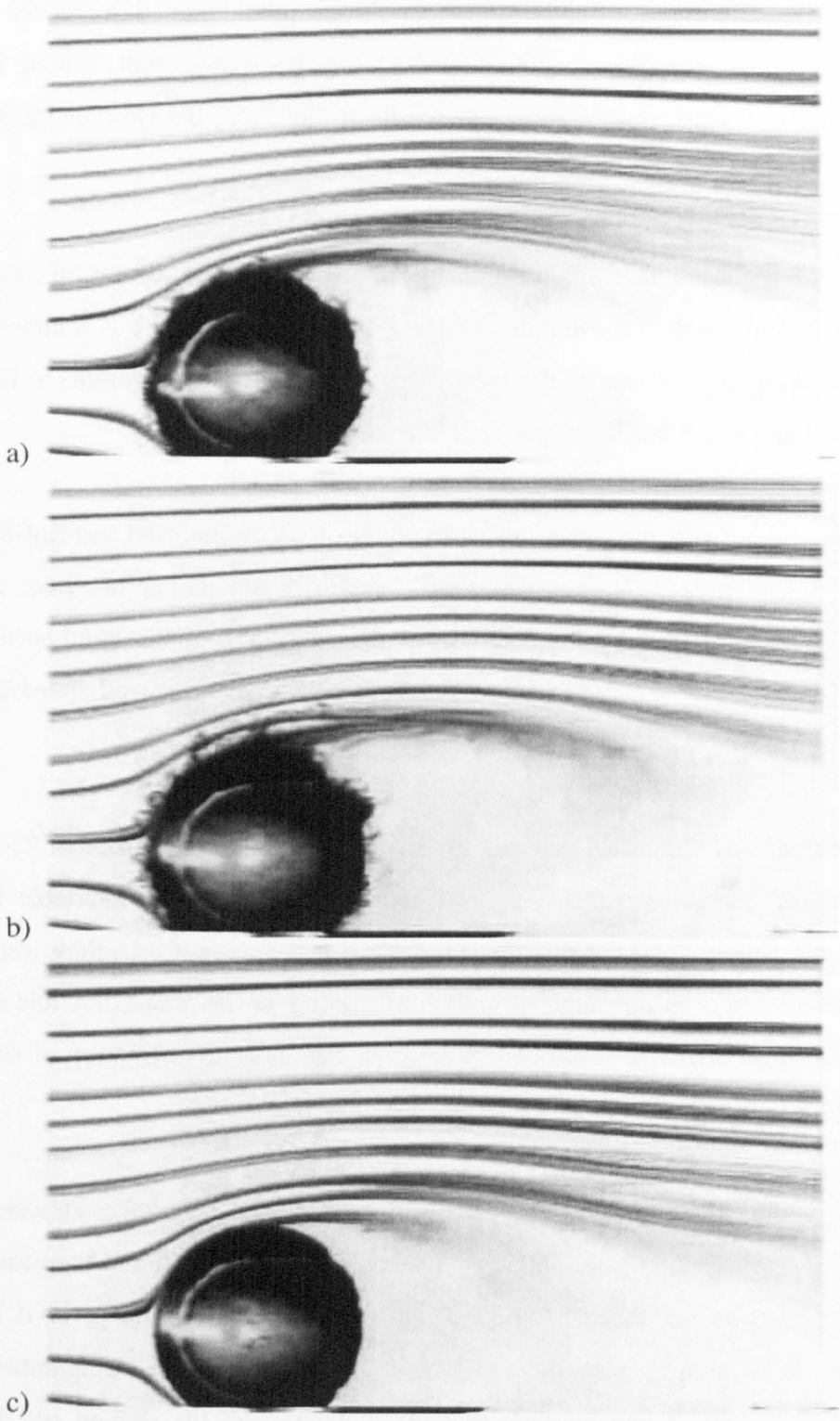

Figure 8.4 Flow around a) normal nap, b) fluffed nap and c) shaved nap non-spinning tennis balls at a wind speed of approximately $2ms^{-1}$ ($Re=2.8x10^4$).

The flow lines are again travelling through the fibres in the nap of the normal and fluffed balls, suggesting that there is an additional drag force exerted due to flow through the fibres. In addition, the second flow line away from the surface of the fluffed ball is significantly affected by the flow around the ball, indeed it appears that the two flow lines closest to the surface appear to cross. It is possible that they have moved onto separate planes caused by the three dimensional properties of the ball.

The maximum wind speed attainable by the wind tunnel was approximately $4ms^{-1}$. Figure 8.5 shows the flow around the three ball types at a wind speed of approximately $4ms^{-1}$ and zero spin.

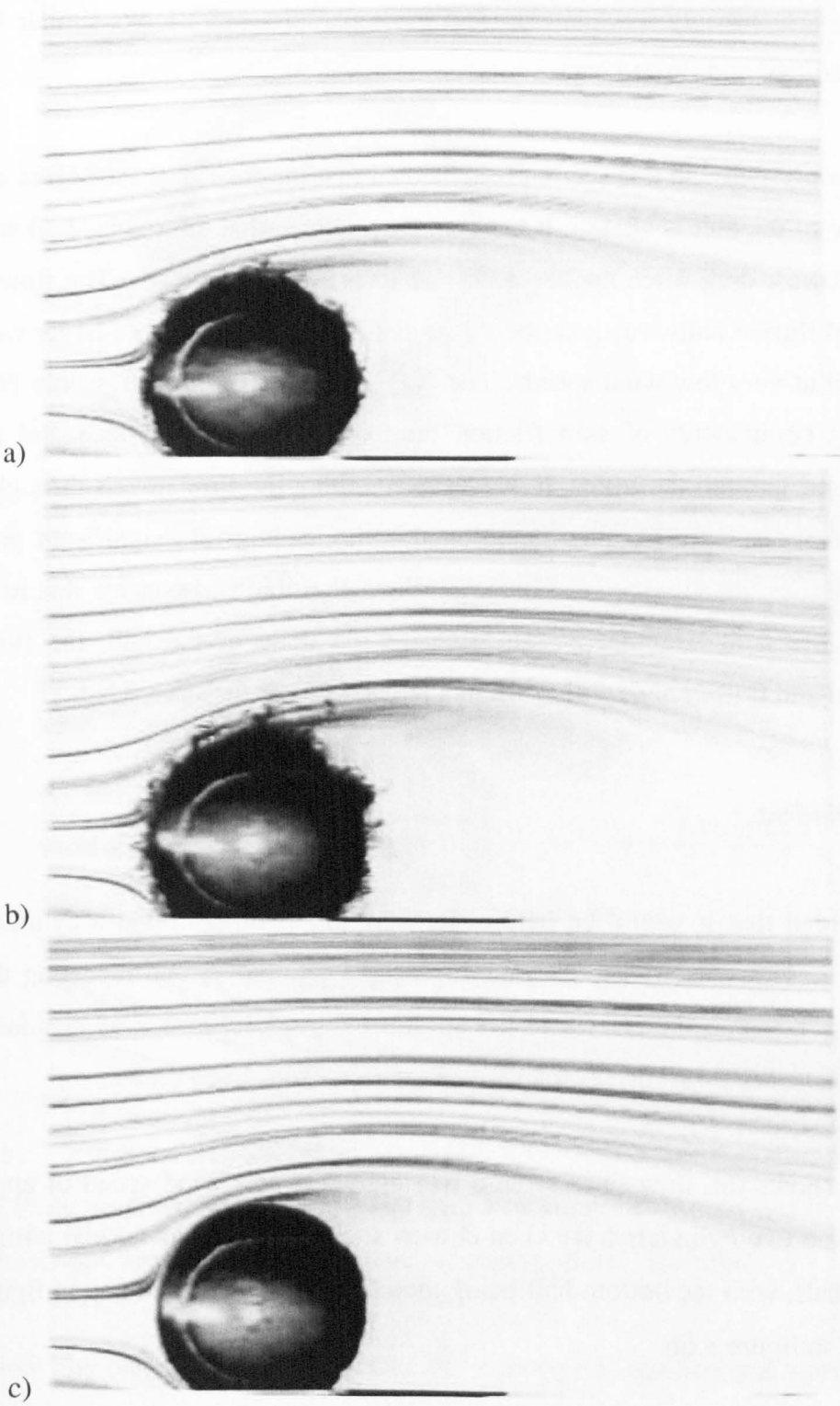

Figure 8.5 Flow around a) normal nap, b) fluffed nap and c) shaved nap non-spinning tennis balls at a wind speed of approximately $4ms^{-1}$ ($Re = 3.5x10^4$).

It can be seen that the flow is less able to deflect around the ball, observed in figure 8.5b where the first two flow lines are now being forced through the nap of the fluffed ball. It is increasingly difficult to differentiate between the flow around the three ball conditions, and the shape of the wake is not visually significantly different. At $4ms^{-1}$, the flow around the shaved ball is probably still laminar, and the separation point looks similar for the balls with unmodified and fluffed naps.

The results presented in this section have shown that the flow over the ball is altered when the surface of the ball is altered. It has also been shown that the shaved ball will probably have the lowest drag force applied to it due to pressure imbalance. The flow around the normal and fluffed balls was less obvious to define, whilst both had a larger wake than the shaved ball at very low wind speeds. The drag on the shaved ball is mainly pressure drag with small components of skin friction drag over the rough surface and microscopic pressure drag through the fibres. It was very clear that the flow travels through the nap of the unmodified and fluffed nap conditioned balls, leading to a significant pressure drag component from the fibres in the airflow. When the drag components due to the surface and fibres are added to the pressure drag of the body of the ball, the flow over the unmodified and fluffed naps will result in a larger C_D than the shaved ball.

8.3.2 Cylinders

It was decided that it would be helpful to view the airflow around a cylinder with nap adhered to it. However, rather than modifying the total cover and repeating the previous test, and the fact that the effects of lift are not being assessed, it was decided to modify opposite sides of the cylinder to enable direct comparisons to be drawn.

Figure 8.6 shows the flow lines around two cylinders at a wind speed of approximately $0.75ms^{-1}$. The two cylinders have been chosen such that each has normal unmodified nap on the top half, with the bottom half being modified to show fluffed nap in figure 8.6a and shaved nap in figure 8.6b.

The distribution of flow lines has been set such that a single filament impinges on the front stagnation point. It can be seen that this flow line follows the route of least resistance in

both cases, rising over the top when the fluffed nap is on the bottom, and underneath when the shaved nap is on the bottom.

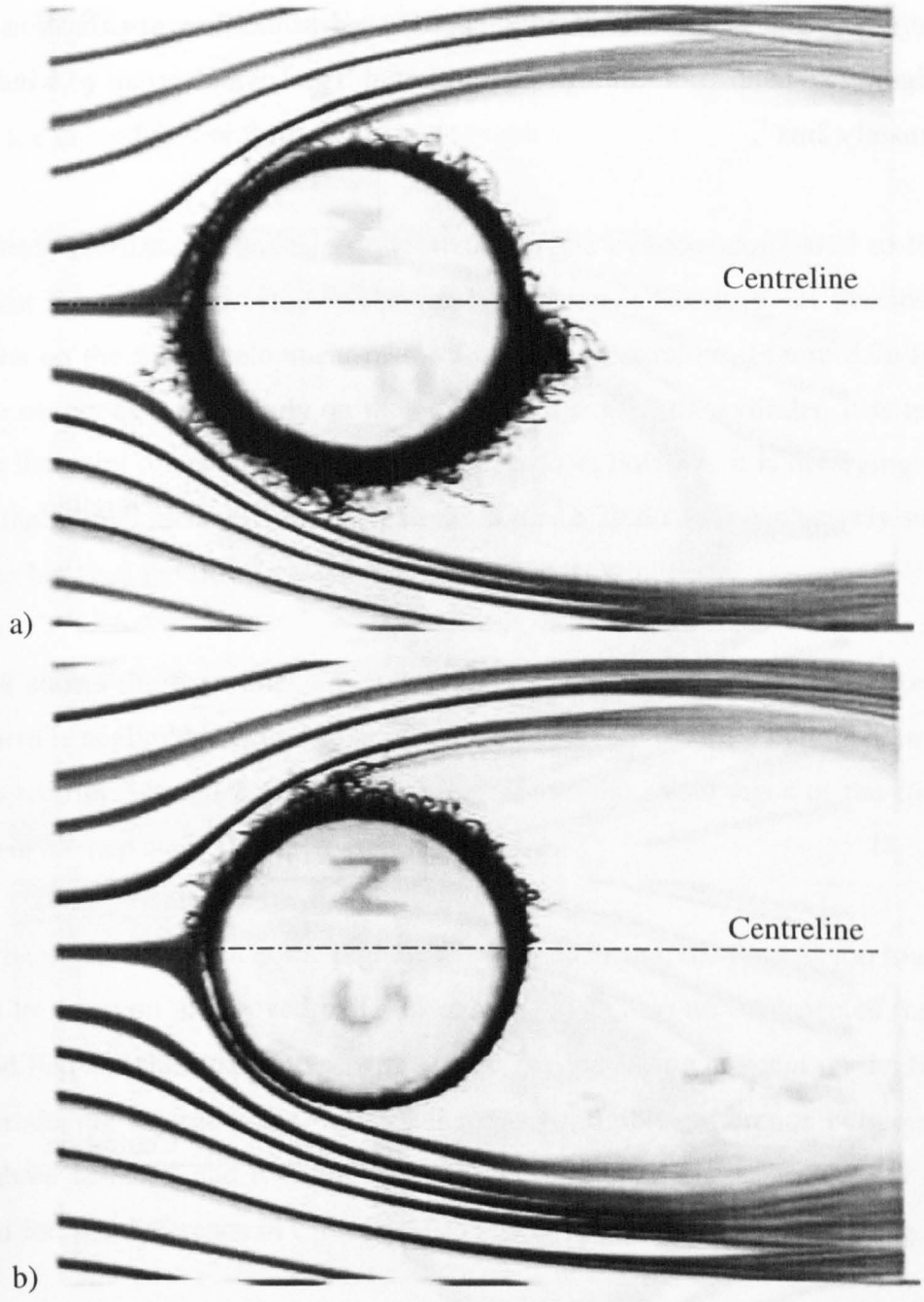

Figure 8.6 Flow observed around a cylinder with a) normal and fluffed and b) normal and shaved nap on opposite sides at a wind speed of approximately $0.75ms^{-1}$.

The first flow line that can be used to assess the flow type is the first one above and below centre. Separation occurs early and the flow lines are diverging on both sides of the cylinder in figure 8.6a. The separation on the shaved surface occurs later than that of the

unmodified nap in the same image and shows signs of stagnation with some turbulent smoke.

Following the same increments of wind speeds used in the flow visualisation around the balls, figure 8.7 shows the flow lines around two cylinders at a wind speed of approximately $2ms^{-1}$.

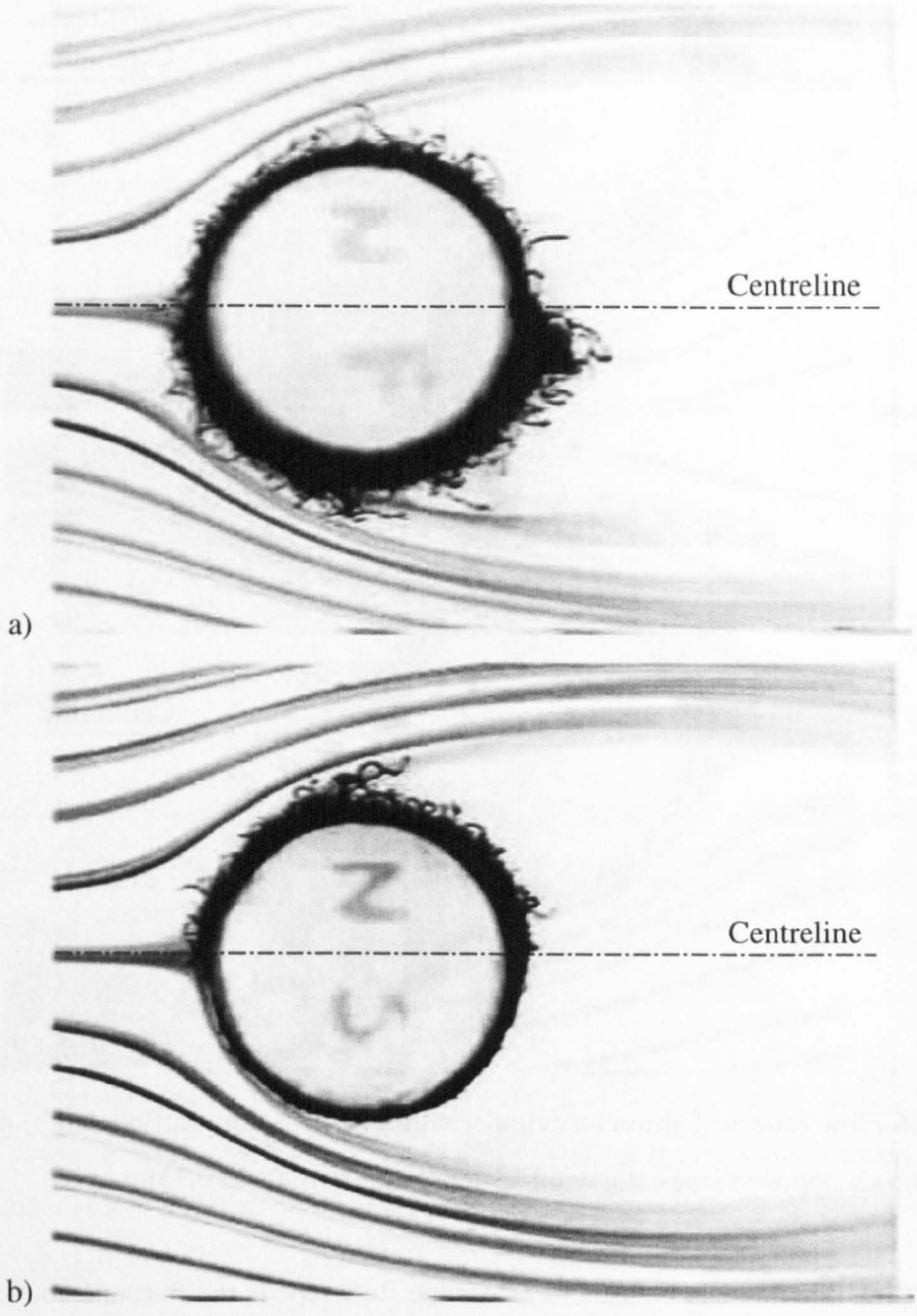

Figure 8.7 Flow observed around a cylinder with a) normal and fluffed and b) normal and shaved nap on opposite sides at a wind speed of approximately $2ms^{-1}$.

It is immediately apparent that the flow line that was passing over the side of least resistance is now flowing over both sides. It is clear that the smoke is travelling through the fibres in the nap in figure 8.7a suggesting the presence of additional drag through the fibres. The flow line over the shaved surface in figure 8.7b can be clearly seen, hence it is not obstructed by nap, and the drag due to flow through the fibrous nap is not as dominant as that on the unmodified or fluffed surface.

There is less information available downstream of the cylinder compared to the images obtained for the cylinder previously shown. It is apparent that it is not possible to draw conclusions on the full development of the flow after separation. Figure 8.7a shows that separation occurs extremely early on the unmodified side of the cylinder, it is less easy to determine the point of separation on the fluffed surface, however it is diverging more than that over the normal surface. The flow lines in figure 8.7b do not conclusively suggest any differences between the flow over the two sides of that cylinder.

Figure 8.8 shows the flow lines around two cylinders at a wind speed of approximately $4ms^{-1}$. There is negligible difference between the flow lines over the cylinders in figure 8.8 and those seen in figure 8.7. Close inspection reveals the initial signs of the flattening of the fibres in the nap due to the increased wind speed.

It should be noted that, even at the highest wind speed tested, the Re was too low to expect transition to occur on the shaved ball. However there is also no evidence of transition on the unmodified and fluffed surfaces, with separation continuing to occur on the front facing surface producing a large wake. Indeed, there is negligible difference between the flow over all three surfaces, and it could be suggested that after effective diameter effects are accounted for, the difference in C_D would be caused by the flow through the nap.

In conclusion, the use of flow lines over the curved surface of cylinders has enabled a clear comparison between flow over/through different nap conditions. The images shown further indicate that the flow is not significantly different for the three surface conditions investigated, with separation occurring on the front facing surface, and hence the additional C_D obtained for unmodified and fluffed balls is due to flow through the fibres.

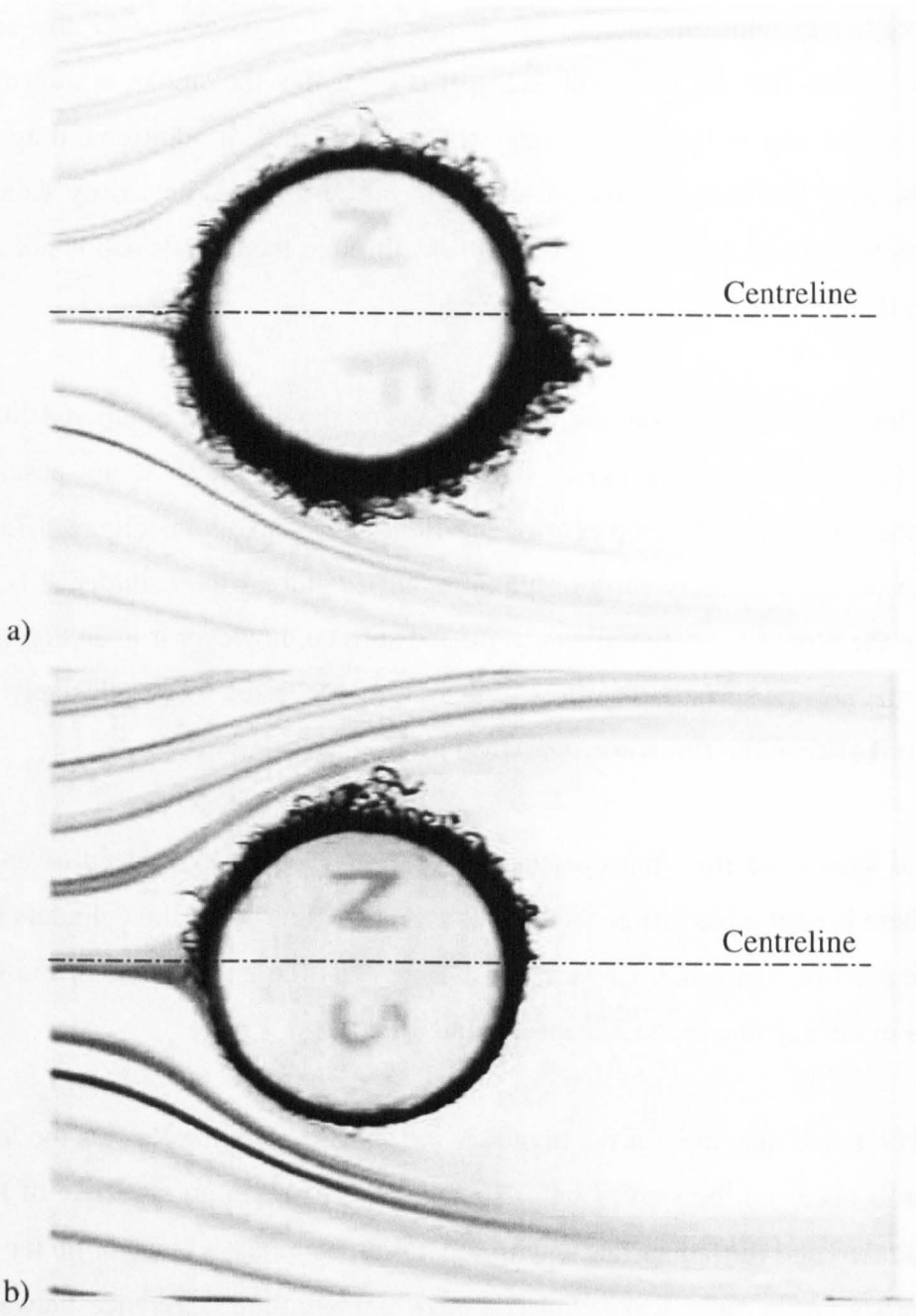

Figure 8.8 Flow observed around a cylinder with a) normal and fluffed and b) normal and shaved nap on opposite sides at a wind speed of approximately 4ms^{-1}.

8.3.3 Effect of spin

The majority of tennis strokes impart spin on the ball, this next section shows the change in aerodynamic properties observed with changing speed and spin. The normal unmodified ball has been used in all results shown in this section. The wind speeds are the same as those used in sections 8.3.1 and 8.3.2, and the spin rates start at approximately 300rpm

with a maximum of approximately 1000rpm. The ball is spinning in the anti clockwise direction in all images.

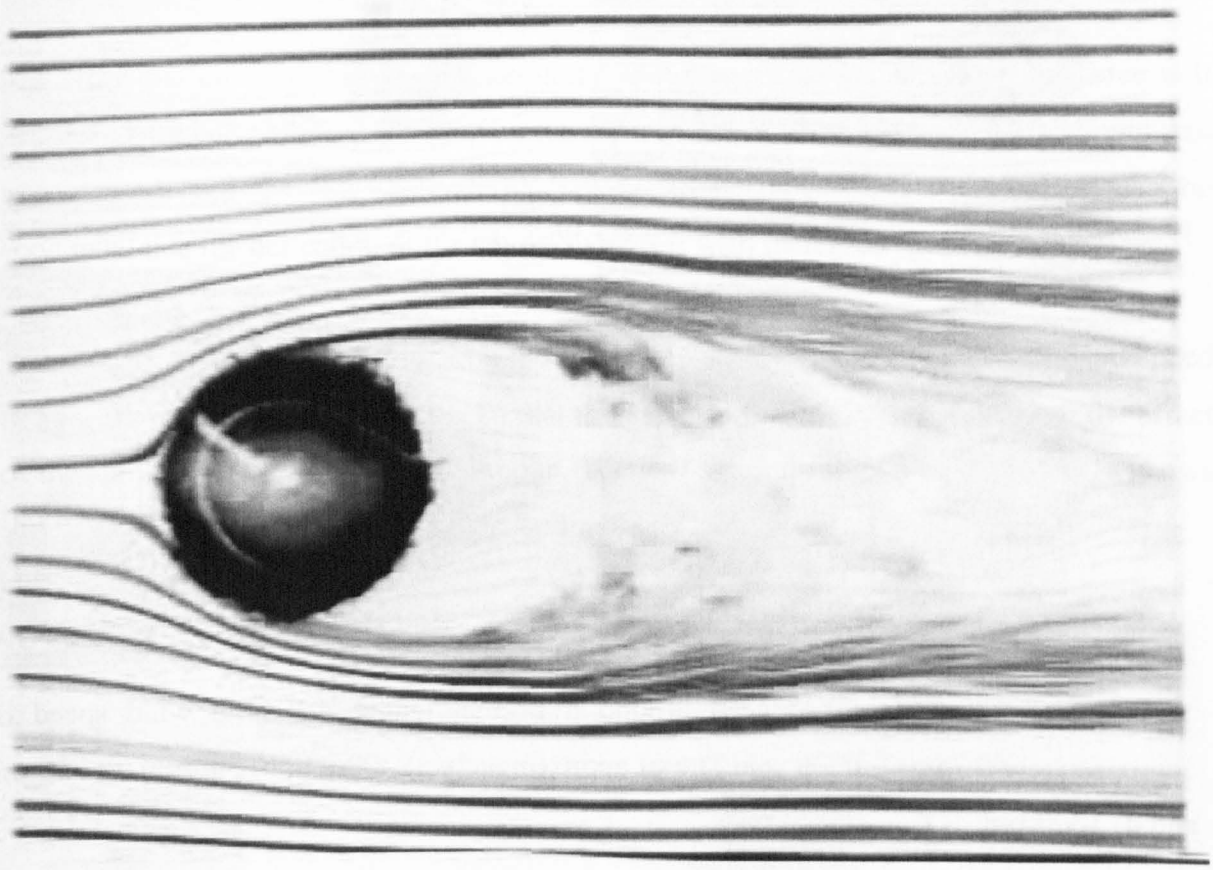

Figure 8.9 Flow lines around a normal unmodified non-spinning ball at a wind speed of approximately $0.75ms^{-1}$.

Figure 8.9 shows the flow lines around a normal unmodified non-spinning ball at a wind speed of approximately $0.75ms^{-1}$. As can be seen, the flow lines have been positioned at equal increments either side of the front stagnation point. Separation occurs on the front face at a similar point at the top and bottom of the ball, and the flow leaves the ball creating a wake directly behind the ball equally spaced around the horizontal axis.

Figure 8.10 shows how the flow around the ball changes with spin for a fixed wind speed of approximately $0.75ms^{-1}$. It can be seen that the flow is immediately deflected upwards upon separation from the ball implying a change in the separation points. The point of separation moves forward on the top surface that is rotating against the airflow, and moves backward on the surface rotating with the airflow. Some of the flow lines that were travelling over the top of the ball have been drawn around the bottom surface.

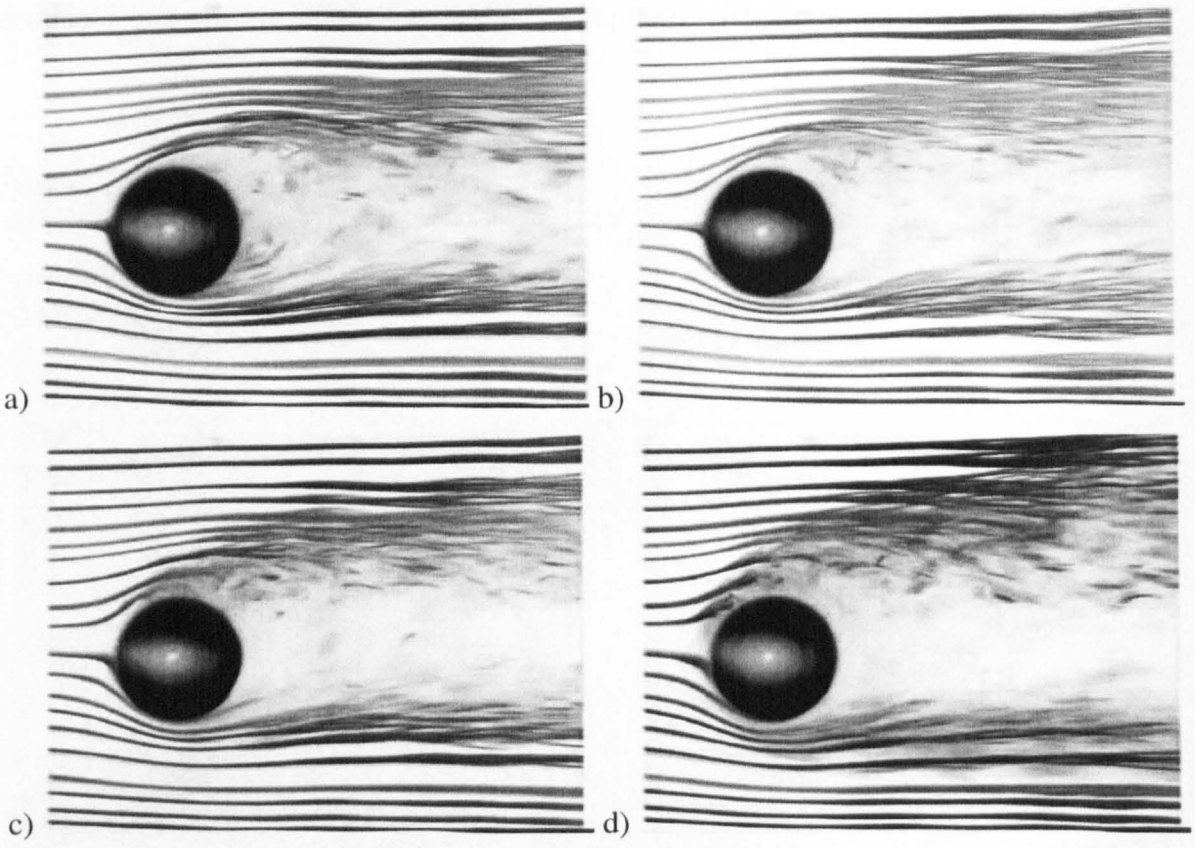

Figure 8.10 Flow lines produced around a normal tennis ball at a wind speed of approximately 0.75ms^{-1} and a spin rate of approximately a) 300rpm, b) 550rpm, c) 750rpm and d) 1000rpm.

There is more than one way to explain the aerodynamic effect (lift) caused by rotation, however asymmetry is always involved. In viscous flow the boundary layer is forced to spin with the ball due to viscous friction, which produces circulation around the ball. At the speeds and spin rates encountered by sports balls, the extra momentum applied to the boundary layer on the retreating side of the ball allows it to negotiate a higher pressure rise before separating and the separation point moves downstream. On the advancing side the reverse occurs and the separation point moves upstream, hence there is asymmetric separation and the wake is deflected (Mehta & Pallis 2001).

Positive (upward) lift is required when an aeroplane is taking off, and is created by lowering the rear of the airfoil. The underside of the airfoil forces the air flowing over it to deflect downwards, hence by Newton's 3rd Law, the air applies an equal and opposite force to the aeroplane, and the resulting wake behind the wing is deflected downwards. Using the same relationship for spinning balls, a downward deflected wake suggests positive lift

force, and an upward deflected wake, as shown in figure 8.10, suggests a negative life force. The lift force derived from rotation is combined with gravitational effects to define the overall direction that the ball will be deflected.

It is clear that circulation will increase as the spin rate increases, hence the lift force will increase. It can be seen that the flow on the top of the ball is affected more as the spin rate is increased, and the flow behind the ball becomes increasingly turbulent. It can be concluded that the deflection of the smoke increases with increased spin rate.

Figure 8.11 shows how the flow around the ball changes with spin for a fixed wind speed of approximately $2ms^{-1}$. It can be seen that the increased wind speed has reduced the effect of the spin on the deflection of the smoke. The low spin rate shown in figure 8.11a shows little evidence of any lift applied to the ball

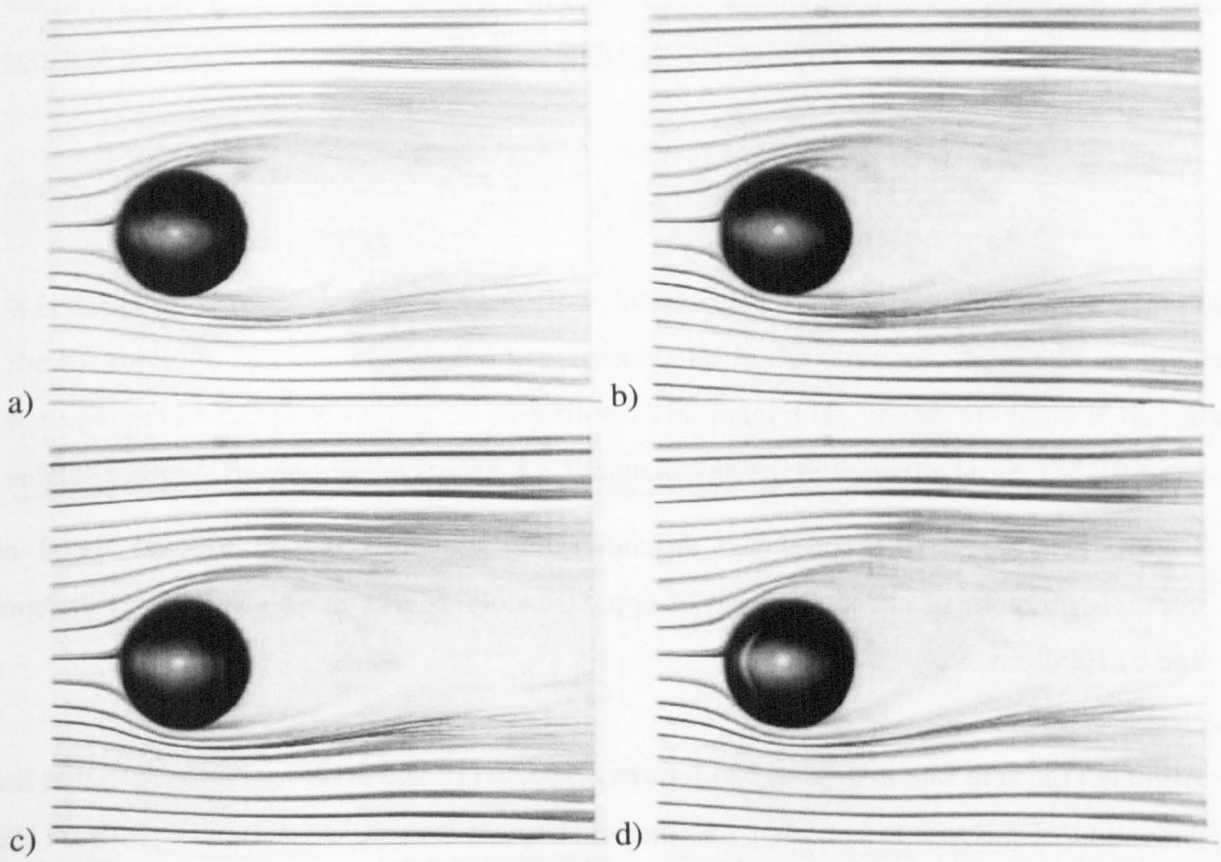

Figure 8.11 Flow lines produced around a normal tennis ball at a wind speed of approximately $2ms^{-1}$ and a spin rate of approximately a) 300rpm, b) 550rpm, c) 750rpm and d) 1000rpm.

The lift coefficient reduces as the spin parameter (ω/v) gets smaller, hence additional increases in wind speed will reduce the spin parameter further. This effect is seen in flow visualisation as a reduced asymmetry in the wake observed at higher wind speeds. Figure 8.12 shows how the flow around the ball changes with spin for a fixed wind speed of approximately $4ms^{-1}$. Whilst there is definitely evidence of some perturbed flow in the streamlines above the ball, even at the highest spin rate in figure 8.12(d) it is becoming increasingly difficult to define the evidence of asymmetric flow.

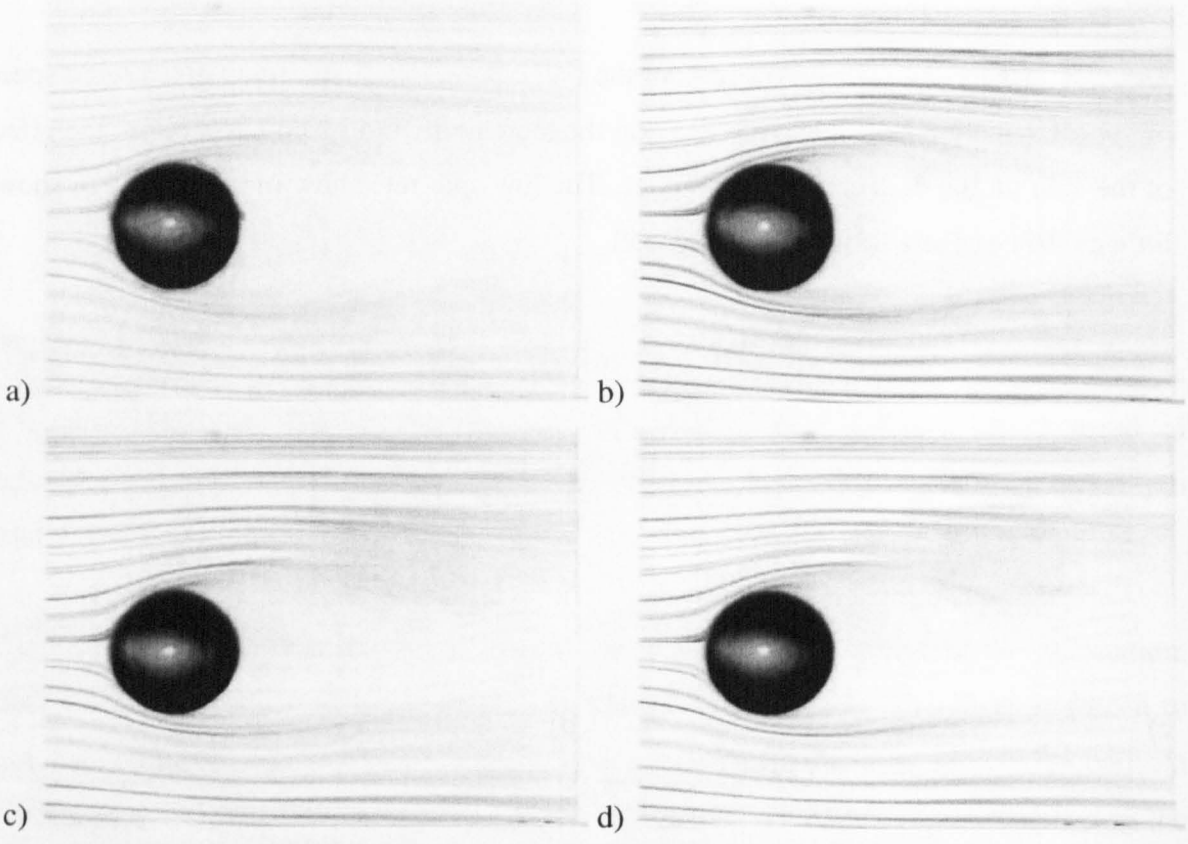

Figure 8.12 Flow lines produced around a normal tennis ball at a wind speed of approximately $4ms^{-1}$ and a spin rate of approximately a) 300rpm, b) 550rpm, c) 750rpm and d) 1000rpm.

Although the spin rate is the same in figures 8.10d, 8.11d and 8.12d, it can be seen that the deflection of the smoke is reduced as the wind speed increases. With guidance from the results obtained in chapter 6, the lift force on the ball in figure 8.12d is less than that on the ball in figure 8.11d, which in turn is less than that on the ball in figure 8.10d. The magnitude of the lift force has been shown to be a function of both spin rate and wind speed, and this section has given visual evidence of the aerodynamic effects of spin.

8.4 Discussion and conclusions

8.4.1 Components of drag

There are two components of drag: pressure drag and skin friction drag. For a bluff body, the overall drag is primarily pressure drag caused by the pressure imbalance between the front and back faces, which can be related to the points of boundary layer separation. Surface drag will always be a proportion of the total drag, and is caused by the viscous interaction of the air over the rough surface, and in general, the rougher the surface the greater the surface drag.

It was clear in all images throughout this chapter that the airflow travels through the nap of the more fibrous surfaces. In these cases, not only is there friction over the surface, there is additional interactions between the air and the fibres. It is therefore concluded that a tennis ball has three components of drag: pressure drag, skin friction drag, and 'nap' drag.

8.4.2 Magnitude of lift

It is tempting to relate the deflection of flow downstream to the magnitude and direction of the lift force. In fact, the lift force acts perpendicular to the direction of motion, or in this case perpendicular to the direction of airflow. The magnitude of the lift force is directly related to the deflection of the smoke, i.e. the greater the deflection the larger the lift force.

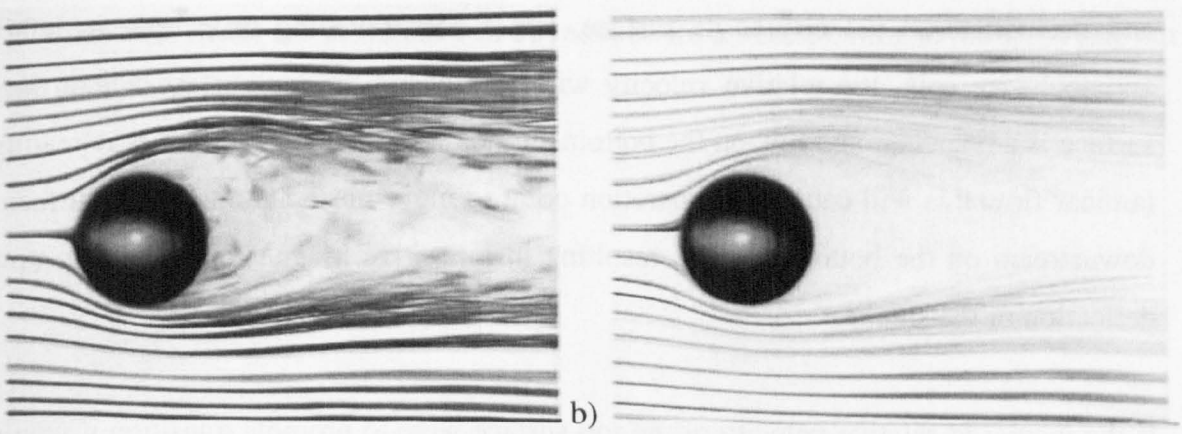

Figure 8.13 Flow lines produced around a normal tennis ball at a) a wind speed of approximately 0.75ms^{-1} and a spin rate of approximately 300rpm and b) a wind speed of approximately 2.5ms^{-1} and a spin rate of approximately 1000rpm.

In chapter 6 it was shown that although a different spin and wind speed may be applied to a ball, providing the ratio of spin to wind speed was the same, the lift and drag force would be the same. Figure 8.13 shows the flow lines around two balls spinning at different rates with wind speed settings such that the spin coefficient is the same for both.

As in previous flow visualisation images, the flow lines are less dense in figure 8.13b due to the increased wind speed. It can be seen that a single flow line is forced beneath the ball and the angle of departure is similar in both images.

8.4.3 Transitional flow

The non-spinning case

When the flow over a sphere becomes turbulent, the separation points move farther around the ball onto the rearward face. It was noted that the wake was large for all surface conditions at all speeds. In this study, it was found that the airflow around the shaved ball condition turns turbulent at a Reynolds number approximately $7x10^4$, as shown in chapter 7. Unfortunately, the maximum Re attainable from the flow visualisation wind tunnel is approximately $1.75x10^4$, hence transition would not be expected.

The spinning case

A spinning ball has two components of velocity: the linear velocity of the centre of the ball and the equatorial velocity at its surface. For a ball travelling from right to left with anticlockwise spin, the relative velocity will be high on the top surface where the ball surface is advancing, and low on the bottom surface where the ball surface is retreating. In laminar flow this will cause the separation point to move upstream on the top surface and downstream on the bottom surface, resulting in a positive Magnus effect and an upward deflection of the smoke.

If the increased relative velocity of the top surface were to promote transition it would be observed by the deflection of smoke switching to a negative Magnus effect with downward smoke deflection. This occurs for a short period whilst the top of the ball is transitional and

the bottom of the ball remains laminar. Once the flow over the bottom of the sphere also becomes turbulent, the deflection reverts to its original upward deflection with positive Magnus effect.

It should be noted that the spinning tests were only performed on the unmodified ball, and there was no sign of a negative Magnus effect over the speed and spin rates tested, the flow is therefore either always fully laminar or fully turbulent.

8.4.4 Implications to the game of tennis

The drag and lift effects on the tennis ball can be dealt with separately. The tennis ball will have a higher rate of retardation, the larger the C_D of the ball. The C_D is directly related to the size of the wake behind the ball, with small additional components due to the flow over and through the nap. It was observed that not only is the size of the wake increased with a fluffed nap, but the airflow is also forced to travel through the fibres of the nap, inducing a higher C_D. A ball with a fluffed nap therefore will slow down more quickly in the air, travelling less far and arriving at the receiver at a lower velocity.

The spinning ball causes asymmetry in the wake, creating a force perpendicular to the direction of motion. The magnitude of the force is related to both speed and spin rate, with a fast spinning slow moving shot having a high side force. The side force causes the ball to deviate from its normal trajectory and the higher the force the greater the deviation. It was observed that the effect of spin on the magnitude of the side force reduced as the wind speed increased, hence the deviation will be reduced for a ball spinning at the same rate but struck with a higher velocity.

THIS PAGE INTENTIONALLY LEFT BLANK

9 PRESSURE DISTRIBUTION AROUND A TENNIS BALL

Previous chapters have discussed experimental methods to determine the aerodynamic forces applied to the ball. This chapter and subsequent chapters will discuss methods used to investigate the flow around the ball, which can then be used to understand the factors that influence the aerodynamic properties.

9.1 Introduction and objectives

The pressure distribution around the surface of a tennis ball can be used as both a visualisation and quantitative tool. Much of the discussion related to the aerodynamic properties of tennis balls refers to the type of flow around the ball, and it is possible to use the pressure distribution around the tennis ball, together with typical data, to discuss whether the flow has become turbulent, or whether it remains laminar throughout.

The effect of changing the properties of the nap was discussed in chapter 7, and investigation of the C_P distribution around the ball can be used to further show why these differences occur.

Several methods have been used thus far to calculate C_D, and manipulation of the C_P distribution will yield an approximate value for C_D.

9.2 Theory

The pressure coefficient, C_P, is derived to compare the pressure differences observed locally with those measured in the flowing air of the wind tunnel (Schlichting, 2000), and is given by:

$$C_p = \frac{p - p_\infty}{q_\infty} \tag{9.1}$$

where: p is the local pressure near the surface of the ball

p_∞ is the free stream pressure

q_∞ is the dynamic pressure

The dynamic pressure was used in previous chapters to calculate the velocity in the working section of a wind tunnel, and is defined by:

$$\textit{Dynamic Pressure} = \textit{Stagnation Pressure} - \textit{Static Pressure}$$

$$\textit{i.e.} \qquad q_\infty = p_0 - p_1 \tag{9.2}$$

C_P is a dimensionless coefficient derived in the same way as C_D and C_L shown in previous chapters. It is commonly used throughout aerodynamic studies, and in many cases a pressure reading will be given in terms of C_P rather than the pressure itself. The local pressure, p, is measured at the surface of a tennis ball, and p_∞ is the free stream pressure. The free stream pressure is identical to the static pressure used in the dynamic pressure measurement, hence reducing the number of measurable parameters required. Rearranging equation 9.1 gives the following:

$$p = p_\infty + q_\infty C_p \tag{9.3}$$

Hence the value of C_P defines how much the local pressure differs from the free stream pressure in multiples of the dynamic pressure. The local stagnation point occurs when the pressure sensor is facing the oncoming airflow. At the stagnation point, C_P is equal to one, hence the local pressure is a magnitude of q_∞ greater than the free stream pressure.

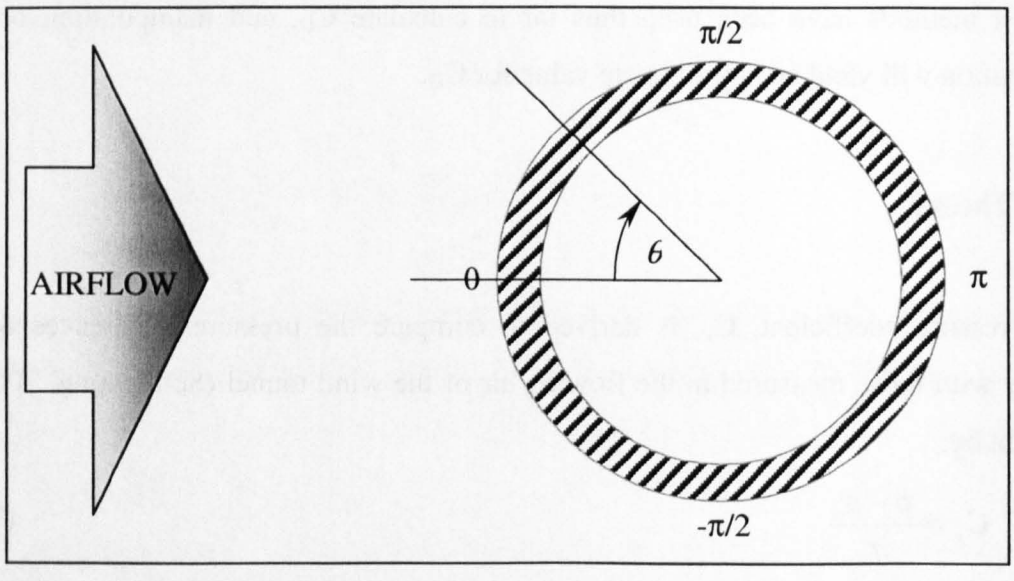

Figure 9.1 Schematic showing a section through a tennis ball at its maximum circumference with airflow impinging at point 0.

Figure 9.1 shows a cross section of a sphere used to define the change in C_P around the surface of the ball. As the velocity of airflow over the surface increases from zero at point 0 to a maximum at the top and bottom (points $\pi/2$ and $-\pi/2$), the pressure reduces from a maximum at point 0 to its minimum at points $\pi/2$ and $-\pi/2$. Hence, it can be deduced that C_P reduces from 1 at the stagnation points, reaching a minimum at the maximum flow rate over the surface.

9.2.1 The theoretical solution

The theoretical inviscid relationship between C_P and the sensing position of the local pressure is defined in Schlichting (8th revision, 2000) as:

$$C_p = 1 - \tfrac{9}{4}\sin^2\theta \qquad (9.4)$$

where the sensing position is measured as an angle to the horizontal shown in figure 9.1.

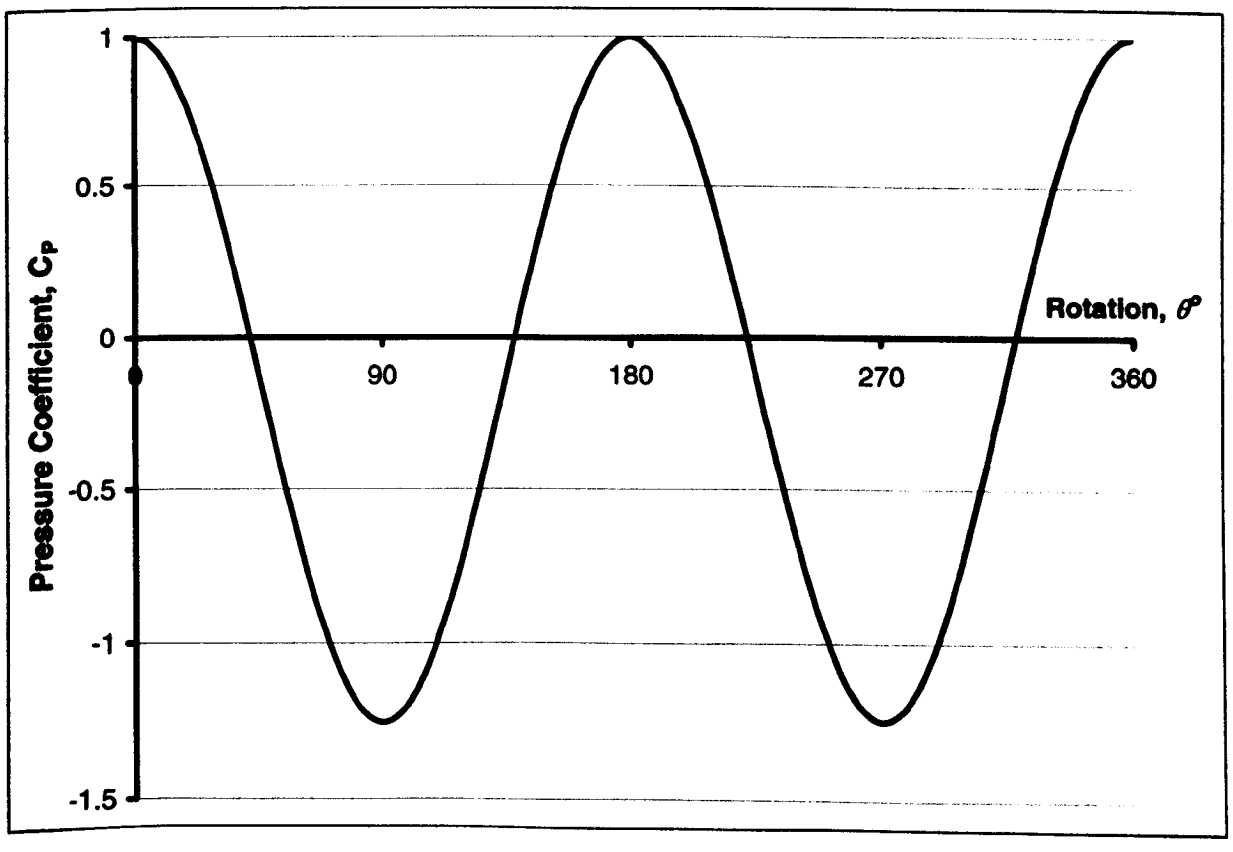

Figure 9.2 Relationship between C_P and pressure sensing point calculated using equation 9.4 defined in Schlichting (8th revision, 2000).

Figure 9.2 shows a graph produced using data created using equation 9.4. It can be seen that C_P starts at a value of 1 and steadily reduces to -1.25 at $\pm\pi/2$, the theoretical points of maximum velocity. The C_P then rises again in the adverse pressure gradient on the back face, returning to 1 at the rear most point. Hence the theoretical solution contains two stagnation points, with the second positioned at the back of the sphere.

In almost all cases, the relationship between C_P and the flow over the ball cannot be described by equation 9.4. It is more normal that the adverse pressure gradient will cause separation at some point around the surface. Literature relating to flow over spheres has shown that the pressure distribution around a tennis ball is more likely to be similar to one of those shown in figure 9.3.

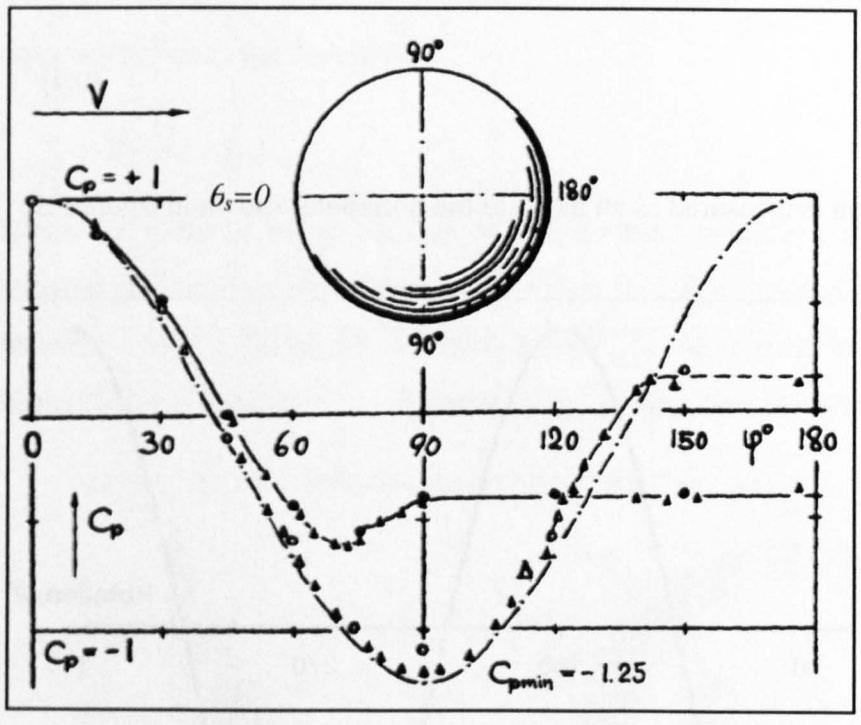

Figure 9.3 Chart showing the typical C_P results obtained around the surface of a sphere for different flow types (Hoerner, 1965).

Figure 9.3 shows two C_P distributions around the circumference of a sphere. It can be seen that the C_P distribution is dependent on the boundary layer separation point, which is dictated by the state of the airflow around the ball. Separation is defined as the point where there is a sudden change in direction of C_P, or where the C_P becomes constant. Separation is easily defined for the laminar flow, occurring near the poles, maintaining a constant pressure in the wake. The turbulent flow has more momentum and is therefore more tolerant of the adverse pressure gradient on the rear face, making it able to recover

significantly. The separation occurs on the rear face creating a small wake with relatively high pressure, and hence less drag.

The question to answer is whether the pressure distribution for a tennis ball is similar to either of the two plots in figure 9.3 or whether it is a combination of the two.

9.3 Apparatus

The apparatus required for this test method involves; a ball mounted in the airflow of a wind tunnel; a rotating fixture to investigate the pressure around the full circumference; and a measuring device to determine the pressure differences.

9.3.1 The wind tunnel

The low-speed wind tunnel that has been used in several of the test methods already described was used for this testing. Doors are fitted along the length of the working section of the wind tunnel in normal operation. One of the doors was replaced for this test method, and replaced by a rotation board. There is a close fit between the board and the wind tunnel such that flow is not disturbed, and it is held in place using screws at each of the four corners. A circular cut out of approximately 300mm diameter, within which the rotation disc was inserted, is at the centre of the board. The rotation plate consists of two parts, the disc that fits in the hole in the board and a larger disc that mounts on the outside of the parent board. Four brackets are attached to the parent board and positioned around the circumference of the larger disc to keep it in place.

9.3.2 Mounting of the ball

In order to investigate the pressure on the surface of a tennis ball, each ball to be tested was modified to incorporate a pressure tapping. Pressure tapping is used widely in aerodynamic studies, and in its most basic form, it is seen as a small hole on the surface. Small diameter tubing was used to translate the pressure experienced by the tapping, measured using a manometer. The surface of a tennis ball is not smooth nor is it solid, hence standard

pressure tapping techniques could not be used. Figure 9.4 shows a tennis ball used in this investigation containing a pressure tapping.

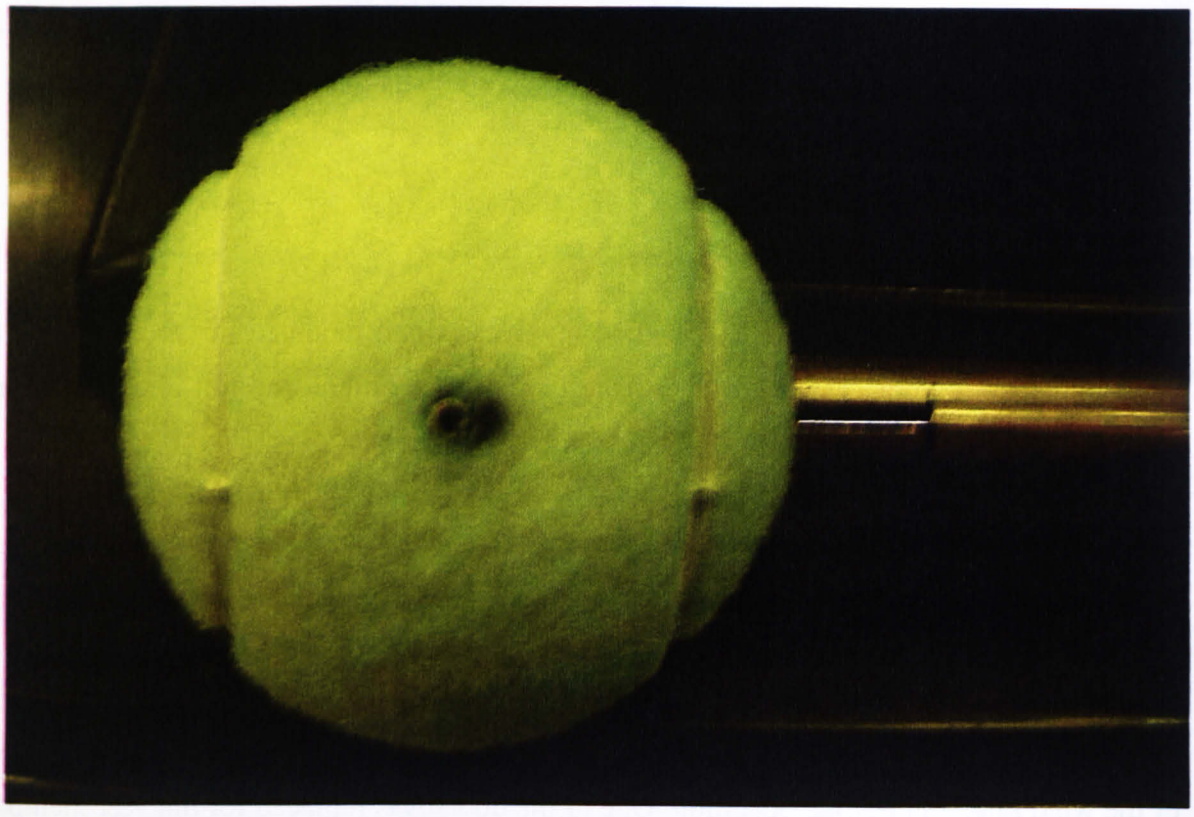

Figure 9.4 Picture showing the pressure tapping in a tennis ball, mounted at the side.

Figure 9.5(a) shows a schematic of a pressure tapping system: this tapping consisted of a short length of 2mm diameter bore brass rod, with flexible 1mm bore tubing fixed within it. A small hole was drilled through the core of the ball, through which the brass rod is inserted. The brass rod was held in place using friction alone, hence the drilled hole is slightly smaller than that of the outside diameter of the rod. A chamfer is machined on one end to enable the rod to be inserted into the ball. After the rod is in place, the tubing is 'threaded' through it from outside to in, with the end being brought out through a larger diameter hole in the side of the ball. The hole in the side of the ball was used for mounting purposes and was created using a cork borer. A length of tubing adequate for connection to a manometer was required and once this had been pulled through, the end was cut off flush with the surface of the brass rod. To further ensure satisfactory flow over the tapping, a small internal chamfer was created in the tubing using a craft knife. The final step requires the pressure tapping assembly to be flush with the surface of the tennis ball, if it was above the surface it may affect the flow over the surface.

a)

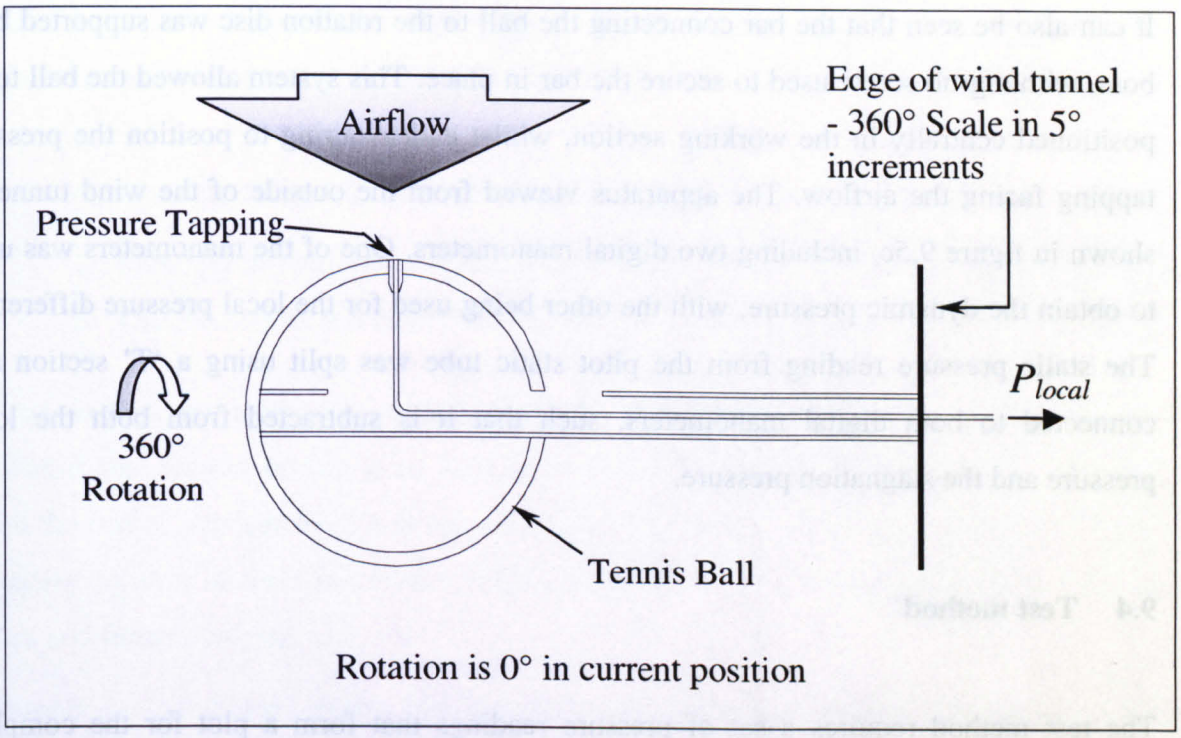

b)

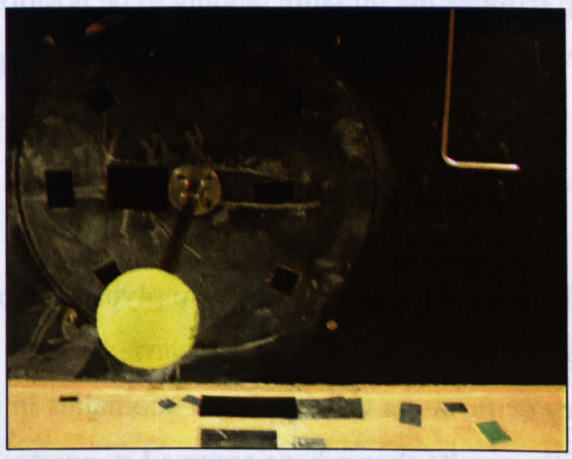

c)

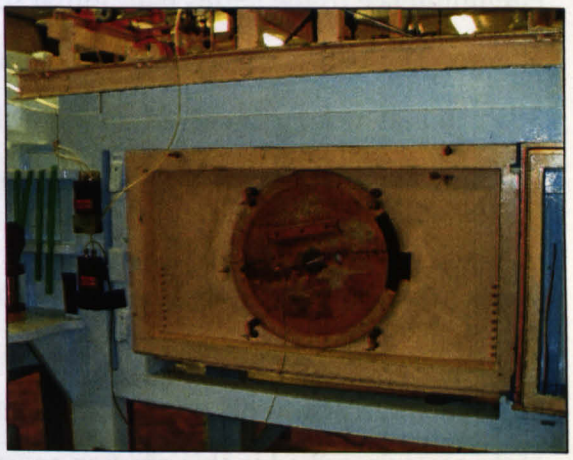

Figure 9.5 Three views; a) schematic; b) the inside of the wind tunnel; and c) the outside of the wind tunnel; of the apparatus used to calculate C_P around a tennis ball.

A hollow bar was used to connect the ball to the edge of the wind tunnel, the same bar was also used as a conduit to deliver the tubing to a manometer. Figure 9.5a shows the ball positioned with the pressure tapping facing the oncoming airflow, at which point a marker on the rotating board lined up with zero on the scale. A full 360° scale was printed around the rotating board in 5° increments. Figure 9.5b shows the apparatus located on the inside of the wind tunnel, including a pitot static tube used for measuring the dynamic pressure in the free stream.

It can also be seen that the bar connecting the ball to the rotation disc was supported by a boss, with a grub screw used to secure the bar in place. This system allowed the ball to be positioned centrally in the working section, whilst endeavouring to position the pressure tapping facing the airflow. The apparatus viewed from the outside of the wind tunnel is shown in figure 9.5c, including two digital manometers. One of the manometers was used to obtain the dynamic pressure, with the other being used for the local pressure difference. The static pressure reading from the pitot static tube was split using a 'T' section and connected to both digital manometers, such that it is subtracted from both the local pressure and the stagnation pressure.

9.4 Test method

The test method requires a set of pressure readings that form a plot for the complete circumference of the tennis ball. Initial set up requires the pressure tapping to be positioned at zero. The ball is then rotated through 5° anticlockwise leaving the marker pointing at 355°. Initial testing involved rotating the ball 370° clockwise in 74 x 5° increments, finishing the test with the marker pointing at 5°.

Literature shows that C_P is symmetrical on the top and bottom surfaces, implying that only half of the ball needs testing. The initial tests with each new ball were carried out on the full circumference to determine the symmetry of flow. As there were no anomalies in any of the tests described in this chapter, most of the results shown have assumed symmetry.

The dynamic pressure is constant throughout each test and it is therefore only noted when a new wind speed setting is required. The readings from the other digital manometer are noted at each 5° increment, and recorded in a spreadsheet. The spreadsheet is designed such that C_P is calculated for each 5° increment and a chart plotted of C_P against rotation.

9.4.1 Calibration

Every manual effort is taken to ensure that the stagnation point coincides with the zero degree position, however it is likely that the stagnation point occurs a few degrees either

side of zero. It is understood that the C_P is equal to one at stagnation, and therefore the apparatus can be used as a yaw meter.

There are two methods by which the results can be used:

1. Unscrew the fixing bar and rotate it a small amount to try to correct its position.
2. Use the results and calculate a correction factor for use in the future analysis.

It was decided that method 1 would not be suitable, not only would it be cumbersome, but it would also require testing after each alteration. Method 2 is less time consuming, and with the use of a spreadsheet it is easy to apply. The correction factor was applied using a separate column in the spreadsheet, which then became the rotation information for the chart and future analysis.

Example: if it were found that the stagnation point occurred at 2.5° anticlockwise (357.5°), then all of the rotation readings would be increased by 2.5°. This will be seen on the chart as a horizontal shift and will not affect the magnitude of C_P in any way.

9.5 Results

The test method will be used to investigate the airflow around four different ball surfaces. Literature widely documents flow around smooth spheres, for comparison purposes, it is useful to commence testing with a smooth ball. Comparison between the results of this test method and previous literature will highlight any problems with the test method itself. The other three balls comprise; a normal pressurised ball; a pressurised ball with fluffed nap; and a pressurised ball with its nap shaved. The normal pressurised ball has been handled only for inserting the pressure tapping and mounting, hence can be assumed to be a true representation of the surface of new ball. The other two tennis balls are used to assess the effect of raising and lowering of the nap that may be expected during play.

9.5.1 Smooth ball

The smooth ball was identical to that which had been used for testing in chapter 7. The results in that test method compared well with previous data, suggesting that the surface

finish on the ball can be considered smooth. Figure 9.6 shows a complete set of C_P versus rotational position results obtained for the smooth ball at the top wind speed of 24.1ms^{-1}. At this speed the Re is approximately 1x10^5, and it was shown in chapter 7 that transition to turbulent flow does not occur until a Re of 3.5x10^5.

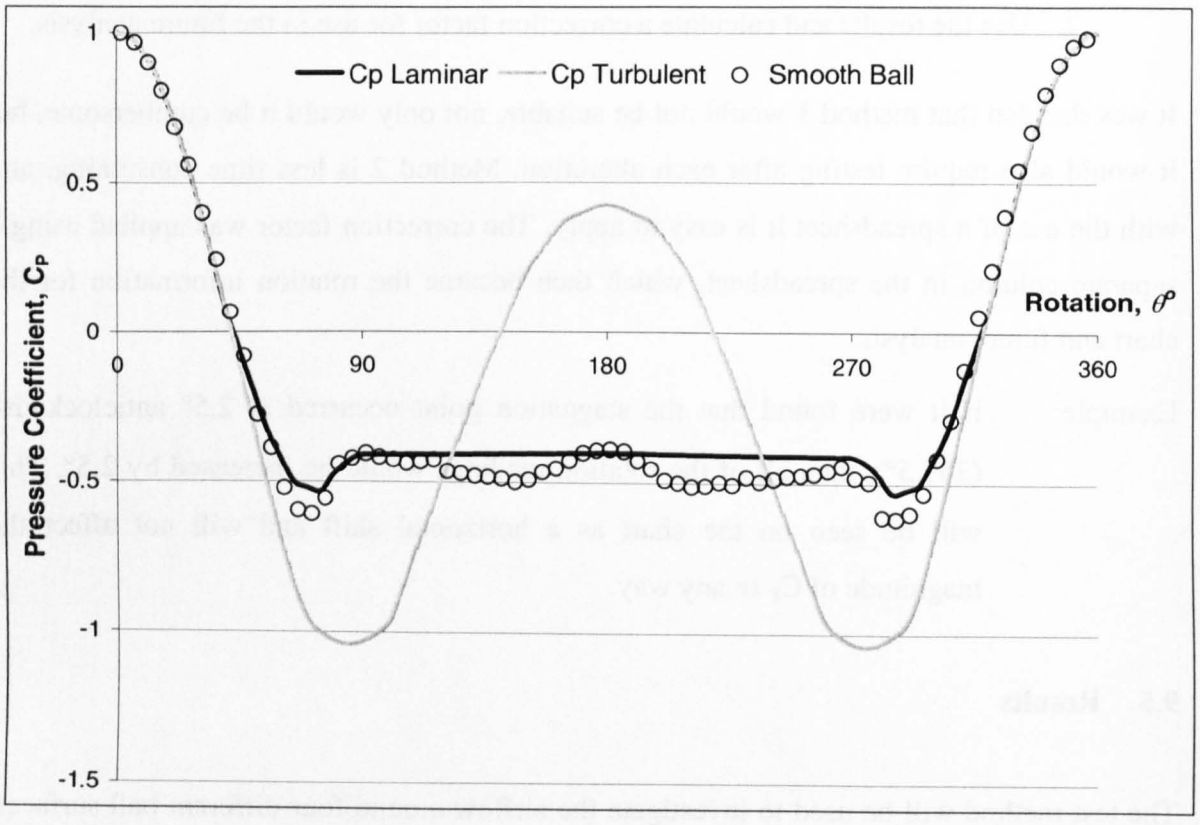

Figure 9.6 Chart of C_P against rotation for a smooth ball at a wind speed of 24.1ms^{-1}.

The C_P plot in figure 9.6 confirms that the airflow over the smooth ball is laminar with the data set comparing well with the typical plot. The separation point for this ball and wind speed is defined at the point where C_P becomes constant, which is at approximately 80°, definitely on the front face. The pressure is relatively constant on the rearward face and has a value slightly less than the free stream pressure. This data set is obtained at the highest wind speed attainable, it was not possible to induce turbulence in the airflow around this ball, moreover it was not required for this analysis.

9.5.2 *Repeatability*

The repeatability of this test method has been assessed by performing multiple tests on the same ball at the same wind speed. Rather than investigating one ball several times, all ball types have been tested twice.

Figure 9.7 shows two C_P distributions obtained around the smooth ball at approximately $25ms^{-1}$. The results were obtained on separate occasions, with the ball being removed from the apparatus between instances. It is clear that the two plots are very similar, containing a small difference on the rear face in one of the tests. It is reasonable to suggest that this test method is repeatable. Any differences observed between different ball types are as a result of the altered airflow caused by the different surface properties.

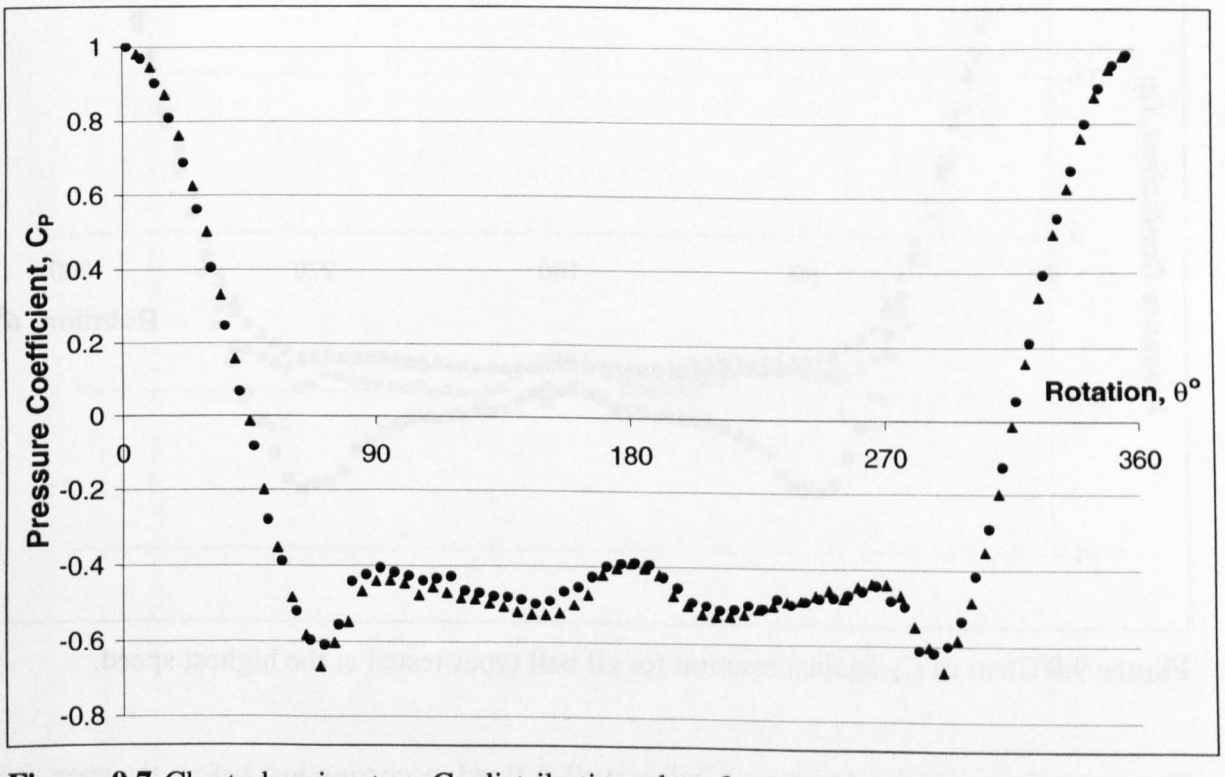

Figure 9.7 Chart showing two C_P distribution plots for a smooth ball at a wind speed of approximately $25ms^{-1}$.

9.5.3 *High-speed*

Although it is more conventional to start at the lowest speed tested and ascend, it may be more useful here to start at the top speed. If turbulent flow were to occur within the

parameters of available from the wind tunnel, it will be observed at the top speed. Should the flow be found to be post critical, the investigation of C_P at the lower speeds will help to uncover the point at which transition occurs.

Figure 9.8 shows a chart plotting C_P against angle tested at the top speeds for all four ball types. The top speed is dependant on several factors, it was observed that the fan in this wind tunnel was able to rotate faster when the generator set had been on for several hours. The speeds used for these tests range from 24.1ms^{-1} to 24.9ms^{-1}, with both the fluffed and shaved balls being approximately 24.9ms^{-1}. Figure 9.8 shows that the airflow around the normal and fluffed balls is similar to that of the smooth ball.

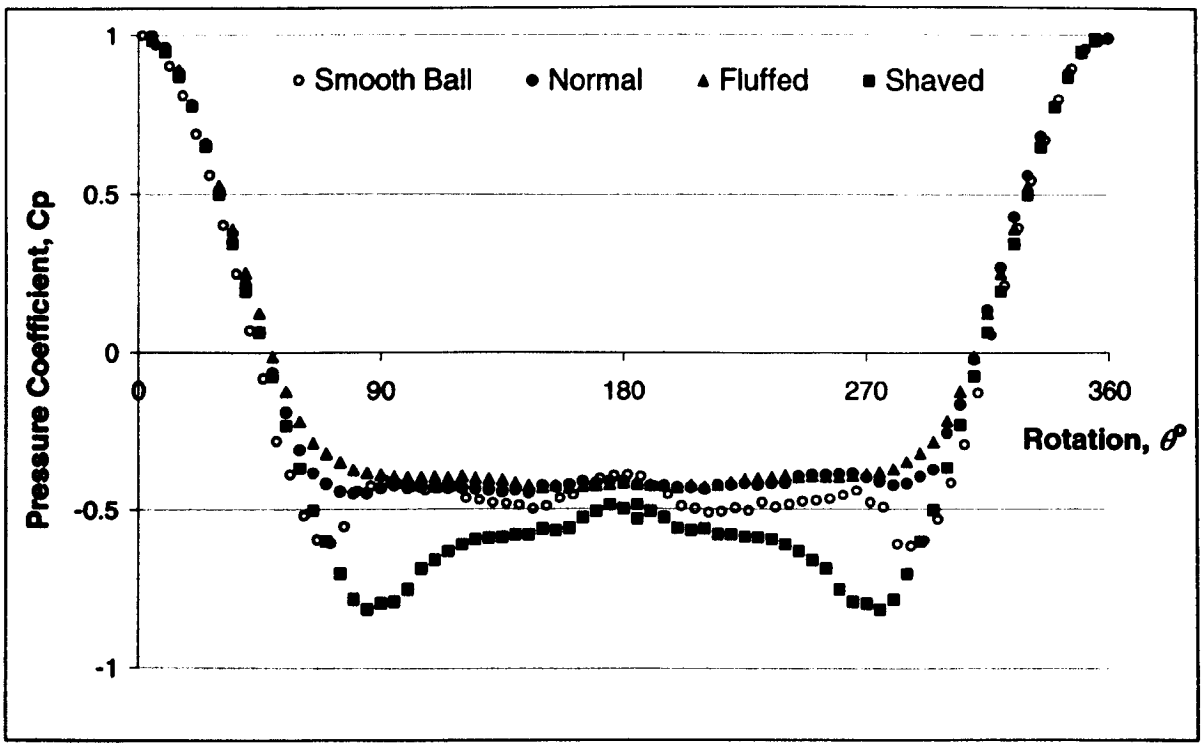

Figure 9.8 Chart of C_P against rotation for all ball types tested at the highest speed.

The separation point for the smooth ball is well defined, occurring just before the apex, it is less obvious for the normal and fluffed balls, however it is possible to conclude that it occurs on the front face, with the constant pressure in the wake starting before 90°. The lack of an adverse pressure gradient infers that the boundary layer is very weak, and that separation has been induced as soon as the adverse pressure gradient is encountered.

The shaved ball is significantly different, with the separation occurring further around on the rear of the ball, maybe as late as 120°. In chapter 7 the C_D of a shaved ball was shown to drop from approximately 0.575 at low wind speeds to just below 0.4 at the maximum wind speed. Therefore, this is a result that may have been expected, and this is a clear indication that the airflow around the shaved tennis ball is transcritical at this wind speed.

9.5.4 Reduced wind speeds

Figure 9.9 shows the C_P results plotted against rotation for all four balls tested at approximately $17ms^{-1}$. It can be seen that there is very little difference between this chart and that seen in figure 9.8. At a wind speed of $17ms^{-1}$, the Re of a shaved ball is approximately 75,000, which is shown to be just beyond Re_{crit} in chapter 7. The separation point has not moved significantly, and the magnitude of the minimum C_P exhibited by the shaved ball is not as low. The plots relating to the normal and fluffed balls are practically identical, and again appear to be very similar to those obtained for the smooth ball, with separation occurring around the apex.

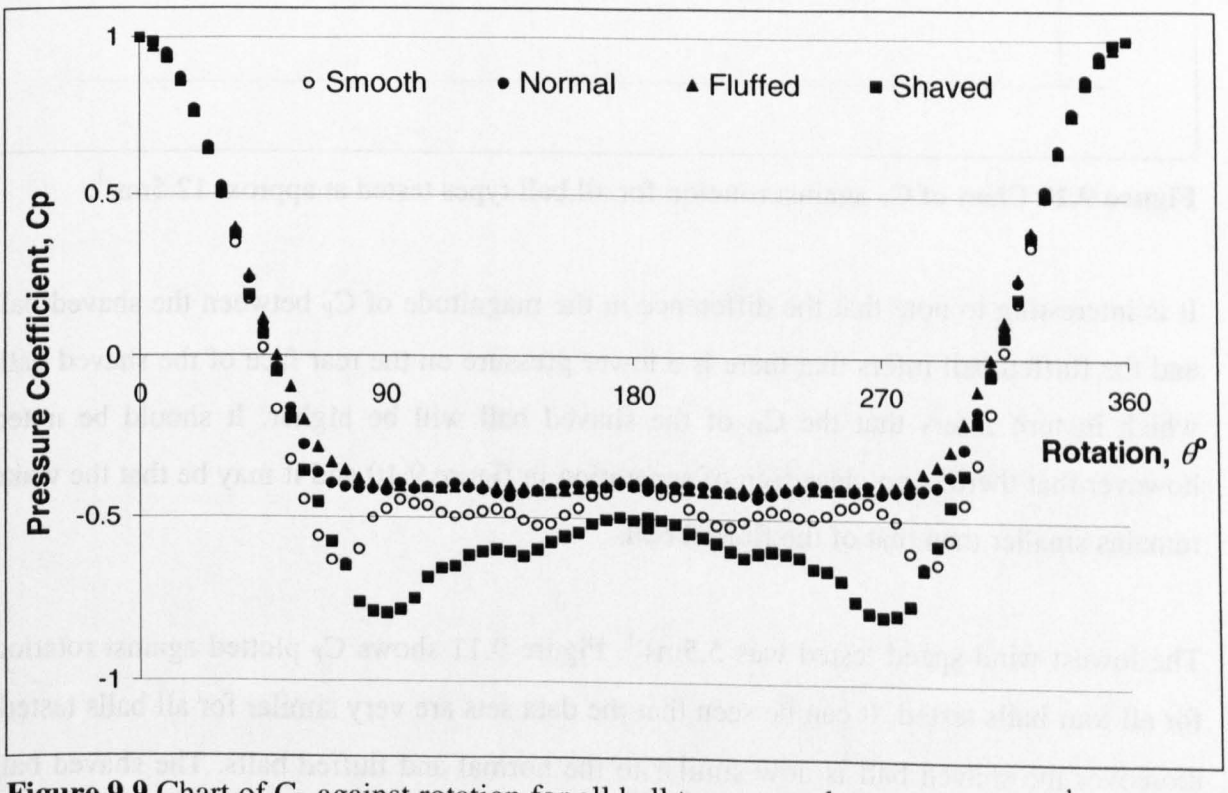

Figure 9.9 Chart of C_P against rotation for all ball types tested at approx. $17ms^{-1}$.

Figure 9.10 shows the C_P results plotted against rotation for all of the ball types at 12.5ms^{-1}. It can be seen that the airflow in the normal and fluffed balls has not changed significantly, and are very similar to the results obtained for the smooth ball. The shaved ball now follows a similar pattern to normal and fluffed balls, although the minimum value is significantly different. A wind speed of 12.5ms^{-1} relates to a Re of approximately 55,000 for the shaved tennis ball, at which point the flow was shown to be critical in chapter 7.

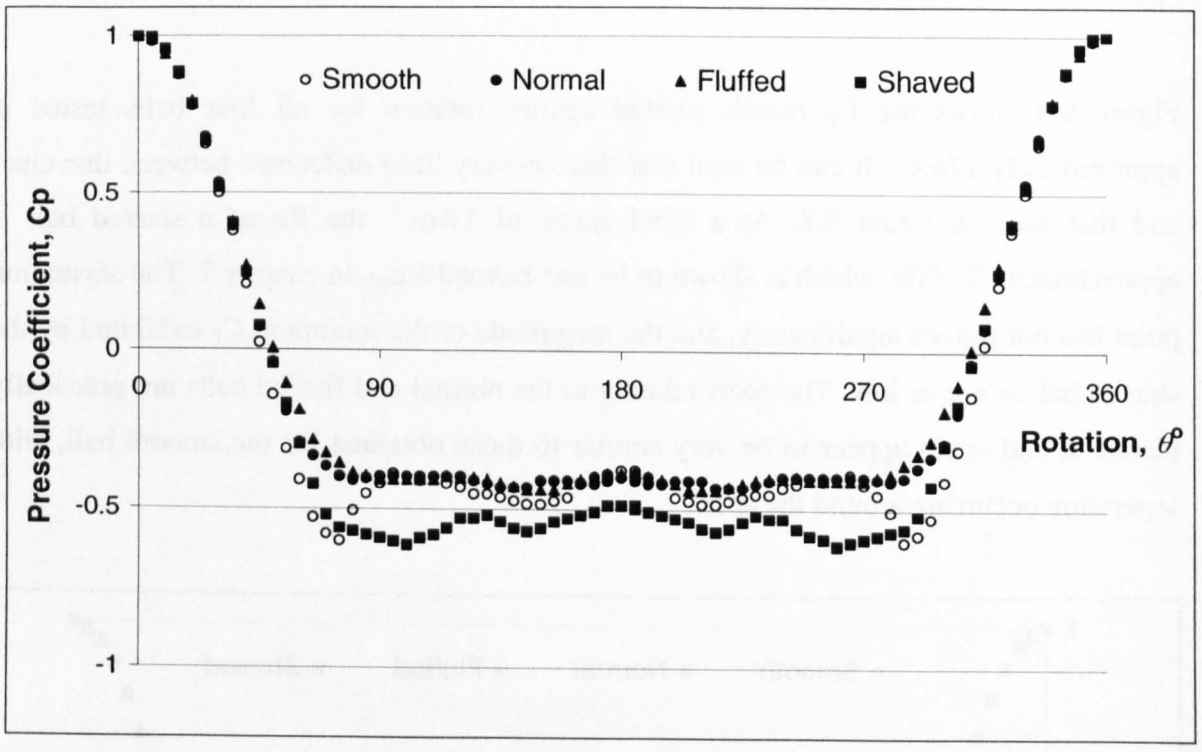

Figure 9.10 Chart of C_P against rotation for all ball types tested at approx. 12.5ms^{-1}.

It is interesting to note that the difference in the magnitude of C_P between the shaved ball and the fluffed ball infers that there is a lower pressure on the rear face of the shaved ball, which in turn infers that the C_D of the shaved ball will be higher. It should be noted however that there is no clear sign of separation in figure 9.10 and it may be that the wake remains smaller than that of the fluffed ball.

The lowest wind speed tested was 5.5ms^{-1}. Figure 9.11 shows C_P plotted against rotation for all four balls tested. It can be seen that the data sets are very similar for all balls tested, moreover the shaved ball is now similar to the normal and fluffed balls. The shaved ball does exhibit a slight recovery, which is not present in either the normal or the fluffed ball

at any speed. A wind speed of 5.5ms^{-1} relates to a Re of approximately 24,000 for the shaved tennis ball, at which point the flow was shown to be laminar in chapter 7.

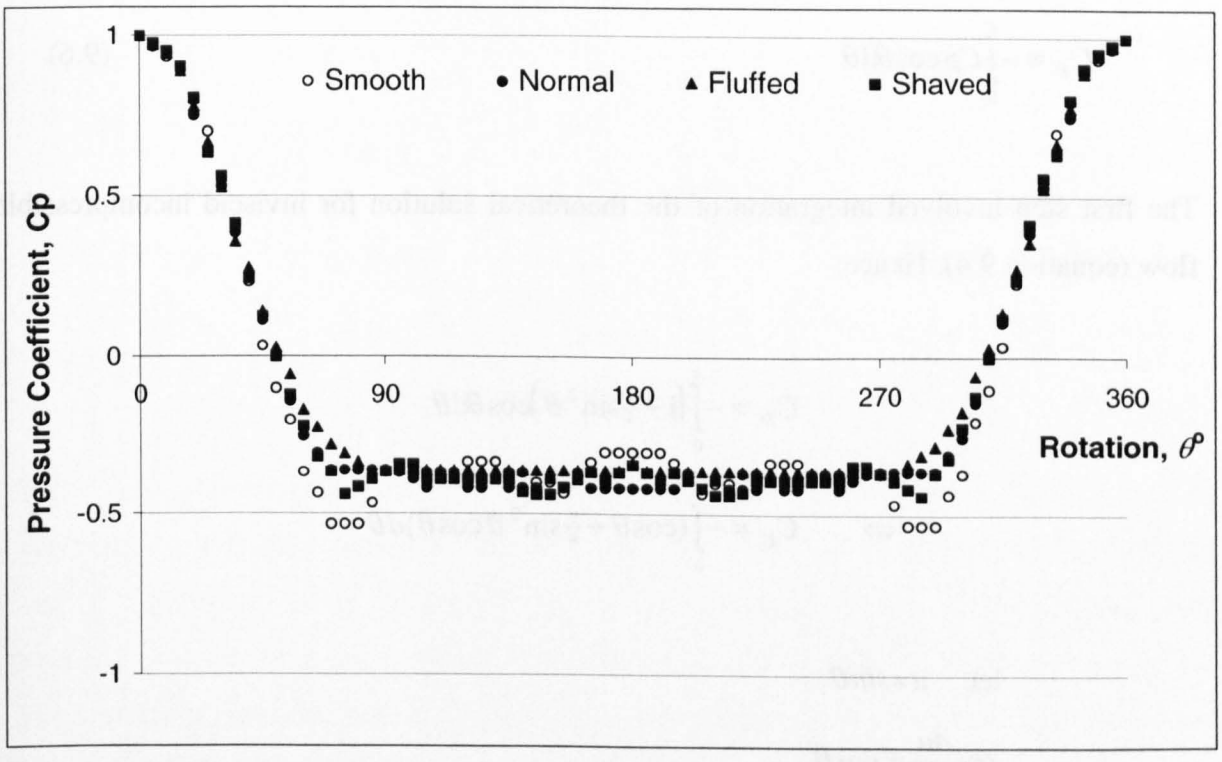

Figure 9.11 Chart of C_P against rotation for all ball types tested at approx. 5.5ms^{-1}.

There are very clear signs of the state of the flow around the shaved and smooth balls. All that can be gained for the normal and fluffed balls however, is that there is a clear indication of the presence of a large wake, with boundary layer separation occurring near the apex.

9.6 Obtaining C_D

The C_P data sets can also be used to approximate the C_D for a given test. All C_P data obtained thus far has been normal to the surface of the ball, however the drag force acts in the same direction as the airflow. The direction can be simply corrected using trigonometry, hence it can be shown that:

$$C_D = -0.5 \int_0^{2\pi} Cp \cos\theta d\theta \qquad (9.5)$$

However, it has also been shown that the flow can be assumed to be symmetrical around the central axis, hence equation 9.5 becomes:

$$C_D = -\int_0^{\pi} Cp\cos\theta d\theta \tag{9.6}$$

The first step involved integration of the theoretical solution for inviscid incompressible flow (equation 9.4). Hence:

$$C_D = -\int_0^{\pi} \left(1 - \tfrac{9}{4}\sin^2\theta\right)\cos\theta d\theta$$

$$\Leftrightarrow \quad C_D = -\int_0^{\pi} (\cos\theta + \tfrac{9}{4}\sin^2\theta\cos\theta)d\theta$$

let $u = \sin\theta$

$$\Leftrightarrow \frac{du}{d\theta} = \cos\theta$$

$$\text{Now} \quad C_D = -\int_0^{\pi} \left(\frac{du}{d\theta} + \frac{9}{4}u^2\frac{du}{d\theta}\right)d\theta$$

$$\Leftrightarrow \quad C_D = -\int_0^{\pi} \left(1 + \frac{9}{4}u^2\right)du$$

$$\Leftrightarrow \quad C_D = -\left[u + \frac{9}{12}u^3\right]_0^0 = 0$$

It is clear that this result does not compare with the results obtained in previous test methods, and on first impression it could be assumed to be incorrect. Figure 9.12 is a chart plotting $C_P\cos\theta$ against rotation, it can be seen that the curve is symmetrical about $C_P=0$, therefore a C_D equal to zero may be expected. This result is known as the D'Alembert's paradox, and occurs in many aerodynamic studies.

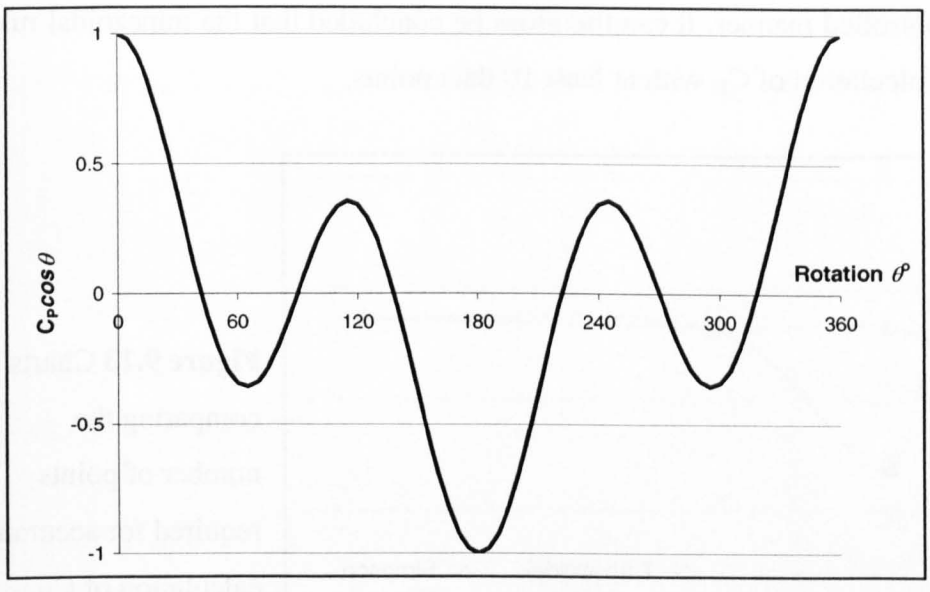

Figure 9.12 Chart plotting $C_P cos\theta$ using equation 8.4 over one complete rotation.

In previous experimental methods in this study it has been possible to create a best-fit polynomial curve which described the data set. It was not possible to do this simply in this part of the study due to the complexity of the curve, hence an alternative integration method to calculate C_D was required. It was decided that both the extended trapezoidal rule and Simpson's extended rule would suit the requirements, and each integration method has been investigated in an attempt to reliably calculate C_D given the available information.

Initial analysis focussed on the number of points required for accurate calculation, comparing the results obtained with each method. There are 72 data points available for each test, with symmetry this can be immediately reduced to 36. It was decided that all available data points should be used in the first calculations, reducing them in convenient increments in subsequent analysis.

Both integration methods involve manipulation of each data point, hence will be more time consuming when there are more points required. Figure 9.13 shows a chart of the results obtained for C_D against number of points required. Smooth ball data at $24ms^{-1}$ was used for the initial analysis, and it can be seen that both of the integration methods give similar results for maximum points (37) and half points (19).

The results obtained using Simpson's rule become unstable with further reduced data points. The trapezoidal rule returns satisfactory results down to 10 data points, and after

that reduced in a controlled manner. It can therefore be concluded that the trapezoidal rule should be used for calculation of C_D with at least 10 data points.

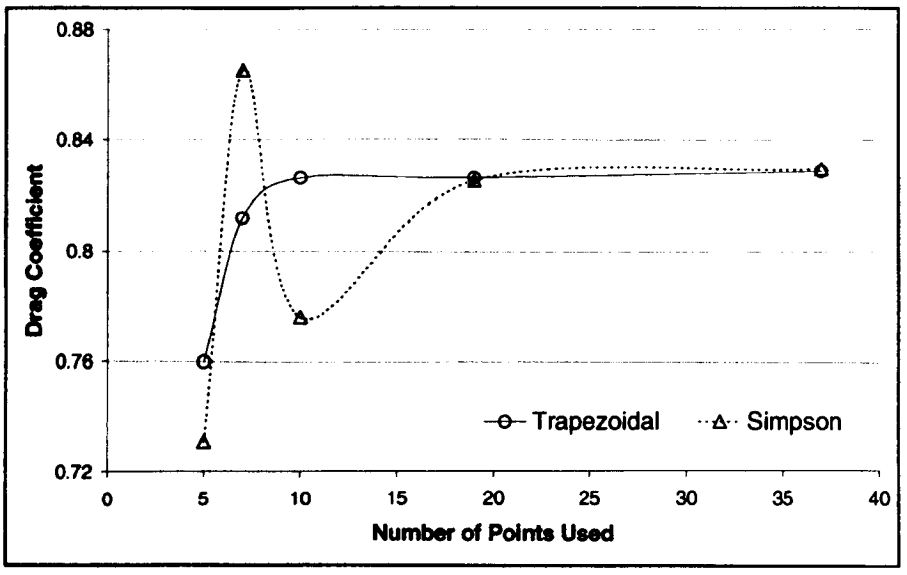

Figure 9.13 Charts comparing the number of points required for accurate calculation of C_D using two different integration methods.

Figure 9.14 shows the chart of the C_D results obtained for the four ball types tested, and it can be seen that the values range from 0.75 up to a little under 0.95. At the lowest wind speed the smooth ball has the lowest C_D, with the fluffed ball slightly lower than both the normal ball and the shaved ball. At all other wind speeds the smooth ball continues to have the lowest C_D, with the normal ball being slightly lower than the fluffed.

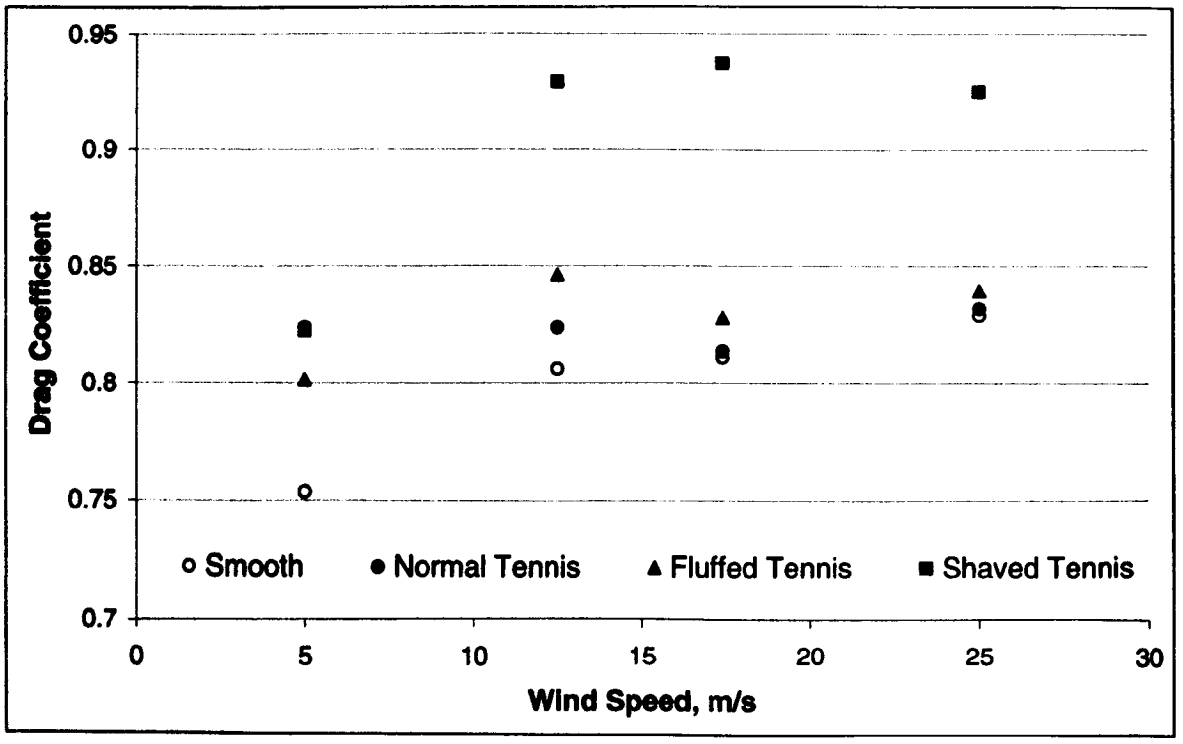

Figure 9.14 C_D results obtained for four different ball types at four different wind speeds.

It is clear that the shaved ball has a significantly higher C_D than the other balls tested for the three highest wind speeds. This result does not tie in with the results obtained in chapter 7, however it was anticipated from the results shown in figures 9.8, 9.9 and 9.10. The C_P for the shaved ball is lower at the rear of the ball for the high wind speeds, implying that the pressure on the rear face is lower. In general, the net imbalance between the front and back faces of the sphere produces a drag force on the sphere in the direction of the low pressure, and the greater the imbalance between the pressures on the front and rear faces of the sphere, the greater the force applied. It should be noted that the pressure tapping experiments were undertaken on two separate occasions, which involved dismantling the set up in between. The C_P distributions for all balls were similar on both occasions, hence this is not an exceptional set of results.

The calculation of C_D using C_P data was not intended as part of this study as there are several other methods that have previously been defined. It was therefore undertaken as a 'quick look see', however it has become clear that the integration methods and equations chosen were not suitable as there is no allowance for three-dimensional relieving. A more accurate estimate of C_D could have been calculated from the C_P data using a more complex spherical integration method, which would reduce the calculated C_D of all balls significantly. More importantly, it has been proposed that the calculated C_D of the shaved ball may reduce more than that of the other ball types using the more accurate calculating process, and hence the results obtained could become more comparative with previously presented data.

9.7 Comparison with flow Visualisation

Pressure tapping results can be used together with flow visualisation to help understand where the separation occurs. Rather than viewing the C_P distribution around the ball, the local pressure distribution is required. In order to calculate the local pressure, the free stream pressures are required. As all of the measurements taken thus far have been comparisons, there are no quantitative values available for the free stream pressure. The atmospheric pressure is readily available, hence a measurement of the atmosphere with respect to the free stream pressure is obtained. This is achieved by removing the

connection to the stagnation pressure tapping before testing commences. An example of the calculations required is as follows:

$$P_{atm} - P_{\infty} = 0.24 \text{ mbar}$$

But, P_{atm} = 1017.51mbar, hence: P_{∞} = 1017.27mbar

The local pressure at each data point can be calculated using equation 9.3.

Figure 9.15 shows the local pressure distribution together with smoke trails around a non-spinning normal ball at approximately 3.5ms^{-1} (equivalent to a Re of around 15,000). The smoke is flowing from left to right, with a clear wake on the rear face of the ball. It can be seen that the pressure is high at the stagnation point, and steadily reduces around the front face. Separation occurs at points A, slightly ahead of top and bottom apexes. The pressure is almost constant in the wake.

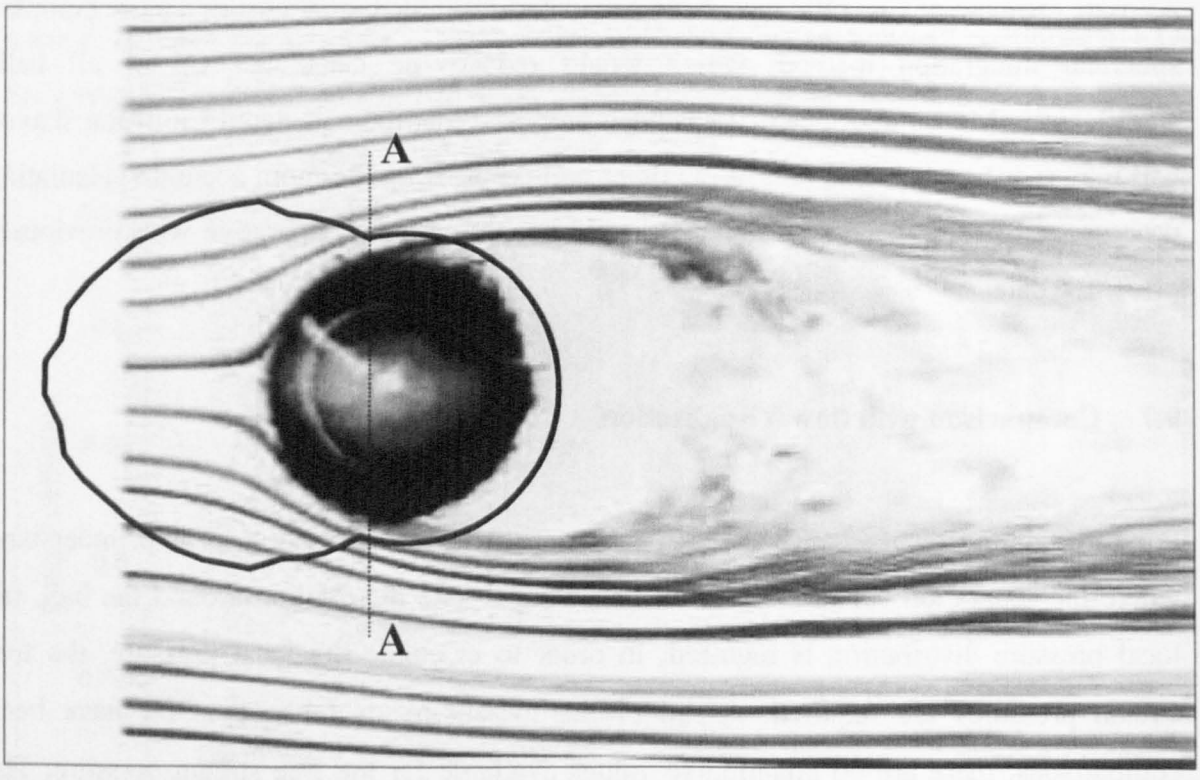

Figure 9.15 Pressure distribution and smoke flow around a normal tennis ball at approximately 3.5ms^{-1}.

Figure 9.16 shows the pressure distribution around the shaved ball at a wind speed of approximately $25ms^{-1}$, with a symbol placed where the ball should be. The small rise in pressure shown in figure 9.8 can be seen in the wake towards the rear most point of the ball.

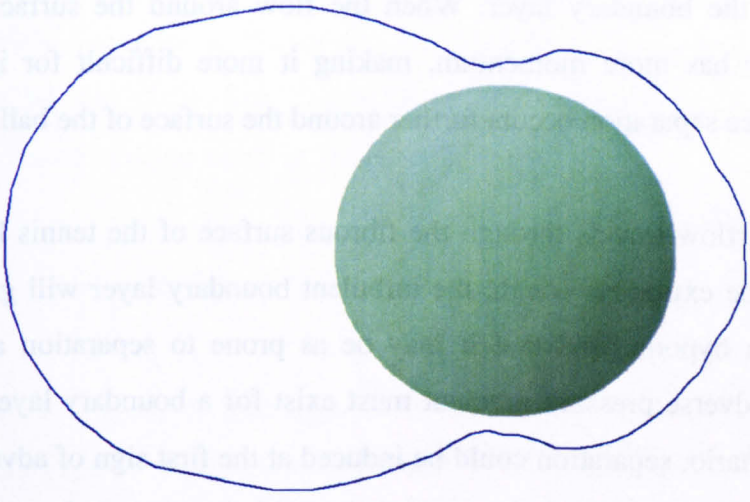

Figure 9.16 Pressure distribution around a shaved ball with a wind speed of approximately $25ms^{-1}$.

The pressure is at a minimum near the apex and begins to rise on the rear of the ball, becoming constant on the rearward surface, with separation occurring at points A, behind the apex. The boundary layer remains attached for longer over the shaved surface than that over the normal surface, and is even shown to withstand a short period of adverse pressure gradient.

9.8 Discussion

An adverse pressure gradient can clearly be seen in the C_P plot for the smooth balls. Theoretically, it commences at the apex, but can begin ahead of the apex due to the curvature effects of the flow close to the ball. In figure 9.6, the adverse pressure becomes apparent at around 70° from the front stagnation point, and separation occurs shortly after that at around 80°, when the C_P becomes constant. Such an ability for the boundary layer to overcome the adverse pressure gradient was also seen in the shaved ball at all wind speeds, but it was not observed on the normal and fluffed balls at any wind speed. Two possible reasons for this observation are discussed in the following sections.

9.8.1 Weak boundary layer

The pressure being measured on the surface of the ball is that in the boundary layer. Separation occurs when the airflow is no longer able to remain attached to the surface of the ball and breaks through the boundary layer. When the flow around the surface is turbulent, the boundary layer has more momentum, making it more difficult for it to separate from the surface, hence separation occurs further around the surface of the ball.

Assuming that some of the airflow travels through the fibrous surface of the tennis ball, which may be considered to be extremely rough, the turbulent boundary layer will grow rapidly. It has therefore been hypothesised that it may be as prone to separation as a laminar boundary layer. An adverse pressure gradient must exist for a boundary layer to separate, therefore, in this scenario, separation could be induced at the first sign of adverse pressure. The observed asymptotic approach to separation could therefore indicate the boundary layer being 'teased' from the surface.

9.8.2 Accuracy of measurement

There is a possibility that the accuracy of the measurements taken near the apex could have been affected by the random fibrous covering. If this were the case, then subtle changes in pressure observed around the separation location could become obscured.

10 DISCUSSION AND CONCLUSIONS

During this study various test methods were developed to enhance the understanding of the aerodynamic properties of tennis balls. Each of the test methods has been defined with a specific aim, and on its own a single test method may not enable a complete understanding. It is the aim of this final chapter to collate the in-depth analyses, and relate the findings to the future developments in the game of tennis.

10.1 Boundary layer – laminar or turbulent

The flow over smooth spheres is laminar up to a Reynolds number of approximately $3.5x10^5$, after which point the boundary layer becomes turbulent. As the surface of the sphere becomes roughened, whether by the addition of grit or by abrasive means, the Re at which transition to a turbulent boundary layer occurs reduces. It is commonly understood that the flow over a tennis ball is complex, however it is possible to use the results from this study to deduce the flow regime witnessed by a tennis ball.

10.1.1 C_D of smooth and rough balls

The flow regime dictates the way the airflow separates from the surface of the ball, and can normally be used to dictate the condition of the boundary layer. Figure 10.1 shows the C_D results obtained by Achenbach (1972) for smooth and rough balls. In addition, the C_D results have been manipulated to show the Re at which transition occurs and the drop in C_D expected, both against a roughness parameter. It can be seen that the Re at which transition occurs drops rapidly when a small amount of roughness is introduced. With additional roughness the Re at which transition occurs continues to drop, and is proposed to occur at a Re of $5x10^4$ for a roughness parameter of $2x10^{-2}$. Assuming that the Re at which transition occurs continues to reduce, it is possible to conclude that the boundary layer of a grossly rough surface (like tennis ball nap) may be turbulent at a very low Re.

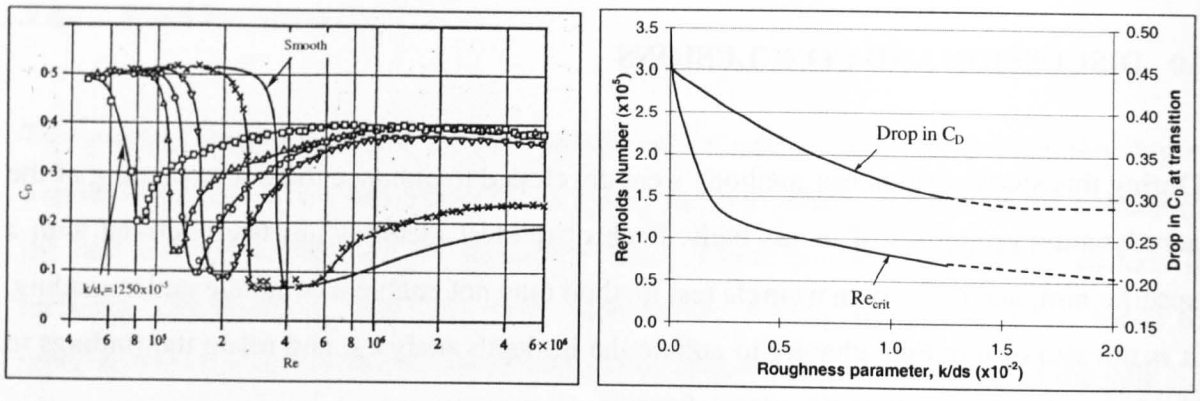

Figure 10.1 Achenbach results presented to show the critical Reynolds number and corresponding drop in C_D that may be expected for a known roughness parameter.

For a smooth ball with a subcritical C_D of around 0.5, the critical C_D has been shown to be less than 0.05. As the roughness is increased, the critical C_D increases, such that a ball with a roughness parameter of $2x10^{-2}$ should have a critical C_D of approximately 0.22. From the gradient of the extrapolated curve, the drop in C_D would not be expected to reduce much further, and hence reports of barely noticeable transitions are not supported by Achenbach's work.

The most important feature that can be observed directly from Achenbach's results is that the transcritical C_D does not return to the subcritical C_D. The transcritical boundary layer of the smooth ball is still developing at a Re of $6x10^6$, however it does not appear to be rising rapidly. Testing on the increased roughness balls reveals that the maximum transcritical C_D appears to be limited to approximately 80% of its subcritical C_D.

The C_D of a tennis ball has been shown to be 0.53 for all Reynolds numbers covered in this study. There are several reasons why the C_D is higher than that of a smooth ball and these will be discussed shortly, it is important to note however, that the C_D does not drop at any point and the C_D is above that shown for a transcritical flow regime. Although it was hypothesised that flow over the very rough surface of a tennis ball should be turbulent, it was originally thought that this data showed that the flow around a tennis ball starts laminar and remains laminar.

The following sections develop the discussion further by looking at some of the test methods adopted by the study.

10.1.2 C_D of an oversized tennis ball

Testing performed using the larger ball was proposed as a method of raising the Re at which the experiments could be performed. Interest in the results was low initially as the use of a larger ball had been excluded due to scaling issues, however, as it happens, it may have been the most important test of the whole study.

Although it may not sound 'interesting', the most interesting result is that there is no indication of a transition at all. The maximum Re attained for the oversized ball was in excess of 500,000, which significantly exceeds the Re_{crit} of a smooth ball in free air of 385,000. This is a clear sign of the flow regime around a tennis ball, as there is no sign of transition it must have occurred very early and the flow around the ball must therefore be turbulent.

10.1.3 Separation point

The pressure distribution around the circumference of the ball can be used to deduce the boundary layer separation points. It is also possible to use the pressure distribution data to calculate C_D, however there are far better means of achieving this, hence this technique was limited to qualitative interpretation only. The pressure is highest at the front stagnation point and reduces around the circumference of the ball. Near the point where the pressure tapping is perpendicular to the flow, the pressure is at a minimum, and starts to rise over the rearward face. Separation occurs due to an adverse pressure gradient, and is observed where the pressure change becomes zero.

Figure 10.2 shows some typical C_P plots taken from Schlichting (8^{th} revision, 2000), with the results for a normal tennis ball in an airflow at 24.6ms^{-1} appended to it. The separation point of a laminar boundary layer is approximately 80° from the front stagnation point, whereas separation occurs on the rearward surface for a turbulent boundary layer. Whilst the normal tennis ball plot is not identical to that of the laminar plot, the pressure change becomes zero at a similar point, if not a little earlier, and therefore separation of the normal tennis ball occurs very early on the advancing side.

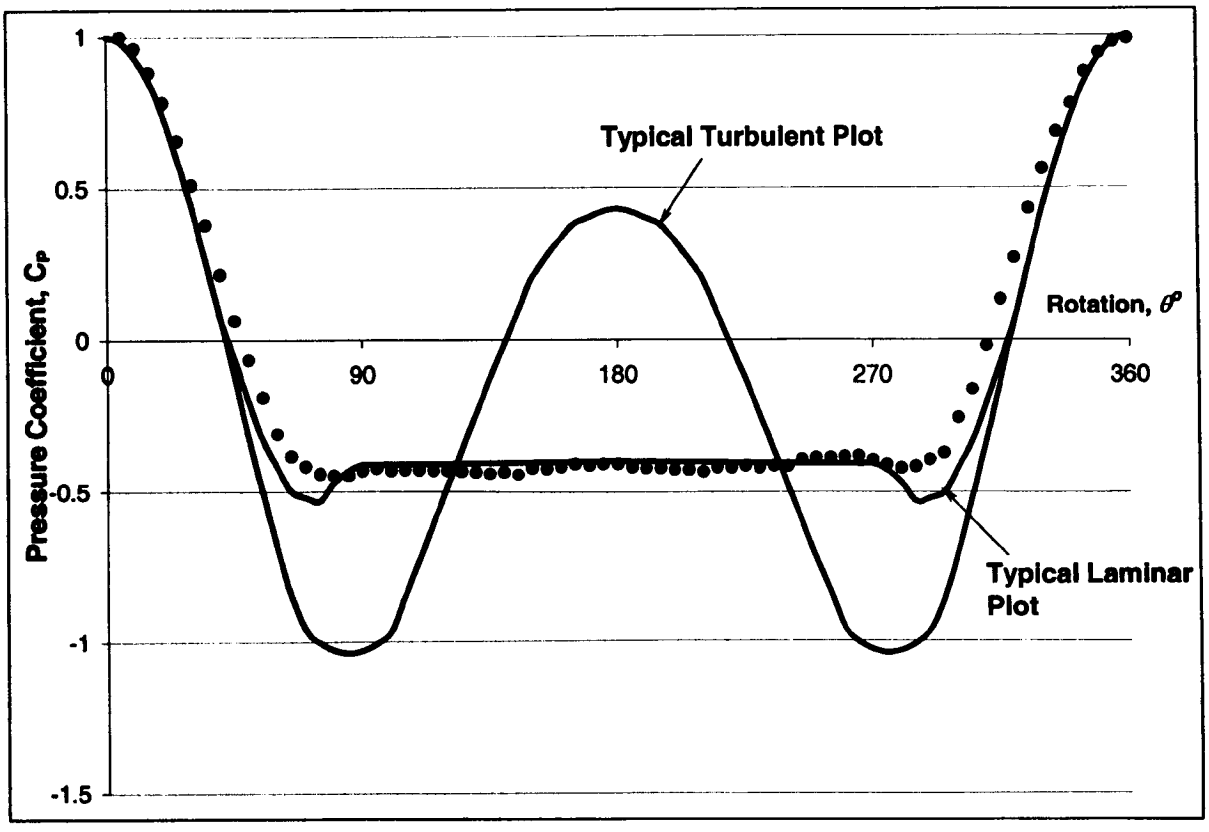

Figure 10.2 Chart of C_P against rotation for a normal ball at a wind speed of 24.6ms^{-1}.

On first inspection, it may be concluded that the flow over the tennis ball is laminar, however the tests on the oversized ball showed that it must be turbulent. There is no sign of an adverse pressure gradient, which possibly suggests that separation has been caused by other means.

In the absence of an adverse pressure gradient inducing separation, a qualitative view of the flow over the surface of a tennis ball needs to be investigated. Figure 10.3 shows the flow lines produced over the surface of a normal tennis ball with unmodified nap at 4ms^{-1}. The separation point is not clear but it can be concluded that it occurs on the front face with flow lines departing near the apex. It can also be concluded that, at low wind speeds, the flow lines appear to travel through the fibrous nap, which infers an additional drag parameter.

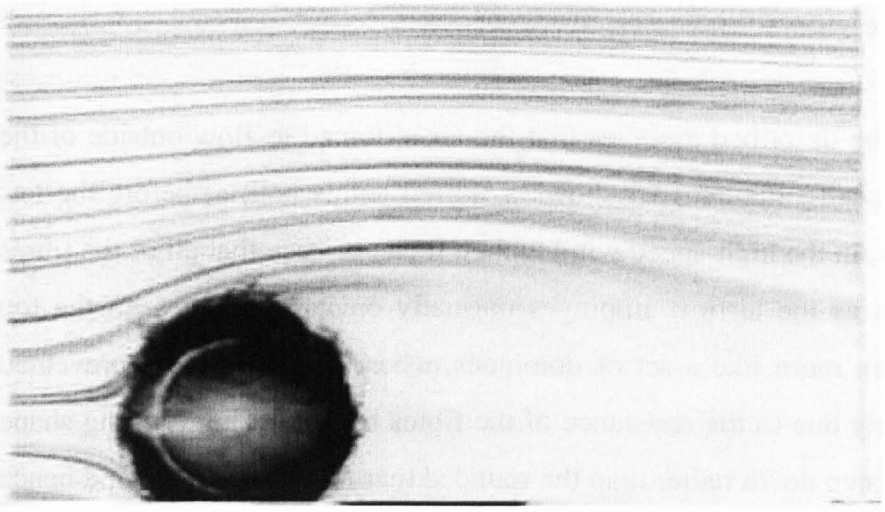

Figure 10.3 Flow lines produced over the surface of a normal tennis ball with unmodified nap at $4ms^{-1}$.

It should be noted that the maximum wind speed used for flow visualisation testing was $4ms^{-1}$, hence it is not clear whether the air continues to flow through the nap when testing at increased wind speeds.

In summary, it has been shown that a tennis ball has a C_D in excess of 0.5 in the transcritical flow regime. Separation has been shown to occur upstream of the apex using both flow visualisation techniques and pressure sensing techniques, which supports the magnitude of the defined C_D. Separation on the forward facing surface of sphere in a transcritical flow regime is not supported by previous studies of flow over rough spheres, hence an alternative separation mechanism should be proposed.

10.1.4 Separation mechanisms

As a tennis ball is a bluff body, the drag acting on it is predominantly due to the pressure imbalance between the front and rear surfaces of the ball, which itself is dependent on the boundary layer separation location. Previous studies had shown the supercritical C_D to rise with increasing Re, with C_D becoming independent of Re in the transcritical regime, reaching a maximum of around 0.4. The data presented for a tennis ball with an unmodified or fluffed nap has consistently been in excess of 0.5 throughout this study, suggesting separation occurring upstream of the apex. An alternative separation mechanism is required for this to occur, and two possible mechanisms will now be discussed.

Airflow over the surface

The first mechanism to be described assumes that the air is forced to flow outside of the nap at increased wind speeds. Figure 10.4 shows a fluffed tennis ball, a) before the test started and b) during test, in the high-speed wind tunnel. It can be seen that all of the fibres on the front face flatten as the airflow impinges normally on it. The fibres on the top surface are seen to flatten more like a set of dominoes, where front fibres are prevented from flattening completely due to the resistance of the fibres beneath. The resulting shape is seen to be more like a step down rather than the rounded rear face of a sphere, and hence may act like a trip.

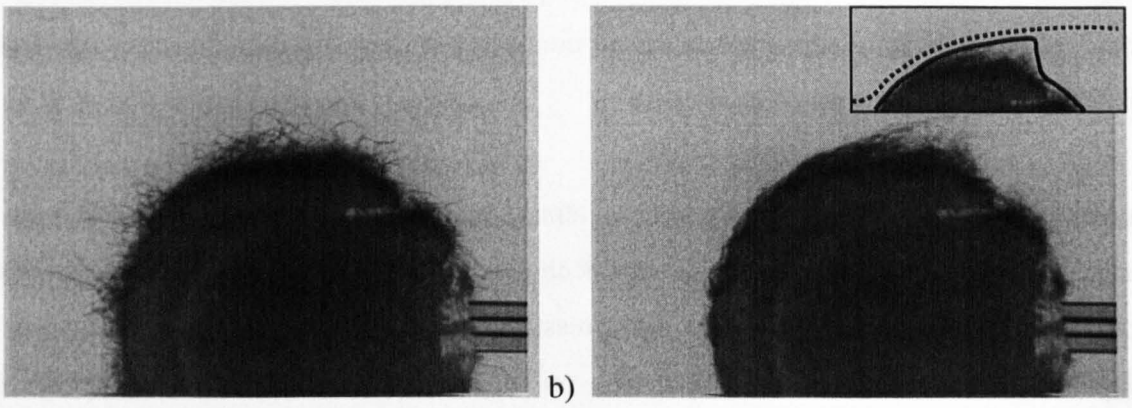

Figure 10.4 Fluffed pressurised tennis ball at wind speeds of approximately (a) zero and (b) 60ms^{-1} in the high-speed wind tunnel.

A trip wire on the front facing surface of a sphere will induce premature transition, however it is proposed that a trip positioned near the apex will induce separation. It is therefore hypothesised that the pressure drop across the step down to the rear surface of the ball is too great for the turbulent boundary layer to overcome and separation occurs. The inset of figure 10.4(b) shows the effective shape that the flow is required to follow, and the dotted line depicts the separated flow. Similar separated flows over normal and fluffed conditioned balls were presented in the flow visualisation study, and this therefore relates to a boundary layer separation point around 80° from the front stagnation point, and hence a C_D of around 0.5.

This mechanism is supported by the 'Brown' effect (discussed in depth in chapter 7), which comes from a dissertation by Brown (1997), where a noduled ball was discussed as

a possible way to increase C_D and hence slow the game of tennis down. It was found that the ball went through a transition expected of a roughened ball, and the C_D dropped to a minimum of just less than 0.3 at a Re of approximately $9x10^4$. As the Re increased, C_D rose steadily in the supercritical regime until at a Re of approximately $2.5x10^5$ (Re_{Brown}), the C_D raised rapidly to in excess of 0.85.

Interpretation of the C_D results revealed that the air flowed through the nodules, and transition occurs relatively early. After Re_{Brown}, the air was forced over the nodules rather than through them, and the additional C_D was shown to be a function of the additional projected diameter to the outer edge of the nodules. This is an important result and helps show that the flow over the surface of tennis ball may not flow through the fibres at increased wind speeds.

It should be noted that there is no large increase observed in the C_D of a tennis ball, therefore the Brown effect for a tennis ball must occur at very low velocities, outside of the test constraints in this study. It has also been shown that airflow appears to travel through the nap of both the normal and fluffed surfaces at $4ms^{-1}$, within the C_D testing range, which would imply that the Brown effect should have been observed in the C_D results had it occurred. If the airflow is assumed to continue to flow through the fibres, even at high wind speeds, then an alternative (or additional) separation mechanism needs to be discussed.

Airflow through the fibres

The second mechanism assumes that air is always forced through the fibres and the roughness of the ball induces separation. As a tennis ball is a bluff body, the drag acting on it is predominantly due to the large wake produced, and if it were considered to be a 'normal' rough sphere, it would have a subcritical C_D around 0.5. It has also been shown that C_D becomes independent of Re in the transcritical flow regime, with the transition points located near the front stagnation and boundary layer separation occurring around 100°, relating to a C_D of around 0.4. It should be noted however, that the transcritical separation points just described are in the region of adverse pressure gradient, and it could therefore be expected that the separation point could continue to move upstream.

With increasing roughness, the boundary layer growth rate is increased resulting in a tendency towards earlier separation. The skin friction coefficient also increases with increasing roughness resulting in a boundary layer that is more resilient to separation. It can therefore be seen that the separation location on a rough sphere is determined by the behaviour of these competing effects. It is entirely possible that for certain types of roughness, such as the round glass beads investigated by Achenbach, that a limit is reached whereby the boundary layer thickening effects are overridden by those due to increasing skin friction coefficient, and the flow remains attached longer. The roughness elements of the tennis ball may be more effective at thickening the boundary layer however, and it is therefore proposed that the absolute limit for turbulent boundary layer separation in the transcritical regime is the same as that for laminar boundary layer separation.

If the turbulent separation location in the transcritical regime is similar to a laminar separation in the subcritical regime ($\theta_s \approx 80°$), then it is suggested that the pressure drag should also be equivalent ($C_D \approx 0.5$), thus giving a total C_D in excess of 0.5.

10.1.5 Airflow through or over nap

In chapter 7, a smooth ball was shown to have a C_D of 0.5 and then the same ball was modified to include fibres. The fluff was added in three stages, and at the first stage the C_D was actually shown to decrease to approximately 0.45, although there was some fluctuation. Only the front portion of the ball was covered with fluff, hence the projected diameter was assumed not to have altered. Such a drop in C_D would be expected during the transition of a boundary layer, therefore it is hypothesised that the added fibres caused the boundary layer to become turbulent.

As the second section of fibres was added, the C_D rose to 0.57. The projected diameter was not altered in the analysis, hence the increase in C_D may have been due to both the effects of an increase in projected diameter and drag on the fibres caused by airflow travelling through the fluff. The third section of fibres completely filled the front face of the ball, and the C_D was found not to change.

It is now clear that the nap of a tennis ball has a significant effect on the flow of air over the surface. The projected diameter was difficult to measure as the fibres were not as densely packed as those on a normal tennis ball, however had the additional diameter been taken into account in the analysis, the C_D would have dropped. It is hypothesised that any additional C_D, above that accounted for by diameter, is then due to the viscosity of the air travelling through the fibres.

10.1.6 Magnitude of C_D of a tennis ball

The C_D of a normal tennis ball with unmodified nap has consistently been shown to be in excess of 0.5. As mentioned in the previous sections, a C_D of around 0.5 would be expected for a sphere with separation near the apex. It is clear that some of the additional drag is due to skin friction, however this may be as low as 2% of the overall drag. In addition, if this were only an additional skin friction effect, then the contribution would be constant at all wind speeds, however C_D has been shown to reduce with increasing Re at low wind speeds, hence there must be an additional drag parameter present for a tennis ball. As with the discussion in the previous section, the explanation differs depending on whether the air flows through the nap or over it.

Airflow over the surface

If the air is forced to flow around the outside of the fibrous cover of the tennis ball, then the projected diameter will be larger than that calculated, hence the increased C_D becomes a function of unaccounted projected area. As a rough guide, a difference of 1% in the calculated diameter will result in a difference of 2% in the calculated C_D.

This theory can be expanded further when consideration of the data at low wind speeds is included. Although the C_D was constant for most of the wind speeds tested, it was found that C_D of the normal and fluffed nap balls was high at low wind speeds and steadily reduced to a constant at increased wind speeds. The fibres in the nap of a tennis ball are normally randomly configured when not moving or no wind is applied. Using the images presented in figure 10.4, it can be seen that the fibres flatten and the projected area of the ball is inclined to reduce as the wind speed increases, indeed a limit will be formed when

the fibres are unable to flatten any further. It can therefore be concluded that part of the drop in C_D will be due to the effect of aerodynamic drag and the flattening of fibres at increased wind speeds.

The flow visualisation images appear to show some air flowing through the fibres at low wind speeds, so it may be that an alternative or additional drag component is present.

Airflow through the fibres

Assuming that reducing projected area effect does not account for the entire drop, and there is air being forced through the fibres, then the rest of the effect can be explained by microscopic pressure drag on each of the fibres.

As the air flows through the fibres, it is hypothesised that it treats each of the fibres as a small cylinder. Figure 10.5 shows classical C_D plots for a sphere and a cylinder for Reynolds numbers from 0.1 up to 10,000,000. If the fibre were considered to be a very thin cylinder with a diameter of 25 microns (about the size of a human hair), then the Re would range from 5 to around 100 for the wind speeds tested in this study.

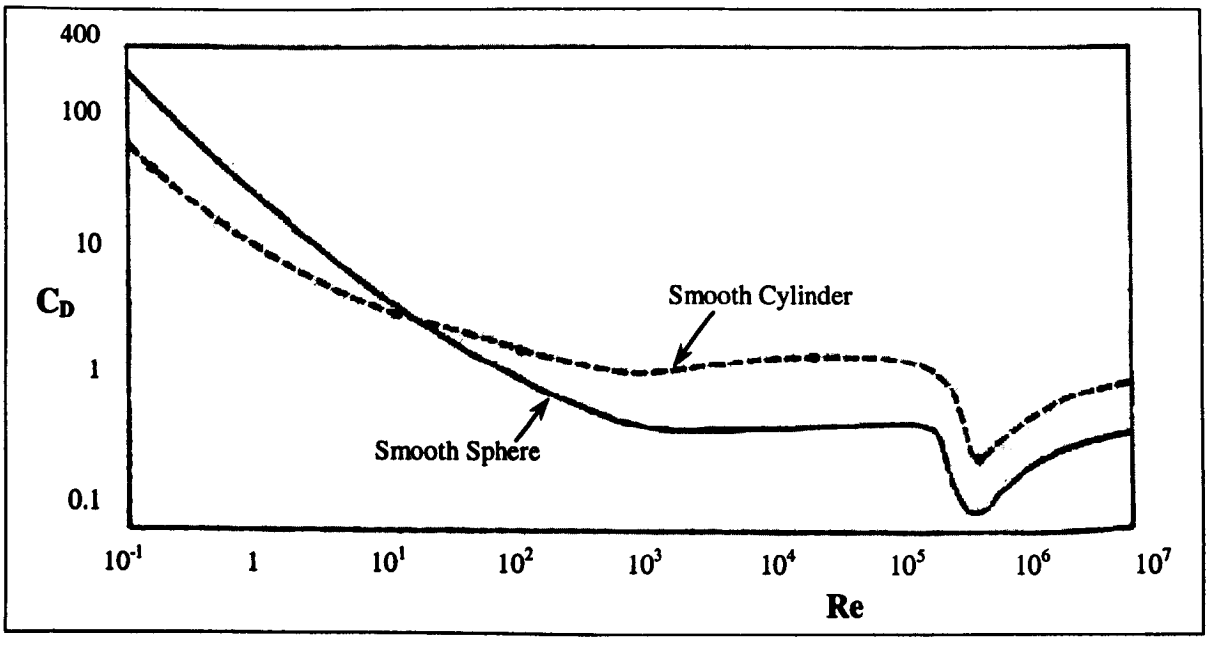

Figure 10.5 C_D for spheres and cylinders at Reynolds numbers from 0.1 up to 10,000,000.

At a Re of 5, it can be seen that the C_D of a cylinder is around 5, and given the fact that there are several hundred fibres in the airflow, the additional drag may be substantial. As the wind speed increases, the orientation of the fibre changes due to the aerodynamic flattening effect, thus reducing the projected area in the airflow, leading to a reduced drag force. It can also be seen that the C_D of a cylinder reduces significantly as Re increases, hence the contribution to the overall drag of the tennis ball will drop substantially at low wind speeds.

At the maximum wind speed, the C_D of the filaments is greater than 1 (one), hence when the fibres are unable to flatten any further, pressure drag on the fibres may remain a significant contributor to the overall drag.

10.2 Diameter effects

The diameter effects have been shown to account for several 'phenomena' throughout this study. It has also been acknowledged that the different C_D results obtained by different research facilities can be explained by the way that the diameter of a tennis ball is measured. In this study, the diameter of the ball is measured using a projection method, which magnifies the ball onto a screen. Other studies replicate the ITF rules by dropping the ball through a ring gauge or vernier callipers. It is commonly found that the diameter obtained using the second method will be smaller than that obtained using the projection method, hence the C_D results will be higher. Rather than creating a common method of measuring the diameter of a tennis ball, the method of presentation can be modified.

*10.2.1 Converting C_D results to C_D*A*

The confusion caused by the effect of the diameter can be eradicated in the analysis phase, achieved by studying the product C_D*A instead of C_D alone. However, as the Re is also a function of the ball's diameter, C_D*A data should be compared against velocity. The resulting plots can be used to compare the drag effects on two similar balls tested in different research institutions. This method is not suitable for comparing balls of different size as the C_D*A results are a function of the size.

Figure 10.6 shows some C_D data that was presented in chapter 7 that has been converted to C_D*A data for shaved, normal and fluffed nap tested in the high-speed wind tunnel. It can be seen that the shaved ball has a lower C_D*A than the normal ball, and the fluffed ball has a higher C_D*A than the normal ball. The trend has not altered, if anything it is more pronounced as the reduced size of the shaved nap ball acted to increase the C_D results hence moving them closer to the normal ball results. Results presented in the form C_D*A versus velocity do not account for differences in size, therefore care should be taken in the interpretation of the plots. Whilst an increase in C_D*A shows a rise in force applied to the ball, it could be due to both an increase in C_D and a larger projected area. However, with the overall aim of the study in mind, a larger C_D*A will help to slow a tennis ball down more quickly.

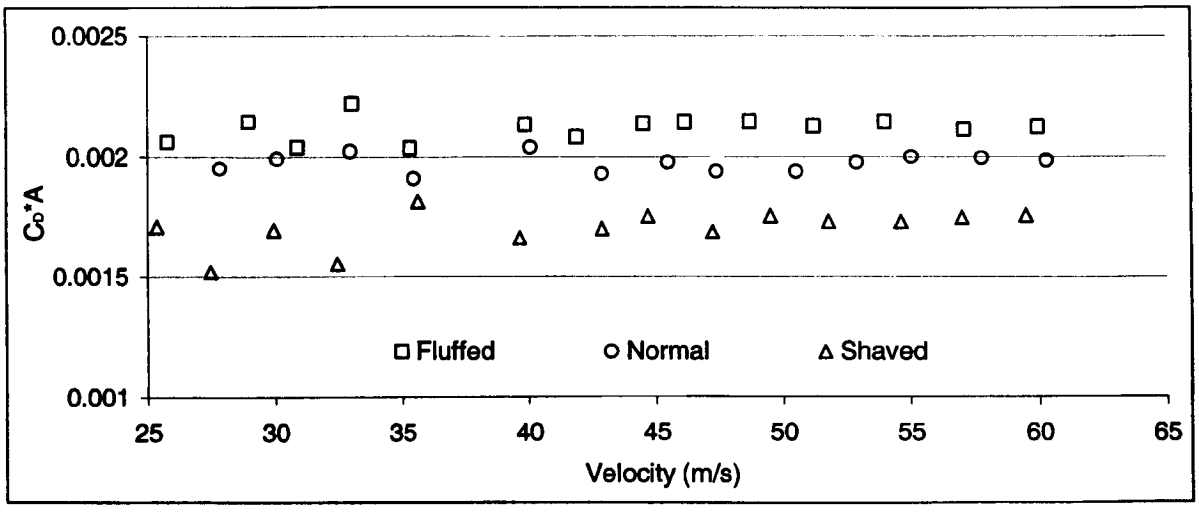

Figure 10.6 C_D*A results plotted against velocity for the shaved, normal and fluffed tennis balls in the high-speed wind tunnel.

Outside of the specific aims of this study, it is currently more conventional to present the data in terms of C_D. This appears to be the first study of sports balls where determination of the diameter has been an issue. Presentation in terms of the dimensionless coefficients of C_D and Re has become expected. For instance, every aerodynamic study uses the well known results for the C_D of a smooth sphere to calibrate a test method. It may be considered that C_D results for tennis balls are meaningless if they cannot be compared directly with other C_D results for tennis balls, however presentation in terms of C_D*A is currently as meaningless if not more so.

10.2.2 Relevant diameter

It has become clear that different methods of measurement have a disabling effect between different research institutions. It is therefore proposed that a common measurement method should be adopted for future studies. Whilst the technique used in this study has been proposed to measure the projected diameter of the tennis ball, it may also lead to some misinterpretation of results. It is clear that air flows through the nap at low wind speeds, and it could therefore be suggested that a measurement method similar to that outlined in the ITF handbook, would give a representative area. As it is known that the pressure drag associated with separation near the apex gives a C_D of around 0.5, any additional drag could be attributed to viscous interaction between the rough surface and the fibres.

However, a possibility remains that the air is forced outside of the fibrous nap and not through it. In this case then the relevant diameter is larger and includes some of the less dense fibrous coating. A measurement method similar to that proposed in this study would then be of interest.

In the absence of a definitive solution, it is proposed that simplicity of measurement method should be considered. The method that utilises calibrated circles to drop the ball through could be considered much simpler than projecting the ball onto a large screen; hence it is proposed that future studies make use of the ITF measurement method.

10.3 Terminal velocity

Several methods to calculate C_D were discussed in chapter 2, however not all of them have been adopted in this study. The method that utilises the terminal velocity of a tennis ball was determined not to be suitable. The drop height required to reach terminal velocity in air is significant, hence this method normally utilises a fluid of higher viscosity than air. It was suggested that water would be suitably viscous, and the tennis ball would reach its terminal velocity within 0.13m.

For accurate analysis the tennis ball would have been required to be soaked in water prior to testing such that all of the air had been removed from the core and the nap. On this

basis, the tennis ball under test would not be in a similar condition to that used in play, and therefore the terminal velocity method was not deemed to be suitable for calculation of representative C_D results.

10.4 Methods to slow the game down

The main aim of this study was to gain an understanding of the aerodynamic properties of tennis balls. As a by-product of this study, methods by which the game of tennis could be slowed down have been determined. There are two main approaches that can be taken to retard a ball more effectively; increase the drag force whilst maintaining the same C_D, or increasing the C_D. The following sections will discuss these two main options and the effects of each on the future of tennis.

10.4.1 Ball size

It rapidly becomes apparent that increasing the size of a sphere can increase the drag force it incurs. It was also well known that the drag of a sphere reduces significantly beyond boundary layer transition. The Reynolds number is a function of the size of the ball, so it is possible that the increased size could induce premature transition at a lower velocity. Overall, the increased drag force is incurred if the flow remains in the subcritical or transcritical regime throughout the flight.

It has been repeatedly shown that there is no significant change in C_D for all of the higher airflow velocities studied, and the flow is in the transcritical regime. The C_D has been shown to increase at reduced wind speeds, however these are significantly less than the projection speeds observed in open play, therefore simple analysis using the following equation:

$$F_D = \frac{1}{2}\rho v^2 C_D A \qquad (10.1)$$

shows that for every 5% increase in the diameter of the ball, there will be an increase of around 10% in the drag force. It can therefore be concluded that the F_D can be increased significantly with a less significant increase in the size of the ball.

10.4.2 Surface properties

The game of tennis has not altered much over the years, with the change in colour from white to yellow being the most significant change to the tennis ball. It is therefore fair to assume that any proposed change will be opposed, and the more significant the requested change, the more fervent the opposition. An increase in the size of the ball is a significant visible change.

In chapter 7 it was shown that the C_D of a tennis ball might be increased by 'fluffing' its surface, the increase can be as much as 6% however there is very little control. Equation 10.1 shows that C_D is directly proportional to drag force, however this increase in F_D is a compound effect as the analysis already accounted for the effect of a larger projected diameter.

Using the results shown in section 7.2.2 as an example, the C_D of the fluffed nap ball was found to be approximately 2.9% higher than that of the ball with the normal nap. The C_D*A results show that the aerodynamic properties of a fluffed tennis ball induce a drag approximately 7.1% greater than that on the ball with a normal nap. It is therefore clear that the properties of the cover of a tennis ball play a significant role on its drag. It can be concluded that a combination of surface properties that induce either increased drag as air flows over and through the porous surface, or early separation if possible, will lead to a higher C_D.

The nap of a tennis ball will change its properties every time it is struck with a racket or impacts with the ground. It is therefore possible that the surface of the ball changes significantly enough for this effect to be seen in the game of tennis currently, and a ball with a normal nap may soon resemble one with a fluffed nap. Although the fluffing of the nap has been shown to produce the desired effect the control of the surface requires improvement. It may be possible that an alternative tennis ball covering could be developed to increase the drag. The aerodynamic properties of tennis balls appear to be unique however, and care must be taken that such that a new covering does not have an adverse effect.

10.4.3 Effect on the game of tennis

A change to the tennis ball will demand interest from tennis players, and any proposed change will require suitable results to support the decision. The 'feel' of the game is of great importance to players, and the more significant the proposed change, the more the feel of the game is likely to be affected. Of the two proposed changes discussed thus far, it is assumed that an increase in the size of the ball is more significant than a change in nap, players will perceive it to feel heavier and may be cause more injuries.

The trajectory model that was developed in chapter 4 can be used to develop a better understanding of the effect of these proposed changes on the flight of the ball. Figure 10.7 shows three simulated trajectories for the normal, fluffed and an 8% oversized ball projected at 60ms^{-1} and an elevation of 2.5°.

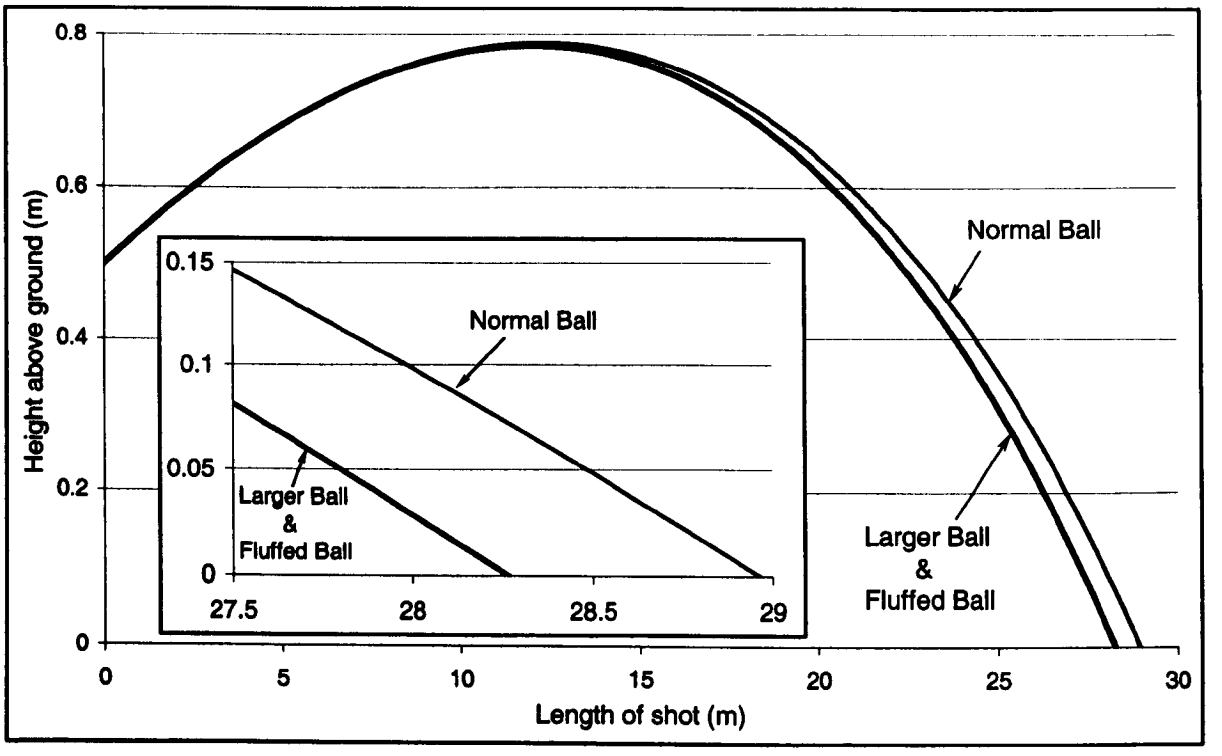

Figure 10.7 Simulated trajectories for a normal ball with normal nap, normal ball with fluffed nap and 8% larger ball with normal nap projected at 60ms^{-1} at an elevation angle of 2.5°, inset shows magnified image of landing area.

The aerodynamic properties and dimensions used in the model are those obtained in this study. It can be seen that both the larger ball and the fluffed ball land approximately 0.75m

shorter than the ball with the normal nap. Even in the magnified inset image of the landing area, it is difficult to distinguish between the two high drag options. It can therefore be concluded that an 8% larger ball with normal nap follows a very similar trajectory to that of a normal sized ball with a fluffed nap.

Although the flight path of the shot is a useful sign of the effect of the proposed change, it is the reduction in speed that is of more interest. Investigation of the trajectory data showed that on impact with the ground, the velocity of the two high drag balls was within 0.05% of each other and almost 5% lower than that of the normal ball with the normal nap.

The time taken to reach the landing points shown thus far are very similar as would be expected, however the large and fluffed balls have travelled less distance. In order to compare the relative flight times and propose the benefits of using the larger or fluffed balls, the length of shot should be similar. By changing the projected elevation angle to 2.65° for the larger and fluffed balls, the landing area of all three trajectories becomes similar, and it takes more than 19ms longer for the larger and fluffed ball to arrive.

It should be noted that this is only an indicative representation, as the effect of these ball changes does not end with the aerodynamics, indeed any change to the ball will probably affect the way it comes off the racquet and impacts with the ground. A broader, more complete investigation is required before enough understanding is available to make definitive conclusions.

10.5 Final conclusions

At the beginning of this study, several objectives were presented, and this section will discuss how these have been achieved.

10.5.1 To develop a method to obtain the aerodynamic forces acting on a tennis ball.

Several methods were developed for calculation of the aerodynamic forces acting on a tennis ball, however it was found that the most reliable results were obtained using a load

cell configuration. Two separate test methods were created such that both non-spinning and spinning C_D results could be obtained.

The C_D of a normal unmodified tennis ball was found to be around 0.53. Modification of the nap to increase the fluff increased the C_D by as much as 6%, conversely, shaving the fibres reduced the C_D by approximately 6%. The shaved ball was shown to act more like a classic rough ball, and a transition was clearly observed. The flow regime of the unmodified and fluffed balls was shown to be transcritical with the use of a large ball.

Spinning tests were performed using an unmodified normal sized tennis ball in the low-speed wind tunnel and the following relationships were developed:

$$C_D = 0.5365 + \left(1.9980 \left(\omega / v \right)^{-2.1887} + 2.8619 \right)^{-0.7069}$$

$$C_L = \left(2.591 \left(\omega / v \right)^{-1.877} + 4.809 \right)^{-0.529}$$

There were three other methods of calculating C_D that were developed throughout this study, however the results obtained were not as reliable as those obtained with the load cell. It is clear however, that with further development and improved apparatus, some of these methods may be improved in the future. This is of specific interest to the combined calculation of both drag and lift, and it is proposed that three-dimensional analysis could be employed. The error analysis developed in this study showed that the methodology was adequate providing that the position of the ball can be accurately modelled, and computer packages available now (and most certainly in the future) will enable improved analysis.

10.5.2 To determine and understand any differences in aerodynamic properties between ball designs.

The C_D results of unmodified pressurised tennis balls and unmodified permanent pressure tennis balls were presented in chapter 5. It was shown that the C_D of both was similar ($\approx$0.53), and within the standard deviation and associated errors of the test method.

10.5.3 To define and use techniques to develop a qualitative understanding of the flow of air over and through the surface of tennis balls.

Two techniques were used to discuss the qualitative properties of the airflow over or through the surface of the tennis ball. Flow visualisation techniques were utilised to assess both non-spinning and spinning balls, whilst pressure distribution methods were utilised for non-spinning balls only.

It was found that both flow visualisation and pressure distribution data showed that separation occurred near the apex, leading to a large wake and therefore large associated pressure drag. By connecting qualitative data together with C_D data obtained using different test methods, it was possible to define laminar and turbulent images and plots.

With the use of flow visualisation, it was also possible to show that air appears to flow through the fibres in the nap of the tennis ball at low wind speeds, which suggested the presence of additional drag parameters.

The lift/side force that acts on a spinning ball is produced by asymmetrical separation that was clearly observed using flow visualisation techniques. The effect of the spin was shown to diminish as the wind speed increased. Similarities were shown between images of similar spin parameter with different spin rates and wind speeds.

10.5.4 To develop a model to predict the behaviour of a tennis ball's flight through the air.

The computational trajectory model was created near the start of the study and was developed throughout, as new data became available. The model was created using the equations of motion for a spinning sphere, and used an iterative process to calculate the co-ordinates of the ball with changing speed, elevation angle, drag and lift.

The resulting trajectory model was presented in chapter 4, and it was shown to predict the flight of captured ball trajectories very well. The analysis covered a range of projection speeds and spin rates and all flight paths were simulated, even the flight time compared

well. Advanced analysis used the computational trajectory model to define the flight paths of several of the ball types used in this study. The differences in flight paths could be used qualitatively, however upon interrogation of the model, quantitative analysis could also be discussed.

10.6 Future work

The understanding of the aerodynamic properties of tennis balls has been advanced significantly by this study, however there is significant scope for further work in this area. The following sections describe future work that may be undertaken to further increase the understanding of the aerodynamic properties of tennis balls.

10.6.1 C_D and C_L of a spinning tennis ball using a specifically designed load cell

The three component wind tunnel balances used in this study were designed as general purpose test equipment. The forces obtained for a tennis ball were a fraction of those that the three component wind tunnel balance was designed for, therefore sensitivity was low. In addition the C_D and C_L results were gathered separately using only the drag component of the balance.

The C_D and C_L results obtained in this study using this equipment were repeatable and contained low associated errors. It is possible to conclude however, that the results could be improved by the use of a load cell specifically designed to measure the lift and drag forces simultaneously on a spinning tennis ball.

Since the completion of this study, the ITF have procured a new wind tunnel with a dedicated load cell system for measuring the drag and lift forces simultaneously. The wind tunnel is currently sited at the University of Sheffield and, along with the load cell system, is undergoing calibration.

10.6.2 Computational Fluid Dynamics (CFD)

Computational Fluid Dynamics has been used widely to analyse the flow over and through a variety of objects. The results obtained using any computational method are only as reliable as the input parameters used to define the problem. A CFD model is therefore meaningless without the empirical wind tunnel data or well developed calculations to back them up. Wind tunnel usage has been in decline in recent years whilst CFD usage has been on the increase. A CFD model will nearly always give a result, however the reliability of the result is not always fully understood. With an accurate model, computational packages are extremely powerful, and may significantly speed up the rate at which results could be obtained.

CFD models have been created for tennis balls where the roughness has been assumed to remain similar throughout. A CFD model created using rough ball relationships between C_D and Re would be suitable for a tennis ball with an extremely well worn surface, as simulated by the shaved nap. It has repeatedly been shown however, that the C_D of a tennis ball is greater than that of a smooth ball and cannot be described by the classical understanding of the aerodynamics around rough spheres. It has also been shown that not only do the fibres continually rearrange themselves whilst the ball moves through the air or moving air flows over it, but the fibres flatten at increased wind speed, so a tennis ball has variable roughness and changes shape as Re increases.

The understanding of the airflow around tennis balls has been expanded significantly during this study, however it is not thought that enough is known at this stage to create an accurate CFD model. It is proposed that a feasibility study should be performed to define the data that is required to develop a computational model. The outcome of such a study would define specific empirical analyses that could be used as the foundation to create a more accurate CFD model for tennis balls.

10.6.3 Acoustic study of the noise levels in the boundary layer

The noise levels in the boundary layer can be used to determine the flow regime in it. In its simplest form the apparatus required for this test method is a stethoscope and a method of

recording the amplitude of noise. The boundary layer of the wind tunnel itself can be used as way of calibration, where the flow over flat plates is well understood. In general, a laminar boundary layer is heard as a 'swishing' noise, whereas the turbulent boundary layer 'crackles'.

Some simple analyses were attempted near the end of the study, but as this test method was not intended as part of this study, the equipment available was not suitable for such a complex requirement. A stethoscope was used to listen to the boundary layer and a microphone was inserted into the earpiece. The microphone was attached to a computer with software capable of converting the noise levels into graphs of amplitude against time. Unfortunately, the system also picked up external noise and gave inconsistent results.

The equipment required to further this investigation is not thought to be complex or expensive, primarily something more suited to the requirements. Whilst more accurate positioning of a delicate sensor is likely to be required, it is more an improvement in the control of the surroundings that will return improved reliability.

10.6.4 Fibres on a smooth flat plate

The addition of fibres to the surface of a smooth ball returned results that have been used to discuss how the flow differs between a smooth ball and a tennis ball. The data obtained was of great interest and showed that a relatively small number of fibres make a significant difference to the type of flow over the ball's surface, and it is proposed that similar analyses could be performed using a flat plate. Analyses of the flow over flat plates are incredibly well understood, and the understanding is far superior to that of flow around spheres. It is therefore proposed that the test method developed in this study should be extended to smooth flat plates, and expanded significantly to help the understanding of the flow over and through the fibres of tennis ball nap.

REFERENCES

Achenbach E. (1972) Experiments on the flow past spheres at very high Reynolds numbers. *Journal of Fluid Mechanics*, **54** (3), 565-575.

Achenbach E. (1974) The effect of surface roughness and tunnel blockage on the flow past spheres. *Journal of Fluid Mechanics*, 65, 113-125.

Asai T. & Akatsuka T. (1998) The physics of football. *Physics World*, **June 1998**, 25-27.

Bartlett R.M. (1986) Floating serve in volleyball. *Crewe & Alsager College of Higher Education.*

Bearman P.W. & Harvey J.K. (1976) Golf ball aerodynamics. *Aeronautical Quarterly*, **27**, 112-122.

Bown W. & Mehta R.D. (1993) The seamy side of swing bowling. *New Scientist*, **139** (1887), 21-24.

Brancazio P.J. (1985) The physics of kicking a football. *The Physics Teacher*, **23**, 403-407

Briggs L.J. (1959) Effect of spin and speed on the lateral deflection (curve) of a baseball; and the Magnus effect for smooth spheres. *American Journal of Physics*, **27**, 589-596.

Brody H. (1987) *Tennis Science for Tennis Players*. Univ. of Pennsylvania Press, Philadelphia.

Brody H. & Cross R. (2000) Proposals to slow the serve in tennis. In: *Tennis Science and Technology: Proceedings of the 1st International Conference on Tennis Science and Technology* (ed S.J. Haake & A.O. Coe), pp. 261-268. Blackwell Science, Oxford.

Brown T.M.C. & Cooke A.J. (2000) Aeromechanical and aerodynamic behaviour of tennis balls. In: *Tennis Science and Technology: Proceedings of the 1st International Conference on Tennis Science and Technology* (ed S.J. Haake & A.O. Coe), pp. 145-153. Blackwell Science, Oxford.

Brown T.M.C. (1997) *Aerodynamics of tennis ball*, 4th year project, Cambridge University.

Cartwright A. (1997) *Tennis ball aerodynamics*, 4th year project, Cambridge University.

Cislunar Aerospace Incorporated (2000) *Sample spin data – U.S. Open (website).*

Cooke A.J. (1992) *The aerodynamics and mechanics of shuttlecocks*, PhD Thesis, New Hall, Cambridge University.

Cooke A.J. (2000) An overview of tennis ball aerodynamics. *Journal of Sports Engineering*, **3**, 123-129.

Daish C.B. (1972) *The Physics of Ball Games.* English Universities Press, London.

Davies J. (1949) The aerodynamics of golf. *Journal of Applied Physics*, **20**, 821-828.

Depra P. (1998) Fluid mechanics analysis in volleyball. In: ISBS '98*: Proceedings of the 16th International Symposium on Biomechanics in Sports* (ed H.J. Riehle & M.M. Vieten), pp. 85-88. UVK - Universitätsverlag Konstanz, Germany.

Douglas P. (1991). *The Handbook of Tennis*. Knopf, New York, NY.

Dryden H.L. & Heald R.H. (1926) Investigation of turbulence in wind tunnels by a study of the flow about cylinders, NACA Report 231, pp. 17.

Dryden H.L. & Kuethe A.M. (1931) Effect of turbulence in wind-tunnel measurements, NACA Report 342, pp. 26.

Dryden H.L., Schubauer G.B., Mock W.C. Jr & Skramstad H.K. (1938) Measurements of intensity and scale of wind-tunnel turbulence and their relation to the critical Reynolds number of spheres. NACA Report 581, pp. 32.

Erlichson H. (1983) Maximum projectile range with drag and lift, with particular application to golf. *American Journal of Physics*, **51**, 357-362.

Frohlich C. (1981) Aerodynamic effects on discus flight. *American Journal of Physics,* **49** (12), 1125-1132.

Frohlich C. (1983) Aerodynamic drag crisis and its possible effect on the flight of baseballs. *American Journal of Physics,* **52** (4), 325-334.

Gobush W., Pelletier D. & Days C. (1994) Video monitoring system to measure initial launch characteristics of golf ball. In: *Science and Golf II: Proceedings of the World Scientific Congress of Golf* (ed A.J. Cochran & M.R. Farally), pp. 327-333. E & FN Spon, London.

Haake S.J., Chadwick S.G., Dignall R.J., Goodwill S. & Rose P. (2000) Engineering tennis – slowing the game down. *Journal of Sports Engineering*, **3**, 131-143.

Hoerner S.F. (1965) *Fluid Dynamic Drag,* Hoerner Fluid Dynamics.

Hubbard M. & Rust H.J. (1984) Simulation of javelin flight using experimental aerodynamic data. *Journal of Biomechnics*, **17** (10), 769-776.

Hubbard M. & Alaways L.W. (1987) Optimum release conditions for the new rules javelin. *International Journal of Sports Biomechanics*, **3**, 207-221.

Lanspeary P.V. (1997) *Establishing very low speed disturbance-free flow for anemometry in turbulent boundary layers*, PhD Thesis, The University of Adelaide.

Lanspeary P.V. & Bull M.K. (1998) A mechanism for laminar three-dimensional separation in duct contractions. In: *Proceedings of the 13th Australasian Fluid Mechanics Conference.*

Lyttleton R.A. (1957) The swing of a cricket ball. *Discovery*, **18**, 186-191

MacColl J.W. (1928) Aerodynamics of a spinning sphere. *Journal of the Royal Aeronautical Society*, **32**, 777-798.

Magnus J.R. & Klaasen F.J. (1999) *The effect of new balls in tennis: four years at Wimbledon.* The Statistician, **48** (2), 239-246.

Massey B.S. (1989) *Mechanics of Fluids* (6th edition), Van Nostrand Reinhold.

McElroy G.K. (1980) Understanding the volleyball float serve. *Sports Coach (Australia)*, 35-37.

McPhee J.J. & Andrews G.C. (1987) Effect of sidespin and wind on projectile trajectory, with particular application to golf. *American Journal of Physics*, **56** (10), 933-939.

Mehta R.D. & Wood, D. (1980) Aerodynamics of the cricket ball. *New Scientist*, **87**, 442-447.

Mehta R.D., Bentley K., Proudlove M. & Varty P. (1983) Factors affecting cricket ball swing. Nature, **303**, 787-788.

Mehta R.D. (1985) Aerodynamics of sports balls. *Annual Review of Fluid Mechanics*, **17**, 151-189.

Mehta R.D. & Pallis J.M. (2001) The aerodynamics of tennis balls. *Journal of Sports Engineering*, **4** (4), 177-191.

Mehta R.D. & Pallis J.M. (2001) Sports ball aerodynamics: effects of velocity, spin and surface roughness. *Material and Science in Sport*, pp. 185-197.

Mehta R.D. (2000) Cricket ball aerodynamics: myth versus science. In: *The Engineering of Sport: Proceedings from the 3rd International Conference on the Engineering of Sport* (ed A.J. Subic & S.J. Haake), pp. 153-167. Blackwell Science, Oxford.

Milne-Thomson L.M. (1973) *Theoretical aerodynamics. - 4th ed.* New York

Neville N.D. (1996) *The aeromechanics of tennis balls*, 4th year project, Cambridge University.

Newton, I. (1672) New theory of light and colours. *Philosophical Transactions of the Royal Society London*, **1**, 678-688.

Pallis J.M. & Mehta R.D. (2000) Tennis science collaboration between NASA and Cislunar Aerospace. In: *Tennis Science and Technology: Proceedings of the 1st International Conference on Tennis Science and Technology* (ed S.J. Haake & A.O. Coe), pp. 135-144. Blackwell Science, Oxford.

Penrose J.M.T., Hose D.R. & Trowbridge E.A. (1996) Cricket Ball Swing: A preliminary analysis using computational fluid dynamics. In: *The Engineering of Sport: Proceedings of the 1st International Conference on the Engineering of Sport* (ed S.J. Haake), pp. 11-19. Balkema, Rotterdam.

Persen L.N. (1972) *Introduction to boundary layer theory.* Tapir Forlag.

Pope A. & Harper J. (1966) *Low-Speed Wind Tunnel Testing.* John Wiley & Sons, New York.

Quyao J. (1989) Aerodynamics and throwing analysis of javelin. In: *The 4th Asian Congress of Fluid Mechanics*, pp. C161-C164.

Raskin J. (1994) Foiled by the Coanda Effect (an alternative way of explaining lift). *QUANTUM The Magazine of Math and Science,* **Sep/Oct 1994**, p4.

Rayleigh Lord. (1877) On the irregular flight of a tennis ball. *Messenger of Mathematics*, **7**, 14-16.

Rex A.F. (1985) The effect of spin on the flight of batted baseballs. *American Journal of Physics,* **53**, 1073-1075.

Rosenhead L. (1963) *Laminar boundary layers.* Oxford, England: Oxford University Press.

Rules of tennis, 2000. ITF

Sayers A.T. (2002) Experimental modelling of the flow around a cricket ball – reverse swing. *Proceedings from the 1st International Conference on Heat Transfer, Fluid Mechanics, and Thermodynamics.*

Schlichting H. *Boundary-layer theory - 8th rev. (2000).* Springer.

Sherwin K. & Sproston J.L. (1982) Aerodynamics of a cricket ball. *Int. J. Mech. Educ.*, **10**, 43-50.

Shapiro A.H. (1964) *Shape and flow: the fluid dynamics of drag.* Anchor, London.

South N. (1996) *Aeromechanical behaviour or the tennis ball,* 4th year project, Cambridge University.

Stepanek A. (1988) The aerodynamics of tennis balls - The topspin lob. *American Journal of Physics,* **56** (2), 138-142.

Tait P.G. (1893) On the path of a rotating spherical projectile (with a plate). *Trans. Roy. Soc. Edin.*, **37**, 427-440.

Tait P.G. (1896) On the path of a rotating spherical projectile II (with a plate). *Trans. Roy. Soc. Edin.*, **39**, 491-506.

Tan A., Frick C.H., & Castillo O. (1986) The fly ball trajectory: An older approach revisited. *American Journal of Physics,* **55** (1), 37-39.

Tennis: a professional guide Distributed by Harper & Row (1984)

Thompson J.J. (1910) The dynamics of a golf ball. *Nature*, **85**, 2151-2157.

Thompson R. (1964) Experimental determination of the lift and drag of a spinning ball. *Mech. Engng. Educ.*, **3**, 9-11

Watts R.G. & Ferrer R. (1987) The lateral force on a spinning sphere: Aerodynamics of a curveball. *American Journal of Physics,* **55** (1), 40-44.

Watts R.G. & Sawyer E. (1975) Aerodynamics of a knuckleball. *American Journal of Physics,* **43**, 960-963.

Zagarola M.V., Lieberman, B. & Smits, A.J. (1994) An indoor testing range to measure the aerodynamic performance of golf balls. In: Science and golf II: Proceedings of the World Scientific Congress of Golf (ed A.J. Cochran & M.R. Farally) pp. 349-354. E & FN Spon, London.

Zayas J. M. (1985) Experimental determination if the coefficient of drag of a tennis ball. *American Journal of Physics,* **54** (7), 622-625.

APPENDIX A: C_D DERIVED USING THE TRAJECTORY OF A PROJECTED BALL

A.1 Introduction

As mentioned in chapter 2, there are three main methods that can be used to find aerodynamic forces on the tennis ball. Two of the methods use motion analysis whilst the third utilises load cells. The methods using motion analysis have many common features, however one utilises a complete trajectory of a projected ball whilst the other uses the trajectory of a ball dropping through the moving air of a wind tunnel. The main advantage to these methods is that experiments to find both drag and lift forces can be set up with relative ease. This chapter documents the theory, methods and results obtained using the trajectory of a projected ball to calculate C_D.

A.2 Theory

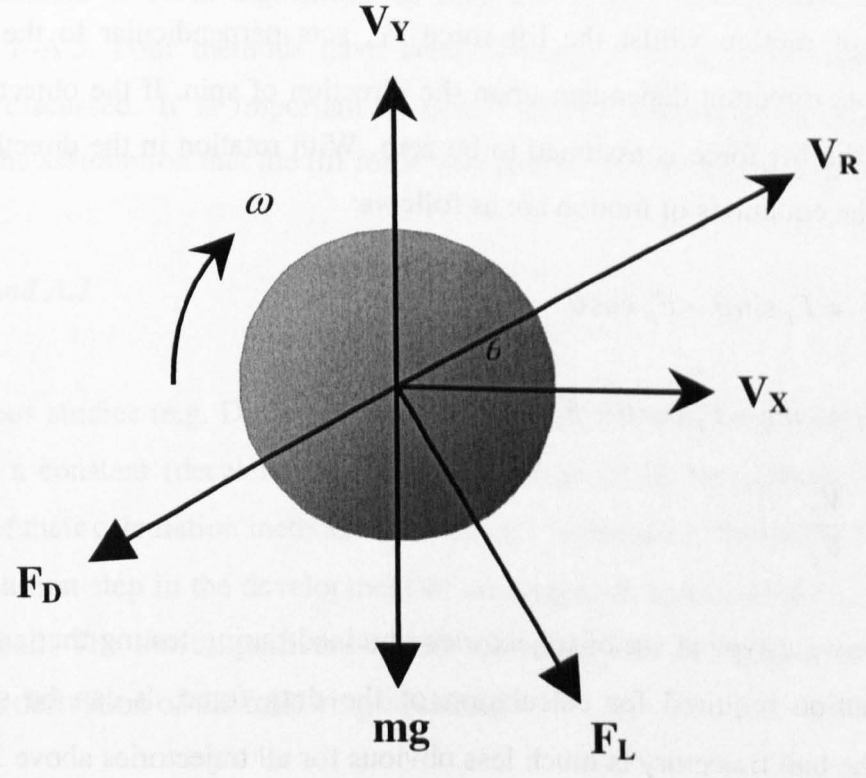

Figure A.1 A force diagram for a ball spinning in the direction of ω travelling at $V_R ms^{-1}$ at θ degrees to the horizontal.

At this point it is useful to remind the reader of the equations obtained when considering an object moving through the air. There are three component forces acting on it; gravity, drag and lift. Both drag and lift forces are functions of the object properties and the atmospheric conditions, and can be described by the following equations:

$$F_D = \frac{1}{2}\rho v^2 A C_D \tag{A.1}$$

$$F_L = \frac{1}{2}\rho v^2 A C_L \tag{A.2}$$

where; F_D and F_L are drag and lift forces respectively

ρ is the density of the fluid within which the object is moving

v is the velocity of the object moving through the fluid, or, the velocity of the fluid moving over the object

A is the *projected* area of the object

C_D and C_L are the drag and lift coefficients respectively

Figure A.1 shows a force diagram for a ball spinning in the direction of ω travelling at $V_R ms^{-1}$ and θ degrees to the horizontal. The drag force, F_D, acts in the opposite direction to the direction of motion whilst the lift force F_L, acts perpendicular to the direction of motion, with its direction dependant upon the direction of spin. If the object is travelling without spin, the lift force is assumed to be zero. With rotation in the direction shown in the diagram, the equations of motion are as follows:

$$m\frac{dV_X}{dt} = F_L \sin\theta - F_D \cos\theta \tag{A.3}$$

$$m\frac{dV_Y}{dt} = -mg - F_L \cos\theta - F_D \sin\theta \tag{A.4}$$

$$\tan\theta = \frac{V_Y}{V_X} \tag{A.5}$$

Figure A.2 shows a typical set of trajectories obtained during testing that can be used to gather information required for calculation of the drag force. It can be seen that the curvature of the ball trajectory is much less obvious for all trajectories above 30mph in the space available for these tests. It can also be seen that the data has been corrected to show the displacement starting at (0,0); rather than plotting a height above the ground, it is the height above the datum or origin.

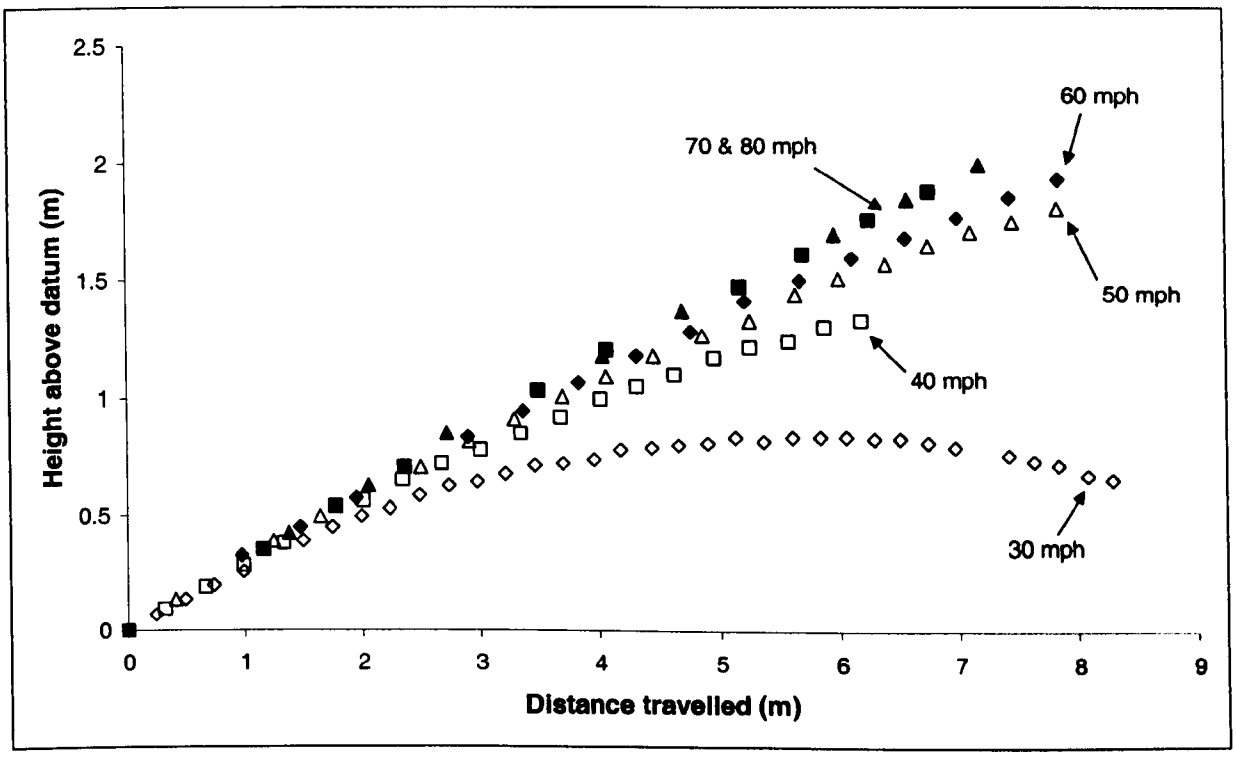

Figure A.2 Graph to show real trajectories obtained during testing for the normal pressurised balls projected at 30mph up to 80mph with zero spin.

It is now possible to form algorithms to find the drag force required by combining equations A.1–A.5. Four methods have been devised in all, and the reasons for each method are discussed. It is important to note that the following methods were made possible by the assumption that the lift force was zero when the ball was not spinning.

A.2.1 Method A.1

Many previous studies (e.g. Davies (1949) & Stepanek (1988)) have used the assumption that there is a constant (decelerating) force applied to a ball throughout its flight as the foundation of their calculation methods. Method A.1 is based on Newton's 2nd law and was designed as a first step in the development of an algorithm to calculate C_D from the flight of a tennis ball. The most significant benefit however, lies in its ease of application as shown in the derivation of the following equations:

$$F_x = ma_x \tag{A.6}$$

$$F_y = m(a_y - g) \tag{A.7}$$

Combining A.6 and A.7 gives:

$$F_D = \sqrt{F_x^{\,2} + F_y^{\,2}} \tag{A.8}$$

Hence C_D can be calculated using equation A.1.

Although it is not clear in figure A.2, the data used in this analysis contains significant scatter. The image analysis technique will be discussed in more detail in section A.5, the following briefly describes some of the difficulties encountered. Due to the large distance to be captured for a complete trajectory, the ball may take up as little as 0.005% of the trajectory image with a resolution of 360 x 240. With the ball accounting for only 4 pixels, and a ball diameter being approximately 66mm, it is clear that significant errors may be introduced. All future calculations of angle, velocity and acceleration will be affected.

The following three methods all start with equation A.1 and are modified to eliminate parameters known to contain significant errors.

A.2.2 Method A.2

The distance travelled in the horizontal direction is significant compared to the height above the datum, thus any errors associated with data collection of vertical displacements should be minimised. Method A.2 is designed to use horizontal data only:

$$F_D = ma = m\frac{a_x}{\cos\theta} = m\frac{\ddot{x}}{\cos\theta} \tag{A.9}$$

$$v = \frac{v_x}{\cos\theta} = \frac{\dot{x}}{\cos\theta} \tag{A.10}$$

Substituting equation A.1 gives:

$$C_D = \frac{2m\ddot{x}\cos\theta}{\rho A\dot{x}^2} \tag{A.11}$$

Thus method A.2 uses $\dot{x}$, $\ddot{x}$ and $cos\theta$ to calculate C_D.

A.2.3 Method A.3

This method is similar to that in method A.2, but rather than reducing equation A.1 to horizontal parameters it is reduced to vertical parameters. It is thought that the constantly changing angle may affect the results obtained. Method A.2 used a cosine term and it may be that the larger variation in the sine term may give preferable results. Method A.3 is designed to use vertical data only:

$$F_D = ma = m\frac{(a_y - g)}{\sin\theta} = m\frac{(\ddot{y} - g)}{\sin\theta} \tag{A.12}$$

$$v = \frac{v_y}{\sin\theta} = \frac{\dot{y}}{\sin\theta} \tag{A.13}$$

Substituting equation A.1 gives:

$$C_D = \frac{2m(\ddot{y} - g)\sin\theta}{\rho A\dot{y}^2} \tag{A.14}$$

Thus method A.3 uses $\dot{y}$, $\ddot{y}$ and $sin\theta$ to calculate C_D.

A.2.4 Method A.4

It has been mentioned that the changing angle might induce large errors into the analysis. In the same way that the analysis concentrates on one direction in methods A.2 and A.3, method A.4 has been minimised so that it does not contain any angle terms. Should there be any problem with the computation of angle, then method A.4 should be an improvement.

$$F_D = ma = m\left(a_x^2 + (a_y - g)^2\right)^{1/2} = m\left(\ddot{x}^2 + (\ddot{y} - g)^2\right)^{1/2} \tag{A.15}$$

$$v = \left(V_x^2 + V_y^2\right)^{1/2} = \left(\dot{x}^2 + \dot{y}^2\right)^{1/2} \tag{A.16}$$

Substituting equation A.1 gives:

$$C_D = \frac{2m\left(\ddot{x}^2 + (\ddot{y} - g)^2\right)^{1/2}}{\rho A\left(\dot{x}^2 + \dot{y}^2\right)} \tag{A.17}$$

Thus method A.4 uses values of $\dot{x}$, $\ddot{x}$, $\dot{y}$ and $\ddot{y}$ to calculate C_D without using sines or cosines of angles.

A.3 Test method

An indoor sports hall was used to record the trajectories of tennis balls to eliminate the effect of weather on the data collection. The width of the sports hall was used for the trajectory, whilst the camera was positioned along the length.

The apparatus for this test method comprises a projection device and a method of recording the trajectory of the ball. A JUGS pitching machine was used to project the balls and is described in detail in section 3.2.1. Two digital high-speed digital video recorders were required in order to capture a complete set of data; one positioned at the exit of the JUGS machine and the other positioned to capture the complete trajectory. Digital KODAK Motioncorders, as described in section 3.3, were used in both positions during this test method, and the following sections describe details required specifically for the projectile test method.

A.3.1 Trajectory capture

The first camera was required to capture balls travelling at speeds up to 100mph. To avoid a blurred image, the exposure was set at a minimum of $1/10{,}000$ second. Also, to ensure that there were sufficient images to obtain accurate output data, the frame rate was set to a maximum of 600 frames per second. The exit of the ball projection device was illuminated using two halogen spotlights to ensure that the image intensity obtained was high enough to allow analysis.

The second camera covered the whole trajectory. During set-up it was decided that the number of points required to accurately depict the trajectory suggested a frame rate of 240 frames per second. This also gives the advantage of a full screen. Three 500W floodlights illuminated the trajectory and the light intensity varied along the trajectory, the exposure rate was set to the minimum required to ensure a complete trajectory could be analysed. As

the natural light source shifted, the light intensity varied and hence the exposure rate was altered to allow for this. Figure A.3 shows a ball soon after leaving the JUGS machine and depicts a typical trajectory.

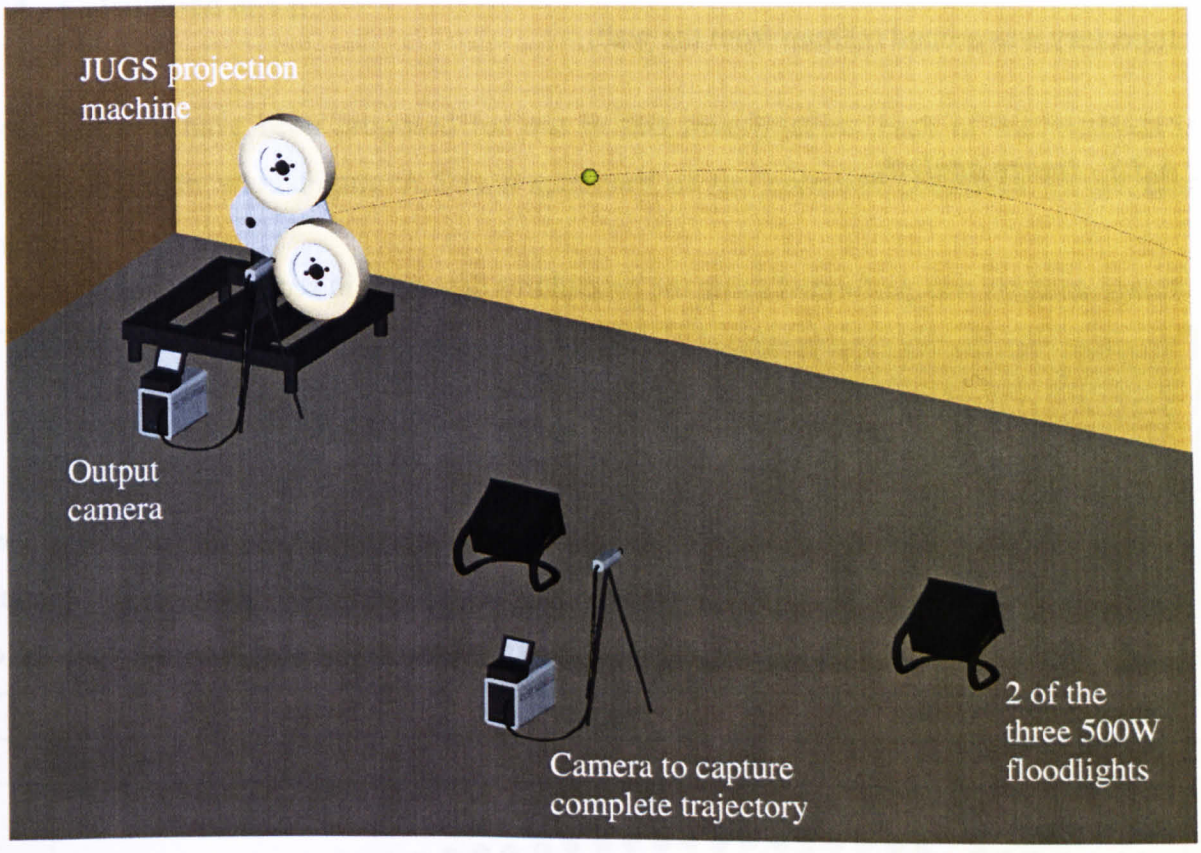

Figure A.3 Picture to show the apparatus used to capture high-speed digital images of a projected tennis ball.

Testing involved setting the dials on the projection device to the desired nominal speed and dropping the ball into the chute. The two cameras were activated at the same instant, triggered using a single impulse. Upon completion of the recording phase, the recorded images were viewed directly from the dynamic memory to find the images of interest. The complete trajectory (including a few frames prior to its start) was recorded directly onto Hi8 videotape at a frame rate of 2 frames per second.

A.3.2 Calibration

A means of calibration was required to ensure that the data obtained from both cameras was applicable. A black board with 100mm squares marked out with white tape was used

for the first camera, positioned in the plane of the trajectory at the output of the bowling machine, and recorded onto the videotape. Reference points positioned 7 metres apart on the wall behind the trajectory were used for the second camera, however stability requirements of the JUGS meant that the base was large, and therefore the plane of the trajectory was around 600mm from the wall.

A.3.3 Image analysis

Image analysis was performed using the procedures described in section 3.3.

A.3.4 Manipulation of data

When all of the co-ordinates for a particular trajectory have been exported, the trajectory can be seen in a graphical form. Figure A.4 shows a graph of distance travelled against height above the origin for a normal pressurised ball projected at a nominal velocity of 30mph with zero spin.

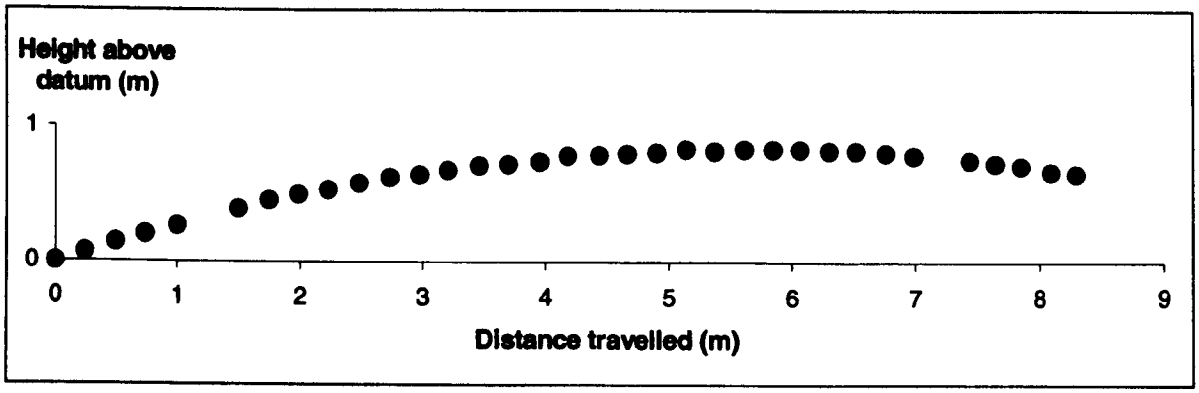

Figure A.4 A typical trajectory for a tennis ball projected with an initial nominal velocity of 30mph, an angle of 16 degrees to the horizontal and zero spin.

The co-ordinates are corrected such that at time equals zero the ball travel and height are zero, hence the origin is set. There are gaps in the data that arise from poor quality images of the ball, caused by either insufficient illumination or interlacing during digitising. The time step between each image is a known constant, hence when a break in data occurs, the time step is multiplied to give the correct data point. Manipulation of the change in distance travelled and height can be obtained with respect to time to give the component

velocities, which can then be used to calculate the accelerations. The angle θ to the ground is constantly changing, and becomes negative as the ball begins to descend.

A.4 Calculation of C_D

Four methods have been proposed for use in this investigation, each of the methods is similar to begin with. Figure A.5 is a summary of the common processes for all four methods.

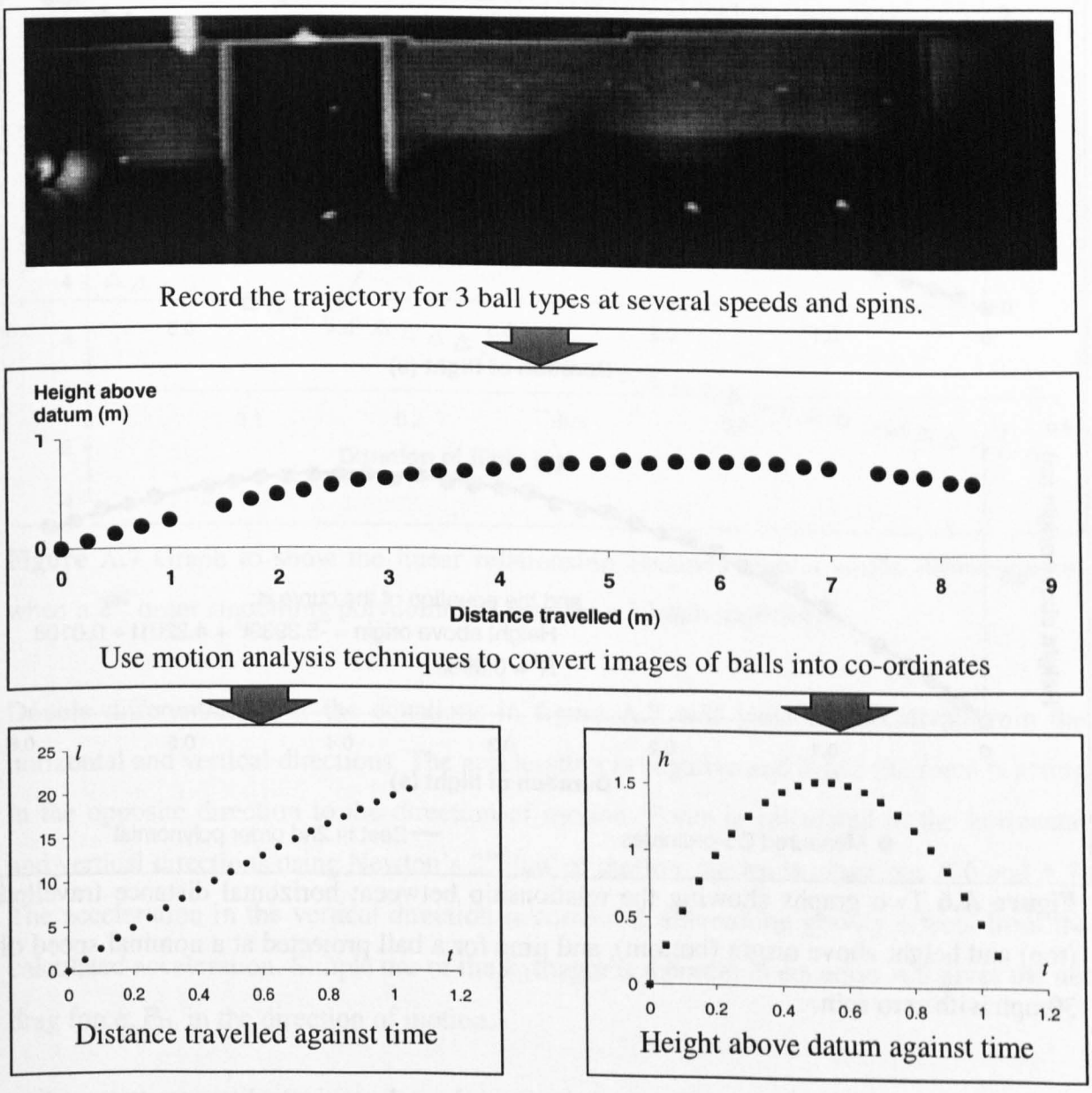

Figure A.5 Flow chart of the preliminary processes used to calculate C_D for all methods. Once the data has reached this stage, the processes used to find C_D with method A.1 differs from that used to find C_D with methods A.2 to A.4.

A.4.1 Using method A.1

An equation to best fit the curves of distance travelled and height above the origin is obtained using the method of least squares. For constant acceleration the best-fit curve should be a 2nd order polynomial ($s \approx ut + \frac{1}{2}at^2$) with respect to time. Figure A.6 shows the set of data obtained for a normal ball projected at a nominal speed of 30mph with zero spin, together with the best-fit quadratic curves and equations.

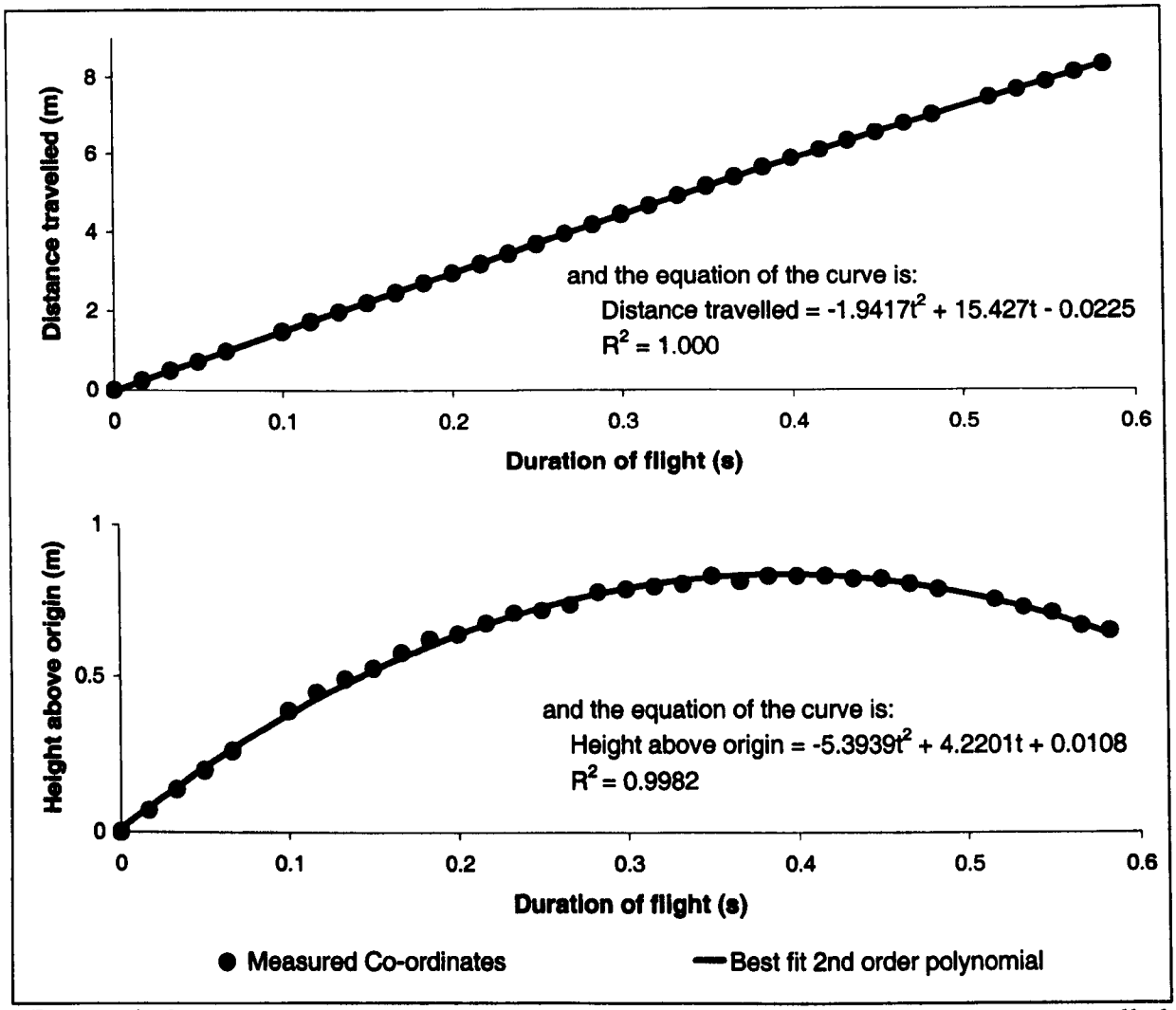

Figure A.6 Two graphs showing the relationship between; horizontal distance travelled (top) and height above origin (bottom), and time for a ball projected at a nominal speed of 30mph with zero spin.

The polynomial best-fit equations of horizontal and vertical distance versus time effectively act as a smoothing process to reduce the effects of the scatter in the motion analysis data. The equations formed were differentiated to form a linear relationship

between velocity and time. Figure A.7 therefore shows the resulting horizontal and vertical velocity profiles for a ball projected at a nominal speed of 30mph with zero spin. Both the horizontal and vertical velocities start positive and reduce steadily with time, however, the horizontal velocity remains positive whilst the vertical velocity turns negative as the ball begins to descend. The equation obtained after a single differentiation is linear, suggesting that there is a constant rate of change of velocity and hence a constant acceleration.

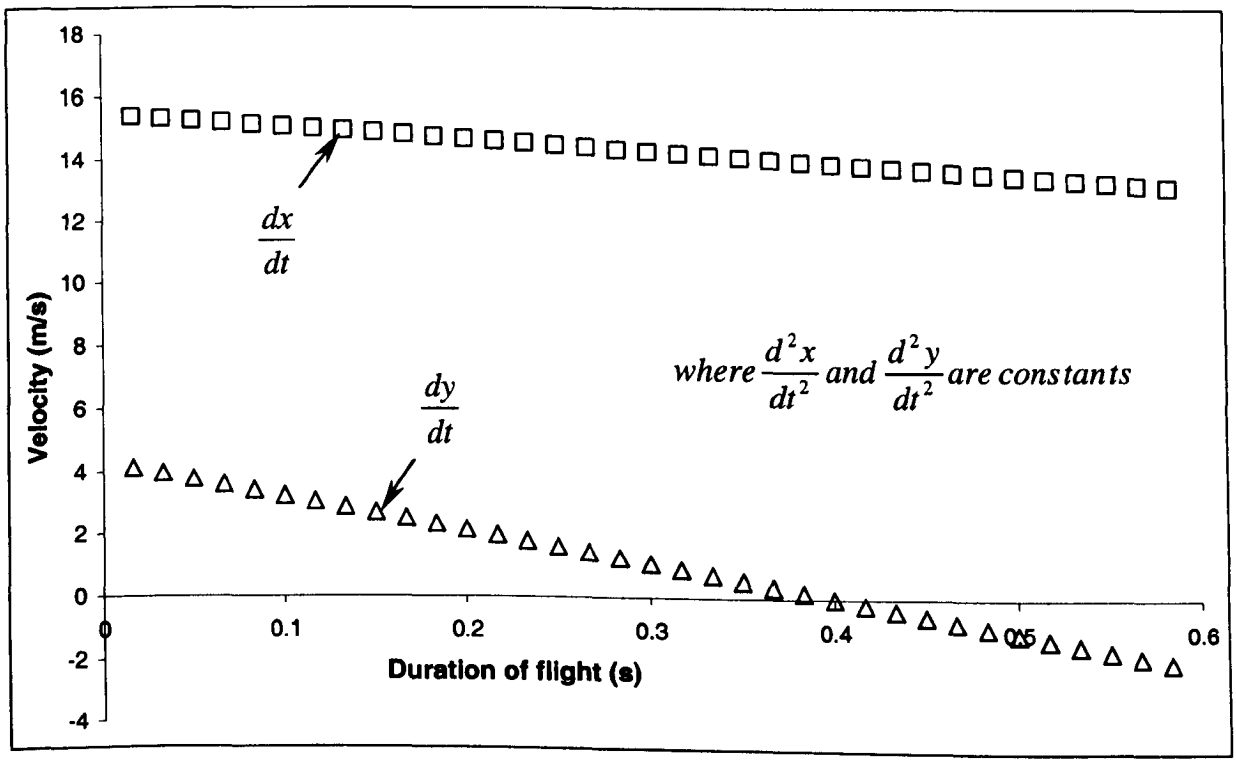

Figure A.7 Graph to show the linear relationship obtained after a single differentiation when a 2nd order smoothing polynomial is used on a 30mph trajectory.

Double differentiation of the equations in figure A.7 will yield the acceleration in the horizontal and vertical directions. The acceleration is negative and hence the force is acting in the opposite direction to the direction of motion. Force is calculated in the horizontal and vertical directions using Newton's 2nd law of motion, shown in equations A.6 and A.7. The acceleration in the vertical direction is corrected, subtracting gravity effects from the calculated acceleration. Simple use of the Pythagoras theorem in equation A.8 gives the net drag force, F_D, in the direction of motion.

The initial ball velocity is required to find the drag coefficient. Although the projection machine is calibrated, it is more accurate to use motion analysis on the images leaving the

projecting machine. Figure A.8 shows a plot obtained for the horizontal data for a normal pressurised ball projected at a nominal speed of 30mph.

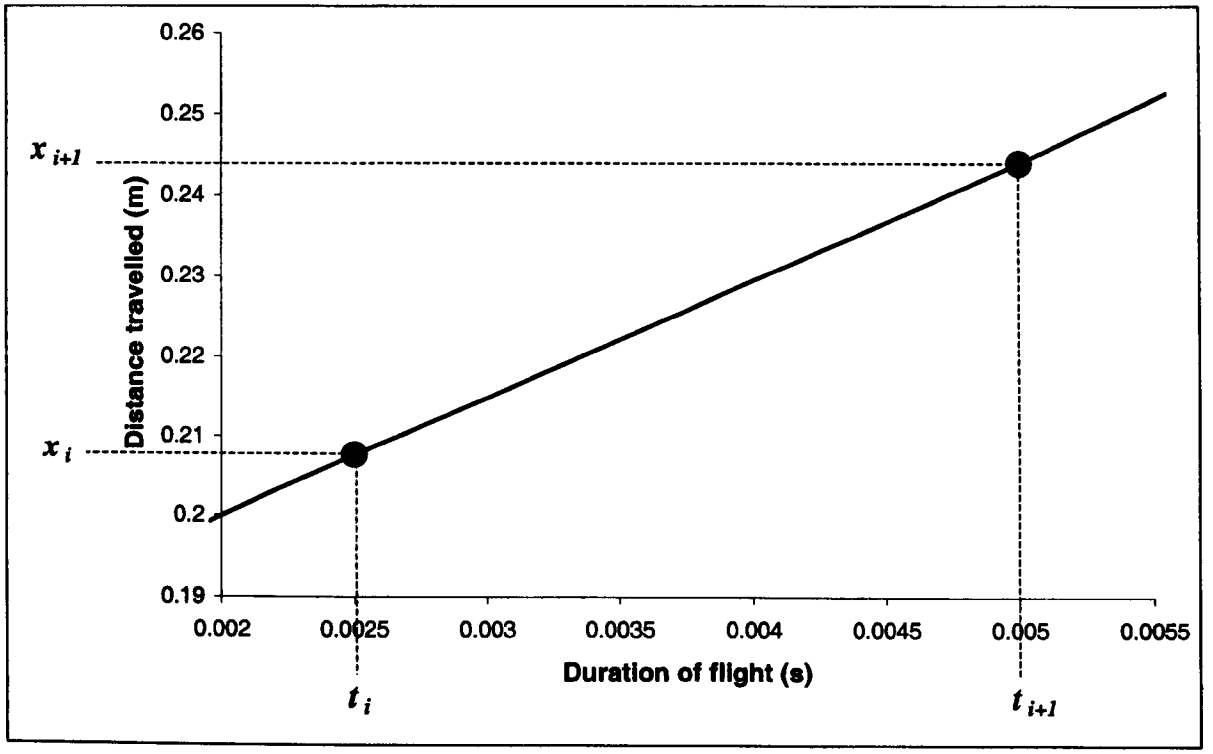

Figure A.8 Graph of two points used to calculate the horizontal velocity out of the JUGS machine for a normal pressurised ball projected at a nominal speed of 30mph.

A similar plot can be obtained for the vertical data, hence V_x and V_y are:

$$V_X = \frac{x_{i+1} - x_i}{t_{i+1} - t_i} \tag{A.18}$$

$$V_Y = \frac{y_{i+1} - y_i}{t_{i+1} - t_i} \tag{A.19}$$

where: x_{i+1} and x_i are the x co-ordinates at times t_{i+1} and t_i.

y_{i+1} and y_i are the y co-ordinates at times t_{i+1} and t_i.

A.4.2 Using methods A.2 to A.4

Rather than using a polynomial function to smooth the horizontal and vertical displacements obtained with respect to time, methods A.2 to A.4 use real time data. Figure A.9 is a flow chart designed to summarise the processes required and the information used

to calculate C_D using these three methods. Each of the three methods uses different parts of a single set of data. The calculations used in method A.2 will be described in the following sections, however the same processes apply to the other two methods using data specific to that method.

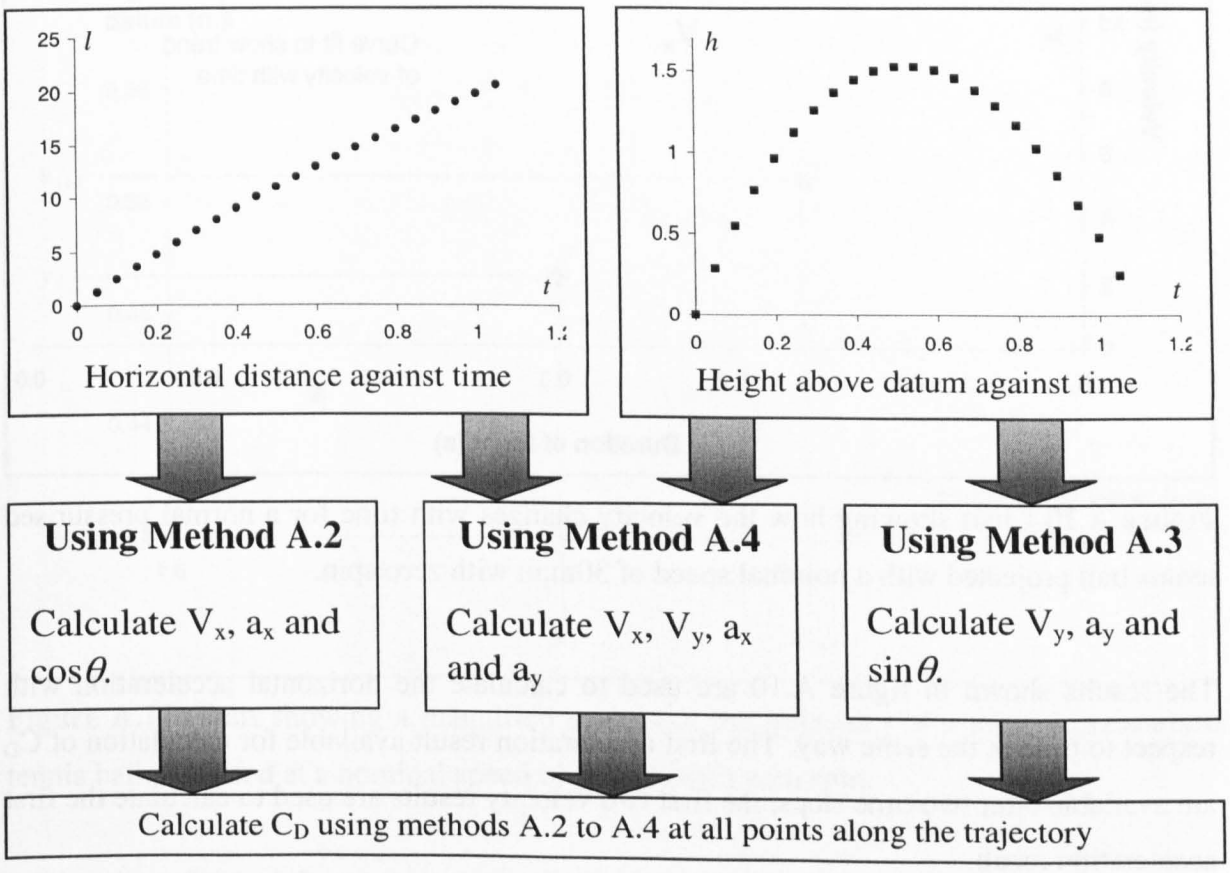

Figure A.9 Flow chart to show the processes required and information used to calculate C_D using methods A.2 to A.4.

The horizontal velocity of the ball is calculated in the same way as described in section A.4.1 using equation A.18 and A.19 for each data point along the trajectory. Figure A.10 shows the horizontal velocity obtained for a normal pressurised ball projected with a nominal speed of 30mph with zero spin. A best-fit curve has been created in Excel to show that the velocity follows a general downward trend with increasing time. A curve has been chosen rather than a line, as methods A.2 to A.4 do not assume constant acceleration. It is important to note that this curve is not used during testing and is annotated to the chart as a visual aid to specifically highlight the scatter in the velocity data. The first velocity result available for calculation of C_D is after one time step, and the first two data points are used to calculate the first velocity result.

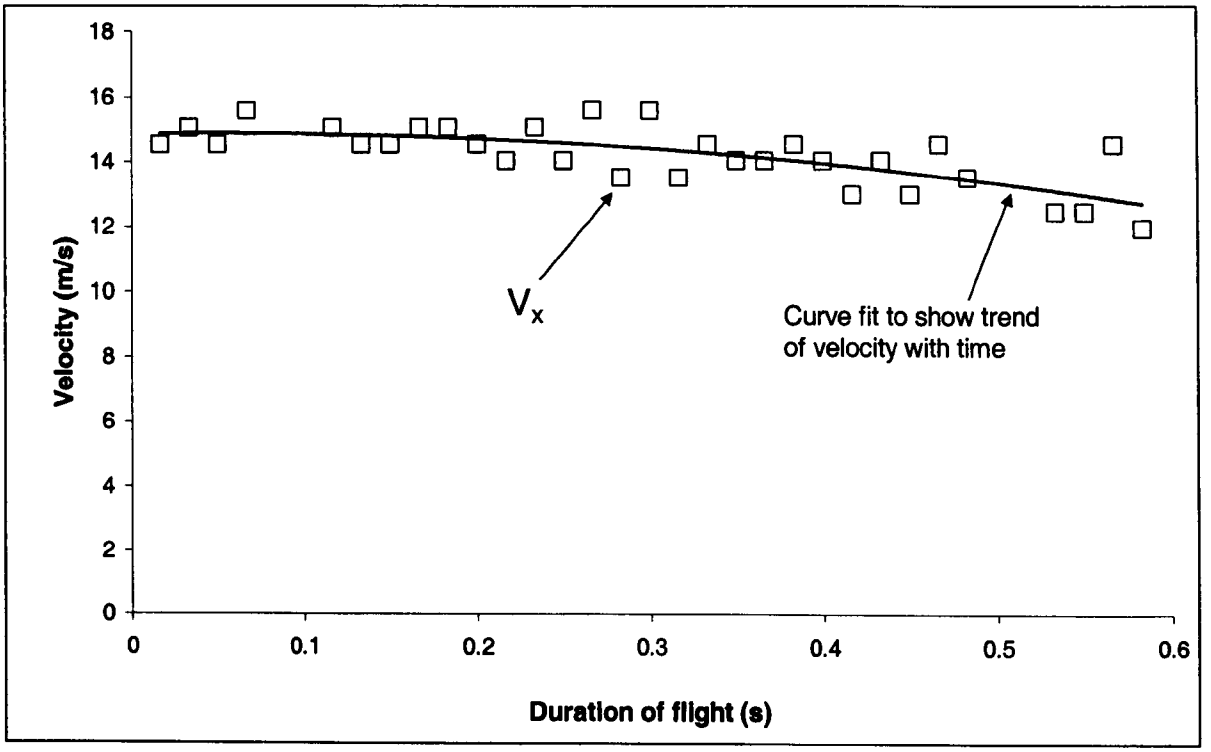

Figure A.10 Chart showing how the velocity changes with time for a normal pressurised tennis ball projected with a nominal speed of 30mph with zero spin.

The results shown in figure A.10 are used to calculate the horizontal acceleration with respect to time in the same way. The first acceleration result available for calculation of C_D are available after two time steps, the first two velocity results are used to calculate the first acceleration result.

Figure A.11 shows a magnified section of the trajectory of a normal pressurised tennis ball projected at a nominal speed of 30mph with zero spin. The direction of travel, θ, is calculated for all data points of the trajectory. The first result available for calculation of C_D is after one time step and the first two displacement data points are used to calculate the first result using the following equation:

$$\theta = \tan^{-1}\left(\frac{y_{i+1} - y_i}{x_{i+1} - x_i}\right) \qquad \text{(A.20)}$$

All of the required parameters are calculated throughout the complete trajectory, and are used to derive C_D using method A.2. C_D is calculated at each data point and could fluctuate significantly due to scattered results shown for velocity in figure A.10, and the resulting

accelerations. Rather than using a single calculated C_D, and to try to overcome any errors caused by the calculation processes, the mean C_D, which is derived from individual C_D results over the complete trajectory, is used.

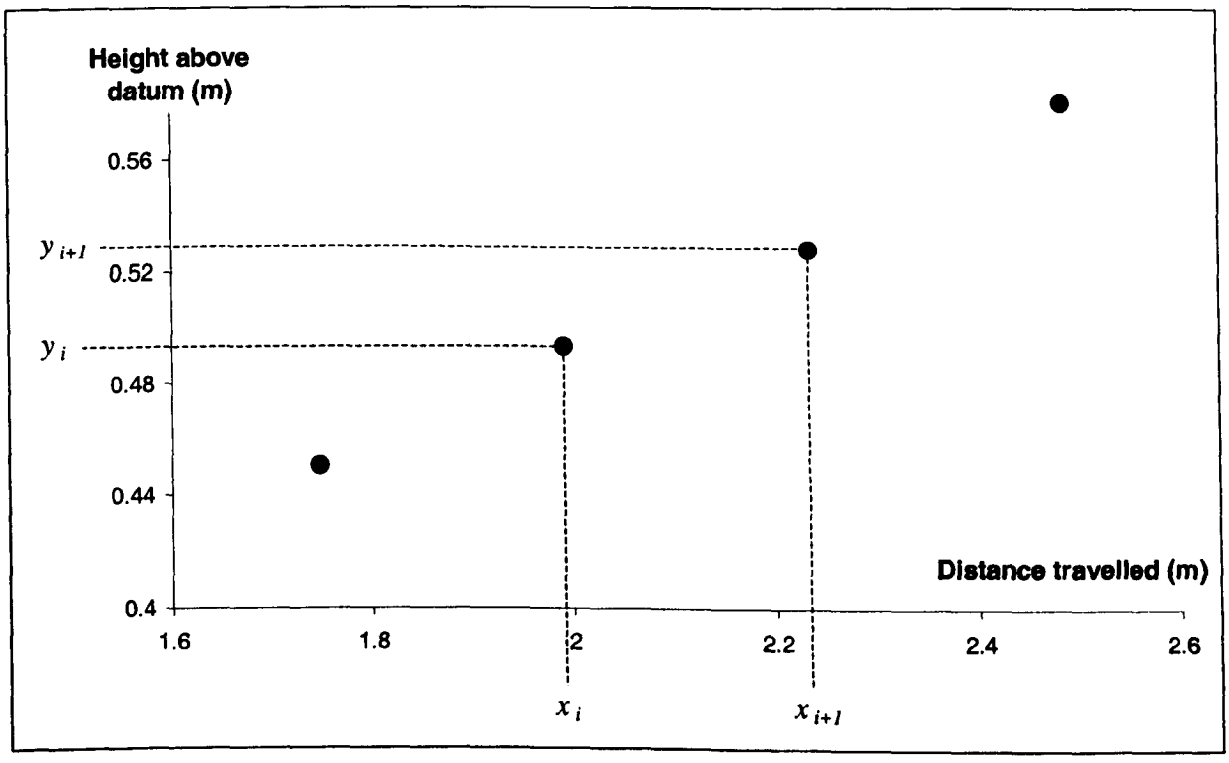

Figure A.11 Chart showing a magnified section of the trajectory of a normal pressurised tennis ball projected at a nominal speed of 30mph with zero spin.

Although methods A.3 and A.4 require different parameters, the same processes are used, and four values of C_D can be obtained for one trajectory. All methods should give the same value for C_D for a given trajectory.

A.5 Error analysis

Initial testing using this method showed that small errors arising from the motion analysis lead to significant errors in the value obtained for C_D. To try to overcome such errors the following analyses were undertaken:

- Analysis time was significant, hence an assessment of the number of points required to accurately define a complete trajectory was undertaken. This was achieved by repeating the analysis using the same data set whilst reducing the number of data points used.

- As the analysis uses a single set of data, the C_D obtained should be the same for each repeat. It was found that the C_D differed between analyses as a result of the induced errors, hence an assessment of the number of repeat analyses required to be confident of the result for C_D was undertaken.

Figure A.12 shows the C_D results obtained using method A.1 for a normal ball projected at a calculated velocity of $13.67ms^{-1}$ and zero spin. The number of points used for the analysis has been reduced by half in four consecutive investigations. The complete trajectory contains 35 data points at this speed.

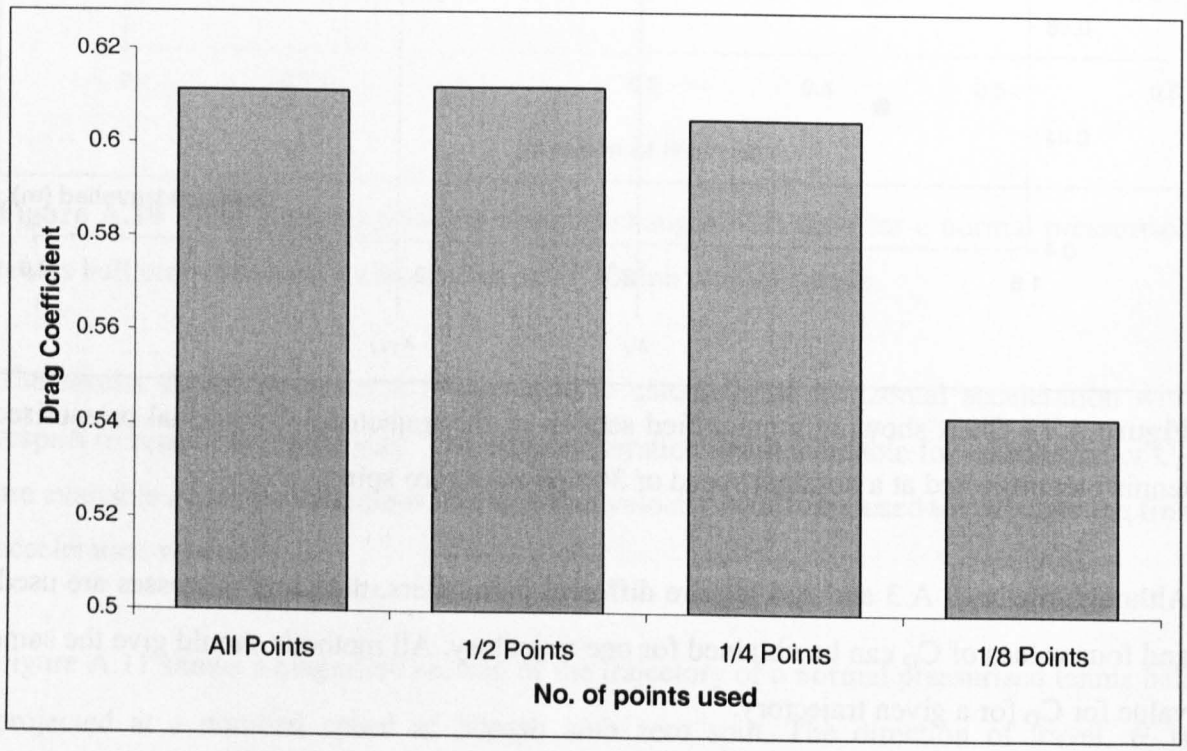

Figure A.12 Graph of the C_D results obtained using method A.1 whilst reducing the number of data points used for analysis of a ball projected at $13.67ms^{-1}$ and zero spin.

It can be seen that there is no apparent difference seen in the first three results, all returning a C_D of approximately 0.61. When 1/8 of the points are used however, the C_D drops to just above 0.54, it could be assumed that this is an unsatisfactory result. In conclusion, at least ¼ of all of the points should be used, however it is recommended that at least 10 points should be used where possible.

The next stage in the investigation used all of the data points of a single trajectory and repeated the analysis to calculate C_D 10 times, this included repeating the manual digitisation of the co-ordinates of the ball trajectory. It can be seen in figure A.13 that the results are scattered, ranging from 0.56 to 0.61, where the scatter is due to the quality of the data provided for analysis. A rolling average has been used to try to make use of the results, and it can be seen that this returns a value of 0.59 for C_D after the 4th repetition. However, the change in rolling average is within the standard deviation of the results after the third repetition. In conclusion, three repetitions should give a suitable result, however four repetitions should be used to ensure greater accuracy.

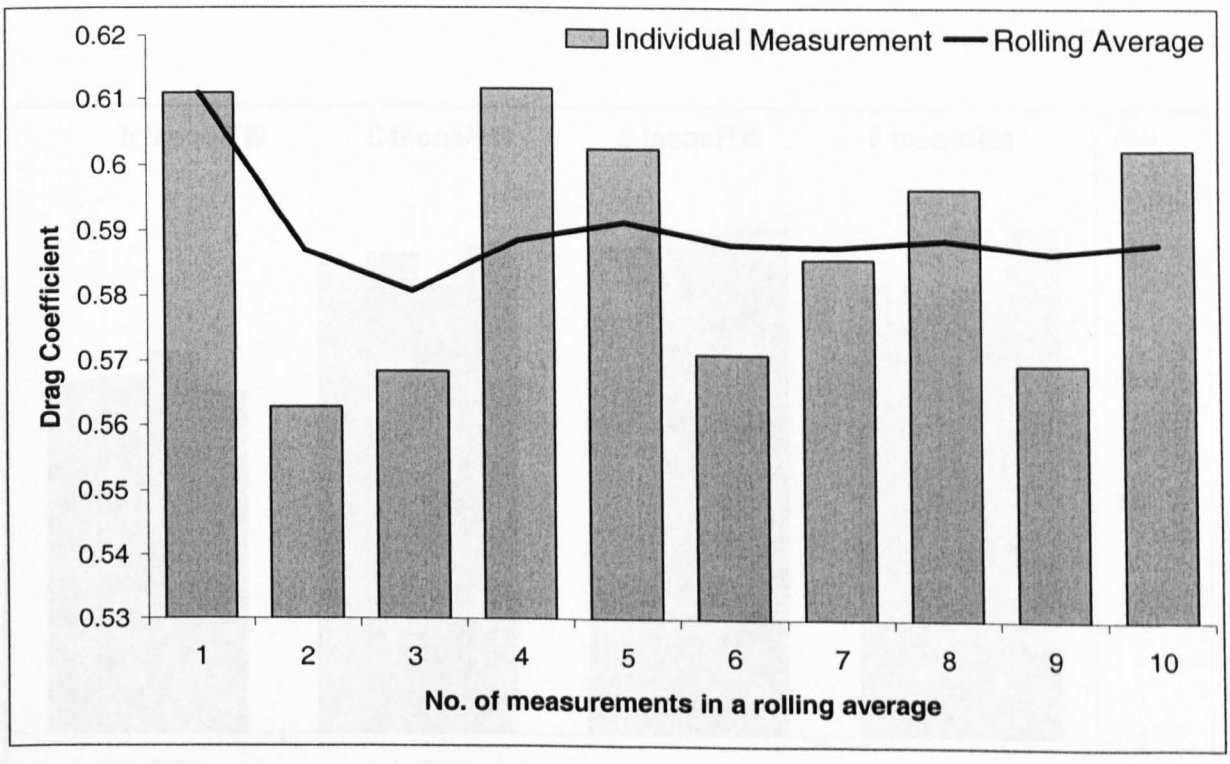

Figure A.13 Chart of a set of 10 individual C_D results obtained using method A.1, the subsequent rolling average obtained using all of the data points of a single trajectory for a normal ball projected at 13.67ms^{-1} with zero spin.

The true C_D for all points shown in figure A.12 was 0.61, as shown by the first bar in figure A.13. Subsequent testing included recapturing the co-ordinates of the trajectory, and hence subtle differences between trajectories would be expected, which therefore lead to different accelerations and drag forces. The variability in this analysis method can be estimated at around 3.2% for the ten C_D results obtained.

Figure A.13 shows that the average C_D obtained using four sets of C_D results are satisfactory when using all of the available data, however this may not be the case when fewer data points are used. Figure A.14 shows the average C_D obtained for the first four C_D results calculated using method A.1 on all of the data available, one half of the available data, one quarter of the available data and one eighth of the available data. The average C_D values obtained range from 0.6 when using $^1/_2$ of all data points down to 0.55 when using $^1/_8$ of all data points. The scatter observed in figure A.13 can be accounted for by the standard deviation of the data set. This analysis was performed on a single set of data, and all results should be the same yet there is a worrying amount of variation between individual C_D results. It was decided that a smoothing method applied to the displacement source data might improve the results.

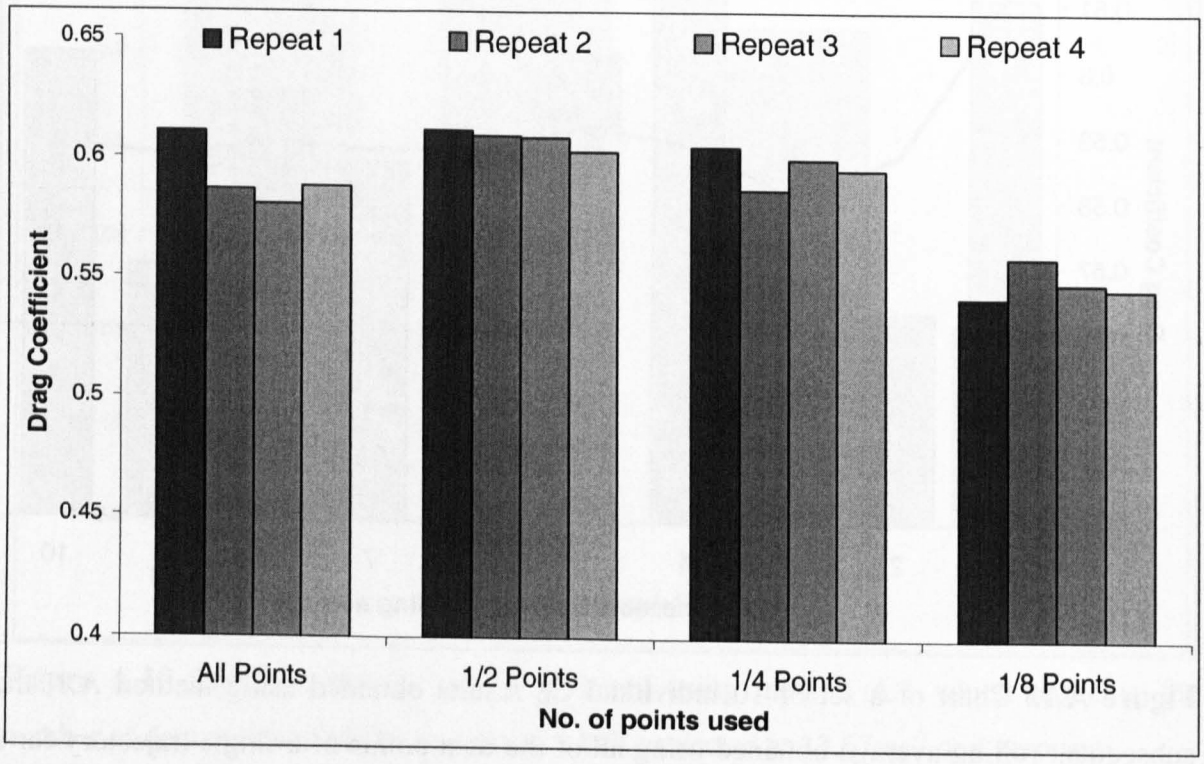

Figure A.14 Graph showing the first four rolling averages obtained for C_D (using method A.1) whilst reducing the number of points used to describe the trajectory for a ball projected at 13.67ms^{-1} with zero spin.

A.6 Smoothing of data

A simulated set of perfect data was formed using a trajectory model. The model was formed using an iterative process with the equations of motion, and this will be discussed

in more detail in chapter 10. The model simulated the trajectory of a ball with a C_D of 0.65 projected at a speed of $26ms^{-1}$ with zero spin and an elevation angle of 15°. The trajectory created using the model has defined input parameters, hence the quality of the results can be assessed.

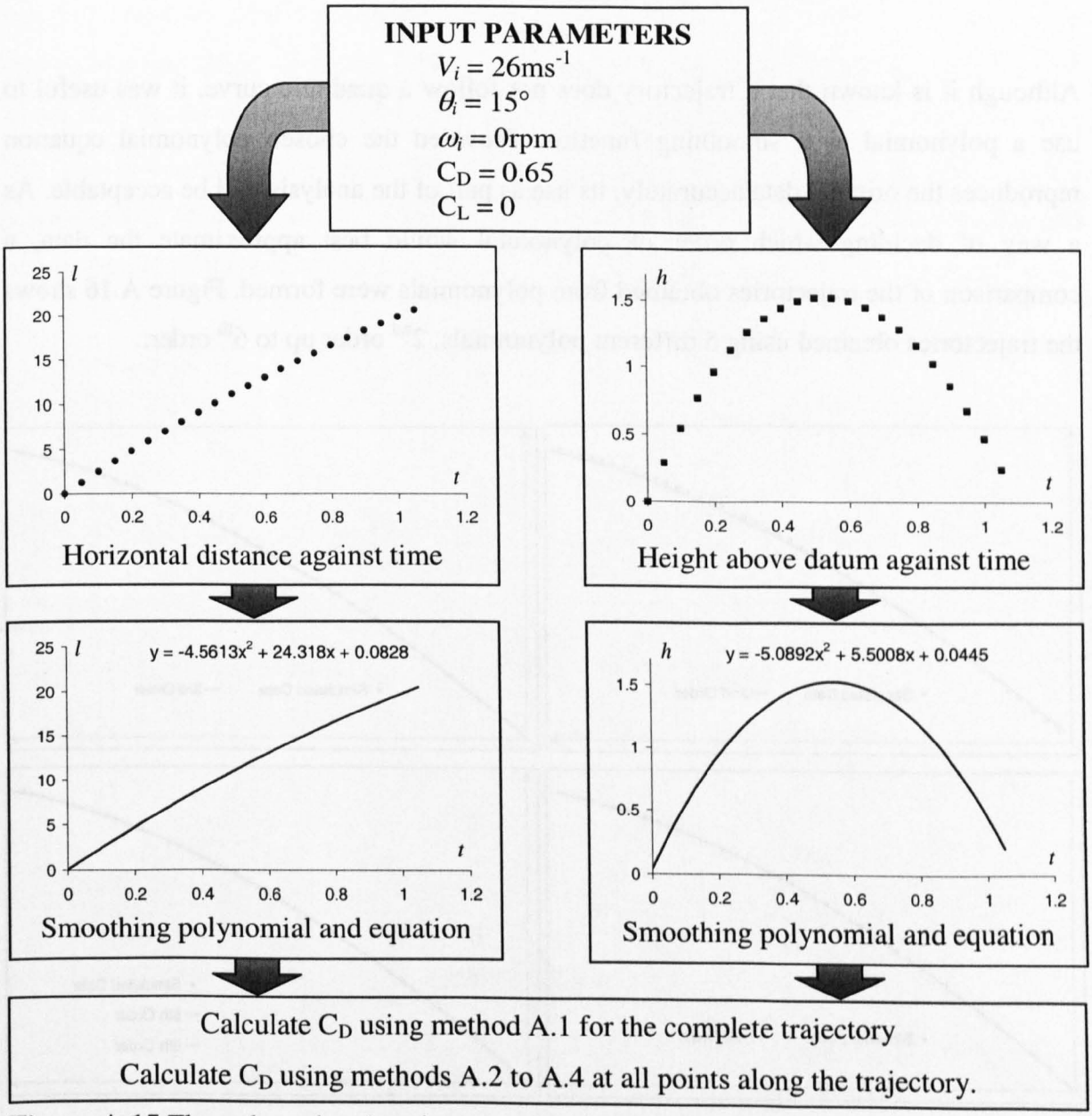

Figure A.15 Flow chart showing the processes involved to calculate C_D using perfect data simulating a ball with a C_D of 0.65 projected with a velocity of $26ms^{-1}$, at an angle of 15° to the horizontal and zero spin.

The trajectory model is used primarily to give a data set similar to that obtained in practice, and after that all calculations are the same as would be used with real data. A smoothing

polynomial is calculated for the source data, and the resulting equation used to plot a new trajectory. The new trajectory is then used to calculate C_D using methods A.1 to A.4 and the flow chart in figure A.15 gives an overview of the processes involved.

A.6.1 Choice of smoothing polynomial

Although it is known that a trajectory does not follow a quadratic curve, it was useful to use a polynomial as a smoothing function. Provided the chosen polynomial equation reproduces the original data accurately, its use as part of the analysis will be acceptable. As a way of deciding which order of polynomial would best approximate the data, a comparison of the trajectories obtained from polynomials were formed. Figure A.16 shows the trajectories obtained using 5 different polynomials, 2nd order up to 6th order.

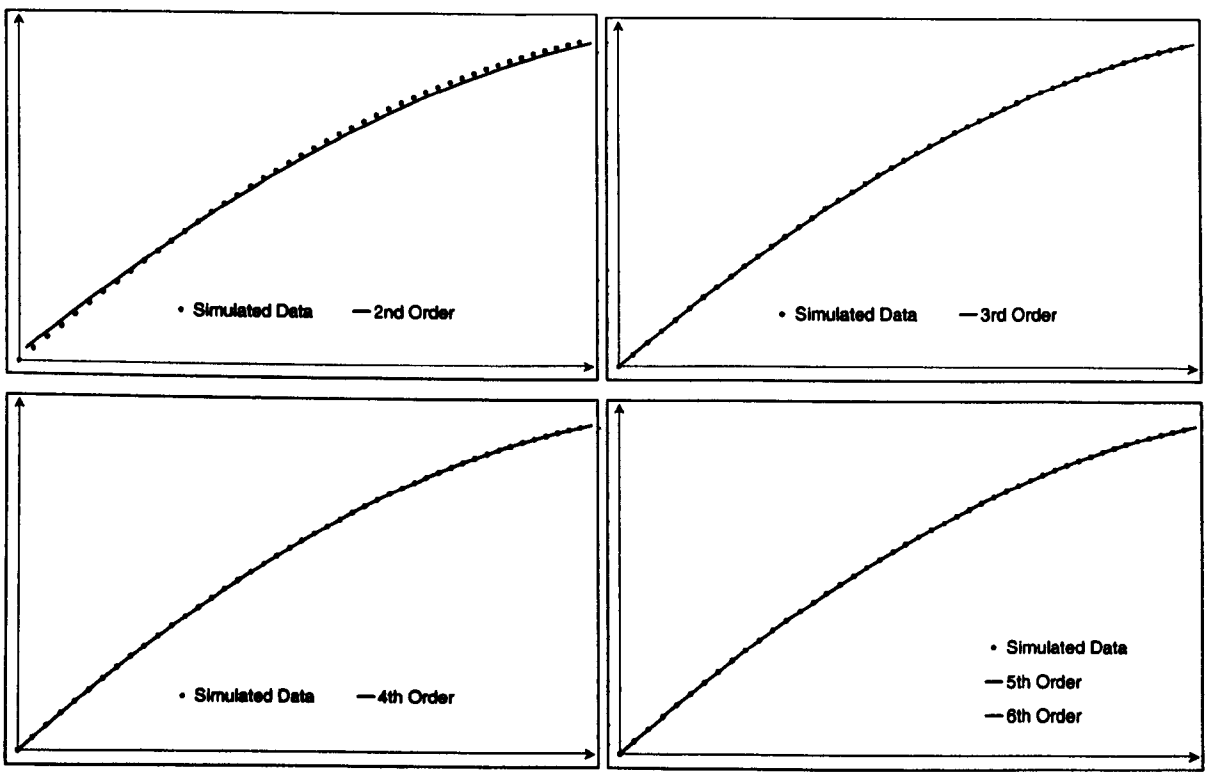

Figure A.16 Graphs to show the first half of the simulated trajectories obtained using different order smoothing polynomials on a ball projected with a velocity of 26ms^{-1}, at an angle of 15° to the horizontal and zero spin.

The charts have been modified to shown only the first half of the trajectory and separated to better distinguish between the analyses. It can be seen that the trajectory plotted using

the 2nd order polynomial does not reproduce the original trajectory adequately. The trajectory reproduced by the other analyses shows little difference between the original data and that simulated using the polynomial equation.

In addition to the above assessment, it is also useful to examine the point at which each trajectory impacts with the ground. Figure A.17 is the magnified view of the last part of each of the trajectories shown in figure A.16. It can be seen that the landing point of the 2nd order data lands almost 250mm short of the model data and the 3rd order data lands approximately 30mm long. It is difficult to distinguish between the 4th, 5th and 6th order polynomials, hence it can be concluded that a fourth order polynomial or higher will approximate the data satisfactorily.

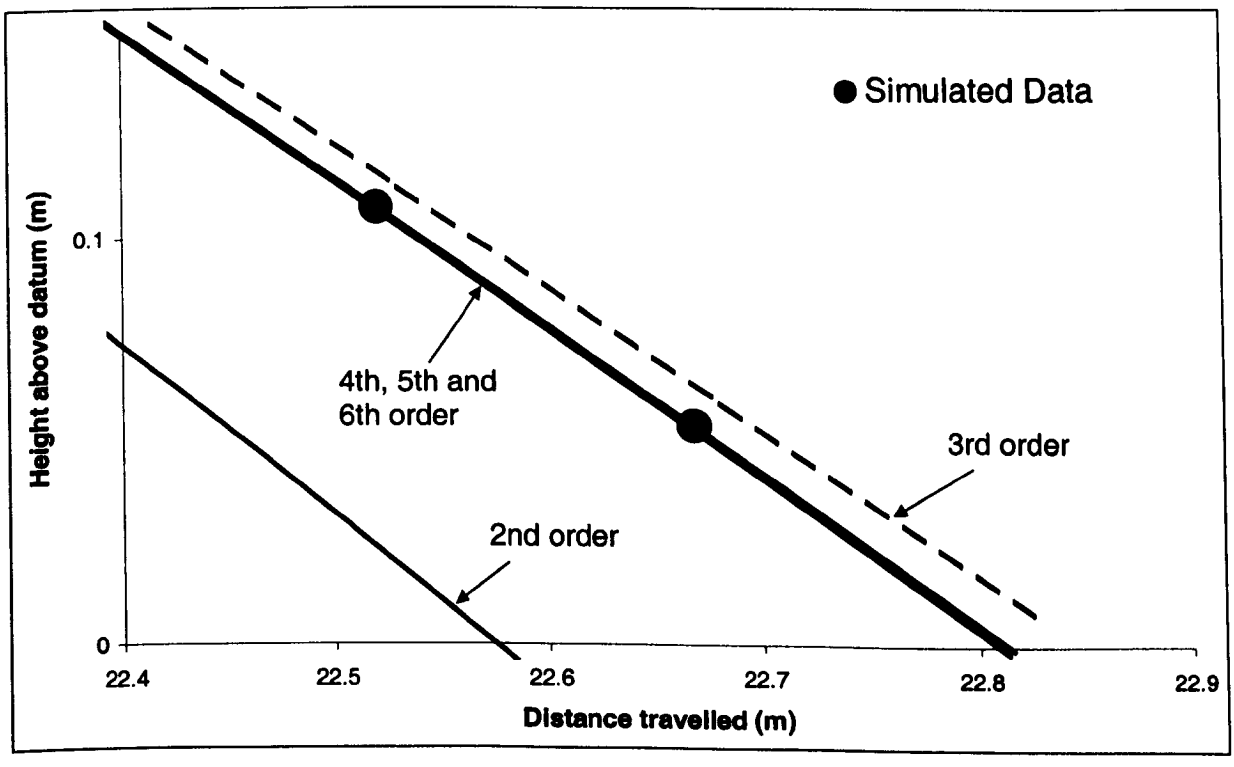

Figure A.17 Graph to show the landings points of the trajectories obtained using different order smoothing polynomials on a ball projected with a velocity of 26ms^{-1}, at an angle of 15° to the horizontal and zero spin.

Although the ball may finish at the correct point, it is not clear what happens during the rest of the trajectory. Figure A.18 shows the average absolute differences obtained at each data point along the trajectory of a ball projected with a velocity of 26ms^{-1}, at an angle of 15° to the horizontal and zero spin. This chart suggests that the average errors for the x co-

ordinates using a 2nd order polynomial were almost 35mm at each data point. When viewing the higher order polynomials it can be seen that these differences are reduced significantly. It appears that the 5th order polynomial simulates the original data better that the 4th or 6th order polynomials, a fact compounded when friction is considered to work against gravity as the ball rises and with gravity as it descends.

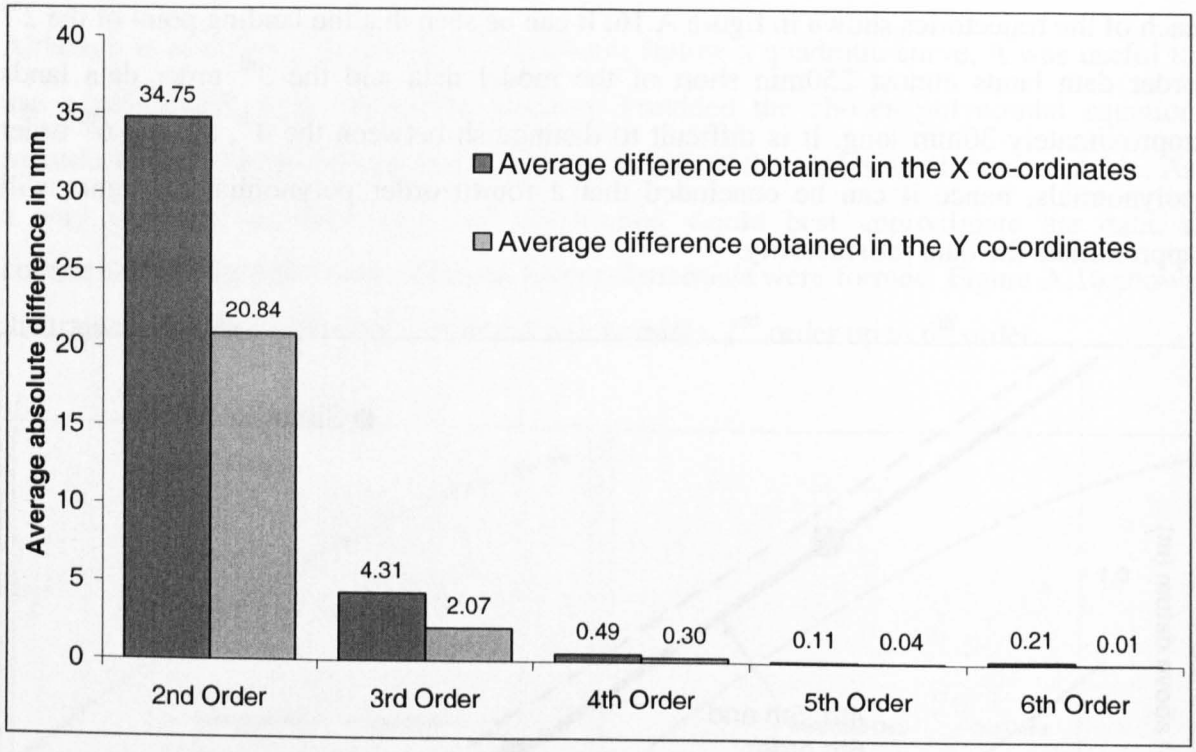

Figure A.18 Graph to show the average absolute differences obtained at each data point along the trajectory of a ball projected with a velocity of 26ms^{-1}, at an angle of 15° to the horizontal and zero spin.

A.6.2 Choice of method

Each of the four methods can now be used to calculate C_D as accurately as possible. Method A.1 can only be used with a quadratic smoothing function, and having performed the analysis in section A.6.1, a 2nd order polynomial is unsuitable for recreating the source data. The C_D obtained using methods A.2 to A.4 are all calculated using a 5th order polynomial for smoothing. The C_D is calculated at all data points and then averaged over the whole trajectory, table A.1 shows the results obtained for all four methods. The C_D should be constant throughout the flight, and investigation of the changes in C_D during the

flight is an indication of a method's stability. The error has been estimated by comparing the calculated C_D against the model C_D.

It can be seen that method A.2 is the most accurate with a value of 0.650 with a standard deviation of 0.001. Method A.4 is slightly less accurate with a value of 0.655 and a standard deviation of 0.003. The C_D obtained using method A.3 is both inaccurate and has a large standard deviation. Method A.1 returns a C_D value that is approximately half of the correct value.

Method No.	Average C_D calculated over all time steps	Standard deviation of C_D for all time steps	Error between calculated C_D and model C_D (0.650)
A.1	0.347	N/A	46.58
A.2	0.650	0.001	0.02
A.3	0.634	0.160	2.54
A.4	0.655	0.003	0.79

Table A.1 Calculated values of C_D obtained using methods A.1 to A.4 with a polynomial smoothing function on simulated trajectory data for a ball with a C_D of 0.65 projected with a velocity of 26ms^{-1}, at an angle of 15° to the horizontal and zero spin.

Reasons behind why method A.1 returns unsatisfactory results are well understood and it would be useful to understand why methods A.2 to A.4 return the results they do. The results for C_D for all methods are obtained by iteratively calculating C_D and averaging over time. It is therefore useful to investigate how the C_D changes with time using each method.

Figure A.19 shows the results obtained for C_D at each data point using methods A.2 to A.4 with a polynomial smoothing function on simulated trajectory data for a ball projected with a velocity of 26ms^{-1}, at an angle of 15° to the horizontal and zero spin. It can be seen that methods A.2 and A.4 calculate a C_D of approximately 0.65 for all points along the trajectory, where the standard deviation is zero to two decimal places. Method A.4 appears to return steadily improving results, starting at 0.66 and reducing to 0.65 at the end of the trajectory. As method A.4 is essentially a combination of methods A.2 and A.3, it is no surprise that the C_D calculated using method A.4 is an improvement over that obtained using method A.3 but not quite as reliable as that calculated using method A.2.

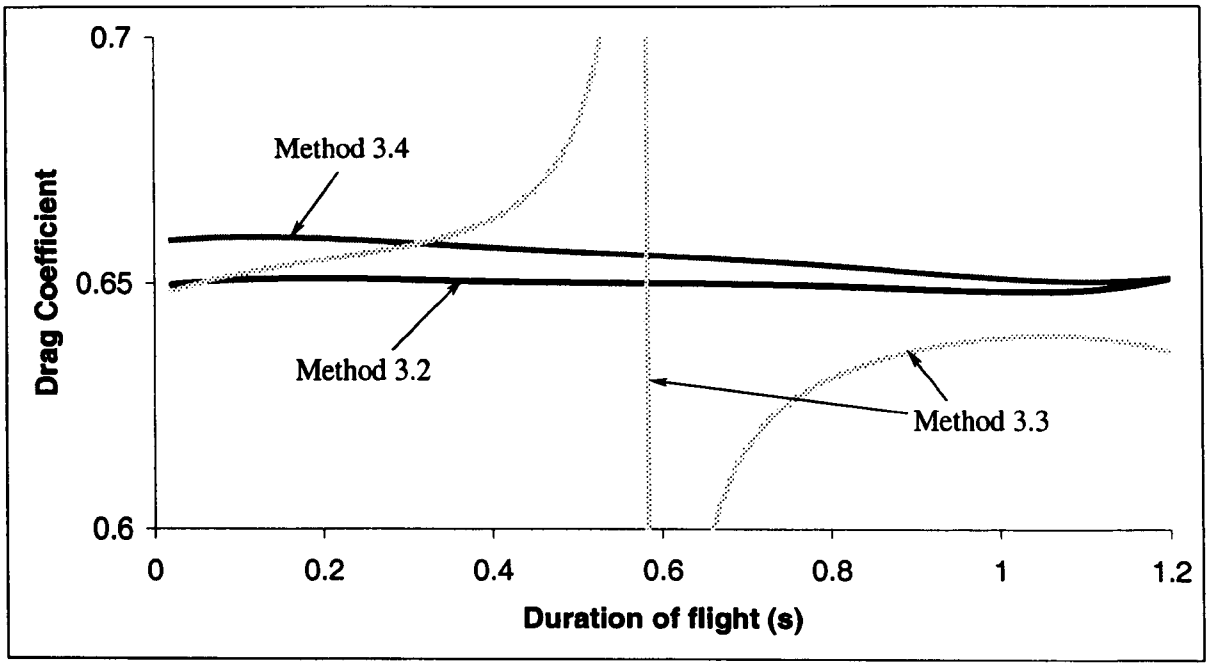

Figure A.19 Chart of C_D against time using methods A.2 to A.4 with a polynomial smoothing function on simulated trajectory data for a ball projected with a velocity of $26ms^{-1}$, at an angle of 15° to the horizontal and zero spin.

Method A.3 returns C_D results that are affected asymptotically approximately half way through the flight. The calculation to find C_D using method A.2 uses only horizontal components of velocity, whereas method A.3 uses only vertical components. Figure A.20 shows how both the horizontal and vertical components of velocity change throughout the duration of the flight.

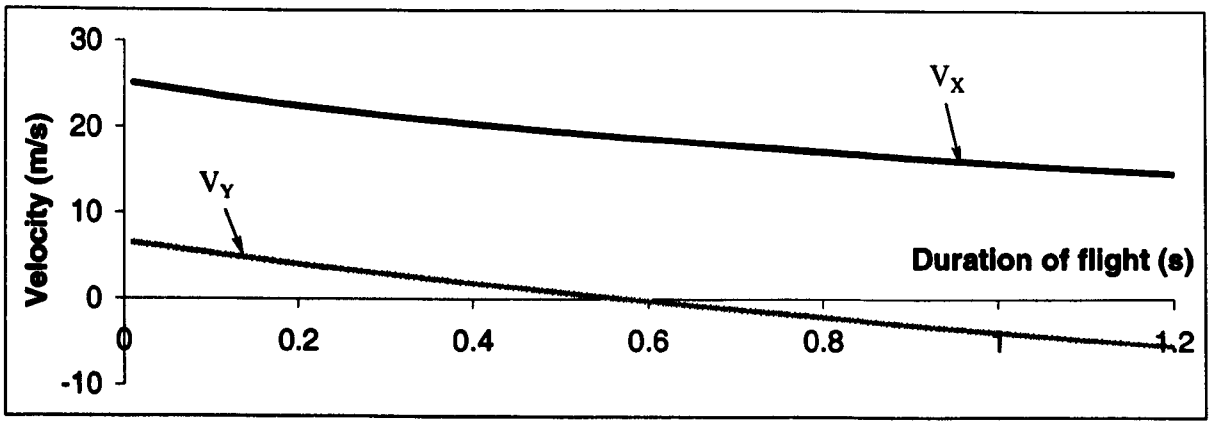

Figure A.20 Chart of the x and y velocity components against time using a 6^{th} order polynomial smoothing function on simulated trajectory data for a ball projected with a velocity of $26ms^{-1}$, at an angle of 15° to the horizontal and zero spin.

It can be seen that V_x is positive for the duration of the flight, whereas V_y starts positive and turns negative as the ball starts to descend. The fact that V_y becomes negative does not affect the analysis, it is the fact that just prior to the ball descending the velocity in the vertical direction will be approximately zero. As V_y tends to zero, the C_D calculated using equation A.14 tends to infinity, and hence explains the changes in C_D throughout the flight shown in figure A.19.

In conclusion, method A.3 is not stable for use and method A.4 is essentially a combination of both methods A.2 and A.3. All formal analyses should use a 5^{th} order polynomial to smooth displacement data against time, and calculation of C_D should use method A.2.

A.7 Results

Initial testing looked at non-spinning balls only, the following parameters were chosen:

Ball Types: Normal sized pressurised
Oversized pressurised
Normal sized permanent pressure

Velocity: Velocity ranged from a nominal speed of 30mph to 100mph, the velocity was obtained using motion analysis techniques described in section A.5.3.

A.7.1 Errors

There are several processes undertaken to calculate C_D when using a trajectory method, all of which count towards errors. The first process that could incur errors is the calibration method, however this is repeated several times and averaged, hence, errors associated with calibration should be negligible.

Errors are compounded when used in several processes, an incorrect point gathered during data collection is also be used to calculate velocity, acceleration and the direction of travel. A smoothing polynomial is used to improve the original data, which should minimise such errors. The trajectory model has been used to assess the errors caused by variation of data

points. A trajectory was formed using the estimate that a single data point could contain a 33mm offset in any direction from its real position. Starting with a perfect 5th order trajectory, the offset was applied to each point randomly. A new set of equations was formed for horizontal and vertical data against time and used to recalculate C_D using method A.2. When compared to the input value of 0.65, the new value of C_D contained a 7.9% error. This figure of error should incorporate errors associated with velocity, acceleration and direction of travel, the offset in deflection was applied to the source data.

A.7.2 Calculated C_D

Figure A.21 shows the results obtained using method A.2 with a 5th order smoothing polynomial for a normal sized pressurised ball projected at nominal velocities from 30mph to 100mph with zero spin.

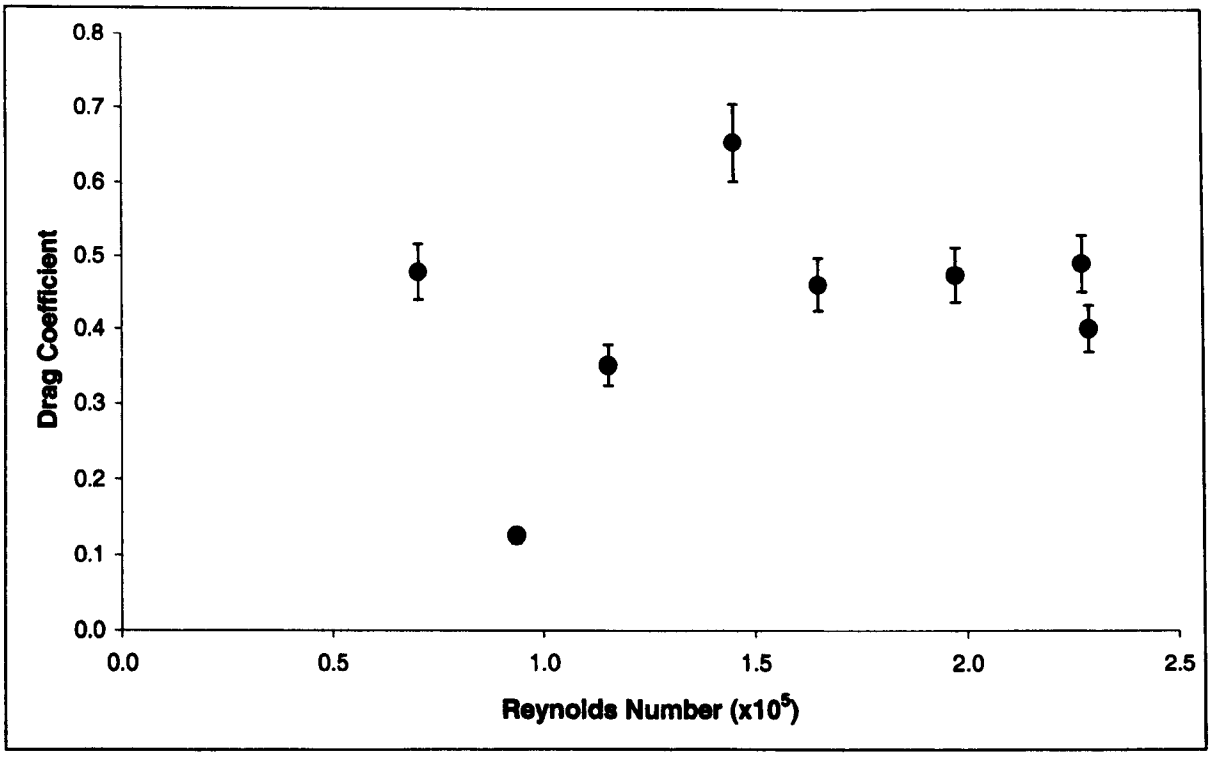

Figure A.26 Graph to show the C_D results obtained using method A.2 with a 6th order best-fit polynomial for a normal pressurised ball projected at nominal velocities from 30mph to 100mph with zero spin.

The error bars have been applied as a percentage of the C_D value for each of the data points. It can be seen that the results show significant scatter, with C_D ranging from a

minimum of 0.12 up to maximum of 0.66. The low C_D result was calculated in the same manner as all of the others and is a sign that there are significant inconsistencies in the calculation method. If the erroneous C_D of 0.12 is ignored, the other results appear to fluctuate around an average C_D of approximately 0.46.

Based on prior work undertaken, a C_D of above 0.5 may have been expected. This fact together with the uncertainty shown suggests that further analysis is required. It should be noted that a method was also devised whereby C_D and C_L results could be calculated, however based on the unpredictable results obtained using the 'simplified' non-spinning analysis, it was decided that the spinning analysis should be ignored at this stage.

A.8 Discussion

A C_D of between 0.5 and 0.6 may be expected for most spheres in the laminar flow regime, and previous work on tennis balls suggests that the C_D for a non-spinning ball should be 0.51 (Stepanek 1988). This is close to that achieved at high velocities, but the results at lower velocities are significantly different.

Several methods have been considered for use in finding the drag force for a projected ball. It was decided that method A.2 used in conjunction with a 5^{th} order smoothing polynomial would give the best results. As can be seen in figure A.22, the C_D results obtained are not consistent, ranging from 0.1 up to almost 0.7. The interesting fact with these results is that they are more closely related to previous work at the higher velocities tested, where there are less data points available for analysis and the curve of the ball is less pronounced.

A.8.1 Spatial resolution errors

It is possible that much of the error comes from the poor quality images used during motion analysis. The ball can be as small as 4 pixels on the screen, which means that the co-ordinates obtained for the position of the ball could easily be out by as much as half of the diameter if the ball. Smoothing has helped to overcome this problem, and errors were estimated to be around 7.9% with simulated trajectories. The C_D results for actual tennis

ball trajectories are showing a large level of inconsistency that reduces confidence in the applicability of this method of analysis.

A.8.2 Errors due to calibration

Calibration was said to cause negligible errors, this is based on the assumption that the calibration image is showing the correct information in the first place. Reference points on the wall, which is positioned approximately 600mm behind the plane of the trajectory, were used for the calibration of the complete trajectory. It is estimated that this could lead to a difference of 3.4% in the calibration factor, increasing the overall length of the trajectory. When applied to the trajectory of a normal pressurised ball projected at 15.9ms^{-1} and 16° to the horizontal, this leads to a change in C_D of 3.1%. This could take the errors to 11% overall, however, the increased length will cause a reduction in C_D. The error bars shown in figure A.21 are corrected to incorporate the new errors associated with calibration and shown in figure A.22.

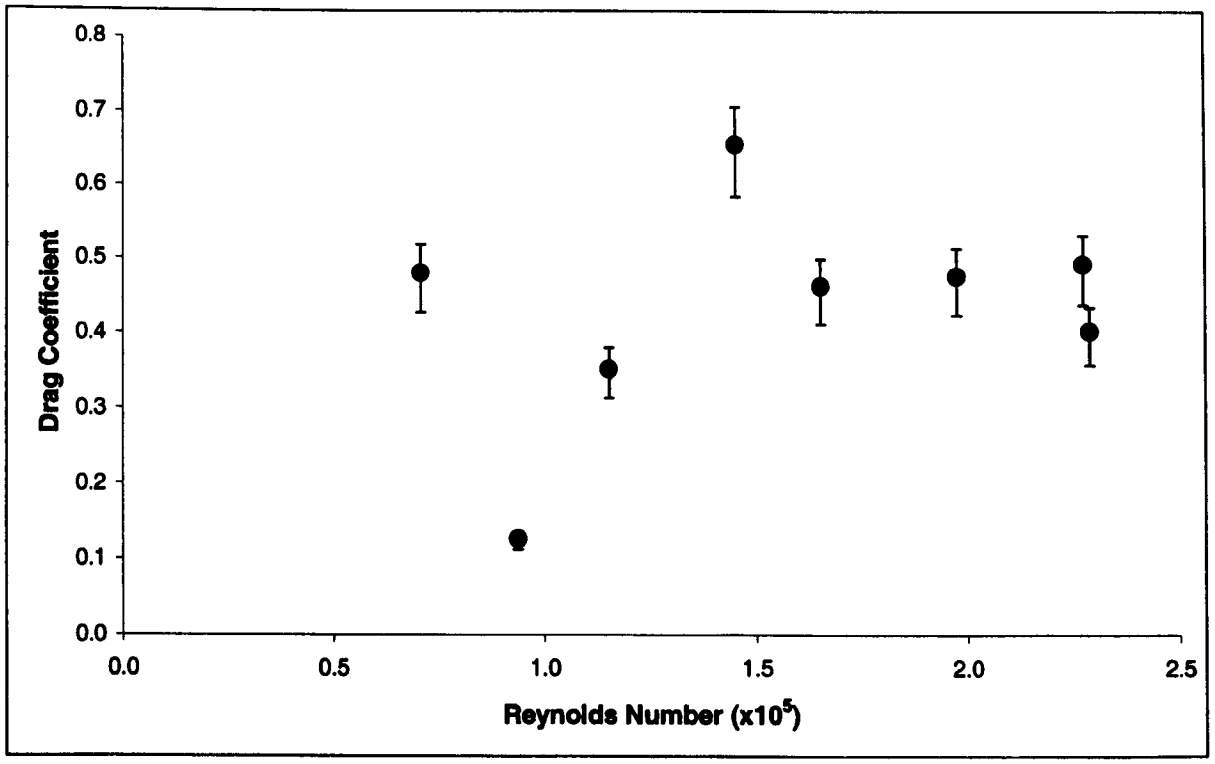

Figure A.22 Graph showing the change in errors associated with calibration for the C_D results obtained using method A.2 with a 6th order best-fit polynomial for a normal pressurised ball projected at nominal velocities from 30mph to 100mph with zero spin

It could now be said that five out of the eight C_D results obtained are similar within the errors associated with the test method, leading to an average C_D of 0.46±0.04.

A.8.3 The knuckle ball effect

Concern remains for the reasons why the scatter is present, error analysis showed that method A.2 should return results with negligible errors. There is a phenomenon associated with non-spinning balls termed 'the knuckle ball effect'. This is taken from the game of baseball, where a ball thrown without spin is shown to deviate in several directions throughout its flight. The deviations are caused by the seam intermittently tripping the boundary layer into turbulent (low C_D) flow on one side, thus creating an asymmetry that induces a side force. The tennis ball has seams similar to a baseball, albeit under the surface rather than being proud. It could be that a non-spinning tennis ball as used in these tests is encountering the knuckleball effect and hence caused some errors in the results.

THIS PAGE INTENTIONALLY LEFT BLANK

APPENDIX B: C_D DERIVED USING THE TRAJECTORY OF A BALL DROP

B.1 Introduction

As with the analysis of the trajectory of the projected ball, the trajectory of a ball dropping through the moving airflow of a wind tunnel can be analysed to determine the drag and lift forces acting on it. Rather than projecting a ball at a given speed, the ball is dropped through the moving airflow of a wind tunnel. The wind tunnel velocity is used in conjunction with the ball velocity to give the effective velocity of the trajectory. The trajectory of a projected ball used the deceleration of the ball through its flight; this method uses the acceleration applied to the ball due to both wind velocity and gravity.

One of the first investigations to utilise this technique was performed by Davies in 1949. Davies studied the deflection of a spinning golf ball dropped from within the wind tunnel. The limitations with technology meant that Davies only used the start and finish point of the trajectory. The vertical height dropped was known therefore the analysis to find C_D and C_L could be conducted. In 1987 Stepanek used the same method to investigate the C_D and C_L of tennis balls.

This study utilises the advances in technology to use motion analysis techniques. The increased information available will enable more complex equations of motion to be developed, and therefore an improved method of calculating C_D and C_L.

The initial tennis ball drop tests were performed without spin, thus simplifying the calculations required to obtain a drag force. The test method was later developed to include spin, which utilised a more complex dropping device.

B.2 Theory

At this point it is useful to remind the reader of the equations obtained when considering an object moving through the air. There are three component forces acting on it; gravity, drag

and lift. Both drag and lift forces are functions of the object properties and the atmospheric conditions, and can be described by the following equations:

$$F_D = \frac{1}{2}\rho v^2 A C_D \tag{B.1}$$

$$F_L = \frac{1}{2}\rho v^2 A C_L \tag{B.2}$$

where: F_D and F_L are drag and lift forces respectively

ρ is the density of the fluid within which the object is moving

v is the velocity of the object moving through the fluid, or, the velocity of the fluid moving over the object

A is the *projected* area of the object

C_D and C_L are the drag and lift coefficients respectively

Figure B.1a shows a picture depicting the drop of a ball through the moving airflow of a wind tunnel, the air is moving from left to right causing the ball to deflect in that direction. A real trajectory is shown in figure B.1b, and the use of these images will be discussed later in this chapter.

a) 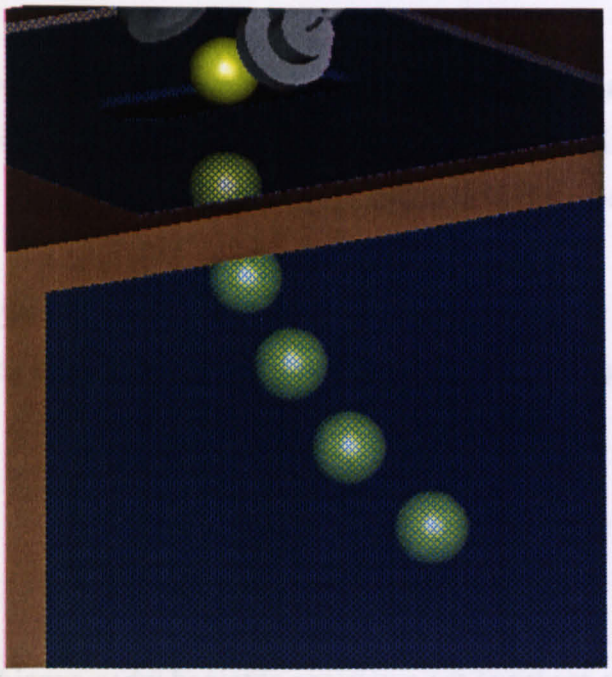 b) 

Figure B.1 Pictures a) depicting a ball being dropped through the moving air of a wind tunnel and being deflected and b) the resulting digitally captured trajectory.

A similar method to that used in appendix A can be used to find the equations of motion for a ball dropping through the moving air of a wind tunnel. Figure B.2 shows the associated force diagram for a ball spinning in the direction of ω, dropping through a wind tunnel with air flowing from left to right at velocity V_W. The picture on the right hand side of figure B.2 shows a typical trajectory obtained during this ball drop investigation.

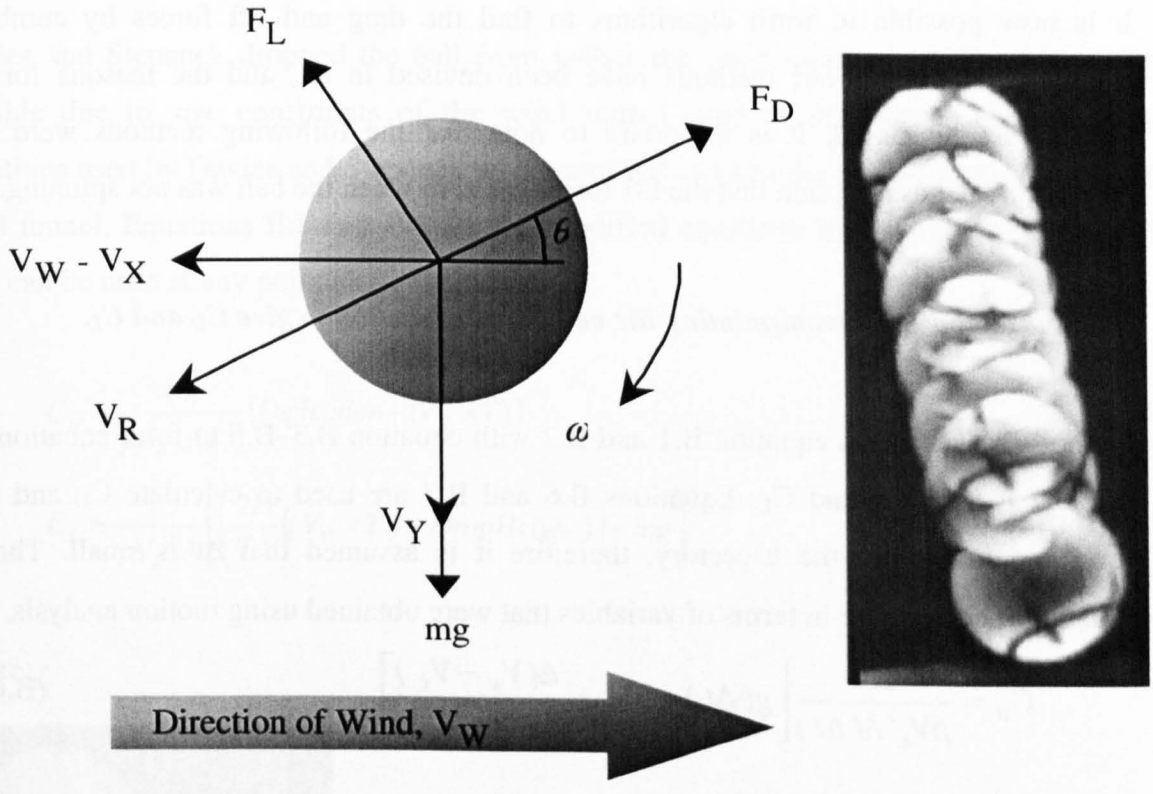

Figure B.2 Diagram showing forces acting on a tennis ball along with velocity components for a typical trajectory of a spinning ball falling through the moving air of a wind tunnel.

The ball was dropped vertically through the airflow, and although the ball was deflected in the direction of the wind and relative to it, with horizontal velocity component V_X and vertical velocity component V_Y, the equivalent direction of motion is that depicted by V_R. The relative velocity, V_R, has components V_W-V_X and V_Y acting in the horizontal and vertical directions. For the given force diagram shown in figure B.2, the equations of motion acting in the direction of the airflow and gravity respectively are:

$$m\frac{d(V_W - V_X)}{dt} = F_L \sin\theta - F_D \cos\theta \qquad \text{(B.3)}$$

$$m\frac{dV_Y}{dt} = mg - F_L\cos\theta - F_D\sin\theta \tag{B.4}$$

$$\tan\theta = \frac{V_Y}{(V_W - V_X)} \tag{B.5}$$

It is now possible to form algorithms to find the drag and lift forces by combining equations B.1–B.5. Four methods have been devised in all, and the reasons for each method are discussed. It is important to note that the following methods were made possible by the assumption that the lift force was zero when the ball was not spinning.

B.2.1 Method B.1 - manipulating the equations of motion to give C_D and C_L.

Method B.1 combines equation B.1 and B.2 with equation B.3–B.5 to form equations B.6 and B.7 to find C_D and C_L. Equations B.6 and B.7 are used to calculate C_D and C_L at several points along the trajectory, therefore it is assumed that Δt is small. The two equations obtained are in terms of variables that were obtained using motion analysis.

$$C_D = \frac{2m}{\rho V_R^{\,2} A(\Delta t)}\left[g(\Delta t) - \Delta V_Y - \frac{\Delta(V_W - V_X)}{\tan\theta}\right] \tag{B.6}$$

$$\Leftrightarrow C_L = \frac{2m\Delta(V_W - V_X)}{\rho V_R^{\,2} A(\Delta t)\sin\theta} + \frac{C_D}{\tan\theta} \tag{B.7}$$

where: V_W is the wind tunnel air stream velocity

V_Y and V_X is the vertical and horizontal components of ball velocity

Δt is the time lapsed between data points

B.2.2 Method B.2 – Davies/Stepanek method

Possibly the most common method used to find C_D and C_L was that utilised by Davies (1949) and later by Stepanek (1988). The analysis assumed acceleration was constant and defined equations in terms of the time taken to drop a known drop height, and the total deflection of the ball due to wind and spin in that time. Davies used carbon paper on the

base of the wind tunnel to plot the landing point of the ball, and hence calculate the deflection. Stepanek video recorded the drop trajectory to improve the analysis but only required the overall deflection as he used the same calculation method. Calculations were simplified with the use of a modified force diagram assuming drag force to be parallel to the wind direction and the lift force to be perpendicular to the wind direction.

Davies and Stepanek dropped the ball from within the wind tunnel, however this is not feasible due to size constraints of the wind tunnel used in this study. The standard equations used by Davies and Stepanek were modified to allow for a drop from outside the wind tunnel. Equations B.8 and B.9 are the modified equations that were developed and they can be used at any point along the trajectory.

$$C_D = \frac{4m}{\rho V_R{}^2 A T^2}\left(Deflection - (V_{Xi} \times T)\right) \tag{B.8}$$

$$C_L = \frac{2}{\rho V_R{}^2 A}\left[\left(\frac{2m}{T^2}\left((V_{Yi} \times T) + DropHeight\right)\right) + mg\right] \tag{B.9}$$

where:

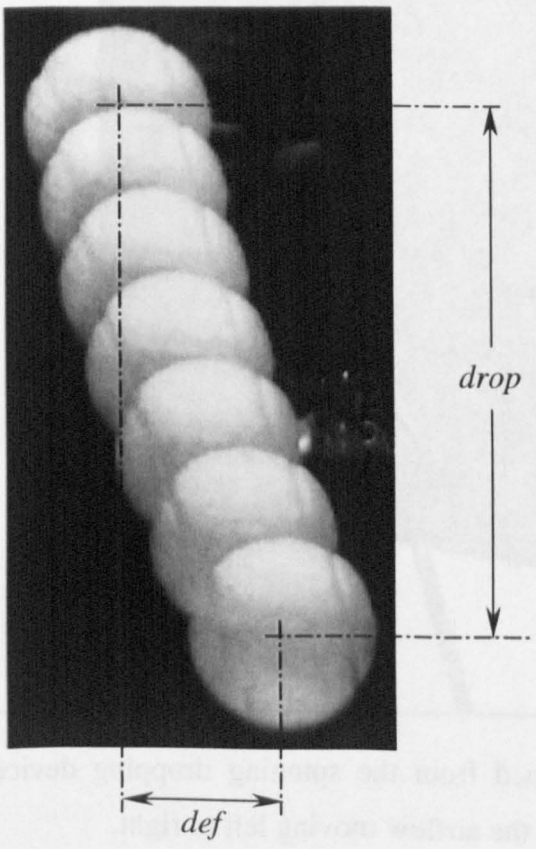

T is the total time taken for the drop
V_{Xi} and V_{Yi} are initial velocities in the x and y directions respectively
def is the deflection
drop is the drop height

B.3 Apparatus and test method

It was mentioned in section B.1 that there were two dropping devices used for this investigation. They have been differentiated by their design criteria, non-spinning and spinning, and are described in section 3.2.2. The non-spinning dropping device was designed and built at the University of Sheffield for a previous project and it was used for early testing, however upon completion, the spinning dropping device was used for all subsequent drop tests. Both types of investigation were performed in the low-speed wind tunnel, and this is described in section 3.1.1.

Figure B.3 shows a picture depicting a ball drop from the spinning dropper and its subsequent trajectory.

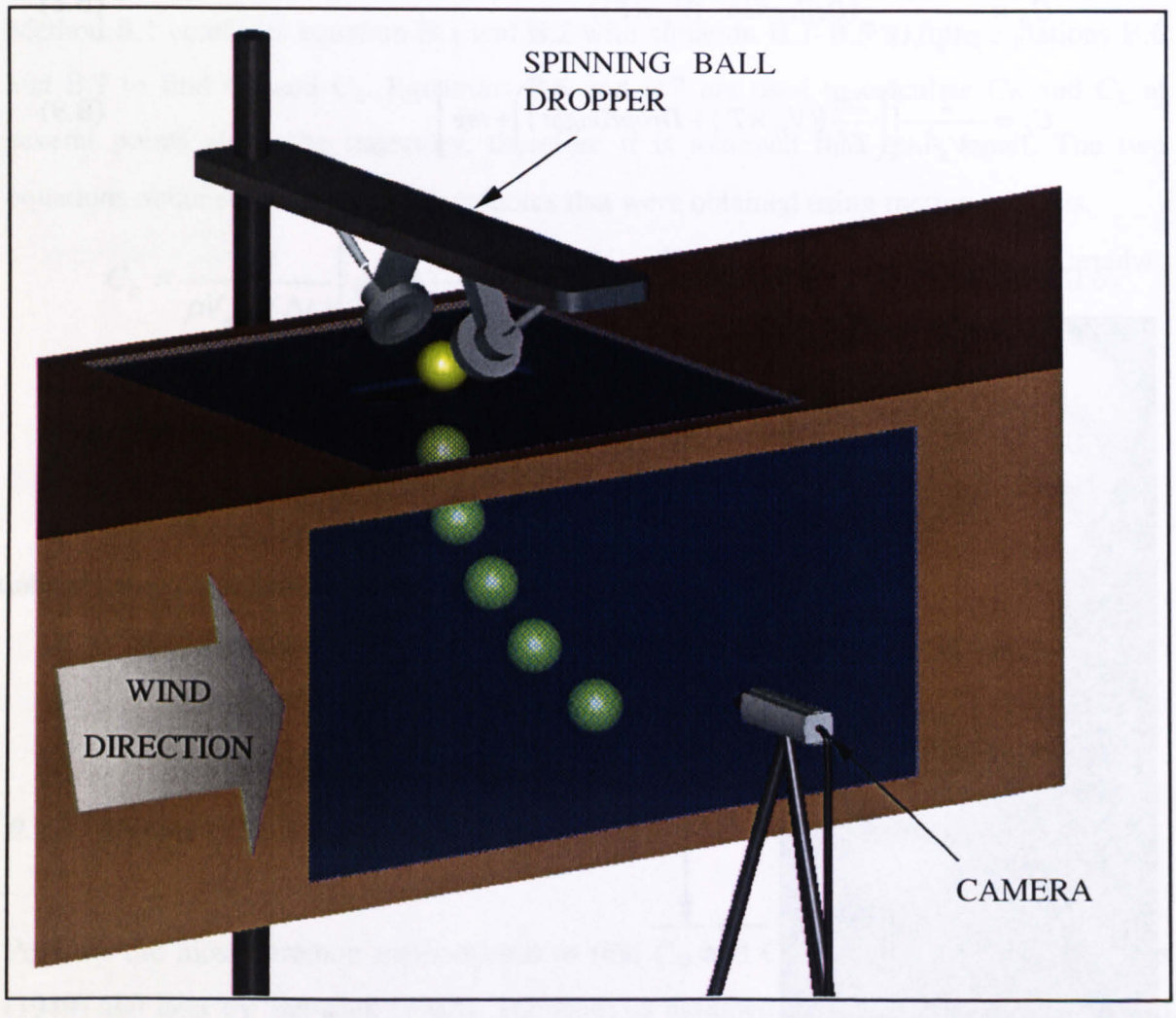

Figure B.5 Picture showing a ball being dropped from the spinning dropping device through the working section of a wind tunnel with the airflow moving left to right.

Upon leaving the dropper, it travels through a hole cut into the top surface of the wind tunnel, the size of the hole is just large enough for the ball to pass through, with a small amount added to ensure no contact between the ball and the top surface. The dropping device is positioned close to the top surface, and therefore the distance travelled by the ball before entering the wind tunnel is small. The ball is shown to deflect in the direction of the wind as it descends through the moving air of the wind tunnel. A camera is positioned such that the complete trajectory of the ball is captured.

The ball was placed between the cups and oriented such that the markings were clearly visible to the camera. The spin rate was calibrated against voltage to give an estimate, however the true spin rate was calculated during analysis. It is important that the ball drops vertically into the wind tunnel, and if the ball was not rotating in a stable fashion, the motor was stopped and the ball removed, rotated and replaced. Once a stable rotation was achieved the camera was set to record and the ball release triggered a short time after.

The KODAK Motioncorder high-speed digital video camera, as described in section 3.3.1, was used to capture the subsequent trajectories. Due to the quality of information required, a frame rate of 240 frames per second was used with an exposure of 1×10^{-4} second.

Both the top and bottom surfaces and the front door of the working section were transparent to enable illumination of the complete trajectory, over 3kW of light in all, enabling analysis of the full flight.

The airflow speed was calculated using pressure differences across the contraction, and the procedure is described in detail in section 3.1.4.

A grating was fixed at the back of the working section to stop the ball from being drawn into the impeller. Although the grating caused blockage within the tunnel, it was deemed sufficiently far down stream of the ball trajectory not to affect its flight. The blockage caused by the grating induced a reduction in the maximum wind speed available from the wind tunnel.

Upon completion of the recording phase, the footage was saved to Hi8 videotape and transferred to computer using the procedures described in section 3.3.2. Each recording

was given an identification number, which was noted down against a description of the trajectory.

Figure B.4 shows the overlaid images for a trajectory of a normal sized pressurised ball dropped with zero spin through the wind tunnel with the airflow travelling from left to right. A typical image used for motion analysis of a spinning ball is shown on the right hand side of figure B.4.

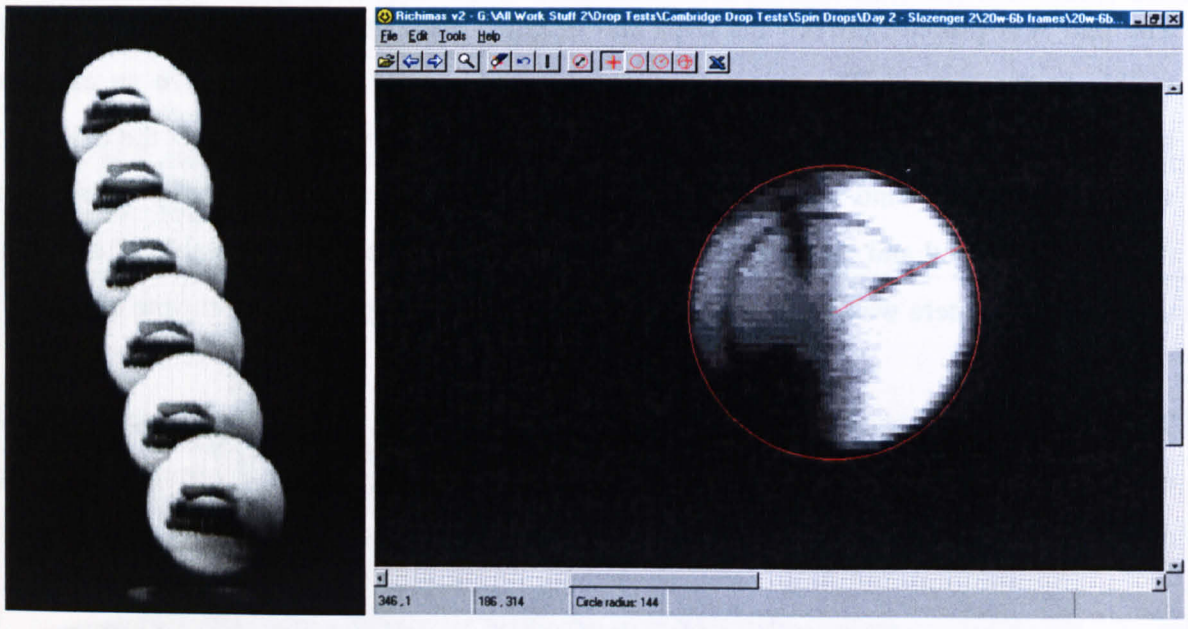

Figure B.4 ***Left:*** showing the overlaid images for the trajectory of a normal pressurised ball dropped with wind travelling from left to right. ***Right:*** showing a typical image used for image analysis.

A red circle surrounds the ball and the co-ordinates at the centre are used for the ball position relative to a datum point. A red line can also be seen emanating from the centre, and this is treated purely as an angle. The information relating to the circle and line is exported to an Excel spreadsheet. Following images are treated in the same way, which enables differences to be formed between data points where the time between images is known.

Images obtained with this method are far superior to those for the projectile method. Only a small trajectory needed to be captured for this investigation, hence the camera was positioned closer giving a larger image. In addition, the illumination was more focussed on

the ball resulting in improved edge definition. The ball has a radius of 36 pixels on average, hence based on a screen size of 360 x 240 pixels the spatial resolution is approximately 4.7%.

A 100mm square grid comprising a board sprayed with matt black paint and white tape was used for calibration purposes. The board was then positioned in the plane of the trajectory and recorded onto videotape. The resulting image was analysed in the same method as the trajectory, however rather than using a circle, points were used to mark diagonal extremes of the viewable area. The resulting co-ordinates were then compared against the known dimensions and a calibration factor was developed and applied.

B.3.1 Manipulation of data

When all of the images were obtained for a particular trajectory, they can be used to create a chart. Figure B.5 shows the graph of deflection due to wind against drop height for a normal pressurised ball at a wind speed of $12ms^{-1}$. The time step between each data point is fixed at 0.0042s.

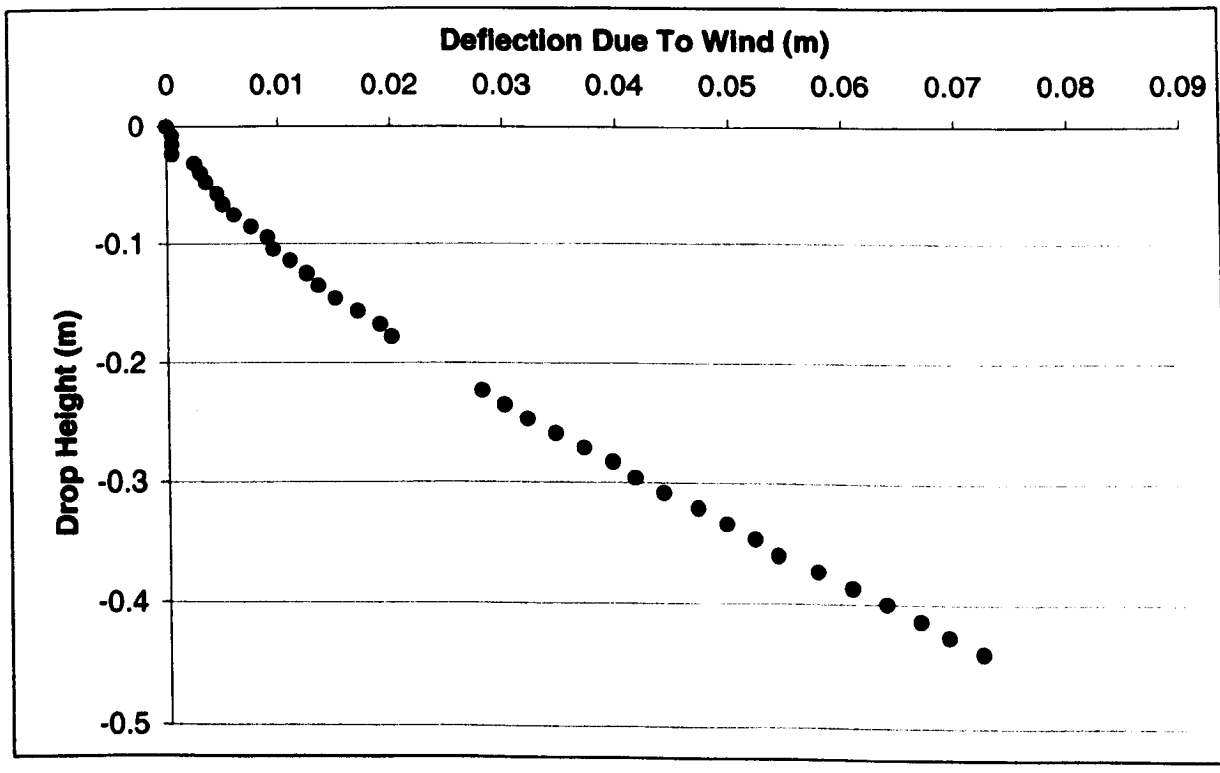

Figure B.5 Graph showing the resulting trajectory for the series of images for a ball dropped with no spin through a wind tunnel with a wind velocity of $12ms^{-1}$.

It can be seen that there are gaps in the data, this is due to interlacing between the video player and the digitising method. Interlacing was easily overcome in the analysis, however initial investigations using the direct data with the algorithms developed in section B.2 did not return satisfactory results. It was decided that an error analysis procedure would uncover any limitations in the algorithms, and therefore lead a more accurate system.

B.4 Error analysis

As utilised in the projectile method, a trajectory model was developed to assess errors for a spinning ball drop through the moving airflow of a wind tunnel. The model uses an iterative process utilising equations B.3 to B.5 developed using the forces diagram in figure B.2. All analyses used a trajectory with a C_D of 0.65, the trajectory was modified to incorporate the effect of spin, starting with $C_L = 0$ denoting zero spin, then increasing it to ± 0.2 simulating clockwise and anti-clockwise spin. To further simulate an actual drop, an initial velocity was introduced, where the ratio of V_{Yi} with V_{Xi} can also be used to modify the incoming angle. A complete description of the computational trajectory model can be found in chapter 4.

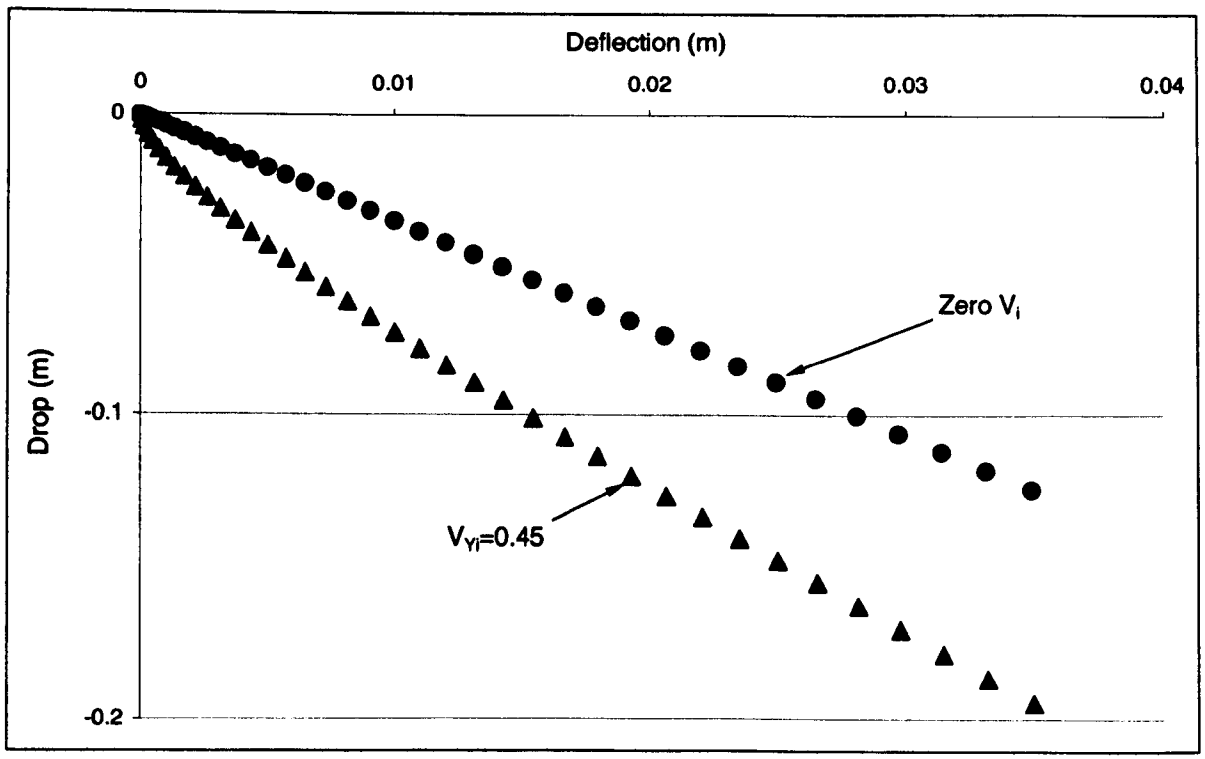

Figure B.6 Chart created with simulated data using a wind speed of 11.7ms^{-1} and showing ball drops with no initial velocity and an initial vertical velocity.

Figure B.6 shows a sample of two trajectories produced using the model, one with zero initial velocity (dropped from within the wind tunnel) and the other having an initial vertical velocity (dropped from outside of the wind tunnel). It can be clearly seen that the small incoming velocity makes a large difference to the trajectory of the ball.

B.4.1 Zero drop velocity

As a test of the trajectory model, the first analysis was based directly on the Davies method, and assumed that the drop velocity was zero. The results obtained for this test are shown in table B.1, as can be seen, the differences between the actual and calculated C_D's and C_L's are significant. The quality of these results is of little consequence, these figures are only required for comparison purposes.

Actual C_D	Calculated C_D	ΔC_D (%)	Actual C_L	Calculated C_L	ΔC_L (%)
0.55	0.559	1.64	-0.2	-0.226	13
0.55	0.555	0.91	-0.1	-0.127	27
0.55	0.551	0.18	0	0.028	N/A
0.55	0.549	0.18	0.1	0.072	28
0.55	0.546	0.73	0.2	0.171	14.5

Table B.1 C_D and C_L results obtained using the original Davies equations with simulated data for a drop with no initial velocity.

The algorithm utilising a modified Davies method can be directly compared against the original to assess the effect of such a modification on the accuracy of the results. The results obtained using method B.2 are shown in table B.2, there is negligible difference between these results and those shown in table B.1. It can therefore be concluded that, not only does the trajectory model work, but the modified equations are also suitable.

Continued analysis using method B.2 showed that the errors in C_D and C_L followed a linear offset, furthermore the results always overestimated the negative lift and underestimated the positive lift scenarios. It was noted that these errors could be reduced to 0.45% for C_D and 0.75% for C_L by averaging the results for C_D and C_L at the same spin rate clockwise and anticlockwise.

Actual C_D	Calculated C_D	ΔC_D (%)	Actual C_L	Calculated C_L	ΔC_L (%)
0.55	0.561	2.00	-0.2	-0.226	13
0.55	0.556	1.09	-0.1	-0.127	27
0.55	0.552	0.36	0	0.028	N/A
0.55	0.548	0.36	0.1	0.072	28
0.55	0.544	1.09	0.2	0.171	14.5

Table B.2 C_D and C_L results obtained using method B.2 with simulated data for a drop with no initial velocity.

In appendix A, it was suggested that the lift component could be ignored if the object was not rotating. As a method of investigation, method B.1 was modified to remove the lift component. Table B.3 shows that the results for zero spin contain zero errors, however errors are introduced when a lift component is present. The error appears to increase with increasing C_L, the rate of increase is in excess of 1% per 0.1 increase in C_L. In conclusion, although the method returned satisfactory results with no lift component applied to the model, when a lift force was present, the results suffered significantly.

Actual C_D	Calculated C_D	ΔC_D (%)	Actual C_L	Calculated C_L	ΔC_L (%)
0.55	0.565	2.73	-0.2	N/A	N/A
0.55	0.557	1.27	-0.1	N/A	N/A
0.55	0.55	0	0	N/A	N/A
0.55	0.544	1.1	0.1	N/A	N/A
0.55	0.538	2.18	0.2	N/A	N/A

Table B.3 C_D results obtained using a modified version of method B.1 with simulated data for a drop with no initial velocity.

The results obtained using the full equations of method B.1 are shown in figure table B.4. It can be seen that the introduction of a lift component improves the quality of results and the difference between the actual and calculated C_D and C_L are eliminated in all cases. The equations of motion are the foundation for the algorithm used in method B.1, hence as they've also been used to develop the trajectory model, a high correlation between input and calculated results should be expected in this analysis. It is important to note however, that this is a clear sign that method B.1 will reliably calculate C_D given high quality data.

Actual C_D	Calculated C_D	ΔC_D (%)	Actual C_L	Calculated C_L	ΔC_L (%)
0.55	0.55	0	-0.2	-0.2	0
0.55	0.55	0	-0.1	-0.1	0
0.55	0.55	0	0	0	0
0.55	0.55	0	0.1	0.1	0
0.55	0.55	0	0.2	0.2	0

Figure B.12 C_D results obtained using method B.1 with simulated data for a drop with no initial velocity.

B.4.2 Including drop velocity

A more realistic approximation of the investigation is that including a drop velocity, simulating the velocity gained by the ball before it enters the wind tunnel. Preliminary analysis of real data showed that the horizontal velocity was small compared to the vertical velocity, for the purpose of this analysis a ratio of 1/20 has been used for V_X/V_Y. The results obtained using simulated data for a ball drop with a C_L of 0.2, C_D of 0.55, and varying drop velocities, are shown in figure B.7.

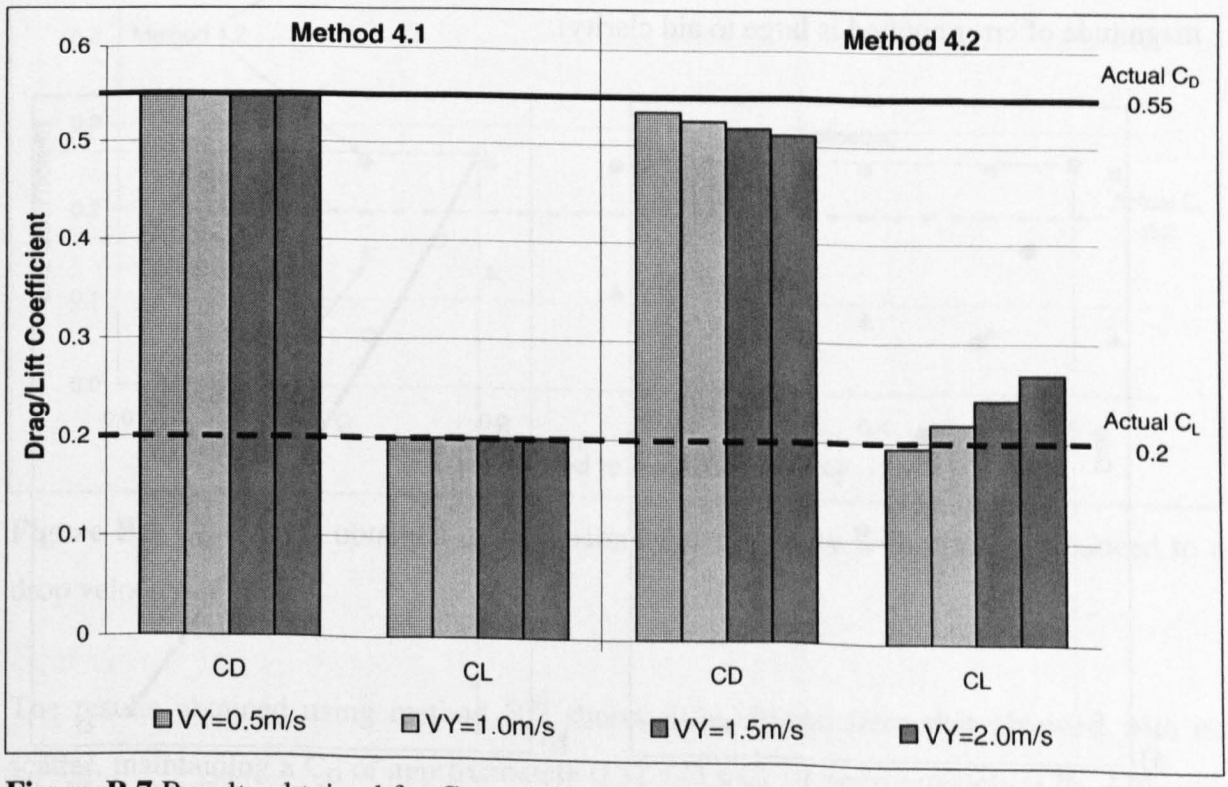

Figure B.7 Results obtained for C_D and C_L using methods B.1 and B.2 with a drop velocity introduced, where the velocity ratio V_X/V_Y is equal to 1/20.

It can be seen that the introduction of in initial velocity does not affect method B.1 and it returns error free results for both C_D and C_L for all drop velocities investigated. The results obtained using method B.2 are seen to gradually deteriorate as the drop velocity increases. The results for C_D start below 0.55 and are closer to 0.51, a difference over 7%, with an initial vertical drop velocity of $2ms^{-1}$. The results for C_L also start lower than the actual C_L, however as the vertical drop velocity is increased, the calculated C_L starts to overestimate, showing an difference of approximately 35% at a C_L of 0.27 when V_Y equals $2ms^{-1}$.

B.4.3 Including scatter

Small errors were introduced at the motion analysis stage, exporting a co-ordinate that may be a few millimetres from the actual trajectory. A typical error in the vertical displacement was found to be 0.04% by repeat analyses of real data, and the corresponding error associated with horizontal displacement was found to be 0.3% (approximately 7 times greater than the vertical error). These errors were applied to the simulated data as deviations from the actual calculated points. In reality the scatter is random, in this analysis the scatter was applied uniformly above and below the original data. Figure B.8 shows a sample of a trajectory produced using this method (all units have been removed as the magnitude of error applied is large to aid clarity).

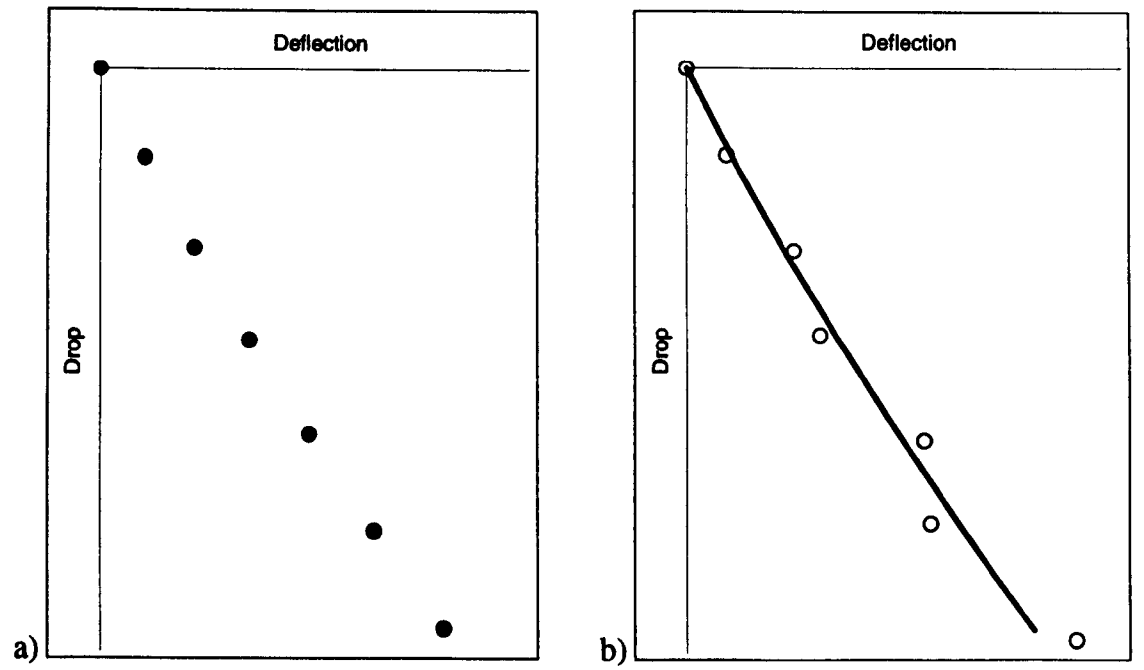

Figure B.8 Charts to show a) a sample of a standard trajectory and b) a trajectory with scatter included next to the standard curve.

It can be seen that the deviation increases as the magnitude of the displacement increases, this is because the error has been applied as a percentage, as observed in the real data. The scatter is applied to both the horizontal and vertical for each point hence the grouping of data points. As the error in the horizontal direction is greater than the vertical, the data points near the bottom of the trajectory are almost in line vertically. This is only apparent in this chart due to the magnitude of scatter applied, the scatter applied in analysis was negligible by comparison.

Figure B.9 shows the results obtained for C_D and C_L using both methods B.1 and B.2 with horizontal and vertical scatter applied in the ratio 7:1. The trajectory was formed using a C_L of 0.2 and a vertical drop velocity of $1.8ms^{-1}$. An error of 0.3% has been observed for the deflection, therefore scatter has been introduced to simulate errors from 0.05 to 0.55 for the horizontal data.

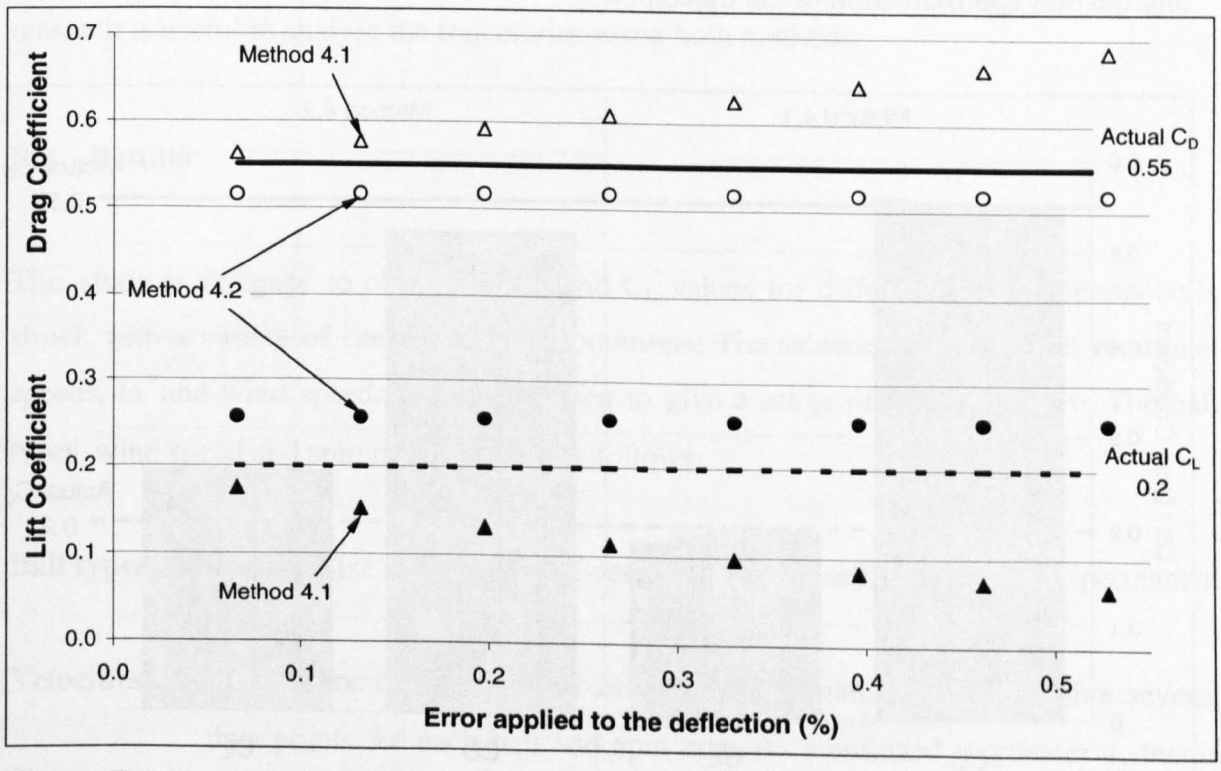

Figure B.9 C_D and C_L obtained using a simulated trajectory with errors introduced to a drop velocity of $1.8ms^{-1}$.

The results obtained using method B.2 shows little change from that obtained with no scatter, maintaining a C_D of approximately 0.52 and a C_L of approximately 0.26. Although method B.1 returns excellent results when errors are negligible, errors in C_D and C_L results

are increased linearly when scatter is increased. The real data showed deviation of approximately 0.3% in the horizontal, the C_D obtained with method B.2 is approximately 0.62, an error of 24% when compared to the actual C_D. The error for C_L is much closer to 50%, which implies that an improved method of analysis is required.

B.4.4 Using a polynomial for smoothing

Both methods returned satisfactory results with the unchanged simulated trajectories. It was hypothesised that the quality of results would return if the quality of data were improved, hence a best-fit polynomial was used. Figure B.10 shows the calculated C_D and C_L values obtained using simulated data from a trajectory with a drop velocity of $1.8ms^{-1}$, wind velocity of $11.5ms^{-1}$, C_L equal to 0.2, a deflection error of 0.3% and a smoothing polynomial. Several different orders of least squares best-fit polynomial have been used to find the best approximation of the trajectory.

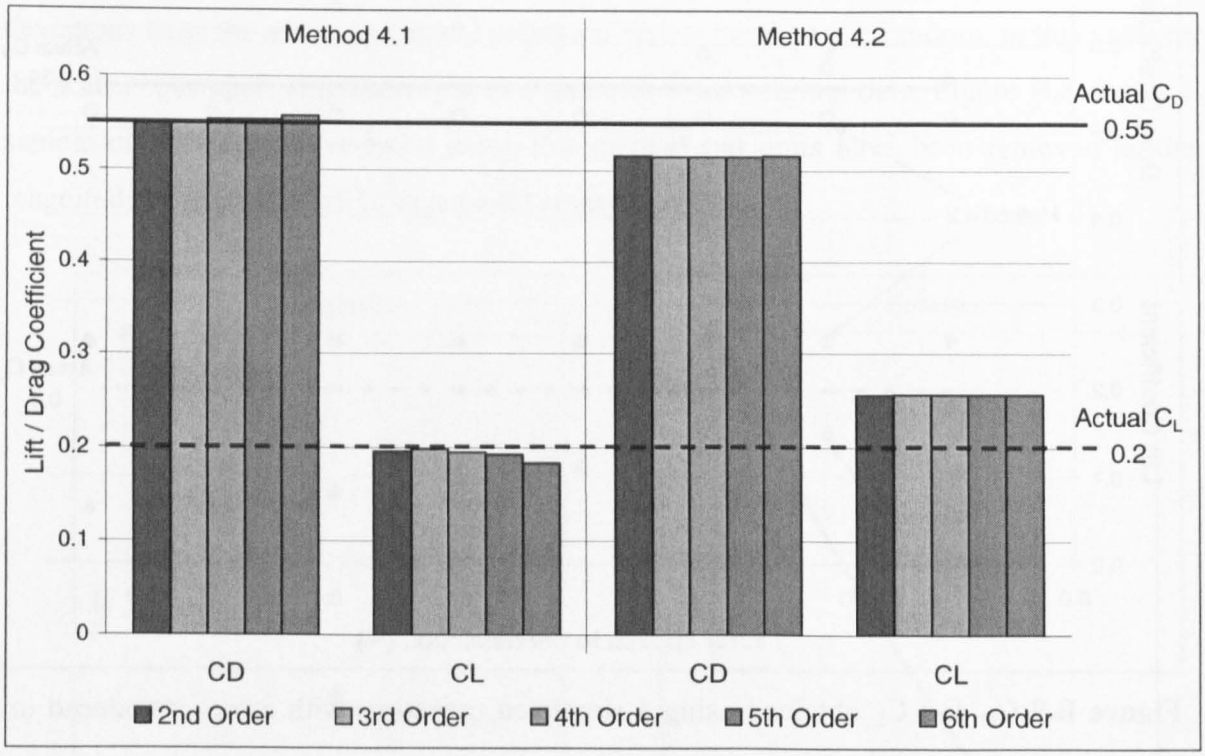

Figure B.10 C_D and C_L obtained for different order polynomial smoothed scattered data.

It can be seen that the results obtained using method B.1 return a good correlation with the values of actual C_D and C_L for all polynomials used. There is negligible difference observed between the 2^{nd} and 3^{rd} order polynomials, however the accuracy reduces from

the 4th order polynomial and upwards. Method B.2 returns very similar results to those obtained in all test scenarios with a clear offset from the actual C_D and C_L. As method B.2 uses only the start and end point of the trajectory, the errors applied and subsequent smoothing function makes little or no difference.

In conclusion, method B.1 returns the best results when using simulated data. When errors were introduced to the perfect data, the accuracy of the results obtained with method B.1 reduced dramatically, whereas method B.2 returned similar results to those without the error. The induced errors were smoothed using a least squares best-fit polynomial. The results obtained using method B.2 remained similar, however the results obtained using method B.1 improved significantly. A 3rd order smoothing polynomial was found to best represent the original data and should be used when analysing the real data. Although method B.2 is shown to be less accurate than method B.1 with good quality data, the results obtained using it remain constant even when the quality of data is poor, for this reason it is useful to analyse the trajectories using both methods.

B.5 Results

This study is designed to obtain the C_D and C_L values for different types of tennis balls struck with a variety of speed and spin conditions. The selection of equatorial rotational speeds, ω, and wind speeds, v, were chosen to give a range of values for ω/v. The ball types, wind speed and spin rates used are as follows:

Ball types: Normal size pressurised; Oversized pressurised; Normal size permanent pressure

Velocities: Wind velocity ranged from zero to approximately $20ms^{-1}$ to give several data points for each ball and spin rate. As mentioned in chapter 1, tennis players hit the ball much harder than $20ms^{-1}$, however this was the maximum velocity of the wind tunnel.

Spin Rates: Spin rate ranged from zero to approximately 2000rpm for both top and backspin. Although the motor is rated at 10,000rpm, at high spin rates the ball often detached itself from the dropping device without being triggered. The spin rate was applied in equal increments of approximately 500rpm.

Figure B.11 shows a sample set of results obtained for a ball dropped through an air stream of 11.6ms^{-1}. The clockwise spinning drop has a spin rate of 1643rpm and the anti-clockwise spinning drop has a rotation of 1685rpm. The ball descending with anti-clockwise spin falls short of the ball dropping with zero spin, which in turn drops short of the ball dropping with clockwise spin. A quick reference to figure 3.9 will show that a ball with a clockwise rotation will have a lift force acting upwards, hence it will stay in the airflow longer, and will therefore deflect further.

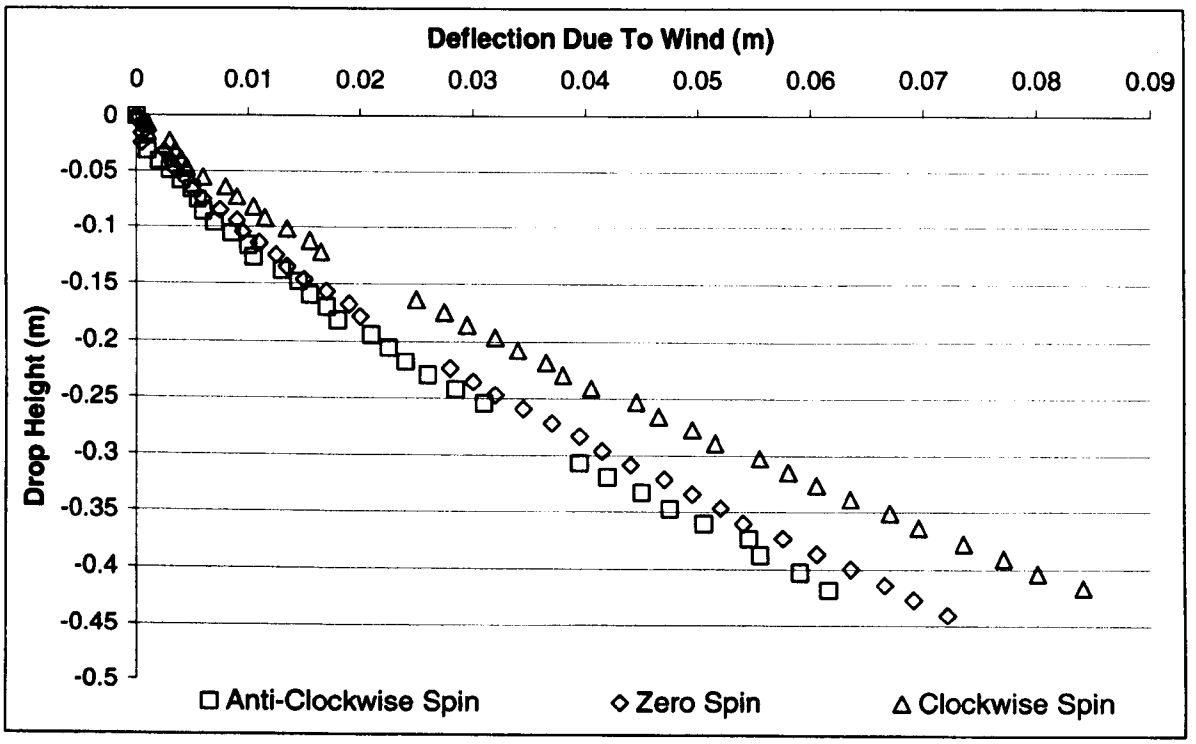

Figure B.11 A graph showing the trajectories obtained for a ball dropped through an air stream of 11.6ms^{-1} and a spin rate of approximately 1600 rpm both anti-clockwise and clockwise.

Table B.5 shows the results obtained from this data, it can be seen that both methods give a C_D of approximately 0.8 for all spin rates. Method B.1 shows C_D increasing with spin rate, whereas method B.2 shows the C_D being higher for the two spinning drops. It is expected that the C_D increases with spin rate, hence thus far it appears that method B.2 returns favourable results. Neither of the methods appear to return suitable results for C_L however. The analysis is designed so that a negative result for C_L shows spin in the anti-clockwise direction, method B.1 shows C_L starting at -0.455 for anti-clockwise spin increasing to -0.046 for clockwise spin. Whilst a result of -0.455 appears a little high when compared to

previously published work, it is in the correct direction, the clockwise spin should be positive however. Method B.2 again returns better results with C_L starting at -0.192 for anti-clockwise spin and increasing to 0.219 for clockwise spin, however at zero spin it appears that C_L is 0.176.

	C_D Method B.1	C_D Method B.2	C_L Method B.1	C_L Method B.2
Anti-clockwise spin	0.772	0.804	-0.455	-0.192
Zero Spin	0.803	0.750	-0.083	0.176
Clockwise Spin	0.856	0.799	-0.046	0.219

Table B.5 Results obtained from the trajectories for a ball dropped through an air stream of 11.6ms^{-1} and a spin rate of approximately 1600rpm both clockwise and anti-clockwise.

When comparing the results obtained using method B.2 to previous results obtained in a similar manner (Stepanek 1987), C_D may be expected to be 0.73 with a C_L of 0.25. These values are not far from those obtained in this study, but it is obvious that results obtained using method B.1 are not satisfactory.

There were several more analyses undertaken, all of which showed that the results obtained with both methods were inconsistent.

B.6 Discussion

B.6.1 Using calculated C_D and C_L in the trajectory model

The trajectory model can be used in conjunction with the C_D and C_L results as a way of testing the results obtained. Figure B.12 shows the trajectories obtained using the C_D and C_L results for clockwise spin using both methods. The actual data set used for analysis is also plotted and used for comparison.

It can be seen that when using the results given by Stepanek the trajectory falls short of the drop data. It is important to remember that these results were obtained for a drop test with an initial velocity of zero, however relative velocities have been used to create the

trajectory. The results obtained using method B.2 appear to compare well with the real data. Given that the time for the complete trajectory is identical for each model, the inset chart shows that these C_D and C_L values cause the ball to slow down too much during the flight. Method B.1 appears to be identical to the real data, with its end point coinciding directly with that of the real data.

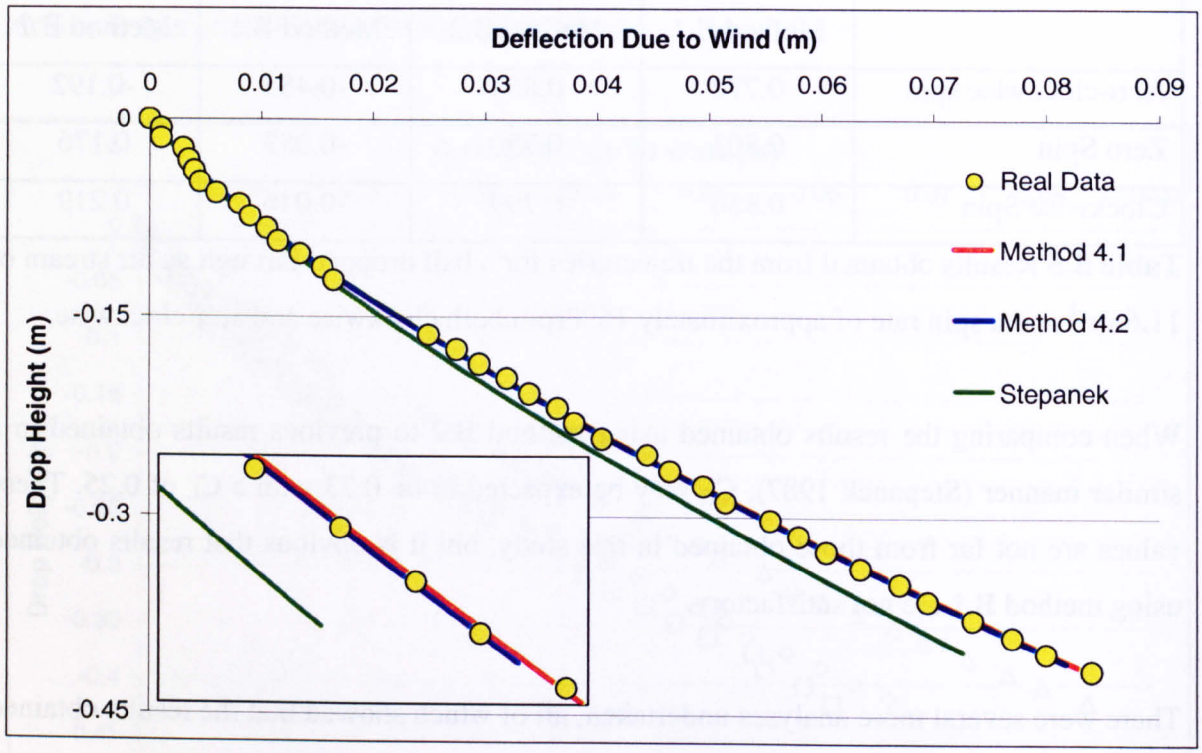

Figure B.12 Graph showing the trajectories obtained using the results for the clockwise spin in the trajectory model along with the actual data set used for analysis (inset shows the end of each trajectory).

The same sort of graph was produced for anti-clockwise spin and it showed that method B.1 again reproduced the data perfectly. The trajectory produced using the results from method B.2 appeared not to decelerate sufficiently and hence showed travel beyond the end of the actual data.

B.6.2 The C_D and C_L of spinning balls moving through the air

The argument from the previous section can be used together with the error analysis presented in this chapter to show that the C_D and C_L of spinning balls moving through the air do not conform to theory and cannot therefore be placed in a table of results.

Unfortunately, the C_D and C_L results obtained for different known spin rates did not show the trends that would have been expected, and therefore they were deemed to be incorrect. Figure B.12 shows that the results obtained using method B.1 create a trajectory that perfectly simulated the real trajectory, it should therefore be concluded that the results are correct.

It is entirely possible that there is more than one set of values for C_D and C_L that could perfectly simulate the real trajectory. Based on this fact, it may be more suitable, and less confusing, to develop a method that combines the lift and drag forces, and hence calculates the aerodynamic force on the ball.

Alternatively, the results for C_D and C_L calculated in this chapter may be correct, and in fact show that static results differ form dynamic results. This hypothesis does not directly correlate with the results obtained in this chapter however, as C_D and C_L was found to vary significantly between trajectories of similar characteristics.

B.6.3 Direction of drop

For a ball dropping with clockwise spin and no wind applied it will deflect to the left, conversely the anticlockwise spinning ball will deflect to the right. It is therefore conceivable that when the wind is applied towards the left, the clockwise ball will deflect less than the anticlockwise spinning ball. It was shown in section B.5 that this is not the case, the clockwise spinning ball in fact deflects more.

Figure B.13 shows the two force diagrams associated with a clockwise spinning ball a) falling through stationary air and b) falling through a wind tunnel with air flowing from left to right. It can be seen that the resulting F_L for the ball falling through stationary air is towards the left. This force acts to deflect the ball to the left inducing a small horizontal velocity component.

The force diagram for a spinning ball falling through the moving air of a wind tunnel is a little more complex. The airflow moving across the ball from left to right is equivalent to

the ball travelling from right to left. The additional horizontal and vertical velocity components due to gravity and the F_D lead to the force diagram shown.

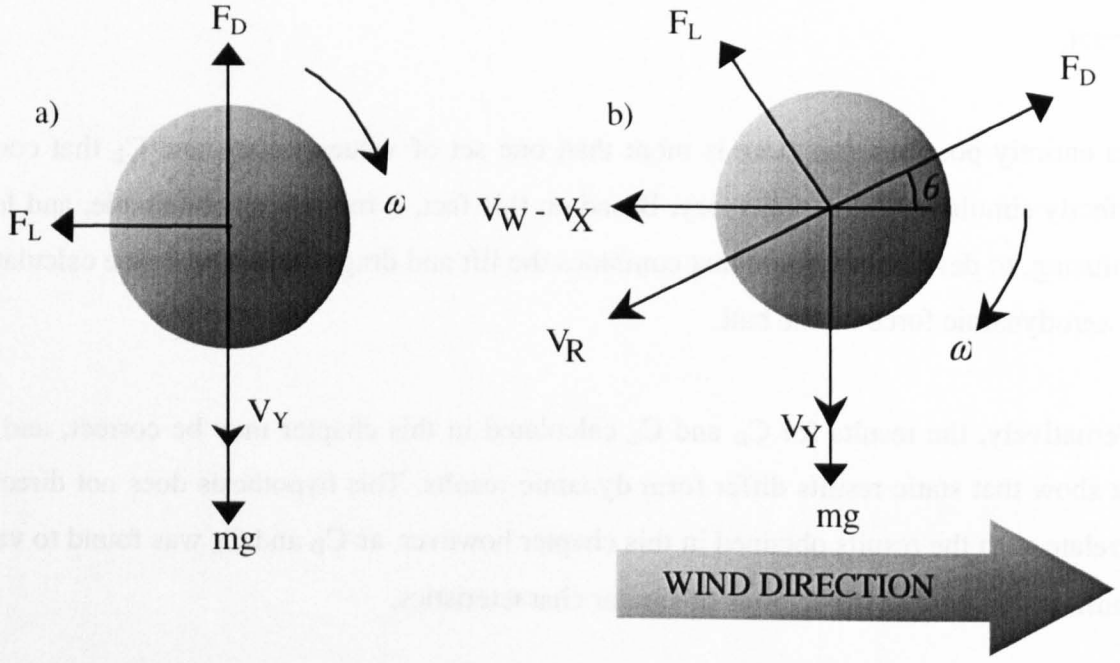

Figure B.13 Shows the two force diagrams associated with a clockwise spinning ball a) falling through stationary air and b) falling through a wind tunnel with air flowing from left to right.

Assuming V_W is large compared to V_Y, and V_Y is larger than V_X, the resultant velocity will act at a small angle below the horizontal. As V_Y and V_X increase, the effect of V_W decreases and the angle of V_R below the horizontal increases. As V_X is induced on the ball due to the wind, it will never be larger than V_W, therefore V_R will always act in the bottom left quadrant of the force diagram. For a ball spinning in the clockwise direction, the F_L will therefore act above the horizontal for a ball travelling from right to left. The lift force always acts perpendicular to the direction of motion and therefore its direction will also move with the V_R.

The effect of F_L therefore changes throughout the flight. When V_W is very large compared to V_Y and V_X, the vertical lift force component is significantly larger causing the flight of the ball to be elongated. As V_Y and V_X increase, the direction of the lift force will rotate and the horizontal component of lift force will increase. It is therefore feasible that as the resultant direction of motion enters the bottom left eighth of the forces diagram, and the

horizontal component of lift force becomes larger than the vertical components, that the clockwise rotating ball may act as it does in still air. The flight duration used in this study were short and therefore V_W was always large by comparison, the clockwise spinning balls always deflected further than the anticlockwise spinning balls.

B.6.4 C_D and C_L obtained using method B.2

In section B.4.1, it was suggested that the errors obtained using method B.2 could be reduced by calculating the C_D and C_L for anti-clockwise and clockwise spin. This manipulation of the results is similar to the procedure undertaken by Davies in his original study, whereby both forward spinning and backward spinning trajectories were required to calculate C_D and C_L at that spin rate. The results thus obtained were for a spin rate, and that spin rate had to be identical in both trajectories.

Method B.2 was designed to be an advance on Davies' original method, whereby the C_D and C_L could be calculated for each trajectory, and moreover could be applied to any trajectory providing the initial velocity could be calculated. It is therefore not suitable to develop this method towards approximating two separate trajectories.

Initial results obtained using simulated data showed method B.2 to calculate the same results as Davies' method showing that it was suitable for further development. Continued error analysis using simulated data showed that method B.2 calculated C_D and C_L with significant differences from the actual values. It is therefore likely that results obtained in studies where Davies' method is utilised will also contain significant errors. The error analysis presented in this chapter has shown however, that the C_D calculated using method B.2 was lower than the actual C_D, and conversely, the C_L was normally higher. This knowledge can be used when assessing the results of future studies using similar methods.

THIS PAGE INTENTIONALLY LEFT BLANK